



HAL
open science

Tectono-stratigraphic evolution and fluid circulations in response to crustal necking: Insights from a fossil necking domain in the Western Alps (Mont-Blanc massif)

Nicolas Dall'Asta

► To cite this version:

Nicolas Dall'Asta. Tectono-stratigraphic evolution and fluid circulations in response to crustal necking: Insights from a fossil necking domain in the Western Alps (Mont-Blanc massif). Geophysics [physics.geo-ph]. Université de Pau et des Pays de l'Adour, 2022. English. NNT : 2022PAUU3070 . tel-04647705

HAL Id: tel-04647705

<https://theses.hal.science/tel-04647705v1>

Submitted on 15 Jul 2024

HAL is a multi-disciplinary open access archive for the deposit and dissemination of scientific research documents, whether they are published or not. The documents may come from teaching and research institutions in France or abroad, or from public or private research centers.

L'archive ouverte pluridisciplinaire **HAL**, est destinée au dépôt et à la diffusion de documents scientifiques de niveau recherche, publiés ou non, émanant des établissements d'enseignement et de recherche français ou étrangers, des laboratoires publics ou privés.

THÈSE

UNIVERSITÉ DE PAU ET DES PAYS DE L'ADOUR

École doctorale des Sciences Exactes et leurs Applications

Présentée

par Nicolas DALL'ASTA

pour obtenir le grade de docteur de l'Université de Pau et des Pays de
l'Adour Spécialité: Sciences de l'Univers

Tectono-stratigraphic evolution and fluid circulations in response to crustal necking: Insights from a fossil necking domain in the Western Alps (Mont-Blanc massif)

**Etude de l'évolution tectono-stratigraphique et des circulations de fluides en
réponse à l'amincissement de la croûte: Exemple d'une marge fossile préservée dans
les Alpes (Massif du Mont-Blanc)**

Membres du jury

Rapporteurs:

Nicolas Bellahsen (MCU)

UPMC Sorbonne Universités

Philippe Boulvais (MCU)

Université de Rennes 1

Examineurs:

Charles Aubourg (PU)

Université de Pau et des Pays de l'Adour

Laurent Jolivet (PU)

UPMC Sorbonne Universités

Gianreto Manatschal (PU)

Université de Strasbourg

Frédéric Mouthereau (PU)

Université Toulouse 3 Paul Sabatier

Magali Rossi (MCU)

Université Savoie Mont-Blanc

Directeur de thèse:

Guilhem Hoareau (MCU)

Université de Pau et des Pays de l'Adour



Tectono-stratigraphic evolution and fluid circulations in response to crustal necking: Insight from a fossil necking domain in the Western Alps (Mont-Blanc massif)

Dall'asta Nicolas

Université de Pau et des Pays de l'Adour

-2022-

Remerciements

Faire une thèse a toujours été un rêve pour moi et enfin après trois années d'effort, j'arrive au point d'orgue de mon parcours universitaire commencé il y a 8 ans à Pau et s'achevant ici à Pau. Et quoi de mieux que le Mont-Blanc comme sujet d'étude. C'est avec un peu de nostalgie et beaucoup de fatigue que je repense à ces trois années de doctorat et aux nombreuses personnes que j'aimerais remercier.

J'aimerais tout d'abord remercier les membres du jury qui ont accepté d'évaluer ce travail, les rapporteurs Philippe Boulvais et Nicolas Bellahsen ainsi que les examinateurs Frédéric Mouthereau, Magali Rossi, Charles Aubourg et Laurent Jolivet.

Je remercie également, mon directeur de thèse Guilhem et Hoareau et mon co-encadrant Gianreto Manatschal. Guilhem, j'ai beaucoup appris à tes côtés et malgré nos façons de travailler un peu différentes parfois m'a guidé patiemment au cours de ces trois années. Je suis très content d'avoir pu faire cette thèse avec toi. Tu as su écouter avec bienveillance toutes mes hypothèses qui par moment étaient un peu tirées par les cheveux. Tu as su me canaliser parfois quand c'était nécessaire et je sais que ce n'est pas toujours facile et faire de moi un chercheur. Je garderai de très bon souvenir de ces missions de terrains autour du Mont-Blanc sous le soleil comme sous la pluie et le froid (le Mont-Blanc est un environnement impitoyable). J'espère que tu n'as pas fait une overdose de détachements. Enfin j'aimerais te remercier d'avoir patiemment corrigé les nombreux « s » manquant dans ce manuscrit, j'imagine ça a du être très énervant... Gianreto que je remercie également de m'avoir accompagné durant ces dernières années. Ce fut un plaisir de travailler avec toi. J'ai beaucoup appris à tes côtés que ce soit sur le terrain ou lors de nos nombreuses discussions. Ta connaissance des Alpes et des marges a été plus qu'indispensable à ce projet. Merci également d'avoir pris du temps pour relire ce manuscrit. Sans vous deux je ne pense pas que j'aurais réussi à mener à bien cette thèse.

Je tiens également à remercier Charlotte Ribes et Jean-François Ghienne grâce à qui j'ai eu la chance de travailler dans cet endroit extraordinaire qu'est le Mont-Blanc et à qui je dois cette thèse.

Malgré le fait que j'ai passé un certain temps à Strasbourg et que je suis parfois un peu un ours solitaire j'ai passé de très bon moment au labo de Pau et je tiens à remercier mes camarades de galère Aurélie, Francho, Gabriel, Thomas et Landry avec qui j'ai commencé ma thèse et surtout partagé des bières. Je tiens aussi à remercier Naim le seul autre naufragé à travailler sur les Alpes à Pau et Stephen le spécialiste des mass balances qui m'a beaucoup aidé durant ma thèse et à qui je dois beaucoup. Enfin je tiens à remercier les permanents du labo qui font de cet endroit un lieu très

agréable où travailler et qui m'ont accompagné depuis la licence. Je voudrais plus particulièrement remercier Jean-Paul et Charles avec qui j'ai pu avoir des discussions enrichissantes et Bertrand pour m'avoir aidé dans la préparation des nombreux échantillons.

La liste des personnes avec qui j'ai pu travailler est longue mais il y a deux personnes en particulier avec qui j'ai vraiment apprécié collaborer, Vincent et Yoann. Je me suis beaucoup amusé à Toulouse avec vous deux et avec toi Yoann sur le terrain. Enfin Amir Khalifi qui m'a gentiment accompagné sur le terrain et avec qui j'ai passé de super moments que ce soit en Espagne (à part le refuge de Cotiella...) ou sur le Mont-Blanc.

Pour mener à bien une thèse, je me suis rendu compte il n'y a pas que l'environnement de travail qui compte mais aussi et surtout l'entourage familial et de ce point de vue je dois avouer que j'ai été très bien entouré. J'ai toujours été soutenu dans les bons comme les mauvais moments. J'aimerais remercier mes parents qui m'ont toujours soutenu dans tous mes projets. Comment exprimer en quelques mots tout ce qu'ils ont fait pour moi ? A ma maman, Laurence qui a toujours su quoi dire quand ça n'allait pas. Tu as toujours su m'écouter et me remonter le moral. A mon papa, Massimo qui m'a transmis la passion de la géologie depuis tout petit. On a eu tellement de discussions passionnées sur la géologie au grand désarroi du reste de la famille. Enfin, ma petite sœur, Julie pour sa bonne humeur et mon frère, François le super codeur pour son aide. J'ai une grande chance d'avoir une famille comme celle-ci et cette thèse est aussi la vôtre. Enfin à ma grand-mère et mes tantes et oncles en Italie et France merci pour vos encouragements. Je voudrai aussi remercier mes beaux-parents Miguel et Monica de m'avoir accueilli pendant un mois à Quito. J'ai pu découvrir ce magnifique pays, l'Equateur et faire une vraie coupure loin de tout. J'aimerais enfin avoir une pensée pour les gens qui ne sont plus ici et qui je pense auraient été fier de moi.

Enfin, Lou qui a partagé ces dernières années avec moi et à qui je dois tellement. Tu m'as supporté durant cette thèse et je sais que ça n'a pas été toujours facile. On a survécu ensemble aux multiples confinements, tu m'as aidé, tu m'as soutenu, tu m'as encouragé. Tu as été plus que patiente avec moi et tu m'as donné tout l'amour que tu pouvais et je n'aurai pas réussi sans toi. Merci d'avoir passé du temps à relire ce manuscrit. J'aimerais tout simplement te remercier et te dire que cette thèse t'appartient également.

Table of content

General introduction	1
Outline of the thesis	11
Chapter I- General concepts related to the Wilson cycle and rifted margins	13
1. From rifting to collision	16
1.1. The Wilson cycle: A keystone to understand the rift to collision evolution	16
1.2. Rifted margins: A century of research and new evolving concepts	18
1.3. Fluid evolution throughout a Wilson cycle.....	28
2. Polyphased rifting at magma-poor rifted margins: the Atlantic-type model.....	35
2.1. Recognition of rift domains.....	35
2.2. Proximal to distal transition: the necking domain	41
2.3. Crustal necking: the least known rift domain	44
2.4. Margin evolution through time.....	52
3. Fault-controlled fluid circulations in extensional system.....	55
3.1. Fault definition	55
3.2. Detachment faults: a key tectonic feature of rifted margins.....	58
3.3. Detachment fault as fluid pathway in rifted margins.....	63
4. Key questions concerning rifted margins.....	65
Chapter II- From rifting to orogeny, concepts developed in the Alps over a century.....	67
1. The Alpine orogen: An inverted fossil rifted margin	70
1.1. The Wilson cycle in the Alps.....	70
1.2. Linking orogenic architecture and paleogeography.....	73
1.3. The External/Internal transition of the Alps.....	76
1.4. Constrains on the pre-rift rheology of the lithosphere	77
2. From the Alpine Tethys to the Alpine orogen.....	80
2.1. Present-day view of the Alpine orogen.....	80
2.2. Large scale view of the Alps	81
2.3. Geophysical transect across the Western Alps	83
2.4. Kinematic and P-T-t evolution of the Western Alps.....	85
3. Case study of the External Crystalline Massifs in the Western Alps	90
3.1. Variscan polymetamorphic basement.....	90
3.2. Alpine evolution of the ECM.....	91
3.3. The Mont-Blanc massif.....	92
4. Key questions associated to the Mont-Blanc massif.....	99
Chapter III- Structural and petrological characteristics of a Jurassic detachment fault from the Mont-Blanc massif (Col du Bonhomme area, France).....	101
1. Geological setting.....	105

2.	Methodology	110
3.	Results	112
3.1.	Alpine metamorphic peak in the Col du Bonhomme area	112
3.2.	Macroscopic description of the basement / sediment contact	112
3.3.	Petrological and microstructural observations	118
4.	Discussion	128
4.1.	Conditions and mechanisms of deformation	128
4.2.	Is the Col du Bonhomme fault a Jurassic extensional detachment fault?	133
Chapter IV- Multiscale element transfer during crustal necking: the Mont-Blanc detachment fault		141
1.	Geological setting	145
2.	Methods	150
2.1.	Analytical techniques	150
2.2.	Mass balance calculations	153
3.	Results	155
3.1.	Mineralogy of the detachment fault	155
3.2.	Host rock.....	156
3.3.	Detachment fault.....	157
3.4.	Bulk-rock chemistry.....	165
3.5.	Mass balance along the fault zone: bulk rock scale	169
3.6.	Mass transfer associated to main mineralogical reactions.....	173
3.7.	Fluid inclusions on veins along the fault zone.....	178
3.8.	Datation of the detachment fault	181
4.	Discussion	184
4.1.	Interpretation of the ages obtain along the detachment fault.....	184
4.2.	Mass balance calculations: evidence of an open system	187
4.3.	Paleo fluid characteristics.....	192
4.4.	Implication of the Mont-Blanc detachment fault	195
Chapter V- Preserved Jurassic Structures in the Northern Mont-Blanc massif (Val Ferret, Switzerland).....		199
1.	Methodology	202
2.	Geological context.....	204
2.1.	Localisation.....	204
2.2.	Alpine deformation	207
3.	Basement characterisation.....	209
3.1.	Definition of basement type.....	209

3.2.	Composition of the magmatic basement.....	212
3.3.	Scaling relation for the Mont-Blanc pluton size.....	214
4.	Autochthonous sedimentary cover.....	215
4.1.	Pre-rift cover.....	216
4.2.	Syn-rift cover.....	217
4.3.	Post-rift sediments.....	220
5.	Tectonized top basement.....	220
5.1.	South Val Ferret.....	221
5.2.	Breya section (section3).....	228
5.3.	Catogne section (section4).....	232
5.4.	Mont-Chemin section (section5).....	233
6.	Discussion: Rift-related model for the Val Ferret.....	238
6.1.	Preservation of the detachment fault.....	238
6.2.	Tectono-stratigraphic evolution.....	240
6.3.	Connexion with the Southern Mont-Blanc detachment fault.....	243
Chapter VI- Large-scale evolution of the Jurassic necking domain of the Alpine Tethys.....		247
1.	Methodology.....	250
2.	Evolution across the necking domain (NW-SE correlation).....	252
2.1.	The Aiguilles-Rouges cover.....	252
2.2.	SW Morcles nappe.....	253
2.3.	The Mont-Blanc cover.....	253
2.4.	Distal Mont-Blanc cover (Wildorn nappe).....	254
2.5.	Ultrahelvetic domain.....	254
2.6.	Correlation across the margin.....	255
3.	Evolution along the necking domain (SW-NE correlation).....	257
3.1.	Aar massif border.....	257
3.2.	Morcle nappe (Ardève).....	258
3.3.	The Mont-Blanc cover.....	259
3.4.	Correlation along the margin (NE-SW profile).....	261
4.	Eustatic evolution of the margin.....	264
5.	Palaeogeographical reconstruction of the necking domain.....	265
5.1.	Helvetic / Dauphinois facies.....	265
5.2.	Paleogeographic evolution.....	267
Chapter VII- Linking ore deposits to crustal necking: Insight from the Western Alps.....		271
1.	What is crustal necking?.....	274
2.	The Case study of the External crystalline massifs.....	277

2.1.	Preserved necking domain in the Mont-Blanc massif.....	277
2.2.	Pre-Alpine mineralisations	279
2.3.	Fluid circulation along necking detachment faults	280
2.4.	Link between detachment fluid circulation and ore deposits.....	281
3.	Discussion	281
3.1.	Fluid migration in the basement and in the cover	281
3.2.	Fluid composition and metal leaching.....	282
3.3.	Predictability of ore deposition in the necking domain	284
Chapter VIII- Discussion, perspectives, and conclusions		287
1.	Recognition of the Mont-Blanc detachment fault	290
1.1.	Southern Mont-Blanc massif	290
1.2.	Northern Mont-Blanc	293
2.	Tectono-sedimentary evolution of the necking domain	294
2.1.	Structural evolution of the necking domain.....	294
2.2.	Recognition of necking detachment faults.....	300
3.	Preservation of the necking domain in orogens	301
3.1.	Alpine overprint on the pre-Alpine structures	301
3.2.	Thermal imprint on the detachment fault	304
3.3.	Evolution of the necking domain during collision	304
4.	Fluid evolution in rifted margins	307
4.1.	Fluid circulation along necking detachment fault	307
4.2.	Ore deposits	308
4.3.	Ore deposits throughout the Wilson cycle.....	309
4.4.	The concept of mineral system applied to crustal necking.....	310
4.5.	A model of evolution of the geochemical signature of the rifting through time.....	313
4.6.	Ore deposits in rifted margins: is it economically viable?.....	314
General Conclusion		322
References.....		329
Appendix.....		402

Appendix

Appendix A	Why large offset detachment faults are mechanically possible?.....	403
Appendix B	Supplementary Material Chapter III	429
Appendix C	Supplementary Material Chapter IV	435
Appendix D	Dating of pre alpine event in the Mont-Blanc massif	450
Appendix E	List and composition of the samples	458
Appendix F	Biostratigraphic data of the Helvetic domain.....	473

Table of figures

<i>Figure I.1: Illustration of the Wilson cycle from ocean opening to ocean closing and continent assembly (from Wilson et al., 2019) describing the different stages defined by Wilson (1968).</i>	17
<i>Figure I.2: Map showing the repartition of the active and passive margins worldwide (from Harris et al., 2014). B- Schematic bathymetric profiles for passive and active margins (from Harris et al., 2014).</i>	19
<i>Figure I.3: A-McKenzie model, also referred to as pure shear (symmetric) or depth uniform rift model. B- Wernicke or lithospheric simple-shear rift model showing a strongly asymmetric rifting with a lithospheric scale detachment fault (modified from Wernicke, 1985).</i>	20
<i>Figure I.4: A- Map of the distribution of the magma-poor, magma-rich and transform margins (from Hauptert et al., 2016). B- Schematic section of a magma-rich and poor margins (from Doré and Lundin, 2015). The magma-poor margins are characterized by the presence of a hyper- thinned crust and exhumed mantle. Magma-rich margins are characterized by the presence of Seaward Dipping Reflectors (SDR).</i>	22
<i>Figure I.5: Evolution of the concepts in rifted margins (from Peron-Pinvidic and Manatschal, 2019) during the 2000's and 2010's.</i>	24
<i>Figure I.6: External and internal factors controlling the architecture of the margin (Sapin et al., 2021). B- Inheritance defined as the deviation from an ideal lithosphere (from Chenin, 2016).</i>	27
<i>Figure I.7: Ore deposits found in passive margins (from Arndt et al., 2017). The proximal domain is characterized by MVT in carbonate platforms while the distal domain is associated to clastic dominated deposits and SEDEX deposits.</i>	30
<i>Figure I.8: Illustration of the fluid circulation associated to the type of ore deposits found along subduction zones (from Zellmer et al., 2015). The water, halogen, sulphur and carbon cycles associated to subduction zones and slab devolatilization are also described showing significant flux of volatile (H₂O, CO₂, S) along the subduction plane and in the volcanic arc.</i>	32
<i>Figure I.9: Ore deposits related to convergence as observed in the Himalayan range (from Hou and Cook, 2009). The ore deposits in the internal part are linked to magmatic activity in response to slab break off and root delamination.</i>	33
<i>Figure I.10: Section of a magma-poor margin at the onset of seafloor spreading (modified from Hauptert et al., 2016). The difference between the upper plate and lower plate is marked by the delaminated H-Block in the lower plate (H(del)). T1, T2, T3 corresponds to the main unconformities between syn-tectonic and post-tectonic sediments.</i>	35
<i>Figure I.11: A- Section of the Iberia margin showing the proximal to distal transition (Alves et al., 2006). The proximal domain is characterized by half-graben basins bounded by high-angle normal faults. B- Half-graben basins from the proximal domain can show growth strata in syn-rift sediments. The sediments are onlapping on the fault plane at a high angle. The half-grabens are sealed by post-tectonic sediments. C- Schematic illustration of a half-graben basin (modified from Tugend et al., 2014).</i>	37
<i>Figure I.12: A- Section of the Iberia margin showing the proximal to distal transition (Alves et al., 2006). B- Section of the distal Iberia margin showing large detachment faults leading to mantle exhumation (HHD = Hobby High detachment, HD = H-detachment; Manatschal et al., 2001). C- Schematic illustration of a detachment fault and its relation with the sedimentary cover showing flat deposits over the exhumed faults associated to large accommodation space (AS), (modified from Tugend et al., 2014).</i>	39

Figure I.13: A-Tectonic and stratigraphic interpretation of the seismic profile of the distal part of the Iberia margin (modified from Ranero and Pérez-Gussinyé, 2010) showing the sequential faulting leading to crustal thinning and mantle exhumation. B- Focus on an area of the seismic profile showing more in detail the stratigraphic architecture of the margin. The distal migration of the deformation is visible through the younger syn-tectonic sediments toward the west (Valanginian-Barremian to Hauterivian lower Albian)..... 40

Figure I.14: A- Section of the Iberia-Bay of Biscay margin showing homogeneous thinning throughout the entire margin (modified from Montadert et al., 1977). B- Section from the Alpine Tethys associated to a wide margin (400 km, modified from Lemoine et al., 1986). 42

Figure I.15: Palinspatic section of the Adriatic margin showing the position of the Pogallo shear zone during Jurassic (modified from Handy, 1987). This shear zone is associated to important crustal thinning in the lower crust..... 43

Figure I.16: Reconstitution of the Adriatic margin from Mohn et al., (2012) showing the upper crust and lower crust conjugated fault leading to embrittlement of the crust. This model implies that the top basement and the Moho correspond to large offset fault and shear zones responsible for significant crustal thinning. 43

Figure I.17: Sketch of a rifted margin showing the architecture and main faults associated to crustal necking and hyperextension (from Osmundsen and Péron-Pinvidic, 2018). The necking domain is composed of two main faults forming the inner and outer necking domain. 44

Figure I.18: A- Example of a necking domain from the Mid Norwegian margin (from Osmundsen and Péron-Pinvidic, 2018) showing the presence of two crustal faults forming the inner and outer necking domain and surrounding a MCC (Metamorphic Core Complex). The syn-rift to post-rift sediments onlap above the basement. B- Example of necking domain in the Norwegian margin showing a large detachment fault crosscutting the upper part of the crust (from Muñoz-Barrera et al., 2021). The fault shows an offset of 22.6 km and is dipping oceanward at a shallow angle (16°). The top of the fault scarp appears eroded. 45

Figure I.19: Illustration of the different types of necking faults according to different rheologies (modified from Osmundsen and Péron-Pinvidic, 2018). A- Thick ductile middle crust will lead to a core complex structure. B- A strong crust will lead to the formation of a fault crosscutting the entire crust. However, due to rotation of the footwall, the initial fault would be crosscut by a secondary set of faults leading to crust-mantle coupling. C- Strong crust associated to thick pre-rift basins. 46

Figure I.20: Numerical modelling of crustal necking in a heterogeneous crust composed of weak and strong layers (from Duretz et al., 2016). A- From 10% of extension, localisation of the deformation is occurring in the crust associated to asthenosphere uplift. B- For 24% of extension, two sets of conjugated faults are visible in the upper and lower crust/ upper mantle leading to progressive coupling. The presence of soft layers in the crust led to the formation of MCC structures associate to significant crustal exhumation. C- For 38% of extension, coupling of the upper and lower crust led to embrittlement of the crust and finally hyperextension. 47

Figure I.21: A- Variations of the heat flow across the rift zone through time for a felsic crust (from Chenin et al., 2020) associated to crustal thickness isopach (yellow=25 km, magenta=20 km, black =15 km). This model shows an increase of the heat flow in the rift shoulders and in the rift centre in response to asthenosphere uplift. B- Crustal section showing the difference of temperature at the end of the necking with the initial temperature and lithospheric section of the rift zone showing the isotherms shallowing in the rift centres associated to asthenosphere uplift (1300°C isotherm). 48

Figure I.22: A- Evolution of the topography through time in response to crustal necking (from Chenin et al., 2019b) showing significant topographic uplift in the rift shoulder. B- Evolution of the crustal thickness through time during necking showing the focalisation of the deformation in response to necking..... 49

Figure I.23: Evolution of a magma-poor margin from a decoupled deformation to a coupled deformation during necking (from Sutra et al., 2013). Crustal necking is associated to a pure-shear, symmetrical deformation while exhumation is associated to a simple-shear deformation leading to an asymmetric margin. 50

Figure I.24: A-Cross section of the Bay of Biscay margin (from Tugend et al., 2014) and associated outcrop observations from the Pyrenean fossil rifted margin. B- Evolution of the syn-rift and post-rift accommodation space (A.S.) across the margins. Potential accommodation space corresponds to the distance between surface and seafloor while the total accommodation space corresponds to the distance between the surface and the top basement. This shows that important accommodation space is found in the distal domains associated to thick sedimentary deposits while the proximal is marked by small accommodation space and thin sedimentary deposits (from Tugend et al., 2014). The necking domain corresponds to the transitional domain between the proximal and distal domains marked by increasing potential accommodation space and moderate sedimentary thickness. The residual continental crust thickness and thinning along the margins are also indicated. 51

Figure I.25: A- Conceptual model of a strike slip fault showing the repartition of the different fault rocks according to the temperature in the crust (for a gradient of 25°C/Km) in relation to the main mechanism of deformation (from Fagereng and Toy, 2011). B- Classification of fault rocks according on the deformation style and content of matrix (from Braathen et al., 2004). C- Illustration of a core zone composed of gouge (from Collettini, 2011) D- Talc-smectite gouge from the Zuccale detachment fault (Elba island) showing SCC' structures associate to viscous flow and mineral precipitation (Collettini, 2011). E- Cataclasite with YPR structures formed under frictional flow along the Zuccale detachment fault (Collettini, 2011). F- Cataclasite from the Grosina detachment fault, Central Alps (Mohn et al., 2012). F- Hydraulic breccia showing jigsaw fractures (from Braathen et al., 2004). 57

Figure I.26: A- AUV microbathymetry images of an Oceanic Core Complex (Mid Atlantic Ridge, Escartín et al., 2017) showing the corrugated surface of the detachment fault with striation parallel to the displacement on the fault. B- Geological interpretation of the exhumed fault from an oceanic detachment (Bonnemains et al., 2017). The fault is partially covered by sediments. C- Rubbles and sediments over the detachment surface (from Escartín et al., 2017). D- Exhumed core zone (composed of gouges) overlaid by syn-rift sediments from the Err detachment, Central Alps (from Masini et al., 2011). 59

Figure II.1: A- Cross section of the Alps from Argand (1924) showing the pro wedge development and retro wedge in the Adriatic crust as well as the main tectonic nappes. B- Cross section of the Western Alps showing the position of the different nappes (modified from Escher et al., 1993 and Pantet et al., 2020). 72

Figure II.2A- Cross section of the Jurassic margin with the different domains highlighted (modified from Mohn et al., 2014). B- Map of the Alps showing the position of the different paleogeographic domains (same color code as A, modified from Schmid et al., 2004; Mohn et al., 2010). The ages of the ophiolites are also indicated on the map. C- Palaeogeographical map of the Alpine realm during the late Jurassic showing the 2 oceanic basins surrounded by the Briançonnais block (modified from Ribes et al., 2019a). D- Cross section of the Alps highlighting the position of the different paleogeographic domains (modified from Escher et al., 1993). 75

Figure II.3: Section of the "Variscan lithosphere" (from Mouthereau et al., 2021) associated to pre-rift rheological profile. 78

Figure II.4: A- Tectonic map of the Alps showing the main units (European derived, Briançonnais-derived, and Adria-derived). The oceanic domain (Liguro-Piemont and Valais) can be found in the internal part of the orogen. B- Satellite image of the Alps (from Google Earth) showing the position of the main geophysical transects. Ag=Argentera, Pv=Pelvoux, Bd=Belledonne, Mb=Mont-Blanc, PFT= Penninic front thrust, Gt= Gottard thrust, PF= Peri-Adriatic faults, Sf=Simplon fault, If=Inntal fault, SEMP= Salzach-Ennstal-Mariazell-Puchberg fault, MMF= Mür-Mürz fault. 80

Figure II.5: A- Profile of the Western Alps (from Pfiffner, 2014) showing the development of a pro wedge over the NW and a retro wedge toward the SE. Folding of the internal nappes of the orogen is visible due to the indentation by the Adria plate B- Section of the Jura Mountain showing thin-skin, fold and thrust belt style related to inversion of a Carboniferous basin at depth (from Guellec et al., 1990; Mugnier et al., 1990) C- Section of across the northern subalpine chains (from Philippe, 1994)..... 81

Figure II.6: A- Section of the Central Alps (from Pfiffner, 2014) showing crustal nappe stacking in the pro wedge and significant backfolding in the retro wedge associated to indentation of the orogenic prism by the Adria plate. B- Section of the Molassic basin showing the propagation of the deformation toward the NW (from Mock and Herwegh, 2017). C- Section of the Aar massif showing thrusting of the basement above the molassic basin (from Nibourel et al., 2021)..... 82

Figure II.7: Section of the Eastern and Southern Alps passing through the Tauern window (from Pfiffner, 2014). 83

Figure II.8: Comparison of the different interpretations of the ECORS-CROP profile (from (Mohn et al., 2014). A- Depth migrated ECORS-CROP profile (from Thouvenot et al., 1996). B-Rift inheritance model showing the role of the ECM as buttress between a thick continental crust in the External domain and a stacked hyper thinned crust in the internal domain (Mohn et al., 2014). C- Lithospheric accretionary wedge model (Lacassin et al., 1990; Nicolas et al., 1990). D- European lower crustal duplex model (from Roure et al., 1996). 84

Figure II.9: A- Vp profile across the Alps (through the Rhône valley) and Pô basin ((Wagner et al., 2012) showing the complex Moho topography below the Alps. B- Vs profiles below the Alps (across the Belledonne massif) showing increase of crustal thickness below the Penninic front (Lu et al., 2018). 85

Figure II.10: Evolution of the subduction of the distal Briançonnais margin (Piemont domain) between 60 and 35 Ma. Underplating of subducted slices along the subduction plane led to exhumation and juxtaposition of subduction remnants with different P-T evolution (Agard, 2021)..... 87

Figure II.11: Switch from subduction in the Liguro-Piemont to the Valais basin leading to progressive burial of the European crust below the accretionary prism. The age of the Valaisan flysch are from Jaquet et al., 2018. 88

Figure II.12: Evolution of the ECM (Aar massif from Herwegh and Pfiffner, 2005). A- Thrusting of the internal units above the ECM (Aa=Aar, Do=Doldenhorn, Wi=Wildhorn). B- Progressive thrusting of the ECM above the External massif which is associated to the extrusion of the Jurassic basins and folding of the internal nappes. C- Late exhumation of the ECM..... 91

Figure II.13: A- Map of the Mont-Blanc and Aiguilles-Rouges massif highlighting the nature of the basement, and the tectonic position of the cover regarding Alpine deformation (autochthonous, para-autochthonous, and allochthonous). B- Section of the Mont-Blanc massif showing the inverted Morcles basins associated to the thrusting on the Mont-Blanc over the Aiguilles-Rouges and Thrusting of the distal Helvetic nappes over the Mont-Blanc massif (modified from Escher et al., 1993). 92

Figure II.14: Section of the Grès Singuliers from Ribes et al., (2020) associated to analysis of the sediments from Dall'Asta (2019.) B- Palinspatic reconstruction (modified from Ribes et al., 2020) of the Helvetic domain during late Jurassic as proposed by Trümpy (1980), Burkhard (1988) and Pfiffner et al.,(2011). C-Reconstruction of the Helvetic domain taking into account the hypothesis of the Mont-Blanc detachment fault (from Ribes et al., 2020). 94

Figure II.15: P-T path of the Mont-Blanc, Aiguilles-Rouge and Morcles nappes showing a prograde path from ca. 32 Ma to 16 Ma and a retrograde path from 16 Ma to present-day (modified from Boutoux et al., 2016). The ages for the Penninic thrust are from Simon-Labric et al., (2009) and the ages for the Mont-Blanc shear zone are from Leloup et al., (2005). The ages associated to the prograde and retrograde path of the Mont-Blanc are from

Rolland et al., (2008), Glotzbach et al., (2008) and Cenki-Tok et al., (2014), and for the Morcles nappe from Kirschner et al., (1996). 95

Figure III.1: A- Tectonic map of the Alps showing the different Alpine tectonic units. Note the presence of the External Crystalline Massifs (ECM) at the transition between the internal and external domains (modified from Mohn et al., 2010; Schmid et al., 2004). The colour code similar to D (except molassic basins in yellow and Tertiary intrusions in red) highlights the paleogeographic position of the different Alpine units. B- Section across the Western Alps (for location see Fig. III.1A; modified from Escher et al., 1993). Colour code similar to D. C- Paleogeographic map of the Alpine realm during the late Jurassic (modified from Ribes et al., 2019a). Sandstones (Ribes et al., 2020) and breccias (Ribes et al., 2019a) related to tectonic activity are also represented. Faults in blue correspond to normal faults associated with stretching, the fault in red corresponds to necking fault thinning the crust, and faults in green correspond to faults exhuming the crust and the mantle. D-Restored section of the Alpine Tethys during the Late Jurassic (Mohn et al., 2010). E- NW-SE directed cross section across the transition zone between the Belledonne and Mont-Blanc massif (Southern Mont-Blanc massif, modified from Eltchaninoff-Lancelot et al. (1982)). The Penninic and Helvetic nappes thrust above the ECM were later deformed by basement deformation leading to the formation of a large antiformal fold. The area of interest corresponds to the basement anticline pinched between the Helvetic nappes to the south and the Roselette nappe to the north. 107

Figure III.2: Map of the Col du Bonhomme area (see location on map in the upper left corner (modified from Meyer, 2002) showing the southern edge of the Mont-Blanc massif. The tectonic contact described by Ribes et al., (2020) is highlighted by the presence of cataclasite and gouge at the transition between the basement and the sediment. Numerous NE-SW and NW-SE Jurassic faults also offset the top basement tectonic contact. The section on the right shows the simplified stratigraphy from the top basement to the Cretaceous with the location of the main decollement levels in the area in the Aalenian and Oxfordian schists. 110

Figure III.3: A-Schematic section of the top basement/sediment contact showing a strain gradient toward the top of the basement. A local loss of the initial rock texture is visible associated with an increase of alteration and brittle overprint. A sharp contact separates the basement and the sedimentary cover. Pre-rift sediments are separated from the basement by a tectonic contact with deformation visible at the base. The Grès Singuliers are lying above both the pre-rift and the basement in a stratigraphic contact. B-Clast of cataclasite reworked in the Grès Singuliers (45°43'46.41"N/ 6°43'47.96"E). C- The top basement is composed of cataclasite and locally black indurated gouge (45°43'39.51"N/6°42'40.25"E). D- Phyllosilicate-rich cataclasite giving an NNE-SSW top to the south sense of shear in the damage zone (45°46'13.36"N/6°43'46.17"E). E- Cataclasite basement with sub-horizontal Variscan foliation is still discernible in the damage zone (45°44'11.21N/6°43'46.85"E). F- Sub-horizontal mylonites affected by brittle deformation. G-Measures of bedding, fault plane orientations (high angle-normal faults and orientations of the top basement tectonic contact) and stretching lineations from the basement and the cover (projected on Schmidt stereograms, lower hemisphere). Note the NE-SW orientation of the basement fold affecting the basement and the cover (limb 1 and 2). 114

Figure III.4: Section of the top basement with sediment infill interpreted as neptunian dykes (45°43'39.6"N/6°42'46"E). The position of the pictures is indicated in the section. A- Contact between the top basement and the Grès Singuliers. B-Profile view of foliated cataclasite overlaid by fractured basement. The fractures are filled with a brownish matrix. C- Upper view of the fractured basement with sedimentary infill. The infill is composed of quartz grains and bioclasts fragments in a brownish matrix. D-View of the bioclasts from the matrix corresponding mainly to crinoids..... 116

Figure III.5: High-angle normal fault offsetting the top basement tectonic contact about 30 m (45°43'53.45"/6°43'51.70"). A sedimentary wedge with thickening of sandstones toward the fault is observed in the Grès Singuliers (15°), indicating a likely Pliensbachian/Toarcian age for the fault..... 117

Figure III.6: Modal composition for some of the different fault rocks found in the Col du Bonhomme area. 119

Figure III.7: A-Lowly altered orthoclase (Or) showing albite (Ab) and white mica (Wm) replacement with creation of microporosity (Scanning Electron microscope- Back Scattered Electron SEM-BSE). B- SEM-BSE image of the alteration of biotite (Bt) to chlorite (Chl) with formation of rutile (Rt). Note the alteration along the cleavage and on the borders of the crystals. Minor deformation such as crenulation is visible in the biotite and chlorite assemblages. C- Closer view of the cataclasite where numerous fractures filled with oxides are observed. Quartz (Qtz) exhibits fractures and minor plastic recrystallisation (bulging, white arrow) associated with undulose extinction (optical photomicrograph, crossed polarized light (XPL)) D- Cataclasite showing important feldspar alteration, with the formation of white micas associated with fracturing and oxides. Minor plastic recrystallization by bulging is visible in the prolongation of fractures (white arrow) (optical photomicrograph, XPL). E- Cataclasite showing fragmentation of the host rock, along with important fracturing of quartz and important hydration of feldspar (optical photomicrograph, plane polarized light (PPL)). Only few remnants of K-feldspars are observed. Partial dissolution of quartz with corrosive wear is clearly visible. Highly deformed quartz veins are observed in the cataclastic matrix, and oxide-rich fractures overprint the cataclasite. F- Hydraulic breccia with calcite cement (left: optical photographs of polished slab; right: XPL photomicrographs). The leucosomes are only affected by perpendicular fractures. The gneiss is affected by stronger alteration and deformation. The rock is overprinted by brecciation and subsequent dolomite (Dol) and ankerite (Ank) formation replaced by later by Mg-calcite (Mg-cal). 122

Figure III.8: A-Microphotograph of the gouge showing a rounded clast embedded in the black matrix. The foliation is highlighted by the elongated clasts. The white arrow points at the cataclastic matrix (M1) of the clast progressively sheared and incorporated into the gouge matrix M2 (XPL). B- Microphotograph of the gouge matrix M1 with clasts of cataclasite showing the progressive shearing (red arrows) and transformation into ultra-fine-grained black matrix M2 (XPL). C- Closer view of the black matrix of the gouge (M2) showing small illite minerals (around 5 μm), small quartz fragments (less than 10 μm) and pyrite (SEM-BSE, unpolished sample) D-Muscovite overgrowth over illite in the gouge (XPL). E- Irregular border between a hyalophane-bearing vein and the gouge. The latter is composed of small Fe-rich bands surrounded by illite-rich matrix. Clasts of hyalophane (Hy) are also observed in the gouge (SEM-BSE). F-Microphotograph of hyalophane and quartz in veins affected by important fracturing. The feldspars show important twinning of the crystals (XPL). 124

Figure III.9: A and B- Microphotograph (XPL and PPL) of the black gouge reworking cataclasite fragments. The elongation of the clasts marks the foliation. Note the reworked clasts of cataclasite in the gouge matrix. C- Example of grain size repartition in gouge and cataclasite samples as obtained from image treatment. All the samples show a fractal dimension between 1.3 and 1.7. Note the progressive grain size diminution toward fault core. D-Grain size circularity of the gouge from image treatment showing a wide range of shapes, from angular to well rounded. E- Grain orientation versus grain size, showing a preferential orientation defining the foliation. 126

Figure III.10: A- Phase map from gouge microprobe mapping (Rt=rutile, Py=Pyrite, Wm=White micas, Qtz=Quartz, Kfs=K-feldspars). B and C - Microprobe maps of Al_2O_3 (B) and TiO_2 (C) showing distinct composition for the Wm phase. This highlights the different composition of the clasts of cataclasite (M1) and fine-grained gouge matrix (M2). The transition from the cataclasite matrix M1 to the gouge matrix M2 shows a loss of Al. Ti is absent from the cataclasite but hosted by rutile in the gouge. D- Profile across the micrometric fault zone for Al_2O_3 and TiO_2 . The Al_2O_3 content has a diffusive profile, contrary to TiO_2 (in red, the zone of gain and in blue the zone of loss). E- Ternary plot of the composition of phyllosilicates from the gouge. $\text{MR}_3 = \text{Na} + \text{K} + 2\text{Ca}$, $2\text{R}_3 = (\text{Al} + \text{Fe}^{\text{III}} - \text{MR}_3)/2$, $3\text{R}_2 = (\text{Mg} + \text{Fe}^{\text{II}})/3$ (Velde, 1985). Ms = Muscovite, Cel = Celadonite, Fsp = Feldspars, Kln = Kaolinite, Prl = Pyrophyllite, Chl = Chlorite, Bt = Biotite, Srp = Serpentinite, Tlc = Talc, Mnt = Montmorillonite. F- Average microprobe composition of the cataclasite matrix and gouge matrix (muscovite to illite) for the major elements. 127

Figure III.11: A- Sketch summarizing the evolution of the fault rocks during exhumation following a retrograde path and a progressive localisation of the deformation in phyllosilicate rich layers (gouge) toward the surface. This is associated with the petrological evolution observed in the Col du Bonhomme from the gneiss to the matrix-supported gouge. The evolution of frictional coefficient is indicated. B- Pliensbachian cross section of

Mont-Blanc showing the crustal architecture and sedimentary infill associated to Mont-Blanc detachment fault (modified from Ribes et al., 2020). Uplift related to the detachment fault led to local erosion and sandstones formation around the massif about the exhumed surface. C- The H-block model for the necking of the crust showing to conjugated fault system in the upper brittle crust and in the lower crust leading to crustal thinning (modified from Mohn et al., 2012)..... 130

Figure IV.1: A-Tectonic map of the Western and Central Alps highlighting the different Alpine tectonic units (modified from Mohn et al. (2010) and Schmid et al.2004)). The colour code similar to C (except Molassic basins in yellow and Tertiary intrusions in red) highlights the position of the different paleogeographic units in the orogen. B- Paleogeographic map of the Alpine Tethys during the late Jurassic (modified from Ribes et al., 2019a). Faults in blue correspond to normal faults associated with stretching, faults in red to necking faults thinning the crust, and faults in green to faults exhuming the crust and the mantle. Sandstones (Ribes et al., 2020) and breccias (Ribes et al., 2019a) related to large scale normal faults and detachment faults are also represented. C - Restored section of the Alpine Tethys during the Late Jurassic (Mohn et al., 2010)..... 145

Figure IV.2: Characteristic evolution of multistage rift from stretching to necking. A- Stretching phase showing decoupled deformation between the upper and lower crust. The deformation is accommodated by high angle normal faults in the upper crust. B- Necking stage corresponding to localisation of the deformation associated to upper lithospheric break up and asthenosphere rising. Crustal necking is responsible for the formation of the central H-block characterised by a thickness below 20 km and surrounded by 2 sets of conjugated faults associated to crustal thinning and progressive coupling of the upper and lower crust. C- Asthenosphere rising is responsible for an increase of temperature as observed from the thermos-mechanical model of Chenin et al., (2020). Thermal gradients were recalculated using heat flow of Chenin et al., (2020). 146

Figure IV.3: A- Map of the Mont-Blanc and Aiguilles-Rouges massifs highlighting the lithology of the basement, and the tectonic position of the cover regarding to Alpine deformation. B- Section of the Mont-Blanc massif showing the inverted Morcles basins associated to the thrusting on the Mont-Blanc over the Aiguilles-Rouges and Thrusting of the Distal Helvetic nappes over the Mont-Blanc massif(modified from Escher et al., 1993). C- Map of the Col du Bonhomme area and associated synthetic stratigraphic section (modified from Dall’Asta et al., 2022). 148

Figure IV.4: A- Section of the top basement detachment and sedimentary cover highlighting the type of deformation observed in the basement and the type of contacts between the pre-rift and syn-rift cover (modified from Dall’Asta et al. 2022). B- Illustration of the pre-rift allochthonous blocks laying over the detachment fault and sealed by the syn-rift deposits, summarizing the observations described in Dall’Asta et al. (2022). 149

Figure IV.5: Cross polarized image of the basement and associated mineralogical map from μ XRF chemical map 156

Figure IV.6: A- Feldspar composition of the basement in the Col du Bonhomme area, and of the Mont-Blanc granite (Bussy, 1990) for comparison. B- Composition of biotite from the host rock. C- Composition of the phyllosilicates observed in the basement and the fault rocks using diagram from (Velde, 1985). D- Composition of chlorites and their precipitation temperatures obtained using the graphical representation of Bourdelle and Cathelineau (2015). Or=Orthoclase, Ab=Albite, An=Anorthite, Fsp=Feldspar, Mu=Muscovite, Ce=Celadonite, Bt= Biotite, Chl=chlorite, Bt=biotite, M=Montmorillonite, Serp=Serpentine, Ta=Talc..... 157

Figure IV.7: A- Plane polarized and B-mineral map of a cataclasite sample from the outer damage zone. C- Optical microphotograph (PPL and XPL) of feldspar and biotite alteration showing pseudomorphic replacement. D- Replacement of orthoclase by white micas associated to creation of microporosity (SEM-BSE image). E- Replacement of albite by white micas associated to creation of microporosity (SEM-BSE image). Fsp=Feldspar, Wm=White micas, Or=Orthoclase, Ab=Albite 158

Figure IV.8: A- Macroscopic image of graphite-rich vein and planes in the cataclasite. B- Thin section view (PPL) of the same graphite rich showing important amount of graphite/illite mixture. C- SEM image of the graphite rich area showing 2 types of graphite material, large graphite zones and illite/graphite mixture. D- Raman spectra of representative graphite associated to titanite..... 160

Figure IV.9: A- Optical image (PPL) of cataclasite from the inner damage zone showing increase of white mica proportion, iron oxides in fractures, and quartz veins reworked in the cataclasite (from Dall'Asta et al., (2022)). B- Phase map of the cataclasite C- Centimetric quartz veins in the inner damage zone reworked in the cataclasite. Two generations of veins are observed, the second generation crosscutting the first one. Fe-ox=Fe oxide, Ill=Illite, Wm=White micas, Or=Orthoclase, Qtz=Quartz 162

Figure IV.10: A- Optical image (PPL) of the gouge showing reworking of cataclasite in the gouge matrix. B- Corresponding phase map. C- Optical image (PPL) of the core zone showing clasts of cataclasite and ultracataclasite reworked in the gouge matrix. D- Optical image (PPL) of the gouge matrix with larger quartz grains and cataclasite clasts. Rt=Rutile, Py=Pyrite, Wm=White micas, Qtz=Quartz 163

Figure IV.11: A- Thin section photograph (XPL) of the quartz-hyalophane veins. B- Composition of hyalophane in a ternary albite-microcline-celsian plot. The light green field corresponds the low-temperature hyalophane, the dark green field corresponds to the hyalophane composition for greenschist conditions, the light blue to lower amphibolite facies and dark blue to upper amphibolite facies (from Essene et al., 2005; Raith et al., 2014). C- Optical image (XPL) of a vein in the gouge showing the vein crosscutting the foliation but also being brecciated and significantly deformed. Note the recrystallized matrix around the vein. D- Optical image (XPL) of the border of the veins showing the transition from recrystallized matrix with Ba-rich white micas to the fine-grained gouge. E- Optical image (XPL) of reworked hyalophane-quartz veins clast in the gouge. 164

Figure IV.12: A-Trace and REE of host rock and fault rock normalized to World Average Shales (Wedepohl, 1971; Bau et al., 2018) as a proxy for the upper continental crust composition. B-Na/(Na+K) vs (Na+K)/Al plots of fault-rock compositions (Wibberley, 1999) showing progressive albite and orthoclase sericitization leading to formation of gouge. 169

Figure IV.13: A, B, C: Log-log plots of the concentration of major, trace and rare-earth elements between the unaltered basement (CO) and the damaged rocks (CA) with A-outer damage zone, B- inner damage zone, C- core zone. The green straight lines are the isocons calculated using Zr and Al as the immobile elements (first method), and the red line is the one calculated using the minimum mass change method. The black straight lines indicate mass change values as percentages. D- Sum of mass change vs volume change showing the minimum of mass change for each sample..... 171

Figure IV.14: A- log-log plot of the concentration of major elements of the orthoclase and muscovite with isocons calculated using the IE (Al immobile) and the MMC methods. B- Histogram of the element mass change using the IE (Al immobile) and the MMC methods. C-Mineral map of the biotite/chlorite and albite/white micas alteration of the basement. D- Log-log plot of the concentrations of major element for the albite-muscovite alteration with isocons calculated using the IE (Al immobile) and the MMC method. E- Same as D but for the biotite-chlorite alteration reaction..... 176

Figure IV.15: EPMA chemical map with associated mass balance calculation. A- Phase map of the gouge-cataclasite transition. Rt=Rutile, Py=Pyrite, Wm=White micas, Qtz=Quartz, Or=Orthoclase. B- Al₂O₃ map (in wt%) for the white mica phase. C- TiO₂ map for the white mica phase showing absence of TiO₂ in the cataclasite and presence of TiO₂ in the gouge matrix. D- BaO map for the white mica phase showing increase of concentration in the Ba in the gouge. E- Log-log plot of the concentration of major elements in the cataclasite and the gouge with isocons calculated using the IE method (Al immobile) and the MMC method..... 177

Figure IV.16: A- Histogram of the Th of fluid inclusions from quartz grains from the 2 generations of veins from the inner damage zone (average with 1σ uncertainty). B- Same as A but for the Tm. C- Optical image (PPL) of an

inclusion from a type 1 quartz vein. D- Optical image (PPL) of an inclusion from a vein 2. E- Histogram of salinity (wt%) obtained with Raman spectrometry for the same 2 generations of veins. F- Histogram of T_e measured for the larger inclusions in the type 2 quartz vein..... 179

Figure IV.17: A- Histogram of the T_h of primary and secondary fluid inclusions of vein-filling quartz grains from the core zone. B- Same as A but for T_m values. C- Optical images (PPL) of the primary inclusions. D- Optical image (PPL) of the secondary inclusions. E- Histogram of salinity (wt%) obtained with Raman spectrometry for the primary fluid inclusions. F- T_h -salinity plot for the fluid inclusions from cataclasite and gouge. 180

Figure IV.18: A- Microphotograph (PPL) of the fault breccia showing a dolomite-ankerite rhombs cemented by calcite overprinted by Mg calcite. The dating was performed on the calcite cement from the ankerite-dolostone primary texture. B- Tera-Wasserburg concordia graph showing the result of U-Pb dating on the calcite. 181

Figure IV.19: A- The $^{40}\text{Ar}/^{39}\text{Ar}$ step-release spectra for the fraction 100-200 μm . B- The $^{40}\text{Ar}/^{39}\text{Ar}$ step-release spectra for the fraction 200-300 μm . C- Isochron diagram for the fraction 100-200 μm . D-Isochron diagram for the fraction 200-300 μm 182

Figure IV.20: A- Thermal evolution of (i) the Mont-Blanc and Aiguilles-Rouge massifs (from Boutoux et al., (2016), based on age data from Leloup et al., 2005), Rolland et al., (2008), Glotzbach et al., (2008) and Cenki-Tok et al., (2014), and (ii) the Morcles nappe (from Kirschner et al., 1996). The thermal peak at 330°C is from RSCM data (Dall'Asta et al.2022). The hyalophane age is also indicated on the graph leading to a cooling age below T_{cl} around 20 to 25 Ma. B- Results of the DIFFARG modeling of a Jurassic feldspar submitted to the alpine thermal evolution from Boutoux et al., (2016). The pre-rift evolution which is not well constrained was chosen to be linear associated to burial under post-rift sediments. This shows a complete reset of the feldspar Ar/Ar age. The case scenarios with and without argon excess are represented..... 186

Figure IV.21: Schematic flow chart showing the mineral transformations and associated element transfers occurring in the detachment fault. The minerals in white correspond to primary phases from the host rock, while the minerals in grey correspond to secondary phases formed in the fault zone. The blue arrows correspond to element transfer in fluid while the black arrows correspond to mineralogical transformations. 189

Figure IV.22: A- Estimation of pH in relation to chloride concentration in a Or-Mu-Ab-Qtz buffered system (Yardley, 2005) B- Temperature-pressure plot with calculated isochore ($\text{H}_2\text{O}-\text{NaCl}$; Bakker, 2018) corresponding to the different generations of inclusion observed in the cataclasite (a. isochore of vein1 and b. isochore of vein 2) and gouge (c.). The geothermal gradient of 50°C/km from numerical models of rifting (Chenin et al., 2020) and chlorite temperatures are indicated, giving a maximum pressure of formation for the inclusions. 192

Figure IV.23:A- Alteration reactions associated to the strain evolution toward the core zone. B- Modelling of the stability of feldspar and biotite during fluid rock interaction for different temperatures compared with the mineralogical observations showing albitization (1) followed by sericitization (2) and (3) and disappearance of chlorite toward the core zone. 193

Figure V.1: Map of the Mont-Blanc showing the location of the Val Ferret. 204

Figure V.2: Map of the north Val Ferret area showing the autochthonous cover of the Mont-Blanc (modified from Swisstopo). The Catogne is characterized by the the presence of pre-rift cover over the basement disappearing southward. The position of the mines in this area is indicated. 205

Figure V.3: Map of the southern Val Ferret showing the syn-rift cover lying above the basement. 206

Figure V.4: Cross section of the Val Ferret in the Ferret Pass area showing the distal units (Helvetic nappes and Penninic nappes) thrust above the Mont-Blanc massif (Trümpy, 1954). 207

<i>Figure V.5: A- Field photograph of the central granite appearing coarse grained with a porphyritic texture and mafic xenoliths. B and C- Border facies of the granite showing an equigranular texture as observed in the area of Breya. D- Microgranite with magmatic inherited texture such as biotite lineation.....</i>	<i>210</i>
<i>Figure V.6: A and B- Foliated magmatic rock with alternating black and with layers corresponding to schlieren. Syn-magmatic folds are visible. C- Optical microphotograph (PPL) of the black layers composed of biotite. Small apatite inclusion typical of magmatic biotite are present. D- Optical microphotograph (XPL) of the black, biotite-rich layers showing the presence of large apatite crystals associated with biotites.....</i>	<i>211</i>
<i>Figure V.7: A- Rhyolite from the Mont-Blanc showing dark biotite phenocrysts in a white matrix. B- Optical microphotograph (PPL) of a corroded quartz characteristic of rhyolites. C- Illustration of quartz shapes in the Mont-Blanc granites and rhyolites. Rhyolite are characterized by strongly corroded quartz (from Marro, 1987).</i>	<i>212</i>
<i>Figure V.8: A- Composition of the different basement samples of the Val Ferret in major elements. B- Composition in trace elements normalized to World Average Shales (WAS; Wedepohl, 1971). C- Composition in Rare Earth Elements normalized to WAS.</i>	<i>213</i>
<i>Figure V.9: A- Schematic view of the Mont-Blanc intrusion (modified from Bachmann and Bergantz, 2008) and its relation with Carboniferous shear zones. The points represent the position of the different samples. B- REE composition normalized to chondrites.</i>	<i>214</i>
<i>Figure V.10: Stratigraphic section (modified from Grasmück, 1961) from the south Val Ferret (L'Amône) and the north Val Ferret (Catogne) associated to the main rifting stages (from Ribes et al., 2019b, 2020).</i>	<i>215</i>
<i>Figure V.11: Pre-rift cover in the Mont-Chemin area. A- Triassic basal arkose with rhyolitic clasts. B- Transition between basal arkose and the Triassic dolostones.</i>	<i>216</i>
<i>Figure V.12: A- Synthetic section drawn from field observations of the late Liassic shale- sandstones alternations from the Col de planches. Classification of turbidites from Bouma (1964) and Mutti (1992). B- Coarse-grained sandstones with belemnites. C- Top of a sandstone bed with laminations and ripples. D- Shales interlayered with the sandstones.</i>	<i>217</i>
<i>Figure V.13: A- Liassic conglomerates from the south Catogne massif showing decimetric clasts of dolostones reworked in the syn-rift sediments. B- Syn-rift sandstones with large basement clasts and fragments of quartz veins.</i>	<i>218</i>
<i>Figure V.14: A- Transition between fossiliferous Aalenian limestones to metric Aalenian shales level and Bajocian limestones. B- Mineralized black shales with yellowish sulphides alteration. C- Black shales with slaty cleavages and small quartz veins.</i>	<i>219</i>
<i>Figure V.15: A-Section (n°1) of the basement sediment-interface in l'Amône showing cataclasite affecting the basement and overlaid by Lower Aalenian conglomerates and sandstones. The arrows indicate the occurrence of mineralized sediments and ore deposits. B- Contact between the sandstone and the conglomerate showing large block sealed by the sandstone deposits. C- Breccias composed of clast of rhyolitic cataclasite. E-Cataclastic bands in the basement.....</i>	<i>221</i>
<i>Figure V.16: A- Optical image (PPL) of a plagioclase phenocryst surrounded by cataclasite in the rhyolite matrix. B-Optical image (PPL) of a quartz phenocryst from the rhyolitic basement. C- Optical image (PPL) of a K-feldspar phenocryst crosscut by quartz filled fractures. D- Optical image of the recrystallized matrix of the rhyolite affected by fractures filled with epidote. E and F- Optical image (XPL and PPL resp.) of a shear zone composed of fine-grained epidote developing in the rhyolite.</i>	<i>222</i>

<i>Figure V.17: A- Contact between the rhyolite and the Aalenian conglomerates. B- Decametric rhyolite rounded clasts in a sandstone matrix. C- Lower Aalenian sandstones showing fine-grained lamination. D- Contact between rhyolite and sandstones interlayered with shales in Saleinaz.</i>	<i>224</i>
<i>Figure V.18: A- Reconstitution of the area of l'Amône during Lower Aalenian with shoreface conglomerates over the basement highlighting the occurrence of a relief nearby. B- Progressive subsidence and smoothing of the relief led to the deposits of marine sandstone above the basement. C- Reconstitution during the Bajocian showing the transgression and progressive drowning of the area.</i>	<i>225</i>
<i>Figure V.19: A- Section of the sediment-rhyolite contact in Saleinaz. B- Orientation of cataclasite planes associated to stretching lineations and orientations of Alpine fractures in a stereogram (Wulf canevas; lower hemisphere).</i>	<i>226</i>
<i>Figure V.20: A and B-Optical microphotograph (PPL and XPL) of cataclasite in rhyolite. C- Fractures in rhyolite associated to cataclastic deformation. Small shear zones are associated to strong comminution. D- Transition from fine-grained to ultra-fine-grained matrix associated to comminution.....</i>	<i>227</i>
<i>Figure V.21: A- Section of the fault zone between the rhyolite and-granite from the Brea area. B- Poles of foliation orientation in the fault zone and stretching lineations associated to the fault zone in a stereogram (Wulf canevas; lower hemisphere).....</i>	<i>228</i>
<i>Figure V.22: A and B- Optical microphotograph (PPL and XPL) of schlieren overprinted by a micrometric shear zone. C- Mylonite in the damage zone overprinted by cataclastic deformation associated to loss of the S/C structures.</i>	<i>229</i>
<i>Figure V.23: A- Optical microphotograph (PPL) of cataclasite in granite associated to strong epidote neoformation. B- Optical microphotograph (PPL) of rhyolitic quartz found in the footwall damage zone.</i>	<i>230</i>
<i>Figure V.24: A- Optical microphotograph (XPL) of the gouge composed of fine-grained white micas chlorite and epidote. B- Optical microphotograph (XPL) of remnants of orthoclase in the gouge. C and D- Optical microphotograph (PPL and reflected light) of the gouge showing darker area composed of graphite.</i>	<i>230</i>
<i>Figure V.25: A-Composition of the Brea fault zone in major elements. B- Composition of the fault zone in trace elements normalized to WAS. B- Composition of REE normalized to WAS.</i>	<i>231</i>
<i>Figure V.26: Section of the basement-sediment interface showing a tectonic contact in the top basement overlaid by syn-rift sediments.</i>	<i>232</i>
<i>Figure V.27: A- Sub-vertical Variscan leucogranite intrusion in the polymetamorphic basement. B- Fractured veins in the polymetamorphic basement.</i>	<i>233</i>
<i>Figure V.28: Image merging of the fault zone in Mont-Chemin showing cataclasite from the damage zone passing to the gouge core zone and to the hanging wall damage zone. Note the presence of large undeformed massive basement lenses.</i>	<i>234</i>
<i>Figure V.29: A and B- Stretching lineations in the gouge. C- Gouge layers in contact with cataclasite reworking large basement clasts. D- Plot of the stretching lineation and of the gouge and cataclasite orientation in a stereogram (Wulf canevas).</i>	<i>235</i>
<i>Figure V.30: A-Microphotograph (PPL) of cataclasite and ultracataclasite overprinting the basement. The microstructures indicates a NE-SW top to the north sense of shear. Y=Y-plane, R=Riedel plane, R'=Antithetic Riedel, P=P-plane. B-Microphotograph (XPL) of gouge reworking a large cataclasite clast. C- Microphotograph (XPL) of gouge overprinting the cataclasite. The gouge is composed of ultra-fine-grained phyllosilicates.</i>	<i>236</i>

<i>Figure V.31: A-Composition of the Mont-Chemin fault zone in major elements. B- Composition of the fault zone in trace elements normalized to WAS. C- Composition of REE normalized to WAS.</i>	<i>237</i>
<i>Figure V.32: Restoration of the Mont-Chemin fault zone back to its Late Liassic position achieved by the rotation of the Liassic sediments back to the horizontal.....</i>	<i>240</i>
<i>Figure V.33: Role of pre-rift basin on the detachment geometry (modified from Epin and Manatschal, 2018) A- Map view of the pre-rift (Permian) basin and the relation between the detachment fault and the basin. B, C and D- Sections perpendicular to the detachment direction showing the reactivation of the Permian basin and the formation of an allochthonous block of Permian. E- Section parallel to the detachment direction showing the relations between the detachment and the Permian faults.....</i>	<i>240</i>
<i>Figure V.34: A- Evolution of the detachment fault during Sinemurian and Aalenian associated to the Carboniferous rhyolites forming allochthonous blocks. B-Proposal of the stratigraphic architecture of the Val Ferret during Late Jurassic. The positions of the different sections are indicated. C- Block diagram of the Val Ferret during crustal necking (Pliensbachian) showing the inverted Carboniferous basin crosscut by secondary faults leading to the formation of allochthonous blocks. The southward termination of the basin leads to the formation of lateral ramps along the Mont-Blanc detachment fault.</i>	<i>242</i>
<i>Figure V.35: Seismic example of allochthonous blocks above a necking detachment fault (1) in the Norwegian margin (modified from Osmundsen and Péron-Pinvidic, 2018). This fault is incised by another detachment fault (4) which is responsible for crustal-mantle coupling. Small syn-rift basins are observed associated to the the allochthonous blocks.....</i>	<i>243</i>
<i>Figure V.36: A- Image of the Mont-Blanc back thrust showing an Alpine fault cross-cutting the basement/sediment interface (credit from J.F. Gienne and C.Ribes). B-Closer view at the contact between the basement and the overturned sediments (credit from J.F. Gienne and C.Ribes). C- Focus on the cover showing undeformed limestones associated to deformed marls showing developed foliation. D- Cataclasite associated to the Mont-Blanc back-thrust.</i>	<i>244</i>
<i>Figure V.37: Connection between the northern and southern Mont-Blanc detachment fault through the Courmayeur area. Stretching lineations associated to fault are indicated with the arrows.....</i>	<i>244</i>
<i>Figure VI.1: A- Map of the External Crystalline Massifs (ECM) from the north Belledonne to the Aar massif highlighting the location of the autochthonous and allochthonous sedimentary cover (modified from Ribes et al., 2020). The location of the sedimentary sections used is indicated on the map as red stars. B- Palinspatic reconstruction of the Belledonne-Aar domain during the late Jurassic (modified from Ribes et al., 2020). M-D = Morcles Doldenhorn, Dol. = Doldenhorn.</i>	<i>250</i>
<i>Figure VI.2: A-Correlation of the sections across the margin from the Aiguilles-Rouge to the Ultrahelvetic domain. B-Reconstitution of the margin during Bajocian associated to the syn-rift sedimentary cover (vertical exaggeration of cover thickness).</i>	<i>256</i>
<i>Figure VI.3: Correlation of the section along the Morcles-Doldenhorn basin using the Aalenian as a datum....</i>	<i>262</i>
<i>Figure VI.4: Correlation of the margin along the necking domain from the Aar to the southern Mont-Blanc massif using the base of Aalenian for datum.....</i>	<i>264</i>
<i>Figure VI.5: Eustatic variations of the Helvetic margin compared to the large scale eustatic variations of the Tethys from Hardenbol et al., 1998. The most striking feature is the Aalenian transgression which is not recorded in the proximal domain (e.g., Jura domain), and which indicates strong tectonic subsidence.....</i>	<i>265</i>
<i>Figure VI.6: Repartition of the Helvetic and Dauphinois facies around the Mont-Blanc and Aar massif (Trümpy, 1971). The isopach line of the Liassic sediments are from (Loup, 1992).</i>	<i>266</i>

Figure VI.7: A- Paleogeographic reconstruction of the Mont-Blanc area during the Sinemurian. Subsidence in the Morcles basin is observed while topographic uplift is starting in the Mont-Blanc. B- Reconstruction during the Pliensbachian showing the emersion of the “Mont-Blanc Island” associated to important clastic deposits around the Mont-Blanc. Sediments are exported toward the distal Ultrahelvetetic domain. C- Reconstruction during the Aalenian showing the progressive transgression on the basement. Clastic deposits are restricted to the Mont-Blanc. Uplift is also observed in the Aiguilles-Rouges massif. D- Reconstruction during the Lower Cretaceous showing progradation of the carbonate platforms. Only a small portion of the Mont-Blanc remained emerged. E- Burial history for the base of the base of the Mesozoic sediments (from Wildi et al., 1989) for the Jura platform, the Helvetic plateau, the Aiguilles-Rouges massif and the Helvetic shelf. 267

Figure VII.1: A- Structural model for the stretching phase and the necking phase. The stretching phase is associated to high angle normal fault bounding half grabens. The crustal necking is associated to large offset detachment faults leading to important topographic uplift. B- Numerical model showing the strain in the lithosphere during the stretching phase and the necking phase. The isotherms are also indicated showing increase of temperature during crustal necking (from (Chenin et al., 2020). 276

Figure VII.2: Map of the External Crystalline Massifs with location of the different mines indicated (based on BRGM, 1984; Ochoa Alencastre and Chenevoy, 1979; Sivade and Thibieroz, 1989; Nögler et al., 1995; Dorignaux, 2017). There is a clear alignment of the mines along the Jurassic faults (from Lemoine and Trümpy, 1987; Ribes et al., 2020 ; Dall’Asta et al., 2022). Some of these ore deposits were dated giving a pre alpine age. Uranium deposits in the Argentera Massif give a Late Sinemurian to Pliensbachian age coeval with crustal necking in the Alps (Geffroy et al., 1964). 277

Figure VII.3: A- Map of the Mont-Blanc massif showing the different basement lithologies. Most of the cover around the Mont-Blanc is para-autochthonous or allochthonous detached above the Aalenian shales. However autochthonous cover is preserved in the internal Mont-Blanc massif. Mines are also indicated on the map (from Tagini, 1951; Chessex and Rivier 1957; Costa and Troilo, 2013; Dorignaux, 2017; Rys, 2020). B- Section of the Mont-Blanc and Aiguilles-Rouges massifs showing the relation between the Carboniferous shear zone, the Jurassic normal fault and the Alpine shear zone (modified from Escher et al., 1993). The Morcles basin correspond to the extruded cover of a half-graben. The Helvetic nappes corresponds to distal sediments thrust over the necking domain. C- Simplified section of the basement showing the relation between the Mont-Blanc detachment fault, the syn-rift to post-rift sediments and the different mineralisations. Qtz = quartz, Hem=Hematite, Ad=Adularia, Au = gold 278

Figure VII.4: A- Sketch of a detachment fault with proposed fluid pathway indicated, based on observation from the Mont-Blanc massif. The downward path of the fluid occurs through crustal fractures in the footwall and faults in the hangingwall associated to calcite precipitation at temperature up to 150°C. The upward path is the detachment fault. Metals are leached from the basement at temperature around 250°C. B- Evolution of the detachment fault showing progressive exhumation. The optimum metal leaching area corresponds to temperatures of around 200 to 250°C. The footwall during exhumation passes from the metal leaching area to the zone of ore formation. 280

Figure VII.5: A- Fluid circulation and element transfer associated to crustal necking based on the example of the Mont-Blanc. At higher temperature, albitisation occurs followed by sericitization and chloritization. Metal-rich brines move upward along the fault leading to formation of ore deposits in the cover. The core zone (gouge) is acting as an impermeable barrier. B- Evolution of the hydrothermal system and fluid signature during rifting. Stretching phase from Hips et al., 2016; Chenin et al., 2020; Barale et al., 2021. The data for the necking stage are from Incerpi et al., 2017; Chenin et al., 2020 and Dall’Asta et al. in prep. The data for the hyperextended stage are from Manatschal et al., 2000; Lescoutre et al., (2019), Saspiturry et al., 2020. Data from the exhumation stage are from Pinto et al., 2015; Quesnel et al., 2019; Coltat et al., 2019, 2021 ; Nteme Mukonzo et al., 2021..... 284

<i>Figure VIII.1: Temperature sensitivity of different thermochronological systems (modified from Doepke, 2017). The lowest and highest Alpine temperature recorded in the Mont-Blanc are indicated (High-T MB and Low-T MB). The method written in red correspond to dating realised in the Col du Bonhomme and presented here. The method written in blue correspond to methods used in the Mont-Blanc (U-Pb on zircon(Bussy et al., 2001), Rb-Sr on muscovite (Leutwein et al., 1970), Ar-Ar on muscovite (Leloup et al., 2005 and Rolland et al., 2008), Fission track on zircon (Glotzbach et al., 2008), ZHe (Boutoux et al., 2016), AHe (Glotzbach et al., 2008 and Boutoux et al., 2016)).</i>	292
<i>Figure VIII.2: A- Model for the Mont-Blanc Belledonne transfer zone showing switch in the rift polarity between the upper and lower plates. B- Section of the lower plate in the Mont-Blanc massif. C- Section of the upper plate in the Belledonne massif.</i>	297
<i>Figure VIII.3: A- Erosional unconformity with the pre-rift truncated and overlaid by syn-rift deposits. B- Tectonic unconformity showing an exhumed fault plane sealed by syn-rift sediments. C- Exhumed detachment fault affected by strong erosion erasing most of the fault remnants. D- Section of the contact between the syn-rift sandstones and the exhumed basement.</i>	298
<i>Figure VIII.4: A- Top view of the beds showing silicified wedge load forming a polygonal network of crests. B- Cross section of the beds showing load casts and soft-sediment deformation structures such as folds.</i>	299
<i>Figure VIII.5: Schematic view of the necking domain showing the truncated necking detachment fault associated to over tilted basins.</i>	300
<i>Figure VIII.6: Impact of the mechanical stratigraphy on the nappe geometry. Thinning of the Aalenian shales toward the Mont-Blanc led to the formation of a ramp in the Upper Jurassic.</i>	301
<i>Figure VIII.7: A- Map showing the geometry of the main thrusts associated to the reactivation of the transfer zone (based on Gourlay, 1982 and Epard, 1990). B- Cross section showing the inversion of a half-graben basin with the extrusion of the sedimentary cover. C- inversion of the detachment fault in the transfer zone with shortcuts leading to the preservation of the pre-Alpine contacts. D- Overtured detachment fault crosscut by back thrust leading to overprint of the pre-Alpine contact (modified from Grocott and McCaffrey, 2017).</i>	303
<i>Figure VIII.8: Proposal of evolution of the necking domain during compression (based on Tavani et al., 2021). The temperature indicated corresponds to the temperature reached by the necking domain. The shortening in the Mont-Blanc and Aar are from Rosenverg et al., 2021.</i>	306
<i>Figure VIII.9: Conceptual model of the relation between the Variscan, rift-related and Alpine ore deposits in the External Crystalline Massifs. Post-Variscan magmatism is responsible for the concentration of some metals in the upper crust, which are remobilized in later tectonic events. The Jurassic deposits are affected by Alpine deformation and metamorphism leading to strong overprint. 1- Marshall et al., 1997; 2-Dall’Asta et al., 2022 ; 3-Rys, 2020; 4-Dorignaux, 2017; 5-Geffroy et al., 1964; 6-Marshall et al., 1998 ; 7-Rossi and Rolland, 2014; 8-Rolland et al., 2003; 9-Polliand and Moritz, 1999; 10-Ochoa Alencastre and Chenevoy, 1979; 11-Chessex and Rivier, 1957; 12-Hofmann, 1994.</i>	309
<i>Figure VIII.10: A- Conceptual sketch of the mineral system according to McCuaig and Hronsky (2014) B- Conceptual sketch of the mineral system according to Dulfer et al., (2016) highlighting the different space and time scales associated to ore deposits.</i>	311
<i>Figure VIII.11: Concept of mineral system applied to crustal necking domain.</i>	312
<i>Figure VIII.12: Evolution of rift-related fluids in a magma-poor margin from the proximal to the exhumed mantle.</i>	313

Figure VIII.13: A- Graph of the critical raw material according to the supply risk and economic importance (from Blengini et al., 2020). The yellow circle indicates material present in necking domains, and green circles material observed in exhumed mantle domains. B- Evolution of the zinc and lead known resources through time (from Sverdrup et al., 2019). The graph presents the total known resources divided in rich, high, low and ultra-low according to the ore grade. The red line corresponds to the supposed peak in the known resources..... 315

Figure VIII.14: A- Size (in tons) of some Pb-Zn deposits found in necking domains. B- Ore-grade (%) of some Pb-Zn deposits found in necking domains. C- Ore grade vs size graph of Pb-Zn, baryte and Mn-oxide from necking domains. D- Proportion of rift and rift-related Pb-Zn deposits through Earth history (from Leach et al., 2010). 318

Table of tables

<i>Table I.1: Common vocabulary defined in rifted margins concerning extensional faulting, morphological features, and rifting processes</i>	25
<i>Table I.2: Summary of the fluid signature of different tectonic settings throughout the Wilson cycle</i>	28
<i>Table I.3: Definition of the different domains observed in magma-poor margins</i>	36
<i>Table I.4: Characteristics of the different rifting stages</i>	53
<i>Table III.1: Results of RSCM thermometry in the Col du Bonhomme area. SD=Standard deviation, SEM= Standard error of the mean, 95% confidence interval</i>	112
<i>Table III.2: Microprobe analysis of minerals from the host rock, the cataclasite and the gouges. The structural formula were calculated with the software AX from (Holland and Powell, 2006). Ferric iron was recalculated according to the method of Holland and Powell, (1998). Wm = White micas, Chl = Chlorite, Bi = Biotite, Fsp = Feldspars, Fap = Fluorapatite, Pg = Paragonite, Ms = Muscovite, Cel = Celadonite, An = Anorthite, Ab = Albite, Or = Orthoclase, Hy = Hyalophane, Cls = Celsian, XMg=Mg/(Mg+Fe).</i>	121
<i>Table IV.1: Composition of the different phases observed in the Col du Bonhomme area. The structural formula were calculated with the software AX from Holland and Powell (2006). Ferric iron was recalculated according to the method of Holland and Powell (1998). Wm = White micas, Chl = Chlorite, Bi = Biotite, Fsp = Feldspars, Pl=Plagioclase, Fap = Fluorapatite, Pg = Paragonite, Ms = Muscovite, Cel = Celadonite, An = Anorthite, Ab = Albite, Or = Orthoclase, Hy = Hyalophane, Ce = Celsian. The composition for each phase corresponds to the average (av.) of the EMPA composition obtained. The Standard deviation (SD) is given as 1σ.</i>	155
<i>Table IV.2: RSCM results on the graphite in the fault zone. SD=Standard deviation, SEM= Standard error of the mean</i>	161
<i>Table IV.3: Composition of the host rock, outer, inner damage zones and core zone in major elements (wt%). The standard deviation is given for 1σ. The normalized spread (R) allows to estimate the heterogeneity of the samples.</i>	166
<i>Table IV.4: Mineral composition (wt% ox.) extracted from the chemical maps. Bt=Biotite, Chl=Chlorite, Or=Orthoclase, Wm=White mica, Ab=Albite, Ill=Illite.</i>	173
<i>Table IV.5: Argon isotopic ratio for each heating stage associated to the calculated age</i>	184
<i>Table IV.6: Parameter used for calculating the temperature of opening, reset, closure following the procedure of Gardés and Montel (2009).</i>	187
<i>Table IV.7: Comparison between different continental detachment faults. The Th given corresponds to homogenization temperature of fluid inclusions in syn-kinematic veins.</i>	197
<i>Table V.1: Location of the different outcrops in the Val Ferret (+ Saillon)</i>	203
<i>Table V.2: RSCM results from the Val Ferret. SD=Standard deviation and SEM= Standard Error of the Mean ..</i>	208
<i>Table V.3: RSCM data for each spectrum of sample MB20c</i>	208
<i>Table V.4: RSCM data for each spectrum of sample MB19d</i>	209
<i>Table VI.1: Sections of the early Jurassic to Mid Jurassic cover between the Belledonne and Aar massifs</i>	252

Table VIII.1: Compilation of ore deposits in fossil-rifted margins and present-day rifted margins providing the type, age, and size of the deposits. The (M) associated to the type of ore deposits means that this deposit has been submitted to metamorphism..... 317

General introduction



View of the Mont-Blanc from the Tête Sud des Fours (Mont-Blanc Massif, France)

Introduction (En)

Rifted margins are one of the most common tectonic settings on Earth forming the transition between an oceanic and a continental lithosphere. The fundamental concept to understand the fate of rifted margins is the **Wilson cycle** (Wilson, 1966). Indeed, rifted margins play a key role in the Wilson cycle as the place of birth (rifting) and death (subduction initiation) of an oceanic domain. The final stage of oceanic closure associated to collision leads to the incorporation of the margin in the orogen with some remnants of rifted margins (fossil rifted margins) partially preserved. The study of rifted margins is fundamental to better understand the process of crustal break-up and oceanisation, as well as to be able to predict the occurrences of **natural resources**. Rifted margins provide most of the hydrocarbon resources and some of the largest metalliferous deposits (Levell et al., (2010), Nemčok, 2016; Arndt et al., 2017). Throughout the years, big steps were made in the understanding of the formation of rifted margins through observations of present-day margins (seismic sections, gravimetric and magnetic survey, wells data see De Charpal et al., 1978; Boillot et al., 1987; Whitmarsh et al., 2001a; Sutra et al., 2013; Sapin et al., 2021), field studies based on fossil rifted margins and hyperextended rift system (e.g., the Alps and the Pyrenees see Lemoine et al., 1981; Lemoine and Trümpy, 1987; Manatschal, 1999 ; Chevalier et al., 2003; Lagabrielle et al., 2010; Mohn et al., 2011, 2014; Tugend et al., 2015; Clerc et al., 2016 ; Ribes et al., 2019c; Lescoutre and Manatschal, 2020; Ducoux et al., 2021; Saspiturry et al., 2021) and numerical modelling (Huisman and Beaumont, 2003; Huisman and Beaumont, 2011; Duretz et al., 2016; Brune, 2018; Lescoutre et al., 2019; Chenin et al., 2020; Lescoutre et al., 2019). These thorough investigations enable to distinguish different type of margins (e.g., magmatic/amagmatic margins and orthogonal/oblique margins) as well as their mechanisms of formation.

This manuscript will be focused on **magmatic-poor margins**, which represent an important part of the rifted margins worldwide. The evolution of these margins appears **polyphased** (Péron-Pinvidic et al., 2013) with each phase characterized by a specific tectono-sedimentary evolution as well as a specific fluid signature (Sutra and Manatschal, 2012; Tugend et al., 2015; Pinto et al., 2015; Incerpi et al., 2017; Ribes et al., 2019d; Barale et al., 2021). The initiation of the rift is associated to **stretching**, which corresponds to minor extension with strong decoupling between the upper crust and the lower crust/mantle (Sutra and Manatschal, 2012). This is followed by **crustal necking** which corresponds to the localisation of the deformation in response to the rupture of the most competent layer (Sutra and Manatschal, 2012; Chenin et al., 2018). The localisation of the deformation leads ultimately to the coupling between the thinned upper and lower crusts and to the complete embrittlement of the continental crust. This allows during the **hyperextension** to thin the crust to zero and exhume the subcontinental **mantle** (Sutra and Manatschal, 2012). The stretching,

hyperextension and mantle exhumation phases have been widely studied, providing strong constraints on the tectonic, sedimentary and thermal evolution of these domains. However, the necking domain remains relatively unknown, despite its key role during rifting. Present-day margins provide information on the crustal structure of the necking domain and the sedimentary geometries associated to necking (Osmundsen and Péron-Pinvidic, 2018; Muñoz-Barrera et al., 2021). Numerical modelling provides more constraints on the topographic and thermal evolution during crustal necking (Chenin et al., 2018, 2019a; Petri et al., 2019; Duretz et al., 2016). However, the stratigraphic evolution as well as the fluid evolution during necking remains largely unconstrained mostly due to the lack of fossil analogues. Key questions concerning the necking domain are:

- **What is the syn- to post-rift stratigraphic evolution of the necking domain?**
- **What is the stratigraphic signature of crustal necking?**
- **Is crustal necking a suitable environment for hydrothermal circulation?**
- **If this is the case, what type of fluid and element transfer are associated to crustal necking?**
- **Is there a characteristic geochemical signature to crustal necking?**
- **Are these circulations associated to specific ore deposits?**

The Alps corresponds to a **fossil Jurassic oceanic domain** inverted since the Late Cretaceous. Preserved remnants of the rifted margins can be found in the pro-wedge and retro-wedge of the orogen. These remnants correspond mostly to **preserved half-grabens** from the proximal domain (Lemoine et al., 1981; Barfety and Gidon, 1984). The distal domain is mostly preserved in the retro wedge, where pre-Alpine **detachment faults** have been identified (Manatschal, 1999). In addition, the necking domain of the Adria margin is partially preserved. Indeed, an upper crustal detachment fault related to necking can be found in the central Alpine Campo-Grosina unit (Mohn et al., 2012). For the European margin it was proposed that the **External Crystalline Massifs (ECM)** correspond to the former **necking domain** (Mohn et al., 2014). The ECM (Aar, Mont-Blanc, Belledonne, Pelvoux, Argentera) are found at the transition between the external and internal parts of the orogen and form nowadays the highest summits of the Alps. In the ECM, and more specifically in the Mont-Blanc, the sedimentary cover is peculiar (Saussure, 1779; Landry, 1976; Eltchaninoff-Lancelot et al., 1982; Epard, 1989). Indeed, it corresponds to clastic sediments ("**Grès Singuliers Fm.**"), which are found nowhere else in the area. They are disconnected from any continental sources and therefore indicate the apparition of a local clastic source. Based on these observations, it was proposed that these sandstones correspond to the **stratigraphic signature of crustal necking** and were formed as a response to basement exhumation in relation to **detachment faulting** (Ribes et al., 2020). The goal of this study is to use this possible fossil necking domain in the Mont-Blanc as an analogue of present-

day necking domains, in order to better understand crustal necking in terms of stratigraphic and fluid evolution, and to fill (partially) the gaps in the knowledge of crustal necking processes. Moreover, more specific questions concerning the evolution of the Mont-Blanc massif and its role during collision are raised:

- **What controls the preservation of some parts of the fossil-rifted margin?**
- **Where are the necking domains best preserved in orogens?**
- **What is the P-T-t pre-Alpine evolution of the Mont-Blanc basement?**
- **What is the role of the rift architecture on the Alpine reactivation?**

The occurrence of fossil necking domains in orogens remains poorly understood. However, their role in the evolution of the orogen might be significant. The reactivation of the necking domain might be the **missing link** to understand the transition between subduction and continental collision explaining the localisation of the deformation in the crust. The necking domain corresponds, by definition, to a crustal taper that can act, during convergence, as a **buttress**. Additionally, necking zones host significant ore deposits, mostly linked to **Pb-Zn-Ba-F mineralizations**. The recognition of necking domains might therefore be a way to predict the occurrence of **ore deposits of economic importance**.

To answer the questions listed above, the work was initially focused on the Col du Bonhomme area where the detachment fault and its sedimentary cover have been previously described (Ribes et al. 2020). Firstly, it was necessary to carefully characterize the contact to better constrain the age and kinematics of the fault zone. To achieve this, mapping of the fault zone associated to structural and microstructural observations on the fault and the cover were realized. This work was complemented by the petrological characterization of the fault zone based on observations and associated to image processing to obtain the evolution of the grain size across the fault. In addition, the Alpine peak temperature in the Col du Bonhomme was determined using Raman Spectrometry on carbonaceous matter (RSCM) on the Aalenian shales and was coupled to structural observations on the Alpine deformation to constrain the Alpine overprint of the rift-inherited contacts. Secondly, geochemical characterization of the fault zone allowed to constrain the fluid circulations associated to the detachment fault. Composition in major, trace element and REE were obtained on bulk fault rock samples associated to μ XRD and EPMA chemical mapping of the fault rocks to highlight chemical changes at a microscale associated to deformation. Mass balance calculations were then realised to evidence element gains and losses between the host rocks and the fault zone. Fluid inclusion analysis on veins in the fault zone based on micro-thermometry analysis and Raman spectrometry on the inclusion was done to obtain more information on the type of fluids along the fault. In addition, Ar-Ar

dating of the hyalophane in the veins and U-Pb dating of calcite from the damage zone were attempted to date the fault zone.

A similar approach was then applied to the northern part of the massif (Val Ferret) to see if the detachment observed in the Col du Bonhomme can be prolonged to the north. This work is based on structural, micro structural and petrological observations associated to chemical analysis of fault rocks found in this area. Similarly, the RSCM data were obtained in this area to constrain the Alpine peak temperature. Compilation of sedimentary sections throughout the Helvetic domain associated to new observations on the syn-rift sediments from the internal Mont-Blanc massif provide an insight on the stratigraphic evolution during crustal necking. Finally, a model of fluid circulations during crustal necking based on the observations from the detachment fault and the cover is proposed linking fluid circulations in the basement to pre-Alpine ore deposit in the internal Mont-Blanc massif.

Introduction (Fr)

Les **marges passives** sont un des environnements tectoniques les plus communs sur Terre formant la transition entre une lithosphère océanique et continentale. Le concept fondamental pour comprendre l'évolution d'une marge au cours du temps est le **cycle de Wilson** (Wilson, 1966). En effet, les marges jouent un rôle primordial dans ce cycle étant le lieu de naissance (rifting) et de disparition des domaines océaniques (initiation des subductions). L'étape finale de la fermeture d'un domaine océanique est la collision continentale menant à l'incorporation de la marge dans l'orogène en formation. Certaines parties de la marge peuvent être partiellement préservées. L'étude des marges est fondamentale afin de mieux comprendre les processus associés au rifting et à l'océanisation et également afin de prédire l'occurrence de **ressources naturelles**. En effet, les marges fournissent la plupart des ressources en hydrocarbure et certains des plus gros gisements en métaux (Levell et al., 2010 ; Nemčok (2016) ; Arndt et al., 2017). Durant les dernières décennies, d'importants progrès ont été réalisés dans la compréhension des marges au travers de l'observation des marges actuelles (lignes sismiques, relevés gravimétriques et magnétiques, données de forages; De Charpal et al., 1978; Boillot et al., 1987; Whitmarsh et al., 2001a; Sutra et al., 2013; Sapin et al., 2021), l'étude de terrain sur les marges et rifts fossiles (e.g., les Alpes et les Pyrénées : Lemoine et al., 1981; Lemoine and Trümpy, 1987; Manatschal, 1999 ; Chevalier et al., 2003; Lagabrielle et al., 2010; Mohn et al., 2011, 2014; Tugend et al., 2015; Clerc et al., 2016 ; Ribes et al., 2019c; Lescoutre and Manatschal, 2020; Ducoux et al., 2021; Saspiturry et al., 2021) et la modélisation numérique (Huisman and Beaumont, 2003; Huisman and Beaumont, 2011; Duretz et al., 2016; Brune, 2018; Lescoutre et al., 2019; Chenin et al., 2020; Lescoutre et al., 2019). Ces travaux approfondis ont permis de distinguer plusieurs types de marges (e.g., magmatique et amagmatique, orthogonal et oblique) ainsi que leurs mécanismes de formation.

Ce manuscrit se concentre sur les **marges amagmatiques** qui représentent une part importante des marges passives dans le monde. L'évolution de ces marges apparaît **polyphasée** (Péron-Pinvidic et al., 2013), chaque étape étant caractérisée par une évolution tectono-stratigraphique particulière et une signature géochimique spécifique (Sutra and Manatschal, 2012, Tugend et al., 2015; Pinto et al., 2015, Incerpi et al., 2017; Ribes et al., 2019b; Barale et al., 2021). L'initiation du rift est associée à la **phase d'étirement** qui correspond à une extension mineure et un fort découplage entre la croûte supérieure et inférieure (Sutra and Manatschal, 2012). Cette étape est suivie par la **phase d'amincissement crustal** qui correspond à la localisation de la déformation en réponse à la rupture de la couche la plus compétente de la lithosphère (Sutra and Manatschal, 2012; Chenin et al., 2018). Cette localisation de la déformation amène finalement au couplage entre la croûte supérieure et inférieure. Cela permet l'**hyperextension** de la croûte jusqu'à **exhumation du manteau** (Sutra and

Manatschal, 2012). Les phases d'extension, d'hyperextension et d'exhumation du manteau ont été étudiées en détail permettant une bonne compréhension de l'évolution tectonique, sédimentaire et géochimiques de ces domaines. Cependant la phase d'amincissement crustal reste relativement peu comprise malgré son rôle clé durant le rifting. Les marges actuelles permettent d'obtenir des informations sur la structure des domaines d'amincissement ainsi que sur les structures sédimentaires associées (Osmundsen and Péron-Pinvidic (2018), Muñoz-Barrera et al., (2021). Les modèles numériques quant à eux permettent de contraindre l'évolution de la température et de la topographie durant l'amincissement (Chenin et al., (2018, 2019a), Petri et al., (2019), Duretz et al., (2016)). Néanmoins, l'évolution à plus petite échelle reste peu contrainte notamment à cause du manque d'analogues fossiles de domaines d'amincissement. **L'évolution stratigraphique** ainsi que les **fluides associés** à l'amincissement crustal restent donc peu compris. Les questions clés concernant les domaines d'amincissement sont :

- **Quelle est l'évolution sédimentaire syn et post-rift d'un domaine d'amincissement crustal ?**
- **Quelle est la signature stratigraphique de l'amincissement crustal ?**
- **Est-ce que l'amincissement crustal est un environnement propice pour des circulations hydrothermales ?**
- **Si c'est le cas, quel type de fluides et quel transfert d'éléments sont associés à cet événement ?**
- **Il y a-t-il une signature géochimique caractéristique de l'amincissement crustal ?**
- **Ces circulations sont-elles associées à des minéralisations ?**

Les **Alpes** correspondent à un **domaine océanique** jurassique inversé depuis le **Crétacé supérieur**. Des lambeaux de l'ancienne marge sont préservés dans les parties externes et internes des Alpes. Ces morceaux de la marge jurassique correspondent principalement à des héli-graben provenant du domaine proximal (Lemoine et al., (1981), Barfety and Gidon (1984)). La partie distale est préservée principalement dans le rétro wedge ou des failles de détachements extensifs jurassiques ont été identifiées. Le domaine d'amincissement de la marge Adriatique est préservé. En effet, une faille de détachement d'âge jurassique affectant la croûte supérieure y est observée. Du côté européen, il a été proposé que les **massifs cristallins externes** (External Crystalline Massifs ou ECM) correspondent à cet ancien domaine d'amincissement (Mohn et al., 2014). Les ECM se trouvent à la transition entre les domaines externes et internes des Alpes et forment aujourd'hui les plus hauts sommets des Alpes. Dans ces ECM et plus spécifiquement dans le massif du Mont-Blanc, la couverture sédimentaire syn-rift présente certaines particularités qui restent inexplicables (Saussure, 1779; Landry; 1976, Eltchaninoff-Lancelot et al., 1982 ; Epard, 1989). En effet, il s'agit de

dépôts clastiques (« **Grès Singuliers** ») qui ne se retrouvent à aucun autre endroit dans la marge fossile. Ils apparaissent déconnectés de toute sources continentales et indiquent la présence d'une source locale. Il a été proposé que ces grès correspondent à la **signature stratigraphique de l'amincissement crustal** et se seraient déposés en réponse à l'exhumation du socle par une **faille de détachement** (Ribes et al., 2020). Le but de ce manuscrit est d'utiliser le Mont-Blanc comme un analogue fossile des domaines d'amincissement dans les marges dans le but de comprendre l'évolution stratigraphique et les circulations fluides associées à l'amincissement crustal. De plus, cela soulève des questions concernant l'évolution du massif du Mont-Blanc et son rôle durant la collision :

- **Qu'est ce qui contrôle la préservation de certaines parties de la marge fossile ?**
- **Où les domaines d'amincissement sont-ils le mieux préservés dans un orogène ?**
- **Quelle est l'évolution P-T-t préalpine du Mont-Blanc ?**
- **Quelle est le rôle des structures préalpines durant la collision ?**

La reconnaissance des domaines d'amincissement fossiles dans les orogènes restent peu répandu. Cependant leur rôle dans l'évolution orogénique semble très important. La réactivation de ces domaines en compressions semble être le lien manquant entre la subduction et la collision continentale expliquant ainsi la localisation de la déformation dans la croûte. Le domaine d'amincissement de la croûte joue le rôle de **butoir** lors de la collision avant propagation de la déformation vers le continent. De plus ces domaines de la marge apparaissent prometteurs en termes de minéralisations et plus particulièrement pour les gisements **Pb-Zn-Ba-F**. La reconnaissance de ces domaines pourrait dès lors permettre de prédire la position de gisements **d'importance économique**.

Afin de répondre à ces questions, le travail c'est principalement concentré sur le Col du Bonhomme où la faille de détachement et sa couverture ont été décrit. Il a tout d'abord été nécessaire de décrire plus en détail ce contact majeur afin de contraindre son âge et sa cinématique. Dans ce but, une cartographie de la zone de faille associé à des relevés structuraux et microstructuraux ont été réalisés. Ce travail est associé à une caractérisation pétrographique basée sur l'observation des paragenèses et du traitement d'image afin de d'obtenir l'évolution de la répartition de la taille des grains le long de faille. De plus, la température du pic métamorphique alpin a été mesurée n'utilisant la spectroscopie Raman sur matière carbonée provenant des schiste Aalénien combinées à des observations structurales sur la déformation alpine dans la zone. Cela dans le but de comprendre l'impact de la phase alpine sur le détachement. Dans un second temps, une caractérisation géochimique de la zone de faille a été réalisé afin de comprendre les circulations fluides le long de la faille. La composition chimique en éléments majeurs, trace et terres rares des roches de failles combinées à à de la cartographie chimique μ XRF et EPMA

afin de mettre en évidence les transformations minéralogiques et les changements chimiques associées à la déformation. Des calculs de bilans de masses ont été également effectués à partir des compositions des roches de failles et de son encaissant afin de mettre en évidence les gains et pertes en éléments le long de la faille. L'étude des inclusions fluides basé sur la microthermométrie et la spectrométrie Raman des veines trouvées dans la zone de faille a permis d'obtenir plus d'informations sur les types de fluides ayant circulés le long de la faille. De plus des datations Ar-Ar sur hyalophane dans les veines ont été effectués afin de mieux contraindre l'âge de la faille.

Une approche similaire a été appliquée dans la partie nord du massif (Val Ferret) afin de voir si le détachement se prolonge plus au nord. Ce travail est basé sur des relevés structuraux et des observations pétrologiques ainsi qu'une caractérisation géochimique des roches de failles. De façon similaire, des données RSCM ont été acquises afin de mieux contraindre les températures alpines dans la zone. La compilation de relevés sédimentaires dans le domaine helvétique associée à de nouvelles observations sur la couverture sédimentaires du Mont-Blanc fournit un aperçu de l'évolution stratigraphique associé à l'amincissement crustal. Enfin, un modèle de circulation de fluides associés aux observations sur le détachement et la couverture est proposé permettant de faire le lien entre les circulations dans le socle et les minéralisations autour du Mont-Blanc.

Outline of the thesis

The first chapter (**General concepts concerning the Wilson cycle and rifted margins**) will present concepts explaining the evolution of rifted margins through time and their importance in the Wilson cycle including the fate of fluids. Second, a focus is made on the evolution of magma-poor margins (Atlantic-type margins) presenting the stratigraphic and tectonic characteristics of the proximal and distal domains based on observations from present-day margins (e.g., Iberia-Newfoundland conjugated margins) and fossil rifted margins (e.g., the Alps). The evolution of necking domains, which are the topic of this work, is presented in detail. Finally, concepts associated to fluid circulations along detachment faults are introduced.

The second chapter (**From rifting to orogeny, concepts developed in the Alps over a century**) presents the Alpine orogenic evolution. The first part concerns the link between the Alpine and Jurassic rift-related palaeogeography and the present-day Alpine tectonic units. An historical perspective showing the evolution of the concepts through time is also proposed. The second part is focused on the Alpine orogen with a first, large-scale description of the Alps before focussing on the Western Alps and more specifically to the External Crystalline massifs.

The third chapter (**Structural and petrological characteristics of a Jurassic detachment fault from the Mont-Blanc massif (Col du Bonhomme area, France)**) focuses on the southern Mont-Blanc, where Ribes et al., (2020) described the Grès Singuliers associated to an extensional detachment fault. This chapter presents new observations of the Mont-Blanc detachment fault described in the Col du Bonhomme (Southern Mont-Blanc) area in order to constrain its extension and evolution through time. The relation between the syn-rift sediments and the exhumed surface are described in detail providing relative age constraints of the detachment fault. The microstructural and petrological evolution is detailed to highlight the main mechanisms of deformation. The impact of the Alpine collision on the Jurassic detachment fault in term of deformation and thermal overprint is discussed. This work was published in the Journal of Structural Geology (Dall'Asta et al., 2022).

The fourth chapter (**Multiscale element transfer during crustal necking: the Mont-Blanc detachment fault**) is focused on the geochemical evolution of the detachment fault. The goal is to identify element transfer along the necking related detachment fault, and to describe the associated properties of the fluids during deformation. This work is based on chemical mapping, mass balance calculations, fluid inclusions in veins as well as geochronology (Ar-Ar on hyalophanes). This chapter is presented under the form of an article in preparation.

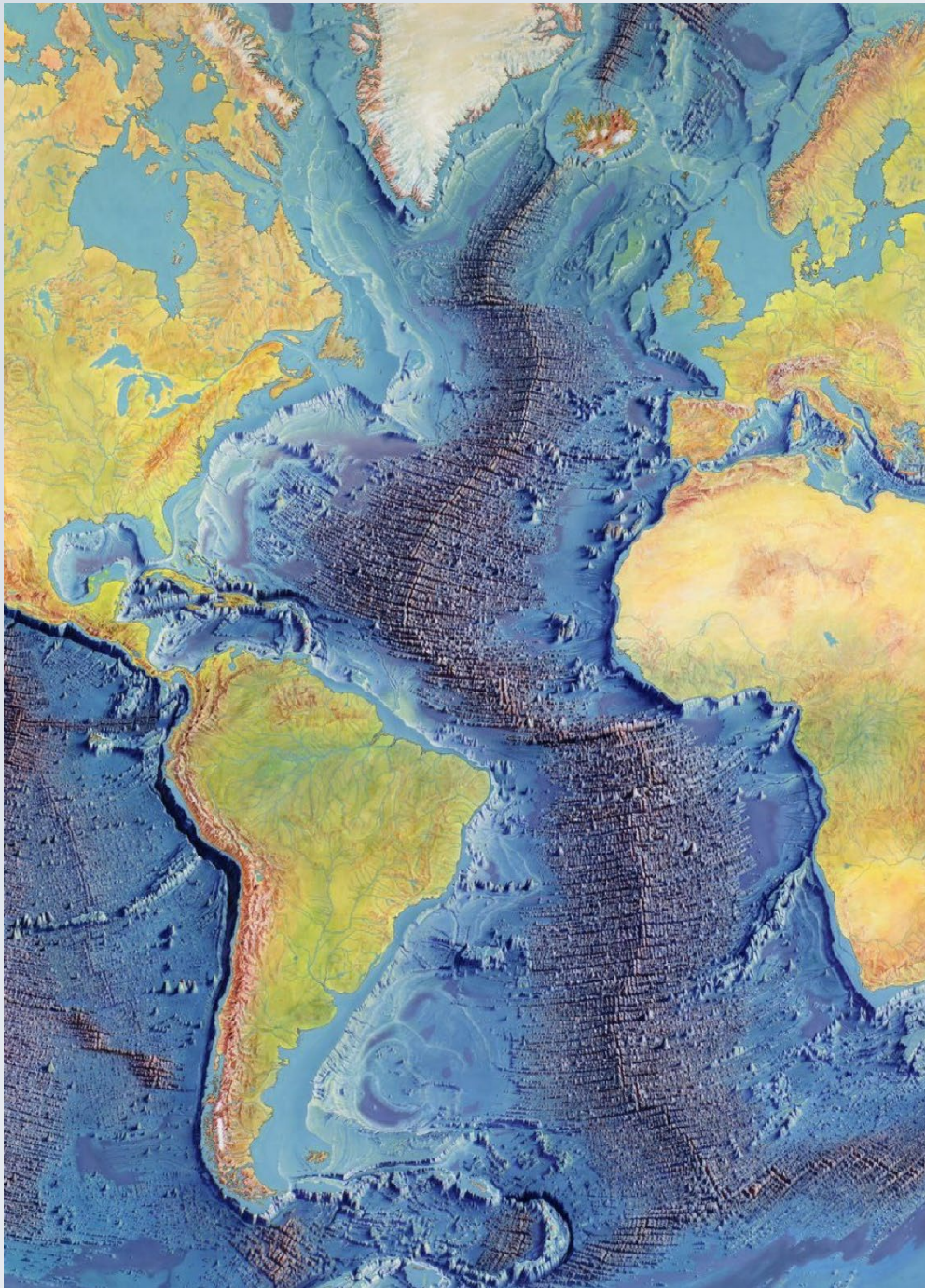
The fifth chapter (**Preserved Jurassic Structures in the Northern Mont-Blanc massif (Val Ferret, Switzerland)**) provides observations of the syn-rift sedimentary evolution as well as the top basement structure in the Val Ferret, to characterize better the prolongation toward the north of the Mont-Blanc detachment fault.

The sixth chapter (**Large-scale evolution of the Jurassic necking domain of the Alpine Tethys**) presents a compilation of sedimentary sections around the Mont-Blanc and Aar to understand better the sedimentary evolution associated to crustal necking. These sections have been correlated across the margin and along the necking domain. The eustatic evolution during the early Jurassic has been reconstructed to isolate large scale sea-level variations in the Western Tethys from local tectonic variations. Finally, paleogeographic reconstructions are presented to illustrate the Mont-Blanc evolution during rifting.

The seventh chapter (**Linking ore deposits to crustal necking: Insight from the Western Alps**) synthesizes the previous structural observations, stratigraphic data, and findings about the fluids along the detachment fault in order to present a model of fluid circulation in necking domains. An additional goal is to integrate the ore deposits found in the cover of the Mont-Blanc massif, in a scenario of crustal necking. The chapter is written under the form of a manuscript in preparation.

The last chapter (**Discussion, Perspectives and Conclusions**) discusses the different aspects tackled in this manuscript. First, a summary of the results is proposed. It is followed by several propositions of further work that can be done to better constrain the Mont-Blanc fossil necking domain. These results are also discussed on a more general perspective regarding the criteria used to recognize necking domains in fossil and present-day margins, the reactivation of necking domains in orogens and the fluid circulation related to crustal necking. Finally, a discussion concerning the importance of rifted margins in the formation of large ore deposits and more specifically elements with economic importance. A review of possible necking related deposits worldwide is proposed to emphasize the role played by the crustal necking in ore formation.

Chapter I- General concepts related to the Wilson cycle and rifted margins



Manuscript painting of Heezen-Tharp "World Ocean floor" map by Berann (1977)

« Je ne savais pas alors que, tôt ou tard, l'océan du temps nous rend les souvenirs que nous y avons enfouis. » (Marina, Carlos Luis Zafon)

Foreword

This introductory chapter briefly presents the different key aspects discussed in this manuscript and related to fossil rifted margins preserved in collisional orogens. First, the links between orogens and rifted margins are briefly discussed in the light of the Wilson cycle. This is followed by a summary of the concepts associated to rifted margins from the early 20th century up to present. Secondly, the magma-poor Atlantic-type margin model will be discussed in detail presenting the characteristics of the proximal and distal domain of magma-poor rifted margins. The section will particularly emphasize the importance of the transition domain between the proximal and distal margins corresponding to the lesser-known necking domain. This necking domain has been recognized only recently and remains yet poorly understood. One of the main questions concerns the dynamics of fluid circulation associated to crustal necking. Therefore, the third part of this introduction concerns fluid circulation along detachment faults, which correspond to important fluid pathways toward the surface or seafloor.

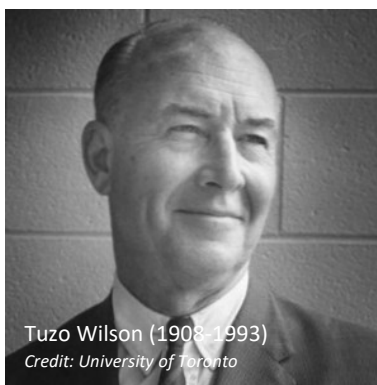
Introduction

Rifted margins form the transition between the continental and oceanic lithosphere and have been identified more than a century ago. They attracted a lot of attention because of the occurrence of resources mostly associated to hydrocarbons exploration. Decades of studies on rifted margins associated to the progress in geophysical imaging enabled to unravel their architecture and evolution. These discoveries demonstrated the existence of two main types of margins, magma-rich and magma-poor and allowed to propose physical models explaining crustal thinning. More specifically, in magma-poor margins, the different rift stages (stretching, necking, hyperextension and mantle exhumation) have been identified and associated to different thermo-mechanical conditions and fluid signatures.

1. From rifting to collision

1.1. The Wilson cycle: A keystone to understand the rift to collision evolution

After 50 years of intense debates regarding the existence of continental drift (Wegener 1922), the progressive acceptance of the concept of plate tectonics in the mid 60's including the concept of mantle convection (Dietz, 1961; Hess et al., 1962), the recognition of magnetic anomalies (Vine, 1966; Heirtzler et al., 1968 ; Le Pichon and Heirtzler, 1968) and the mapping of mid-oceanic ridges by Heezen and Tharp (1965) led to a change of paradigm. In complement, a mechanism to explain the consumption of the oceanic lithosphere was provided through the discovery of the Wadati-Benioff plane (Wadati, 1935; Benioff, 1949). Its interpretation as the result of a subducting oceanic lithosphere (Oliver and Isacks, 1967) became a major building block of the plate tectonic model. The knowledge that oceans can appear and disappear throughout the Earth history had a major impact on the geoscientist community and changed the interpretation of basin and mountain formation.



Tuzo Wilson (1908-1993)
Credit: University of Toronto

Opening of the North-Atlantic as mentioned by Wilson et al., (2019) was already proposed by various authors such as Wegener (1922), Argand (1924), Du Toit (1937) and more recently Bullard et al., (1965) and Le Pichon et al., (1977). On the other hand, new ideas concerning orogenic processes were also proposed in the Alps. An embryonic model of the formation of

orogens was proposed by Argand (1916) through closure of marine basins (geosynclines) by nappe stacking. The idea was further developed by Choubert (1935) who proposed formation of orogens through collision of cratons. However the link between orogenic processes and plate tectonics was made by Tuzo Wilson in a paper with a thought provoking name, “DID THE ATLANTIC CLOSE AND THEN RE-OPEN?” (Wilson, 1966) in which he recognized the presence of a Cambro-Ordovician Ocean (Iapetus ocean) which closed during Cambrian leading to the formation of a common ‘Atlantic’ faunal realm between Europe and America, preceding the opening of the North Atlantic. This enabled Wilson to suggest multiple cycles of opening and closing of oceans through time. This work was then continued leading to a deeper understanding of the different stages of opening and closing of oceanic basins through time (Wilson, 1968) from an embryonic rift to a mature ocean followed by the thermal equilibration and then subduction of the oceanic lithosphere followed by the onset of collision and formation of mountain belts (Fig. I.1).

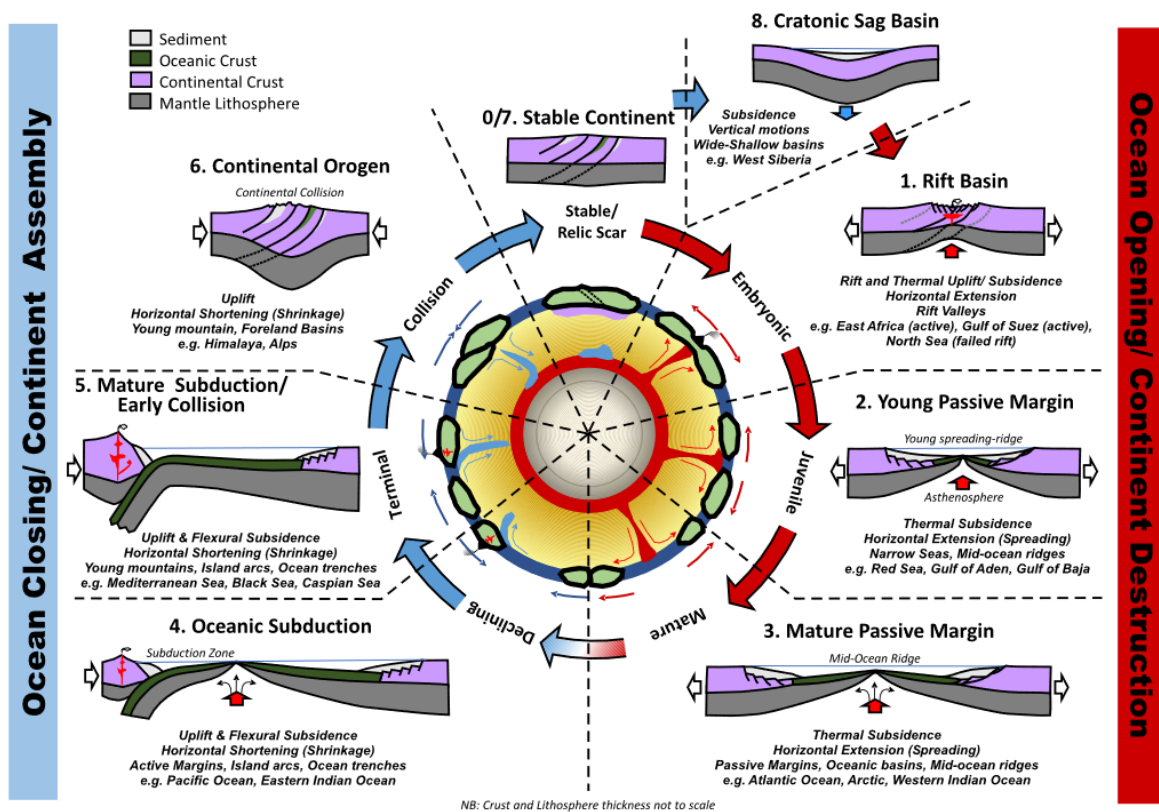


Figure I.1: Illustration of the Wilson cycle from ocean opening to ocean closing and continent assembly (from Wilson et al., 2019) describing the different stages defined by Wilson (1968).

The concept of the “Wilson cycle” was widely accepted by the community. Oceanic sutures started to be recognized in orogens worldwide (Burke et al., 1977). New mechanisms of rift initiation and their link with hot spots were proposed in regard to the Wilson cycle (Dewey and Burke, 1974). Progressively, the Wilson cycle gained a broader definition and was associated to continental amalgamation and break up (Wilson et al., 2019). As highlighted by Wilson et al. (2019),

supercontinent evolution (Nance et al., 2014) and the Wilson cycle became synonyms although they describe phenomena at different temporal and spatial scales.

Even if the embryonic plate tectonic model from Argand (1924) was derived from observations in the Alps, Alpine geologists expressed reserves regarding the newly evolving ideas of the plate tectonic theory (see Trümpy, 2001; Schaer, 2011). Despite these first reluctances, the acceptance of plate tectonics by Alpine geologists, integrating structural, stratigraphic, and geophysical data, was realized giving fruitful new interpretations (Schaer, 2011), and leading to propose of the subduction of the Liguro-Piemont domain (Boccaletti et al., 1971; Hawkesworth et al., 1975; Dewey et al., 1973; Frisch, 1979). Finally, increasing knowledge of passive margins led to the identification of remnants of Jurassic margins in the Alps (Trümpy, 1975; Lemoine et al., 1986).

Sixty years after the proposal of the Wilson cycle, significant progress was achieved on the knowledge of both rifted margins and orogenic belts. The identification of inverted rifts led to the definition of aborted Wilson cycles. The recognition of various types of margins with different sizes, thermal histories, magmatic budgets highlighted the importance of the pre-rift collisional inheritance (Chenin et al., 2019c). On the other hand, the margin architecture and the size of the oceanic domain appear to control the orogenic architecture (Chenin et al., 2017). These findings led to revisit the definition of subduction (Benioff-type oceanic subduction vs Ampferer-type continental subduction; McCarthy et al., 2020; Chelle-Michou et al., 2022), and to introduce intermediary stages in the Wilson cycle. Nevertheless, important questions remain such as the role played by inheritance during rifting and collision. In that perspective, the Alps, with about 300 years of ongoing research remain an incredible laboratory for testing new ideas on rifting and orogenic processes in the light of the Wilson cycle.

1.2. Rifted margins: A century of research and new evolving concepts

1.2.1. What is a rifted margin?

Margins are, at a first order, the locations bridging the continental and oceanic lithospheres. They usually correspond to “**offshore zones consisting the continental shelf, slope, and abyssal plane**” (Collins dictionary). They are divided into tectonically active (35% of the margins, Fig. 1.2) and passive margins (65% of the margins; Harris et al., 2014). They are also characterized by different geomorphological features such as the width of the shelf or the presence of rises and trenches (Fig. 1.2B; Shepard et al., 1963). Rifted (passive) margins correspond to the transition between oceanic crust and continental crust with different densities and thickness (7 km for the oceanic crust and a tapering crust (from 30+/-5 km to zero) as a result of the progressive thinning of the continent due to large-scale motion of continents

General concepts related to the Wilson cycle and rifted margins

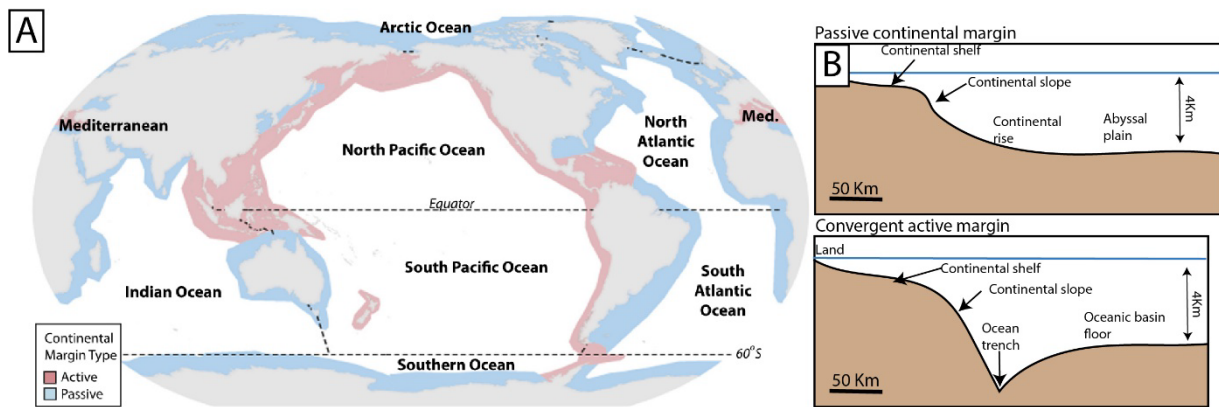


Figure 1.2: Map showing the repartition of the active and passive margins worldwide (from Harris et al., 2014). B- Schematic bathymetric profiles for passive and active margins (from Harris et al., 2014).

Rifted margins have been studied for more than a century and various models for their formation had been proposed (Bond and Kominz, 1988; Boillot, 2012) following the main scientific theory of their time.

1.2.2. Evolution of the concepts through time

1.2.2.1. Precursors of the rifted model: the geosyncline theory (1860-1960)

As the result of worldwide geological exploration at the end of the 19th century (Suess, 1904) identified 2 types of margins named “Atlantic coast” and “Pacific coast” corresponding to the modern passive and active margins. This distinction was based on characteristic features such as seismicity, magmatic activity, and topography of the coast. Moreover, the concept of geosyncline was proposed to explain the local accumulation of sediments in basins, and continental margins (Lemoine, 2006). It corresponds in fact to a basinal area surrounded by topographic highs forming the margins of the basins. It was first introduced by de Beaumont and Brongniart (1828) to explain accumulation of pelagic sediments in the Alps. This concept was later reused and popularized by Dana (1873) and Hall (1882) and referred to as the “geosyncline”. Following these initial works, mapping of structures in orogens allowed Haug (1900) to propose a first description of the repartition of Mesozoic basins worldwide. Concerning continental margins, they were interpreted first as geosynclines filled with thick sedimentary successions derived from the adjacent continental areas.

The recognition of ophiolites in geosynclines in orogens, which was difficult to explain at that time, led to the distinction between miogeosyncline (with ophiolites) and eugeosyncline (without ophiolites). The composition of the Alpine-type ophiolites (serpentinites, diabases, radiolarites) was described precisely in the Central Alps by Steinmann (1905). It was accepted that the ophiolites were part of a large geoanticline separating two geosynclines (Aubouin, 1961). The description of magmatic intrusions forming a topographic high dividing the two geosynclines reminds the position

General concepts related to the Wilson cycle and rifted margins

of the mid-oceanic ridges described during the second half of the 20th century in present-day oceans.

Most of the characteristics of modern rifted margins such as the crustal taper, sedimentary architecture and topographic highs were already known at the beginning of the 20th century. The dynamics of these basins were well characterized even if the mechanisms behind this evolution was yet little understood. A lack of knowledge concerning the oceanic crust composition led to a miscomprehension of the origin of ophiolite units. The revolution of plate tectonics associated to the new discoveries from the continental margin and oceanic crust led progressively to the abandonment of the concept of geosyncline during the late 60's.

1.2.2.2. The plate tectonic revolution (1960's-1980's)

The plate tectonic theory was a game changer for the understanding of rifted margins, as it provided a mechanism for rifting and formation of oceanic crust through seafloor spreading. Most of the work was done initially on the proximal parts of margins, which focused the attention due to their economic significance in term of hydrocarbon exploration (Peron-Pinvidic et al., 2019). Fewer attention was drawn on the more distal parts of the margin. As a result, the nature of the transition between continental and oceanic crusts remained unclear and a similar geometry was postulated for the proximal and distal parts of margins. Crustal thinning was achieved through high-angle normal faults, leading to a succession of tilted blocks until the oceanic crust.

1.2.2.3. McKenzie vs Wernicke model (1970's-1980's)

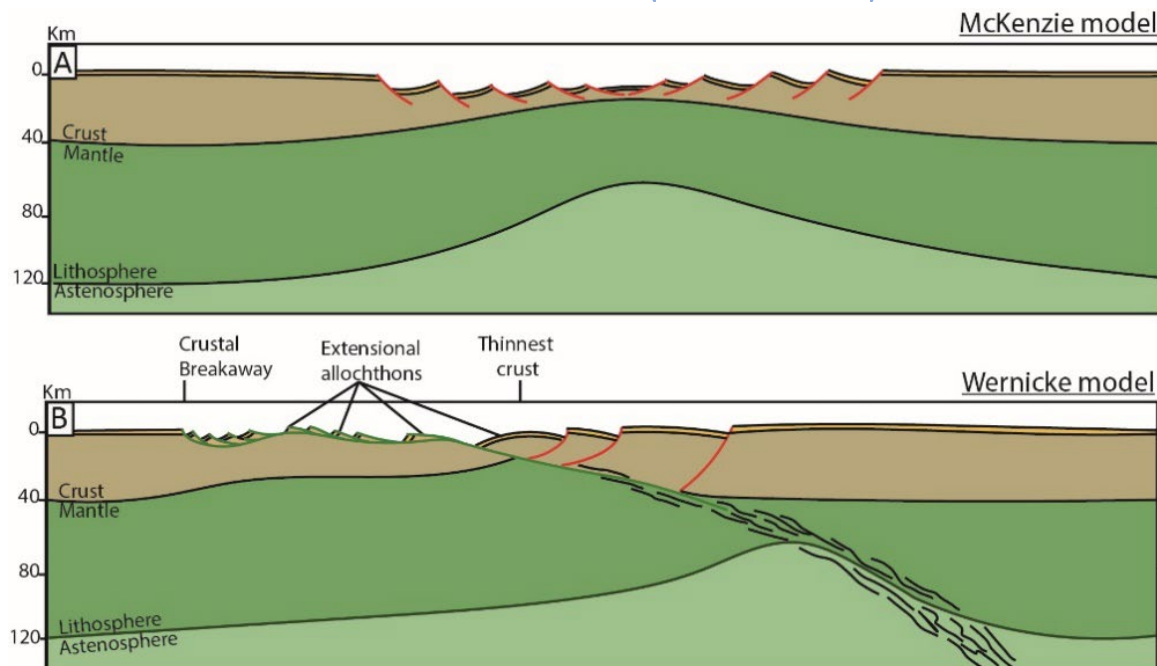


Figure 1.3: A-McKenzie model, also referred to as pure shear (symmetric) or depth uniform rift model. B-Wernicke or lithospheric simple-shear rift model showing a strongly asymmetric rifting with a lithospheric scale detachment fault (modified from Wernicke, 1985).

Different modes of extension were proposed to explain the formation of rifted margins. A first model assuming pure-shear deformation at a lithospheric and crustal scale is known as the McKenzie model (Fig. 1.3A). This model, proposed by McKenzie (1978), explained the observed important post-rift subsidence in the North-Sea as the result of thermal equilibration of the lithosphere post-dating the rift event. Important extension (high β) leads to high thermal gradients in response to asthenosphere uplift and is followed by major thermal subsidence. The rise of the asthenosphere during rifting can also explain melt formation through mantle decompression (White et al., 1987) and the progressive increase of magmatic activity as a function of increasing β -values during rift.

However, observations from the Basin and Range (USA) led to a different model. Indeed, in this area extension was accommodated by low-angle detachment faults. The fault initiated as rolling hinge faults. The large offset on the faults lead ultimately to fault flattening toward the surface due to isostatic rebound (Wernicke and Axen, 1988). The observations of long-offset extensional detachment faults inspired Wernicke (1985) to propose the so-called Wernicke-model (Fig. 1.3B) that assumed that rifting was accommodated by simple-shear deformation at a lithospheric scale. In this type of rift model, rift systems are profoundly asymmetric. In the footwall, the top basement corresponds to exhumed fault zones exhuming deep parts of the crust and mantle, while the hanging wall appears relatively undeformed (Lister et al., 1986).

An everlasting debate followed regarding the type of deformation occurring during rifting. The two models lead to significant differences in the evolution of subsidence and melt production during rifting (Buck et al., 1988; Latin and White, 1990). It was proposed that the North Sea was formed by pure-shear deformation (Klemperer, 1988) while other rift systems like the Red Sea (Voggenreiter et al., 1988) and fossil rifted margins such the Alpine Tethys (Lemoine et al., 1987; Favre and Stampfli, 1992) were formed by lithospheric simple-shear deformation.

However, new observations from rifted margins showed that the reality was probably a combination of both models (Mutter and Larson, 1989; Nissen et al., 1995). Models combining pure-shear and simple shear were summarized by Lister et al., (1991). They combined pure-shear deformation in the lithospheric mantle and in the lower crust with simple-shear associated to a detachment fault in the crust (Coward, 1986). These models of differential stretching lead to different thermal evolutions and therefore different amounts of subsidence and uplift. Indeed, Uniform stretching of the lithosphere leads to larger net subsidence while the presence of crustal detachment and pure shear lithospheric deformation leads to less net subsidence.

1.2.2.4. Magma-rich vs magma poor margins (1990's and 2000's)

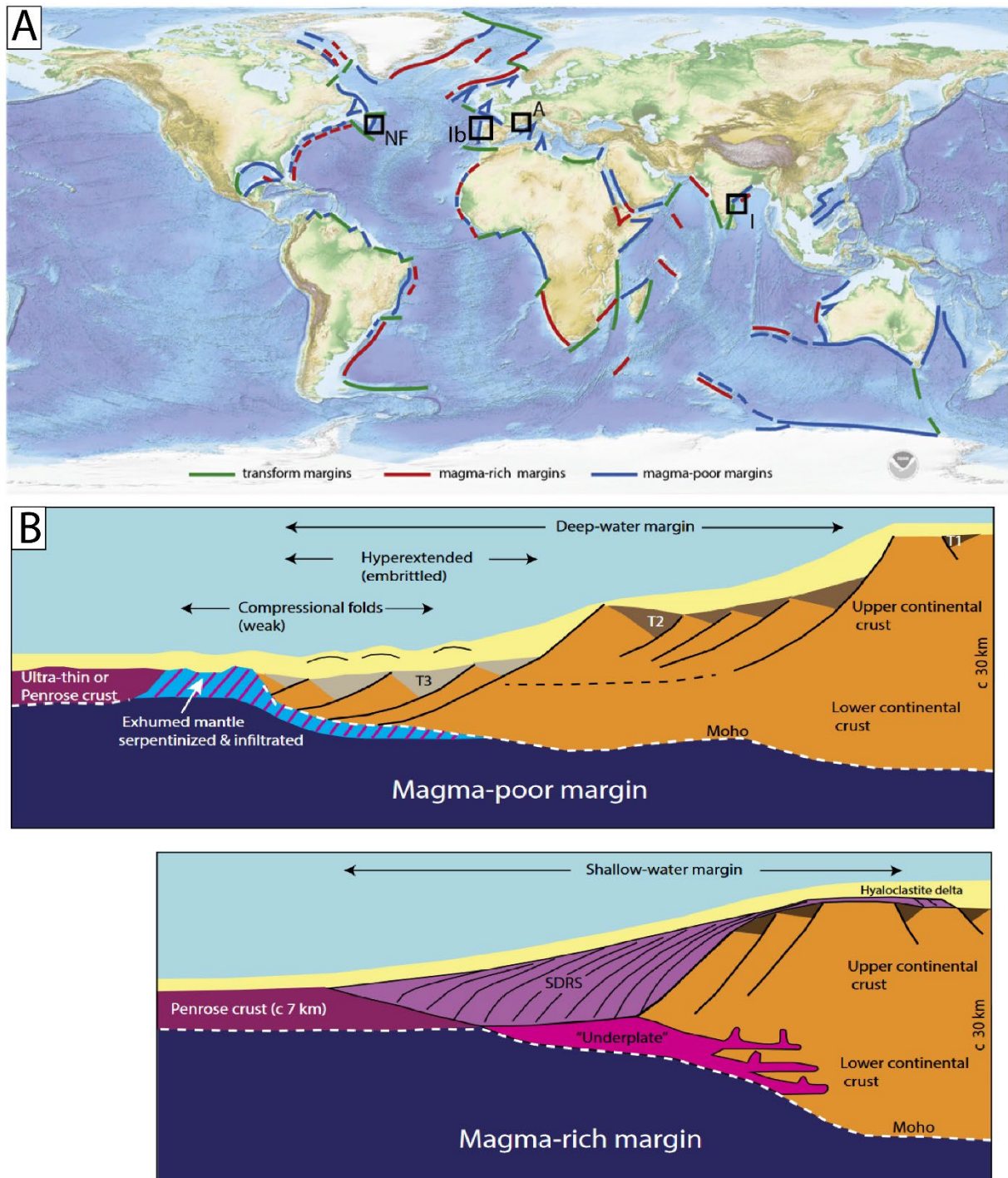


Figure 1.4: A- Map of the distribution of the magma-poor, magma-rich and transform margins (from Haupert et al., 2016). B- Schematic section of a magma-rich and poor margins (from Doré and Lundin, 2015). The magma-poor margins are characterized by the presence of a hyper-thinned crust and exhumed mantle. Magma-rich margins are characterized by the presence of Seaward Dipping Reflectors (SDR).

A distinction started to appear around the late 80's in the classification of margins. It appeared that some margins such as the Norwegian-Greenland conjugated margins are formed in their distal part by huge volcano-clastic successions located at the transition between the continental crust and the oceanic crust. These volcanic deposits are characterised by Seaward Dipping Reflectors

(SDR; Fig. 1.4B). On the contrary, other margins (e.g., Bay of Biscay and Newfoundland-Iberia; Boillot et al., 1987) show no volcanic successions and a continent-ocean transition formed by thinned to hyper-thinned continental crust and exhumed mantle (Fig. 1.4B). These observations led Mutter et al., (1988) and White and McKenzie (1989) to classify the margins into 2 categories, the volcanic margins and the non-volcanic margins (Fig. 4A). According to Mutter et al., (1988), magma is formed through “convective partial melting” related to thermal increase associated to asthenosphere uplift. Initial melts are produced by partial melting of the lithospheric mantle, followed by decompression melting of the asthenosphere (tholeiites). Convective cells in the rising asthenosphere develop because of strong lateral thermal gradients related to lithospheric breakup. White et al., (1987) and Mutter et al., (1988) proposed that volcanic margins are associated with pure-shear deformation, while simple shear-dominated margins would not create vigorous convection nor produce important melt. They therefore related the deformation mechanism to the magmatic budget. Due to a different thermal history, subsidence would vary greatly between volcanic and non-volcanic margins.

As mentioned by Tugend et al., (2020) this duality between volcanic and non-volcanic rifting started to erode due to the recognition of magmatism in so-called non-volcanic margins (e.g., the Alpine-Tehys fossil rifted margins (Desmurs et al., 2002) and Iberia margin (Whitmarsh et al., 2001b)). At present, it is well shown that all rifted margins, including those where mantle is exhumed, are linked to the formation of magmatism during rifting. This is not surprising as the end of rifting is marked by the onset of seafloor spreading and hence, magmatic activity. A change in terminology from volcanic vs non-volcanic to magma-rich vs magma-poor was therefore proposed to consider these new observations (Peron-Pinvidic et al., 2013). Magma-rich margins are recognized through key characteristics such as the presence of SDR, of dense lower crustal bodies, and of relatively shallow marine syn-rift sediments (Fig. 1.4B; Franke, 2013). In contrast, magma-poor margins are characterised by an extreme crustal thinning and deep water sediments (Fig. 1.4B; Doré and Lundin, 2015). The diversity of margins reflects various magmatic budgets during rifting, before break up (Tugend et al., 2020). These variations question the simple link between extension (β) and magmatic budget proposed by White and McKenzie (1989) in their depth-uniform McKenzie model.

1.2.2.5. New concepts in rifted margins (2010's)

The significant improvement of the quality of the seismic images of present-day rifted margins as well as the recognition of remnants of fossil rifted margins in mountain belts led to an important progress on the comprehension of the rifting evolution through time. This enables a more accurate description of morphological features of rifted margins such as marginal highs, platforms, terraces, continental ribbons and microcontinents (Table 1.1; Peron-Pinvidic and Manatschal, 2019). In addition to morphological terms, these improvements led to a reinterpretation of the evolution of

rifts and the mechanisms and processes explaining their formation. Despite large variability, first order similarities are observed from different margins around the world (Reston, 2009; Peron-Pinvidic et al. 2019). As stated by Franke (2013) and Peron-Pinvidic et al. (2019), these similarities highlight identical underlying mechanism of formation. These new processes (Fig. 1.5) correspond to polyphase faulting, sequential faulting, deformation migration and ductile deformation and explains the architecture of the distal domain of rifted margins.

One of the fundamental result of rifted margin research has been the recognition of polyphased rifting, which is the consequence of the interaction between deep seated mantle deformation and crustal deformation during rifting (Péron-Pinvidic et al, 2019). This polyphased deformation results in the formation of different structural domains across the margin, which correspond to the proximal domain, the necking domain, the hyperextended domain, and the oceanic domain. The final architecture of the margin is related to key parameters controlling the rift evolution (Peron-Pinvidic et al. 2019). These key elements comprise the initial lithospheric thermal state, the extension rate, the amount of crustal and mantle hydration during extension as well as the obliquity. They have an impact on the strain partitioning during extension as well as on the rheological evolution of the lithosphere.

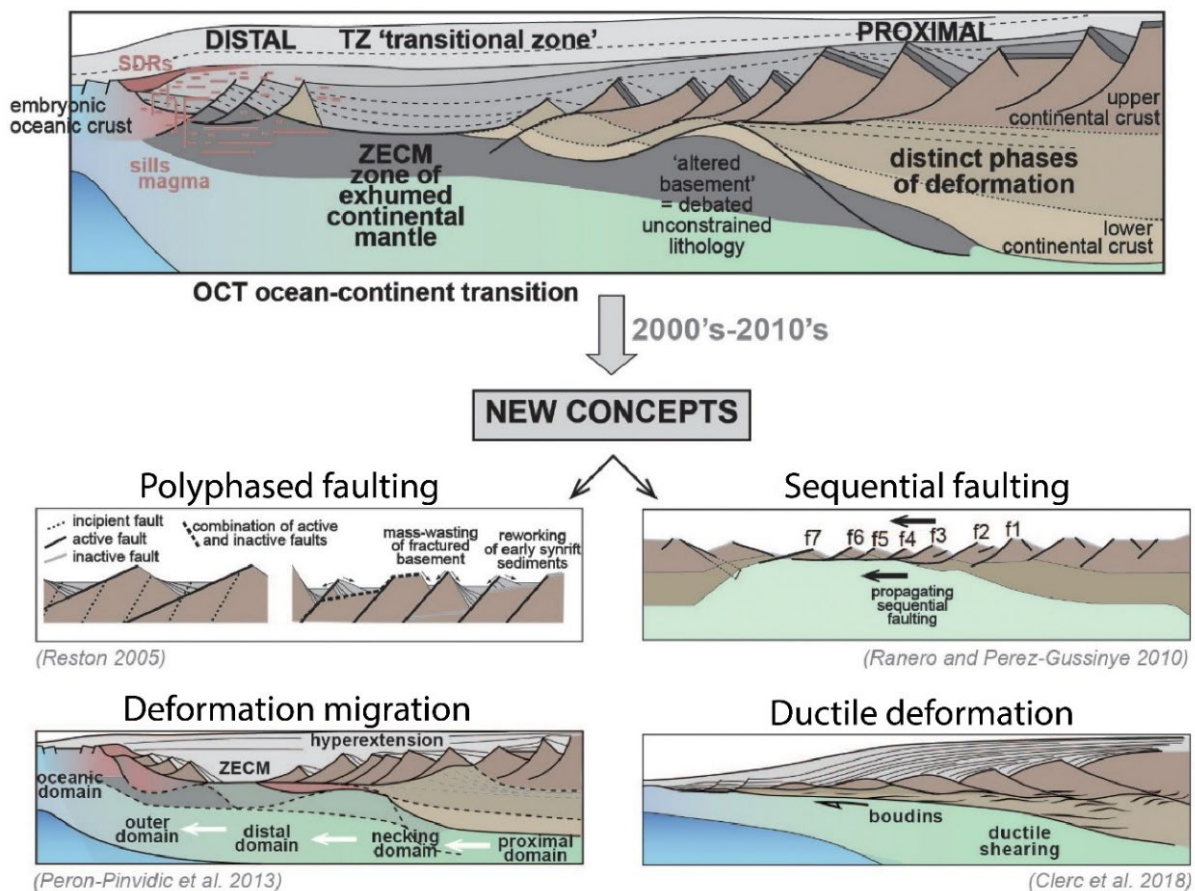


Figure 1.5: Evolution of the concepts in rifted margins (from Peron-Pinvidic and Manatschal, 2019) during the 2000's and 2010's.

	Term	Definition	References
Rifting	Polyphased rifting	Complex spatial and temporal evolution that cannot be explained using classical pure shear and/or simple shear rift models alone. It is associated to strain migration and localisation.	Péron-Pinvidic and Manatschal (2009)
Morphological features	Micro-continent	> 15 km thick crust, surrounded by oceanic crust	Péron-Pinvidic and Manatschal (2010)
	Continental Ribbon	> 20 km thick crust, separated by hyperextended basins, to normal thickness continent crust	Péron-Pinvidic and Manatschal (2010)
	H-Block	< 20 km thick crust, bounded by thinning and exhumation faults, preserves pre-rift sediments (see also keystone)	Péron-Pinvidic and Manatschal (2010); Lavier and Manatschal, 2007)
	Extensional allochthons	< 5 km thick crust, soled by exhumation fault	Péron-Pinvidic and Manatschal (2010)
	Sedimentary allochthons	Remnants of the cover detached from the hangingwall and lying above the detachment fault	
Faulting	High angle normal fault	Normal fault dipping at a steep angle (>50°) accommodating moderate deformation	
	Detachment fault	Shallow dipping normal fault (<30°) leading to large offset and basement exhumation	
	Sequential faulting	Sequential formation of single faults cross cutting in the hanging wall of the previous fault	Ranero and Pérez-Gussinyé (2010)
	Polyphased faulting	Back rotation of normal faults leading to fault lock-up and formation a new fault cross cutting the first fault generation	Reston (2005)

Table I.1: Common vocabulary defined in rifted margins concerning extensional faulting, morphological features, and rifting processes

The data collected from different types of margins worldwide led ultimately to a discussion on margin classifications to encompass the margin diversity and to emphasize the different forcing parameters (Sapin et al., 2021). Rifting appears to be controlled by the interplay of external parameters (extension rate, sedimentation rate, occurrence of mantle plume) and inherited parameters (pre-rift structuration, crustal and mantle composition) resulting in a large diversity of rifted margins, which is hard to capture by simple classifications (Sapin et al., 2021). The characteristics of external parameters is the fact that they can change at any stage of rifting leading to the significant change in the margin final architecture (Sapin et al., 2021). One of the other key parameters controlling rifted margin architecture is rift obliquity. In fact, strong obliquity tends to favour narrow margins, which is clearly observed in oblique and transform margins (Basile, 2015) while orthogonal rifting will favour wider margins (Jammes et al. 2010).

It appears that some domains such as the proximal and necking ones are always present, while others are characteristic of specific types of margins. The exhumation domain is symptomatic of magma-poor margins, and the SDR of magma-rich margins. Weak margins are characterized by an important length while strong margins are characterized by narrow width. Young warm crust, thin lithospheric mantle and low extension rate are related to weak margins, while high extension rates, and old rigid cold lithosphere are related to strong margins. The absence of magma is related to the presence of a depleted mantle and/or low extension rate while high magmatic budgets are related to high extension rates and/or a fertile mantle. There is a continuum between four end-members: magma-rich vs magma-poor and strong margin vs weak margin (Fig. I.6A).

The last point which drew most of the attention in these past years is the role of pre-rift inheritance and its control in the following rifting history which corresponds to the deviation from an ideal lithosphere (Fig. I.6B) and can affect the rheological profile of the lithosphere. This inheritance can be decomposed into 3 main points which are compositional inheritance, thermal inheritance, and structural inheritance (Manatschal et al., 2015, 2021). Compositional inheritance can modify the overall rheology of the crust and therefore exert a strong control on the final architecture of the margin. It was proposed by Chenin et al., (2019a) that the localisation of the rift is strongly influenced by the inherited lithospheric composition. It appears that mantle depletion and crustal mafic underplating prevent the reactivation of overlying weaknesses (such as faults) explaining why the North-Atlantic rifting avoided the Variscan domain associated to strong underplating and depleted mantle. Compositional inheritance can also have an impact on the timing of break up, heat flow and magmatic budget as observed along the Labrador sea (Gouiza and Naliboff, 2021).

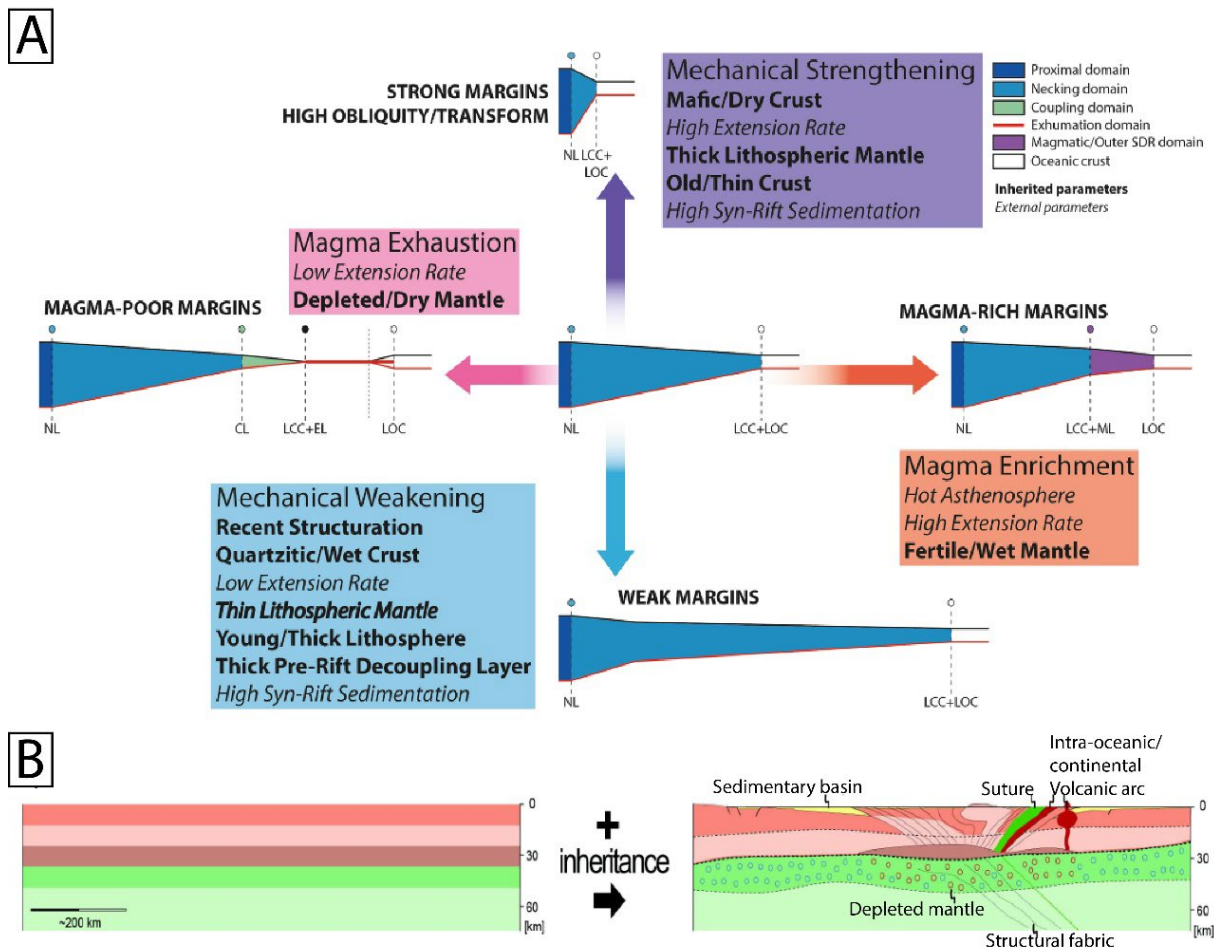


Figure 1.6: External and internal factors controlling the architecture of the margin (Sapin et al., 2021). B- Inheritance defined as the deviation from an ideal lithosphere (from Chenin, 2016).

The structural inheritance plays also a role at smaller scale as observed by Muñoz-Barrera et al., (2020) on the Norwegian margin. Inherited Caledonian crustal scale core complexes seemed to control the orientation and segmentation of the subsequent rifting. Insights from analogue modelling show that inherited structures can create complex fault geometries during rifting (Zwaan et al., 2022).

Finally, thermal inheritance exerts a strong impact on the crustal rheology. Indeed, a non-re-equilibrated crust, which is anomalously warm will be affected by ductile deformation and affect the margin architecture and overall length of the margin. These thermal anomalies are, however, short-lived. As soon as the source of the thermal anomaly ceases, the anomaly will resorb over tens of millions of years.

In conclusion, the result of decades of research on rifted systems and breakup processes led to a good comprehension on the architecture of rifted margins and their mechanisms of formation. The links between thermal evolution, extension rates, inheritance, and margin structures are quite well understood. Nevertheless, many questions remain and define directions of future research on rifted

margins concerning the role of inheritance as well as the evolution from proximal to distal parts of the margin, which remain poorly understood.

1.3. Fluid evolution throughout a Wilson cycle

Different fluids are observed associated to different tectonic settings during rifting and collision. These differences can form a distinct geochemical signature of a specific tectonic environment and can lead to different ore deposits.

1.3.1. Fluid signature during rifting

	<i>Tectonic environment</i>	<i>Thermal gradient (°C/Km)</i>	<i>Type of fluids</i>	<i>Fluid temperature (°C)</i>	<i>Element transfer</i>	<i>Gaz content</i>	<i>References</i>
<i>Rifting (magma-poor)</i>	Stretching phase	30-40	Hydrothermal brines	100-150	Ca, Mg, Fe	???	Hips et al., 2016; Salomon et al., 2020; Chenin et al., 2020 ; Barale et al., 2021
	Crustal thinning	40-60	Hydrothermal brines	???	???	???	Chenin et al., 2020 ;
	Hyperextension	80-100	Hydrothermal brines	>280	Cu, Mg, Ni, Cr	???	Manatschal et al., 2000; Incerpi et al., 2019
	Mantle Exhumation	80-100	Hydrothermal brines		Cu, Fe, Mg Zn, Ni, Cr	CO ₂ , H ₂ , CH ₄	McCullom and Bach, 2009; Cannat et al., 2010; Pinto et al., 2015 Nteme Mukonzo et al., 2021 Coltat et al., 2021
<i>Post-rift</i>	Mid-oceanic ridges	80-100	Hydrothermal brines	180 to 380°	Cu, Fe, Mg Zn, Ni, Cr	CO ₂ , H ₂ , CH ₄	Ding et al., 2005; Debret et al., 2018
	Passive margin	15-40	Oil Hydrothermal brines			CO ₂ , CH ₄ (biotic origin mostly)	Suess, 2014; Mazzini and Etiope, 2017 Gholamrezaie et al., 2018
<i>Convergence</i>	Subduction	10-20	Hydrothermal brines		B, Sr, Rb, Ba, La, Ce, Pb, Th	CO ₂ , N ₂	Philippot et al., 1995; Scambelluri and Philippot, 2001; Kessel et al., 2005; Bebout and Penniston-Dorland, 2016; Prigent et al., 2018 Bebout and Penniston-Dorland;
	Collision	15-30	Hydrothermal brines	120-400	Pb, Zn, Ag, Au Sn, W, Mo	CO ₂ , CH ₄ , N ₂	Zhang et al., 2022 Sindern et al., 2012

Table I.2: Summary of the fluid signature of different tectonic settings throughout the Wilson cycle

Rifting is associated with a progressive increase of the thermal gradient as a consequence of asthenosphere uplift and magma production which increases from proximal to distal (Table I.2). This characteristic evolution from thick cold continental crust to exhumed mantle and proto-oceanic crust is linked to an increase of the thermal gradient and a clear change in the geochemical signature on the fluids (Table I.2). Indeed, the initial stretching phase is associated to fluid circulations in the sedimentary cover and shallow crust. The fluid temperature is relatively low around 100 to 150°C with a composition of H₂O and NaCl mostly. They are characterized by carbonate mineralizations

around the fault with dolostone and ankerite formation highlighting mobilisation of Ca, Mg, Fe (Hips et al., 2016; Salomon et al., 2020; Barale et al., 2021).

The mantle exhumation is characterized by high temperature fluids, above 280°C in a H₂O-CO₂-NaCl system (Table I.2; Nteme Mukonzo et al., 2021). The different nature of the protolith (lithospheric mantle) compared to the more proximal domains leads to mobilisation of Cu, Fe, Mg, Cr, V associated to mantle serpentinization (Pinto et al., 2015; Klein and Le Roux, 2020). This mantle serpentinization is also responsible of the formation of H₂ and abiogenic CH₄ (McCollom and Bach, 2009; Cannat et al., 2010).

In between, these two events corresponding to rift initiation and termination, the fluid evolution is not well understood (Table I.2). The crustal thinning is associated to a progressive change from a crustal fluid signature to a mantle fluid signature. The occurrence of crustal fluid signatures is characterized by a slight increase of temperature, a change in the isotopic signature (decrease of $\delta^{13}\text{C}$, low $^3\text{He}/^4\text{He}$) highlighting a crustal component and a change from carbonate-dominated to silica-dominated (Incerpi et al., 2019). These observations are, however, made from diagenetic transformation of pre-rift sediments. Therefore, the fluid origin, pathway, and composition remain unconstrained. The distal, hyperextended margin is characterized by a significant gain in mantle-derived elements (Manatschal et al., 2000) indicating fluid penetration in the mantle before circulating in the hyperextended domains with temperatures up to 200°C recorded along the fault.

1.3.2. Fluid signature during post-rift evolution

The post-rift evolution of the margin is associated to a progressive cooling of the margin. Most of the hydrothermal activity appears concentrated around the spreading centre, where really high thermal gradients are reached associated to magmatism (Table I.2). Differences in the fluid pathway can be observed between fast and slow ridges but the element transfer appears relatively similar and corresponds to Cu, Fe, Zn, Mg, Ni, Cr (Debret et al., 2018). Fluid have a temperature ranging from 180 to 300°C at seafloor with slightly acidic pH (Ding et al., 2005).

Fluid circulation on passive margins is mostly restricted to the sedimentary cover and associated to hydrocarbon and water migration inside the cover and diagenetic transformation of the sediments (Table I.2). The fluids are derived from intraformational water expelled during or from dehydration associated to smectite-illite transformation during burial. Cold seeps (Suess, 2014) are also observed in the continental slope associated to methane and water leakage toward the surface associated to mud volcanoes (Mazzini and Etiope, 2017).

1.3.3. What resources associated to fluid circulation in rifted margins?

The study of rifted margins has been strongly linked with that of natural resources, mostly for oil and gas exploration. Indeed, around 35% of the giant oil fields worldwide were found in passive margins and 31% in continental rift systems corresponding to the main tectonic settings for oil discoveries (Mann et al., 2003). However, ore-deposits in rifted margins have not drawn much attention.

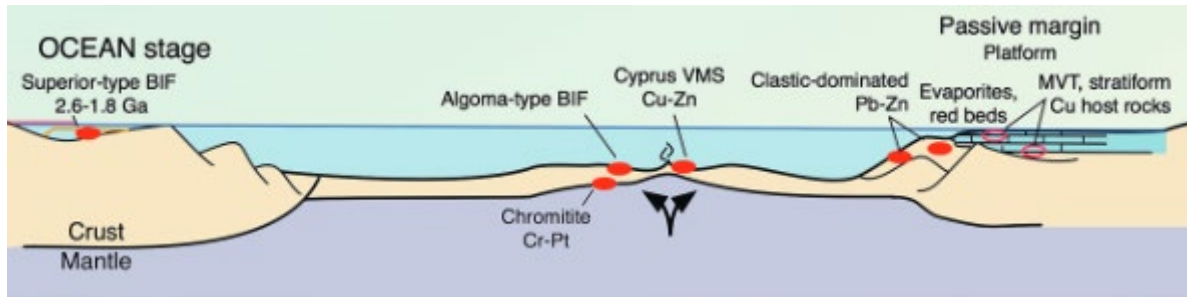


Figure 1.7: Ore deposits found in passive margins (from Arndt et al., 2017). The proximal domain is characterized by MVT in carbonate platforms while the distal domain is associated to clastic dominated deposits and SEDEX deposits.

Ore deposits have been described in aborted rifts and rifted margins (Pirajno and Cawood, 2009; Arndt et al., 2017; Zappettini et al., 2017). A clear distinction is visible between the type of ores associated to continental rifting, and the ones associated to mantle exhumation (Fig. 1.7). This difference is obviously related to the different geochemical reservoirs involved (continental crust vs mantle) as well as the different heat flows (Lescoutre et al., 2019; Saspiturry et al., 2020). The exhumed mantle domain is characterized by the presence of volcanogenic massive sulphide deposits similar to black smokers (Coltat et al., 2021). They are characterized by Fe-Cu-Zn-rich to Cu-Co-Zn-(Ni)-(Au)-rich deposits.

Deposits associated to continental rifting are not as well understood. Sedimentary hosted mineralisations such as SEDimentary EXalative (SEDEX) and Mississippi-Valley-Type (MVT) in carbonate platforms have been described both in present-day and fossil margins (Fig. 1.7; Leach et al., 2010; Arndt et al., 2017). Other types of sedimentary hosted deposits such as clastic deposits (CD) are also observed. They are associated to deposits of Zn-Pb-Cu-Ba-F \pm Fe-Ag-Au (Pirajno and Cawood, 2009). MVT are associated to carbonate platforms in the proximal domain of the margins, while SEDEX and clastic deposits are found in their more distal part (Leach et al., 2010). Porphyry epithermal deposits associated to syn-rift magmatic intrusions such as Mo-Au ores and Sn-REE- Nb-F ores in granites (Arndt et al., 2017) are also observed along magmatic rifted margins.

1.3.4. Fluid evolution during subduction

1.3.4.1. Fluid signature of subduction zones

Subduction is characterized by cold thermal gradient (10-20°C/Km; Bebout and Penniston-Dorland, 2016) and by HP-LT metamorphic facies (Table I.2). However, important burial led to important devolatilization and decarbonation of the sediment and hydrated oceanic crust during prograde metamorphism (Fig. I.8). Fluid inclusion studies show that the fluids corresponds to H₂O-CO₂-NaCl ± KCl (Philippot et al., 1995). Minor amounts of N₂ have been also observed in the fluids (Andersen et al., 1989). Another characteristic is the mobilisation of LILE and LREE in the fluid phase (Scambelluri and Philippot, 2001; Kessel et al., 2005; Bebout and Penniston-Dorland, 2016; Prigent et al., 2018). The fluid salinity is variable and up to 50 wt% NaCl equiv. (Svensen et al., 1999). They migrate along the subduction zone by porous flow associated to shear zones at the subduction interface (Prigent et al., 2018). Part of this LILE-rich fluids also migrate in the mantle wedge above the subduction zone (Pirard and Hermann, 2015).

1.3.4.2. What resources associated to fluid circulation in subduction zones?

Fluids related to dehydration and devolatilization reactions are responsible for ore deposits of different types at the surface around the volcanic arc (Wang and Xiao, 2018). The deposits correspond mostly to orogenic and epithermal Au, Cu-Mo and Cu-Au porphyry iron oxide copper gold (IOCG) and VMS-type deposits (Herrington and Brown, 2011; Wang and Xiao, 2018).

In the fore-arc and in the accretionary prism, Au-rich VMS type deposits can be observed and are related to sulphide rich fluids derived from the slab. Orogenic gold can also be observed associated to CO₂-rich fluids derived from the slab and circulating along shear zones (Wang and Xiao, 2018). However, most of the ore-deposits are related to magmatic activity in the arc (Wang and Xiao, 2018). This is the case for Cu-Mo and Cu-Au porphyry deposits and IOCG deposits. The magmas are characterized by high water, halogen and CO₂ content derived from the slab and relatively oxidant due to the high sulphate contents (Zellmer et al., 2015). The upward migration of the magma leads to exsolution of CO₂, H₂S and SO₂ and progressively to the precipitation of sulphate and sulphides and ore deposit formation (Zellmer et al., 2015).

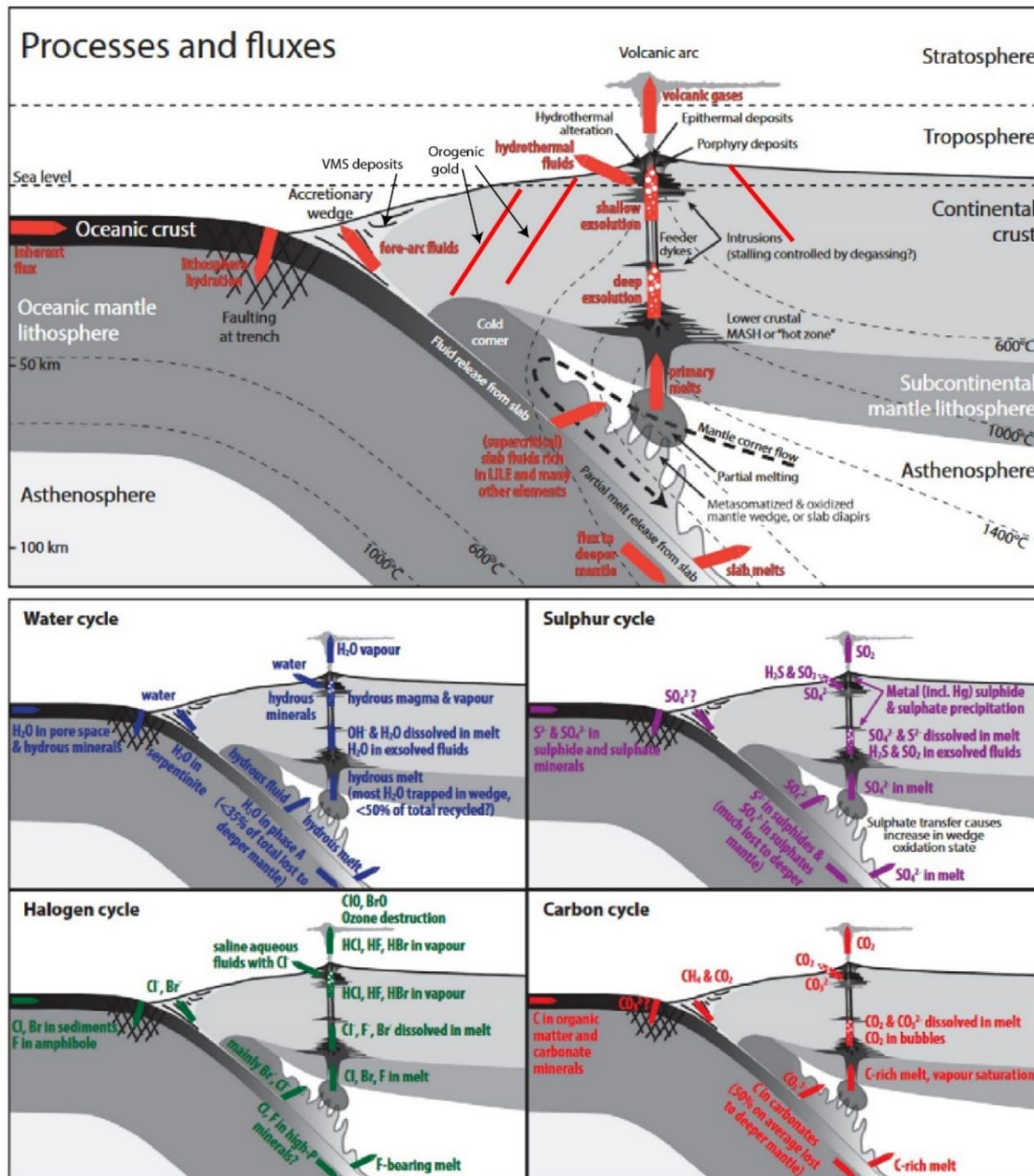


Figure 1.8: Illustration of the fluid circulation associated to the type of ore deposits found along subduction zones (from Zellmer et al., 2015). The water, halogen, sulphur and carbon cycles associated to subduction zones and slab devolatilization are also described showing significant flux of volatile (H_2O , CO_2 , S) along the subduction plane and in the volcanic arc.

1.3.5. Fluid evolution during continental collision

1.3.5.1. Fluid signature of continental collision

Continental collision is characterized by nappe stacking leading to progressive increase of temperature under thermal gradient of 15 to 30°C (Table I.2; Zhang et al., 2022) followed by delamination and magmatic intrusions during late- to post-orogenic evolution. Different fluids are observed associated to different places in the orogen. The external part of the orogen is associated to H_2O -NaCl±KCl fluids under temperature of 100 to 200°C (Sindern et al., 2012). The internal part of the orogen is associated to significant dehydration and devolatilization leading to the occurrences of

metamorphic fluids. These fluids are characterized by higher temperatures and important content of CO₂, CH₄ and N₂ and are enriched in K, Ca, Mg (Sindern et al., 2012).

1.3.5.2. What resources associated to fluid circulation in orogens?

Ore deposits associated to continental orogens are relatively diverse. Indeed, Ag-Pb-Zn, Mo-porphyry, Cu-Au porphyry and gold-rich quartz are relatively common in orogenic domain. There is a spatial and temporal repartition of these deposits. The external part of the orogen is characterised by Pb-Zn-Ag deposits (Fig. I.9). Sediment-hosted deposits correspond to MVT-type deposits related to fluid circulations from the internal to the external part of the orogen until reaching carbonated platforms in the foreland basins (Sverjensky, 1986) leading to the formation of large Pb-Zn deposits.

However, the main drivers of ore deposits are the late orogenic magmatic intrusions, which lead to porphyry deposits. These magmatic intrusions are located mostly in the internal domain (Fig. I.9). The heat necessary to generate these magmatic intrusions is associated to lithosphere break-off or delamination. These magmas formed by crustal anatexis forming hydrous felsic melts enriched in Sn, W and Rb, Cs, Li, Y (Hou and Cook, 2009). The ore deposits related to magmatic intrusions are mostly Mo-Cu-Au deposits, Fe-rich skarn deposits and Sn-W deposits. Large deposits of REE are related to carbonatite intrusions found in the late stage orogenic evolution as observed in the Himalayan orogen (Hou and Cook, 2009).

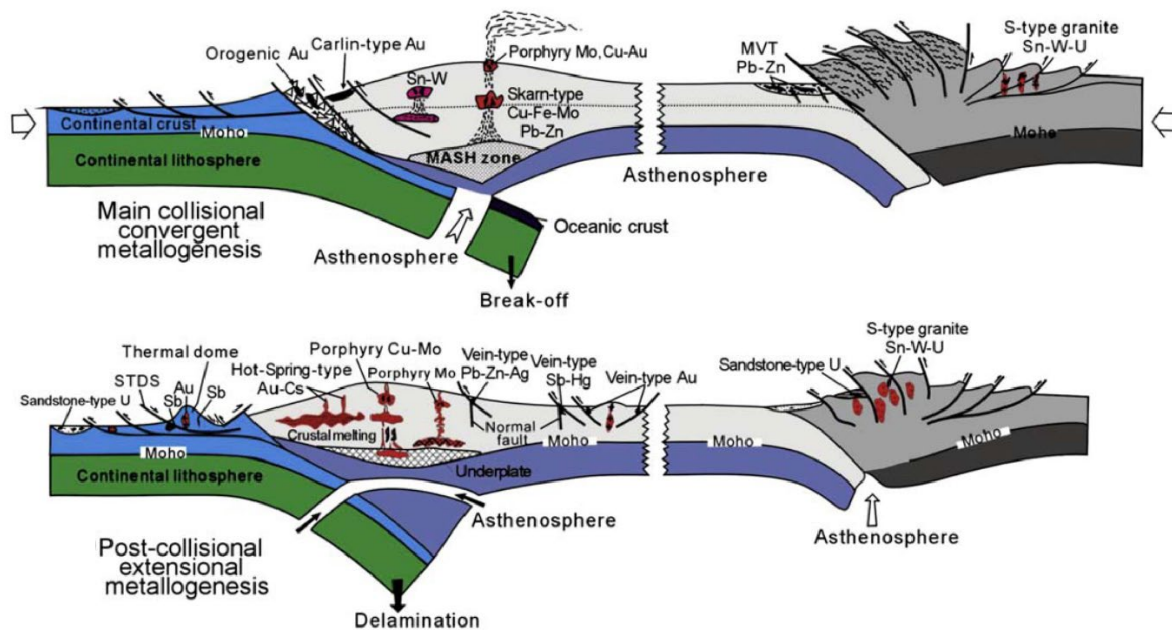


Figure I.9: Ore deposits related to convergence as observed in the Himalayan range (from Hou and Cook, 2009). The ore deposits in the internal part are linked to magmatic activity in response to slab break off and root delamination.

Gold deposits are common in orogenic setting (Goldfarb et al., 2001). Different Au deposits are observed such as Carlin-type Au (“sediment-hosted, disseminated precious-metal deposits”; Bagby and Berger, 1985) and orogenic Au (associated to peak metamorphism; Hou and Cook, 2009). While Carlin-type are associated to magmatic intrusions and might represent the distal portion of Au-skarns, orogenic gold deposits are associated to devolatilization metamorphic reactions leading to CO₂ rich fluids migrating along faults (Kerrick et al., 2000). Late- to post-collisional extension is associated to vein-type Au deposits.

Take-home message

- Orogenic inheritance controls rifting and rift inheritance controls evolution and architecture of collisional orogens.
- The evolution of rift concepts led to the identification of different rift stages (stretching, necking, hyperextension, exhumation) and the understanding of internal and external forcing parameters controlling the final margin evolution and architecture.
- Different fluids are associated to the different stages of the Wilson cycles with different signatures and ore deposits.

2. Polyphased rifting at magma-poor rifted margins: the Atlantic-type model

2.1. Recognition of rift domains

2.1.1. Archetype of magma-poor and sediment starved margin

The archetype magma-poor margin was defined using both seismic and well observations from the present-day Iberia-Newfoundland rifted margin and outcrop observations from the fossil Alpine Tethys analogue. Analogies between the present and fossil margin are based on similar observations recognized and described in numerous papers. This model is known as the Atlantic-type model and corresponds to the magma-poor, sediment starved endmember model of rifted margins.

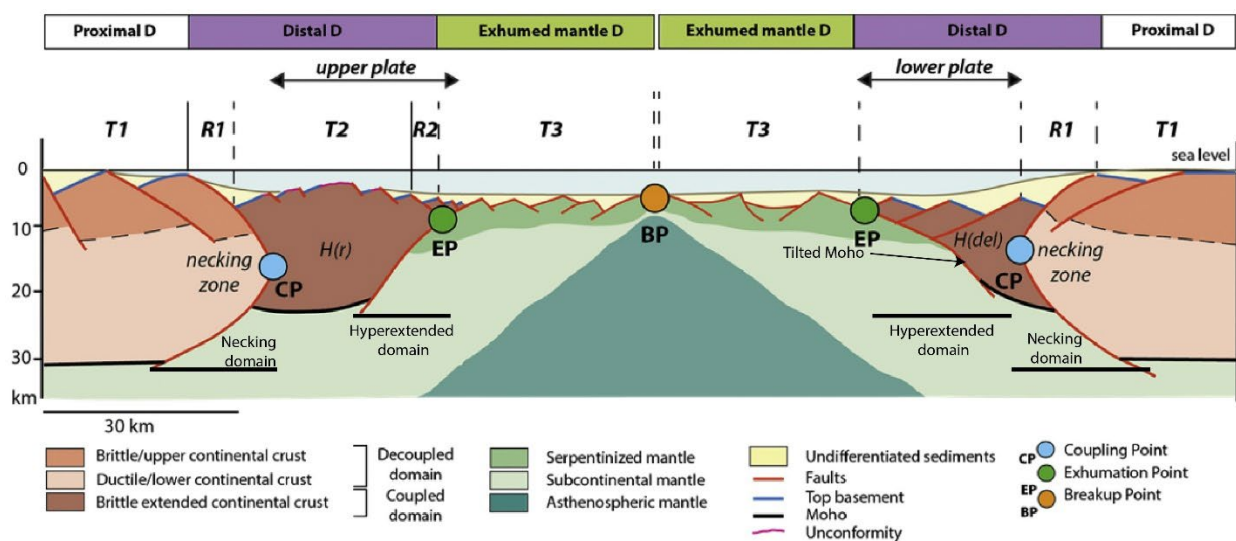


Figure I.10: Section of a magma-poor margin at the onset of seafloor spreading (modified from Hauptert et al., 2016). The difference between the upper plate and lower plate is marked by the delaminated H-Block in the lower plate ($H(\text{del})$). T1, T2, T3 corresponds to the main unconformities between syn-tectonic and post-tectonic sediments.

Conjugated rifted margins can be described in terms of upper plate and lower plate (Fig. I.10). The different domains (Table I.3) such as: 1) the proximal domain, 2) the necking domain, 3) the hyperextended domain, and 4) the exhumed mantle domain are found both in the upper and lower plate, but their size and structure vary (Hauptert et al., 2016). The definition of upper plate proposed by Lister et al., (1986) is related to the lithospheric simple shear Wernicke model. The upper plate corresponds the hanging wall of this lithospheric detachment fault. The lower plate corresponds therefore to the footwall of this structure. In reality, this model cannot explain rifted margins, and the upper and lower plates and only set up at the end of necking, when the crust is thinned to less than 10km and within the brittle domain. At this stage the upper plate is characterised by a narrow hyperextended domain (Fig. I.10) while the lower plate corresponds to a much wider, hyperextended domain that is tapering toward the ocean (Fig. I.10; Hauptert et al., 2016).

<i>Domain</i>	<i>Definition</i>	<i>Deformation mode</i>
<i>Proximal domain</i>	Domain associated to minor extension accommodated by high angle normal faults. The crust is 25 ± 5 km thick and with decoupling levels between the upper and lower crust; accommodation is minor outside rift basins	Stretching (e.g., McKenzie, 1978)
<i>Necking domain</i>	Domain characterized by thinning of the crust from 25 ± 5 to 10 km with converging top and base of the crust. During necking, the domain remains shallow and rapidly subsides post necking.	Necking (Mohn et al., 2012; Chenin et al., 2020), (remnants of the previous stretching mode can be preserved)
<i>Hyperextended domain</i>	Domain characterized by continental tapering from 10 to 0 km and detachment faulting linked to intense fluid rock interactions	Hyperextension (Nirrengarten et al., 2016) (remnants of the previous stretching and necking can be preserved in allochthonous blocks)
<i>Exhumed mantle domain</i>	Domain associated to exhumed mantle to the seafloor linked to deep water sedimentation and massive hydration (serpentinization)	Mantle exhumation (Manatschal, 2004) (remnants of the previous modes can be preserved in allochthonous blocks)

Table I.3: Definition of the different domains observed in magma-poor margins.

2.1.2. Proximal domain architecture

2.1.2.1. General characteristics

The proximal domain is the most continentward of the domains found in rifted margins (Fig. I.11A). It shows only minor crustal thinning with thickness of 25 ± 5 km and a thinning factor below 0.2 (Gómez-Romeu et al., 2020). The Moho is relatively flat and horizontal. The top basement appears offset by series of high-angle normal faults defining half-graben basins (Fig. I.11A). The accommodation space is minor outside rift basins which is shown by the thinner post-rift deposits compared to the distal part indicating minor post-rift subsidence.

These basins were the first to be identified in present-day (e.g., Jeanne d'Arc basin) and fossil rifted margins (e.g. Bourg d'Oisan half-graben, and the Lombardian basin in the Western Alps; Bernoulli, 1964; Lemoine et al., 1981; Bertotti, 1990; Bertotti et al., 1993). These faults are rooted in the ductile crust leading to listric normal fault geometries. They accommodate minor extension as reflected by their low offset (1000 m for the Ornon fault (Chevalier, 2002) and low β factors.

General concepts related to the Wilson cycle and rifted margins

Additionally, this minor crustal thinning led to the absence of significant increase of the geothermal gradient in the crust (Chenin et al., 2018).

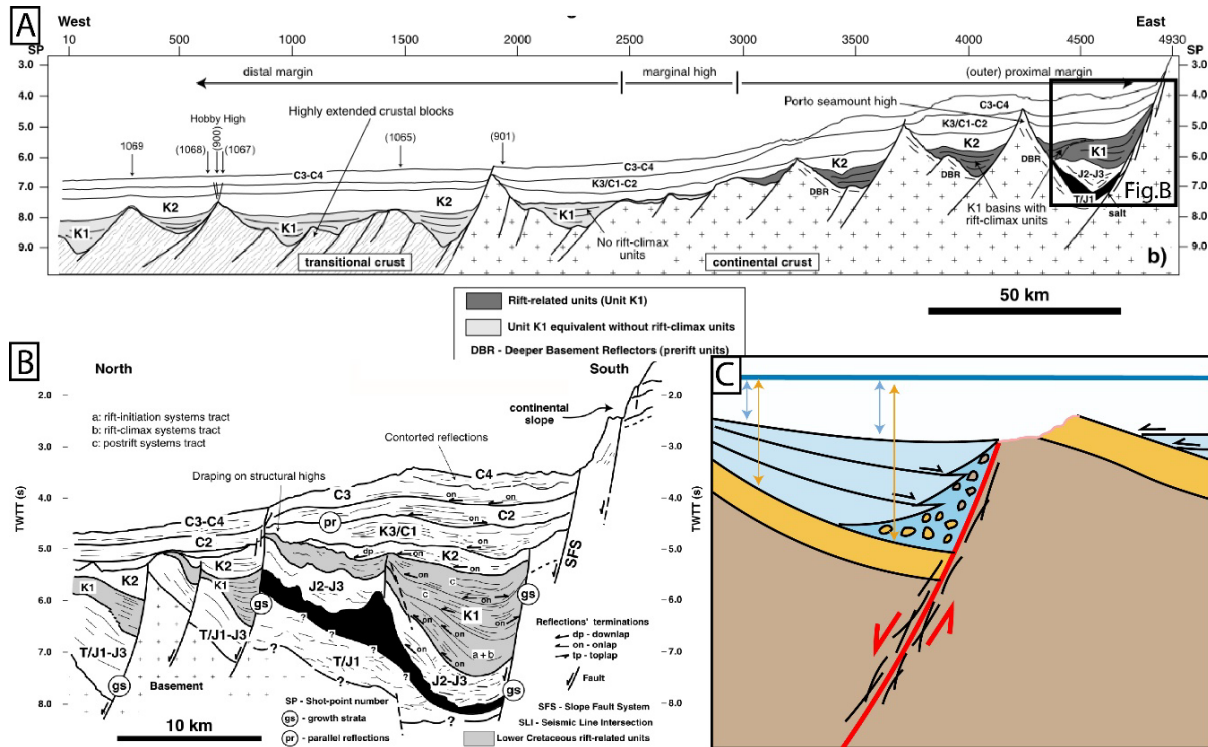


Figure I.11: A- Section of the Iberia margin showing the proximal to distal transition (Alves et al., 2006). The proximal domain is characterized by half-graben basins bounded by high-angle normal faults. B- Half-graben basins from the proximal domain can show growth strata in syn-rift sediments. The sediments are onlapping on the fault plane at a high angle. The half-grabens are sealed by post-tectonic sediments. C- Schematic illustration of a half-graben basin (modified from Tugend et al., 2014).

2.1.2.2. Sedimentary architecture

The progressive sedimentary infilling of the half-graben basins leads to an increase of the sediment thickness toward the fault (Barr, 1987). This results in the formation the typical wedge shape of the syn-rift sedimentary sequence thickening toward the fault plane (Fig. I.11B and C). These wedges are the main characteristic to recognize the syn-rift sediments in these half-grabens and allow to date the fault activity as observed in many seismic sections from rifted margins (e.g. Iberia-Newfoundland margin and Norwegian-Greenland margin; Driscoll et al., 1995; Alves et al., 2006; Müller et al., 2005).

The sedimentary architecture in these half-graben basins depends on the sedimentation rate and the subsidence rate. The net subsidence is a combination of regional eustatic variation and tectonic subsidence. Tectonic subsidence is related to regional subsidence associated to crustal scale processes (e.g. thermal support or thermal relaxation) and fault slip rate (Doglioni et al., 1998). The syn-rift subsidence in the proximal domain is mostly controlled by the rate of slip along faults during rifting. For example, the Ornon fault (Bourg d'Oisans; Chevalier et al., 2003) showed that significant

subsidence occurred in the basin while subsidence outside the basin was minor. Moreover, their results showed that fault offset occurred over a very short time (ca. 1-2Ma).

2.1.2.3. Sedimentary deposits

Clastic-dominated basins are filled by fluvio-lacustrine clastic deposits or by marine sediments (Leeder and Gawthorpe, 1987). The type of environment depends on the subsidence rate vs the sedimentation rate as well as on the local base level. In the case of over-filled basins, the subsidence rate is equal to the sedimentation rate. Under a low base level, the fault scarp is incised by river systems leading to the formation of alluvial fan deposits in the basin (Leeder and Gawthorpe, 1987). The connection to important clastic sources leads to the filling of the basin by fluvial coarse sediments alternating with lacustrine sediments. In underfilled basins subsidence rate is more important than the sedimentation rate. The fault scarp is still partially emerged on the top and is marked by the presence of fan delta deposits and slumps while the deeper part of the basin is filled by turbiditic systems derived from the delta. An example of this system is the Gulf of Corinth where Gilbert deltas controlled by the fault activity were deposited while the basin was (under)filled by turbiditic systems (Ford et al., 2013; Gawthorpe et al., 2018).

Carbonate-dominated systems are characterized by the lack of landmasses able to provide clastic sediments and associated to a high local base level. The fault scarp is marked by the presence of breccias derived from the carbonate platform in the margin border. In the topographic highs, reefs and carbonate build-ups are visible whereas the deeper parts of the basin are filled by marls (Leeder and Gawthorpe, 1987). An example of these type of environment is the Bourg-d'Oisans basin, which corresponds to the proximal domain of the Alpine Tethys and opened in an epi-epireic sea disconnected from continental clastic input (Thierry, 2000). The fault plane is composed of tectonic breccias partially reworked in the sediments. Larger fragments of the pre-rift cover forming decametric olistoliths can be observed along the fault plane (Barfety and Gidon, 1984).

2.1.3. The Hyperextended domain

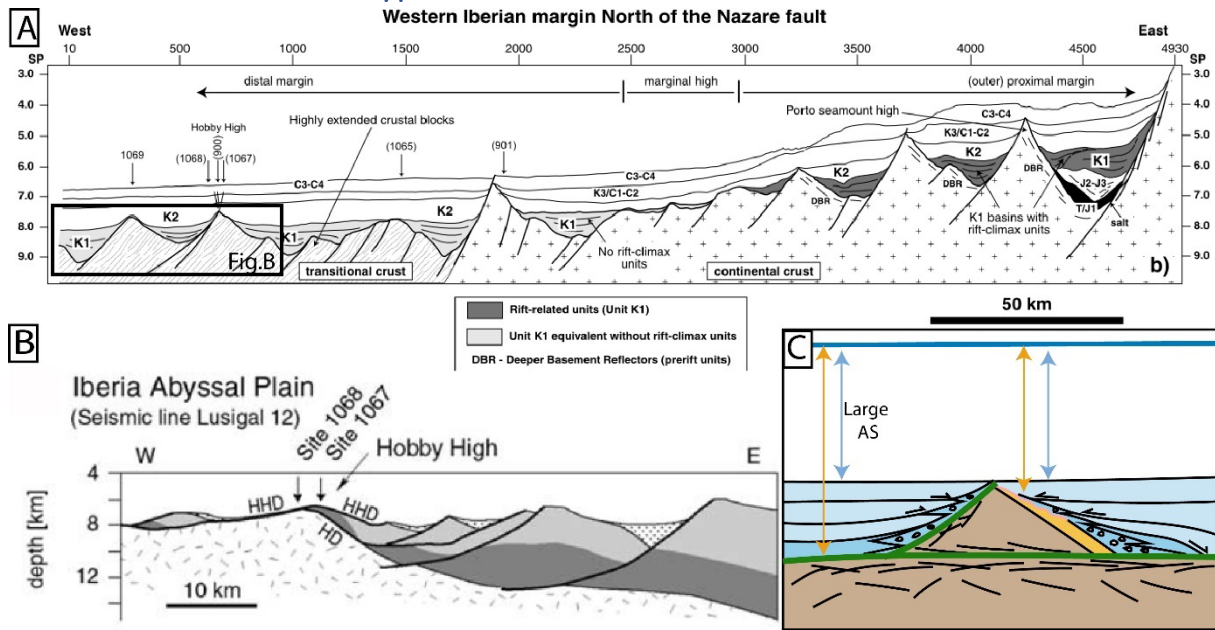


Figure I.12: A- Section of the Iberia margin showing the proximal to distal transition (Alves et al., 2006). B- Section of the distal Iberia margin showing large detachment faults leading to mantle exhumation (HHD = Hobby High detachment, HD = H-detachment; Manatschal et al., 2001). C- Schematic illustration of a detachment fault and its relation with the sedimentary cover showing flat deposits over the exhumed faults associated to large accommodation space (AS), (modified from Tugend et al., 2014).

2.1.3.1. General characteristics

The hyperextended domain (Fig. I.12A) is characterised by a thin continental crust (below 10 km) passing progressively to the exhumed mantle on the seafloor (exhumed mantle domain). The syn- to post-rift sedimentary cover is thick, and the water depth is commonly greater than 2 km indicating strong syn- and post-rift subsidence. The Moho appears tilted toward the continent until reaching the surface where the mantle is exhumed. The top basement corresponds to large scale detachment fault rooted in the mantle as a result of a strong coupling and embrittlement of the whole lithosphere during the final stages of rifting (Fig. I.12B). The detachment faults appear in seismic sections as strong reflectors in the crust and the top basement such as the S-reflector of the Galicia margin (Reston et al., 1996; Reston, 2009) and H-reflector of the Southern Iberia margin (Manatschal et al., 2001). Other strong reflectors observed in the crust at the distal part of the margin corresponds to the upper crust-lower crust boundary (Manatschal et al., 2001). Minor magmatic activity through sills and dyke formation in the cover and the basement is also observed.

2.1.3.2. Fault geometry

The deformation in the hyperextended domain corresponds to on-sequence faulting leading to the formation of detachment faults (Reston and McDermott, 2011; Epin and Manatschal, 2018). The fault appears to form in sequence, each fault crust cutting the crust thinned beforehand by previous faults (Fig. I.13; Ranero and Pérez-Gussinyé, 2010). This sequential faulting leads to the

General concepts related to the Wilson cycle and rifted margins

isolation of small allochthonous blocks over the detachment fault. The detachment faults offsets appear to decrease toward the exhumed mantle domain (Epin and Manatschal, 2018).

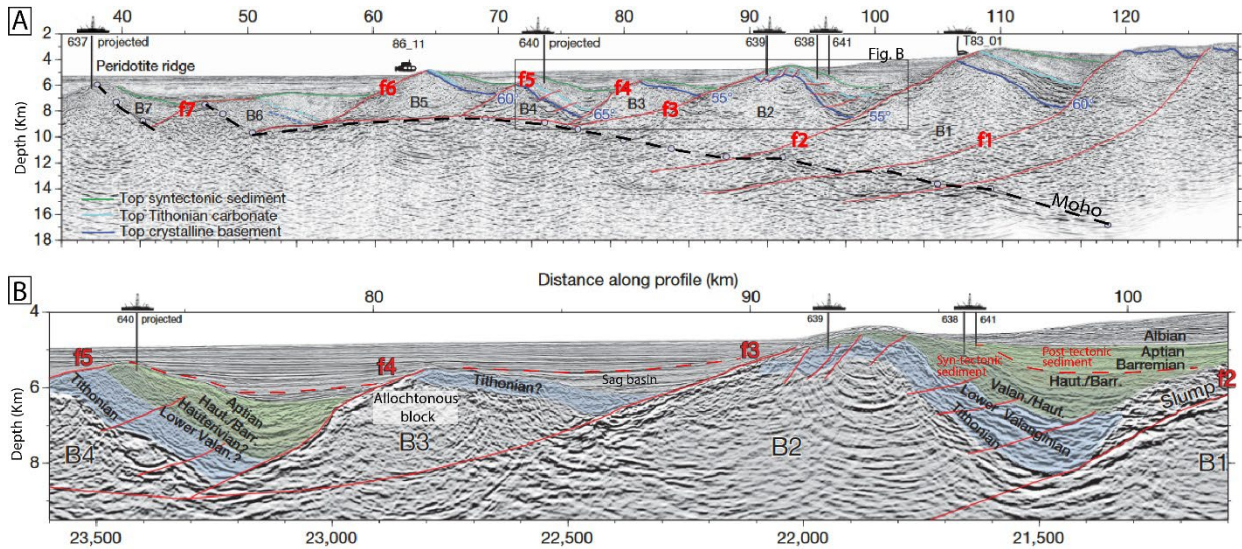


Figure I.13: A-Tectonic and stratigraphic interpretation of the seismic profile of the distal part of the Iberia margin (modified from Ranero and Pérez-Gussinyé, 2010) showing the sequential faulting leading to crustal thinning and mantle exhumation. B- Focus on an area of the seismic profile showing more in detail the stratigraphic architecture of the margin. The distal migration of the deformation is visible through the younger syn-tectonic sediments toward the west (Valanginian-Barremian to Hauterivian lower Albian).

The application of the Coulomb wedge theory describes quite well the evolution of the distal, hyperextended domain (Nirrengarten et al., 2016). Indeed, this theory applied in compressional settings is also applied in extensional domain (Xiao et al., 1991). In the case of hyperextension, the total embrittlement of the distal domain led to a friction dominated deformation. The slip surface or decollement level corresponds to the serpentinized mantle below the thinned crust. The decollement dip measured in various magma-poor margins is comprised between 4 and 27° and the slope angle between -2 and 6.5° (Nirrengarten et al., 2016). These detachment faults are controlled by the geometry of the extensional prism.

2.1.3.3. Sedimentary architecture

The syn-rift deposits appear undeformed and over the detachment fault (Fig. I.12C) and show downlap geometries and wedge shape terminations toward the ocean and continent, over the hyperextended domain. These pseudo-conformable sediments above the hyperextended domain contrast with the geometries previously described from the proximal domain. Post-rift sediments are sub-horizontal and offlap toward the ocean (Fig. I.12C and I.13; Chenin et al., 2022).

2.1.3.4. Sedimentary deposits

The sediments are best studied in fossil distal margins such as the Err nappe from the Central Alps where portions of detachment faults from the distal Adria margin and their sedimentary infill are preserved (Masini et al. 2011; Epin and Manatschal, 2018; Ribes et al., 2019).

The base of the syn-rift sediments in the hyperextended domains correspond to polymictic breccia composed of reworked sedimentary clasts and basement clasts from the detachment fault flooring the basin. These breccias show minor transport and are related to the tectonic activity along the detachment fault. The sedimentary clasts are derived from the hanging wall while the basement clasts are derived from the exhumed detachment fault and the underlying footwall (Masini et al., 2011). These types of deposits are submitted to constant reworking pointing to an extremely dynamic environment. A gradual thinning of the deposits is observed upward, associated to a change in the transport direction from perpendicular to parallel to the basin axis (Masini et al., 2011).

Preserved portions of the exhumed mantle domain are also found in the Alps such as the Platta nappe in the Central Alps (Epin et al., 2019; Ribes et al., 2019) and in the Tasna area (Ribes et al., 2019c). The sediments deposited above the exhumed mantle correspond to reworked centimetric mantle clasts from the detachment fault, intercalated with radiolarian chert levels and basaltic pillow lava (Ribes et al., 2019c). Locally, black shales can be recognized, marking local anoxia in small depressions on the seafloor (Ribes et al., 2019c). Exhumation of the detachment faults led to the creation of complex surfaces with chaotic breccias reworking the fault rocks and remnants of the pre-rift cover. These remnants can be decametric and can be observed above the continental crust but also exhumed mantle.

2.2. Proximal to distal transition: the necking domain

The transition between the distal and proximal domains corresponds to a key domain as it is associated to: (i) significant crustal thinning, and (ii) a characteristic subsidence history, and (iii) a change in the thermal state of the margin. However, it is only recently that its peculiar geometry and sedimentary architecture have been investigated (Osmundsen and Redfield, 2011; Mohn et al., 2012; Ribes et al., 2020).

2.2.1. First model of crustal thinning

The first seismic sections from the Iberia margin were showing progressive crustal thinning from the proximal domain to the distal domain (Fig. I.14A; Montadert et al., 1977; De Charpal et al., 1978). The top basement appeared to be composed of a succession of tilted blocks associated to deeper basins toward the ocean, overlying a crustal taper thinning toward the ocean. The Moho appeared to be gently tilted toward the continent. This interpretation was underlined by the hypothesis that the physical processes associated to rifting remained the same throughout the whole rifting. As a consequence, older interpretations assumed that the same formation processes controlled the proximal and distal parts of the margin and that tilted blocks occurred across the whole margin.

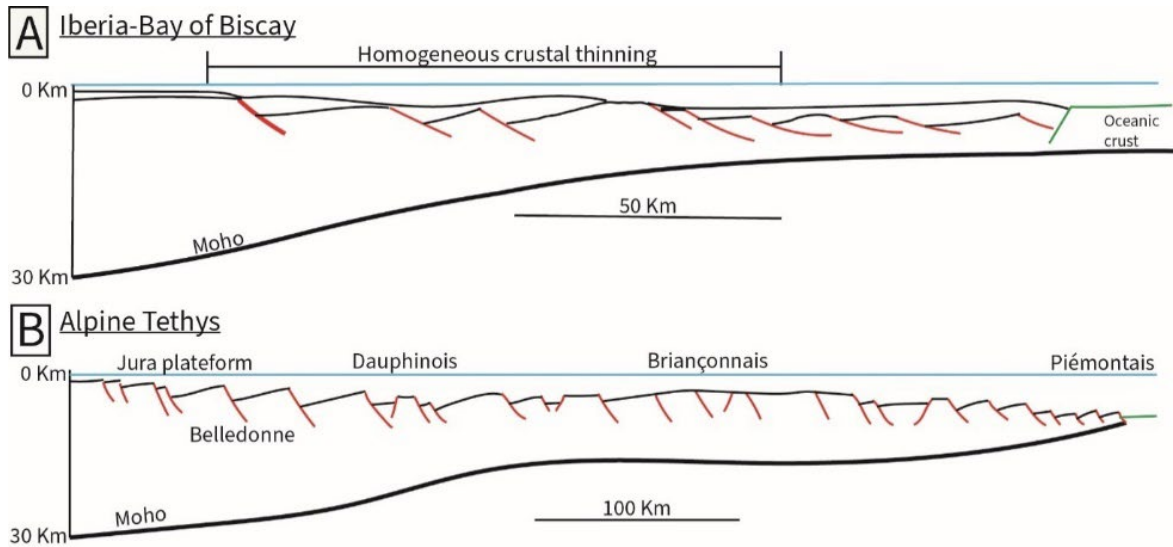


Figure I.14: A- Section of the Iberia-Bay of Biscay margin showing homogeneous thinning throughout the entire margin (modified from Montadert et al., 1977). B- Section from the Alpine Tethys associated to a wide margin (400 km, modified from Lemoine et al., 1986).

The same type of geometries have been postulated in the Alps for the fossil European margin (Fig. I.14B; Lemoine et al., 1981) by comparison with the present-day Iberia and Bay of Biscay margins. The restored margin is extremely wide (up to 400 km), and corresponds to a succession of tilted blocks nowadays preserved in only few locations (Barfety and Gidon, 1984; Lemoine et al., 1981). At present, such a margin geometry is not supported anymore by field observations.

2.2.2. The recognition of crustal necking

The occurrence of amphibolite to sub-greenschist facies mylonites identified along the Pogallo shear zone (Handy, 1987) and dated by the Rb-Sr and K-Ar methods on muscovites and biotites, ranging mostly from 230 to 160 Ma were a first hint for crustal thinning during Jurassic rifting. This shear zone is composed of high grade mylonites (ca. 500°C) passing to low grade mylonites (ca. 350°C), and locally cataclasites. Greenschist deformation is dated at 180 Ma. Restoration of the shear zone to its pre-Alpine position leads to a continentward-dipping shear zone with a normal sense of shear. The total crustal thinning along the Pogallo shear zone has been estimated in the order of about 10 km (Handy, 1987; Schmid et al., 1987). This lower crustal shear zone, when put in perspective with the upper crustal Jurassic normal faults preserved in the same area, led to the recognition of rift-related crustal necking by Mohn et al., (2012). Therefore, crustal thinning is not homogeneous along the margin but is instead localised along major structures both in the upper and lower crust (Fig. I.13).

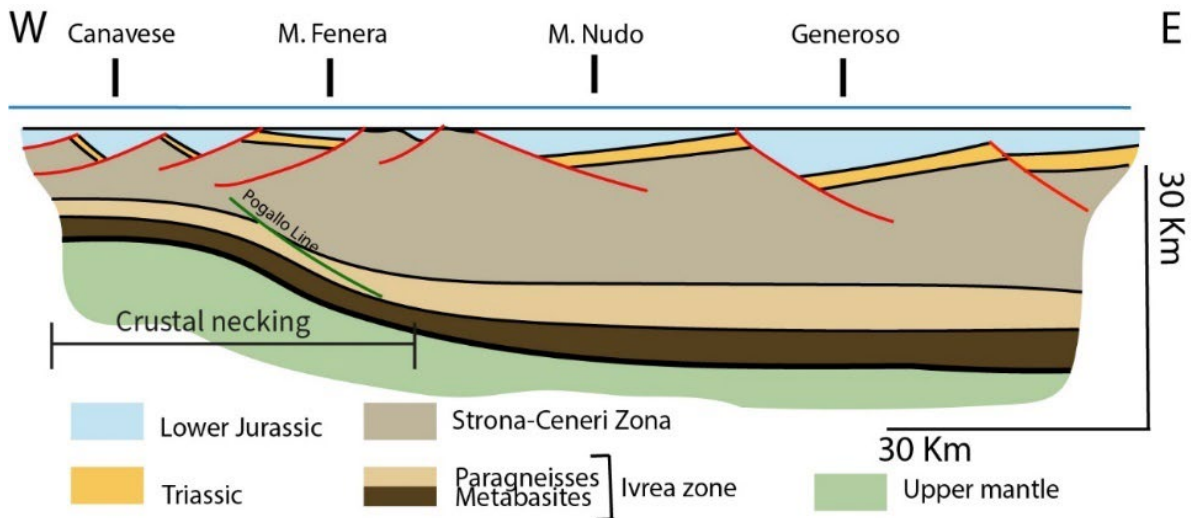


Figure I.15: Palinspatic section of the Adriatic margin showing the position of the Pogallo shear zone during Jurassic (modified from Handy, 1987). This shear zone is associated to important crustal thinning in the lower crust

Preserved remnants of the necking domain were also found in the Central Alps (Campo-Grosina nappe; Mohn et al., 2010; Mohn et al., 2011). They consist of large detachment faults (comprising cataclasites and gouges) in the top basement. This detachment was responsible for the exhumation of a greenschist mylonitic zones (Eita shear zone) interpreted as the former brittle-ductile transition indicating significant crustal exhumation (Fig. I.16; Mohn et al., 2012). Therefore, crustal thinning is not progressive but discontinuous, showing that different, successive mechanisms are playing a role.

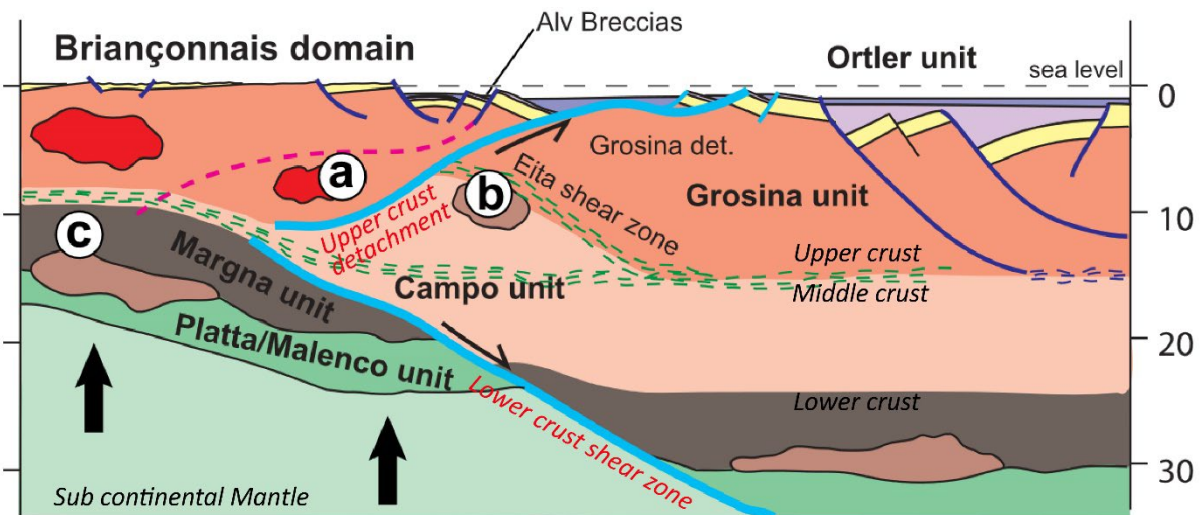


Figure I.16: Reconstitution of the Adriatic margin from Mohn et al., (2012) showing the upper crust and lower crust conjugated fault leading to embrittlement of the crust. This model implies that the top basement and the Moho correspond to large offset fault and shear zones responsible for significant crustal thinning.

2.3. Crustal necking: the least known rift domain

2.3.1. The necking domain in present-day margins

2.3.1.1. General characteristics

Nowadays, crustal necking is recognized at all rifted margins. The compilation of data from margins worldwide (n=21; Chenin et al., 2017) shows a wide range of widths for the necking domain, which range from 10 up to 200 km width with an average of 50 km (Chenin et al., 2017). There is no correlation neither with the size of the other domains, nor with the existence of a mature oceanic domain (> 1000 km). This is not surprising as the architecture of the necking domain is acquired before the onset of sea floor spreading.

2.3.1.2. Necking architecture

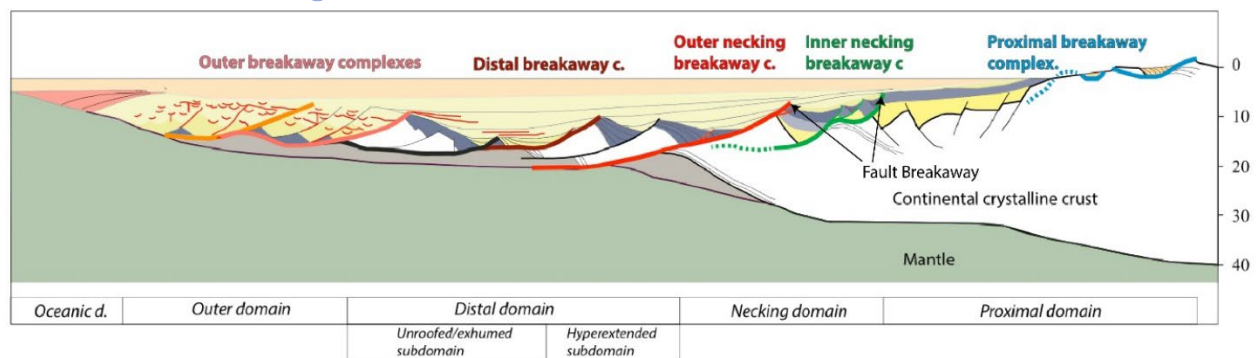


Figure I.17: Sketch of a rifted margin showing the architecture and main faults associated to crustal necking and hyperextension (from Osmundsen and Péron-Pinvidic, 2018). The necking domain is composed of two main faults forming the inner and outer necking domain.

Detailed descriptions of the necking domain architecture were proposed in the Iberia-Newfoundland margin, the Bay of Biscay and the Mid Norwegian margin (Osmundsen and Redfield, 2011; Péron-Pinvidic et al., 2013; Tugend et al., 2015; Osmundsen and Péron-Pinvidic, 2018; Muñoz-Barrera et al., 2021). The necking domain can be separated into an outer and an inner necking domain as observed in the Mid Norwegian margin (Osmundsen and Péron-Pinvidic, 2018).

Fault breakaways correspond to the intersection between the fault and the surface (Axen, 2004). The fault breakaway of the inner necking domain is located at the oceanward termination of the proximal domain (Fig. I.17). The faults correspond to large detachments accommodating important offsets responsible for the exhumation of middle crust as observed with the mid crustal granulite found on the seafloor of the north Iberian margin (e.g., Le Danois high; Capdevila et al., 1980; Fügenschuh et al., 2003; Cadenas et al., 2021). A second set of large detachment faults can be observed in some margins and forms the outer necking domain (Fig. I.17) leading to the coupling

between the crust and the mantle.

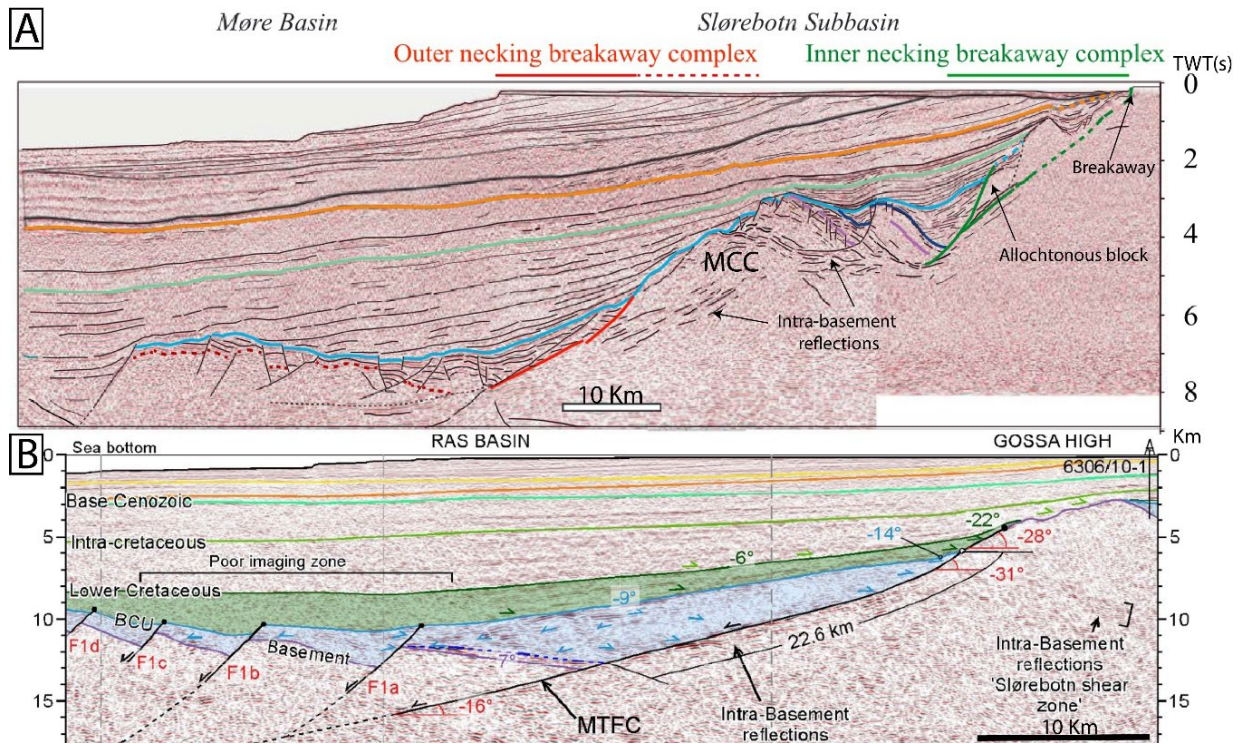


Figure I.18: A- Example of a necking domain from the Mid Norwegian margin (from Osmundsen and Péron-Pinvidic, 2018) showing the presence of two crustal faults forming the inner and outer necking domain and surrounding a MCC (Metamorphic Core Complex). The syn-rift to post-rift sediments onlap above the basement. B- Example of necking domain in the Norwegian margin showing a large detachment fault crosscutting the upper part of the crust (from Muñoz-Barrera et al., 2021). The fault shows an offset of 22.6 km and is dipping oceanward at a shallow angle (16°). The top of the fault scarp appears eroded.

The faults show various geometries from a ramp-flat geometry to large planar faults. These geometries are controlled by the rheology of the crust. Ductile middle crust will lead to the formation of a flat exhumation geometry the middle crust before a second fault incises the lower crust coupling the continental crust with mantle (Fig. I.18A). A strong crust will lead to a planar fault cutting the whole crust (Fig. I.18B). The rotation of the fault during extension will lead to the deformation of a second large fault incising the crust. These models relating fault geometries and rheology explain a lot of the observations made in the necking domains. The rheology of the crust is controlled by the crustal composition and the thermal gradient (Fig. I.19).

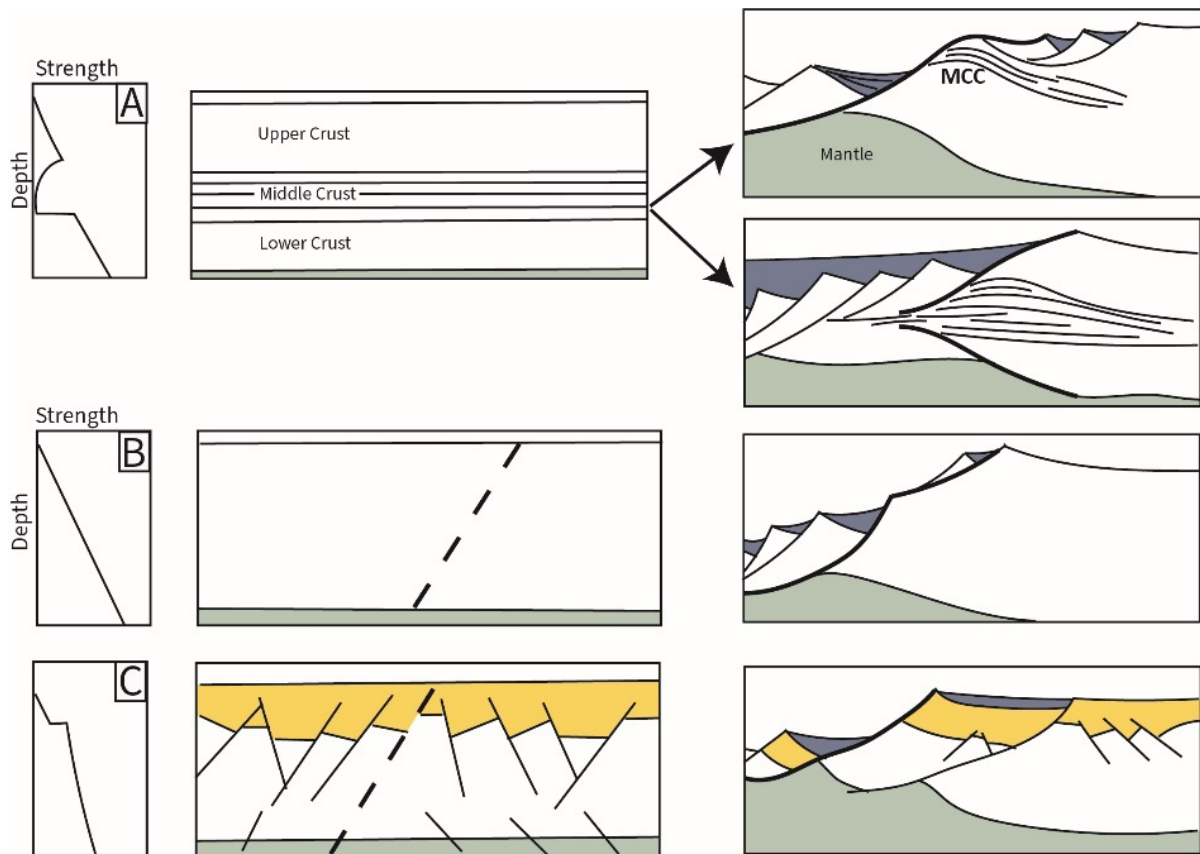


Figure 1.19: Illustration of the different types of necking faults according to different rheologies (modified from Osmundsen and Péron-Pinvidic, 2018). A- Thick ductile middle crust will lead to a core complex structure. B- A strong crust will lead to the formation of a fault crosscutting the entire crust. However, due to rotation of the footwall, the initial fault would be crosscut by a secondary set of faults leading to crust-mantle coupling. C- Strong crust associated to thick pre-rift basins.

2.3.1.3. Necking detachment faults

The fault plane of detachment faults shows complex geometries. Across the main fault plane, crustal allochthons or rieder blocks are observed and correspond to new faults forming as the main detachment is unfavourably oriented during exhumation (Osmundsen and Péron-Pinvidic, 2018). The presence of pre-rift evaporites can lead to strong decoupling between the pre- and post-evaporite layers that last until the evaporites are consumed. This results in the presence of large allochthons made of post-evaporite sedimentary sequences lying above the exhumed surface (Jammes et al., 2010). The remnants of the former evaporite layer from so called cagneules (or corgneule), which are often associated with fault zones containing basement clasts and cover breccias (Motus et al., 2022).

2.3.1.4. Along strike variability

Important variability of the fault geometry and width of the necking domain is observed along strike (Osmundsen and Redfield, 2011; Osmundsen and Péron-Pinvidic, 2018; Muñoz-Barrera et al., 2020). Laterally, the fault offset can decrease and as a consequence, a detachment fault can pass laterally to a high-angle normal fault. Besides, the geometry of the necking detachment faults can change drastically. These variations are related to inheritance due to different crustal

compositions and the reactivation of inherited pre-rift shear zones (Muñoz-Barrera et al., 2020; Muñoz-Barrera et al., 2021).

2.3.2. Crustal necking: A transient process through time

The present-day necking domain is the result of a transient process, itself called crustal necking. The necking domain is usually relatively similar on each conjugated margin. This rifting stage is controlled mostly by the rheology. Indeed, the strength of the lithosphere is controlled by the strongest layer. Therefore, the failure of this strong layer will control the rupture of the whole lithosphere leading to focalisation of the deformation and asthenosphere uplift.

2.3.2.1. Crustal deformation

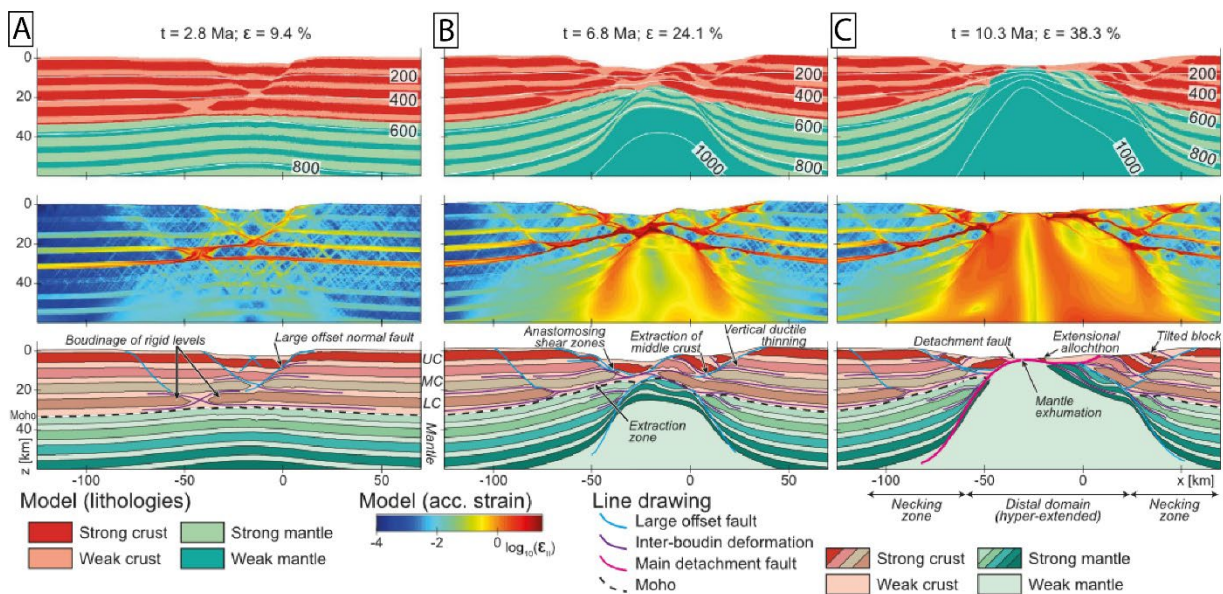


Figure 1.20: Numerical modelling of crustal necking in a heterogeneous crust composed of weak and strong layers (from Duretz et al., 2016). A- From 10% of extension, localisation of the deformation is occurring in the crust associated to asthenosphere uplift. B- For 24% of extension, two sets of conjugated faults are visible in the upper and lower crust/ upper mantle leading to progressive coupling. The presence of soft layers in the crust led to the formation of MCC structures associate to significant crustal exhumation. C- For 38% of extension, coupling of the upper and lower crust led to embrittlement of the crust and finally hyperextension.

The deformation appears accommodated by two sets of conjugated faults in the upper crust and in the lower crust followed by a migration of the deformation (Chenin et al., 2018). This type of faults have geometries of extraction faults (Froitzheim et al., 2006), which can lead to the extrusion of the material found in between the two faults. In this case, the extraction of the ductile crust leads to embrittlement of the crust. Moreover, the heterogeneities of the crust such as magmatic intrusions can lead to strain softening of the crust, thereby modifying the fault architecture (Duretz et al., 2016; Petri et al., 2019). If strong enough, such strain softening is associated exhumation of deep crustal levels up to the surface and formation of core complex (Fig. 1.20; Duretz et al., 2016).

2.3.2.2. Thermal evolution

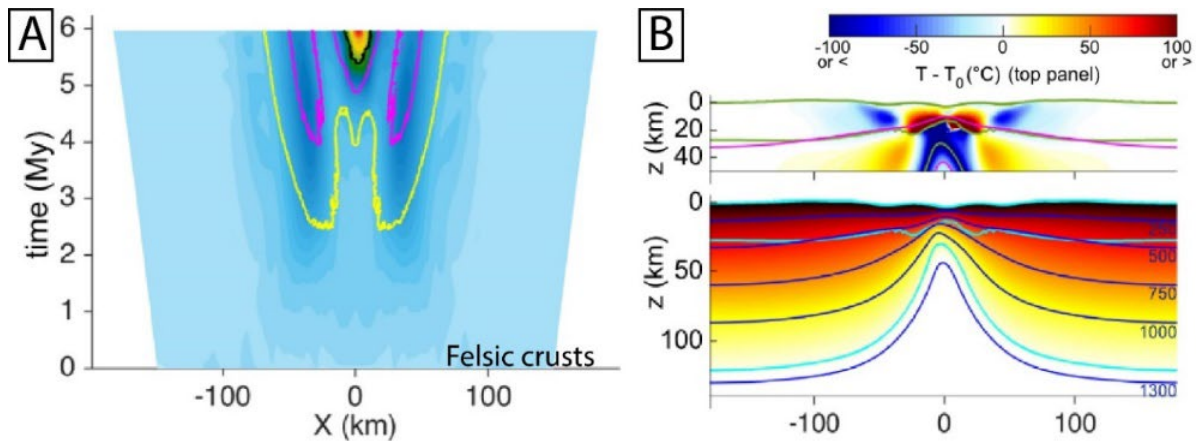


Figure I.21: A- Variations of the heat flow across the rift zone through time for a felsic crust (from Chenin et al., 2020) associated to crustal thickness isopach (yellow=25 km, magenta=20 km, black =15 km). This model shows an increase of the heat flow in the rift shoulders and in the rift centre in response to asthenosphere uplift. B- Crustal section showing the difference of temperature at the end of the necking with the initial temperature and lithospheric section of the rift zone showing the isotherms shallowing in the rift centres associated to asthenosphere uplift (1300°C isotherm).

The rising of the asthenosphere during the necking is responsible for increase of the temperature in the rift zone. This temperature increase is not homogeneous in the crust (Fig. I.21A). Indeed, while the rift centre shows higher thermal gradients than the adjacent borders the proximal domain is already colling. The increase can reach more than 100°C at the base of the crust. Surface heat flow reaches 100 mW.m² on the rift border and 160 mW.m² in its centre, which corresponds to a thermal gradient of ca. 60°C/km. The crustal faults bounding the basins are also separating two domains with a different thermal history. The hanging wall of the fault corresponds to a domain with higher thermal gradients, whereas the footwall shows lower thermal gradients (Fig. I.21B). Cooling of the footwall of ca. 50°C compared to initial temperature is even expected (Chenin et al., 2020). This leads to strong vertical and lateral thermal gradients. The post-rift stage in the necking domain is associated with a progressive thermal relaxation, responsible for the fast initial subsidence and drowning of the necking domain.

2.3.2.3. Topographic evolution

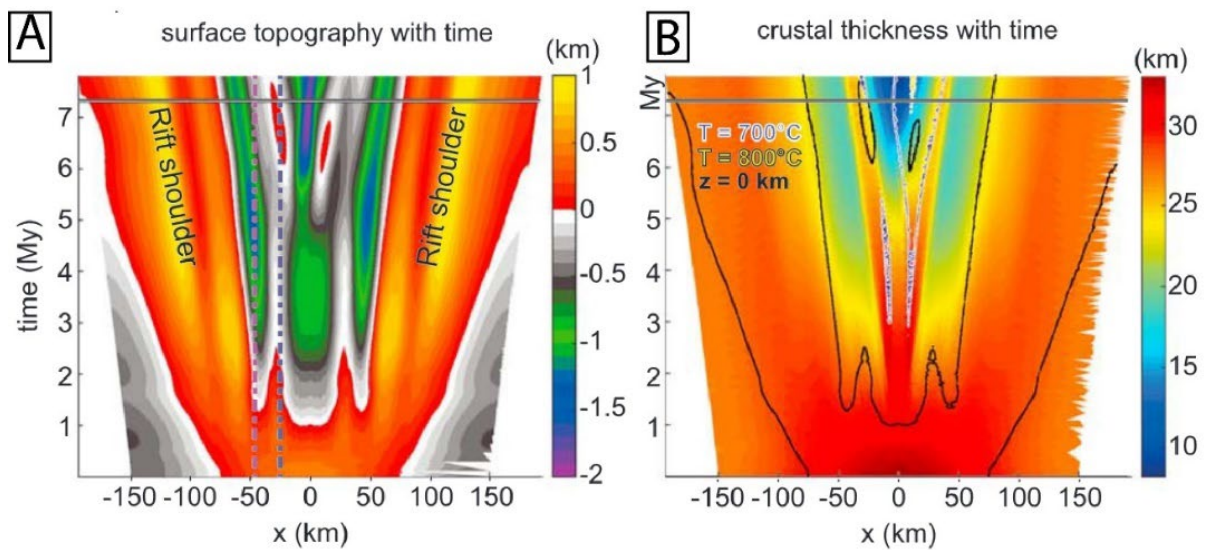


Figure 1.22: A- Evolution of the topography through time in response to crustal necking (from Chenin et al., 2019b) showing significant topographic uplift in the rift shoulder. B- Evolution of the crustal thickness through time during necking showing the focalisation of the deformation in response to necking.

Important uplift is expected on the rift borders and the rift centre as a response to necking (Fig. 1.22). One of the key parameters for the isostatic uplift is the thickness of the elastic layer which is controlled by the composition of the crust and the temperature (Lavie et al., 2000; Chenin et al., 2020). Large elastic thickness will lead to important uplift. In addition, part of this uplift is related to thermal support due to asthenosphere rising (Chenin et al., 2018). Depending on the crustal composition, the uplift ranges from 500 to 2000 m in the rift borders.

2.3.3. Necking evolution through time

The two pairs of conjugated faults lead to extraction of the ductile crust and embrittlement of the remaining, thinned continental crust (Fig. 1.23). This results in the connection between the upper and lower crusts. The focal point where the main pairs of conjugate faults are joining is called coupling points and the area found in between the bounding faults is called H-Block (Lavie and Manatschal, 2006; Sutra et al., 2013). The H-Block, or also referred to as the key-stone, will become the future hyperextended domain. Rift architecture during necking appears mostly symmetrical in “pure-shear” style with increase of asymmetry during hyperextension (Sutra et al., 2013; Chao et al., 2021).

Crustal necking is a transient process and is relatively short-lived. Numerical models show that necking lasts between 4 and 8 Ma (Chenin et al., 2022) and is followed by migration of the deformation in the future distal part. Transgression over the uplifted basement is expected in the necking domain.

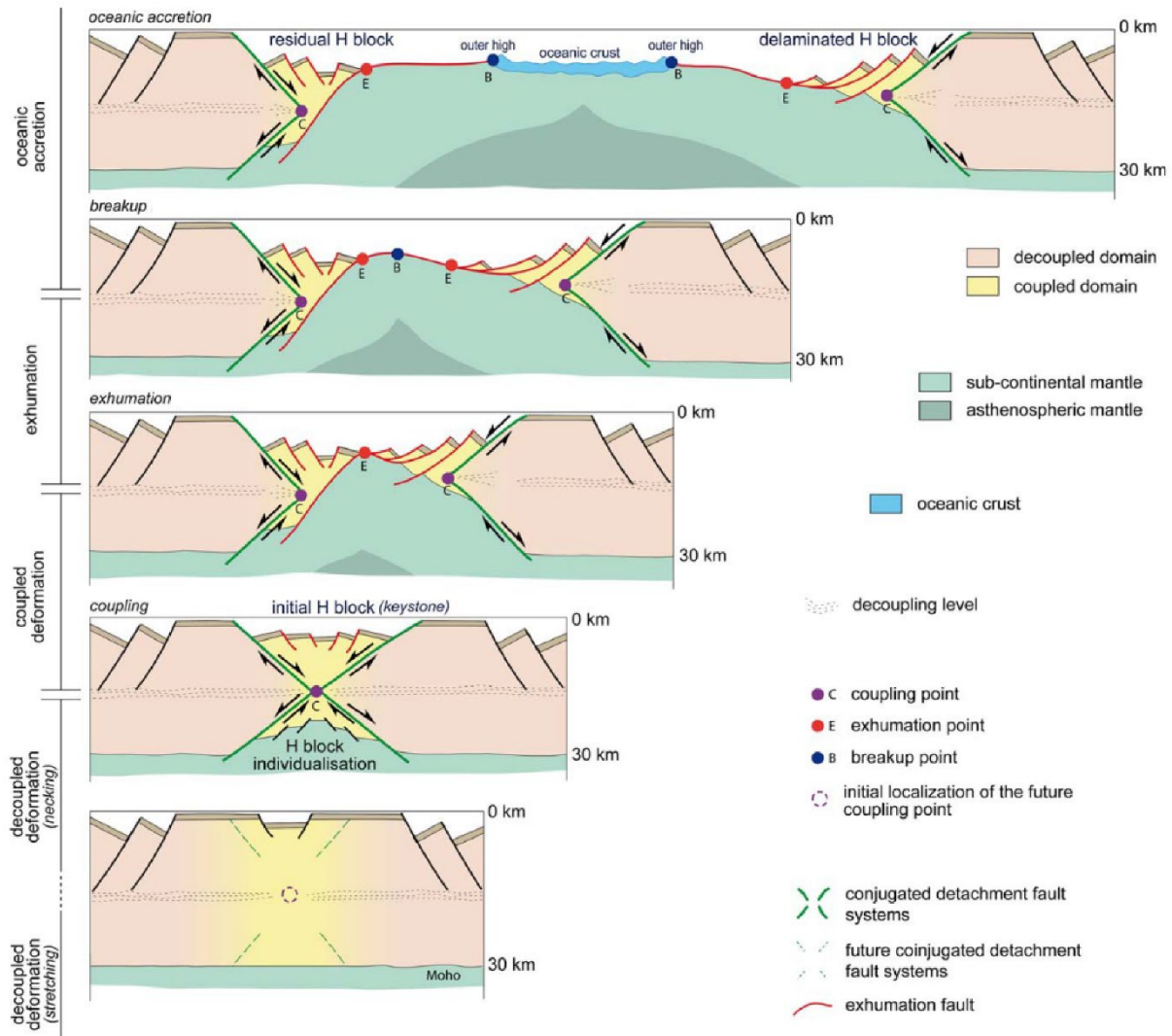


Figure 1.23: Evolution of a magma-poor margin from a decoupled deformation to a coupled deformation during necking (from Sutra et al., 2013). Crustal necking is associated to a pure-shear, symmetrical deformation while exhumation is associated to a simple-shear deformation leading to an asymmetric margin.

2.3.4. Stratigraphic response to crustal necking

Crustal necking is associated to a specific sedimentary record and a characteristic sedimentary architecture (Chenin et al., 2022). The onset of rifting is marked by an unconformity (Ribes et al., 2019b) visible throughout the rift domain. In the necking domain, the syn-necking sediments are lying directly above the exhumed basement and the pre-rift cover, which marks the necking unconformity (Fig. 1.24A). This unconformity is also highlighted by the occurrence of post-rift deposits above the basement marking a long-term emersion of the basement (Fig. 1.24A). In contrast, in the proximal domain a change from wedge shape deposits to passive infills is observed (Ribes et al., 2019b). In the rift centre, important uplift can lead to significant erosion and karstification as observed for example in the Briançonnais block in the Alps (Hauptert et al., 2016).

The architecture of the syn-necking deposits is also complex. Indeed, the switch from a high-angle normal fault to a detachment fault is related to a change in the sedimentary architecture.

General concepts related to the Wilson cycle and rifted margins

Initial sediments form a wedge, but the progressive flattening of the fault as necking proceeds leads to the deposition of the syn-rift sediments conformably over the exhumed fault (Masini et al., 2011). Early syn-rift sediments of the stretching phase or pre-rift sediments can lay over the detachment fault as allochthons (Chao et al., 2021).

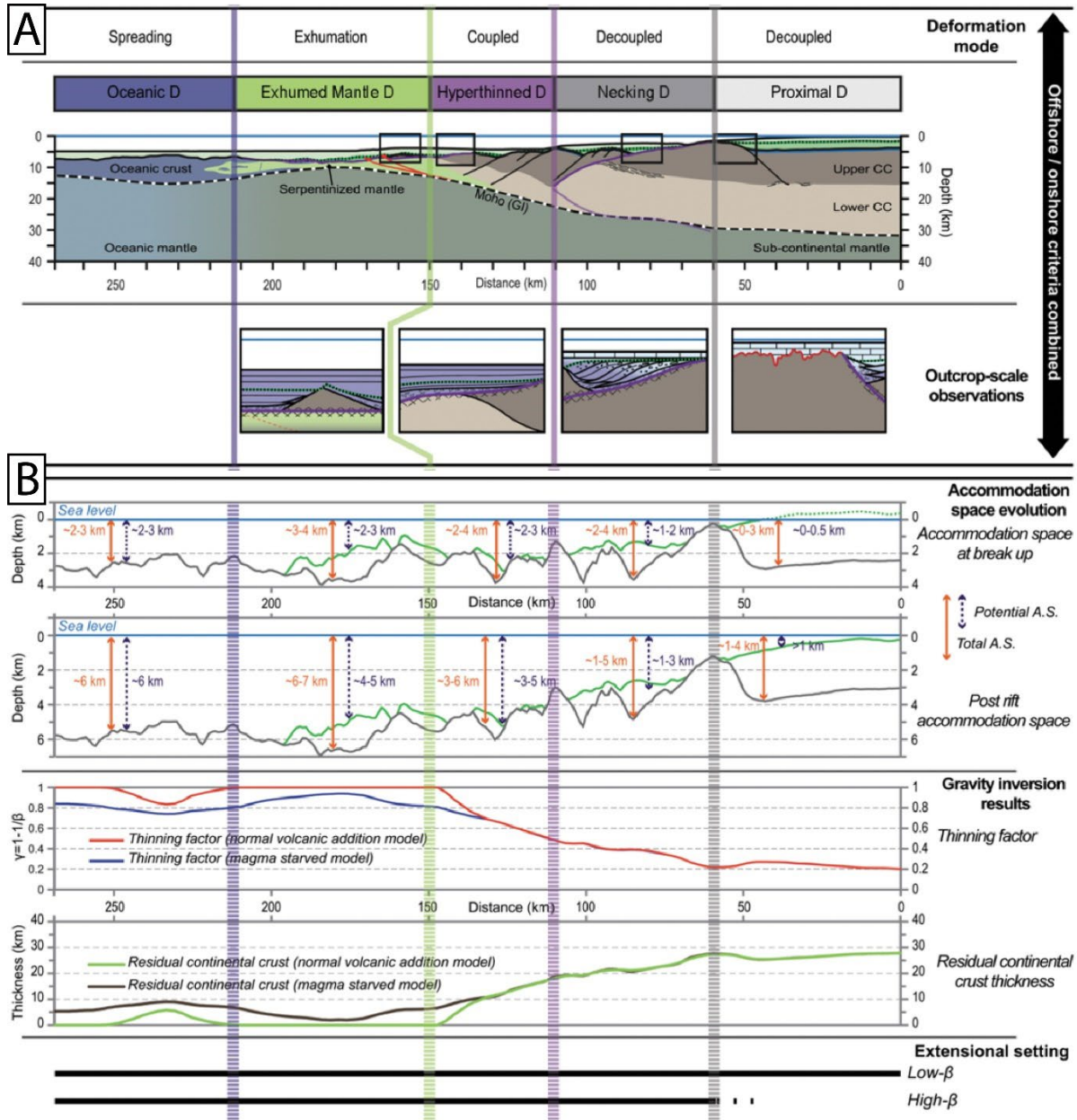


Figure 1.24: A-Cross section of the Bay of Biscay margin (from Tugend et al., 2014) and associated outcrop observations from the Pyrenean fossil rifted margin. B- Evolution of the syn-rift and post-rift accommodation space (A.S.) across the margins. Potential accommodation space corresponds to the distance between surface and seafloor while the total accommodation space corresponds to the distance between the surface and the top basement. This shows that important accommodation space is found in the distal domains associated to thick sedimentary deposits while the proximal is marked by small accommodation space and thin sedimentary deposits (from Tugend et al., 2014). The necking domain corresponds to the transitional domain between the proximal and distal domains marked by increasing potential accommodation space and moderate sedimentary thickness. The residual continental crust thickness and thinning along the margins are also indicated.

The evolution of the accommodation space is a key parameter controlling the stratigraphic evolution. Reconstruction of accommodation space using the syn- and post-rift stratigraphic record

provides key information about crustal and lithospheric thinning during and after rifting (Tugend et al., 2015). The necking domain marks an increase of the accommodation space compared to the proximal domain. This change of accommodation space is associated to a change of crustal thickness and syn-rift lithospheric thinning. During post-rift subsidence, the necking domain is also affected by a strong increase of the accommodation space compared to the proximal domain (Fig. I.24B).

In terms of lithology, important basement uplift in response to upper mantle rupture leads to the formation of large clastic deposits. This is clearly visible in the Mont-Blanc massif and its surrounding areas where large sandstone deposits have been interpreted as the stratigraphic response to necking (Ribes et al., 2020). These sandstones are lying above the pre-rift deposits and the basement or are interfingered with the time-equivalent Early Jurassic carbonate deposits of Pliensbachian age. These clastic deposits are composed of conglomerates at the base passing progressively to fine-grained tidal deposits. The conglomerates show reworking of the sedimentary cover and the basement while the sandstones are derived exclusively from the basement. An important transgression surface is observed above the sandstones with deposits of black shales. In the proximal and distal domains, syn-necking sediments correspond to turbidite to calci-turbidites (Epard, 1989, Ribes et al., 2019a) related to a progressive increase of source distance. In the distal parts of the basin, the sediments are characterized by very fine-grained, shale-rich deposits (Trümpy, 1951).

2.4. Margin evolution through time

These different domains of rifted margins (Table I.4) are the result of different physical processes during rifting that range from decoupled deformation dominated by pure-shear to coupled deformation dominated by simple-shear under an increasing thermal gradient. The proximal domain is the result of the stretching phase (Fig. I.23). The key parameter is the decoupling between the upper crust and lower crust. This decoupling is achieved because of the presence of a ductile “weak” felsic middle and lower crust. The occurrence of mafic underplating at the base of the crust leads to the formation of more competent lower crust. Rift initiation is associated to diffuse extension accommodated by high-angle normal faults in the upper crust leads to the formation of a low- β basin.

Crustal necking is responsible for the localisation of the deformation in the H-Block, which will become the future distal domain due to rupture of the most competent layer and for the crustal thinning in the H-Block below 20km. This event leads to the progressive increase of the temperature in the rift centre. This localisation is accommodated by crustal scale basins bounding detachment faults leading to the progressive coupling between the lower and upper crust corresponding to the future necking domain. The rift at this moment appears relatively symmetrical (Hauptert et al., 2016).

The total coupling of the upper and lower crust at the end of the necking stage in the H-Block is associated to the coupling point.

<i>Rift stage</i>	<i>Thermal gradient</i>	<i>Type of fault</i>	<i>Basin architecture</i>	<i>Type of sediments</i>	<i>Preservation in rift domain</i>
<i>Stretching</i>	30-40°C/km	High-angle normal fault	Half-graben with formation of growth strata towards the faults	Continental clastic deposits to shallow marine sediments	Proximal domain In the necking domain and hyperextended domain remnants of such basins can be preserved
<i>Crustal necking</i>	From ca. 30°C/km to 60°C/km	Large offset detachment faults	Conformable syn-tectonic sediments over the fault	Clastic sediments derived from basement uplift	Necking domain
<i>Hyper extension</i>	60 to 80°C/km	Sequential detachment faults	Conformable syn-tectonic sediments over the fault+ sag basins	Reworking of exhumed basement; turbidites and/or pelagic sediments	Hyperextended domain
<i>Mantle exhumation</i>	80-100°C/km	Large offset detachment faults	Conformable syn-tectonic sediments over the fault+ sag basin	Mantle reworking turbidites and pelagic sediments (e.g., radiolarian cherts)	Exhumed mantle domain

Table I.4: Characteristics of the different rifting stages

The following stage defines the future upper and lower plate. Indeed, the hyperextension phase is restricted to the H-block/key stone where the crust is completely embrittled enabling sequential detachment faults to thin and delaminate the crust until mantle exhumation to the seafloor occurs (Fig. I.23). This sequential faulting leads to the formation of an asymmetric margin

under simple shear deformation defining the upper and lower plate. Remnants of the previous rift stages can be found in allochthonous blocks where the syn-stretching and necking deposits are preserved.

The hyperextension is associated to an increase of the temperature due to the continuous asthenosphere rising. The end of the hyperextension is marked by the onset of mantle exhumation marked by the exhumation point.

Mantle exhumation is related to detachment faulting with increasing magmatic imprint overprinting detachment faulting (Fig. I.23) (Coltat et al. 2020). The magmatic activity increases until a steady-state magmatic system is achieved marking the onset of seafloor spreading associated to the break-up point. Structures similar to oceanic core complex are formed, which correspond to a dome-shaped detachment faults crosscut by later high angle normal faults (Epin et al., 2019). While mantle exhumation is achieved, the necking and proximal continue to subside as the lithosphere cools.

Take-home message

- The Iberia-Alpine model is the archetype of the magma-poor sediment starved margin. The model was developed combining observation from the present-day Iberia margin and outcrops from the Alps.
- The different domains of the margin (proximal/ necking/ hyperextended and mantle exhumed domains) were formed during different stages of the rifting (stretching/ necking/ hyperextension and mantle exhumation) associated to migration and a narrowing of the rift zone.
- The proximal domain which is affected only by the stretching phase is characterized by minor extension accommodated by high-angle normal faults. The upper and lower crust are decoupled.
- The hyperextended domain is characterized by detachment faults accommodating large offsets leading to mantle exhumation. They record the stretching to hyperextension stages. The crust and the mantle are coupled.
- The necking domain is characterized by the progressive thinning of the crust from 25 ± 5 km to 10 km and is associated to the progressive coupling between the upper crust and lower crust.
- This coupling is achieved during crustal necking, which corresponds to the localisation of the formation in response to the rupture of the strongest layer of the lithosphere, which is the upper mantle. This event associated to significant thermal increase and topographic uplift isolate the proximal domain from the future distal domain (H-Block).

3. Fault-controlled fluid circulations in extensional system

3.1. Fault definition

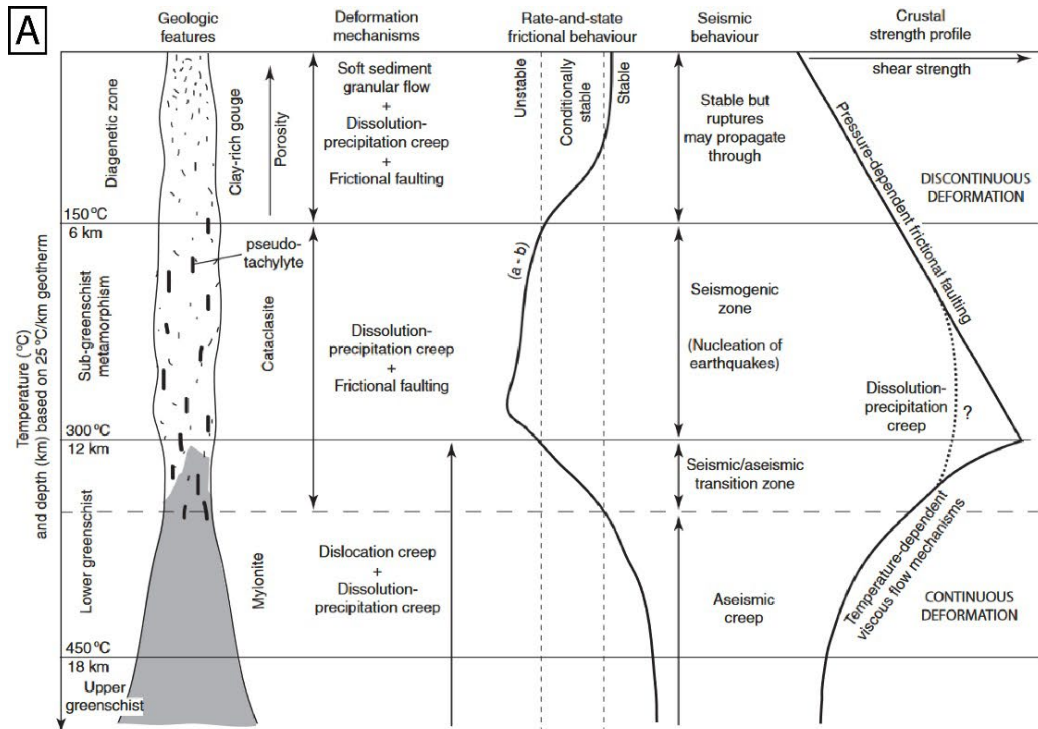
Fault zones are discontinuities in the brittle parts of the crust and mantle accommodating large shear strains. A fault is characterized by an offset corresponding to the accumulated displacement on the fault. Fault mechanics is controlled by the interplay between shear stresses and normal stresses. High shear stresses favour slip while high normal stresses prevent slip. They are related by the equation: $\tau = C_o + \mu\sigma_n$ (1) with σ_n the normal stress at the surface, τ the shear stress, C_o the cohesion of the material and μ the coefficient of internal friction. Moreover, increase of pore pressure decreases normal stresses favouring fault slip. The fault angle to the principal stress axis is related to the friction: $\theta = 45^\circ - \frac{\varphi}{2} = 30^\circ$ (2) with $\varphi = \tan^{-1}\mu$. Friction of 0.65 as postulated by Byerlee (1978) for the crust corresponds to an angle of ca. 30° to the principal stress axis.

3.1.1. Fault structure

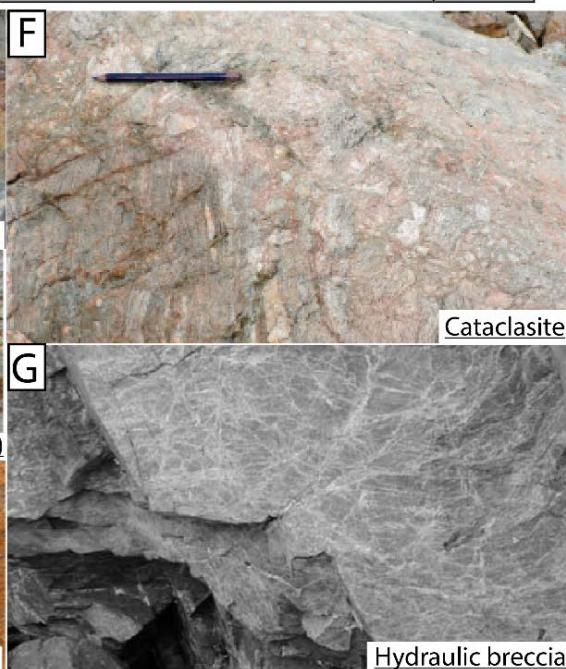
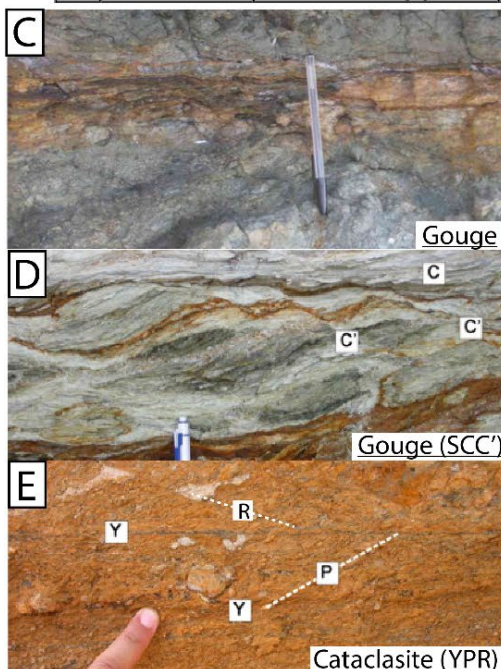
A fault zone is composed of a damage zone and a core zone with various thicknesses. The core zone is the part of the fault where most of the slip is accommodated at shallow depth (less than 5 km depth). The damage zone corresponds to the deformed basement bounding the fault core. There are no clear scaling relations between the thickness of the damage and core zones, and the offset.

Fault rocks are the rocks formed along the fault zone in response to strain in the crust. The response of the rock to the strain depends on the temperature and the pressure at which deformation occurs. Two main mechanisms are found in nature, plastic and frictional deformation (Fig. I.25A). First, at temperature between 150 and 300 °C deformation is brittle, which means that it is accommodated by fractures sliding and abrasion of the grains leading to grain comminution and important dissolution precipitation (Boulton et al., 2009; Collettini et al., 2009). Second, at high temperature (above 300°C), the rocks are deformed under plastic flow and deformation is continuous. For quartz, the transition from brittle to plastic flow occurs at around 300°C (Stipp et al., 2002). For a quartz-feldspathic crust with a normal geothermal gradient of 30°/km, it corresponds to about 10 km depth. However, for feldspars the transition occurs at higher temperature (above 450°C). Fault rock classifications (Fig. I.25A and B) are based on the mechanism of deformation, the amount of cementation and the ratio of the matrix vs clasts (Braathen et al., 2004). When deformation is dominated by plastic flow the fault rocks are called mylonite or phyllonites depending on the content of phyllosilicates. When frictional deformation dominates, the fault rocks correspond to cataclasites, pseudotachylites, breccias and gouges.

General concepts related to the Wilson cycle and rifted margins



Brittle		← Deformation style →			Ductile		% matrix and grain-size	
Frictional flow		← Dominant deformation mechanism →			Plastic flow			
Non-cohesive		Secondary cohesion		Primary cohesion				
		Cemented HB	Indurated HB	> 50% phyllosilicate	< 50% phyllosilicate			
Hydraulic breccia (HB)	Breccia series	Proto-breccia	Cemented proto-breccia	Indurated proto-breccia	Proto-cataclasite	Proto-phyllo-nite	Proto-mylonite	0-50% matrix
		Breccia	Cemented breccia	Indurated breccia	Cataclasite	Phyllo-nite	Mylonite	50-90% matrix
		Ultra-breccia	Cemented ultra-breccia	Indurated ultra-breccia	Ultra-cataclasite	Ultra-phyllo-nite	Ultra-mylonite	90-100% matrix
	Gouge	Cemented gouge	Indurated gouge					Sub-microscopic matrix
		Pseudotachylite						



General concepts related to the Wilson cycle and rifted margins

Figure I.25: A- Conceptual model of a strike slip fault showing the repartition of the different fault rocks according to the temperature in the crust (for a gradient of 25°C/Km) in relation to the main mechanism of deformation (from Fagereng and Toy, 2011). B- Classification of fault rocks according on the deformation style and content of matrix (from Braathen et al., 2004). C- Illustration of a core zone composed of gouge (from Collettini, 2011) D- Talc-smectite gouge from the Zuccale detachment fault (Elba island) showing SCC' structures associate to viscous flow and mineral precipitation (Collettini, 2011). E- Cataclasite with YPR structures formed under frictional flow along the Zuccale detachment fault (Collettini, 2011). F- Cataclasite from the Grosina detachment fault, Central Alps (Mohn et al., 2012). F- Hydraulic breccia showing jigsaw fractures (from Braathen et al., 2004).

The term cataclasite (Fig. I.25E and F) corresponds to coarse to fine-grained rocks with a mechanism of deformation at the transition between plastic and frictional flow, keeping cohesion during deformation (primary cohesion). Pseudotachylites correspond to ultra-fine-grained rocks formed during seismic slip and local slip-induced melting (Kirkpatrick and Rowe, 2013). At macroscale they form dark veins corresponding to melt injections in the basement and are characterized at microscale by the presence of silica glass and volcanic textures such as amygdules and spherulites (Kirkpatrick and Rowe, 2013). Pseudotachylites are usually strongly altered and hard to recognize.

The term breccia (Fig. I.25G) is used for coarse-grained rocks with low matrix content whereas the term gouge (Fig. I.25C and D) is used for ultra-fine-grained rocks (Braathen et al., 2004). These breccias and gouges can be cemented or indurated (secondary cohesion).

The type of deformation in cataclasites and gouges varies depending on the total amount of phyllosilicates and the presence of fluids. Indeed, purely frictional deformation as observed mostly in cataclasite and ultracataclasite leads to the formation of YPR structures (Fig. I.23E). Strong shearing is accommodated by the main Y-plane. Secondary R (Riedel), R' (antithetic Riedel) and P planes are visible at a certain angle to the Y-plane. This is similar to the structures defined at macroscale along fault zone (Dresen, 1991). Indeed, frictional deformation is scale independent and therefore, structures observed at the macroscale can be observed at the microscale. However, frictional-viscous deformation associated to the precipitation/recrystallisation and sliding of the phyllosilicates lead to the formation of SCC' (Imber et al., 2008) structures similar to mylonite (Fig. I.23D). This type of deformation is observed mostly in gouges and phyllonites.

3.1.2. Mechanisms of fluid circulation along faults

Fault zones are characterized by important anisotropy along and across the fault plane (Evans et al., 1997). Significant dilation can lead to local increase of permeability enabling fluid circulation (Sibson, 1996; Wibberley and Shimamoto, 2003). In the damage zone of granitic hosted faults with very low initial permeability (10^{-19} m^2) such as the Median Tectonic Line strike slip fault in Japan permeability is relatively important (10^{-14} m^2). In the core zone, permeability is instead heterogeneous, from high values up to 10^{-14} m^2 to very low ones (10^{-19} m^2) in the phyllosilicate-rich zone (Wibberley and Shimamoto, 2003). Permeability also depends on time and deformation. Indeed, mineral precipitation can lead to progressive fault sealing while ongoing deformation can

create new fractures keeping the permeability high (Woodcock et al., 2007). It is therefore clear that faults can act both as conduits or barriers for fluid flow (Scholz, 1990). It was proposed by Caine et al., (1996) that the behaviour of a fault as a conduit, a barrier or both is controlled by the proportion of core zone vs damage zone along the fault. High core zone/damage zone ratio is associated to a barrier behaviour whereas low core zone/ damage zone ratio is associated to a conduit behaviour.

Local fluid overpressures associated to barriers can form along the fault, leading to that of disconnected fluid reservoirs. Release of fluids can occur during rupture of the fault, corresponding to a 'fault valve behaviour' (Sibson, 1990; Claesson et al., 2004; Zhu et al., 2020). The result is the formation of crack and seal veins associated to the sudden release of fluids along the fault (Ramsay, 1980), finely crystallized veins with clear euhedral crystals (Boullier et al., 2004), or cockade structures (Berger and Herwegh, 2019). Mixing of fluids with different origins is also commonly observed (Claesson et al., 2004). The veins formed along the fault can be submitted to subsequent deformation associated to fault activity (Boullier et al., 2004; Klee et al., 2021). Another effect of fluids along the fault zone is their role in earthquake initiation. Fluid overpressure can initiate rupture and trigger earthquakes (Sibson, 2014). Aftershocks are thought to reflect fluid migration in response to fluid liberation during the earthquake (Miller, 2013).

3.1.3. Crustal faults as pathway for fluid

Different geochemical reservoirs can exist in the crust associated to different fluid sources. Meteoric water is characterized by a low salinity. Seawater and sedimentary brines are characterized by important salinity especially in the upper crust. They are associated to low temperature reservoir (< 300°C) in sedimentary basins and in the upper crust. Moreover, fluids in the upper crust are mostly found under hydrostatic pressure (Müller et al., 1997). Metamorphic fluids derived from devolatilization and decarbonation show really low salinity and high content in gas especially CO₂ while magmatic fluids have a wide range of salinity and significant gas content (Yardley, 2005). They are associated to high temperature reservoirs (> 300°C) in the middle crust at the base of the seismogenic crust (15 to 20 km; Sibson, 2019). These different reservoirs are not always connected with each other, and overpressure can develop. Large crustal scale faults can connect these over pressured reservoirs with the surface leading to the concept of arterial faults (Sibson, 2019).

3.2. Detachment faults: a key tectonic feature of rifted margins

3.2.1. Definition of detachment faults

Detachment faults correspond to shallow dipping (< 30°) at the surface. They were first defined in the Basin and Range (Wernicke, 1981). They are usually associated to large offsets (kilometric displacement), which in the case in the Basin and Range can be up to 20 km (Wernicke, 1981; ; Zhao et al., 2018). Since the first discovery, detachment faults have been described from

General concepts related to the Wilson cycle and rifted margins

many other tectonic settings such as hyperextended magma-poor rifts (e.g., Iberia margin (Reston et al., 1996), Alpine Tethys (Manatschal, 1999), Corinth gulf (Rietbrock et al., 1996)) or post-orogenic collapse in the Alps (e.g., Simplon fault; Grasemann and Mancktelow, 1993; Mancktelow and Pavlis, 1994; Steck, 2008) or in the Himalaya (Searle, 2010)). Different types of detachments faults have been recognized associated to different mechanisms of formation. Some of the faults are flattened toward the surface due to footwall rotation, whereas they dip more steeply at depth (Wernicke and Axen, 1988; Lavier et al., 2000). On the other side, detachment faults can initiate at low angle (Collettini, 2011).

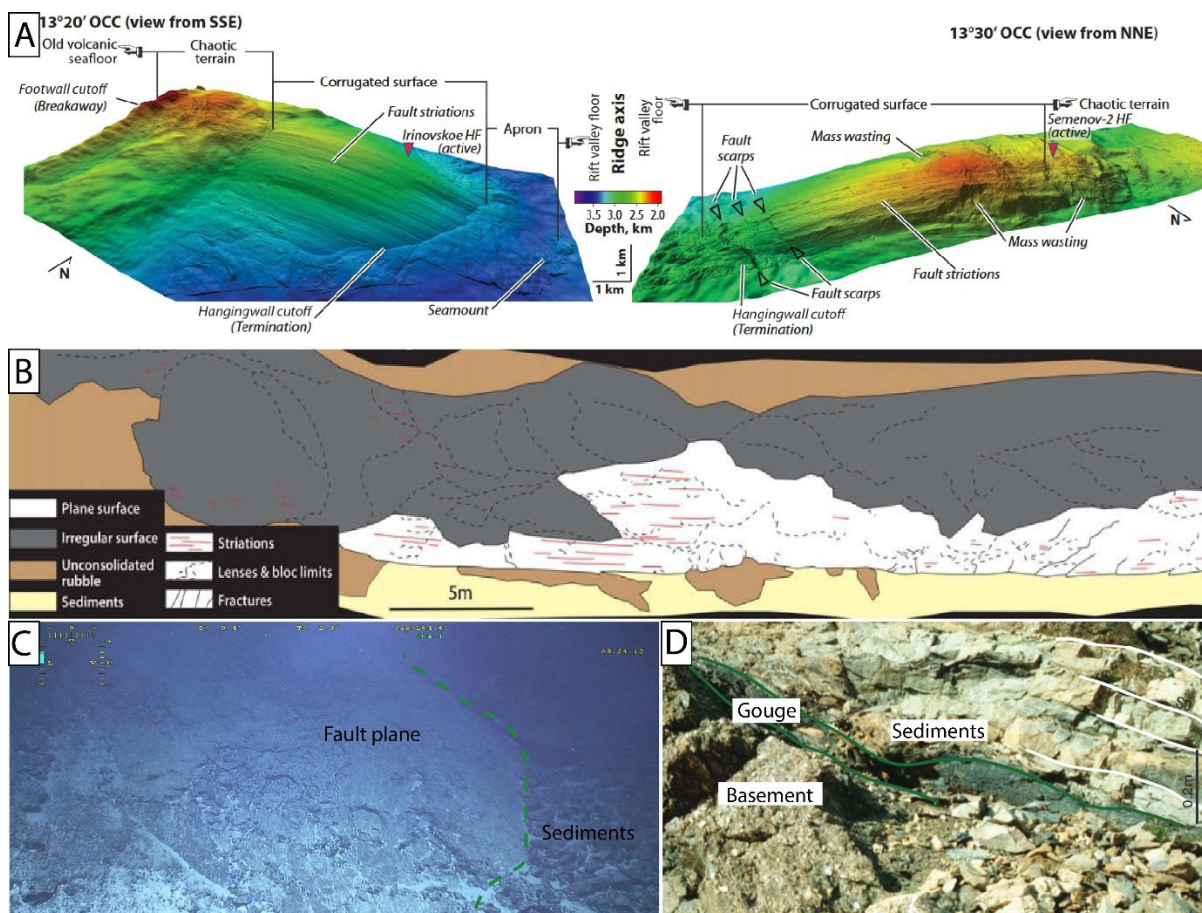


Figure 1.26: A- AUV microbathymetry images of an Oceanic Core Complex (Mid Atlantic Ridge, Escartín et al., 2017) showing the corrugated surface of the detachment fault with striation parallel to the displacement on the fault. B- Geological interpretation of the exhumed fault from an oceanic detachment (Bonnemains et al., 2017). The fault is partially covered by sediments. C- Rubbles and sediments over the detachment surface (from Escartín et al., 2017). D- Exhumed core zone (composed of gouges) overlaid by syn-rift sediments from the Err detachment, Central Alps (from Masini et al., 2011).

Large offset detachment faults are associated to exhumation of the footwall to the surface. This exhumed fault plane can be extremely complex. It is composed of gouges and cataclasites overlaid by sedimentary breccias (Wagner and Johnson, 2006; Christie-Blick et al., 2007; Masini et al., 2012; Escartín et al., 2017). Oceanic core complexes provide a good overview of the structure of an exhumed fault plane (Cannat et al., 1995). In the exhumed fault planes, corrugations are observed (Fig. 1.26A). They correspond to large undulations of the fault plane (50 to 100 m wide) parallel to the

slip direction (Parnell-Turner et al., 2018). These corrugations are formed due to the coalescence of anastomosed fault surfaces at depth. Additionally, large rubbles, sediments and breccia are observed above the exhumed fault plane (Fig. I.26B and C). Reworking of fault rocks such as cataclasites and even indurated black gouges have been described in fossil detachment faults in the Alps (Masini et al., 2011). One of the key characteristics is that syn-tectonic sediments are deposited conformably above the fault plane (Fig. I.26D), which is not possible for high-angle normal faults.

3.2.2. Mechanisms controlling detachment fault formation

Anderson theory tells that normal faults form at a high angle. Therefore, the existence of detachment faults appears at first, counterintuitive and physically impossible. This raised important debates in their mechanisms of formation (see Appendix A).

Fault flattening occurs in response to isostatic rebound triggered by unroofing of the footwall and possible thermal support associated to elevation of the temperature due to rifting (Wernicke and Axen, 1988; Lavier et al., 2000). A first model developed in the Basin and Range implies a listric fault, which is a normal fault with a dip angle of 60° near the surface and flat at depth where it is rooted into a decoupling level (Wernicke and Axen, 1988). As the extension continues, the footwall is pulled out underneath the hanging wall. As a consequence of the unloading, the footwall is isostatically compensated and uplifted, resulting in a low angle geometry of the former listric fault. A second model implies an initial high-angle normal fault (Lavier et al., 2000). Important extension on a normal fault should lead to significant vertical movement. However, the physical work to overcome gravitational forces and the flexure of the plate is too strong to allow any vertical movement (Forsyth, 1992). The only possibility for accommodating more displacement on the fault is to minimize the vertical movement. Therefore, the fault must be flattened when reaching the surface to maximize the horizontal movement (transforming the vertical offset into horizontal offset). This gives a convex upward shape to the normal fault. Important back-rotation leading to fault flattening can also lead to fault abandonment because of unsuitable fault orientation (Webber et al., 2022).

Fault initiation at shallow angle is usually associated to non-Andersonian stress orientations with rotation of the principal vertical stress. Deviation of the stress field can be related to large-scale anomalies such as a Moho bulge (Spencer and Chase, 1989), flow of ductile crust leading to important shear stress (Yin, 1989) or to local perturbation in the stress field such as high fluid pressure or dyke (Parsons and Thompson, 1993). Besides, reactivation of thrusts can lead to low angle normal fault formation (Axen, 1993).

3.2.3. The importance of hydration reactions for fault behaviour

3.2.3.1. Friction reduction of fault rocks

Fluid flow has a strong influence on fault mechanics. Indeed, strong fluid rock interaction leads to important mineral changes. In quartzo-feldspathic rocks, hydration reactions along the fault zone lead to feldspars saussuritization (replacement of Ca- plagioclase by epidote, chlorite and white micas) and sericitization (replacement of albite and orthoclase by white micas) under temperature of ca. 150 to 300°C (Manatschal, 1999; Wibberley, 1999). Mg-rich mafic rocks are affected by serpentinization and important chloritization (Evans et al., 2013; Pinto et al., 2015; Bonnemains et al., 2017; Quesnel et al., 2019). Formation of phyllosilicate-rich fault zones can lead to a change of physical properties such as friction. Low friction enables fault slip and facilitate formation of large offset detachment faults (Forsyth, 1992; Buck, 1993; Collettini, 2011). This process is referred to as strain weakening (Wintsch et al., 1995) and is described in many active and paleo-faults (e.g., San Andreas fault, US (Evans and Chester, 1995; Lockner et al., 2011), the Alpine fault in New Zealand (Warr and Cox, 2001), the Err detachment in Eastern Switzerland (Manatschal, 1999); Le Moine thrust in Scotland (Wibberley, 2005), the Median Line in Japan (Jefferies et al., 2006)). Indeed, phyllosilicates have in general a low friction explained by their crystallographic structure (sliding along the 001 plane; Faulkner et al., 2018). Talc is the mineral with the lowest friction coefficient between 0.1 and 0.2 (Ikari et al., 2011; Moore et al., 2016). Serpentine has also friction coefficient lower than 0.2 (Tesei et al., 2018). Clay minerals show a wide range of friction coefficients, between 0.4-0.1. The absorption of water, which can be significant in such minerals (e.g. montmorillonite) can decrease drastically the friction (Morrow et al., 2000). Illite minerals have a friction coefficient of around 0.3-0.2 (Tembe et al., 2010). Decrease of friction between muscovite and illite is explained by the lack of interfoliar cation in illite leading to a less efficient bonding of the layers.

3.2.3.2. Thermal evolution of the footwall

Exhumation of the footwall is associated with exhumation of deeper and hotter basement resulting in an increase of the advective heat resulting in a higher geothermal gradient which in turn can reduce the elastic thickness of the crust (Lavie and Buck, 2002). This can result in the formation of a secondary fault and the abandonment of the main detachment fault. Strong hydrothermal circulation can help cooling the crust and the related hydration reactions can keep the detachment fault zone weak (Manatschal, 1999; Lavie and Buck, 2002; Collettini, 2011). As an example, footwall cooling was observed along the Whipple Mountain detachment fault (USA), associated with strong thermal gradients observed over very short distance (decrease of 80°C over 40 m; Morrison and Anderson, 1998).

3.2.4. Fluid circulation associated to detachment faults

Fluid circulations along detachment faults are responsible for intense fluid-rock interactions. The type of interaction depends on the type of rocks and the composition of the fluid. The fluids are mostly composed of meteoric and seawater derived aqueous solutions (Fricke et al., 1992; Manatschal et al., 2000) with various dissolved gas observed depending on the fluid origin and the tectonic context.

3.2.4.1. Element transfer associated with detachment faulting

Fluid circulation is associated with element transfer along faults. The mobility of elements depends on the type of rocks altered but also fluid temperature, pH-eh conditions and the fluid composition. Indeed, the solubility of metals in aqueous fluids depends on the type of complexes they will form and on the type of ligands. Lithophile elements are usually classified as hard and soft metals. Hard metals (e.g. Na, K, Mg, Ca, Rb, Sr, Ba) tend to form complexes with fluorine or with species where the electron donor is oxygen, such OH^- or SO_4^{2-} (Vance and Little, 2019). Soft metals (e.g., Pb, Zn, Sn, Sb, Ga, Ge) are characterized by an important number of electron valence. They tend to form strong complexes with Cl and Br (Vance and Little, 2019). Transition metals (e.g., Mn, Fe, Cu, W) form a specific category with specific properties. Their wide number of valence states enables them to form a large variety of aqueous species (Vance and Little, 2019).

Elements such as Si, Na, Ca and K are released from the basement through hydration reactions such as sericitization and chloritization (Keith and Reynolds, 1980). Continental detachment faults show enrichment of Mn, Cu, Pb, Zn and Ba in fault rocks along a detachment fault as observed in the Basin and Range (Roddy et al., 1988). Such element transfer along faults can possibly result in large Cu, Pb, Ag ore deposits (Spencer and Welty, 1986), highlighting the significance of detachment faults as major fluid pathway.

3.2.4.2. K-metasomatism along detachment faults

Fluid circulation along continental detachment faults have been mostly studied in the Basin and Range, where excellent outcropping conditions are met (Spencer and Reynolds, 1989; Roddy et al., 1988). The footwall of the detachment faults are characterized by chlorite-epidote alteration associated to reductive conditions under retrograde metamorphism (Zappettini et al., 2017). Base metals sulphides can form in the footwall and are associated to fluid temperature of 300 to 350°C and salinity between 5 and 15 wt% NaCl equiv. (Roddy et al., 1988; Long, 1992). The hangingwall is characterized by K-metasomatism associated to circulation of oxidizing basin brines. This K-metasomatism corresponds to the replacement of plagioclase by orthoclase (Roddy et al., 1988). The deposits in the hanging wall correspond to Mn oxides and Ba-F veins. They are also observed in the syn-rift basin in association with iron oxides (e.g., hematite).

3.2.4.3. Mg-metasomatism along detachment faults

Detachment faults linked to oceanic core complexes and mantle exhumation are associated to important Mg metasomatism. They have been studied mostly in fossil rifted margins such as in the Pyrenees and the Alps. Mantle serpentinization is associated to release of Mg-Cr rich fluids (Lagabrielle et al., 2019). Mg-metasomatism is characterized by talc and Mg-chlorite formation (Moine et al., 1989). They show fluid temperatures between 160 to 280°C and high salinities, between 12 to 38 wt% NaCl equiv. (Nteme Mukonzo et al., 2021). The fluids are also characterized by high CO₂ and CH₄ content leading to significant carbonation.

3.3. Detachment fault as fluid pathway in rifted margins

3.3.1. Fluid circulation in the hyperextended domain

Fluid circulation has been studied in detail at fossil hyperextended domains found in the Central Alps. The detachment fault appears as a major pathway for fluids. Significant hydration of fault rocks is commonly associated with the breakdown of feldspars (Manatschal, 1999). Additionally, this strong hydration appears as one of the main drivers for the detachment formation through fault weakening associated to low friction minerals such as chlorite and white micas. Enrichment in Ni and Cr along fault zones indicate that fluid reacted with the mantle before circulating along fault zones in the hyperextended crust back to the seafloor (Pinto et al., 2015). Further observations based on isotopic Sr ratio provides a better constrain on the fluid pathway (Hochscheid et al., 2022). Downflow of seawater derived fluids along normal faults through a hyperextended crust into the mantle resulting in serpentinization is shown by the Sr isotope signature. This channelized fluid flow along detachment faults is a key element during the first step of serpentinization associated to hyperextension.

3.3.2. Fluid circulation associated with crustal necking

The increase of the thermal gradient in the necking domain associated with important crustal and lithospheric thinning makes that this domain represents a favourable tectonic setting for hydrothermal circulation in the basement. However, no studies clearly focused on fluid circulations in the necking domain. Due to the difficulty in accessing necking zones in present margins, fossil analogues are mandatory to get a better comprehension of hydrothermal systems in these domains.

Few examples of necking detachment faults have been described so far (Mohn et al., 2012; Bot et al., 2016). These faults are affected by significant fluid circulations and related breakdown of feldspars. Few information is however available concerning the type of fluids which circulated along these faults. Enrichments in K and Fe have been noticed along the fault zones (Bot et al., 2016).

Some work has been done on the fossil Adria rifted margin in relation to fluid circulation. In the pre-rift cover, important syn-necking (Pliensbachian to Toarcian; Incerpi et al., 2019)

hydrofracturing and dedolomitization processes were described, indicating significant fluid flow linked to hydrothermal activity in the cover with homogenization temperatures of the fluid up to 160°C. Silica rich-fluids have been identified to form during the necking stage. These fluids were enriched in highly radiogenic Sr and had $^3\text{He}/^4\text{He}$ pointing toward a crustal source (Incerpi et al., 2019). This indicates significant fluid circulations in the crust. However, no data from the cover of the necking domain has been collected so far because of its poor preservation in the Adria margin. Therefore, the pathway of the fluids from the cover to the basement, the fluid temperature and the element transfer associated to crustal necking are only poorly constrained at this stage.

Take-home message

- Detachment faults enable to accommodate important extension and are associated with the formation of significant topographic relief.
- Fluid rock interactions are key for detachment formation through friction reduction along fault planes.
- Detachment faults are fluid pathways which enable element transfer at large scale between the crust and the cover.
- Detachment faults are important pathways for fluids during hyperextension and mantle exhumation.
- Few examples of necking detachment faults are available therefore, the type of fluids and the fluid pathways during crustal necking remains unknown.
- Few data from the pre-rift cover in the Central Alps indicate a switch from carbonate-rich to silica-rich fluids associated to an isotopic crustal signature.

4. Key questions concerning rifted margins

The comprehension of magma-poor rifted margins increased dramatically during these last 20 years. The main parameters controlling the architecture of the margin and its thermal evolution have been identified. The main questions concern the role of pre-rift inheritance in the evolution of rifted margins. It was pointed out that structural inheritance and compositional inheritance have an impact on the overall architecture of the margin as well as on the magmatic budget during rifting. These questions are driving most of the attention nowadays. However, another aspect of the rifted margins, which is not well constrained, is crustal necking.

The necking domain corresponds to the least understood domain of rifted margins despite the key role of crustal and lithospheric necking on the rift evolution and final rift architecture. From the first recognition by Mohn et al. (2012) to present, many studies have been accomplished concerning the structure of the necking domain as well as the evolution of the crust and mantle during necking based on numerical modelling (Chenin et al. 2020). From these studies, it appears clear that necking of the crust is related to significant crustal thinning associated to basement exhumation. The response to this event is important topographic uplift and increase of temperature due to asthenosphere uplift. However, there is a lack of constraints based on observations on present-day and fossil rifted margins. Preliminary work on the Western Alps highlighted the presence of massive sandstones around the Mont-Blanc interpreted as the sedimentary response to crustal necking. This study by Ribes et al. (2020) showed that the necking domain might be partially preserved around the Mont-Blanc providing a fossil analogue for the necking domain.

The key questions concerning the necking domain are related to the tectono-sedimentary and fluid evolution of the necking domain. The sedimentary evolution can be observed only at a large-scale on present-day margins and few information is available concerning the environment of deposits and their evolution during crustal necking. Therefore, main questions that remain are:

- **What is the timing of the topographic uplift and the extent of the topographic high created during necking?**
- **What is the clastic source and the extent of the clastic deposits related to the crustal necking?**
- **What is the tectono-sedimentary evolution of the necking domain?**

Other questions remaining unresolved concerns the thermal evolution associated to crustal necking and its relationship with fluid circulation. Questions addressed in this study are:

- **What is the thermal evolution of the necking domain?**
- **What are the fluid characteristics and pathways associated to necking?**
- **What is the geochemical signature of fluids related to crustal necking?**
- **Are there ore deposits related to crustal necking?**

Chapter II- From rifting to orogeny, concepts developed in the Alps over a century



View of the Mont-Blanc from the Tête Nord des Fours (France)

« La continuité des grands spectacles nous fais sublimes ou stupides. Dans les Alpes, on est aigle ou crétin » (Victor Hugo)

From rifting to orogeny, concepts developed in the Alps over a century

Foreword

This chapter will focus on the Alps and more specifically on the External Crystalline Massifs (ECM) in the Western Alps. The first part of the chapter will introduce the paleogeographic evolution of the Alpine domain and the related concepts, as discussed from the late 19th century to modern time. Finally, a discussion on the pre-rift rheology of the crust in the Western Alps is proposed to understand the type of inheritance encountered during rifting.

The second part of the chapter focus on the present-day architecture of the Alpine orogen from map view, crustal sections and geophysical transects. In a second time, a general evolution of the Western Alps from subduction to collision is presented.

The third and last part of this chapter focuses on the ECM and more particularly on the Mont-Blanc area, which is the topic of the work presented here. A presentation of the structure of the massif and its Alpine history are briefly introduced. A discussion on the two rift models for the Mont-Blanc, the high-angle normal fault vs the detachment fault and their implication is proposed.

Introduction

The Alps have been studied over more than 200 years and have been the birthplace of many theories and concepts concerning the formation of orogens (e.g., discovery of thrust nappes in the late 19th century (Bertrand, 1884) and of continental subduction (Chopin, 1984)). However, the Alps were not only a fertile place to understand orogenic processes but also for investigating rifting processes. The early recognition of marine Mesozoic rift basins (Bernoulli et al., 1979) led to the first attempt of paleogeographic reconstructions. In addition, the application of the plate tectonic theory to the Alps led to the recognition of the Jurassic Alpine Tethys oceanic domain. The link between the paleogeographical domains of the Jurassic rifted margins and the Alpine tectonic units helped understanding the evolution from rifting to collision. Moreover, rift-related structures are locally well preserved in the Alps. The identification of exhumed mantle and its interpretation as remnants of the former Alpine Tethys distal margins make of the Alps a key place to understand the formation of magma-poor rifted margins.

However, one of the remaining questions in the Alpine evolution is the role of the External Crystalline Massifs (ECM) during rifting and Alpine collision. In addition, debates concerning the interpretation of the ECM as the former necking domain of the European margin raised also numerous questions concerning the pre-Alpine and Alpine evolution of these ECM.

1. The Alpine orogen: An inverted fossil rifted margin

1.1. The Wilson cycle in the Alps

1.1.1. Recognition of the oceanic basins and embryonic nappe tectonics

The Alps are the birth place of various concepts in structural geology and tectonics (Schaer, 2010, 2011). By the end of the 19th century and the beginning of the 20th, thrust and folds were recognized in the Alps both in the internal part (e.g., Penninic domain (Lugeon and Argand, 1905), the external part (e.g., Glarus (Bertrand, 1884), Helvetic domain (Lugeon, 1902), Prealps (Schardt, 1893) and the Jura (Buxtorf, 1907)).

The recognition of different sedimentary environments with different ages was a key problem for understanding the tectonic structures described previously. In the 19th century, the recent improvement of palaeontology applied to the Prealps in Switzerland raised some major questions as summarized by Masson (1976). The juxtaposition of rocks of similar age but different paleo-environments was indeed an important problem (e.g., shallow marine and deep-water sediments). The situation was even more complex with the juxtaposition of extremely different

From rifting to orogeny, concepts developed in the Alps over a century

terrane both in ages and paleo-environments. Vertical and horizontal movements were already recognized and accepted at the end of the 19th century (Schaer, 2010). Vertical movements were related to continental uplift or subsidence, and horizontal displacement was related to folding (Termier, 1922). These movements were tentatively explained by the contraction of Earth by cooling (de Beaumont, 1829). The problem of the lateral displacement was brilliantly solved by Marcel Bertrand (1884) and Hans Schardt (1900, 1907), who introduced the concept of nappes to explain the juxtaposition of different terrains. His works, based on one century of observations from De Saussure to Heim, put the basis for a modern interpretation of the Prealps. After that, different nappes were described such as the Prealps Mediane nappes, the Brèche nappe and the Ultrahelvetetic nappes (see references in Masson (1976)). With the identification of the nappes, attempts to restore them to their paleogeographic positions were made by Schardt (1898). He mentioned for the first time an affinity of some of the Prealps nappes with the 'intra-Alpine Briançonnais', highlighting the possible large transport of these nappes during Alpine orogeny. The Briançonnais block has been intriguing for geologists since the beginning of Alpine geology. This domain, by its stratigraphic and structural position was called 'exotic block'.



Emile Argand (1879-1940)
Credit: C.E. Wegmann

The beginning of the 20th century marked a major change in the geologic community with the massive adoption of the nappe theory (Masson, 1976). The distinction between the internal metamorphic units and the external unmetamorphosed units was proposed. Geologists started then to work on the position of the nappe roots and on the paleogeography using stratigraphic and structural arguments. Mapping of the different nappes in the Alps was achieved by Argand (1916) and identified the axial trace of the large scale

folds in the internal part of the orogen. On the same time, Heim (1918) recognized the importance of decollement levels such as evaporites in the Jura even if he could not identify a satisfactory mechanism for the emplacement of basement nappes from the more internal domains.

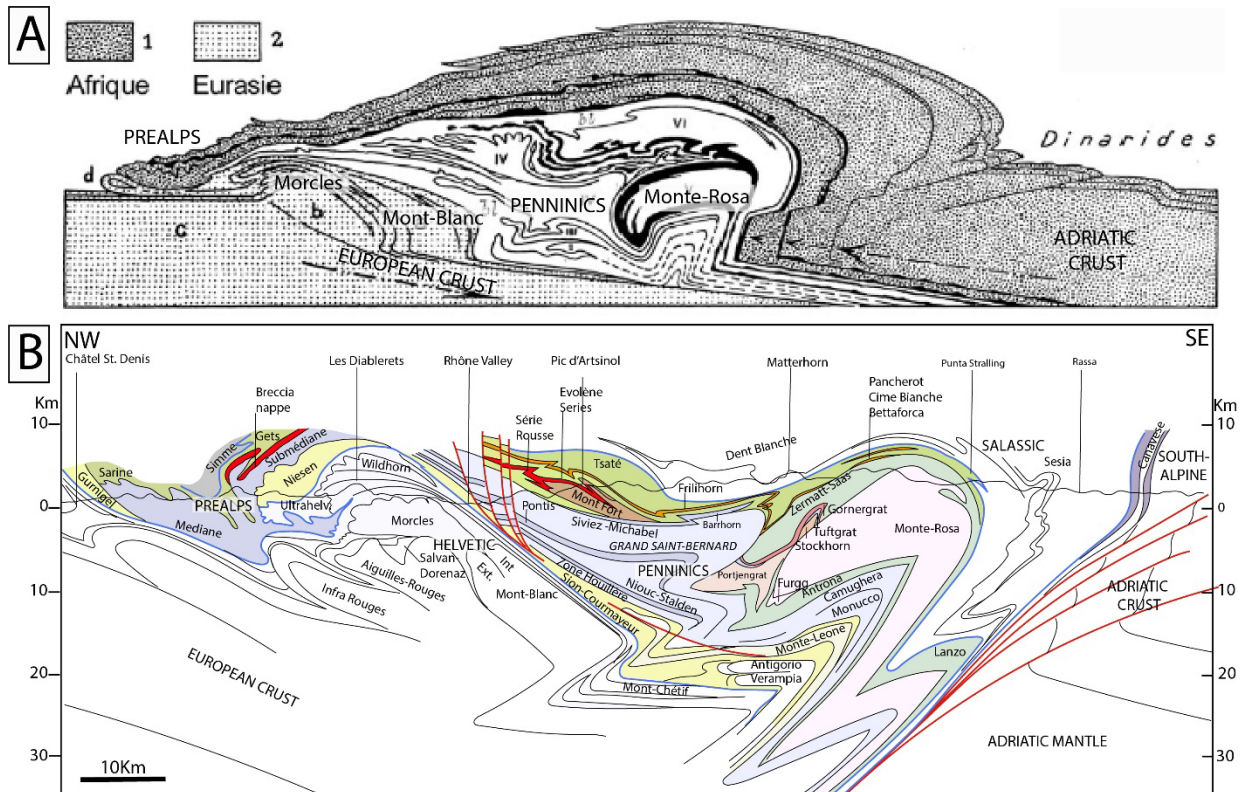


Figure II.1: A- Cross section of the Alps from Argand (1924) showing the pro wedge development and retro wedge in the Adriatic crust as well as the main tectonic nappes. B- Cross section of the Western Alps showing the position of the different nappes (modified from Escher et al., 1993 and Pantet et al., 2020).

The last advance was the recognition of crustal stretching leading to deep-water sedimentation before compression and nappe formation. As stated by Argand (1924) “A geosyncline will result, in general, from horizontal extension which stretches the raft of sial [continental crust] ... This explains the frequent association of greenstones with bathyal or abyssal sediments”. This interpretation hence reconciled a lot of observations from stratigraphy and structural geology with large displacements along the thrusts. The last major problem was the presence of ophiolites and their tectonic significance. Pioneering work by Steinmann (1905) led to the identification of ophiolites in the Eastern Alps interpreting them as “passively involved in the nappe” indicating an older age for these ophiolites (Bernoulli et al., 2003). This led to the first mapping of the different nappes in the Alpine realm, the identification of the main Alpine units, and the division between the external and internal domains (Fig. I.1A; Argand, 1924). The section proposed by Argand is close to the modern section of the Western Alps (Fig. II.1B). The pro wedge and retro wedge were already identified as well as the main tectonic units.

1.1.2. The problem of thin crust vs subducted continental crust

The revolution of plate tectonics led to a complete reinterpretation of the Alps and to the confirmation of some earlier work. However, a problem was identified quite rapidly. Crustal

thickening (45 km of crust) appeared relatively low in regard to the important displacements on the main thrusts (Trümpy, 1975). This led to two different explanations with different implications.

It was proposed, in analogy with present-day margins (especially the Red Sea), that the absence of crustal thickening is due to the collision of thinned crustal domains of the margin, allowing significant displacement without important overthickening of the crust (Helwig, 1976; Trümpy, 1975). This interpretation was proposed considering the latest observations from rifted margins in orogenic building. Postulating a pre-Alpine thinned crust (to less than 10 km thick) can indeed explain the present-day crustal thickness without any root delamination (Ménard et al., 1991).

The other interpretation is the removal of large portions of the orogenic root in the mantle (Daly, 1942). Crustal subduction as defined by Ampferer and Hammer (1911) was proposed as a mechanism for the removal of large volumes of crust. Densification of the crust can lead to slab break-off and sinking of the detached slab. This explanation was used to explain low crustal thickness and post orogenic magmatism, as well as the exhumation of UHP rocks in the internal domain of the Alps (von Blanckenburg and Davies, 1995).

1.2. Linking orogenic architecture and paleogeography

1.2.1. Link between orogenic units and margin domain

The early work of Argand identified the link between the paleogeography and the orogenic structure. The application of plate tectonics in the Alps led to a better comprehension of the link between the paleogeography of the Alpine Tethys and the orogen architecture. The internal domain corresponds to the distal and oceanic domains of the marge (Fig. II.2A and D; Trümpy, 1975; Favre and Stampfli, 1992). They are formed of highly deformed metamorphic units. On the other side, the external units correspond to the former proximal domain of the margin and is formed of little to unmetamorphosed units (Fig. II.A and D). They are separated by a main tectonic contact, the Penninic thrust. However, these major tectonic units correspond also to major domains of the rifted margin. Indeed, in the external domain, series of half-graben filled with shallow-marine sediments and overlaid by prograding platforms are characteristic of the proximal domain (Bernoulli et al., 1979; , 1986; Ramsay, 1981). On the other side, the internal domain corresponds to distal and oceanic domains (Trümpy, 1975; Froitzheim and Eberli, 1990; Manatschal , 1999).

Internal nappes are frequently composed of high pressure metabasic rocks such as eclogites and amphibolites that are the witnesses of the former oceanic domain. HP continental rocks are interpreted as remnants of the distal margin dragged into the Cretaceous subduction (Boccaletti et al., 1971; Elter, 1971; Stampfli and Marthaler, 1990; Stampfli et al., 1998; Handy et al., 2010; Agard and Handy, 2021). However, mapping of ophiolitic remnants shows that large continental units are

From rifting to orogeny, concepts developed in the Alps over a century

found in between oceanic units (Fig. II.2.B and C). This is interpreted as the presence of the two oceanic basins (e.g., Valais and Liguro-Piemont basins of Dumont et al., 1984; Lemoine and Tricart, 1986; Lagabrielle, 1987; Bousquet et al., 2002; Schmid et al., 2004; Loprieno et al., 2011; Beltrando et al., 2012; Ribes et al., 2019c) separated by a continental block constituting the Briançonnais domain (Fig. II.2A). This interpretation of the Briançonnais as a continental ribbon to the south is an explanation for many observations indicating the presence of two margins on each side of the Briançonnais (Lower Penninic and Upper Penninic; Stampfli, 1993). The Briançonnais block disappears progressively toward the northeast and is not observed in Eastern Alps (Fig. II.2C; Lemoine and Trümpy, 1987).

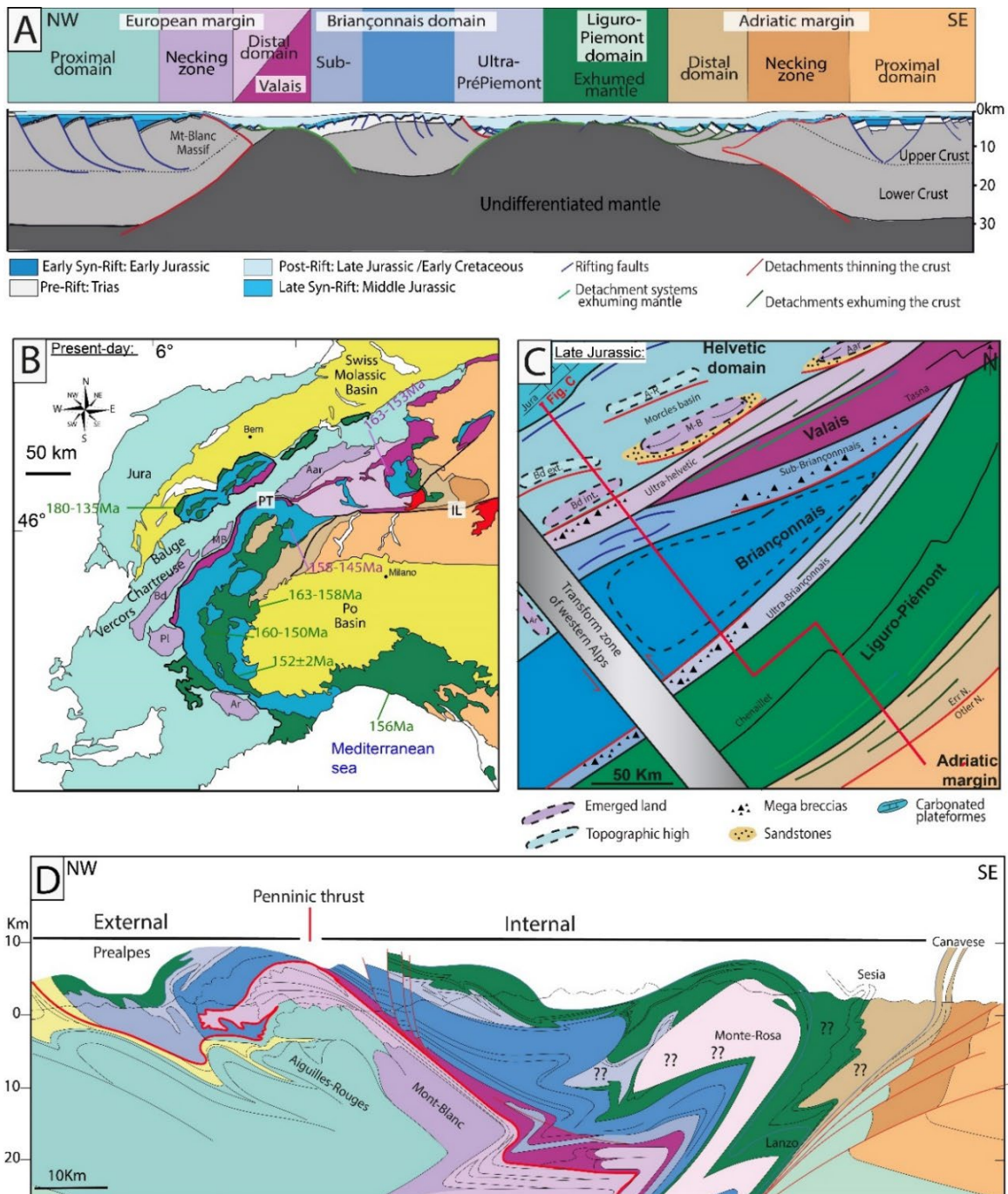


Figure II.2A- Cross section of the Jurassic margin with the different domains highlighted (modified from Mohn et al., 2014). B- Map of the Alps showing the position of the different paleogeographic domains (same color code as A, modified from Schmid et al., 2004; Mohn et al., 2010). The ages of the ophiolites are also indicated on the map. C- Palaeogeographical map of the Alpine realm during the late Jurassic showing the 2 oceanic basins surrounded by the Briançonnais block (modified from Ribes et al., 2019a). D- Cross section of the Alps highlighting the position of the different paleogeographic domains (modified from Escher et al., 1993).

1.2.2. Age of the oceanic domain

The age of the Liguro-Piemont oceanic domain is widely accepted by the community. The recognition of Late Jurassic to Early Cretaceous sediments lying in stratigraphic contact with exhumed mantle and gabbros and extrusive basalts put a strong constrain on the age of the ophiolites from the Liguro-Piemont domain (Elter, 1971). The sedimentary cover of these ophiolites corresponds to radiolarian cherts, and pelagic mudstones followed by *Palombini* bearing black shales deposit. Radiolarian cherts from ophiolites of Alpine Corsica gave ages between the Callovian and the Kimmeridgian (De Wever et al., 1987). Additionally, various magmatic rocks have been dated in the Alpine ophiolites. These radiometric ages yielded Alpine ages due to the subduction and collision but also clear pre-Alpine ages (Fig. II.2B). Early dating of ophiolites from the Prealpes (nappe des Gets) gave ages on gabbros between 180-165 Ma and 150-135 Ma using K-Ar (Delaloye and Bertrand, 1976). Plagiogranite in the Iherzolites and gabbros from the Liguria domain gave ages of ca. 156 Ma (U-Pb on zircons; Borsi et al., 1996). Dating of the Montgenèvre ophiolite (U-Pb on zircons from a leucogranite) gave ages between 160 to 150 Ma (Costa and Caby, 2001). Dating on metaplagiogranite from the high-grade ophiolite of the Monte-Viso yielded ages of 152 ± 2 Ma (U-Pb on zircons; Lombardo et al., 2002). Finally, ages (U-Pb on zircons from Fe-Ti gabbros) in the region of Lanzo (Piemont, Italy) gave ages from 163 to 158 Ma (Kaczmarek et al., 2008).

However, the age of the Valais was submitted to important controversy. Two main hypotheses were debated, which were (i) a late Jurassic opening of the Valais, coeval to the Liguro-Piemont basin (Lemoine and Trümpy, 1987) or (ii) an Albian-Cenomanian opening in relation to Pyrenean rifting and opening of the Bay of Biscay (Stampfli, 1993). The main arguments for the second hypothesis was the thick Cretaceous sedimentary cover in the Valais basin compared to the thin Jurassic cover (Loprieno et al., 2011). However, the Jurassic sedimentation is starved even in the Liguro-Piemont domain (De Graciansky et al., 2010). The recognition of late Jurassic sediments lying over the exhumed mantle in the Lower Penninic units from the Valais basin (Beltrando et al., 2012) is a strong argument in favour of the Jurassic opening of the Valais. Radiometric ages from ophiolites belonging to the Valais gave ages of 153 to 157 Ma, coeval to the Liguro-Piemont basin (Liati et al., 2005). These elements are clearly demonstrating an opening of the Valais basin during the Upper Jurassic.

1.2.3. Nature of the syn-rift deposits

Study of the sedimentary architecture of syn-rift deposits located in the internal and external domains helped constraining the margin paleogeography. Jurassic breccias on the cover were used as a proxy for the identification of paleo normal faults. Large scale breccias have been described in different domains of the Alps and interpreted as the sedimentary remnants of large fault scarps (Ribes et al., 2019a). They are observed in the External Crystalline Massifs from the European margin, such as the Moûtier breccia in the Belledonne massif (Fig. II.2C). The age of these breccias range from Lower Jurassic to Lower Cretaceous and the breccias are composed of cover and basement clasts (Antoine, 1971; Collart, 1973). Large olistoliths can be found in the breccias (Ribes et al., 2019a). Other large scale breccias can be found in the “Breccia nappe” (Chessex, 1959; Hendry, 1972; Weidman, 1972), corresponding to the Briançonnais margin (Pré-Piemont domain) dated as Toarcian to Berriasian (Fig. II.2C). They correspond to a 1700 m-thick succession of breccias composed of metric blocks to centimetric clasts (Ribes et al., 2019a). Finally, large scale breccias are also observed in the sub-Briançonnais domain, which corresponds to the Valais margin of the Briançonnais domain. These breccias have again an age ranging from the early Jurassic to the early Cretaceous, with at the base Triassic to Jurassic clasts and basement clasts upward. These breccias witness large faults which were not preserved during Alpine collision (Ribes et al., 2019a), so that they help precising Alpine paleogeography.

More local breccias (< 100 m thick) were also recognized in the more distal units of the Valais domain (Ultrahelvetic (Trümpy, 1954), Niessen (Badoux and Homewood, 1978) and Lower Penninic nappes (Jeanbourquin and Burri, 1991; Spring et al., 1992; Loprieno et al., 2011), and in the Piemont domain (Pantet et al., 2020)). They also contain sedimentary clasts and basement clasts and highlight the presence of local fault scarps and paleo faults.

Another important feature is the presence of large-scale unconformities recognized in the Alps and more specifically in the Briançonnais domain (Baud et al., 1977; Hauptert et al., 2016). The pre-rift Triassic cover of the Briançonnais appears eroded and affected by important karstification. This emersion occurring during the Early Jurassic was related to a sudden uplift of the Briançonnais domain. Karstification was at least 300 m deep (Baud and Megard-Galli, 1975). This emersion was followed by a Bajocian transgression indicating the drowning of the Briançonnais block. This major unconformity is visible throughout the entire Western Alps (Baud and Megard-Galli, 1975; Baud et al., 1977).

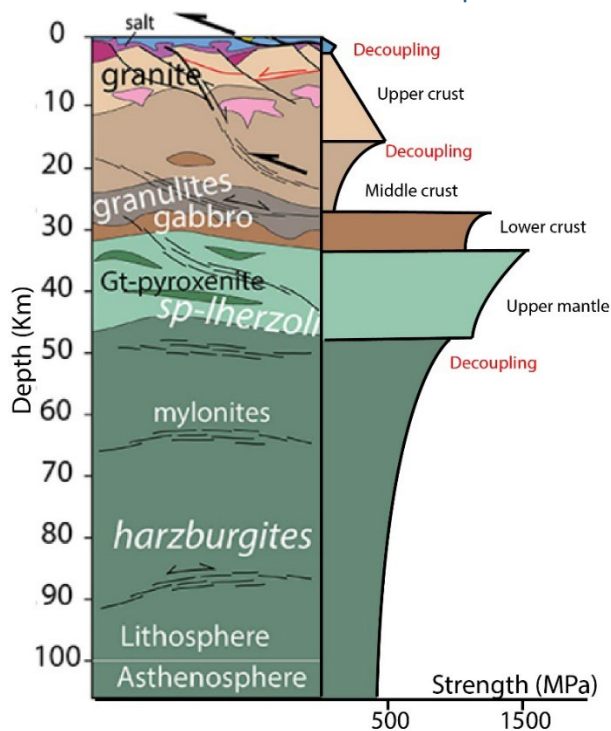
1.3. The External/Internal transition of the Alps

The External Crystalline Massifs (ECM) correspond to large area of the European basement uplifted and forming at present the highest mountains in the Alpine belt. The ECM correspond now

at the transition between the internal and external domains of the Alps forming the footwall of the Penninic thrusts (Fig. II.2D). Thick-skin deformation is observed in these massifs with large shear zones leading to the incorporation of the ECM in the orogenic wedge (Herwegh and Pfiffner 2005; Leloup et al., 2005; Bellahsen et al., 2012). Besides, Butler (1986) noticed that the amount of the amount of crustal shortening (64 km) calculated on a section across the Pelvoux by Goguel (1948) could not be restored at depth and that an homogeneous shortening throughout the crust would lead to an pre-Alpine crustal thickness of less than 18 km. However, Rosenberg et al., (2021) proposed a less important shortening (28 km) in the external massifs. The decoupled deformation between the upper crust and lower crust in the opposite could be restored but implies a humongous shortening (180 km; Butler, 1986) to fit with the model of Menard and Thouvenot (1984) which is greater than shortening proposed by Rosenberg et al. (2021) for the whole Alpine section of the Pelvoux (93 km).

However, the ECM are also found at the transition between the distal margin (Helvetic nappes) and the proximal domain of the European margin. A change of sedimentary facies and sedimentary thickness can be observed (Trümpy, 1951) with an increase of thickness toward the distal margin (Loup, 1992). The ECM corresponds also to the breakaway of the Cretaceous carbonate platforms highlighting a change in the bathymetry (Ramsay, 1981). The abrupt change of pre-Alpine crustal thickness in the ECM mentioned by Butler (1986) might be associated to the proximal to distal transition (e.g., necking domain).

1.4. Constrains on the pre-rift rheology of the lithosphere



From rifting to orogeny, concepts developed in the Alps over a century

Figure II.3: Section of the “Variscan lithosphere” (from Mouthereau et al., 2021) associated to pre-rift rheological profile.

As mentioned in the previous chapter (1.2.2.4 and 2.1.3.2), the pre-rift rheology of the crust is a key factor controlling the architecture of the rifted margin including the necking domain. This rheology is controlled by thermal inheritance as well as compositional and structural inheritance (Manatschal et al., 2021).

At the European scale, post-Variscan Carboniferous extension is widespread throughout the Variscan realm and led to crustal thinning of the crust and partial reequilibration at ca. 30 km. The “Variscan” lithosphere (inherited from Variscan and post-Variscan event) was however, relatively thin (ca. 50 km) compared to the adjacent cratons (e.g., Baltic craton ca. 200 km) which is explained by small edge convection cells leading to thermal erosion of the lithosphere (Mouthereau et al., 2021) and weak coupling between the the plate and the mantle.

Concerning the Alpine Tethys, some observations from the Variscan to post-Variscan basement as well as the pre-rift cover allows to fix some constrains on the role of compositional inheritance. Indeed, the exposed mantle and lower crust from the Ivrea zone show the occurrence of Permian gabbros underplating the crust, and resulting in associated granulitisation in the lower crust (Fig.II.3). This mafic underplating inherited from post-Variscan Carboniferous extension forms a competent layer compared to the weak quartz-rich middle crust. In addition, the occurrences of large felsic Carboniferous intrusions in the middle and upper crust lead to significant softening of the crust (Petri et al., 2019).

The pre-rift thermal state of the crust is much more difficult to asses. The subsidence pattern in the pre-rift basins can help constraining the thermal state of the crust before the onset of rifting. It appears that larger Triassic dolostone deposits in the Briançonnais compared to the European domain are related to magmatic activity during Permian leading to stronger subsidence while the magmatic activity in the European domain ceased at the end of Carboniferous (Ballèvre et al., 2018). This thermal anomaly seems to be reequilibrated at the end of Triassic where when thin shallow marine carbonate deposits are observed thougout the Alpine realm, indicating the absence of strong subsidence. It appears that the Post-Variscan thermal event was mostly reequilibrated at the end of Triassic. However, in the south of the Western Alps (Belledonne massif and Pelvoux), Triassic basaltic intrusions are present (Vatin-Pérignon et al., 1972; Vatin et al., 1974). These mafic intrusions can be linked to the mafic intrusions observed in the Pyrenees and might be related to the Central Atlantic Magmatic Province (Rossi et al., 2003). The role and extent of this magmatic event in the Alps remains however unknown.

Finally, the role of structural inheritance is also difficult to constrain. Large Variscan and post-Variscan shear zones in the Alpine basement are well characterized (von Raumer et al., 2009; Vanardois et al., 2022). However, their role during the Jurassic rifting is not well understood. An

example could be the East Variscan shear zone which is visible in the ECM. It was postulated that this crustal shear zone is responsible for the difference of magmatic activity observed during the Permian between the Briançonnais and the European domain and might also be responsible for the localisation of the Valais basin (Ballèvre et al., 2018).

To summarize, it appears that the “Alpine” lithosphere corresponds to a thin warm lithosphere, thermally reequilibrated crust scale associated to upper crust-lower crust decoupling (Fig. II.3).

Take-home message

- The ‘Wilson cycle’ highlights the strong link between the rift related paleogeographic domains of the Alpine Tethys and the tectonic units of the Alpine collisional orogen.
- The internal domain corresponds to remnants of the Valais and Liguro-Piemont basins that are at the origin ophiolite bearing units under and overlying the Briançonnais units.
- The external units correspond to remnants of the proximal domain of the European and Adria margins.
- The transition between the external and internal units (e.g., ECM) corresponds to former necking domain.
- The ‘Wilson cycle’ is a key concept for understanding the transition from rift/oceanic domains to subduction and collision.

2. From the Alpine Tethys to the Alpine orogen

2.1. Present-day view of the Alpine orogen

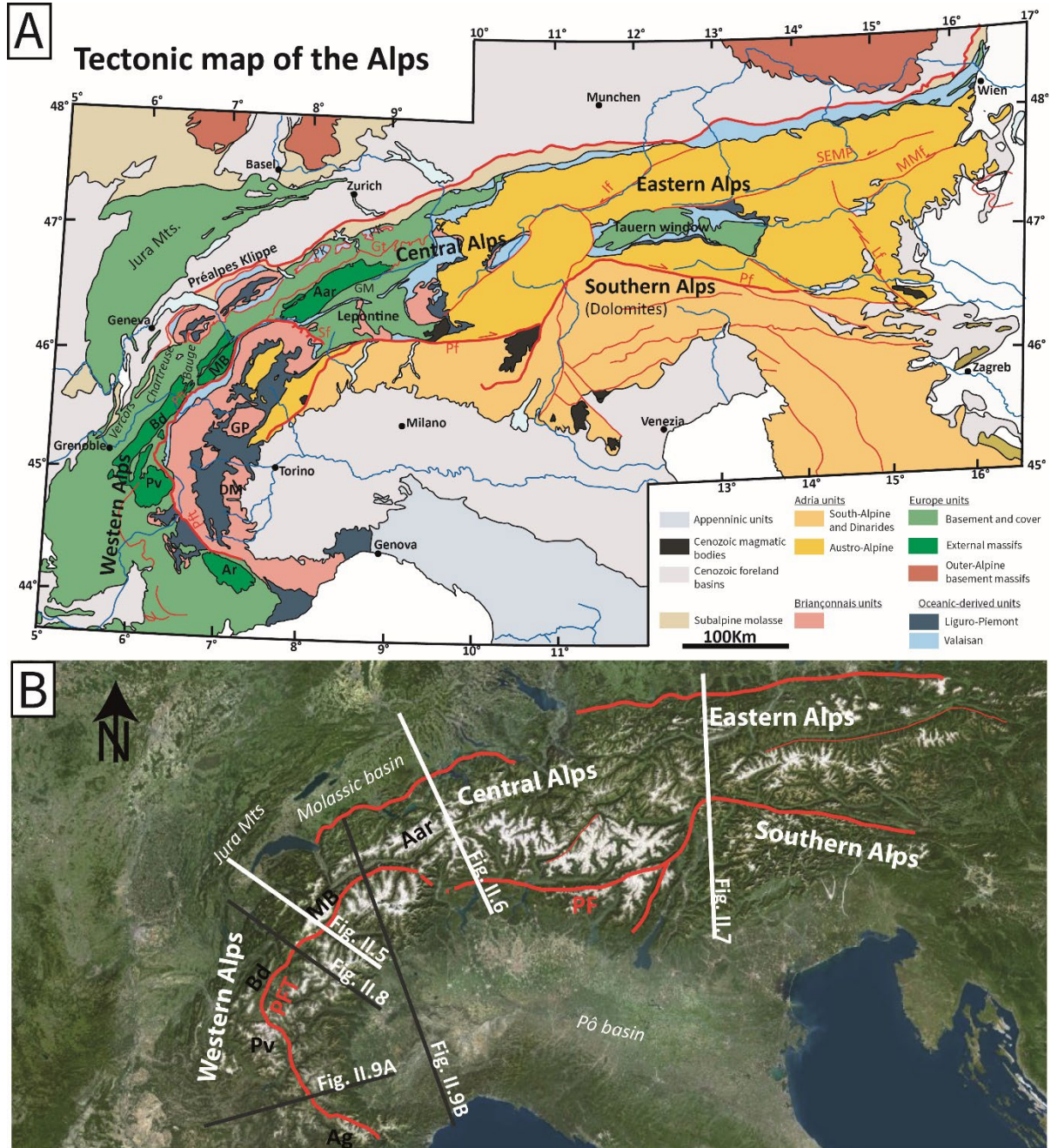


Figure II.4: A- Tectonic map of the Alps showing the main units (European derived, Briançonnais-derived, and Adria-derived). The oceanic domain (Liguro-Piemont and Valais) can be found in the internal part of the orogen. B- Satellite image of the Alps (from Google Earth) showing the position of the main geophysical transects. Ag=Argentera, Pv=Pelvoux, Bd=Belledonne, Mb=Mont-Blanc, PFT= Penninic front thrust, Gt= Gottard thrust, Pf= Peri-Adriatic faults, Sf= Simplon fault, If=Inntal fault, SEMP= Salzach-Ennstal-Mariazell-Puchberg fault, MMF= Mür-Mürz fault.

The Alps correspond to a non-cylindrical fold belt extending from the Swiss basin to the north to the Pô and venetian basin to the south. The Alps are an asymmetric double verging belt, 150 to

300 km wide (Fig. II.4). They are divided into four different domains with different tectono-sedimentary history, the Western, Central, Southern and Eastern Alps (Fig. II.4).

2.2. Large scale view of the Alps

2.2.1. The Western Alps

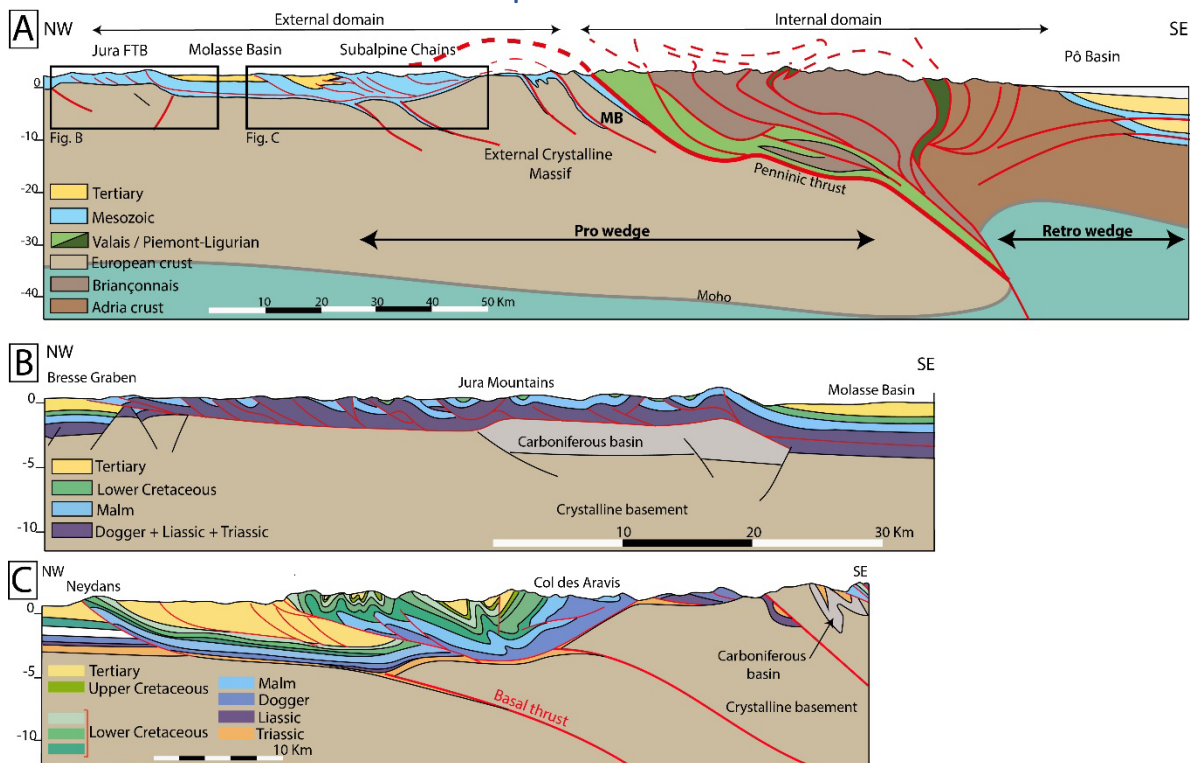


Figure II.5: A- Profile of the Western Alps (from Pfiffner, 2014) showing the development of a pro wedge toward the NW and a retro wedge toward the SE. Folding of the internal nappes of the orogen is visible due to the indentation of the Adria plate B- Section of the Jura Mountain showing thin-skin, fold and thrust belt style related to inversion of a Carboniferous basin at depth (from Guellec et al., 1990; Mugnier et al., 1990) C- Section of across the northern subalpine chains (from Philippe, 1994).

The arcuate part of the Alps corresponds to the Western Alps going from the Mediterranean Sea to the Mont-Blanc massif. It is an asymmetric orogen with a pro-wedge developing toward the NW and a retro-wedge associated to backfolding of the internal nappe toward the SE. The Internal units correspond to the former oceanic domain and the Briançonnais thrust above the European margin forming the external units of the Alps. The propagation of the deformation led to the formation of fold and thrust belt in the external part of the orogen (Fig. II.5).

The External Alps are characterized by thin skin thrust imbrication (e.g., Vercors, Bauges, Chartreuses massifs) overlying the Molassic basin. To the north, the presence of thick evaporitic sequence enabled propagation of the thrust westward until an inverted Carboniferous basin where the thrust emerges forming the Jura fold and thrust belt. The External Crystalline Massifs (Argentera, Belledonne, Pelvoux, Aiguilles-Rouges, Mont-Blanc) are formed by basement nappe stacking exhuming the European basement. In the retro wedge, the structures are buried under the Pô basin.

The internal unit above the European basement corresponds to a high-grade metamorphic (greenschist to eclogite facies) domain that is thrust above the European domain along the Penninic thrust. In the internal domain, subduction remnants formed an eclogitic belt (Gran Paradiso, Dora Maira, Zermaat-Saas) corresponding to subduction remnants.

2.2.2. The Central Alps

The Central Alps go extend from the north of the Mont-Blanc massif to the Tauern window (Fig. II.4). The External massifs resembles to those of the Western Alps with thrusting of the cover and basement above the Molassic basin. The External Crystalline Massif (Aar) is formed by crustal nappe stacking (Fig. II.5) overlying the Molassic basin (Fig. II.6B). The Internal domain is composed of the distal part of the European margin, which is absent in the Western Alps, and remnants of the oceanic domain (Valais and Liguro-Piemont). Indeed, the highly metamorphosed distal European margin (Leontine dome) was exhumed by the late Alpine Simplon detachment fault (Fig. II.4). This detachment fault is found at the junction between the Simplon-Rhone fault and the Peri Adriatic fault. The other difference with the Western Alps is the presence of large and shallow mantle bodies (Ivrea) sandwiched between the European and Adria units (Fig. II.4 and II.6A).

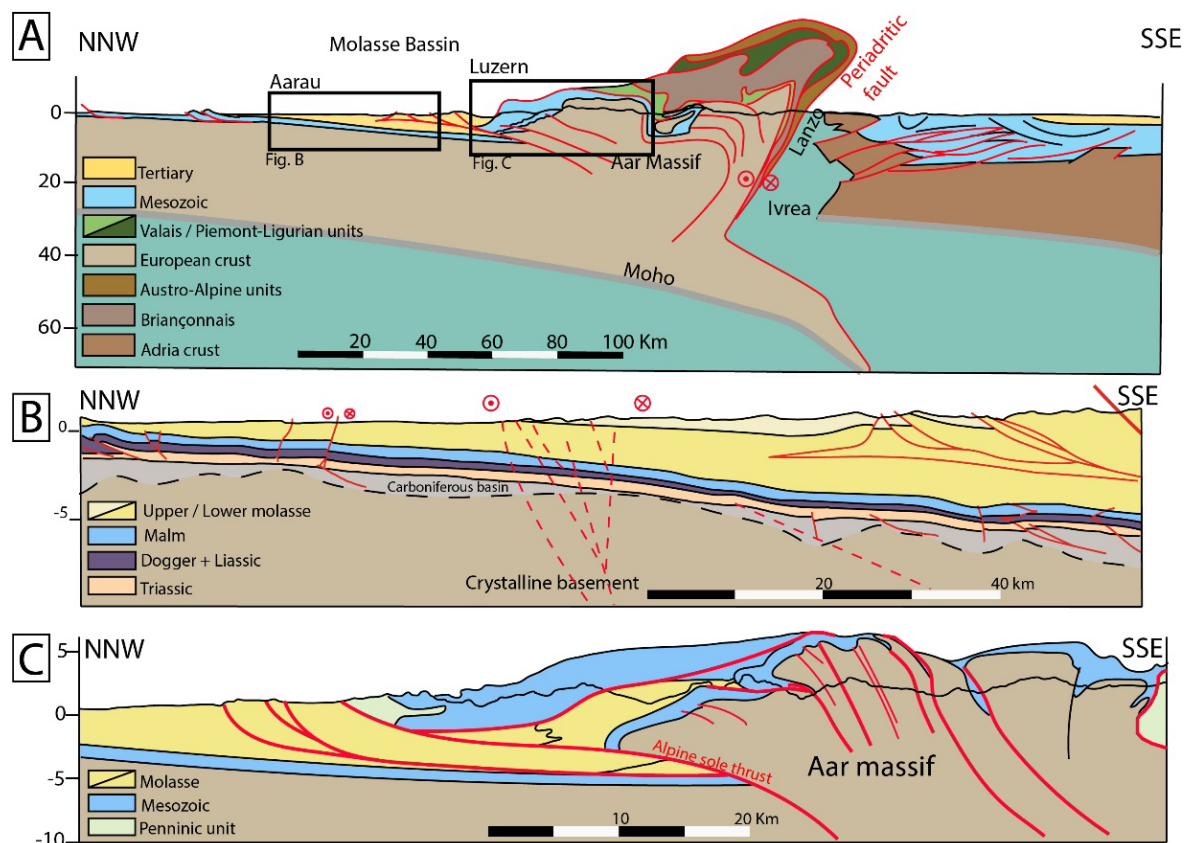


Figure II.6: A- Section of the Central Alps (from Pfiffner, 2014) showing crustal nappe stacking in the pro wedge and significant backfolding in the retro wedge associated to indentation of the orogenic prism by the Adria plate. B- Section of the Molassic basin showing the propagation of the deformation toward the NW (from Mock and Herwegh, 2017). C- Section of the Aar massif showing thrusting of the basement above the molassic basin (from Nibourel et al., 2021).

2.2.3. The Southern and Eastern Alps

The Eastern Alps extend in a E-W direction from the Tauern window to the Pannonian basin (Fig. II.4). To the south, the Peri Adriatic line separates the Southern Alps from the Eastern Alps. Cenozoic magmatic intrusions (ca. 43 to 16 Ma e.g. Adamello intrusion; Schaltegger et al., 2019) are present along the Peri Adriatic fault. The Eastern Alps are mostly composed of Austroalpine units overlying the oceanic domain and European domains (Fig. II.7). The European basement outcrops only in large antiformal stacks forming tectonic windows (Fig. II.7). It is also important to note the disappearance of the Briançonnais domain in the Eastern Alps (Rosenberg et al., 2021).

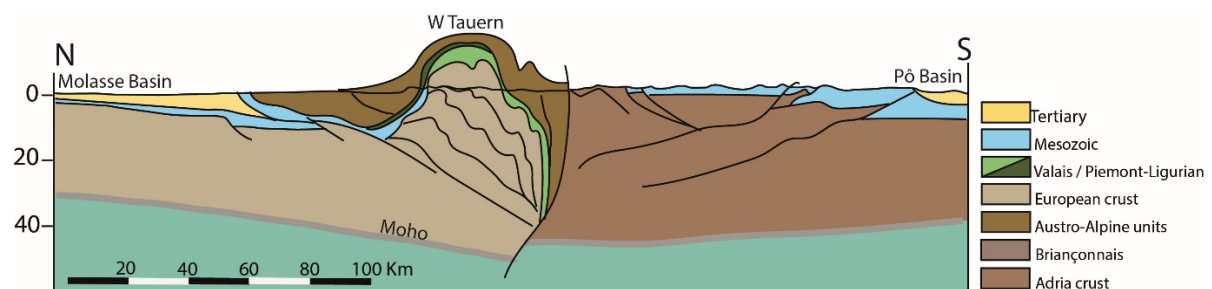


Figure II.7: Section of the Eastern and Southern Alps passing through the Tauern window (from Pfiffner, 2014).

2.3. Geophysical transect across the Western Alps

2.3.1. ECORS profile

Long offset seismic surveys associated to gravimetric and magnetic survey were realised across the Western Alps in 1985 (ECORS-CROP; Nicolas et al., 1990). NW-SE profiles were realized roughly parallel to transport directions.

This profile shows a general image of the crustal structure of the Alps from the external to the internal domains. The European crust, which is about 30 km in the external domain, is characterized by a strong reflection at around 20 to 25 km (a). A strong reflector dipping to the east and corresponding to the Penninic thrust marks the transition to the internal domain (b). Another strong reflector dipping in the opposite direction is found in the lower crust (c). The internal domain is characterized by sub-horizontal reflectors. Below the External Crystalline Massifs, the Moho starts dipping shallowly towards the east reaching ca. 50 km below the internal domains.

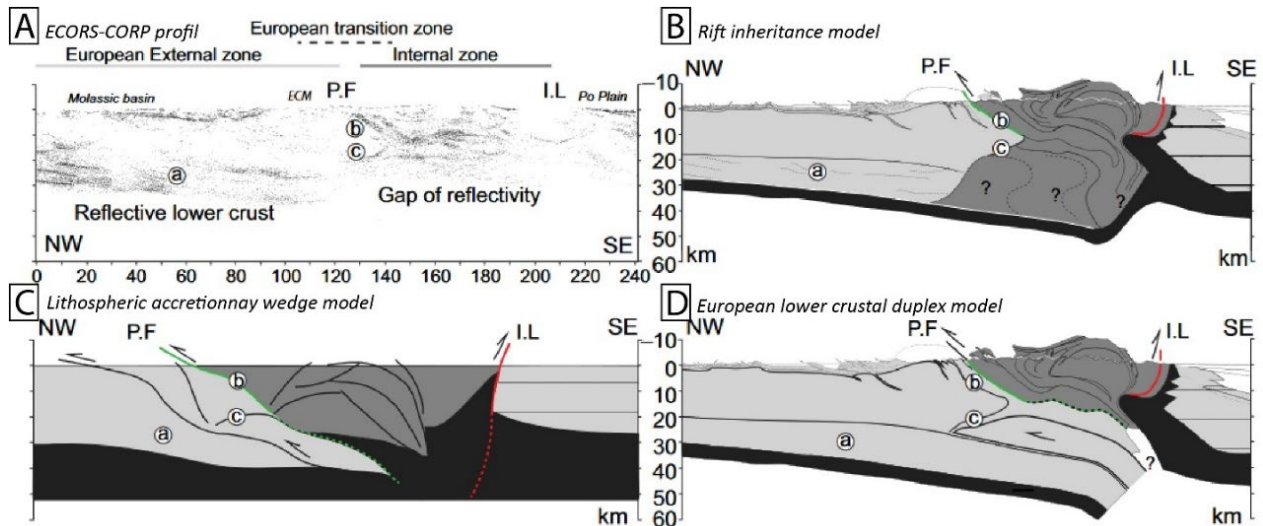


Figure II.8: Comparison of the different interpretations of the ECORS-CROP profile (from (Mohn et al., 2014)). A- Depth migrated ECORS-CROP profile (from Thouvenot et al., 1996). B-Rift inheritance model showing the role of the ECM as buttress between a thick continental crust in the External domain and a stacked hyper thinned crust in the internal domain (Mohn et al., 2014). C- Lithospheric accretionary wedge model (Lacassin et al., 1990; Nicolas et al., 1990). D- European lower crustal duplex model (from Roure et al., 1996).

Different interpretations of the ECORS profile (Fig. II.8A) were given implying different mechanisms of crustal accretion (Fig. II.8). The first model is referred as lithospheric accretionary wedge (Fig. II.8C; Lacassin et al., 1990; Nicolas et al., 1990). This model corresponds to an accretion of large lithospheric nappes accommodated by crustal scale thrusts including the Penninic thrust. However, the lower crust reflector (c) is not explained by this model. The second model corresponds to the formation of lower crustal duplex in the European basement (Fig. II.8D; Roure et al., 1996; Schmid and Kissling, 2000). Therefore, the reflector (c) corresponds to the indentation of the upper crust by the lower crust. The last interpretation takes into account the rift-related inheritance (Fig. II.8B; Mohn et al., 2014). This model proposes that the External Crystalline Massifs which correspond to the former necking domain played the role of buttress on which the internal domain was accreted.

2.3.2. Tomography of the Alps

New tomography data using combined Controlled-Source Seismology (CSS) and Local-Earthquake Tomography (LET) were used to constrain the Moho topography below the Alps (Wagner et al., 2012). Three Moho surfaces are defined, a European Moho, an Adriatic and a Ligurian Moho (Fig. II.9A). The European Moho is dipping eastward and passes from 30 km to 50 km below the Internal domain. There is a significant Moho step corresponding to the Ivrea anomaly and separating the European and Adria Moho. The Adria Moho is dipping eastward from less than 30 km to 40 km below the Pô basin.

The CIFALP project corresponds to a passive seismic experiment launched during the 2010's with the aim to provide better constraints on the deep structures of the Alps (Malusà et al., 2021). It corresponds to a transect between France and Italy passing between the Pelvoux and Argentera

massif. The depth of the Moho in the CIFALP section ranges from 40 km below the External massif to more than 60 km (Malusà et al., 2021) in the Internal domain which is associated with continental subduction (Zhao et al., 2015). A Moho overlap is observed between the European and Adria plates. The depth of the Adria Moho ranges from less than 20 km to almost 40 km below the Pô basin.

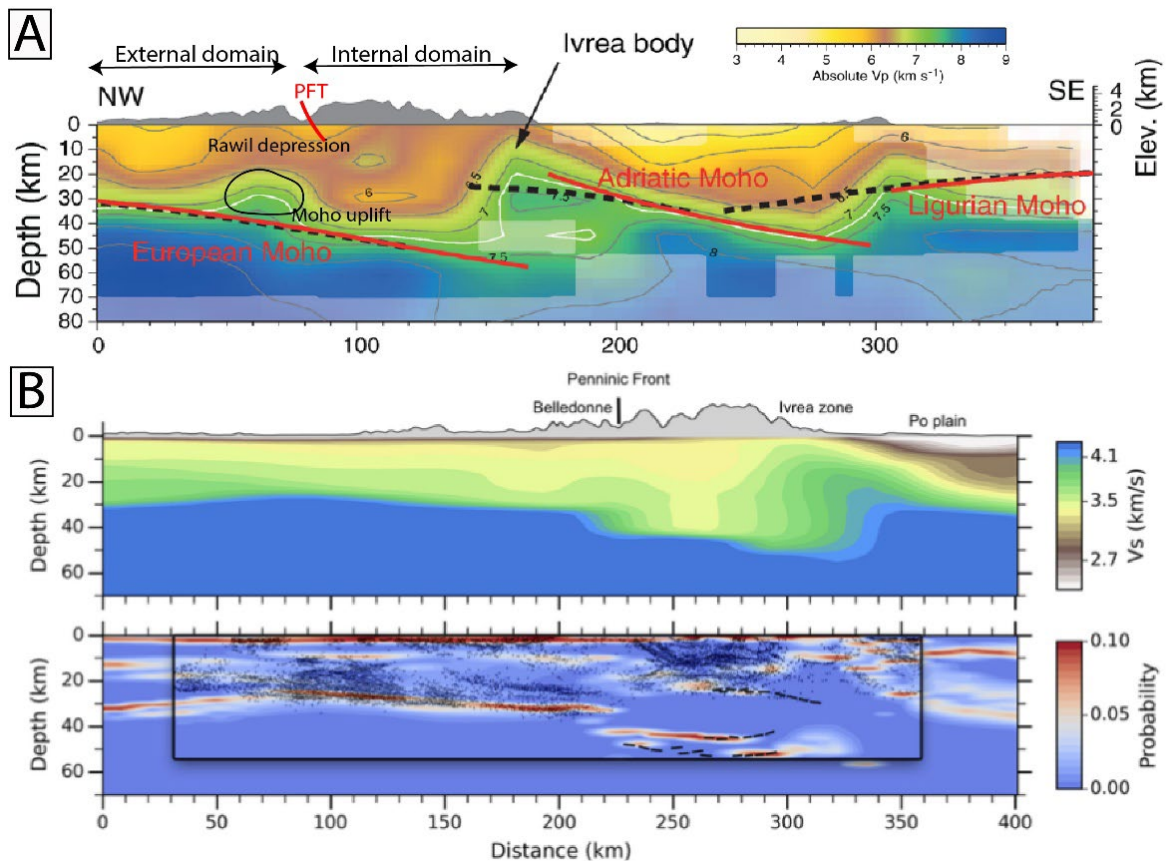


Figure II.9: A- Vp profile across the Alps (through the Rhône valley) and Pô basin ((Wagner et al., 2012) showing the complex Moho topography below the Alps. B- Vs profiles below the Alps (across the Belledonne massif) showing increase of crustal thickness below the Penninic front (Lu et al., 2018).

AlpArray is a European project of passive seismic acquisition in the Alpine domain (Hetényi et al., 2018). The Vs map and profile across the CIFALP and ECORS profile revealed a more complex Moho topography with a Moho step associated to the Penning thrust (Fig. II.9B). The Moho depth is below 40 km in the External domain of the Alps and passes to almost 50 km below the internal domain (Lu et al., 2018, 2020).

2.4. Kinematic and P-T-t evolution of the Western Alps

2.4.1. The subduction stage

Onset of convergence in the Alpine Tethys is ca. 84Ma (Macchiavelli et al., 2017). It was proposed by Angrand and Mouthereau (2021) that the opening of the southern North Atlantic Ocean resulted in the eastward movement of the Iberia block. This led to the closure of the Alpine Tethys (Angrand and Mouthereau, 2021). The subduction initiated along the Adria margin associated to

strong strike slip due to the NE movement of the Adria plate relatively to the European plate (Le Breton et al., 2021; Angrand and Mouthereau, 2021). Late Cretaceous N-S movement of the African plate led to an acceleration of the closure of the Alpine Tethys with convergence rate between 12.6 and 7.1mm/a (Handy et al., 2015; van Hinsbergen et al., 2020; Le Breton et al., 2021). The subduction of the oceanic domain was associated to the formation and accretion of Cretaceous flysch (e.g., Helminthoid flysch). It is worth noting the total absence of volcanic clasts (Trümpy, 1975) and Cretaceous detrital zircons (McCarthy et al., 2018) indicting the lack of volcanic activity. This is known as the Eo-Alpine phase which is well constrained in the Central and Eastern Alps (Kurz and Fritz, 2003) where it is dated from the age of the first flysch at ca. 100-90 Ma and from amphibole zoning at 83 to 91 Ma (Villa et al., 2000).

During the Palaeocene–early Eocene, ca. 110 km of shortening were accommodated by the subduction system (Malusà et al., 2011a). Subduction below the Adria plate led to the formation of an accretionary prism with incorporation of tectonic slivers that underwent greenschist to amphibolite facies conditions (Herviou et al., 2022). This was followed by a beginning of continental subduction with part of the hyperextended domain dragged into the subduction (Fig. II.10; Agard and Handy, 2021; Herviou et al., 2022). During the middle to late Eocene, a change in kinematics with a strong left lateral movement resulted in 30 km of extension normal to the trench (Malusà et al., 2011a). This led to mechanical slicing (Fig. II.10) of the subducted oceanic domain and subsequent exhumation (Herviou et al., 2022) and to the formation of a high pressure belt in the internal domain of the Alps. These remnants correspond mostly to the exhumed mantle (Piemont) and proto-oceanic domain (Liguro-Piemont). They reached eclogitic facies (Fig. II.10) with a peak metamorphic age between 65 and 45 Ma for a maximum depth of 45 to 90 km and a temperature of 350 to 450°C (Herviou et al., 2022). Ultra-high pressure metamorphism was also achieved in the Dora Maira massif as observed with the presence of coesite indicating a maximum burial depth of above 90 km (Chopin, 1984). The exhumation of these HP to UHP units was achieved between 44 and 34 Ma followed by stacking of these units (Herviou et al., 2022). However, no remnants of the oceanic crust were recovered from the subduction.

From rifting to orogeny, concepts developed in the Alps over a century

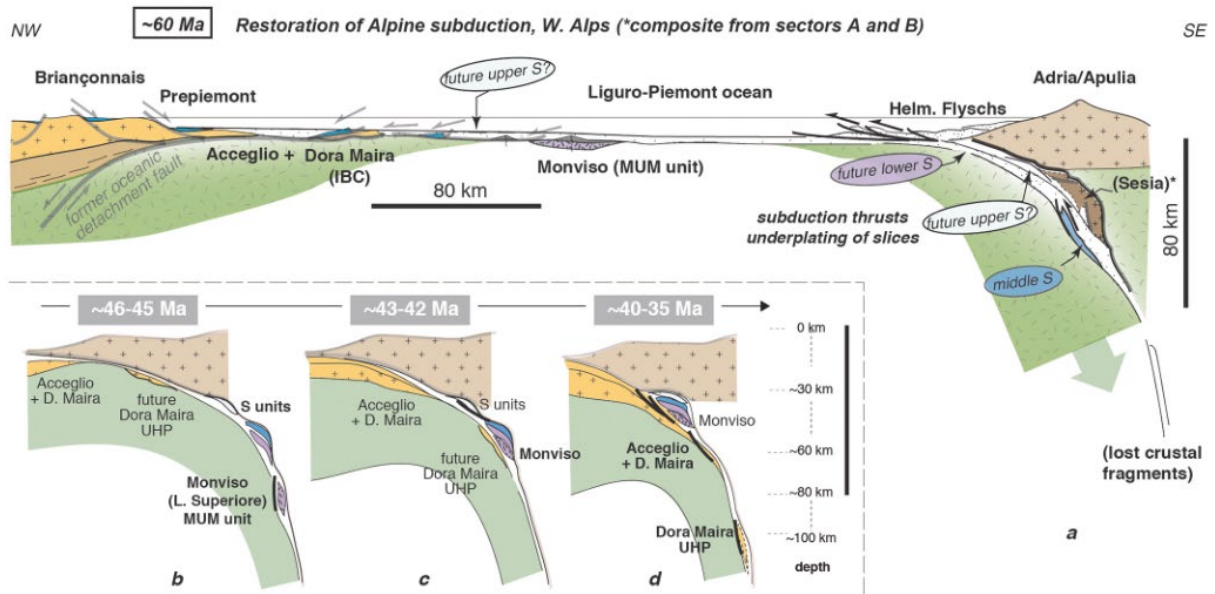


Figure II.10: Evolution of the subduction of the distal Briançonnais margin (Piemont domain) between 60 and 35 Ma. Underplating of subducted slices along the subduction plane led to exhumation and juxtaposition of subduction remnants with different P-T evolution (Agard, 2021).

The timing of closure of the Valais basin is less constrained. Subduction of the Valais started roughly around 45-40 Ma following the closure of the Liguro-Piemont basin (Rosenbaum and Lister, 2005). This is followed by the thrusting of the accretionary prism above the European crust through the Penninic thrust. The advance of the Penninic units is marked by the younger age of the flexural basin and flysch toward the continent (Fig. II.11; Jaquet et al., 2018).

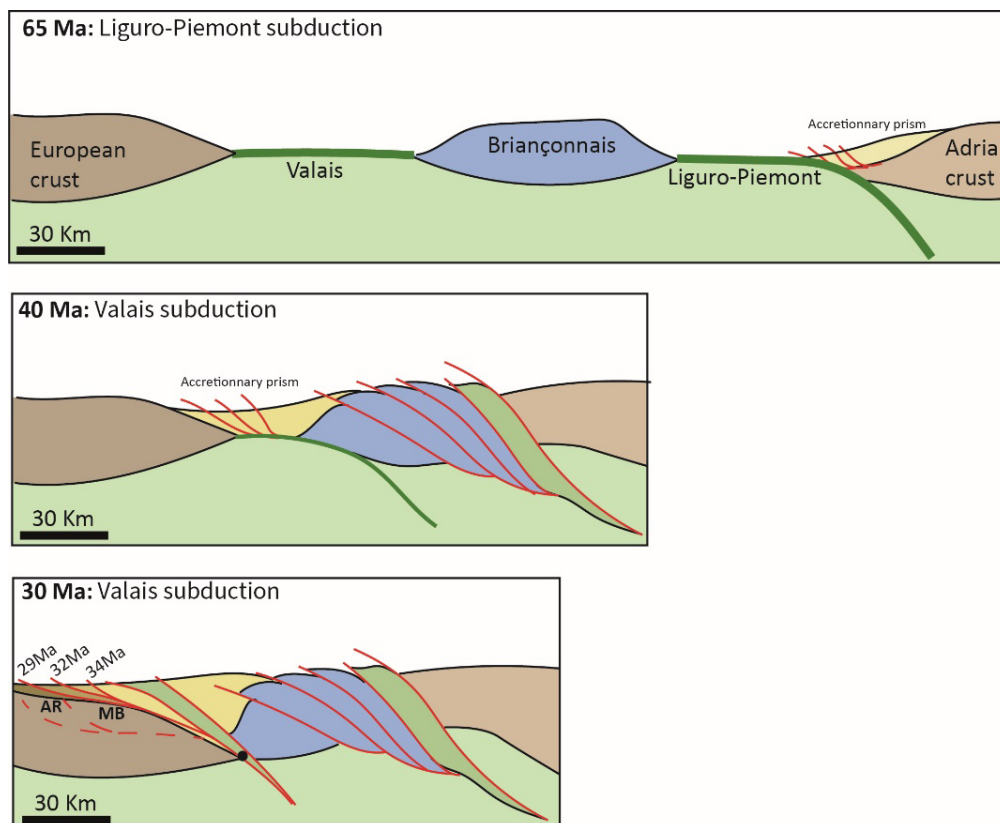


Figure II.11: Switch from subduction in the Liguro-Piemont to the Valais basin leading to progressive burial of the European crust below the accretionary prism. The age of the Valaisan flysch are from Jaquet et al., 2018.

2.4.2. The collision stage

During the Oligocene, a switch from subduction/accretion to collision is observed with the propagation of the deformation toward the continent. The collision was marked by a decrease of the convergence rate (8.9 to 6mm/a; Piromallo and Faccenna, 2004; Handy et al., 2015; van Hinsbergen et al., 2020; Le Breton et al., 2021).

Firstly, the Internal domain was thrust above the European basement, which marks the activation of the Penninic thrust after 35 Ma (Schmid and Kissling, 2000; Simon-Labric et al., 2009). It was associated to an increase of the geothermal gradient from ca. 18 to 30°C/Km (Malusà et al., 2006). This increase of thermal gradient was also linked to an increase of magmatic activity with the emplacement of calc-alkaline to ultrapotassic intrusions (Fig. II.4A; Venturelli et al., 1984). Oligocene volcanoes appear to be reworked in Oligocene sediments and followed by exhumed Oligocene plutons (Malusà et al., 2011b). This magmatic activity is explained by slab break-off, which lead to heating of the crust by the rising asthenosphere (von Blanckenburg and Davies, 1995; Davies and von Blanckenburg; 1995). This concept of slab break-off may explain various phenomenon observed in the internal domain such as rapid surface uplift and therefore, various slab break-off ages were proposed by different authors (Garzanti et al., 2018).

Secondly, propagation of the deformation toward the continent led to the switch from thin to thick-skin deformation in the European margin (Herwegh and Pfiffner, 2005; Bellahsen et al., 2012). Large shear zones developed in the basement under greenschist conditions leading to localization of the deformation along ultra-mylonitic shear zones (Bellahsen et al., 2012). These shear zones are responsible for the shortening of inherited Jurassic basins and extrusion of the syn-rift cover as observed in the Morcles nappes (Ramsay, 1981) or in the Bourg d'Oisan half basin (Bellahsen et al., 2012). These basement shear zones were ultimately responsible for the uplift and exhumation of the External Crystalline Massifs. The migration of the deformation toward the continent led to the activation of the Belledone/Aiguilles-Rouges basal thrust (Kalifi et al., 2021) at 18 Ma and to the propagation of the deformation into the External domain of the Alps (Vercors, Chartreuse, Beauge). The External domain corresponds to an imbrication of thrust nappes in the cover possibly connected at depth to the Belledonne basal thrust (Kalifi et al., 2021). The presence of a thick decollement level further north (evaporites) led to the propagation of the deformation below the Molassic basin and formation of the Jura mountains. In addition, it was proposed that the Jura thrusts and the External domain thrusts are in lateral continuity (Kalifi et al., 2021).

Take-home message

- The Alps corresponds to an asymmetric double-verging orogen.
- Subduction of the Liguro-Piemont ocean occurred during the Lower Cretaceous, and during the Oligocene for the Valais basin.
- Continent-Continent collision occurred from Oligocene to present-day.

3. Case study of the External Crystalline Massifs in the Western Alps

3.1. Variscan polymetamorphic basement

The External Crystalline Massifs are composed of polymetamorphic and magmatic rocks formed between 500-600 Ma and 300 Ma through a Wilson cycle (Von Raumer et al., 2002; von Raumer and Stampfli, 2008). The ECM corresponds to the active Gondwana margin (von Raumer and Stampfli, 2008) submitted to significant Cambrian back-arc rifting (e.g. Chamrousse ophiolite; Ménot et al., 1988) followed by the closure of these basins linked to significant Ordovician magmatism associated to the opening of the Rheic ocean, which were strongly metamorphized during Variscan orogeny and forms nowadays augen gneiss (Von Raumer et al., 2002; Schaltegger et al., 2003).

Closure of the Rheic ocean led to the Variscan orogeny during Silurian to Carboniferous times (Von Raumer et al., 1993). Remnant of eclogites dated as Silurian followed by decompression from eclogitic facies to amphibolitic facies are found in the ECM (Paquette et al., 1989). This decompression is also observed on granulites found in the ECM (Colombo et al., 1993; Ferrando et al., 2007). Devonian to Carboniferous nappe stacking was associated with a rise of the geothermal gradient as indicated by kyanite bearing parageneses associated with the production of the first Variscan melt (Von Raumer et al., 1993).

Two main magmatic phases are observed during the Carboniferous. Indeed, Barrovian conditions led to generation of significant crustal melting throughout the entire Alpine realm. The first magmatic phase corresponds to Mg-K magmatism from 340 to 330 Ma with both crustal and mantle sources (Bussy et al., 2001). This magmatic phase was coeval with strong strike slip deformation associated to transpression (von Raumer et al., 2009; Vanardois et al., 2022). Melt extraction appears to be related to the shear zones as observed in the Aiguilles-Rouges massif migmatites (Genier et al., 2008). The second magmatic phase corresponds to Fe-K magmatism emplaced between 305 and 295 Ma; Debon and Lemmet, 1999; Bussy et al., 2001). They mark an increase of the mid-crustal source associated to stronger crustal melting. The Late Carboniferous is characterized by the development of intracontinental basins (e.g. Salvan-Dorenaz basin in the Aiguilles-Rouges massif (Capuzzo et al., 2003) in a transtensional setting. The intrusions were emplaced along strike-slip shear zones at mid crustal levels (von Raumer et al., 2009). The source of heat necessary for this widespread magmatism came mostly from basaltic underplating of the crust associated with asthenospheric flow in response to slab break-off or crustal delamination (Bussy et al., 2001). The late Carboniferous extension, which is widespread throughout the Variscan realm (Faure, 1995) is explained by the orogenic collapse of the warm and weak overthickened crust (Burg et al., 1994; Rey et al., 1997), back-arc extension (Faure et al., 1997; Stampfli et al., 2001) or to the

development of a right lateral strike slip associated with the motion of the African plate relative to the Siberian plate (Arthaud and Matte, 1977).

3.2. Alpine evolution of the ECM

The ECM are characterized by 3 main Alpine tectonic phases defined in the Aar massif but also recognized in the Mont-Blanc and in some extent also in the Belledonne and Pelvoux massifs. The Prabé phase (38-20 Ma) was characterized by the thrusting of the Penninic domain as well as the emplacement of the Helvetic nappes from the distal European margin over the ECM (Fig. II.12A; Herwegh and Pfiffner, 2005). This corresponds to the prograde P-T path of the ECM. Maximum peak temperature observed in the Aar massif is above 500°C in the internal part of the massif while the External part reached temperatures below 300°C (Nibourel et al., 2021) and was dated at 21 Ma (Ar/Ar on biotite; Rolland et al., (2009)). Peak metamorphism in the Mont-Blanc is around 400°C (Rolland et al., 2003) and is dated between 30 Ma (Cenki-Tok et al., 2014) and 16 Ma (Rolland et al., 2008). The cover reached temperatures below 350°C.

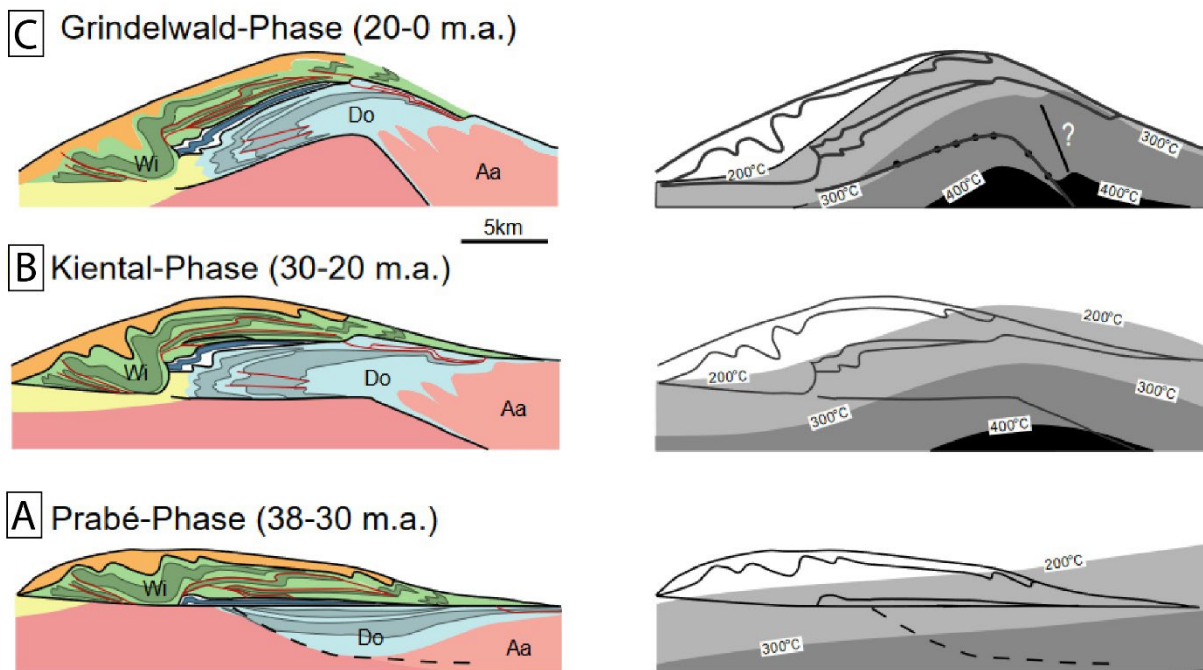


Figure II.12: Evolution of the ECM (Aar massif from Herwegh and Pfiffner, 2005). A- Thrusting of the internal units above the ECM (Aa=Aar, Do=Doldenhorn, Wi=Wildhorn). B- Progressive thrusting of the ECM above the External massif which is associated to the extrusion of the Jurassic basins and folding of the internal nappes. C- Late exhumation of the ECM.

The Kiental phase (Fig. II.12B) was associated to the extrusion of the cover of the Morcles-Doldenhorn basin and the folding of the Helvetic nappes. High temperatures up to 380°C (Girault et al., 2020) are observed in the Morcles Doldenhorn nappes associated to plastic deformation of carbonates (Herwegh and Pfiffner, 2005). The same evolution was observed in the Belledonne massif with a slightly lower temperature of the cover up to 350°C (Bellanger et al., 2015). This closure of the half-graben was associated to the development of large basement shear zones leading to significant

basement shortening, which is possible due to the high temperature that reached more than 300°C (Bellahsen et al., 2012; Bellanger et al., 2015).

The Grindelwald phase (Fig. II.12) corresponds to exhumation of the nappe stacking. The exhumation is related to the initiation of the Belledonne-Aiguilles-Rouges basal thrust and is coeval of the formation of the External massif and Jura mounts. Strike-slip is observed along the External crystalline massifs (Rolland et al., 2009) in relation to the Simplon-Rhône fault zone .

3.3. The Mont-Blanc massif

3.3.1. Structure of the Mont-Blanc massif

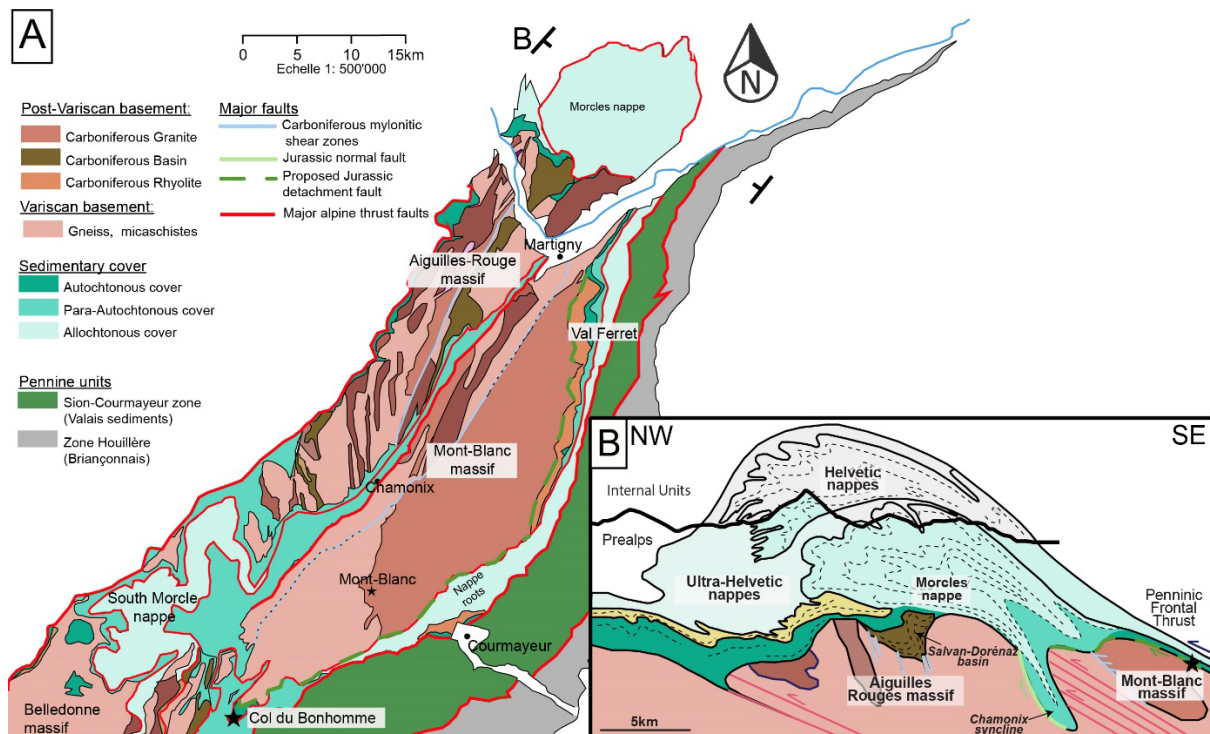


Figure II.13: A- Map of the Mont-Blanc and Aiguilles-Rouges massif highlighting the nature of the basement, and the tectonic position of the cover regarding Alpine deformation (autochthonous, para-autochthonous, and allochthonous). B- Section of the Mont-Blanc massif showing the inverted Morcles basins associated to the thrusting on the Mont-Blanc over the Aiguilles-Rouges and Thrusting of the distal Helvetic nappes over the Mont-Blanc massif (modified from Escher et al., 1993).

The Mont-Blanc basement is composed of a migmatite intruded by a kilometric scale Fe-K granite dated at 303 Ma (Bussy et al., 2001). The external part of the massif is composed of a large shear zone (Mont-Blanc shear zone (MBSZ); Leloup et al., 2005) thrusting the Mont-Blanc above the Aiguilles-Rouge massif (Fig. II.13). This shear zone is ca. 2 km wide and is dated between 20 and 10 Ma. However, the para-autochthonous sedimentary cover was described in the southern part of the External Mont-Blanc (Epard, 1986), overprinted by the MBSZ. Further north, the cover appears detached from the basement.

Pre-Alpine mylonites (Fig. II.13A) were described along the Mont-Blanc granites formed under greenschist conditions (Belliere, 1988). A first generation (N30) anterior to the granite

intrusion, a second generation (N30) affecting the intrusion and a third generation (N45) found only locally at the border of the intrusion (Belliere, 1988). The intrusion is formed by a granite at pressures of 3.8 kbar (Marshall et al., 1997). Besides, the absence of contact metamorphism (Bussy, 1990) indicating relatively high temperature of the basement. The granite is intruded by leucogranites, which crystallized under high p_{H_2O} (1.5 kbar; Marro, 1987). The Mont-Blanc intrusion led to formation of skarn at the contact with marble lenses giving a pressure of formation of 6 to 8 kbar and a temperature of 400 to 500°C (Marshall et al., 1997).

The internal Mont-Blanc is composed of autochthonous sedimentary cover including Triassic to Mid-Jurassic sediments. The Early Liassic sediments correspond to marl and limestone deposits mostly while late Liassic sediments correspond to the massive sandstone deposits (Grès Singuliers; Ribes et al., 2020) overlaid by Aalenian shales. The Grès Singuliers outcrop clearly in the southern Mont-Blanc. The base of the formation is composed of conglomerate passing to coarse-grained sandstones (Fig. II. 14A). Paleo current in the area are N-S to NE-SW. Petrographical analysis of the sediments show a decrease of the grains is visible in the formation followed by coarsening toward the top of the formation under tidal environment (as observed with bundle and tidal bars). These sandstones are composed of granitic and metamorphic lithic clasts. In addition, the feldspar content increase toward the top (Fig. II. 14A). These sandstones deposits are also visible in the northern part of the Mont-Blanc massif (Catogne and Mont-Chemin). Moreover, on the northern part of the massif (Val Ferret, Switzerland), rhyolites dated at 307 ± 2 Ma (Capuzzo and Bussy, 2000) are observed at the contact with the Mont-Blanc granite (Marro, 1987).

The internal Mont-Blanc is bounded locally by the Mont-Blanc back thrust (Antoine et al., 1975). This back-thrust was interpreted as an overturned normal fault as it seems to bound Jurassic basin. Moreover, laterally, the fault trace disappears and the basement is overlaid by Cretaceous sandstones (Compagnoni et al., 1964; Elter et al., 1965; Butler, 1985). Guermani and Pennacchioni (1998) described the contact as made by cataclasites and ultracataclasites overprinted by mylonites. Mylonites cross-cut brittle faults at relatively high angle. Above the basement overturned Liassic shales are visible, only weakly deformed (Butler, 1985).

3.3.2. Jurassic-rift related structures

The External Mont-Blanc massif corresponds to the westward termination of the Morcles basin (Fig. II.14A) which corresponds to an half-graben which formed during Liassic extension (Burkhard, 1988; Epard, 1990).

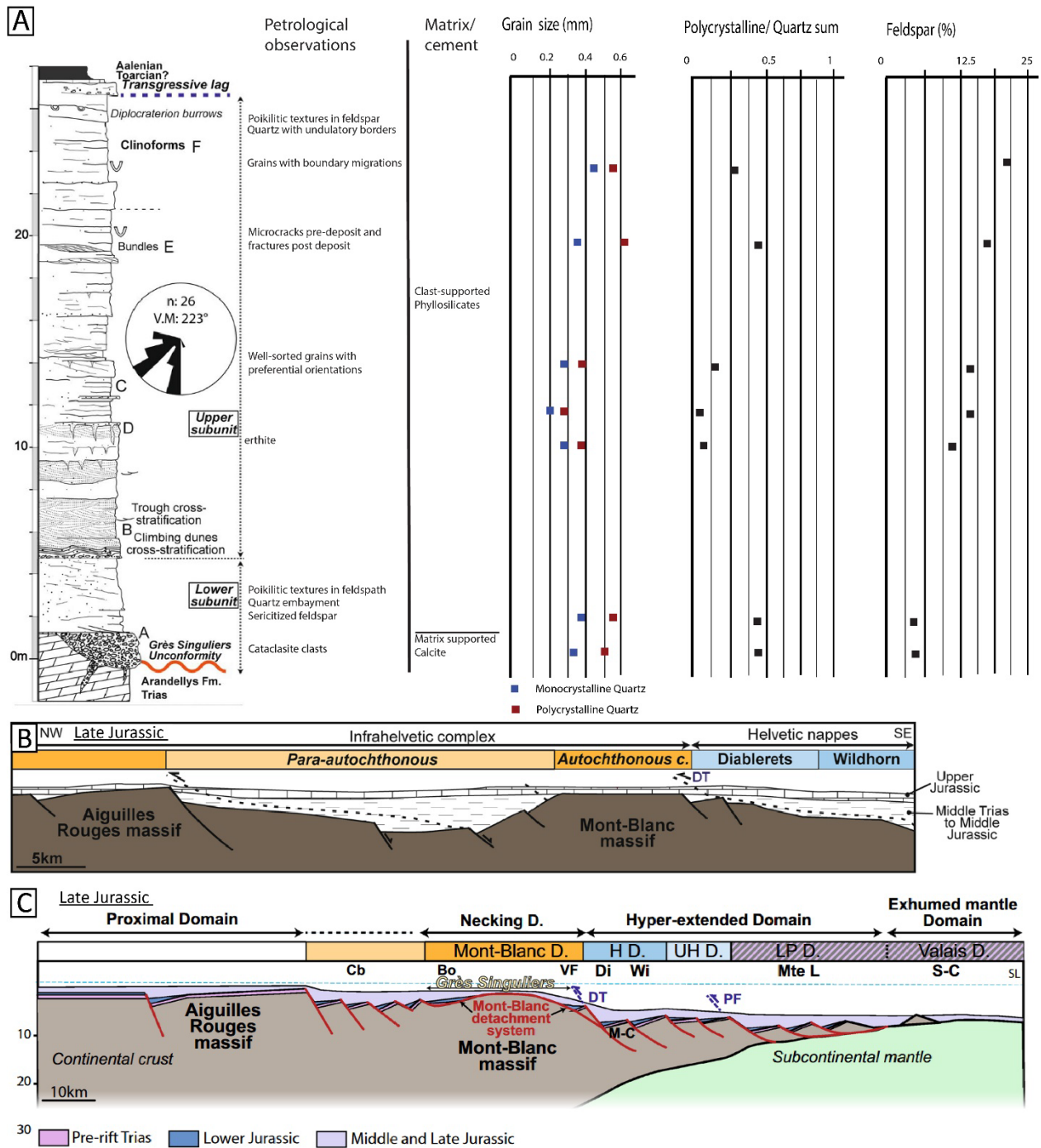


Figure 11.14: Section of the Grès Singuliers from Ribes et al., (2020) associated to analysis of the sediments from Dall'Asta (2019.) B- Palinspatic reconstruction (modified from Ribes et al., 2020) of the Helvetic domain during late Jurassic as proposed by Trümpy (1980), Burkhard (1988) and Pfiffner et al., (2011). C-Reconstruction of the Helvetic domain taking into account the hypothesis of the Mont-Blanc detachment fault (from Ribes et al., 2020).

Different hypotheses concerning the rift-related architecture of the internal Mont-Blanc massif have been proposed. The first interpret the internal Mont-Blanc as the footwall of a high-angle normal fault (Fig. 11.14B) delimitating another basin westward (Diableret and Wildhorn units). However, this fault accommodated only minor extension. The overall area was later covered by upper Jurassic carbonate platforms.

However, the occurrence of massive syn-rift sandstone (Grès Singuliers) deposits in the internal part of the massif indicates important basement uplift. These sandstones observed in the Mont-Blanc domain are not visible in the Aiguilles-Rouges massif, which shows that a different tectonic activity occurred in the Mont-Blanc domain. Associated to these sandstones is a tectonized top basement that is described and interpreted as a Jurassic detachment fault (Ribes et al., 2020). The syn-rift sandstones are therefore interpreted as the result of the basement exhumation related to tectonic activity along the detachment fault (Fig. II.14C).

These two different interpretations have drastically different consequences. First, the significant basement exhumation associated to the detachment indicates that the Mont-Blanc granite was not exposed at the surface until the Jurassic (at least the section found nowadays in the internal Mont-Blanc massif), while the minor extension accommodated by the normal faults assumes that the granite was already exposed at the surface before Jurassic times. This has an impact on the post-Variscan P-T path of the Mont-Blanc basement. Secondly, the detachment is responsible for significant crustal thinning, which led to the presence of thinned to hyper thinned crust east from the Mont-Blanc massif (Fig. II.14B).

3.3.3. Alpine deformation and P-T-t conditions

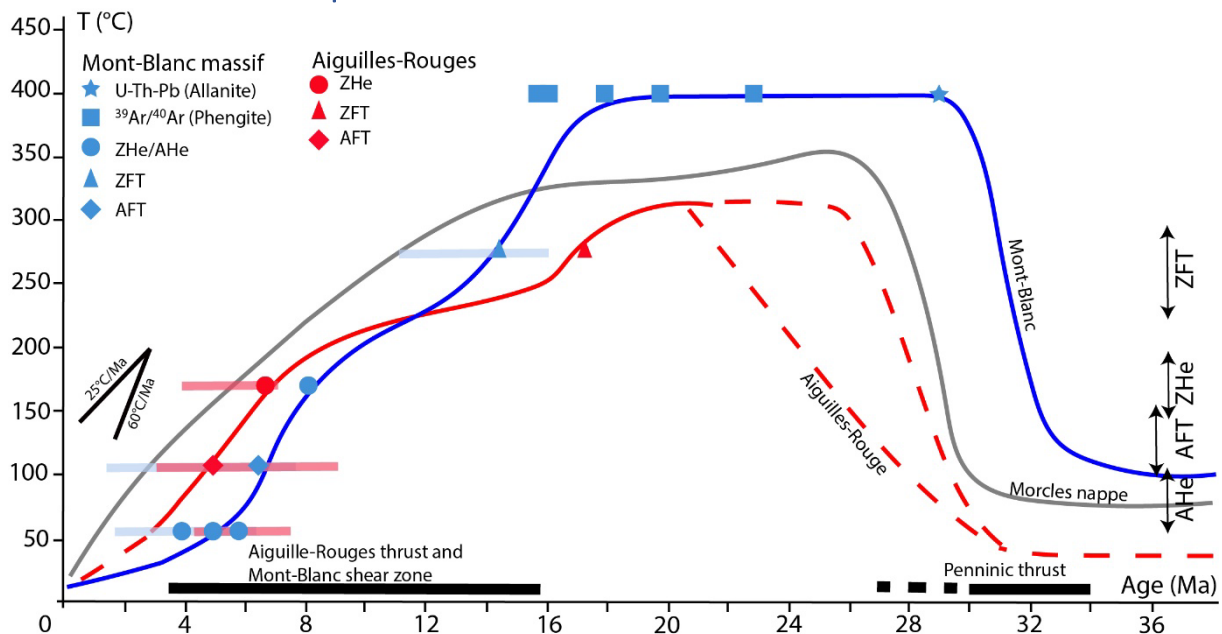


Figure II.15: P-T path of the Mont-Blanc, Aiguilles-Rouge and Morcles nappes showing a prograde path from ca. 32 Ma to 16 Ma and a retrograde path from 16 Ma to present-day (modified from Boutoux et al., 2016). The ages for the Penninic thrust are from Simon-Labric et al., (2009) and the ages for the Mont-Blanc shear zone are from Leloup et al., (2005). The ages associated to the prograde and retrograde path of the Mont-Blanc are from Rolland et al., (2008), Glotzbach et al., (2008) and Cenki-Tok et al., (2014), and for the Morcles nappe from Kirschner et al., (1996).

The Mesozoic cover of the Mont-Blanc massif is locally unconformably overlaid by Tertiary sediments. This is observed mostly in the SW Mont-Blanc cover and indicates an early erosion of the cover possibly associated to tectonic activity (Butler, 1989). However, the tectonic burial of the

massif under the accretionary prism was achieved only during the Oligocene. The Taveyennaz Flysch dated at 30-34 Ma (U-Pb zircon, Lu et al., 2020) and Ar-Ar on amphibole, Féraud et al., 1995) indicates a tectonic burial younger than 34 Ma. Dating of the Penning thrust (Ar-Ar on phengite) provides an age of 31 to 34 Ma (Simon-Labric et al., 2009). The displacement of the flexural basins toward the continent is related to a migration of the accretionary prism (Fig. II.11).

The Mont-Blanc massif was buried under the Helvetic and Penninic units from the distal European margin and Valais basin. The peak temperature conditions registered in the cover are between 300 and 350°C in the southern Mont-Blanc and above 350°C in the northern part of the massif. The stilpnomelane-epidote-calcite veins in the northern part of the massif give a temperature of 360 to 420°C for a pressure of 2.3 to 5.2 kBar (Marshall et al., 1998a). Syn-kinematic allanites along shear zones in the basement gave an age of 29 Ma (Cenki-Tok et al., 2014) for the metamorphic peak at a temperature of ca. 400°C (Boutoux et al., 2016). These high temperatures lasted ca. 10 Ma in the basement before exhumation of the massif, leading to basement cooling (Fig. II.15).

The exhumation of the massif is related to the formation of the the Mont-Blanc shear zone in the Lower Miocene (Leloup et al., 2005) responsible for the thrusting of the Mont-Blanc above the Aiguilles-Rouge. This exhumation path is well constrained using zircons and apatite fission track and AHe and ZHe ages (Boutoux et al., 2016).

3.3.4. Alpine fluid circulations in the ECM

3.3.4.1. Alpine veins

Different types of Alpine veins are found in the Western Alps especially in the ECM. Quartz-chlorite, quartz-muscovite, and quartz-adularia-calcite are the most common veins observed (Marshall et al., 1998a; Rossi and Rolland, 2014). They appear mostly as sub-vertical veins and have an age (Ar-Ar on adularia) of ca. 10 Ma and were emplaced during exhumation of the ECM. In addition, gold-rich quartz veins are also observed locally (Marshall et al., 1998b). They are associated with adularia and provides an age similar to the quartz-adularia calcite veins.

3.3.4.2. Fluid composition

The fluid inclusions from these different vein types show significant variability. Fluid inclusions are composed of H₂O-NaCl and CO₂ which vary between 0 up to 14% of the inclusion volumes corresponding to XCO₂ of 0.016. The salinity ranges between 6 and 12% (Poty et al., 1974; Marshall et al., 1998a). The composition from inclusion leaching gives a ratio Na/K of 5.7 for the quartz-chlorite inclusions and of 2.9 for quartz-muscovite veins. No Ba is observed in the fluids and the amount of F is comprised between 900 and 1500 ppm. The B content is found between 500 and 1200 ppm. Few Zn (<100 ppm) and no Cu and As are observed (Marshall et al., 1998a). In addition,

the homogenization temperatures (Th) found in these inclusions are comprised between 140 and 230°C (Marshall et al., 1998a).

Along Alpine shear zones, element transfer associated to fluid circulations are observed. This is the case for the Mont-Blanc where mobilisation of REE is described (Rolland et al., 2003). Indeed, the presence of REE-rich phases in the mylonite indicates REE gain (allanite, monazite, bastnanite for LREE and aeschynite for HREE) along the shear zone. Leaching of the REE from the deformed basement and increase of LREE in the mylonites are associated to the presence of complexing agent such as SO_4^{2-} and F^- while precipitation is associated to the occurrence of CO_2 (Rolland et al., 2003).

3.3.4.3. Alpine ore deposits

Ore deposits found in the External domain are composed mostly of Pb-Zn-Ag deposits found in the basement or in the sedimentary cover (Polliand and Moritz, 1999). This type of deposits is explained by the dehydration of Mesozoic sediments at depth leading to the formation of metamorphic fluids migrating toward the surface along thrusts.

Vein-type gold was observed in the Mont-Blanc massif (Marshall et al., 1998b). These veins show a concentration in gold up to 40.7ppm corresponding to 4g/t of Au (Clinton (2011), Kuehnbaum (2011)). Besides, U-Cu deposits are also found for example in the Aiguilles-Rouges massif (Siviez, Marecotte). These deposits are composed of Cu-rich sulphides and secondary malachite associated uraninite and uranophane up to 8 wt%. The working hypothesis is the occurrence of U- rich brines penetrating at the basement-sediment interface during Alpine orogeny and precipitated at the contact with Carboniferous volcanic rocks (Clinton, 2011).

Take-home message

- The External Crystalline Massifs correspond to a Variscan polymetamorphic basement intruded by post-Variscan Carboniferous aluminous to metaluminous granites.
- The ECM were submitted to greenschist facies during Alpine collision.
- The Mont-Blanc massif preserves syn-rift massive sandstone deposits raising the question of their origin.
- Different interpretations for the rift architecture have been proposed for the Mont-Blanc massif with different tectonic implications.
- One of the hypotheses considers that the sandstones were the result of significant basement uplift in response to detachment faulting.

4. Key questions associated to the Mont-Blanc massif

The first main question concerns the architecture of the margin. Indeed, Jurassic exhumed mantle from the Valais was observed in the Penninic units SW of the Mont-Blanc massif (Petit Saint-Bernard, Beltrando et al., (2012)). This is indicating that crust had to be thinned significantly between the Mont-Blanc massif and the Penninic units. This questions the architecture of the European margin and leads to the following fundamental questions:

- How was this crustal thinning achieved in the European margin?

Mohn et al., (2014) and Ribes et al., (2020) proposed that the Mont-Blanc massif corresponds to the former necking domain indicating that crustal thinning was accommodated in the Mont-Blanc massif. The distal part of the Mont-Blanc massif to the SW would correspond to the hyperthinned crust subducted during closure of the Valais basin. This provides a partial answer to the problem of the crustal thinning. However, this new model for the rift-related history of the Mont-Blanc massif proposed by Ribes et al., (2020) raises questions concerning the pre Alpine P-T-t evolution of the Mont-Blanc granite. Indeed, most of the constraints concerning the evolution of the Mont-Blanc massif are associated to the condition of emplacement of the granite and the late Alpine evolution of the massif. Therefore, the Permian and Triassic evolution remains unconstrained. This problem is similar to the "granulite conundrum" in the Pyrenees (Manatschal et al., 2021) concerning the timing of exhumation of granulite, during Permian post-orogenic extension or during Cretaceous rifting. This conundrum led to drastically different interpretation of the rift-related history.

The identification of major detachment faults is one of the keys to solve the problem of crustal thinning. Nevertheless, the occurrence of a pre-Alpine detachment faults in the Mont-Blanc massif also raises the question of the preservation of such structures in the External Crystalline Massif. This concerns possible reactivation of the fault and also the impact of Alpine metamorphism on these pre-Alpine contacts. The main questions concerning the necking domain in the Western Alps are:

- What are the characteristics of pre-Alpine detachment faults and what are the fingerprints that allow to identify them?
- What is the impact of Alpine collision on the pre-Alpine tectonic contacts?

From rifting to orogeny, concepts developed in the Alps over a century

Chapter III- Structural and petrological characteristics of a Jurassic detachment fault from the Mont-Blanc massif (Col du Bonhomme area, France)

Nicolas Dall'Asta^{*1}, Guilhem Hoareau¹, Gianreto Manatschal², Stephen Centrella¹, Yoann Denèle³, Charlotte Ribes⁴, Amir Kalifi^{1,4}

¹ Université de Pau et des Pays de l'Adour, E2S UPPA, CNRS, LFCR-France

² Université de Strasbourg, CNRS, ITES UMR 7063, Strasbourg F-67084, France

³ Géosciences Environnement Toulouse, Université de Toulouse, CNRS, IRD, UPS, CNES, F- 31400 Toulouse, France

⁴ TotalEnergies SE - Centre Scientifique et Technique Jean Féger (CSTJF) – TOTAL – France



View of the Grès Singuliers from the Col du Bonhomme (France)

« Quelques brumes fumaient sur les pentes des Alpes, effaçaient les vallées en rampant vers les sommets dont les crêtes dessinaient une immense ligne dentelée dans un ciel rose et lilas » (La Vie errante, Guy de Maupassant)

Structural and petrological characteristics of a Jurassic detachment fault from the Mont-Blanc massif
(Col du Bonhomme area, France)

Foreword

The autochthonous cover of the Mont-Blanc corresponds to pre-rift cover overlaid by massive syn-rift sandstones (Upper Sinemurian -Pliensbachian) which are found unconformably lying above the pre-rift cover and the basement. (Ribes et al., 2020) reinterpreted the facies evolution as well as the tectonic environment related to the sandstones. Indeed, these clastic sediments were interpreted as the stratigraphic response to crustal necking. It is proposed that during Jurassic rifting, crustal necking led to significant topographic uplift in the Mont-Blanc massif which led to the formation of the syn-rift sandstones found in the internal Mont-Blanc massif. In addition, (Ribes et al., 2020) proposed that this necking event was accommodated by large detachment fault which are partially preserved.

This fault appeared mostly preserved in the Col du Bonhomme area (southern Mont-Blanc massif, France) where a top tectonized basement was described. Besides, the best outcrop for the syn-rift sandstones is in this specific area where the stratigraphic evolution is well constrained. For these reasons, the following chapter focuses on this specific area preserving pre-alpine contacts. The results presented here characterized this top tectonized basement presented as a detachment fault. These results provide better constraints on the tectono-sedimentary architecture of this tectonic contact as well as its kinematics. Petrographical and microstructural characterization of this tectonized basement is also provided. Finally, the alpine thermal evolution of the Col du Bonhomme is better constrained to better understand the alpine overprint on this pre-alpine contact.

This work presented here in the form of an article was published in the *Journal of Structural Geology* 2022, volume 159, special edition in honour of J. Ramsay. The supplementary figures associated to this article can be found in the Appendix B of the manuscript.

Introduction

Recent investigations suggest that orogens resulting from a Wilson cycle (Wilson 1966; Wilson et al., 2019) are strongly controlled by rift-related inheritance (e.g., Jammes and Huismans, 2012; Chenin et al., 2017; Jourdon et al., 2019). Such inheritance is largely responsible for the position of major decoupling levels that can be reactivated during convergence, and thus control the final architecture of the orogen, as recently demonstrated for the Pyrenean system (Cadenas et al., 2018; Espurt et al., 2019; Izquierdo-Llavall et al., 2020; Labaume and Teixell, 2020; Lescoutre and Manatschal, 2020; Manatschal et al., 2021) or the eastern Alps (Mohn et al., 2011, 2014). Paleogeographic reconstructions suggest that the same may apply to the Western Alps (Mohn et al., 2011). Indeed, the present-day External Crystalline Massifs (ECM) are located at the transition between the proximal and the distal domains of the former European margin, which formed during Jurassic rifting and hyperextension (Mohn et al., 2014). However, little work has yet been done on rift-related, pre-Alpine structures in the internal part of the ECM, and their possible impact on the subsequent Alpine reactivation (Butler, 1986, 2017). Jurassic rift-related faults were identified such as the Ornon fault (Belledonne massif; Barfety and Gidon, 1984; Lemoine et al., 1986) or inferred from variations in the thickness of lower Jurassic sedimentary rocks on either side of the ECM (Lemoine and Trümpy, 1987; Bellahsen et al., 2012, 2014), and interpreted as a high-angle normal fault associated with limited crustal thinning. The geometry of these faults contrasts with the large offset normal faults expected at the transition between the proximal and distal domains, as observed at present-day rifted margins (e.g. Osmundsen and Péron-Pinvidic, 2018). Recently, Ribes et al., (2020) proposed the presence of a rift-related, Jurassic detachment fault in the internal Mont-Blanc massif, responsible for the tectonic exhumation of the basement leading to a local emersion and reworking of the Variscan basement in the sediment, as documented in the Lower Jurassic sandstones of the Grès Singulier Formation. The occurrence of such a detachment system predicts important crustal thinning, which is not only in accordance with observations made at present-day rifted margins (Osmundsen and Péron-Pinvidic, 2018; Muñoz-Barrera et al., 2020; Ribes et al., 2020) but is also compatible with the subsidence history observed at the transition between the proximal and distal domains in the Alpine domain (Masini et al., 2014; Ribes et al., 2019b). However, this interpretation is mostly based on field structural and sedimentological observations, calling for a more detailed structural, petrological, and geochemical characterization of the detachment fault previously proposed by Ribes et al. (2020). Corroborating the existence of such a detachment surface is not only important for the understanding of the pre-Alpine evolution and the structure of the European margin, but it also strongly impacts the interpretation of the Alpine orogenic evolution. Its existence would have major implications for the evolution of the Mont Blanc massif and on a larger

scale for the interpretation of how the transition between the internal and external parts of the Western Alps can be interpreted and how far they are linked/controlled by rift inherited structures.

In this contribution, we focus on the Col du Bonhomme area, where the proposed detachment surface has been described in most detail by Ribes et al. (2020). Field, microstructural and petrological observations, and elemental geochemical analyses are used to elucidate the kinematics, the mineralogical and geochemical characteristics, and the relative timing of this structure. Our aim is to determine whether this structure was inherited from Jurassic rifting or if it has an Alpine origin.

1. Geological setting

The Alpine orogen was formed as a result of the closure of the Alpine Tethys since the Cretaceous. Its evolution is linked with a complex, polyphase kinematic evolution leading to the subduction of the oceanic, proto-oceanic and exhumed subcontinental mantle domains and the subsequent collision of the Jurassic Adriatic and Europe margins (Fig. III.1; Ford et al., 2004; Rosenbaum and Lister, 2005). Several studies pointed out the link between the main Alpine tectonic units, and the fossil rift domains of the Alpine Tethys (Argand, 1916; Debelmas and Lemoine, 1970; Lemoine et al., 1986; Lemoine and Trümpy, 1987; Stampfli and Hochard, 2009; Bellahsen et al., 2014; Mohn et al., 2014). Indeed, wide-spread Jurassic rifting, which initiated with distributed extension during the Early Jurassic (e.g. Bourg d'Oisans basin; Lemoine et al., 1981; Barfety and Gidon, 1984; Chevalier, 2002), resulted in a complex arrangement of hyperextended, exhumed mantle and proto-oceanic domains (e.g., Valais and Liguro-Piemont domains of Dumont et al., 1984; Lemoine and Tricart, 1986; Lagabrielle, 1987; Bousquet et al., 2002; Schmid et al., 2004; Loprieno et al., 2011; Beltrando et al., 2012; Ribes et al., 2019c) during the late Middle Jurassic to Cretaceous. The external units (Jura, Bauges, Bornes, Chartreuse, Vercors) have been commonly assigned to the proximal domain of the former European margin (Fig. III.1 A,B,C,D; Tricart et al., 2000). They are characterised by the presence of high-angle normal faults of lower Jurassic age associated to half-graben type basins filled with shallow marine sediments (Lemoine et al., 1981). In contrast, the internal units originate from the distal part of the European margin, corresponding to the hyperextended domain, the exhumed mantle and the oceanic domain. Due to important Alpine tectonic overprint, most of the distal parts of the margin have been intensively deformed during subduction (e.g. Pré Piémont domain Pantet et al., 2020), collision and subsequent exhumation (e.g. oceanic domain HP-LT Schistes Lustrés units; Elter, 1971; Lagabrielle et al., 2015). Consequently, rift-related structures are only preserved in a few places (e.g. Petit Saint Bernard (Beltrando et al., 2012), Tasna (Ribes et al., 2019c), Chenaillet (Manatschal et al., 2011), Aiguille Rouge D'Arolla (Decrausaz et al., 2021)). A key

Structural and petrological characteristics of a Jurassic detachment fault from the Mont-Blanc massif (Col du Bonhomme area, France)

result of these studies is that the external and internal units show contrasting features not only in their stratigraphic and metamorphic imprint, but also in their inherited structures with major implications for their Alpine tectonic history.

The ECM (e.g., Aar, Mont-Blanc, Belledonne, Pelvoux, Argentera Massifs), which belong to the external units of the Alps, are commonly interpreted to derive from the transition between the proximal and distal domains of the European margin (former necking domain Fig. III.1C and D; Butler 1986; Butler, 1989; Mohn et al., 2014). At present, they floor the Helvetic and Penninic nappes (Fig. III.1B), and reached greenschist P-T conditions during Alpine nappe stacking (Bousquet et al., 2008; Rosenberg et al., 2021). Most of the rift-related structures have been overprinted by Alpine deformation, as for example the reactivation of former normal faults in the Aar massif (Nibourel et al., 2021). Therefore, most of the rift history has been deduced from the facies, thickness and paleo bathymetric evolution of the syn- and post-rift deposits (e.g., Sangle unit; Epard, 1990) and Ultrahelvetetic units (Trümpy, 1951) and from the difference of geometry between large fold and thrust nappes (e.g., Vervex unit (Epard, 1990) or Morcles-Doldenhorn nappe (Kiss et al., 2020)).

Structural and petrological characteristics of a Jurassic detachment fault from the Mont-Blanc massif (Col du Bonhomme area, France)

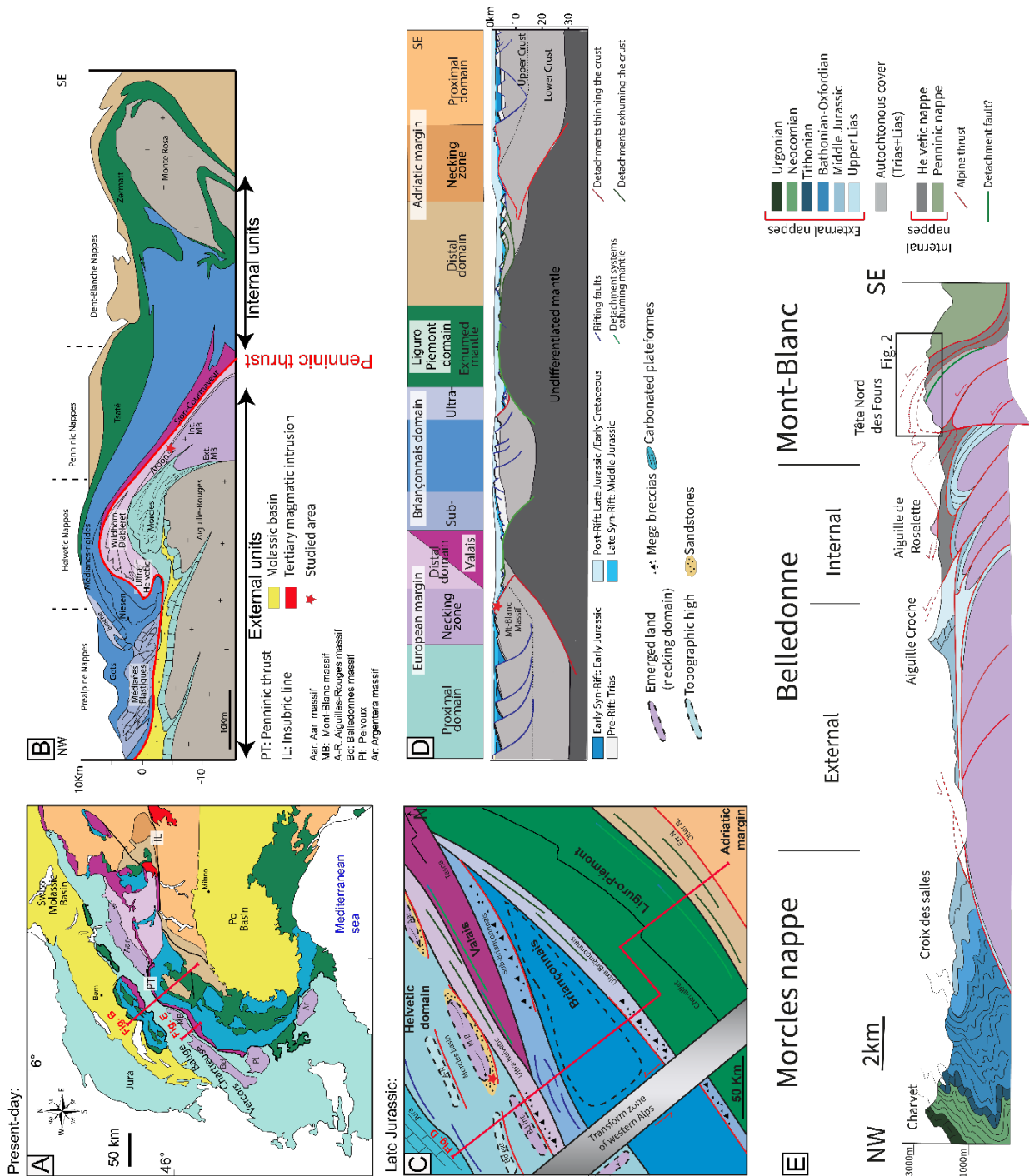


Figure III.1: A- Tectonic map of the Alps showing the different Alpine tectonic units. Note the presence of the External Crystalline Massifs (ECM) at the transition between the internal and external domains (modified from Mohn et al., 2010; Schmid et al., 2004). The colour code similar to D (except molassic basins in yellow and Tertiary intrusions in red) highlights the paleogeographic position of the different Alpine units. B- Section across the Western Alps (for location see Fig. III.1A; modified from Escher et al., 1993). Colour code similar to D. C- Paleogeographic map of the Alpine realm during the late Jurassic (modified from Ribes et al., 2019a). Sandstones (Ribes et al., 2020) and breccias (Ribes et al., 2019a) related to tectonic activity are also represented. Faults in blue correspond to normal faults associated with stretching, the fault in red corresponds to necking fault thinning the crust, and faults in green correspond to faults exhuming the crust and the mantle. D- Restored section of the Alpine Tethys during the Late Jurassic (Mohn et al., 2010). E- NW-SE directed cross section across the transition zone between the Belledonne and Mont-Blanc massif (Southern Mont-Blanc massif, modified from Eltchaninoff-Lancelot et al. (1982)). The Penninic and Helvetic nappes thrust above the ECM were later deformed by basement deformation leading to the formation of a large antiformal fold. The area of interest corresponds to the basement anticline pinched between the Helvetic nappes to the south and the Roselette nappe to the north.

Structural and petrological characteristics of a Jurassic detachment fault from the Mont-Blanc massif (Col du Bonhomme area, France)

The Mont-Blanc massif, which is part of the ECM, is a Variscan polymetamorphic basement made up of paragneisses, cordierite-bearing migmatites and granitic intrusions in its western part (external Mont-Blanc massif), and by a large pluton of metaluminous, ferro-potassic granite surrounded by migmatites in its eastern part (internal Mont-Blanc massif; Bussy, 1990). The pluton corresponds to a post-orogenic magmatism related to extensional tectonic (orogenic collapse or back-arc extension), with a mantle-derived source associated to crustal contamination (Bussy et al., 2001). U-Pb dating of the cordierite-bearing leucosomes and of the granites showed that this late Carboniferous magmatic event lasted about 10 Ma in the ECM (migmatite formed at ca. 307 ± 2 Ma (Capuzzo and Bussy, 2000) and granite emplacement took place between 307 ± 3 Ma (Montenvers granite) and 303 ± 2 Ma for the Mont-Blanc granite (Bussy et al., 2001)). The absence of a clearly defined metamorphic contact aureole around the Mont-Blanc granite, noted by Bussy (1990), may indicate an emplacement at significant depth, with pressures up to 3.8 kbar at the top of the intrusion, i.e., an assumed intrusion depth at 9 to 12 km for the pluton roof (Marshall et al., 1997). Cooling ages and P-T conditions were obtained from skarns located immediately around the granite (i.e., on the pluton walls), providing temperatures of 400/500°C and pressures of 4/8 kbar (based on Ti-thermometry on amphibole and stable isotopes) in Mont-Chemin ore deposits, dated at 303-335 Ma using Ar/Ar on amphiboles (Marshall et al., 1997). Most studies assumed that post-Variscan exhumation to the surface of the external Mont-Blanc massif was achieved during the Permian (Marshall et al., 1997). It was followed by the development of a Permo-Triassic erosional surface, as observed in the external Mont-Blanc massif and the Aiguille-Rouge massif located westward (Epard, 1986). In the western areas, the exhumation was further constrained by the occurrence of Ladinian to Carnian tidal sandstones (Demathieu and Weidmann, 1982) known as the Vieux Emosson Formation (Epard, 1989) directly overlying the basement. Upper Triassic dolostones and evaporites (Arrandellys Fm. ; Epard, 1989) complete the Triassic sequence.

The conditions of exhumation in the internal Mont-Blanc massif are more debated. Most studies considered that similarly to the external part of the massif, the Triassic deposits form a primary, stratigraphic contact with the eroded basement (Eltchaninoff-Lancelot et al., 1982; Epard, 1990). In contrast, Ribes et al. (2020) have proposed that the contact between the pre-rift deposits and the basement corresponds to a Jurassic detachment fault, i.e., that they are allochthonous relative to the underlying exhumed basement. A key observation is the presence of early syn-rift sandstones (Sinemurian/Pliensbachian) corresponding to the Grès Singuliers Formation (Landry, 1976; Eltchaninoff, 1980; Epard, 1989; Ribes et al., 2020) that overlies a deformed and exhumed basement (Fig. III.2). These sandstones, up to 50 meters thick, have been interpreted as the result of local uplift and erosion of the Mont Blanc basement associated either with a normal fault (Epard, 1990; Meyer, 2002), or a large offset extensional detachment fault (Ribes et al., 2020). Ribes et al.

Structural and petrological characteristics of a Jurassic detachment fault from the Mont-Blanc massif (Col du Bonhomme area, France)

(2020) proposed that exhumation and related uplift of the internal Mont Blanc basement occurred during rift-related necking at around 185 ± 5 Ma (Pliensbachian), resulting in sub-areal exposure of a core complex type structure. It is interesting to note that the Mont-Blanc core complex of Ribes et al. (2020) can be well compared to the Mont-Blanc island whose presence was proposed and discussed in Trümpy (1971) and Loup (1992) to explain the occurrence of the Grès Singuliers and its primary contact with the basement. During the Aalenian transgression, the core complex/island was drowned and the Triassic to lower Jurassic deposits were covered by Aalenian to Oxfordian black shales of the Dugny Formation (Fig. III.2; Lemoine et al., 1986; Meyer, 2002). These were followed by Upper Jurassic to Cretaceous limestones.

In the Mont-Blanc massif, the Alpine deformation corresponds to: (i) the thrusting of the more internal Helvetic and Penninic nappes over the Mont-Blanc during the Late Eocene to Early Miocene (Leloup et al., 2005; Egli and Mancktelow, 2013); followed by (ii) thick-skin deformation leading to the closure of the Morcles basin (Escher et al., 1993 ; Herwegh and Pfiffner, 2005) ; and (iii) to thrusting of the Mont-Blanc basement over the Aiguille-Rouges basement (Mont-Blanc shear zone) from middle Miocene to early Pliocene (Leloup et al., 2005). This thrusting was associated with the back thrusting of the basement over sediments along the eastern/internal border of the massif (Guermani and Pennacchioni, 1998; Leloup et al., 2005; Egli and Mancktelow, 2013). Studies of metamorphic assemblages (muscovite-biotite-chlorite-epidote), U-Th-Pb geochronology on allanite and Ar/Ar geochronology on phengite, biotite and phlogopite indicate that the Alpine metamorphic peak was reached between 28 and 15 Ma, with pressures of 0.5 GPa and temperatures up to 400°C in the basement (Rolland et al., 2003 ; Rolland et al., 2008; Cenki-Tok et al., 2014). It was followed by Neogene to present day exhumation of the massif (Glotzbach et al., 2008; Boutoux et al., 2016; Herwegh et al., 2020).

Structural and petrological characteristics of a Jurassic detachment fault from the Mont-Blanc massif (Col du Bonhomme area, France)

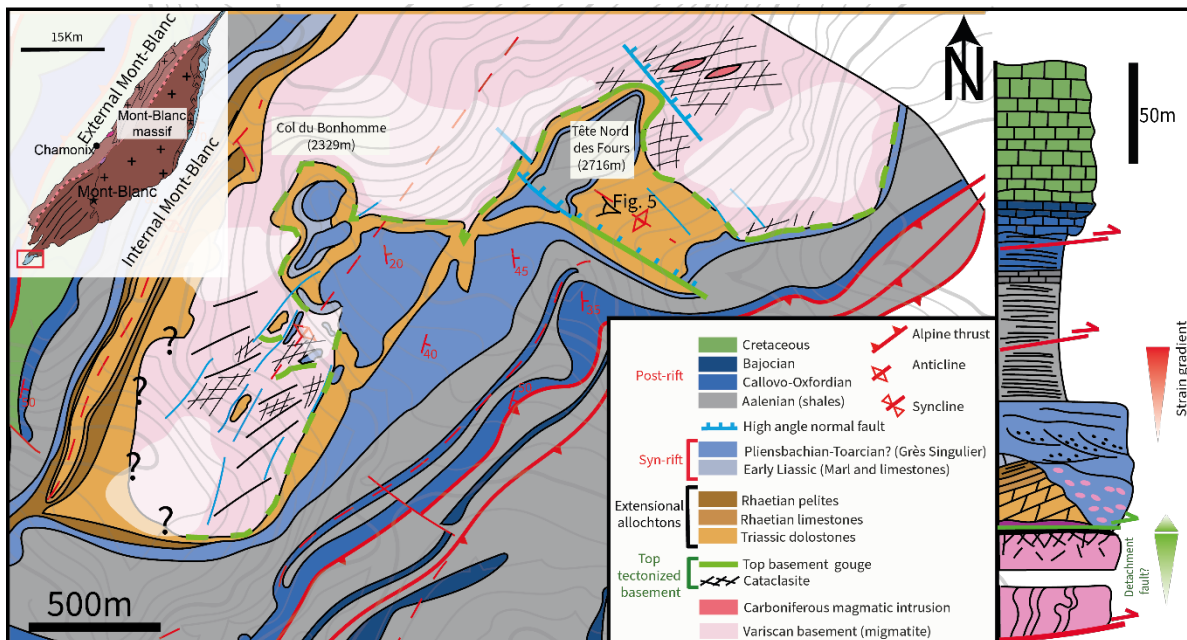


Figure III.2: Map of the Col du Bonhomme area (see location on map in the upper left corner (modified from Meyer, 2002) showing the southern edge of the Mont-Blanc massif. The tectonic contact described by Ribes et al., (2020) is highlighted by the presence of cataclasite and gouge at the transition between the basement and the sediment. Numerous NE-SW and NW-SE Jurassic faults also offset the top basement tectonic contact. The section on the right shows the simplified stratigraphy from the top basement to the Cretaceous with the location of the main decollement levels in the area in the Aalenian and Oxfordian schists.

In this study, we focus on the Col du Bonhomme area located to the NW of Bourg St-Maurice (France). It corresponds to an antiformal fold (Fig. III.1E) preserving the cover of the southern Mont-Blanc massif below the Helvetic nappes, thus giving access to the pre-Alpine contacts. In this area (Fig. III.2B), the syn-rift Grès Singuliers lie unconformably above the pre-rift Triassic cover and the basement. The nature, age, and significance of the contact between the sedimentary cover and the basement is the main goal of our study.

2. Methodology

The geological maps of Meyer (2002) and Ribes et al. (2020), complemented by Google Earth satellite images, field observations and drone acquisitions, were used to build a new 11 km² map of the area (Fig. III.2). Field observations were focused on the facies and thickness distribution of the syn- and pre-rift sedimentary cover, their relationship with the basement, as well as on the recognition and structural characterization of different fault generations and related fault rocks (cataclasites, fault breccias and gouges). In total 71 samples were collected (33 fault rocks; 33 samples from the sedimentary cover and 5 from the unfractured basement).

In order to quantify the peak metamorphic temperatures reached during Alpine metamorphism in the Col du Bonhomme area, Raman spectroscopy of carbonaceous material (RSCM) analyses were performed on 2 polished thin sections of organic-rich Aalenian shales and one

Structural and petrological characteristics of a Jurassic detachment fault from the Mont-Blanc massif (Col du Bonhomme area, France)

section of pre-rift limestone. A total of 55 Raman spectra were acquired with a Horiba Jobin-Yvon Labram II spectrometer coupled to a microscope, at the Institut des Sciences Moléculaires, Université de Bordeaux, France. Acquisitions parameters include a 514.5 nm argon laser, an extended scanning mode (500-2000 cm^{-1}) and an acquisition time of 30s. Spectra of the first-order region of carbonaceous material were processed using the Fityk software (Wojdyr, 2010). Each spectrum was fitted with 4 bands (D1, D2, D3, and the graphite band G) with Voigt profiles. The calibration of Beyssac et al. (2002), based on the parameter $R2 = D1/(G + D1 + D2)$ was used.

Petrographic observations of polished thin sections from sampled rocks ($n = 71$) were performed with a Nikon LV150ND optical microscope, and by cathodoluminescence (CL) using a Cathodyne system (OPEA) with an operating condition of 15 kV–18 kV and a gun current of 300–350 mA under a 60 mTorr vacuum (LFCR, Pau, France). Other techniques include a Zeiss EVO50 scanning electron microscope (SEM) coupled to EDS mapping (20kV beam; PLACAMAT, Pessac, France). Electron Probe Micro-Analyzer (EPMA) analyses were carried out on polished thin sections using a Cameca SXFive instrument at the Centre de Microcaractérisation Raymond Castaing in Toulouse (France), calibrated with natural and synthetic in-house standards: aluminium oxide (Al), wollastonite (Si, Ca), sanidine (K), manganese titanite (Mn), hematite (Fe), albite (Na), barite (Ba), celestine (Sr). For the determination of major element compositions on silicate from the fault rocks and phosphate in the basement minerals, the operating conditions were set at 15 kV, with a probe current of 50 nA, and a 2 μm beam. For elemental mapping, similar conditions, and a step size of 2 μm were used.

Following microscopic acquisitions, the XMapTools software (Lanari et al., 2014, 2019) was used to build quantitative X-ray electron microprobe maps, and the AX software (Holland and Powell, 2006) to recalculate the structural formulas of the different mineral phases observed. Optical photomicrographs of the fault rocks were processed with ImageJ (Rasband, 1997) to calculate the surface area, the orientation and the circularity of each grain, and the detection of microfractures. Grain size was calculated using the equal area diameter. These parameters were used to calculate several fault parameters such as the fractal dimension β , the cut-off sharpness α and the characteristic diameter D_c (μm), by fitting the curve obtained with the equation $P\left(\frac{N}{N_t}\right) = \left(1 + \left(\frac{D}{D_c}\right)^\alpha\right)^{-\frac{\beta}{\alpha}}$ (Otsuki, 1998; Monzawa and Otsuki, 2003), with P the number of grains (N) larger than a certain diameter (D in μm) with N_t the total number of grains. Similarly, the microfracture density (μm^{-1}) was calculated using the circle inventory method (Davis et al., 2011; Rossetti et al., 2010), consisting in dividing the total length of microfractures within a circle by the area of this circle.

3. Results

3.1. Alpine metamorphic peak in the Col du Bonhomme area

The peak temperatures calculated from the RSCM analyses of the Aalenian shales and pre-rift limestone samples are 322 ± 18 °C, 336 ± 25 °C and 335 ± 22 °C (Table III.1 and Appendix B Tab. B1,2,3). Since these shales are rich in organic carbon and are post-tectonic relative to the rifting in the Mont-Blanc/proximal domain, these values likely correspond to the peak temperatures reached during the Alpine metamorphic overprint. These results, which point to lower greenschist facies conditions, are in good agreement with illite crystallinity values measured in the area (1.35; Eltchaninoff and Triboulet, 1980), and with the compilation of RSM data by Rosenberg et al. (2021), giving a temperature below 350°C for the southern part of the Mont-Blanc area. Petrographic observations on the Grès Singuliers highlight the impact of such metamorphism on the mineralogy of the Jurassic deposits in the internal Mont Blanc massif where alpine metamorphism resulted in a static thermal overprint marked by overgrowth of muscovite over illite (see Appendix B Fig. B.1).

Sample	Location	Lithologies	Coordinates	Nb of spectra	R1	R2	T (°C)	1σ SD (°C)	95% SD (°C)	95% SEM (°C)
CB20-40	Col des Fours	Aalenian shales	45°45'52.06"N 6°44'9.68"E	21	2.47	0.71	322	6.52	18	3.96
CB20-41	Col des Fours	Aalenian shales	45°45'51.37"N 6°44'7.22"E	18	1.73	0.68	336	7.2	25.6	6.02
MB1c	Col des Fours	Liassic Carbonate	45°45'55.10"N 6°44'16.06"E	16	2.53	0.71	325	7.4	22.5	5.62

Table III.1: Results of RSCM thermometry in the Col du Bonhomme area. SD=Standard deviation, SEM= Standard error of the mean, 95% confidence interval.

3.2. Macroscopic description of the basement / sediment contact

In the Col du Bonhomme area, the contact between the Mont-Blanc basement and the overlying Triassic and Liassic sediments crop out at several places as shown in Fig. III.2.

3.2.1. Basement and tectonized top basement

The basement is composed of a cordierite bearing migmatitic gneiss with a sub-vertical NNE-SSW striking foliation (Fig. III.3G). It is intruded by meter-thick magmatic bodies corresponding to aplite.

Towards the top of the basement, the gneiss is progressively deformed over about 40 meters, showing a gradational transition from the well-preserved gneiss to a cataclasite and a gouge at the basement/cover contact (Fig. III.3). Locally, sub-horizontal foliation is visible, possibly corresponding to Variscan mylonites cross cutting the sub-vertical foliation. They are parallel to the top basement contact (Fig. III.3A, F and G) and show a brittle overprint forming tectonic breccia. In more detail, the damage gneiss is characterized by a network of anastomosed fault zones of

Structural and petrological characteristics of a Jurassic detachment fault from the Mont-Blanc massif (Col du Bonhomme area, France)

cataclastic gneiss with lenses/clasts of preserved gneiss (Fig. III.3A), that we define as the damage zone. These anastomosing fault zones form a progressively denser network towards the top, clearly showing a strain gradient toward the top basement. The leucosomes of the migmatitic gneiss are good markers for the strain at the macroscale. Far from the contact, the initial texture of the leucosomes is preserved. Upsection, they are affected by important, centimetre scale fractures without displacement, indicating an increase of the brittle overprint toward the basement/sediment contact (Fig. III.3E). Closer to the contact (< 10 m Fig. III.3A), the fracture network becomes denser, the fragments of leucosomes get smaller and gradually develop into cataclasites. The brittle overprint of the former host rock includes the disaggregation of the fabric and the alteration of the feldspars, leading to an increase of the phyllosilicate content upsection. Kinematic markers of fault-related structures are sparse and commonly difficult to interpret. They mainly consist of few lineations giving a N-S direction. In phyllosilicate-rich zones, the kinematics is clearer as the foliation is more marked. S/C' structures are observed, where the C' plane has an orientation 200/36 with a top to the SSW sense of shear.

The core of the fault (i.e., the core zone; < 1 meter-thick, Fig. III.3A and C) corresponds to a matrix-supported fault rock with a high content of phyllosilicates, here referred to as indurated gouge. It appears as a dark, fine grained discontinuous layer with a well-developed foliation. It forms a sharp contact with the underlying cataclasites forming the damage zone (Fig. III.3A). Centimetric injections of material from the gouge are visible in the cataclasite (Fig. III.3A). Veins parallel to the foliation are also observed (Fig. III.3C). The gouge has the same appearance at the macro and micro-scale with the alternation of matrix-rich and clast-rich bands, showing N-S lineated clasts (Fig. III.3F).

Structural and petrological characteristics of a Jurassic detachment fault from the Mont-Blanc massif (Col du Bonhomme area, France)

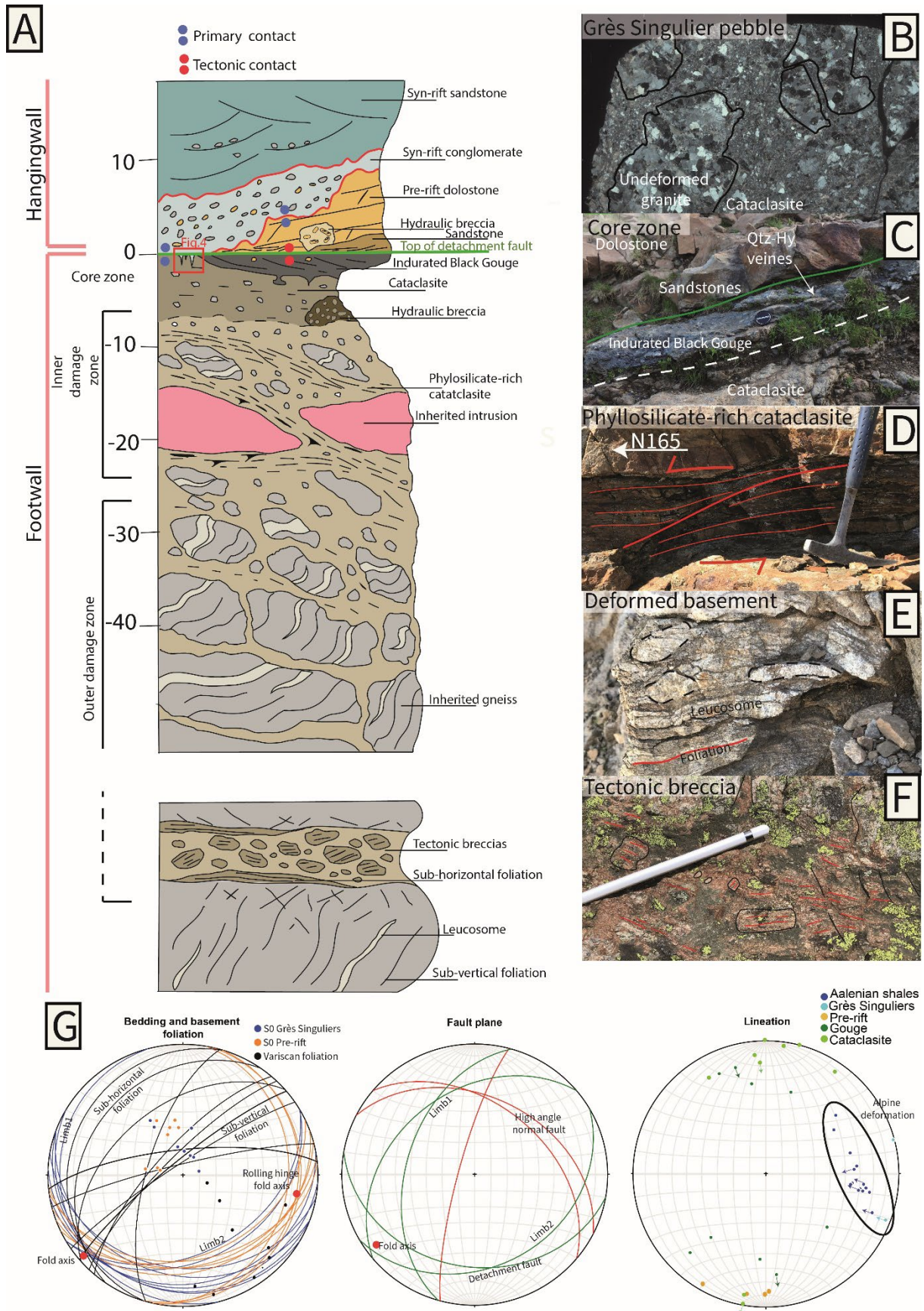


Figure III.3: A-Schematic section of the top basement/sediment contact showing a strain gradient toward the top of the basement. A local loss of the initial rock texture is visible associated with an increase of alteration and brittle overprint. A sharp contact separates the basement and the sedimentary cover. Pre-rift sediments are separated from the basement by a

Structural and petrological characteristics of a Jurassic detachment fault from the Mont-Blanc massif (Col du Bonhomme area, France)

tectonic contact with deformation visible at the base. The Grès Singuliers are lying above both the pre-rift and the basement in a stratigraphic contact. B-Clast of cataclasite reworked in the Grès Singuliers (45°43'46.41"N/ 6°43'47.96"E). C- The top basement is composed of cataclasite and locally black indurated gouge (45°43'39.51"N/6°42'40.25"E). D- Phyllosilicate-rich cataclasite giving an NNE-SSW top to the south sense of shear in the damage zone (45°46'13.36"N/6°43'46.17"E). E- Cataclasied basement with sub-horizontal Variscan foliation is still discernible in the damage zone (45°44'11.21N/6°43'46.85"E). F- Sub-horizontal mylonites affected by brittle deformation. G-Measures of bedding, fault plane orientations (high angle-normal faults and orientations of the top basement tectonic contact) and stretching lineations from the basement and the cover (projected on Schmidt stereograms, lower hemisphere). Note the NE-SW orientation of the basement fold affecting the basement and the cover (limb 1 and 2).

3.2.2. Pre-rift, tectonized sedimentary deposits

Pre-rift sediments locally lie above the tectonized basement. Four types can be distinguished, whose spatial distribution is variable along the contact. The first one, which is common, corresponds to discontinuous 20 cm-thick lenses of sandstones composed of micrometric angular lithic fragments and carbonate clasts within a calcite cement (Fig. III.3C). The second type consists to a limestone containing millimetric to centimetric, euhedral quartz crystals with 100µm-large rectangular anhydrite inclusions (see Appendix B Fig. B.2). The third type corresponds to upper Triassic brownish dolostone (Arandellys Fm.), whose thickness ranges from 0 to approximately 10 meters, and which covers the sandstone lenses and limestones with quartz nodules (Fig. III.2,3A and 3C). Although the dolostone origin is sedimentary, it is now significantly deformed up to forming both, metric asymmetric boudins and monomictic breccias. The dolostone layers form an angle of about 10-15° with the tectonic contact separating the basement from the pre-rift sediments suggesting an angular unconformity. In addition, the dolostone boudins can lie directly above the tectonized basement and are associated with tectonic breccias. These breccias are either polymict containing angular to sub-angular pluri-cm to pluri-dm clasts of both dolostones and basement or monomict (see Appendix B Fig. B.3 A, B) including dolostone and minor quartz-bearing limestone clasts characterized by a jigsaw geometry (Fig. B.3C, D). Clasts of dolostone embedded in the gouge are frequently observed (Fig. B.3E and F). Finally, the fourth type of pre-rift sediments includes Lower Jurassic (Hettangian) calcschists and limestones preserved in the Rocher du Bonhomme.

3.2.3. Syn-rift sediments sealing the contact

At some places, the gouge and cataclasites within the top basement are crosscut by subvertical cracks, which are filled with a sedimentary breccia containing cataclastic material, clasts of gouges and quartz veins floating in a brownish matrix (Fig. III.4). The cracks are tens of cm-large and deep and can be best interpreted as neptunian dykes (Fig. III.4A). The brown sedimentary infill corresponds to a calcite-rich indurated mud containing quartz grains and bioclasts, mostly crinoids (Fig. III.4C, D). The same matrix is also locally observed above the basement gouge and is found within the cracks (Fig. III.4B). This observation suggests that the meter-thick brown breccia made mainly of basement clasts, forms a stratigraphic contact with the tectonized basement.

Structural and petrological characteristics of a Jurassic detachment fault from the Mont-Blanc massif (Col du Bonhomme area, France)

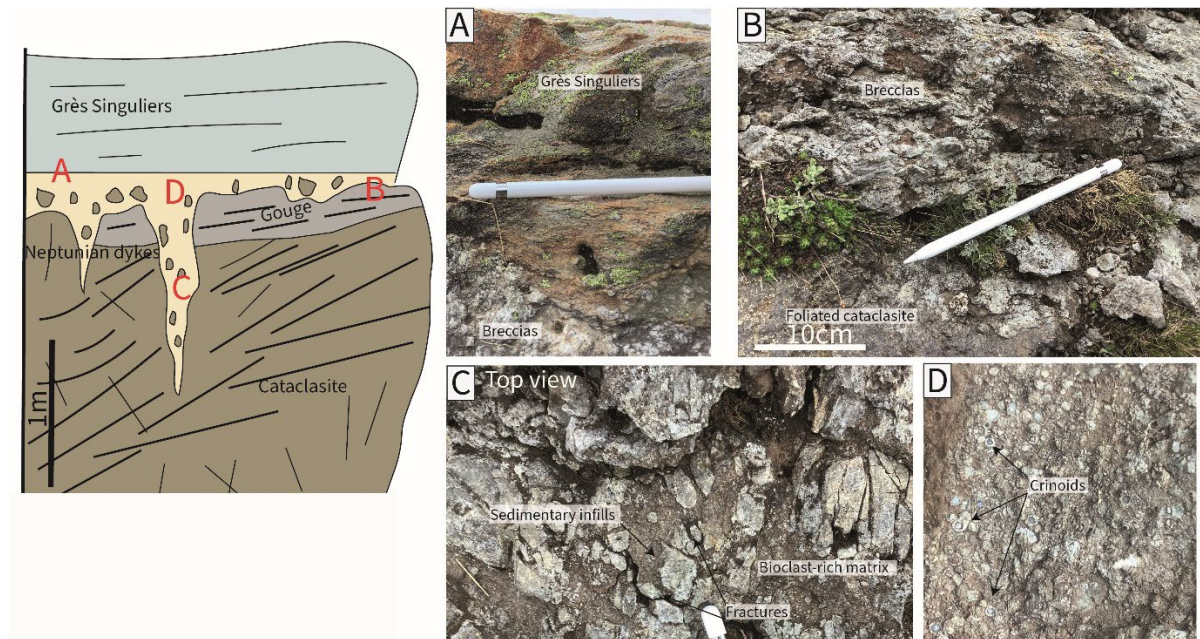


Figure III.4: Section of the top basement with sediment infill interpreted as neptunian dykes ($45^{\circ}43'39.6''N/6^{\circ}42'46''E$). The position of the pictures is indicated in the section. A- Contact between the top basement and the Grès Singuliers. B-Profile view of foliated cataclasite overlaid by fractured basement. The fractures are filled with a brownish matrix. C- Upper view of the fractured basement with sedimentary infill. The infill is composed of quartz grains and biotoclast fragments in a brownish matrix. D-View of the biotoclasts from the matrix corresponding mainly to crinoids.

The pre-rift dolostones and limestones are truncated by an erosional surface at its top, and are unconformably overlain, along a stratigraphic contact, by Liassic syn-rift sandstones and conglomerates of the Grès Singuliers Fm (Fig. III.2, III.3 and Appendix B Fig. B.3F). These sandstones, 10 to 30 meters thick, can also seal directly the tectonized basement at places where the pre-rift deposits are absent. The lower part of the Grès Singuliers corresponds to: (i) monomictic conglomerates (pluri-dm angular carbonate pebbles derived from the pre-rift limestones and dolostones), with a N-S paleocurrent direction as deduced from pebble imbrications different from the NW-SE paleocurrent measurements from the upper part of the formation (Ribes et al., 2020), or (ii) polymictic conglomerates (sub-angular to rounded pebbles of carbonates and basement). Pebbles of cataclasites are also observed ($45^{\circ}43'46.41''N/6^{\circ}43'47.96''E$), indicating reworking of the fault rocks from the underlying exhumed basement (Fig. III.3) into the sediments. The upper part of the Grès Singuliers corresponds to shoreface and foreshore sandstones with strong tidal influence (Ribes et al., 2020). Well-preserved sedimentary figures such as cross beds, small tidal laminations and bioturbations are common.

At the top of the Formation, NW-SE stretching lineations related to Alpine deformation are commonly associated with millimetre-thick proto-mylonite shear zones and a pervasive cleavage. Above the sandstones, Aalenian shales belonging to the Dugny Fm. show important deformation with C/S structures giving a top to the NW sense of shear (Fig. III.3F). These structures correspond to the decollement level of the Helvetic nappes above the Mont-Blanc massif (Eltchaninoff-Lancelot et

Structural and petrological characteristics of a Jurassic detachment fault from the Mont-Blanc massif (Col du Bonhomme area, France)

al., 1982; Egli and Mancktelow, 2013). It is important to note that the base of the Grès Singuliers is little deformed and that there is a clear strain gradient upsection towards the main Alpine thrust.

3.2.4. High-angle faults

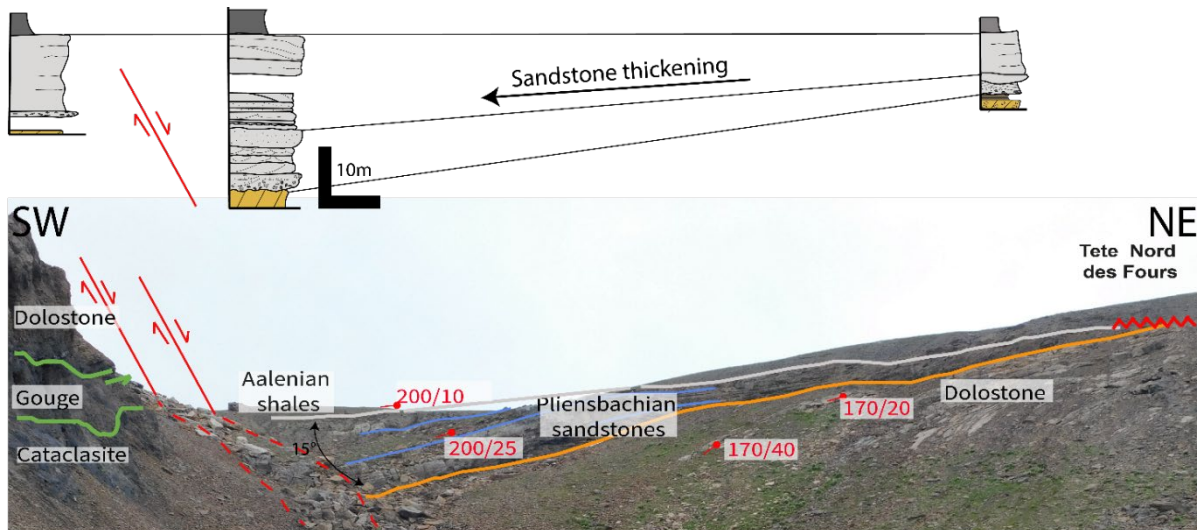


Figure III.5: High-angle normal fault offsetting the top basement tectonic contact about 30 m ($45^{\circ}43'53.45''/6^{\circ}43'51.70''$). A sedimentary wedge with thickening of sandstones toward the fault is observed in the Grès Singuliers (15°), indicating a likely Pliensbachian/Toarcian age for the fault.

Both the basement and the pre-rift deposits are offset by two sets of high-angle normal faults, one striking NE-SW and the second NW-SE. The NE-SW striking normal faults show small offsets (few meters) of the top basement. The NW-SE faults offset the basement and the pre-rift but also the Grès Singuliers and the Aalenian shales. In the Col des Fours area, a NW-SE fault (30/45) offsets the top basement, including the gouges and cataclasites, by about 35 m (Fig. III.5). A sedimentary wedge (15°) formed by the Grès Singuliers is visible in the hanging wall of the fault (Fig. III.5). Thickening of the sandstones toward the fault plane is compatible with the Grès Singuliers being syn-tectonic to this fault and suggesting a fault activity being Pliensbachian-Toarcian. A roll-over anticline (fold axis 100/14) accommodates the deformation of the pre-rift cover. Slickensides on planes parallel to the fault strike (pitch of 18°) and on secondary planes oblique to the fault (strike: N150) show an important strike-slip component, possibly related to an Alpine reactivation of the fault (coherent with the WSW strike slip direction measured in the area by Egli and Mancktelow, 2013, in the Helvetic cover).

3.2.5. Synthesis of macroscopic observations

A strain gradient is observed in the basement toward its top. Variscan foliation is overprinted by brittle deformation, leading to cataclasite and gouge formation. This progressive localisation of the deformation is marked by an increase in the content of phyllosilicates which make most of the gouges. This tectonized basement is overlaid by pre-rift and syn-rift sediments, but the nature of the relationship between basement and its sedimentary cover differs between both types. The pre-

rift/basement contact is tectonic while the syn-rift/basement contact is stratigraphic. Therefore, the syn-rift deposits seal an exhumed tectonized top basement, as well as its overlying pre-rift sediments. The syn-rift Grès Singuliers, are affected by a strain gradient as can be seen at its top, which increases toward the overlying Aalenian shales. This alpine deformation is the most intense in the Aalenian shales, which acted as an important decollement during emplacement of the Helvetic nappes (Eltchaninoff-Lancelot et al., 1982; Egli and Mancktelow, 2013).

3.3. Petrological and microstructural observations

3.3.1. Host rock: Variscan gneiss

At distance from the tectonic contact, the subvertical foliation of the migmatitic gneiss basement (quartz (43%), biotite (18%), and feldspar (37%), Fig. III.6) is highlighted by the alternation of biotite and quartz-feldspar bands. Accessory minerals are mostly fluorapatite found with biotite. Leucosomes related to melt infiltration are parallel to the gneiss foliation. They are composed of coarse quartz and feldspars. Micro textural analysis shows that quartz grains were affected by grain boundary migration (GBM) and sub-grain rotation with the myrmekitization of some plagioclase feldspars. The migmatites are intruded by aplite veins characterised by a high amount of quartz. The latter are typical of high temperature rock fabrics of migmatitic gneisses.

The high temperature (HT) gneiss fabric is also overprinted by microfractures affecting the feldspars, locally forming micro veins showing bulging recrystallisation where the fractures propagate in the quartz. These fractures are mostly transgranular and crosscut the previous HT foliation. They are associated with alteration of feldspars with formation of white micas, albite and microporosity (Fig. III.7A). Small kinks and crenulation with rutile-rich micro fractures highlight the deformation in the phyllosilicate-rich zones (Fig. III.7B). This deformation is associated with hydration of the host rock leading to alteration of feldspar and biotite and the formation of white micas. Primary biotite is strongly altered with formation of chlorite and rutile. Alteration is stronger on the border of the crystals and along their cleavage, where rutile is observed, whereas the core of the crystals is better preserved. Chlorite corresponds to an intermediate composition between chlinochore, Fe-sudoite and amnesite (Table III.2). The paragenetic association of the hydration of the host rock is $K\text{-Fsp} + \text{Ab} + \text{Bi} \leftrightarrow \text{Chl} + \text{Mu} + \text{Rt} \pm \text{Qtz}$ with a total amount of phyllosilicate of around 10%.

Structural and petrological characteristics of a Jurassic detachment fault from the Mont-Blanc massif (Col du Bonhomme area, France)

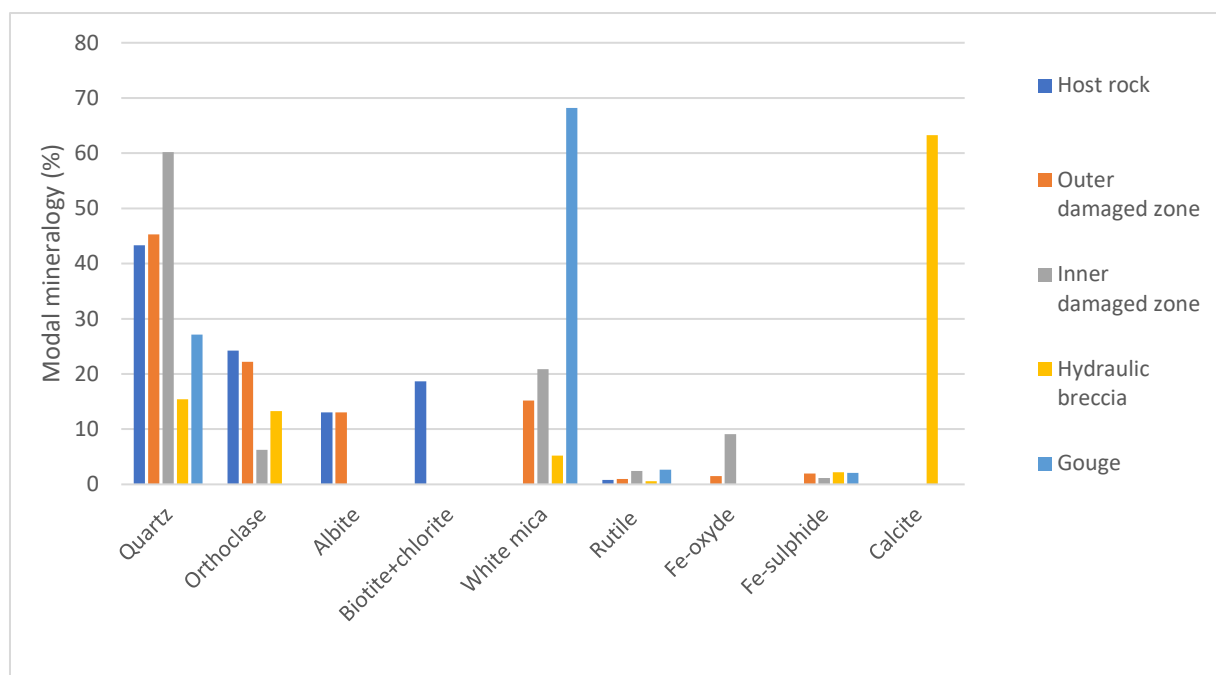


Figure III.6: Modal composition for some of the different fault rocks found in the Col du Bonhomme area.

3.3.2. Damaged zone

In the damage zone, the gneiss host rock is highly altered and affected by brittle deformation. It is composed mainly of quartz, plagioclase and K-feldspars, white micas, sulphides (pyrite and arsenopyrite) and iron oxide minerals. Minerals inherited from the gneiss host rock correspond to quartz, remnants of feldspars and small zircons. Chlorite, fluorapatite and biotite, which were present further away from the tectonic contact, are absent. This fabric is overprinted by fractures filled mostly with iron oxide.

In the outer damage zone (>20 m), feldspar constitutes 30% of the rock (10% for plagioclase and 20% for K-feldspar, Fig. III.6). Feldspars show various amounts of alteration (hydration). Poorly altered K-feldspars show the replacement of orthoclase by albite and small white micas, and formation of secondary porosity (Fig. III.7A). Highly altered feldspars are mostly replaced by white micas (Fig. III.7D). Most of the plagioclase has a high proportion of albite. Patches of quartz + micas are common mostly along crystal twins. Minor bulging recrystallisation is related to propagation of transgranular fractures in quartz and undulose extinction of quartz crystals is observed (Fig. III.7C, D).

Close to the top basement / sediment contact (inner damage zone: < 20 m), the amount of feldspar (Fig. III.6) decreases (6% of orthoclase and no more albite), correlated with an increase of white micas (20%). Highly altered feldspars show extensive, up to complete white mica replacement (Fig. III.6D). The rock is clast-supported, dominated by quartz clasts. Most of the clasts are derived from the gneiss, and the phyllosilicates are a by-product of feldspar alteration leading to the formation of a white mica matrix (M1). White micas are zoned, with an increase of Si and a decrease of Al toward their rims (Table III.2). This results a composition departing from the ideal composition

Structural and petrological characteristics of a Jurassic detachment fault from the Mont-Blanc massif (Col du Bonhomme area, France)

of muscovite and being closer to that of the illite-phengite group. Most of the white micas have a grain size below 50 μm , corresponding to sericite (Eberl et al., 1987), but locally larger micas are observed (> 100 μm). Both quartz crystals inherited from the gneiss (where HT dynamic recrystallisation is visible) and from the syn-kinematic veins (coarse grain blocky texture with no dynamic recrystallisation of quartz and locally elongated to fibrous texture) commonly have a lobate crystal border (Fig. III.7C) similar to a corrosive wear pattern and indicating quartz dissolution.

Sample	CB20-10										5a		5c					
	Host rock										Cataclasite		Gouge					
	Chl	Chl	Bi		Fsp	Fsp			Fap		Wm	Wm	Wm	Wm		Hy	Hy	
SiO2	24.89	24.88	35.28	SiO2	65.13	63.98	68.63	CaO	52.18	SiO2	51.82	49.14	48.25	51.09	SiO2	54.49	53.50	
TiO2	0.00	0.00	3.35	TiO2	0.00	0.00	0.23	MnO	0.98	TiO2	0.10	0.47	2.87	0.27	TiO2	0.00	0.00	
Al2O3	20.81	20.68	19.15	Al2O3	19.09	18.46	18.88	FeO	0.57	Al2O3	25.95	26.66	29.73	27.92	Al2O3	20.17	20.17	
Cr2O3	0.00	0.00	0.00	Cr2O3	0.00	0.00	0	F	2.67	Cr2O3	0.00	0.00	0.00	0.00	Cr2O3	0.00	0.00	
Fe2O3	0.00	0.00	0.00	Fe2O3	0.00	0.00	0.17	MgO	0.03	Fe2O3	0.00	0.25	0.00	0.00	Fe2O3	0.00	0.00	
FeO	28.30	27.51	17.96	FeO	0.00	0.00	0	Cl	0.07	FeO	2.56	1.76	1.47	1.99	FeO	0.04	0.04	
MnO	0.44	0.44	0.35	MnO	0.00	0.00	0	P2O5	43.02	MnO	0.03	0.09	0.00	0.00	MnO	0.04	0.01	
MgO	11.56	11.66	8.45	MgO	0.00	0.01	0.02	SrO	0.01	MgO	3.71	3.64	1.95	3.16	MgO	0.00	0.00	
CaO	0.04	0.00	0.00	CaO	0.17	0.00	0.05	SO3	0	CaO	0.00	0.01	0.02	0.07	CaO	0.00	0.06	
Na2O	0.00	0.02	0.38	Na2O	2.18	0.36	11.07	Na2O	0.09	Na2O	0.04	0.01	0.08	0.08	BaO	11.75	13.22	
K2O	0.04	0.07	9.00	K2O	13.03	15.87	0.46	SiO2	0.06	K2O	10.78	10.58	9.61	10.33	Na2O	0.43	0.46	
Total	86.08	85.26	93.92		99.60	98.68	99.51		99.67		94.99	92.62	93.98	94.91	K2O	10.94	10.43	
															Total	97.86	97.89	
Oxygens	14.00	14.00	11.00		8.00	8.00	8.00				11.00	11.00	11.00	11.00		8.00	8.00	
Si	2.72	2.74	2.71	Si	2.98	2.99	3.012			Si	3.47	3.38	3.24	3.40	Si	2.79	2.76	
Ti	0.00	0.00	0.19	Ti	0.00	0.00	0.008			Ti	0.01	0.02	0.15	0.01	Ti	0.00	0.00	
Al IV	1.28	1.26	1.73	Al	1.03	1.02	0.977			Al IV	0.53	0.63	0.76	0.60	Al	1.22	1.23	
Al VI	1.41	1.42		Cr	0.00	0.00	0			Al VI	1.52	1.53	-0.76	-0.60	Cr	0.00	0.00	
Cr	0.00	0.00	0.00	Fe3	0.00	0.00	0.006			Cr	0.00	0.00	0.00	0.00	Fe3	0.00	0.00	
Fe3	0.00	0.00	0.00	Fe2	0.00	0.00	0			Fe3	0.00	0.01	0.00	0.00	Fe2	0.00	0.00	
Fe2	2.59	2.53	1.15	Mn	0.00	0.00	0			Fe2	0.14	0.10	0.08	0.11	Mn	0.00	0.00	
Mn	0.04	0.04	0.02	Mg	0.00	0.00	0.001			Mn	0.00	0.01	0.00	0.00	Mg	0.00	0.00	
Mg	1.89	1.91	0.97	Ca	0.01	0.00	0.002			Mg	0.37	0.37	0.20	0.31	Ca	0.00	0.00	
Ca	0.01	0.00	0.00	Na	0.19	0.03	0.942			Ca	0.00	0.00	0.00	0.01	Ba	0.24	0.27	

Structural and petrological characteristics of a Jurassic detachment fault from the Mont-Blanc massif (Col du Bonhomme area, France)

Na	0.00	0.00	0.06	K	0.76	0.95	0.02 6			Na	0.01	0.00	0.01	0.01	Na	0.04	0.05
K	0.01	0.01	0.88							K	0.92	0.93	0.82	0.88	K	0.71	0.69
Sum	9.94	9.93	7.71	Sum	4.98	4.99	4.97			Sum	6.97	6.98	6.85	6.93	Sum	5.00	5.00
XMg	0.42	0.43	0.46	XAn	0.83	0.00	0.21			XPg	0.48	0.09	0.96	0.98	XCls	23.7 4	26.7 3
				XAb	20.1 2	3.37	97.1 1			XMs	50.3 4	56.1 2	72.2 3	57.3 9	XAb	4.30	4.60
				XOr	79.0 5	96.6 3	2.68			XCel	49.1 9	43.7 9	26.8 1	41.6 3	XOr	71.9 6	68.6 6
										Charge deficit	0.93	0.93	0.84	0.90			

Table III.2: Microprobe analysis of minerals from the host rock, the cataclasite and the gouges. The structural formula were calculated with the software AX from (Holland and Powell, 2006). Ferric iron was recalculated according to the method of Holland and Powell, (1998). Wm = White micas, Chl = Chlorite, Bi = Biotite, Fsp = Feldspars, Fap = Fluorapatite, Pg = Paragonite, Ms = Muscovite, Cel = Celadonite, An = Anorthite, Ab = Albite, Or = Orthoclase, Hy = Hyalophane, Cls = Celsian, XMg=Mg/(Mg+Fe).

The inherited gneissosity is completely overprinted by brittle deformation (Fig. III.7C, D, E). In the clast-rich areas, the clasts are rather angular, while in the areas with a higher matrix-to-clast ratios, quartz grains are more rounded (Fig. III.7E). Most fractures and veins are intergranular, but clusters of intragranular fractures are locally observed. These fractures are branched with each other with an acute angle up to 45° (Fig. III.7E). Several events of quartz fracturing are also highlighted by different generations of fluid inclusion trails in single quartz grains, which have a fracture density of 28 μm^{-1} . Therefore, deformation is achieved by fracturing associated with significant hydration and mineral neoformation (white micas and quartz precipitation in the veins). These types of “chaotic fault rocks” maintaining cohesion during deformation are typical of cataclasites (Braathen et al., 2004). The grain size shows fractal distribution with a fractal dimension between 1.38 and 1.5.

The fabrics described previously are later overprinted by larger transgranular veins (Fig. III.7E). These veins are filled either with quartz or with iron sulphide or oxide. The quartz veins (> 100 μm -thick) are themselves affected by fracturing and progressively reworked in the cataclastic matrix corresponding to continuous vein formation throughout deformation. The iron sulphide to oxide veins, which crosscut the quartz veins, are thinner (> 10 μm -thick). Far from the contact, only sulphides are observed (6%), while closer to the contact only 1% of pyrite is present, for 2% of rutile and 8% of iron oxide. No specific orientation of the clasts nor the veins is visible.

Structural and petrological characteristics of a Jurassic detachment fault from the Mont-Blanc massif (Col du Bonhomme area, France)

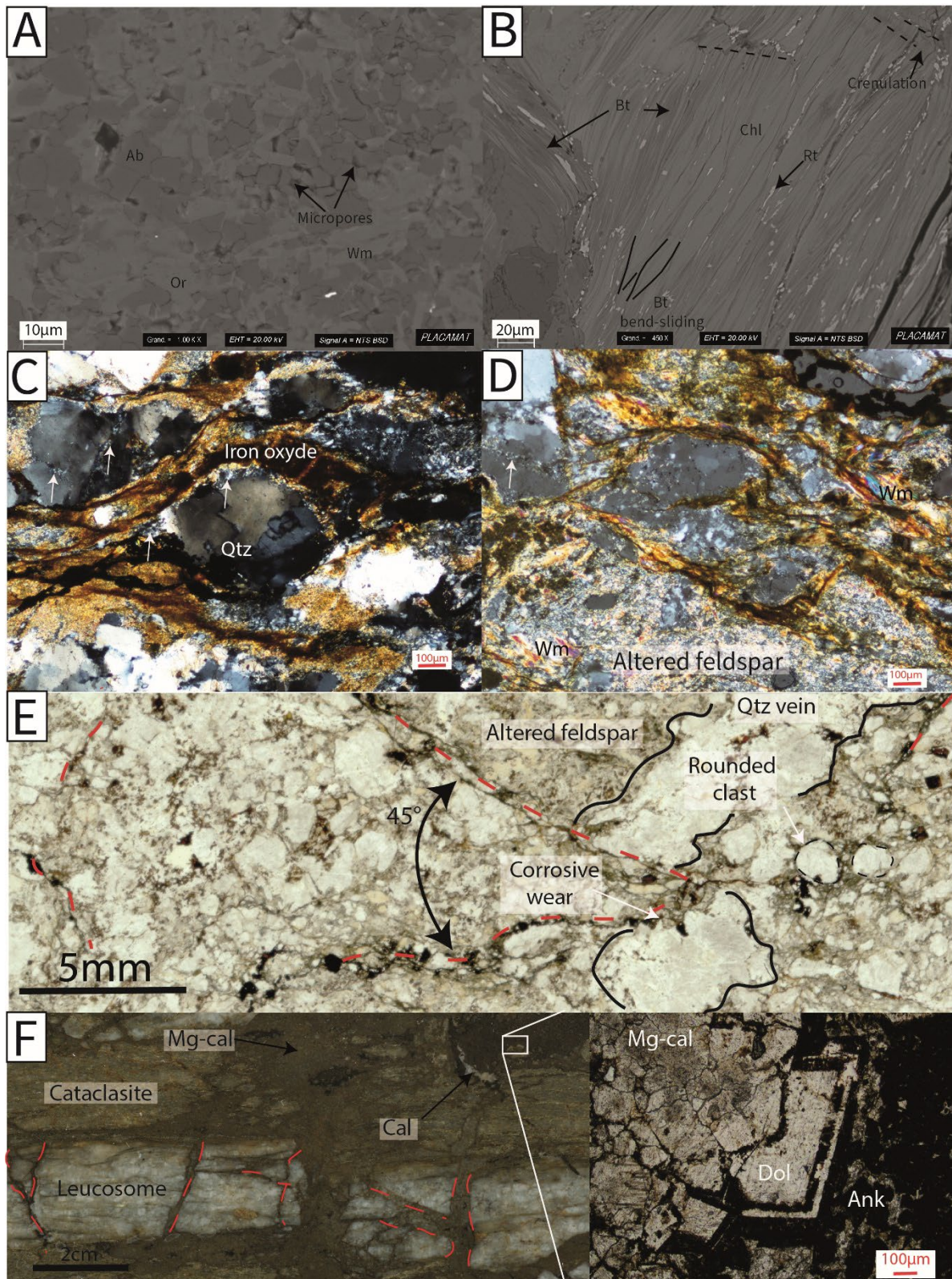


Figure III.7: A-Lowly altered orthoclase (Or) showing albite (Ab) and white mica (Wm) replacement with creation of microporosity (Scanning Electron microscope- Back Scattered Electron SEM-BSE). B- SEM-BSE image of the alteration of biotite (Bt) to chlorite (Chl) with formation of rutile (Rt). Note the alteration along the cleavage and on the borders of the crystals. Minor deformation such as crenulation is visible in the biotite and chlorite assemblages. C- Closer view of the cataclasite where numerous fractures filled with oxides are observed. Quartz (Qtz) exhibits fractures and minor plastic recrystallisation (bulging, white arrow) associated with undulose extinction (optical photomicrograph, crossed polarized light (XPL)) D- Cataclasite showing important feldspar alteration, with the formation of white micas associated with fracturing and oxides. Minor plastic recrystallization by bulging is visible in the prolongation of fractures (white arrow) (optical photomicrograph, XPL). E- Cataclasite showing fragmentation of the host rock, along with important fracturing of

Structural and petrological characteristics of a Jurassic detachment fault from the Mont-Blanc massif (Col du Bonhomme area, France)

quartz and important hydration of feldspar (optical photomicrograph, plane polarized light (PPL)). Only few remnants of K-feldspars are observed. Partial dissolution of quartz with corrosive wear is clearly visible. Highly deformed quartz veins are observed in the cataclastic matrix, and oxide-rich fractures overprint the cataclasite. F- Hydraulic breccia with calcite cement (left: optical photographs of polished slab; right: XPL photomicrographs). The leucosomes are only affected by perpendicular fractures. The gneiss is affected by stronger alteration and deformation. The rock is overprinted by brecciation and subsequent dolomite (Dol) and ankerite (Ank) formation replaced by later by Mg-calcite (Mg-cal).

Along the fault (core) zone, calcite-rich fractures are locally visible (Fig. III.7F). Calcite fills fractures in the cataclasite with a jigsaw monogenic fabric. Cement is brown-coloured, with locally preserved banded texture (2-3 mm). The cement is iron-rich, with a zoned iron composition. The initial texture is composed of large dolomite rhombs with small ankerite rhombs and formation of calcite filling the space between the former minerals. It is affected by static recrystallization leading to formation of equigranular twinned Mg- calcite. Along the contact between the calcite-cemented fractures and the cataclasite, part of the white micas and feldspars are also replaced by calcite forming patches. The jigsaw fabric with important dilation points toward hydraulic fracturing resulting in breccias. Textural relationships suggest that breccia formation corresponds to one of the latest deformation events along the fault plane.

3.3.3. Core zone

The core zone is made of gouges, which are dark, fine-grained matrix-supported rocks, which rework fragments of cataclasites (Fig. III.8A and B,). The rock shows the same appearance microscopically as macroscopically, with the alternation of clast-rich and matrix-rich layers. The high content in phyllosilicate points toward an indurated black gouge following the definition of Braathen et al. (2004). In the clast-rich layers (at the microscale), the quartz grains range from 1 mm to less than 10 μm in size. The grain size distribution follows a power law with a fractal dimension β between 1.58 and 1.7 (Fig. III.9C). The shape of the clasts is variable, ranging from angular to well-rounded (up to 0.9 circularity) with a mean circularity of 0.59 (Fig. III.9F). Deformation of the clasts lead to the formation of σ -clasts (Fig. III.8A), associated with small folded cataclasite clasts (Fig. III.8B). Preferential orientation of the clasts (Fig. III.9E, e.g., Manatschal, 1999) highlights the foliation. The asymmetric clasts are good kinematic markers. Asymmetric clasts are visible in the direction parallel to the N-S stretching lineation indicating a top to the south sense of shear. The gouge matrix (M2) corresponds mostly to illite-rich material less than 5 μm in size, with lower amounts of quartz and pyrite (Fig. III.8C). Neoformed illite growing perpendicularly from the pyrite walls in pressure shadows are also present. Small zircons (less than 50 μm) inherited from the gneiss are affected by fracturing and minor dissolution at the micro-scale. Oxide-rich bands represent 5% of the whole samples (2% of iron oxide and 2.7% of rutile, Fig. III.8E). Most of the pyrite was dissolved, leaving holes in the rock surrounded by quartz pressure shadows. Post-kinematic mineralogical transformations are also observed. Only a small amount of pyrite is preserved or weathered to jarosite. Coarser white micas (up to 100 μm long, $X_{\text{M}} > 0.7$) are visible in the gouge and the

Structural and petrological characteristics of a Jurassic detachment fault from the Mont-Blanc massif (Col du Bonhomme area, France)

cataclasite clasts. They appear post-dating the gouge growing sometimes over the gouge foliation (Fig. III. 8.D). Finally, micrometric hematite-filled fractures can locally be observed in the gouge, where they crosscut and thus postdate the foliation.

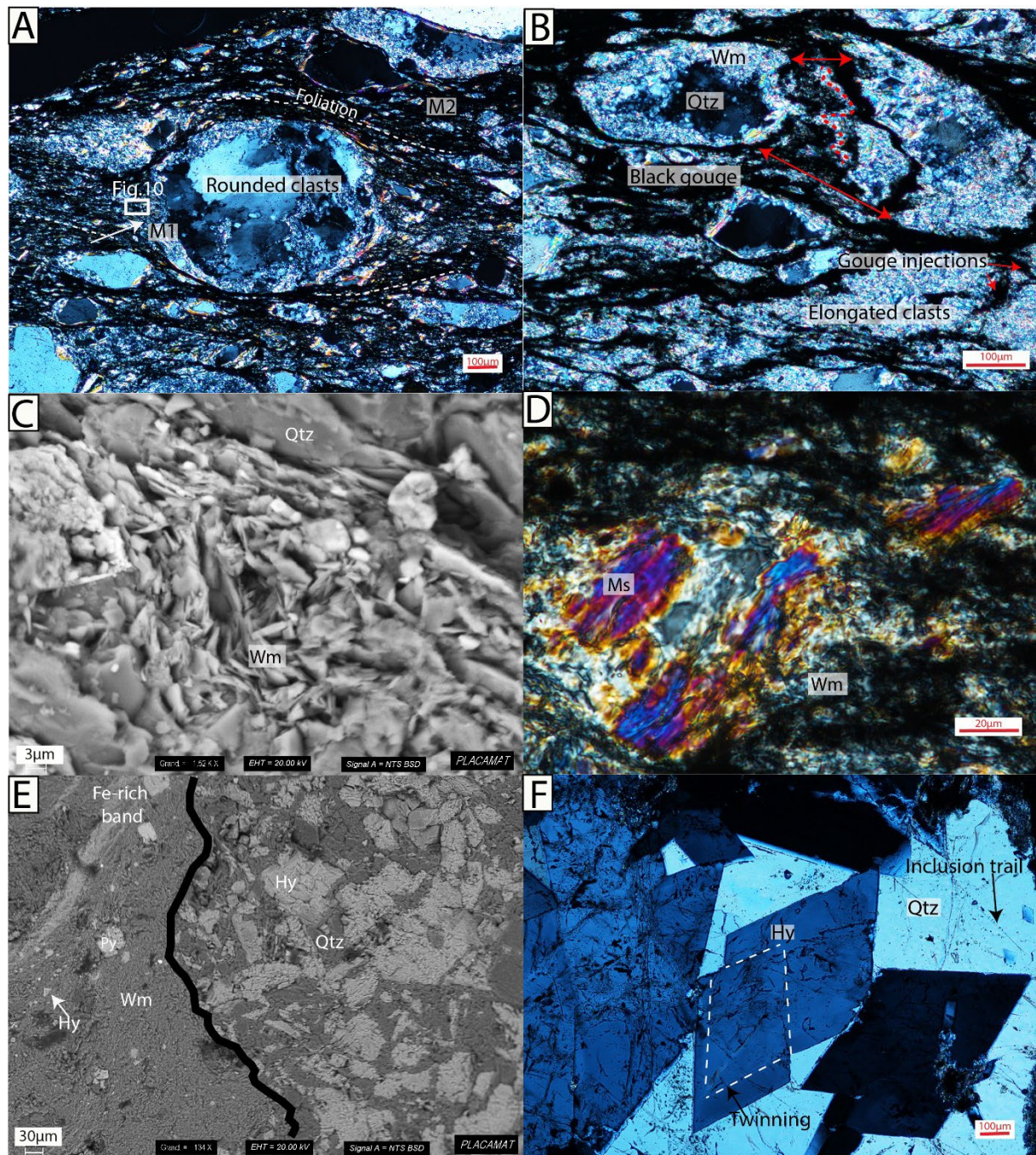
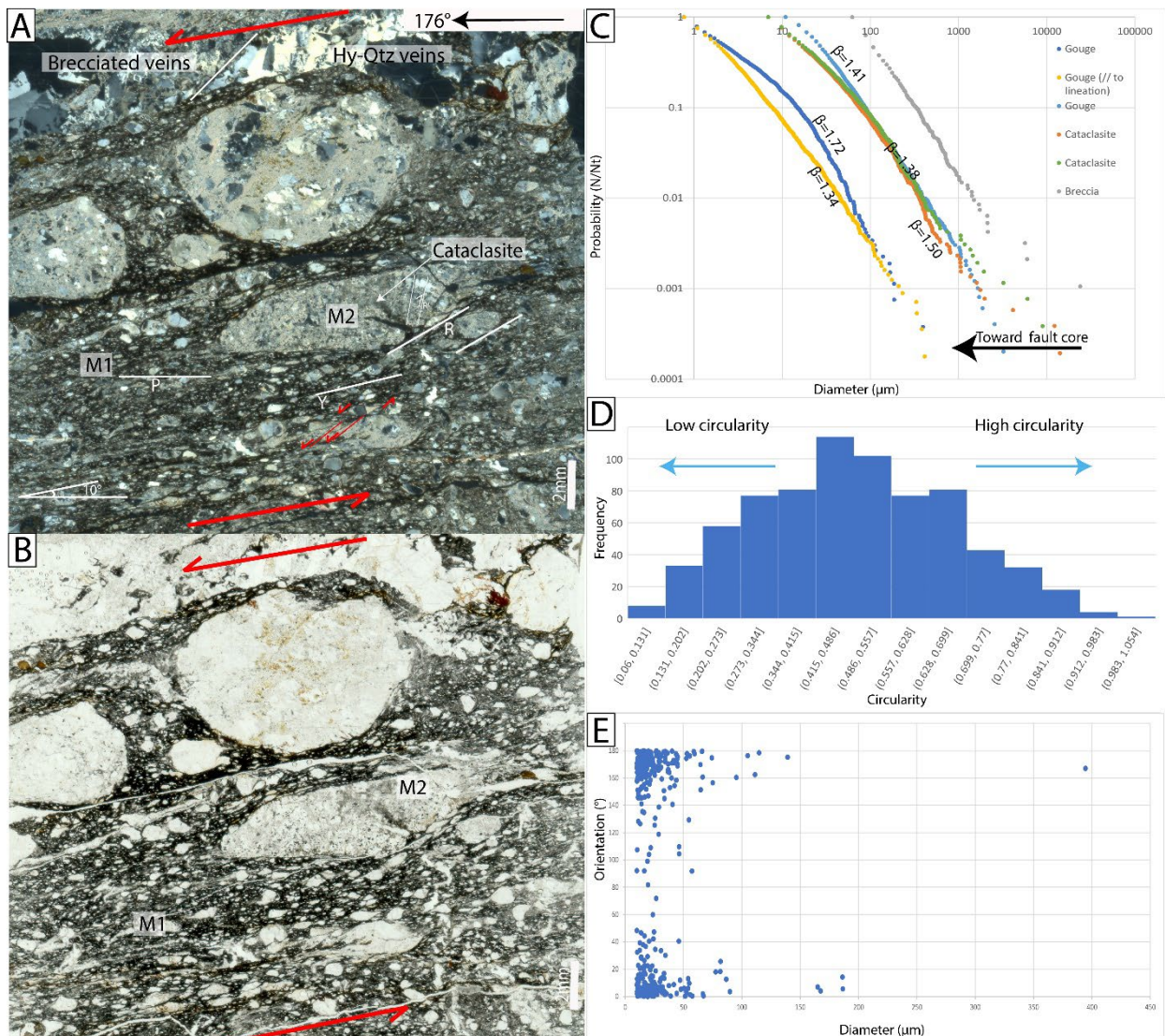


Figure III.8: A-Microphotograph of the gouge showing a rounded clast embedded in the black matrix. The foliation is highlighted by the elongated clasts. The white arrow points at the cataclastic matrix (M1) of the clast progressively sheared and incorporated into the gouge matrix M2 (XPL). B- Microphotograph of the gouge matrix M1 with clasts of cataclasite showing the progressive shearing (red arrows) and transformation into ultra-fine-grained black matrix M2 (XPL). C- Closer view of the black matrix of the gouge (M2) showing small illite minerals (around 5 μm), small quartz fragments (less than 10 μm) and pyrite (SEM-BSE, unpolished sample) D-Muscovite overgrowth over illite in the gouge (XPL). E- Irregular border between a hyalophane-bearing vein and the gouge. The latter is composed of small Fe-rich bands surrounded by illite-rich matrix. Clasts of hyalophane (Hy) are also observed in the gouge (SEM-BSE). F-Microphotograph of hyalophane and quartz in veins affected by important fracturing. The feldspars show important twinning of the crystals (XPL).

Structural and petrological characteristics of a Jurassic detachment fault from the Mont-Blanc massif (Col du Bonhomme area, France)

Dilation and vein formation also occurred in the core zone. Small (2 mm-thick), fractured quartz veins are visible in the matrix. Some veins crosscut the foliation and are affected by fracturing with millimetric offsets, while other veins are parallel to the foliation. Pressure shadows filled with fibrous quartz can have developed around quartz vein fragments. Besides, thin (< 100 μm -thick) iron oxide rich veins parallel to the foliation plane are present. A last vein generation corresponds to centimetre-thick veins visible at the macroscale, parallel to the gouge foliation (Fig.III.8E, III.9A and B). They are not observed in the adjacent cataclasites. The veins are filled by quartz and Ba-rich feldspar (hyalophane, Fig. III.E and F). The Ba content of hyalophane is around 11 to 15% wt, corresponding to a composition of 23% Celsian, 4% Albite and 71.9% orthoclase. The hyalophane crystals, which are euhedral, show no compositional zoning. They are partially replaced by quartz mainly along their cleavage (Appendix B Fig.B.4). On the border of the veins, hyalophane crystals are highly fractured, with reworking of some fragments in the gouge. An important amount of transgranular fractures affecting quartz and hyalophanes are also visible (fracture density of $18 \mu\text{m}^{-1}$) with some corresponding to healed fractures with fluid inclusion trails.



Structural and petrological characteristics of a Jurassic detachment fault from the Mont-Blanc massif (Col du Bonhomme area, France)

Figure III.9: A and B- Microphotograph (XPL and PPL) of the black gouge reworking cataclasite fragments. The elongation of the clasts marks the foliation. Note the reworked clasts of cataclasite in the gouge matrix. C-Example of grain size repartition in gouge and cataclasite samples as obtained from image treatment. All the samples show a fractal dimension between 1.3 and 1.7. Note the progressive grain size diminution toward fault core. D-Grain size circularity of the gouge from image treatment showing a wide range of shapes, from angular to well rounded. E- Grain orientation versus grain size, showing a preferential orientation defining the foliation.

More information on the processes occurring during the formation of gouge M2 from the cataclasite is obtained with quantitative compositional mapping by electron probe micro-analyser (EPMA), highlighting the behaviour of major elements and the textural evolution during deformation (Fig. III.10). Phase maps (Fig. III.10A) show quartz and feldspars grains in a white mica matrix. For the white micas, a reduction of the grain size is visible for white micas larger than 10 μm in the cataclasite and smaller than 10 μm in the gouge matrix M2 (Fig. III.10B). The progressive shearing of the cataclasite matrix M1 has an impact not only on the grain size but also on the composition of the micas (Fig. III.10B and C). Except for the K_2O and SiO_2 contents, which remain stable (10 wt%), and the Al_2O_3 that decreases, other major element contents increase between the cataclasite and the gouge matrix (Fig. III.10F). The increase is particularly important for TiO_2 as visible in the chemical map (Fig. III.10C), the chemical profile (Fig. III.10D) highlighting the absence of TiO_2 in the cataclasite and presence in the gouge matrix. Recalculation of structural formulas show a slight decrease of Al VI and Al IV between the cataclasite matrix and the gouge matrix (1.75 +/- 0.07 apfu (atom per formula unit) to 1.67 +/- 0.04 apfu and 0.58 +/- 0.06 apfu to 0.55 +/- 0.040 apfu for Al VI and Al IV, respectively). Detailed compositional analysis of the phyllosilicates from the gouge matrix (M2 see Fig. III.10E and Table III.2) show departure from the Mu-Ce line (phengite). This indicates that Si-Al substitution is not achieved through a tschermak substitution ($\text{Al}^{\text{IV}}\text{Al}^{\text{VI}} \leftrightarrow \text{Si}^{\text{IV}}(\text{Mg}, \text{Fe}^{2+})^{\text{VI}}$) but through a pyrophyllite substitution ($\text{Al}^{\text{IV}}\text{M}^{\text{I}} \leftrightarrow \text{Si}^{\text{IV}}\square^{\text{I}}$) and illite substitution $\text{Al}^{\text{VI}}\square^{\text{I}} \leftrightarrow \text{Mg}^{\text{VI}}\text{M}^{\text{I}}$, leading to charge deficit and formation of illite (Meiller, 2013) with interfoliar charge between 0.8 and 0.9 (Meiller, 2013).

Structural and petrological characteristics of a Jurassic detachment fault from the Mont-Blanc massif (Col du Bonhomme area, France)

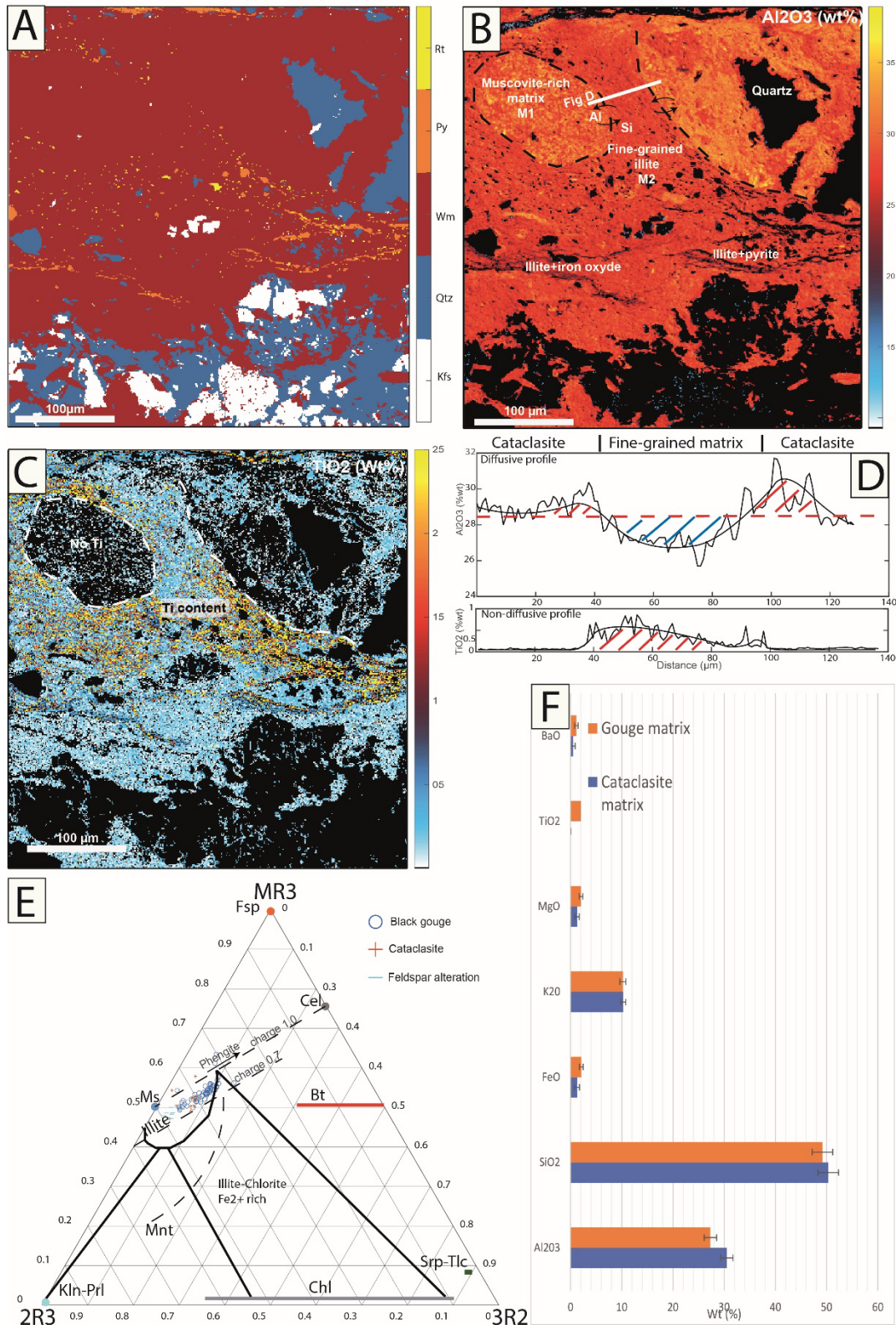


Figure III.10: A - Phase map from gouge microprobe mapping (Rt=rutile, Py=Pyrite, Wm=White micas, Qtz=Quartz, Kfs=K-feldspars). B and C - Microprobe maps of Al_2O_3 (B) and TiO_2 (C) showing distinct composition for the Wm phase. This highlights the different composition of the clasts of cataclasite (M1) and fine-grained gouge matrix (M2). The transition from the cataclasite matrix M1 to the gouge matrix M2 shows a loss of Al. Ti is absent from the cataclasite but hosted by rutile in the gouge. D - Profile across the micrometric fault zone for Al_2O_3 and TiO_2 . The Al_2O_3 content has a diffusive profile, contrary to TiO_2 (in red, the zone of gain and in blue the zone of loss). E - Ternary plot of the composition of phyllosilicates from the gouge. $MR_3 = Na+K+2Ca$, $2R_3 = (Al+Fe^{III}-MR_3)/2$, $3R_2 = (Mg+Fe^{II})/3$ (Velde, 1985). Ms = Muscovite, Cel = Celadonite, Fsp = Feldspars, Kln = Kaolinite, Prl = Pyrophyllite, Chl = Chlorite, Bt = Biotite, Srp = Serpentine, Tlc = Talc,

4. Discussion

4.1. Conditions and mechanisms of deformation

4.1.1. Progressive deformation in retrograde conditions

Detailed petrographical and microstructural observations suggest that the studied rocks forming the top basement of the internal Mont Blanc massif can be best interpreted as belonging to a fault zone. The fault rocks record the overprint of an initially high-temperature Variscan fabric in the gneissic basement, by a cataclastic deformation at much lower temperatures. In the gneiss, the observation of sub-grain rotation and grain boundary migration during dynamic recrystallisation of quartz grains points to temperatures of around 450 to 600°C during the formation of a first, primary foliation (Stipp et al., 2002). Such high temperature fabrics would correspond to depths of 15 to 20 km considering an average gradient of 20°C/km (determined using P-T date on skarns (Marshall et al., 1997)). These depths are similar to those of emplacement of the lower part Mont-Blanc pluton at around 15 km (6 to 8 Kbar north Mont-Blanc massif; Marshall et al., 1997), suggesting that this Variscan fabric was acquired during the Carboniferous, before any significant exhumation. In the damage zone, this fabric is first overprinted by feldspar fracturing, minor quartz bulging recrystallisation and hydration (Fig. III.11A). The association of brittle behaviour of feldspars and minor plastic deformation of quartz is indicative of a deformation temperature of around 275°C to 300°C (Stipp et al., 2002), corresponding to a depth of about 7 km assuming a geothermal gradient of 40°C/km (derived from heat flow modelling during necking of the crust, Chenin et al., (2020)). This deformation was associated with significant hydration of the basement, as seen by widespread feldspar sericitization and chloritization of biotite (Fig. III.11A), still under lower greenschist facies metamorphic conditions. Toward the fault core zone, deformation is more intense and accompanied by an almost complete feldspar replacement by muscovite and illite, and the disappearance of both biotite and chlorite. These metamorphic reactions occurred simultaneous to an increasing brittle overprint during which the host rock lost its initial HT fabric to become a clast supported cataclasite, with an increase of the phyllosilicate content toward the core zone. Cataclastic flow as observed here is found at depth ranging between 12 to 5 km (Sibson, 1986), which is in agreement with a decrease of the overburden during deformation and simultaneous exhumation. The progressive alteration of the rock during brittle deformation resulted in the localisation of deformation in phyllosilicate-rich zones, resulting in the matrix supported core zone (black gouge M2). The observation of rounded clasts of cataclasite in this gouge supports the interpretation that the gouge formed within a previously brittle deformed and altered basement. Petrographical and geochemical observations demonstrate that the gouge matrix was formed by progressive shearing of the cataclasite matrix,

Structural and petrological characteristics of a Jurassic detachment fault from the Mont-Blanc massif (Col du Bonhomme area, France)

associated with a change in composition and grain comminution (Fig. III.11A). The decrease of Si in the white micas in the cataclasite and corresponding increase in the gouge is consistent with fluid-mediated diffusion of Si and Al across the fault zone and progressive enrichment in Si in the fine-grained gouge matrix, along with the neof ormation of illite. The absence of crystal plastic recrystallisation of quartz during gouge formation indicates that frictional deformation was the dominant deformation mode. This restricts the temperature to below 275°C, which corresponds to the onset of plastic deformation (Stipp et al., 2002). Brittle behaviour is also visible through the high microfracture density of cataclasite grains, as well as through the significant grain comminution in the gouge. Indeed, the low fractal dimension ($\beta = 1.3-1.7$) calculated in the gouge is an illustration of this friction-dominant, scale independent process leading to grain size reduction. It is in the range of both generic and detachment gouges (Boulton et al., 2009), which have been shown to be commonly formed at levels shallower than 5 km depth (Sibson, 1986), where conditions for extensive clay formation are met (low T and low P) . Finally, transition from plastic/frictional deformation to pure frictional deformation and reworking of cataclasites in the gouge points to exhumation along a retrograde path as deformation proceeded. This exhumation of the basement reached the surface where formation of fissures filled with a crinoid mud affected the already tectonized basement and was sealed by the Grès Singuliers.

Structural and petrological characteristics of a Jurassic detachment fault from the Mont-Blanc massif (Col du Bonhomme area, France)

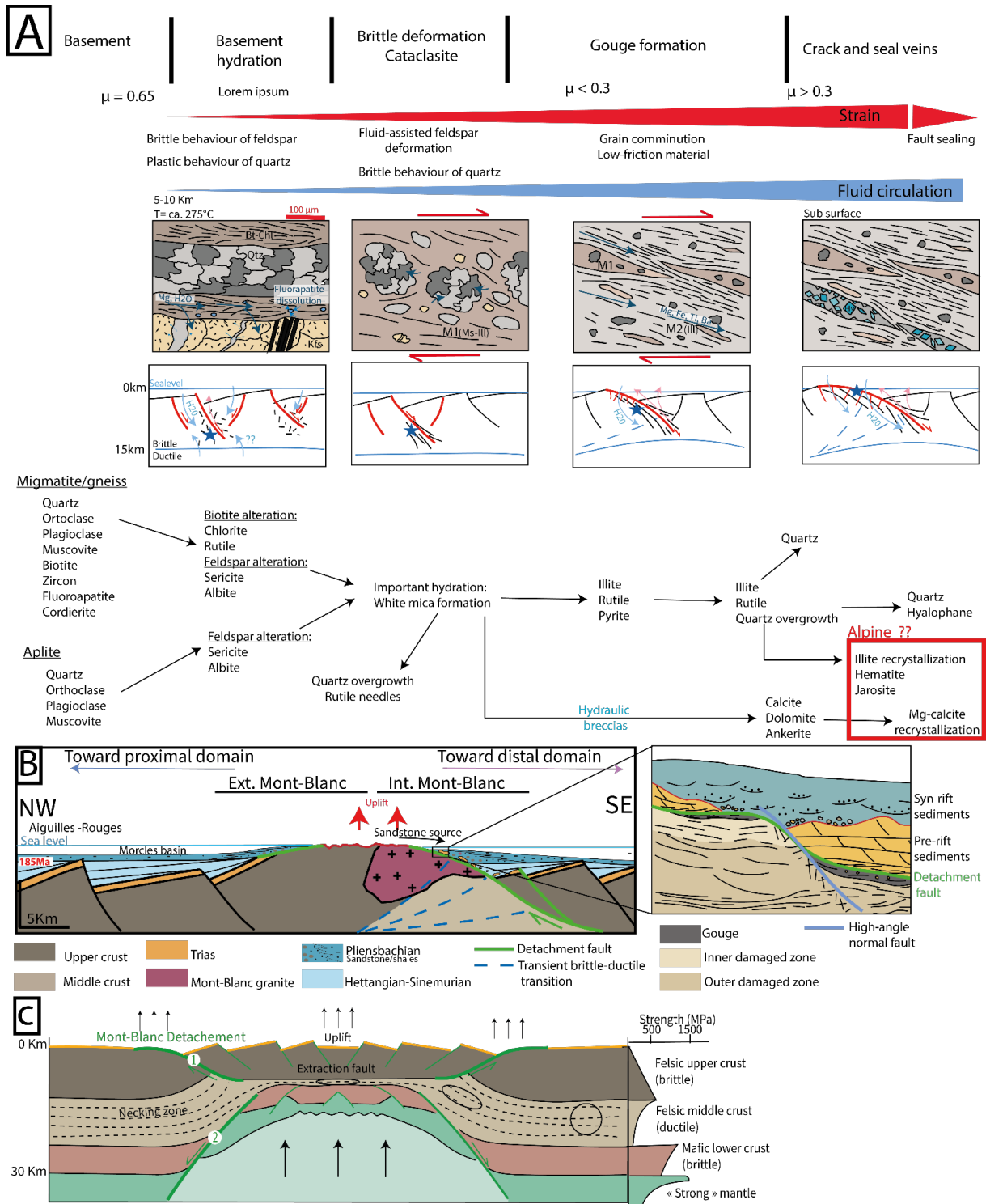


Figure III.11: A- Sketch summarizing the evolution of the fault rocks during exhumation following a retrograde path and a progressive localisation of the deformation in phyllosilicate rich layers (gouge) toward the surface. This is associated with the petrological evolution observed in the Col du Bonhomme from the gneiss to the matrix-supported gouge. The evolution of frictional coefficient is indicated. B- Pliensbachian cross section of Mont-Blanc showing the crustal architecture and sedimentary infill associated to Mont-Blanc detachment fault (modified from Ribes et al., 2020). Uplift related to the detachment fault led to local erosion and sandstones formation around the massif about the exhumed surface. C- The H-block model for the necking of the crust showing to conjugated fault system in the upper brittle crust and in the lower crust leading to crustal thinning (modified from Mohn et al., 2012).

4.1.2. Strain softening due to phyllosilicate neoformation along brittle fault plane

Deformation at retrograde, fluid assisted alteration was associated with important phyllosilicate replacement and neoformation in the cataclasite and particularly in the gouge. It is thus likely that the phyllosilicates played a key role in the mechanical evolution and behaviour of the fault (e.g. Wintsch et al., 1995; Jefferies et al., 2006; Wibberley 2005; Imber et al., 2008; Wallis et al., 2015). Indeed, from the proportion of illite to quartz (80% of clay) in the gouge M2, and using the experimental work on gouge friction of Tembe et al. (2010), the gouge can be estimated to have had a friction coefficient (μ) lower than 0.3 (Fig. III.11A), without considering the possible impact of fluid pressure in facilitating slip along the fault plane. Such a low-friction coefficient must be compared with that of gneissic rocks, which is expected to be >0.6 (Ikari et al., 2011). This behaviour is best explained by the neoformation of phyllosilicates, which led to significant strain-softening at the transition from a clast to matrix/phyllosilicate supported fabric, promoting, and facilitating slip along the fault plane. In clays, this frictional sliding is enhanced by the presence of interlayer water (when present) and a deficit in interlayer cations, leading to a low bonding of the octahedral and tetrahedral layer facilitating slip (Morrow et al., 2000). In addition to the phyllosilicates, the injection of gouge matrix (M2) into the cataclasites, both at macroscopic and microscopic scales, shows that the gouge locally behaved like a fluid. This is best explained by local fluid overpressure developing in the gouge during transient deformation events (e.g., Manatschal, 1999), likely associated with gouge compaction and pore reduction during shearing (e.g., Faulkner et al., 2018). However, several observations suggest that the mechanical behaviour of the fault gouge evolved from low- to high-friction. The last event affecting the gouge was the formation of quartz-hyalophane veins emplaced parallel to the gouge foliation. Although the age of the veins is not well constrained, the brecciation of some veins and the presence of clasts of hyalophane in the gouge M2 and the cataclasite tends to indicate a syn-kinematic emplacement of these veins. At present-day the gouge is indurated, which is not compatible with a low friction coefficient. Induration may be explained by syn-kinematic quartz precipitation and presence of Si-rich pervasive fluid or recrystallisation of the illite matrix, possibly during Alpine orogenesis, as discussed later (Fig. III.11A). The fact that only cataclasites but no gouge clasts were found in the syn-rift sediments might point toward the second hypothesis. Nevertheless, adularia similar to the hyalophane variety from the veins are found commonly reworked in the Grès Singuliers (Appendix B Fig. B.4).

4.1.3. Fault-related basement hydration and fluid circulation

The mineral assemblages observed in the damaged basement and the fault rocks highlight the widespread presence of fluids during Jurassic deformation, while their chemical composition suggests the migration of some elements along the fault zone linked to fluid channelling. Indeed,

Structural and petrological characteristics of a Jurassic detachment fault from the Mont-Blanc massif (Col du Bonhomme area, France)

several syn-kinematic metamorphic minerals are hydrated, mostly chlorite and white micas. Chlorite formed in replacement of biotite, which is a common reaction at greenschist facies conditions (Parry and Downey, 1982; Parneix et al., 1985). Chloritization was spatially restricted to the lowly deformed basement. The most important evidence of widespread hydration is the partial transformation of the K-feldspars to sericite and albite, followed by their complete replacement by white micas as deformation continued. The reaction was likely triggered by significant fracturing at both the macro and the microscale in the fault zone, increasing the permeability in the basement, facilitating fluid circulation (e.g., McCaig, 1988; Sibson, 2000; Manatschal et al., 2000; Wibberley and Shimamoto 2003; Rossetti et al., 2010). Such effect is highlighted by important alteration around microfractures in the damage zone, which indicates that fracturing at the micro scale increased the reactive surface available for fluid rock interaction (Plümper et al., 2017). In addition to phyllosilicates, several minerals precipitated in veins or locally in the fault gouge during deformation, such as iron rich sulphide/oxides, quartz, hyalophane, or rutile. Some minerals containing elements found in large concentrations in the host rock, such as quartz (Si) or iron sulphides/oxides (Fe), could have easily precipitated in a closed system, triggered by dissolution/precipitation mechanisms (e.g., Jefferies et al., 2006; McAleer et al., 2017). However, the presence of rutile and Ti-rich illite in the gouge matrix, or of hyalophane in veins, which are rich in Ti and Ba respectively, requires element transfer in a more open system. The systematic enrichment of the gouge matrix (M2) in Ti points to mobility of this element during gouge formation. Indeed, the gouge matrix was formed by shearing of the cataclasite matrix (M1), which is devoid of Ti. This indicates at least a minimum amount of Ti transfer in an open system at micro-scale, which is unexpected as this element is usually considered as immobile during fluid-rock interaction (Rubin et al., 1993; Van Baalen, 1993). In the same way, the presence of hyalophane mostly in late veins suggests the input of an external Ba-rich fluid. Such fluid mobility is not surprising, since faults can act as a conduit for fluids both in sedimentary basins and at crustal scales (McCaig, 1988; Manatschal et al., 2000; Sibson 2000; Rossetti et al., 2010). However, fault permeability is extremely heterogeneous (Wibberley and Shimamoto, 2003). In the damage zone (cataclasite), permeability reaches values of 10^{-14} - 10^{-16} m², controlled mainly by mineral precipitation and dissolution, and by fracture development (Wibberley and Shimamoto, 2003). Dynamic permeability (crack and seal behaviour) related to local fluid overpressure build up along the fault during an interseismic cycle with fluid release during coseismic slip might have contributed to the overall permeability (Sibson, 1990; Sibson, 1992; Poulet et al., 2021). In the core zone (gouges), permeability is generally lower (10^{-17} - 10^{-20} m²) and anisotropy associated with the planar fabric of the phyllosilicates higher (Kopf, 2001; Wibberley and Shimamoto, 2003). In the studied fault, most of the veins observed are parallel to the foliation, where one could expect the highest permeability. It is thus likely that the gouge fabric had strong control of vein formation and related fluid circulation.

Nevertheless, the origin of external fluids, such as a crustal source (dehydration of hydrated rocks) or the infiltration of water from the surface, remains to be determined. Ongoing mass-balance calculations should help to quantify more precisely the conditions of fluid mobility during fault-related deformation in the Col du Bonhomme area.

4.2. Is the Col du Bonhomme fault a Jurassic extensional detachment fault?

4.2.1. Sedimentological evidence for superficial exhumation along a detachment

An extensional detachment fault corresponds to an fault dipping gently ($< 30^\circ$) and which can appear sub-horizontal at the surface (Boulton et al., 2009). Thus, syn-rift sediments can be deposited conformably above an exhumed fault surface, which is not possible for a thrust fault that results in burial. The extensional fault can either initiate at a low-angle, or alternatively initiate at a high-angle and rotate subsequently during exhumation at a low-angle near or at the surface. Isostatic uplift and low elastic strength in the footwall favour such a rotation (Axen and Hartley, 1997) and can lead to an important, kilometre-scale offset (Forsyth, 1992). Such faults are also referred to as rolling hinge faults (Wernicke and Axen, 1988; Lavier and Buck, 2002). They are usually associated with low frictional material along the fault plane. If the fault is exhumed under aerial or marine conditions, it can be submitted to erosion. In such a case, the fault surface can be eroded and becomes difficult to observe. The reworking of the fault rocks in the syn-exhumation sediments is a diagnostic feature of exhumed faults as observed for instance in the Basin and Range (Yin and Dunn, 1992). Epin et al. (2017) defined diagnostic criteria to identify pre-Alpine, rift related detachment faults. A key observation is the presence of fault rocks at the top basement, overlaid by either pre-rift sediments along a tectonic contact, or by syn- to post-tectonic sediments in which case the contact is stratigraphic. Indeed, deposition of sediments above a fault plane is geometrically possible only above an extensional detachment fault, where the footwall is pulled out underneath its hanging wall. Both features are clearly observed in the Col du Bonhomme area.

First, remnants of pre-rift Triassic deposits are overlying cataclasites and gouges capping the basement along a tectonic contact. Similar examples have been described in the Pyrenees (Lagabrielle et al., 2010; Jammes et al., 2010) but also in the Alps, where pre-rift remnants are found over the exhumed crust in the necking, the distal and the exhumed mantle domains of the Adriatic margin (Mohn et al., 2010; Epin, 2017). These pre-rift blocks can range from tens of meters to kilometres. Many authors discussed the role of evaporites as potential decoupling levels controlling the preservation of supra-salt pre-rift cover sequence as allochthonous hanging-wall blocks over exhumed footwall (e.g., Jammes et al., 2010; Epin and Manatschal, 2018). In the case of the Col du

Structural and petrological characteristics of a Jurassic detachment fault from the Mont-Blanc massif (Col du Bonhomme area, France)

Bonhomme, the anhydrite-bearing quartz locally found in recrystallized carbonates at the base of the pre-rift deposits suggests the former presence of evaporite levels below the dolomites, suggesting that they may have played a role during exhumation.

Second, the syn-rift deposits are sealing the exhumed fault surface, creating a stratigraphic contact. Field observations suggest that the oldest sediments deposited onto the detachment correspond to the crinoid-rich, brown-coloured breccias. The latter fills neptunian dykes that crosscut the basement cataclasites and gouges and is therefore necessarily younger than the fault rocks. A more recent age is also supported by reworking of the cataclasites and gouges in the breccias. A similar breccia, marked by the presence of lamellibranches, echinoderms and *Pentacrines* crinoids was also described by Landry (1976), 2km southeast from the Col du Bonhomme (Crête des Gittes; 45°42'51.6"/ 6°42'37.39"). The first occurrence of crinoids in the Helvetic/Dauphinois domain began in the Hettangian, with massive deposition of crinoid-bearing limestones during the Sinemurian/Pliensbachian in the Grande Rousse, Belledonne, and Morcles massifs (Roux et al., 1988; Loup, 1992; Barfety, 1985; Gillcrist, 1988; Chevalier, 2002; Epard, 1989). A similar, early syn-rift age for the breccia would be consistent with these studies, but also with the age of the overlying Grès Singuliers which is assumed to be Sinemurian to Pliensbachian. Like the breccias, the Grès Singuliers are in stratigraphic contact with the tectonized basement, but also rework the diagnostic cataclasites. This not only indicates that the fault had to be exhumed at the surface, but also supports its pre-Alpine age.

Finally, in the Col du Bonhomme area, an unconformity of 10 to 20° is observed between the Grès Singuliers and the top basement surface. Assuming horizontal deposition, which is likely at least in the top Grès Singuliers, where no sedimentary structures indicative of deposition on a major slope were observed, a shallow, < 20° dip-angle between the sediments and the top basement can be reconstructed. All these observations are compatible with an interpretation in which the Mont Blanc massif is capped by a Jurassic low-angle, extensional detachment fault. The shallow dip at the surface may be due to the rotation of the fault due to isostatic uplift in response to fault activity (removal of the hanging wall; Lavier et al., 2000; Lavier and Buck, 2002). This uplift may have lead ultimately to the formation of the Mont-Blanc Island of Trümpy (1971) and Loup (1992), thus providing a source for the detrital syn-rift Grès Singuliers sandstones found around the Mont-Blanc massif (Fig. III.11B; Ribes et al., 2020).

4.2.2. Interpretation of kinematic markers

Most of the Alpine deformation related to the emplacement of the Helvetic nappes in the Col du Bonhomme area was accommodated in the Aalenian shales overlying the Grès Singuliers, as already noted by Egli and Mancktelow (2013). This may explain why the pre-Alpine, rifted related cover-basement relationships at the Col du Bonhomme were not significantly affected by Alpine

deformation. In the damage and core zones of the studied fault, a limited imprint is also supported by the lack of typical Alpine deformation recorded elsewhere in the Mont-Blanc basement, characterized by mylonitic shear zones. In addition, our kinematic measurements obtained in the pre-rift and in the basement (Fig. III.3G) are consistent with a normal fault having a top to the south sense of shear, which is hardly compatible with the Alpine directions measured in the area (E-W to NW-SE directions with top to the west or to the north-west sense of shear; Meyer, 2002; Egli and Manckletow, 2013).

N-S directed syn-rift movement in the Mont-Blanc detachment differs from the NW-SE direction generally assumed for the extensional direction of the Alpine Tethys rift system (Lemoine and Trümpy, 1987; Fig. III.1). However, these local measurements cannot be directly compared to the direction of regional extension without considering the specificities of the Alpine Tethys European margin whose three-dimensional characteristics is poorly known. Such scale discrepancies may reflect kinematics complexities related to rift segmentation and inheritance. Many examples both from fossil and present-day margin, show the complex kinematics occurring along faults network, where locally sense of shear can be oblique to the direction of extension. The necking system along the Norwegian margin shows complex fault geometries at large scale (Osmundsen and Péron-Pinvidic, 2018), with fault orientations spreading over 90°, controlled mostly by inheritance (Muñoz-Barrera et al., 2020). More generally segmentation in extensional systems could be associated with the development of transfer zones where local stretching can be highly oblique to the direction of regional extension as demonstrated in metamorphic core complex (Le Pourhiet et al., 2014) and reproduced in rift segment boundaries (Le Pourhiet et al., 2017). Segmentation of the Alpine Tethys rift system by major NW-SE transfer zones have been postulated by many studies in particular between the Pelvoux and Argentera massif and possibly between the Belledonne and Mont-Blanc massif (e.g. Lemoine et al., 1989; Decarlis et al., 2017; Ribes et al., 2019a). It is also worth noting that recent studies in the Pyrenean rift have also emphasised that rift segment boundary is better preserved from subsequent underthrusting during orogeny than rift segment centres (Manatschal et al., 2021). For all these reasons, our N-S stretching measurements in the Mont-Blanc preserved detachment may suggest rift segmentation in the southern western border of the internal Mont-Blanc massif.

4.2.3. Mineralogical and geochemical evolution: Jurassic exhumation versus Alpine metamorphism

In addition to the arguments presented above, the exhumation of the footwall can be deduced from the retrograde path recorded by with the mineralogical assemblages of the fault rocks, which show a progressive decrease of temperature associated with the exhumation from sub-greenschist conditions to the surface. Most mineralogical assemblages identified are diagnostic of

lower greenschist metamorphic conditions, with temperatures lower than $\sim 300^{\circ}\text{C}$. These temperatures are very close to those reached during the Alpine metamorphic peak in the Col du Bonhomme ($\sim 330^{\circ}\text{C}$). These temperatures preclude the formation of biotite but are high enough to allow that of muscovite, raising the question of the preservation of the parageneses related to Jurassic fault exhumation. Indeed, our observations show that such syn-kinematic parageneses correspond to extensive phyllosilicate formation, either muscovite in the cataclasite or illite in the gouge, and minor formation of rutile, quartz/hyalophane veins, iron sulphides and calcite. From these minerals, some could clearly have been altered or recrystallized during Alpine prograde metamorphism. This applies first to the white micas. It is not excluded that the present-day illite matrix of the gouge results from the prograde recrystallisation of a lower temperature clay. However, if illite formed during Jurassic extension, its preservation would not be surprising since illite-type white micas are stable until 350°C for the illite end-member, with complete disappearance of smectite above ca. 300°C (Velde, 1985; Merriman, 1999; Rosenberg, 2002; Meunier et al., 2004). In addition, illite whose presence is widespread in the Grès Singuliers and the Aalenian shales (Eltchaninoff and Triboulet, 1980), is known to form at least until 320°C (Eberl et al., 1987; Battaglia, 2004; Meunier et al., 2004). Then, the age of the white micas (sericite-type) observed in the pressure shadows of quartz fragments and sulphides is hard to assess, and an alpine age is possible. Minor muscovite static recrystallisation was also observed locally as overprinting the gouge matrix, possibly as a consequence of prograde metamorphism.

For some phases appearing the latest in the sequence (hyalophane-quartz veins, calcite), doubts remain as to a Jurassic or Alpine origin. In the gouge, the hyalophane-quartz veins are deformed and can be broken to clasts, which favours an early, Jurassic formation. The presence of detrital adularia in the Grès Singuliers clearly points in the same direction. However, the composition of the latter needs to be analysed in more detail to confirm a common origin with the hyalophane crystals of the veins. Finally, the Alpine overprint is likely responsible for the static recrystallisation of calcite in the basement, where the initial texture was almost completely lost and replaced by equigranular calcite.

To conclude, the contact between the tectonized top basement and the sediments is clearly pre-Alpine, and the Alpine metamorphic overprint seems mostly static with partial recrystallisation of low temperature minerals such as the gouge clay matrix and calcite.

4.2.4. Large scale implication of the Mont-Blanc detachment fault

The presence of a rift-related detachment fault in the Mont-Blanc massif might have a variety of implications for its Alpine history. First, this study shows that major rift-related structures can be preserved even in deformed parts of an orogen, in accordance with previous observations in the Alps (Barfety and Gidon, 1984; Lemoine and Trümpy, 1987; Manatschal, 1999; Cardello and Mancktelow,

Structural and petrological characteristics of a Jurassic detachment fault from the Mont-Blanc massif (Col du Bonhomme area, France)

2014; Epin and Manatschal, 2018; Pantet et al., 2020; Nibourel et al., 2021) and the Pyrenees (Izquierdo-Llavall et al., 2020; Espurt et al., 2019; Labaume and Teixell, 2020; Lescoutre and Manatschal, 2020). Indeed, the large-scale architecture of the Mont-Blanc massif proposed by Ribes et al. (2020) put the Mont-Blanc at the transition between the proximal and the distal domains of the former European margin, indicating a specific crustal architecture.

The thinning of the crust is highlighted by the increase of the accommodation space and the presence of exhumed mantle (Beltrando et al., 2012). According to the model of the H-Block (Fig. III.11C; Lavier and Manatschal, 2006), thinning during the necking of the crust is accommodated by two conjugated faults located in the upper brittle crust and in the lower crust. The Mont-Blanc detachment fault could correspond to the upper crust detachment where the deformation is mostly (if not entirely) brittle. The lower crust conjugate fault might have been preserved as interpreted from the ECORS-CROP profile (Thouvenot et al., 1996; Mohn et al., 2014).

Preservation was probably better in the southern edge of the Mont-Blanc massif, where the rift-related structures are oblique to the main thrust axis, and therefore likely transported passively. At present, the thrust nappes from the external part of the Mont-Blanc (former proximal domain) present polyharmonic folds (e.g., Morcles nappe; Ramsay, 1989; Epard, 1990), whereas in the internal part of the Mont-Blanc Massive, the thrust nappes are characterized by disharmonic folding (e.g., Wildhorn and Diableret nappes; Ramsay, 1989). Fold nappes in the external domains are generated by half-graben inversion as shown by field evidence (e.g., Bourg d'Oisan basin; Chevalier, 2002) or by numerical models (Bauville and Schmalholz, 2015; Kiss et al., 2020). The geometry of the disharmonic thrust nappes from the internal Mont-Blanc may thus be explained by the role of structural inheritance from the Mont-Blanc detachment fault, leading to a different Jurassic basin architecture and position of decollement level.

In addition, important hydration of the basement around the detachment level during Jurassic rifting, in part linked with an open fluid circulation, could have changed the rheological behaviour of the crust, by diminishing its strength (Wintsch et al., 1995), as postulated for example in the Axial zone of the Pyrenees by Bellahsen et al. (2019) and Airaghi et al. (2020). Indeed, thin-skinned and thick-skinned fold thrust belts are controlled by thermal inheritance but also by structural (Mohn et al., 2014; Tavani et al., 2021) and chemical inheritance (Lacombe and Bellahsen, 2016). A rheologically weakened basement following fault-related hydration promotes thick-skin style of deformation during shortening, and could accommodate large amounts of deformation through a localised or diffused deformation zone, which is observed in the external crystalline massifs of the Alps (Bellahsen et al., 2014; Bellanger et al., 2015; Nibourel et al., 2021; Rosenberg et al., 2021). Finally, because of its potential role in both collision-related deformation and fluid flow

during Alpine metamorphism, our study shows that the extent of Jurassic deformation and associated basement hydration clearly deserves further characterisation.

Conclusion

This work was focused on the field, petrographic, microstructural, and geochemical characterization of a tectonic surface recently discovered in the Col du Bonhomme area as part of the Mont-Blanc massif, and previously described as a Jurassic detachment fault. The tectonic surface affects mostly the gneissic basement of the massif, which is heavily deformed into cataclasite above which Sinemurian to Pliensbachian sediments were deposited.

In detail, the cataclastic basement is increasingly deformed toward its top. Deformation was exclusively the brittle field and associated with hydration of the basement, visible through the increase of phyllosilicate neoformation, which is likely responsible for the observed strain localisation. Overall, the transition from sub-greenschist brittle deformation to gouge formation with low-T clays points towards a retrograde path during fault activity, leading ultimately to exhumation to the surface, which is also supported by the reworking of clasts of fault-rocks in the overlying syn-rift sandstones. All these observations are fully consistent with an interpretation of the top basement as a Jurassic extensional detachment fault. They also suggest that important hydration of the basement and vein formation could be related to fluid circulation along the fault plane, although additional work is needed to confirm this interpretation.

Finally, the description of a pre-Alpine detachment fault in the Mont-Blanc massif shows that preservation of such rift-related structures is possible in the External Crystalline massifs despite significant Alpine deformation. It also raises the question of the role played by this structure during Alpine shortening. Nevertheless, this detachment also provides a field analogue for the necking domain of rifted margins where both the sedimentary cover and the tectonic structure of the basement are preserved.

Structural and petrological characteristics of a Jurassic detachment fault from the Mont-Blanc massif
(Col du Bonhomme area, France)

Structural and petrological characteristics of a Jurassic detachment fault from the Mont-Blanc massif
(Col du Bonhomme area, France)

Chapter IV- Multiscale element transfer during crustal necking: the Mont-Blanc detachment fault

Nicolas Dall'Asta^{*1}, Guilhem Hoareau¹, Stephen Centrella¹, Gianreto Manatschal², Patrick Monié³

¹ Université de Pau et des Pays de l'Adour, E2S UPPA, CNRS, LFCR-France

² Université de Strasbourg, CNRS, ITES UMR 7063, Strasbourg F-67084, France

³ Géosciences Montpellier, UMR-CNRS 5243, Université de Montpellier, Place Eugène Bataillon, 34095 Montpellier Cedex 05, France



View of the Col des Fours et Tête Sud des Fours (Mont-Blanc massif, France)

« L'œil étonné aperçoit les pics des Alpes, toujours couverts de neige, et leur austérité sévère lui rappelle des malheurs de la vie ce qu'il en faut pour accroître la volupté présente. » (La Chartreuse de Parme, Stendhal)

Foreword

This chapter is the continuation of the previous chapter and will be focused again on the Col du Bonhomme area. While the previous chapter focused on the tectono-stratigraphic and petrographical evolution of a detachment fault, this chapter will concentrate on the paleo fluid characteristics along the fault. This work is based on bulk and mineral chemistry, mass balance calculation, fluid analysis and dating of syn-kinematic phases.

The goal is to identify the main characteristics of fluid associated to crustal necking and to identify element transfer occurring along the fault. This chapter is presented under the form of an article. This chapter corresponds to the extended version of the article draft. The supplementary material can be found in the Appendix C.

Introduction

Polyphase rifting is characterized by the transition from wide rifting (stretching phase) to narrow rifting (necking phase), controlled by lithospheric break up and leading ultimately to crustal thinning (hyperextension) and mantle exhumation (Péron-Pinvidic et al., 2013). In magma-poor rifted margins, crustal architecture resulting from polyphase rifting is composed of a proximal domain with a thick continental crust, a necking domain characterized by crustal thinning down to 10 km, and a hyperextended domain (Sutra et al., 2013). Rifting is usually associated to intense hydrothermal activity, due to an increase of the thermal gradient associated to significant fracturing and faulting of the crust, providing pathways for fluid flow within the basement (Oliver et al., 2006). However, the evolution in composition and temperature of the fluids involved in these successive rifting phases is only partly elucidated.

In detail, the stretching phase shows superficial fluid circulation mostly restricted to the sedimentary cover, under cold geothermal gradient (30-40°C/km; Chenin et al., 2018; Lescoutre et al., 2019; Saspiturry et al., 2020). This leads mostly to mobility of Ca and Mg (Hips et al., 2016; Salomon et al., 2020; Barale et al., 2021). On the contrary, the numerous studies focused on the distal part of margins, associated to the last stages of rifting (hyperextension and mantle exhumation) demonstrated that marine fluids can penetrate into the basement and the mantle (Bayrakci et al., 2016; Barale et al., 2021; Hochscheid et al., 2022) in the presence of high geothermal gradients (80-100°C/km see Hart et al., 2017; Ducoux et al., 2019; Saspiturry et al., 2020; Lescoutre et al., 2019; Manatschal et al., 2021). Associated fluid-rock interactions favour mantle serpentinization, as well as important continental- and mantle-derived transfer of elements (Mg, Cr, N, Si) into overlying syn-rift sediments (Pinto, 2014). Fluid pathways and element mobility associated to the necking phase have been far less studied but tend to indicate significant circulation of continental-crust derived fluids (e.g., Bot et al., 2016; Incerpi et al., 2017,2019). However, crustal necking is characterized by a localization of the deformation and significant increase of the geothermal gradient (60°C/km see Chenin et al., 2020), which raises the question of the fate of the fluids in such context.

To overcome this lack of knowledge, we study the fluid signatures recorded along a fossil detachment fault in the Mont-Blanc massif (Western Alps), the former necking domain of the Jurassic margin. The structural, microstructural and tectono-sedimentary characteristics of this detachment fault were recently described by Ribes et al., (2020) and Dall'Asta et al., (2022). Here, mass balance calculations, alteration parageneses and syn-tectonic veins are used to constrain more precisely the type of fluids linked to the detachment, and thus to crustal necking associated to the Jurassic opening of the Alpine Tethys.

1. Geological setting

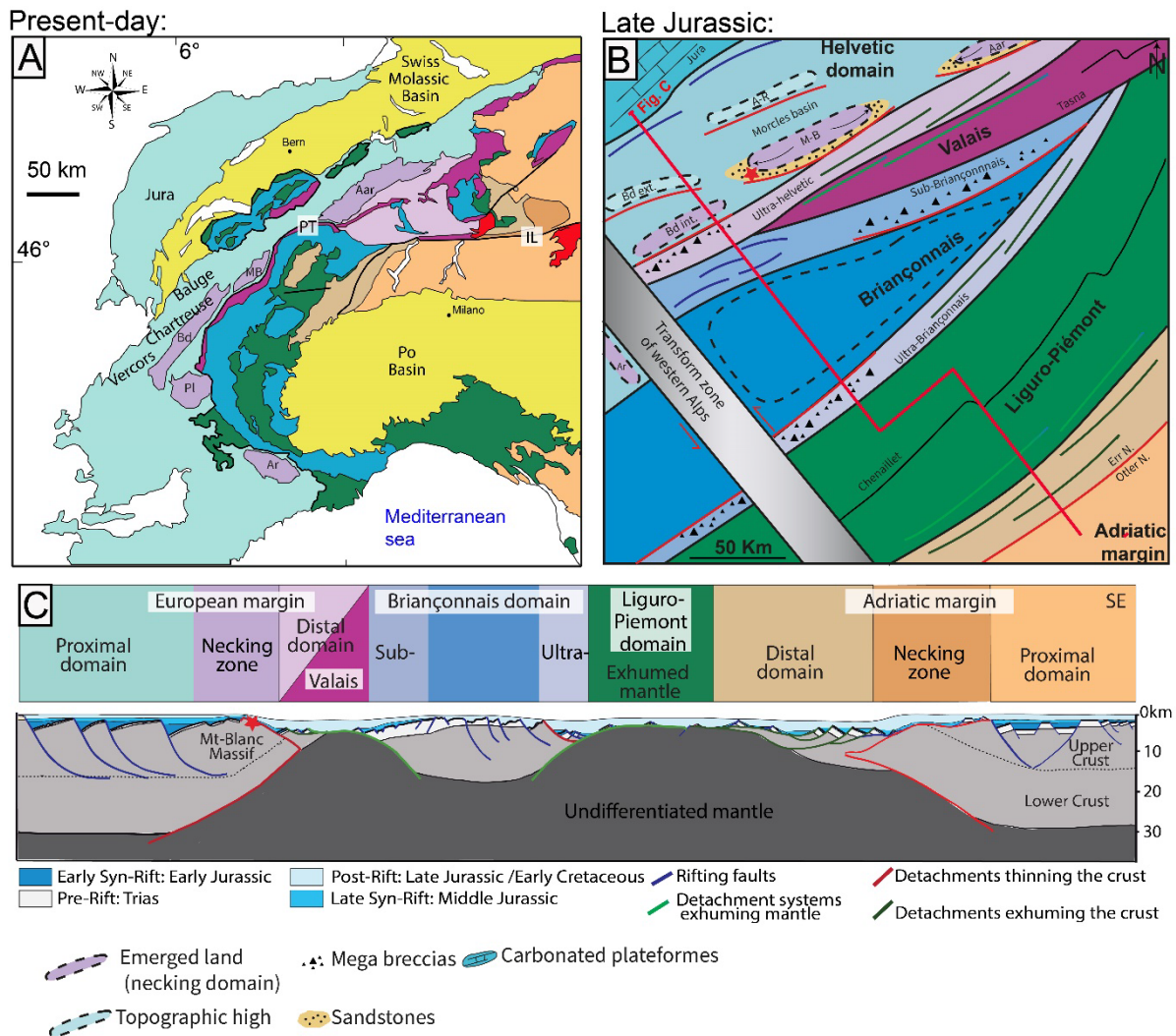


Figure IV.1: A-Tectonic map of the Western and Central Alps highlighting the different Alpine tectonic units (modified from Mohn et al. (2010) and Schmid et al. 2004)). The colour code similar to C (except Molassic basins in yellow and Tertiary intrusions in red) highlights the position of the different paleogeographic units in the orogen. B- Paleogeographic map of the Alpine Tethys during the late Jurassic (modified from Ribes et al., 2019a). Faults in blue correspond to normal faults associated with stretching, faults in red to necking faults thinning the crust, and faults in green to faults exhuming the crust and the mantle. Sandstones (Ribes et al., 2020) and breccias (Ribes et al., 2019a) related to large scale normal faults and detachment faults are also represented. C - Restored section of the Alpine Tethys during the Late Jurassic (Mohn et al., 2010)

The Western Alps correspond to two Jurassic oceanic basins (Valais and Liguro-Piemont; Argand, 1916; Debelmas and Lemoine, 1970; Lemoine et al., 1986; Lemoine and Trümpy, 1987; Stampfli and Hochard, 2009; Bellahsen et al., 2014; Mohn et al., 2014) that started to close from the late Cretaceous along with subduction of proto-oceanic domains, followed by the collision of the European and Adria plates (Ford et al., 2004; Rosenbaum and Lister, 2005). Rifting initiated during the Hettangian with a distributed deformation, followed by localized deformation during the crustal necking phase of Pliensbachian age (Beltrando et al., 2015). This crustal necking stage was first recognized in the fossil Adria margin by Mohn et al., (2012). Handy (1987) described a Jurassic lower crustal shear zone (Pogallo shear zone). Mohn et al., (2012) on the other hand described the Grosina

Multiscale element transfer during crustal necking: the Mont-Blanc detachment fault

fossil detachment fault (Grosina detachment) affecting the upper crust. Besides, Mohn et al. (2014) also proposed that the External Crystalline Massifs in the Western Alps corresponds to the fossil necking domain of the European margin. Recent numerical models (Duretz et al., 2016; Petri et al., 2019;), fossil examples (Mohn et al., 2012; Ribes et al., 2020) and present-day analogues (Sutra and Manatschal 2012; Sutra et al., 2013; Péron-Pinvidic et al., 2017 ; Osmundsen and Redfield, 2011; Osmundsen and Péron-Pinvidic, 2018; Muñoz-Barrera et al., 2020; Muñoz-Barrera et al., 2021; Chao, 2021) demonstrate that crustal necking is a short-lived event (ca 10 Ma), associated to an increase of heat flow in response to asthenosphere uplift (Fig. IV.2C; Chenin et al., 2018, 2020) and to large-offset detachment faults (Mohn et al., 2012; Petri et al., 2019; Chenin et al., 2019c), which may have applied to the Western Alps as well.

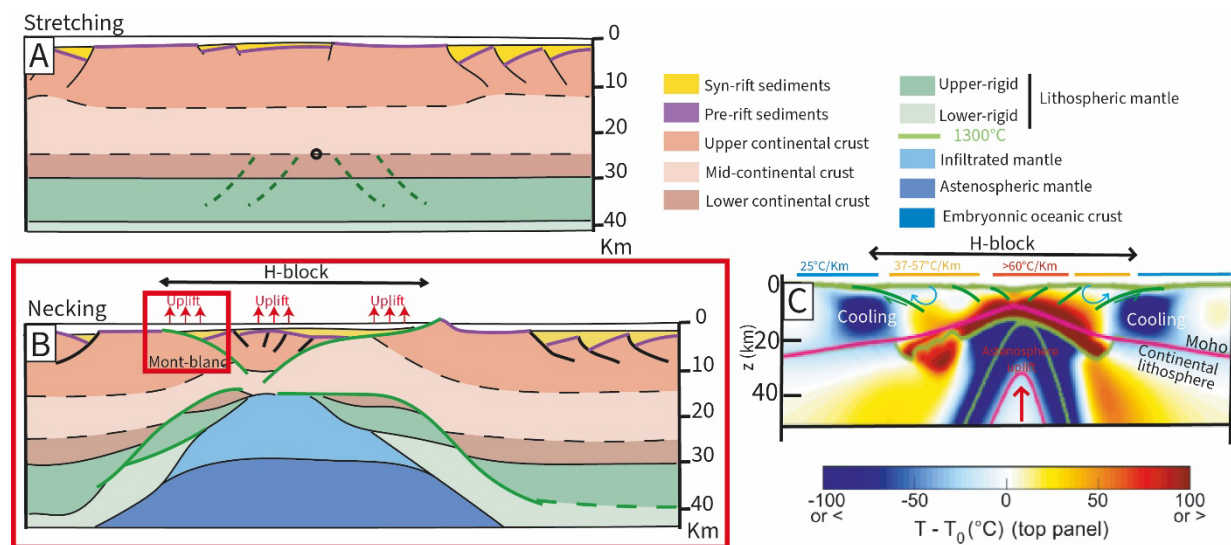


Figure IV.2: Characteristic evolution of multistage rift from stretching to necking. A- Stretching phase showing decoupled deformation between the upper and lower crust. The deformation is accommodated by high angle normal faults in the upper crust. B- Necking stage corresponding to localisation of the deformation associated to upper lithospheric break up and asthenosphere rising. Crustal necking is responsible for the formation of the central H-block characterised by a thickness below 20 km and surrounded by 2 sets of conjugated faults associated to crustal thinning and progressive coupling of the upper and lower crust. C- Asthenosphere rising is responsible for an increase of temperature as observed from the thermomechanical model of Chenin et al., (2020). Thermal gradients were recalculated using heat flow of Chenin et al., (2020).

Rifting led ultimately to a succession of hyperextended, exhumed mantle and proto-oceanic domains (Valais and Piemont-Ligure basins; Fig. IV.1B and C) separated by a continental ribbon (Dumont et al., 1984; Lemoine and Tricart 1986; Lagabrielle, 1987; Bousquet et al., 2002; Loprieno et al., 2011; Beltrando et al., 2012; Ribes et al., 2019d). The closure of these domains by subduction started in the late Cretaceous in the Liguro-Piemont basin (Stampfli et al., 1998), and in the upper Eocene in the Valais basin (Rosenbaum and Lister, 2005). It was followed by thrusting of the hyperextended and exhumed mantle domains above the more proximal domain along the Penninic thrust during late Eocene-Oligocene (Cardello et al., 2019). Migration of deformation toward the continent resulted in a change from subduction/accretion to collision during the Oligocene, along

with a change in the deformation pattern from thin to thick-skin (Herwegh and Pfiffner, 2005; Leloup et al., 2005; Egli and Mancktelow, 2013).

The External Crystalline Massifs (Aar, Mont-Blanc, Belledonne, Pelvoux, Argentera) are located at the transition between the external part of the Alps, corresponding to the former proximal domain of the margin, and their internal part, corresponding to the hyperextended and exhumed mantle domains (Beltrando et al., 2012; Mohn et al., 2014). The external domain shows no Alpine metamorphic overprint to low greenschist metamorphism, whereas the internal domain is associated to greenschist and blueschist facies (Bousquet et al., 2008; Rosenberg et al., 2021). The ECM located in-between have experienced only lower greenschist facies (Bousquet et al., 2008). Mohn et al., (2014) explain the present-day location of the ECM by the role of crustal buttress played by the necking domain during convergence.

The Mont Blanc massif is part of the ECM. Its external part (to the west) is formed by a large Alpine shear zone (Mont-Blanc shear zone) while its internal part (to the east) preserved autochthonous cover (Fig. IV.3 A and B see Grasmück, 1961; Eltchaninoff, 1980; Leloup et al., 2005). The massif consists mainly of a polymetamorphic basement (mostly Variscan gneiss, Von Raumer et al., 1993). In the internal part, the basement is intruded by a post-Variscan metaluminous, ferro-potassic carboniferous granites (Mont-Blanc granites, 303 Ma, Bussy et al., 2001), and overlaid by Triassic sandstones and dolostones marking a transgression above the basement (Epard, 1986, 1989). An increase of subsidence in the basin around the Mont-Blanc is observed from 190 to 180 Ma (Wildi et al., 1989), contemporaneous to the Mont-Blanc uplift and deposition of sandstones. This points toward a major tectonic event, which was interpreted as the crustal necking of the European crust during Alpine Tethys opening (Mohn et al., 2014; Ribes et al., 2020; Dall'Asta et al., 2022). In the internal Mont-Blanc massif, the sandstones (Grès Singuliers) were interpreted as the sedimentary response to important basement in response to crustal necking (Ribes et al., 2020; Dall'Asta et al., 2022). These detrital deposits have a late Sinemurian and Toarcian age and are found all along the internal Mont-Blanc, lying directly above the exhumed basement. They are overlaid by Aalenian black shales marking the onset of subsidence of the area and the progressive drowning of the Mont-Blanc. Finally, prograding carbonate platforms of upper Jurassic and Lower Cretaceous form the youngest deposits in the area (Landry, 1976).

Multiscale element transfer during crustal necking: the Mont-Blanc detachment fault

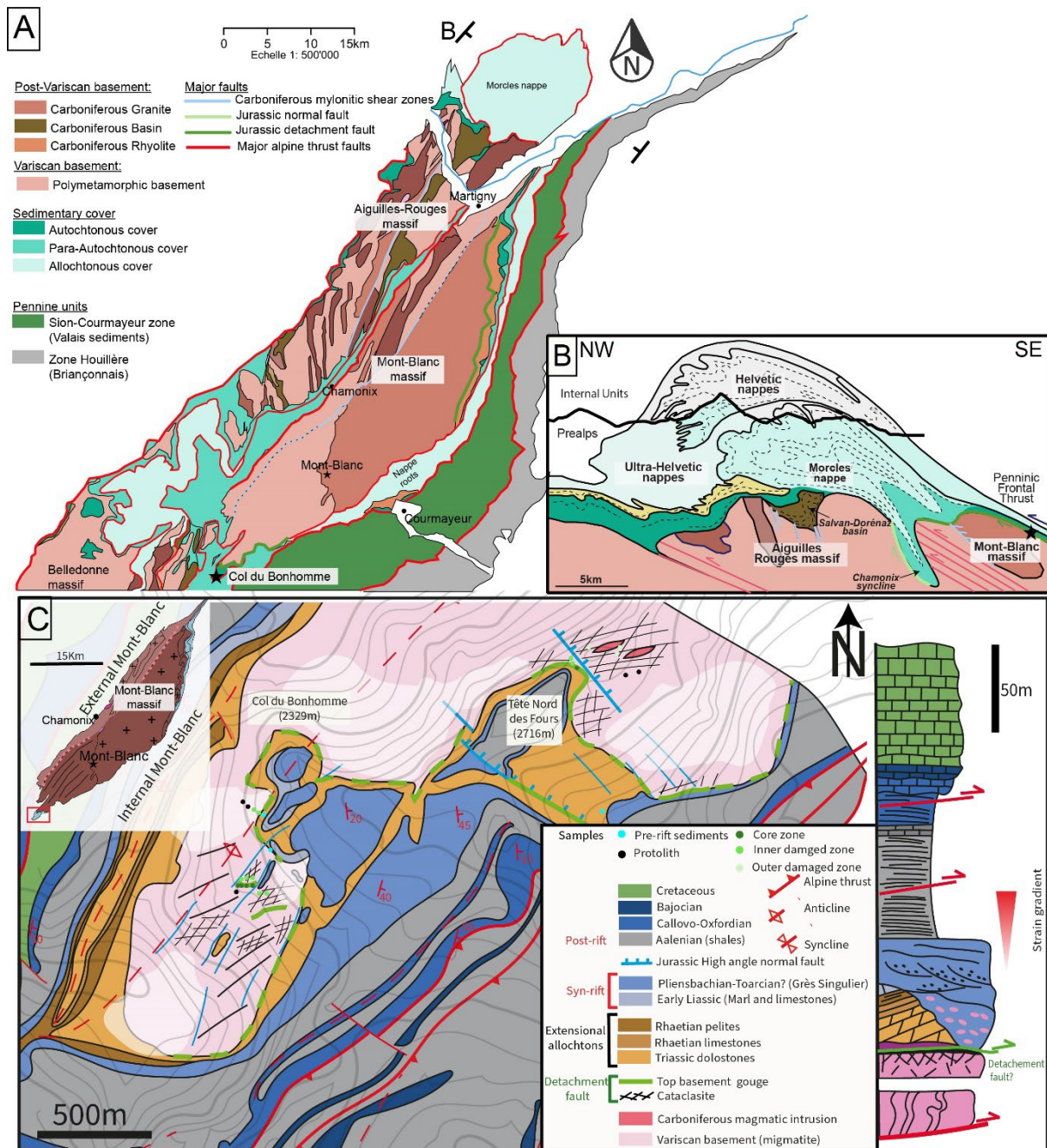


Figure IV.3: A- Map of the Mont-Blanc and Aiguilles-Rouges massifs highlighting the lithology of the basement, and the tectonic position of the cover regarding to Alpine deformation. B- Section of the Mont-Blanc massif showing the inverted Morcles basins associated to the thrusting on the Mont-Blanc over the Aiguilles-Rouges and Thrusting of the Distal Helvetic nappes over the Mont-Blanc massif(modified from Escher et al., 1993). C- Map of the Col du Bonhomme area and associated synthetic stratigraphic section (modified from Dall'Asta et al., 2022).

In the Mont-Blanc massif, Alpine deformation corresponds to: (i) thrusting of the more internal nappes (Helvetic and Penninic) over the Mont-Blanc massif during the Late Eocene to Early Miocene (Leloup et al., 2005; Egli and Mancktelow, 2013), followed by (ii) thick-skin deformation (Escher et al., 1993; Herwegh and Pfiffner, 2005), and (iii) to thrusting of the Mont-Blanc basement over the Aiguille-Rouges basement (Mont-Blanc shear zone) from the middle Miocene to early Pliocene (Leloup et al., 2005). Studies of metamorphic assemblages (muscovite-biotite-chlorite-

Multiscale element transfer during crustal necking: the Mont-Blanc detachment fault

epidote), U-Th-Pb geochronology on allanite and Ar/Ar geochronology on phengite, biotite and phlogopite indicate that the Alpine metamorphic peak was reached between 28 and 15 Ma, at pressures of 0.5 GPa and temperatures up to 400°C in the basement (Rolland et al., 2003; Rolland et al., 2008; Cenki-Tok et al., 2014). The cover and cover/basement interface were submitted to lower temperatures. RSCM thermometry gives a temperature of around 320 to 330°C for the southern Mont-Blanc area (Rosenberg et al., 2021; Dall'Asta et al., 2022), corresponding to the lower greenschist facies.

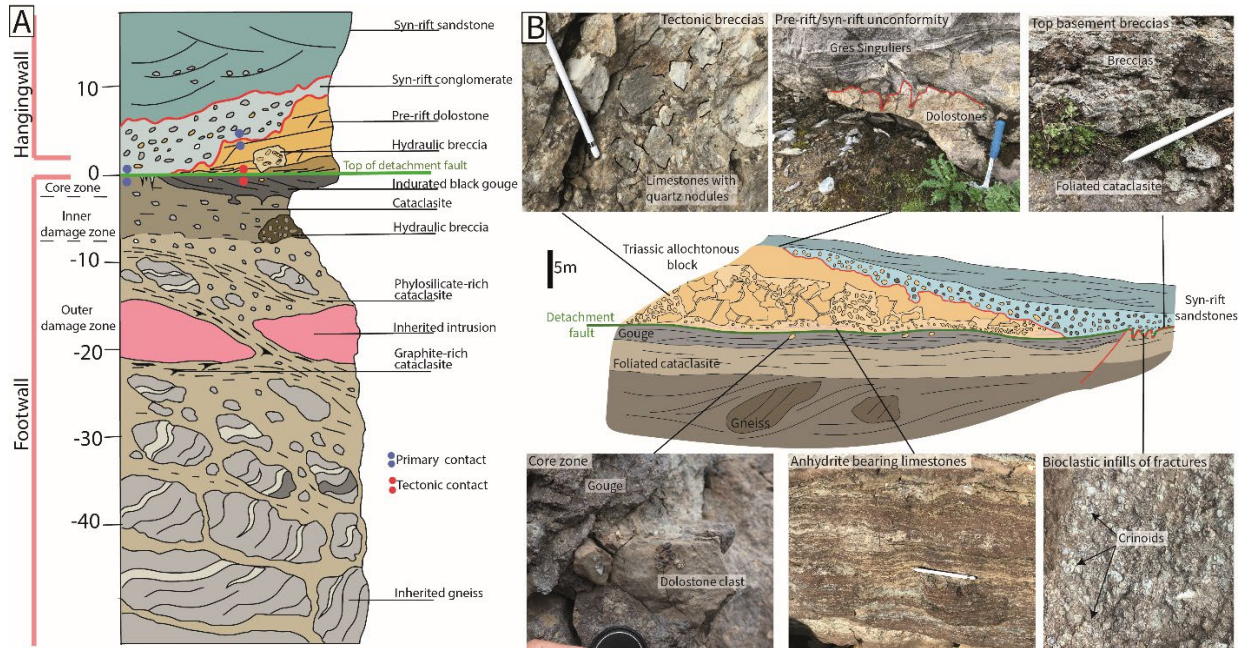


Figure IV.4: A- Section of the top basement detachment and sedimentary cover highlighting the type of deformation observed in the basement and the type of contacts between the pre-rift and syn-rift cover (modified from Dall'Asta et al. 2022). B- Illustration of the pre-rift allochthonous blocks laying over the detachment fault and sealed by the syn-rift deposits, summarizing the observations described in Dall'Asta et al. (2022).

The detachment fault itself is not preserved everywhere. In the Col du Bonhomme area (Fig. IV.3C), south of the Mont-Blanc massif, the detachment fault is well preserved below the Aalenian shales (Dall'Asta et al., 2022). It appears on the field as a tectonized top basement overlaid by pre-rift and syn-rift sediments (Fig. IV. 4A and B). This tectonized basement shows a progressive increase of the brittle deformation toward the top basement forming the damage zone of the fault, and leading to a complete overprint of the Variscan foliation (Dall'Asta et al., 2022). The damage zone can be separated into an outer and an inner part (~20 m and 5 m of thickness, respectively), overlaid by a core zone (fault core). The outer damage zone shows widespread cataclasite, while the inner zone presents foliated cataclasite. In the core zone (~20-50 cm-thick), deformation is stronger, with gouge locally preserved. The inner damage zone and core zone are strongly hydrated over 10 m in thickness. The fault is overlaid by pre-rift dolostones which are significantly deformed especially at their base, as shown by the presence of breccias and asymmetric boudins associated to strong

shearing. Therefore, the contact between the pre-rift sediments and the basement is tectonic, with the pre-rift deposits interpreted as an allochthonous block (Dall'Asta et al., 2022). In contrast, the syn-rift sediments are in primary contact either with the basement and/or the pre-rift. The first sediments over the exhumed detachment correspond to a bioclastic mud, filling fractures in the basement. These bioclasts correspond mostly to Sinemurian crinoids (Dall'Asta et al., 2022). The bioclastic muds are covered by Pliensbachian-Toarcian syn-rift sandstones (Grès Singuliers). This clearly indicates that the Grès Singuliers are sealing the exhumed detachment fault. Besides, reworked cataclasite is visible in the Grès Singuliers (Dall'Asta et al., 2022).

2. Methods

2.1. Analytical techniques

A total of 81 samples were collected from the fault ($n = 36$) the basement ($n = 5$) and the cover ($n = 40$). Corresponding polished thin sections were observed petrographically with a Nikon LV100ND optical microscope (LFCR, Pau, France), and a Zeiss EVO50 scanning electron microscope (SEM) coupled to EDS mapping (20 kV beam; PLACAMAT, Pessac, France).

Micro-XRF chemical mapping of thin sections ($n = 6$) was realized at the Institut Terre et Environnement Strasbourg (Strasbourg, France) using a Bruker M4 Tornado with an Rh anode and voltage of 50 kV, an anode current of 400 μA , and a pixel size of 25 μm . The data were treated using the SMap code (Munoz et al., 2006; Ulrich et al., 2014) and the XMapTools software (Lanari et al., 2014, 2019).

Electron Probe Micro-analyzer (EPMA) analyses were carried out on 4 polished thin sections using a Cameca SXFive instrument at the Centre de Microcaractérisation Raymond Castaing in Toulouse (France), calibrated with natural and synthetic in-house standards: aluminium oxide (Al), wollastonite (Si, Ca), sanidine (K), manganese titanite (Mn), hematite (Fe), albite (Na), barite (Ba), celestine (Sr). For the determination of major element compositions on silicate from the fault rocks and phosphate in the basement minerals, the operating conditions were set at 15 kV, with a probe current of 50 nA, and a 2 μm beam. For elemental mapping, similar conditions, and a step of 2 μm were used. The XMapTools software was used to build quantitative X-ray electron microprobe maps, and the AX software (Holland and Powell, 2006) to recalculate the structural formulas of the different mineral phases observed. Optical photomicrographs of the fault rocks were processed with ImageJ (Rasband, 1997).

Raman spectroscopy of carbonaceous material (RSCM) analyses were performed on 2 polished thin sections of cataclasite and one thin section of the gouge. A total of 55 Raman spectra were acquired with a Horiba Jobin-Yvon Labram II spectrometer coupled to a microscope, at the Institut des Sciences Moléculaires, Université de Bordeaux, France. Acquisitions parameters include a 514.5

nm argon laser, an extended scanning mode (500 - 2000 cm^{-1}) and an acquisition time of 30 s. Spectra of the first-order region of carbonaceous material were processed using the Fityk software (Wojdyr, 2010). Each spectrum was fitted with 4 bands (D1, D2, D3, and the graphite band G) with Voigt profiles. The calibration of Beyssac et al. (2002), based on the parameter $R2 = D1/(G + D1 + D2)$ was used.

Bulk rock analysis for major, trace and rare-earth elements was realized on 27 powdered samples from the basement and 3 from the sedimentary cover ($< 80 \mu\text{m}$) at the SARM (Service d'Analyse des Roches et Minéraux) in Nancy (France) using an ICP-OES (Inductively coupled plasma - optical emission spectrometry) for major elements and an ICP-MS (Inductively coupled plasma mass spectrometry) for trace and rare earth elements.

Fluid inclusion (FI) petrography was performed on 15 doubly polished thick sections ($100 \mu\text{m}$) to identify FI assemblages (Goldstein et al., 2003) in quartz and hyalophane from veins in the core zone. Microthermometric analyses were performed on 10 selected thick sections using a Linkam THMSG600 heating-cooling stage connected to a Nikon Eclipse LV100ND microscope at the LFCR. Due to the small size of the inclusions, Raman spectrometry was performed to determine chlorinity (Dubessy et al., 2002; Frezzotti et al., 2012) and to validate the results from T_m measurements. This was performed using a LabRAMHR spectrometer (Horiba Jobin Yvon) equipped with a $600 \text{ g}\cdot\text{mm}^{-1}$ grating and an edge filter, as well as an excitation light provided by an Ar^+ laser at 457 nm at a power of 200 mW at the Georessources laboratory (Nancy, France). Chloride content was calculated using the calibration of Caumon et al., (2013) based on the ratio of intensity of the bands 3425 and 3260 cm^{-1} . The effect of quartz birefringence was avoided using the procedure explained by Caumon et al., (2015). Finally, isochores were calculated using the program AqSo_NaCl (Bakker, 2018) by taking into account the composition and salinity of the inclusions.

$^{40}\text{Ar}/^{39}\text{Ar}$ analyses were conducted in the Noble Gas laboratory of Géosciences at the University of Montpellier 2, France, using a multicollector mass spectrometer (Thermo Scientific Argus VI MS) with a nominal mass resolution of ~ 200 and a sensitivity for argon measurements of 3.55×10^{-17} moles/fA at 200 μA trap current. The mass spectrometer is housing a Nier-type source and a fixed array of five Faraday detectors and one Compact Discrete Dynode (CDD) detector used to measure ^{36}Ar . It is linked to a stainless-steel gas extraction/purification line and CO_2 laser system for step-heating which produces after focusing a 1 mm diameter beam that is used for step heating. The samples selected for dating were irradiated for 20 hours in the core of the Triga Mark II nuclear reactor of Pavia (Italy) with several aliquots of the Taylor Creek sanidine standard ($28.61 \pm 0.03 \text{ Ma}$, Renne et al., 2011) as flux monitor. Argon isotopic interferences on K and Ca were determined from irradiation of KF and CaF_2 pure salts from which the following correction factors were obtained:

$(^{40}\text{Ar}/^{39}\text{Ar})_{\text{K}} = 0.00945 \pm 0.00075$, $(^{38}\text{Ar}/^{39}\text{Ar})_{\text{K}} = 0.0127 \pm 0.00030$, $(^{39}\text{Ar}/^{37}\text{Ar})_{\text{Ca}} = 0.0006135 \pm 0.000061$

and $(^{36}\text{Ar}/^{37}\text{Ar})_{\text{Ca}} = 0.000259 \pm 0.000025$. After loading in the sample chamber, the samples were baked at about 120 °C during 24 hours to remove atmospheric argon from the sample surface. Air aliquots from an automated pipette system were analysed prior to the sample analyses to monitor mass discrimination and detector bias. Line blanks were analyzed between every 3 sample analyses and were subtracted from succeeding sample data. Step-heating experiments on two single adularia grains were conducted with a duration of heating of 60 seconds at each step. A custom-made software is used to control the laser intensity, the timing of extraction/purification and the data acquisition. The ArArCalc software© v2.5.2 (Koppers 2002) was used for data reduction and plotting, with the decay constants proposed by Renne et al. (2011). All the data were corrected for system blanks, radioactive decay, isotopic interferences and mass discrimination. Atmospheric ^{40}Ar is estimated using a value of the initial $^{40}\text{Ar}/^{36}\text{Ar}$ ration of 298.6 (Lee et al., 2006). Calculated ages are reported at the 2σ level and include uncertainties in the J-values.

U-Pb geochronology via the in-situ Laser Ablation Inductively Coupled Mass Spectrometer (LA-ICP-MS) method was conducted at the Institut des Sciences Analytiques et de Physico-Chimie pour l'Environnement et les Matériaux (IPREM) laboratory (Pau, France). All the samples (polished chips) were analyzed with a femtosecond laser ablation system (Alfamet, Novalase S.A., France), coupled to an 8900 Triple Quadrupole ICP-MS (ICP-QQQ; Agilent) The aerosol produced by the ablation was carried to the ICP-MS by a tube (1/16" internal diameter) using a Helium stream (450 mL min⁻¹). Measured wash out time of the ablation cell was ~500 ms for helium gas considering the 99% criterion. To improve sensitivity, 10 mL min⁻¹ of nitrogen was added to the twister spray chamber of the ICP-MS via a tangential inlet while helium flow was introduced via another tangential inlet located at the very top of the spray chamber. Measurements were performed under dry plasma conditions. The fs-LA-ICP-MS coupling was tuned on a daily basis in order to achieve the best compromise in terms of sensitivity, accuracy, particles atomization efficiency and stability. The additional Ar carrier gas flow rate, torch position and power were adjusted so that the U/Th ratio was close to 1 +/- 0.05 when ablating the NIST SRM612 glass. Detector cross-calibration and mass bias calibration were checked daily using the appropriate sequence of the ICP-MS software.

The femtosecond laser operates at an IR wavelength of 1030 nm, delivers 360 fs pulses. The laser source can operate within a wide range of repetition rates (1 Hz to 100 kHz) and energy ranging from 200 µJ per pulse below 1 kHz to 1 µJ at 100 kHz. Complex trajectories can be realized by moving the laser beam (15 µm diameter at full energy) across the surface of the sample using the rapid movement of galvanometric scanners combined with a high repetition rate. For in situ U-Pb dating, we have defined a laser trajectory with the galvanometric scanners (5 mm.s⁻¹ speed) allowing to obtain 100 µm square ablation craters at a repetition rate of 200 Hz, for 35 s of ablation. Samples were pre-ablated during 3 s with 150 µm square craters to remove possible contamination. Final

crater depth reached $\sim 100 \mu\text{m}$. The ^{238}U , ^{232}Th , ^{208}Pb , ^{207}Pb , and ^{206}Pb masses were selected, reaching a total mass sweep times of about $\sim 30 \text{ ms}$, before mass sweep averaging of $\sim 150 \text{ ms}$. The limits of detection for ^{206}Pb and ^{238}U were ~ 0.8 and $\sim 0.5 \text{ ppb}$, respectively, as calculated by Iolite 4 using the equation of Howell et al. (2010).

U-Pb data from 2 sessions were processed using Iolite 4 software (Paton et al., 2011) and the VizualAge_UcomPbine Data Reduction Scheme for background correction and normalization (Chew et al. 2014). Prior to normalization, a Python script was used to remove obvious spikes on background corrected signal (higher than 2sd of the median value of a rolling window of size 5).

Normalization used standard sample bracketing to NIST SRM614 glass (Woodhead and Hergt, 2001) for Pb/Pb and Th/U ratios, and WC1 calcite reference material (age $254.4 \pm 6.4 \text{ Ma}$; Roberts et al., 2017) for Pb/U ratios (WC-1; Roberts et al., 2017), using the method of Roberts et al. (2017). Three (3) NIST and 5 WC1 spots were measured every 20 analyses of the unknown. The Duff Brown Tank limestone (Age 64.04 ± 0.67 ; Hill et al., 2016) was used as validation reference material. No common lead correction nor downhole fractionation correction were made.

The uncertainties of the mean isotope ratios of the unknown and validation samples are the standard errors at the 95% level, to which the excess uncertainties, as calculated by Iolite based on the NIST614 reference material, are added (all ratios). Additional systematic uncertainties are propagated onto the final age (Horstwood et al., 2016). These include (2s) decay constant uncertainties (0.1%), an estimate of the long-term reproducibility of the method (2%) and the uncertainty on the reference material age (2.75%; Roberts et al., 2017).

U-Pb ages were determined from lower intercepts on a Tera-Wasserburg plot, as implemented in the IsoplotR software (Vermeesch, 2018). Uncertainties are quoted as age $\pm x/y$, where x is without systematic uncertainties and y is with. The ages obtained for Duff Brown Tank were $66.1 \pm 3.7 \text{ Ma}$ and $68 \pm 1.1 \text{ Ma}$ (2 sessions, 10 spots each, anchored to common Pb value of 0.74). These ages are similar to or slightly higher than the reference age of $64.0 \pm 0.7 \text{ Ma}$.

2.2. Mass balance calculations

Composition and volume changes during metasomatic alteration of a phase A to B are related by the Gresens equation (Gresens, 1967): $x_n = \left(f_v \left(\frac{\rho_A}{\rho_B} \right) c_n^B - c_n^A \right) 100$ where x_n is the mass change (wt% or ppm) of an element n during metasomatism, f_v is the volume change, c_n^B is the concentration of an element n in the phase B, c_n^A the concentration of an element n in the phase A and $\frac{\rho_A}{\rho_B}$, the density ratio. The density was calculated from the modal composition of the sample. Moreover, the similar density between the samples lead to a ratio close to 1 implying that changes of density are secondary parameters on the mass balance calculations. The estimation of the volume change f_v usually relies on the determination of one or several immobile elements (Grant, 1986). The

elements commonly considered as immobile are HFSE (Zr, Nb, Ta), as well as Ti and Al (MacLean and Kranidiotis, 1987). An alternative way to estimate f_v is the minimization of mass transfer (Centrella et al., 2021):

$$\text{Min} (\text{Sum } |X_n|) = \text{Min} \left(\sum_{n=1}^i \left| \left(f_v \left(\frac{\rho_b}{\rho_a} \right) C_n^b - C_n^a \right) 100 \right| \right)$$

where (Sum |X_n|) is the sum of the absolute values of mass transfer for major elements for various volume changes. The volume change used is the one corresponding to the minimum of mass transfer. In this study, the two methods are used and compared. Zr and Al are considered as immobile (Ferry, 1979; Steyrer and Sturm, 2002) and therefore are chosen as the reference for mass balance calculation on bulk rock samples. EPMA measurements of mineral compositions only give the major elements. The results are plotted using a log-log isocon diagram (Grant, 1986). The heterogeneity of the samples (R) for each element is calculated by normalizing the spread of the mean value of concentration in a specific element, following the procedure of Grant (1986): $R = \frac{X_{max} - X_{min}}{\sum_{i=1}^n X} n$ with X the concentration of a given element and n the number of samples as shown in Steyrer and Sturm (2002). The heterogeneity of the sample composition can be classified as homogeneous (0 < R < 0.5), heterogeneous (0.5 < R < 1), or very heterogeneous (R > 1) (Steyrer and Sturm, 2002).

3. Results

3.1. Mineralogy of the detachment fault

The paragenetic evolution of the detachment fault described in (Dall'Asta et al., 2022) is completed here by new data of mineral composition (Table IV.1) and complemented by phase maps for each fault rock.

Min	Altered basement										Cataclasite		Gouge					
	Core Chl (n=21)		Bi (n=3)		Fsp (n=6)		Pl (n=4)			Fap	Wm (n=14)		Wm (n=57)			Hy (n=35)		
	Av.	SD	Av.	SD	Av.	SD	Av.	SD			Av.	SD	Av.	SD		Av.	SD	
SiO ₂	26.0	0.8	36.3	1.6	64.8	1.3	67.9	0.8	CaO	52.2	SiO ₂	50.1	1.1	50.2	1.0	SiO ₂	54.7	2.4
TiO ₂	0.1	0.1	3.6	0.6	0.0	0.0	0.0	0.0	MnO	1.0	TiO ₂	0.2	0.2	0.3	0.4	TiO ₂	0.0	0.0
Al ₂ O ₃	19.8	0.6	20.1	1.7	18.9	0.8	19.0	0.2	FeO	0.6	Al ₂ O ₃	29.1	2.5	27.9	1.4	Al ₂ O ₃	20.1	1.4
Cr ₂ O ₃	0.0	0.0	0.0	0.0	0.0	0.0	0.0	0.0	F	2.7	Cr ₂ O ₃	0.0	0.0	0.0	0.0	Cr ₂ O ₃	0.0	0.0
Fe ₂ O ₃	0.0	0.0	0.0	0.0	0.0	0.0	0.2	0.0	MgO	0.0	Fe ₂ O ₃	0.0	0.0	0.0	0.0	Fe ₂ O ₃	0.0	0.0
FeO	29.0	0.8	17.9	1.1	0.1	0.1	0.2	0.2	Cl	0.1	FeO	2.4	0.9	2.0	0.4	FeO	0.0	0.0
MnO	0.3	0.1	0.3	0.1	0.0	0.0	0.0	0.0	P ₂ O ₅	43.0	MnO	0.0	0.0	0.0	0.0	MnO	0.0	0.0
MgO	10.9	0.6	7.5	1.4	0.1	0.1	0.0	0.0	SrO	0.0	MgO	2.4	0.7	3.2	0.6	MgO	0.0	0.0
CaO	0.0	0.0	0.0	0.1	0.1	0.1	0.2	0.2	SO ₃	0.0	CaO	0.0	0.0	0.0	0.0	CaO	0.0	0.1
Na ₂ O	0.0	0.0	0.3	0.1	2.5	3.3	11.1	0.3	Na ₂ O	0.1	Na ₂ O	0.1	0.0	0.1	0.0	BaO	11.2	2.5
K ₂ O	0.2	0.3	7.9	2.2	12.3	5.3	0.3	0.2	SiO ₂	0.1	K ₂ O	10.5	0.4	10.5	0.4	Na ₂ O	0.4	0.1
Total	86.4	0.6	93.8	0.7	98.7	0.5	98.8	1.0		99.7	F	0.3	0.1	0.7	0.2	K ₂ O	11.0	0.8
											Total	95.5	1.0	94.3	1.3	Total	97.9	97.9
Oxygen	14		11		8		8					11		11			8	
Si	2.8	0.1	2.7	0.1	3.0	0.0	3.0	0.0			Si	3.3	0.1	3.4	0.1	Si	2.8	0.1
Ti	0.0	0.0	0.2	0.0	0.0	0.0	0.0	0.0			Ti	0.0	0.0	0.0	0.0	Ti	0.0	0.0
Al IV	1.2	0.1	1.8	0.1	1.0	0.0	1.0	0.0			Al IV	0.7	0.1	0.7	0.1	Al	1.2	0.1
Al VI	1.4	0.1	0.0	0.0	0.0	0.0	0.0	0.0			Al VI	1.6	0.1	1.6	0.2	Cr	0.0	0.0
Cr	0.0	0.0	0.0	0.0	0.0	0.0	0.0	0.0			Cr	0.0	0.0	0.2	0.1	Fe ₃	0.0	0.0
Fe ₃	0.0	0.0	0.0	0.0	0.0	0.0	0.0	0.0			Fe ₃	0.0	0.0	0.0	0.0	Fe ₂	0.0	0.0
Fe ₂	5.3	0.2	1.1	0.1	0.0	0.0	0.0	0.0			Fe ₂	0.1	0.1	0.1	0.1	Mn	0.0	0.0
Mn	0.1	0.0	0.0	0.0	0.0	0.0	0.0	0.0			Mn	0.0	0.0	0.0	0.0	Mg	0.0	0.0
Mg	3.5	0.2	0.9	0.2	0.0	0.0	0.0	0.0			Mg	0.2	0.1	0.3	0.1	Ca	0.0	0.0
Ca	0.0	0.0	0.0	0.0	0.0	0.0	0.0	0.0			Ca	0.0	0.0	0.0	0.0	Ba	0.2	0.1
Na	0.0	0.0	0.0	0.0	0.2	0.3	0.9	0.0			Na	0.0	0.0	0.0	0.0	Na	0.0	0.0
K	0.1	0.1	0.8	0.2	0.7	0.3	0.0	0.0			K	0.9	0.0	0.9	0.1	K	0.7	0.1
											F	0.1	0.0	0.15	0.05			
Sum	9.9		9.9		5.0		5.0				Sum	7.0		6.9			5.0	
XMg	0.4		0.0		XAn	0.5	XAn	0.7			XPg	0.8		1.0		XCe	21.8	
				XAb	23.3	XAb	97.8				XMs	56.4		58.2		XAb	3.6	
				XOr	76.2	XOr	1.5				XCel	42.9		40.8		XOr	77.3	
											F/Cl	13		50				

Table IV.1: Composition of the different phases observed in the Col du Bonhomme area. The structural formula were calculated with the software AX from Holland and Powell (2006). Ferric iron was recalculated according to the method of Holland and Powell (1998). Wm = White micas, Chl = Chlorite, Bi = Biotite, Fsp = Feldspars, Pl=Plagioclase, Fap = Fluorapatite, Pg = Paragonite, Ms = Muscovite, Cel = Celadonite, An = Anorthite, Ab = Albite, Or = Orthoclase, Hy =

Hyalophane, Ce = Celsian. The composition for each phase corresponds to the average (av.) of the EMPA composition obtained. The Standard deviation (SD) is given as 1σ .

3.2. Host rock

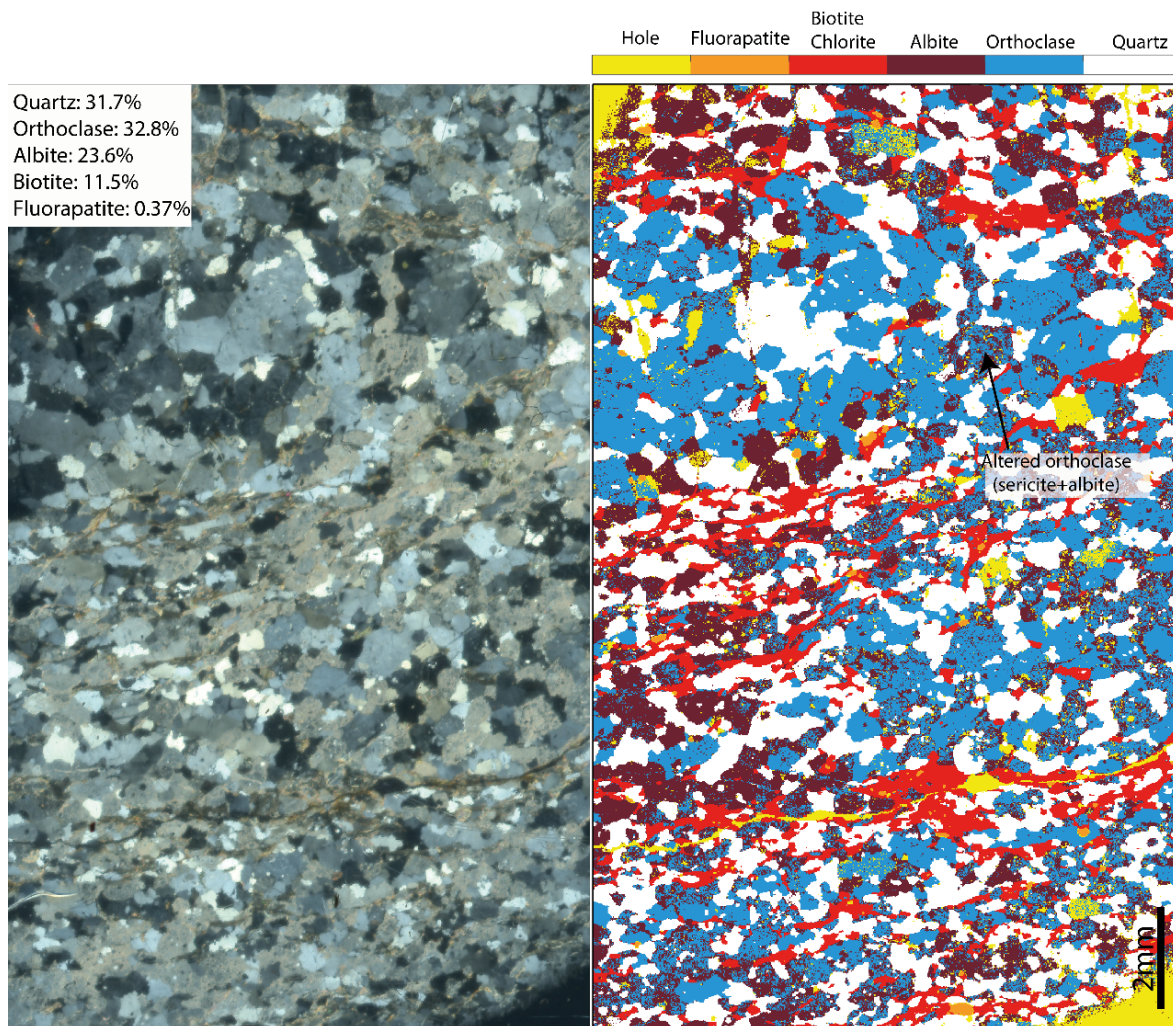


Figure IV.5: Cross polarized image of the basement and associated mineralogical map from μ XRF chemical map

The basement of the Col du Bonhomme area corresponds to a migmatitic gneiss with a subvertical NW-SE foliation and meter-thick magmatic intrusions. The mineralogy corresponds to feldspars (mostly orthoclase and minor plagioclase), quartz, brown biotites and accessory phases such as fluorapatite and zircons (Fig. IV.5, Appendix C Fig. C.1). Orthoclase and quartz grains are several hundreds of micrometres in size. At the microscale, grain-boundary migration and sub-grain rotation of quartz points to a temperature of deformation in the range 450°C to 600°C. Feldspar composition corresponds to orthoclase with some anorthoclase, and to pure albite (Fig. IV.6A). This plagioclase composition differs from the An_{20-22} up to An_{30} found elsewhere in the Mont-Blanc granite (Bussy, 1990). Biotite corresponds to Fe-biotite (Fig. IV.6B) The magmatic intrusions correspond to aplite with a granitic composition. They are composed of muscovite, orthoclase, albite and quartz with scarce biotite.

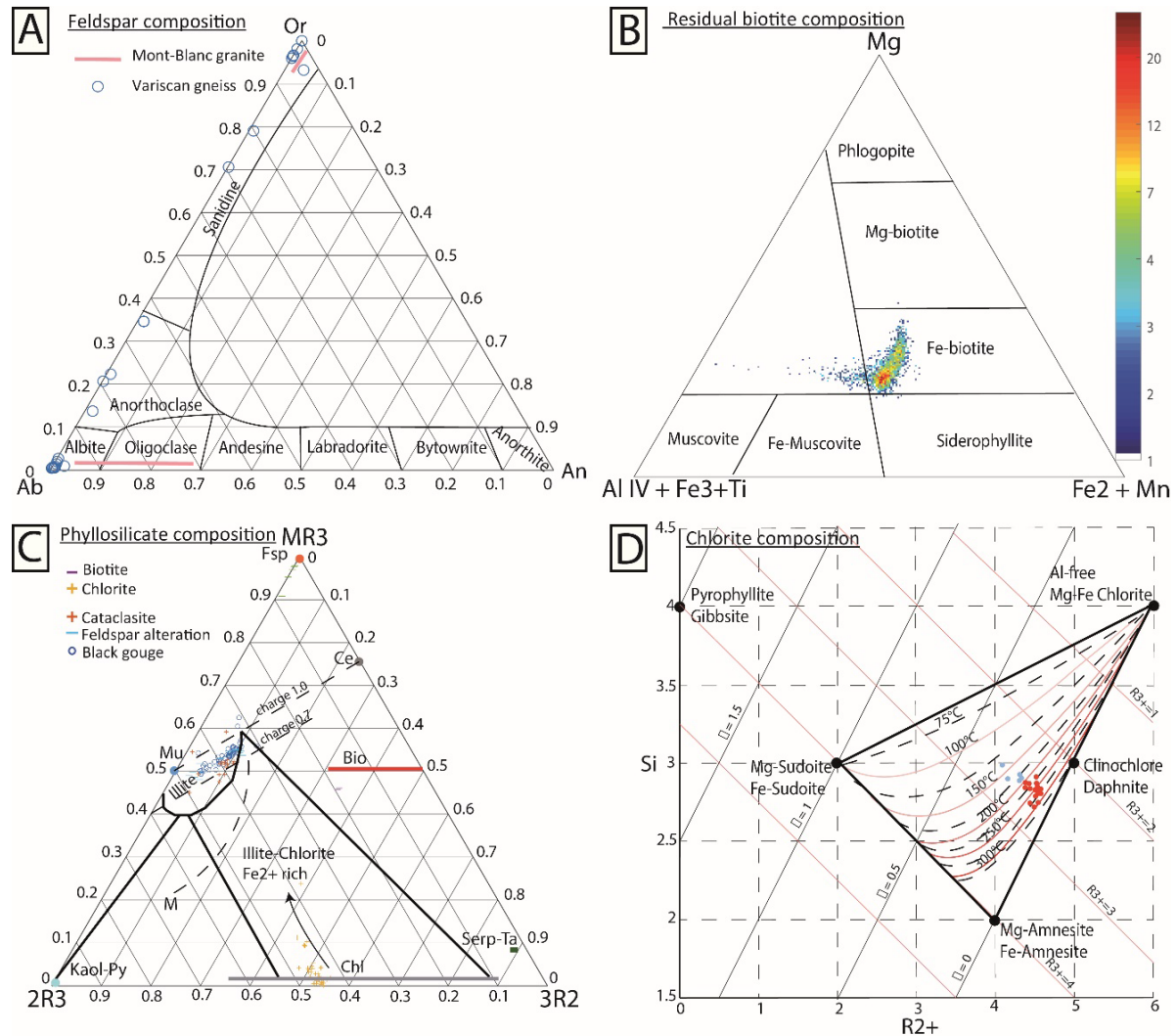


Figure IV.6: A- Feldspar composition of the basement in the Col du Bonhomme area, and of the Mont-Blanc granite (Bussy, 1990) for comparison. B- Composition of biotite from the host rock. C- Composition of the phyllosilicates observed in the basement and the fault rocks using diagram from (Velde, 1985). D- Composition of chlorites and their precipitation temperatures obtained using the graphical representation of Bourdelle and Cathelineau (2015). Or=Orthoclase, Ab=Albite, An=Anorthite, Fsp=Feldspar, Mu=Muscovite, Ce=Celadonite, Bt= Biotite, Chl=chlorite, Bt=biotite, M=Montmorillonite, Serp=Serpentine, Ta=Talc.

3.3. Detachment fault

The fault damage zone is composed of quartz and feldspars inherited from the host rock, chlorite, white micas, rutile, Fe-oxides and sulphides replacing feldspars and biotite (Dall’Asta et al., 2022).

3.3.1. Outer damage zone

The outer damage zone (Fig. IV.7A and B, Appendix C Fig. C.2) is marked by a decrease of the amount of feldspar compared to the host rock, correlated to an increase in white micas and the replacement of biotite by chlorite (Fig. IV.6). The orthoclase minerals show a two-stage alteration. The first one corresponds to its replacement by albite. The second one is the pseudomorphic replacement of albite and relics of orthoclase by white micas (Fig. IV.7C), with conservation of the mineral shapes and cleavage in the case of albite (Fig. IV.8C). The replacement of orthose and albite

Multiscale element transfer during crustal necking: the Mont-Blanc detachment fault

by white micas led to creation of respectively 6 and 5% of porosity (Fig. IV.7D and E). Biotite-to-chlorite replacement was coeval to feldspar alteration. The replacement is pseudomorphic with locally rutile exsolutions along chlorite cleavage. Chlorite also fills micrometric fractures in the surrounding orthoclase. It corresponds to Mg/Fe-sudoite, clinocllore and Mg/Fe-amnesite (Fig. IV.6D). Residual biotite is Fe-rich (45-55% annite, 20-30% phlogopite; Fig. IV. 6B).

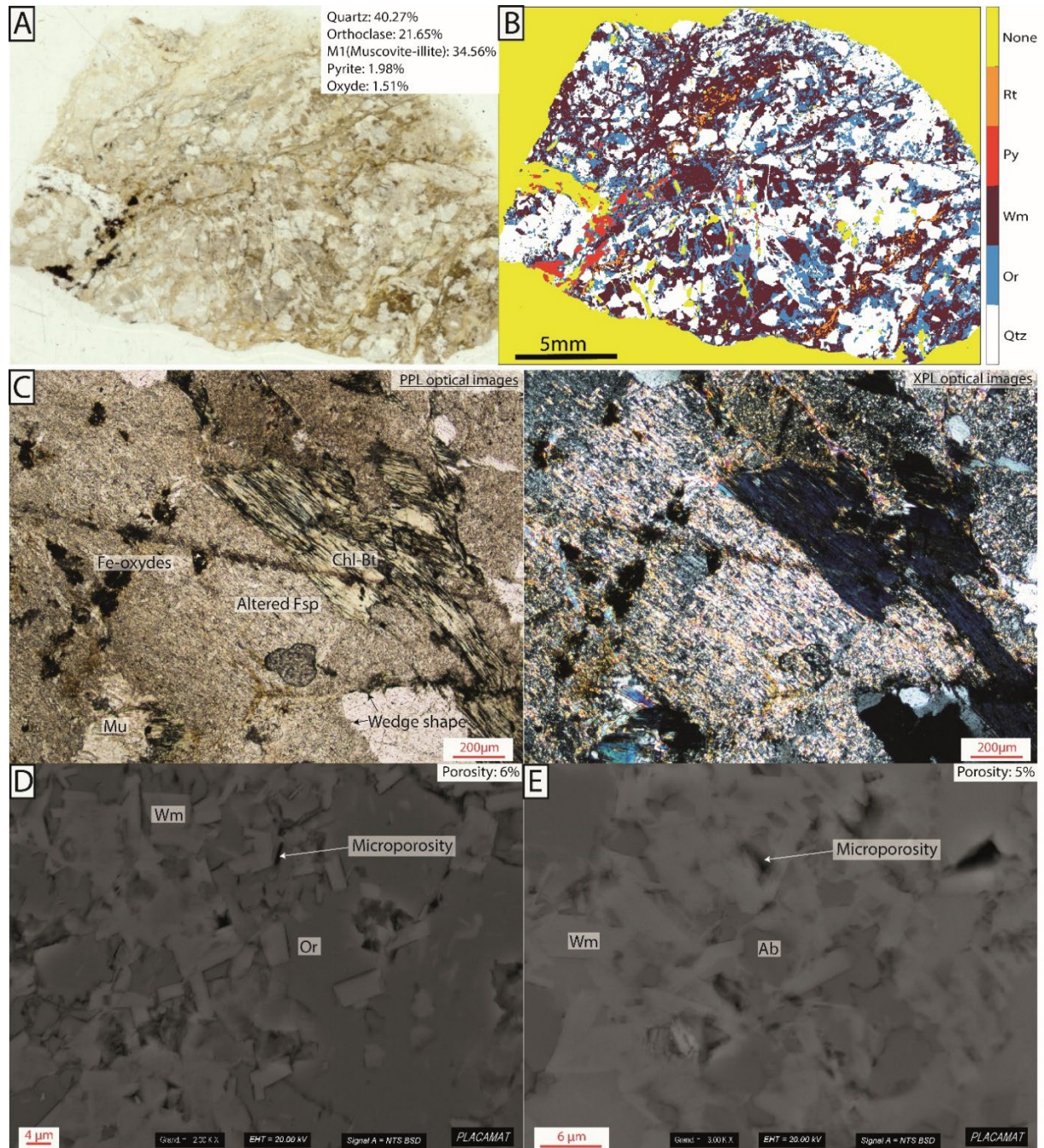


Figure IV.7: A- Plane polarized and B-mineral map of a cataclasite sample from the outer damage zone. C- Optical microphotograph (PPL and XPL) of feldspar and biotite alteration showing pseudomorphic replacement. D- Replacement of orthoclase by white micas associated to creation of microporosity (SEM-BSE image). E- Replacement of albite by white micas associated to creation of microporosity (SEM-BSE image). Fsp=Feldspar, Wm=White micas, Or=Orthoclase, Ab=Albite

Several thermometers were used to calculate the temperature of formation of chlorite based on their composition. Using the empirical calibrations of Kranidiotis and MacLean (1987), Cathelineau (1988) and Jowett (1991) chlorite temperature between $233\pm 31^{\circ}\text{C}$ and $255\pm 36^{\circ}\text{C}$ (Appendix C Fig. C.3) were obtained while the semi-empirical thermometer of Inoue et al., (2009) gives a lower temperature of $193\pm 33^{\circ}\text{C}$. Graphical representation of Bourdelle and Cathelineau (2015) gives a temperature comprised between 200 and 300°C (Fig. IV.7D) for the core of chlorite, with a decrease in the border below 200°C .

Important dilatancy is observed through the formation of quartz veins, which are affected by cataclastic deformation (Fig. IV.7A and B). The veins are observed in the entire damage zone. In the outer damage zone, their size ranges from several micrometres up to hundreds of micrometres. Several quartz textures are observed, with either fibrous or blocky crystals ($100\ \mu\text{m}$) with euhedral facets. Pyrite is locally observed in the centre of the vein.

Locally, graphite-rich veins and joints are observed in the outer damage zone (Fig. IV.8A), where they surround lowly deformed to undeformed Carboniferous aplite intrusions. They form mm-thick layers along graphite-rich joints and centimetric black veins in the cataclasite. This graphitic material, not described in Dall'Asta et al. (2022), represents around 12% of the outer damage zone around the intrusion. The black veins are centimetre-thick and originate from the graphite-rich planes, indicating a link between opening of the veins and shearing along the joints. The borders of the veins show sharp edges, and abundant clasts of cataclasite are observed in the veins at the macro and microscale (Fig. IV.8B).

The joints are marked by a discontinuous thin layer composed of a grey matrix (M1). Injection of this matrix is observed in the cataclasite. It is composed of scarce micrometric quartz fragments in an altered dark matrix overprinted by micrometric sericite. This grey matrix which can be found only in the graphite joints passes to a graphite-rich matrix (M2).

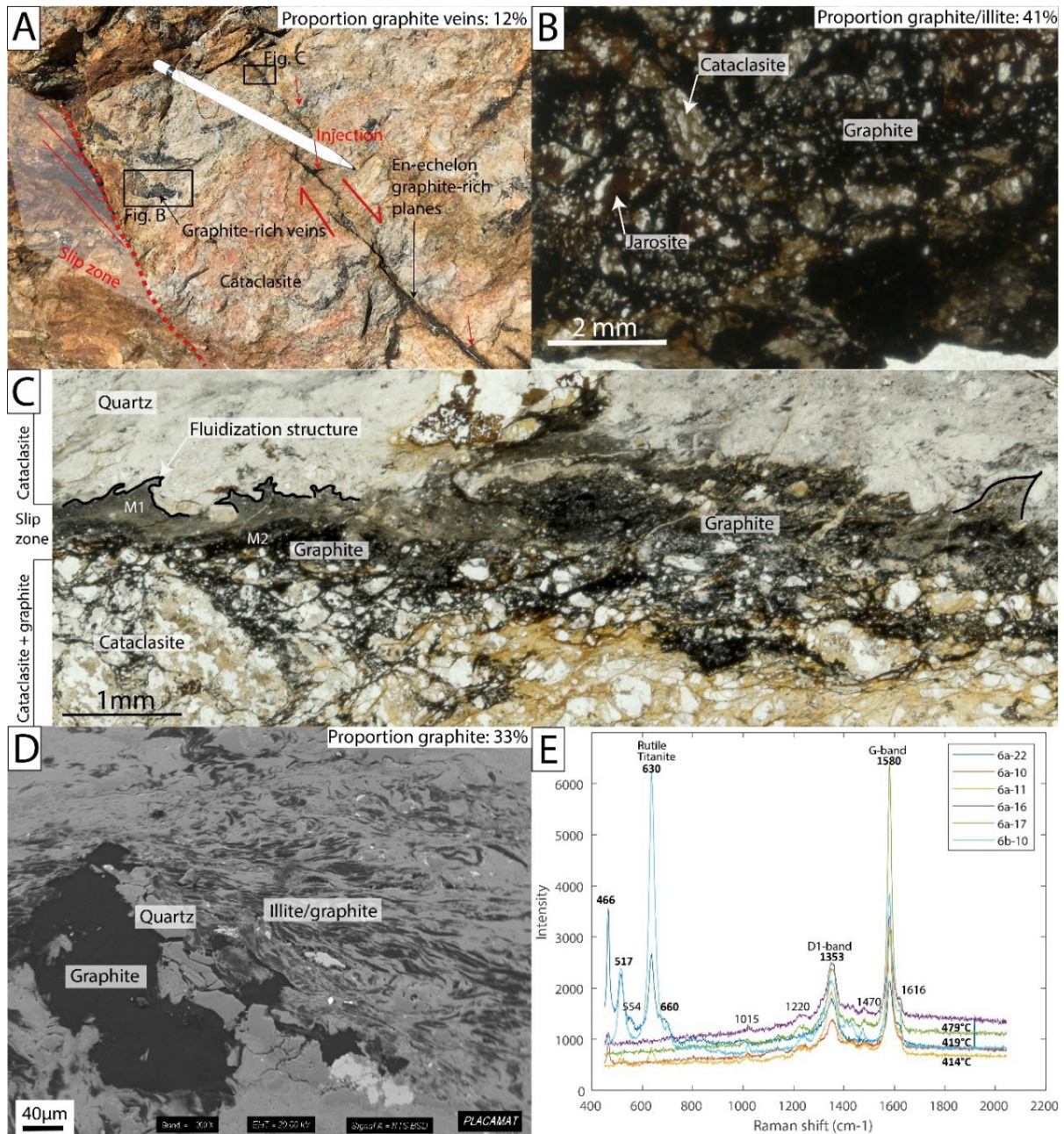


Figure IV.8: A- Macroscopic image of graphite-rich vein and planes in the cataclasite. B- Thin section view (PPL) of the same graphite rich showing important amount of graphite/illite mixture. C- SEM image of the graphite rich area showing 2 types of graphite material, large graphite zones and illite/graphite mixture. D- Raman spectra of representative graphite associated to titanite.

Two types of graphite material are observed in the vein and along the joints (Fig. IV.8C and D). The first one corresponds to large (100 μm thick) graphite aggregates. It is associated with hundred-micrometre-large sulphide grains (mostly pyrite and arsenopyrite), small sulphide droplets (20 μm) and quartz veins with a microcrystalline texture. The second type corresponds to graphite flakes mixed with illite. These flakes show deformation such as micro-folds and shearing (Fig. IV.8C). Graphite is also found locally in the core zone.

<i>Sample</i>	<i>Location</i>	<i>Lithologies</i>	<i>Coordinates</i>	<i>Nb of spectra</i>	<i>R1</i>	<i>R2</i>	<i>T(°C)</i>	<i>1σ (°C)</i>	<i>SEM (95%)</i>
<i>CB20-6a</i>	Tête Nord des Fours	Graphite veins	45°44'11.3''N 6°43'46.6''E	13	0.39	0.42	451	24.82	19.14
<i>CB20-6b</i>	Tête Nord des Fours	Graphite veins	45°44'11.3''N 6°43'46.6''E	16	0.39	0.44	443	25	22.19
<i>MB5c</i>	Rocher du Bonhomme	Gouge	45°43'39.5''N 6°42'40.3''E	16	0.48	0.77	423	18	15.98

Table IV.2: RSCM results on the graphite in the fault zone. SD=Standard deviation, SEM= Standard error of the mean

Raman spectrometry of the graphite shows well-developed G-bands and an important D1-band corresponding to high-grade carbonaceous matter (crystallized graphite). Rutile and minor titanite can be observed on the Raman spectra (Fig. IV.8D) with a main peak at 600 - 660 cm^{-1} depending on the crystallinity (Zhang et al., 2013; Nakamura et al., 2015). The temperatures obtained using (Beyssac et al., 2002) calibration range from $451 \pm 23^\circ\text{C}$ to $443 \pm 24^\circ\text{C}$ for the graphite veins and joints (Table IV.2, Appendix C Tab. C.1,2,3). A similar temperature range is obtained for graphite from the gouge ($417 \pm 30^\circ\text{C}$), pointing to possible reworking of vein / joint graphite material into the gouge. This temperature is 100°C higher than the Alpine metamorphic peak measured in the overlying sediments (330°C ; Dall'Asta et al., 2022).

3.3.2. Inner damage zone

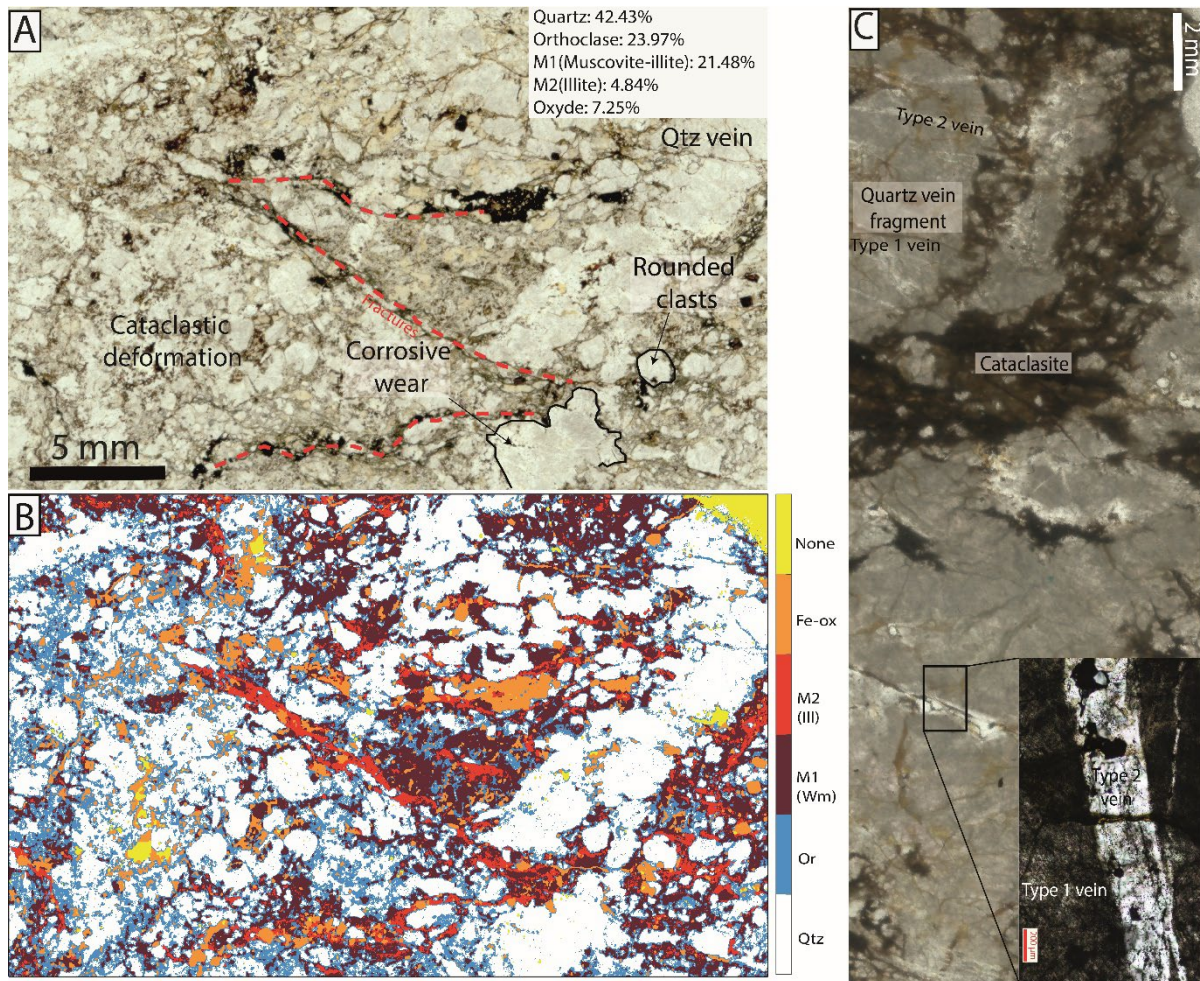


Figure IV.9: A- Optical image (PPL) of cataclasite from the inner damage zone showing increase of white mica proportion, iron oxides in fractures, and quartz veins reworked in the cataclasite (from Dall'Asta et al., (2022)). B- Phase map of the cataclasite C- Centimetric quartz veins in the inner damage zone reworked in the cataclasite. Two generations of veins are observed, the second generation crosscutting the first one. Fe-ox=Fe oxide, Ill=Illite, Wm=White micas, Or=Orthoclase, Qtz=Quartz

The inner damage zone is marked by the complete disappearance of albite and the presence of Fe-oxides mostly along fractures (Fig. IV.9A and B, Appendix Fig. C.3). Centimetric quartz veins are also observed. They are crosscut by secondary quartz veins and small oxide veins and can be reworked in the cataclasite as micrometric to centimetric clasts (Fig. IV.9C). Locally, tectonic breccias overprint the cataclasite (Appendix C Fig. C.4). These breccias are composed of cataclasite clasts. The cement is composed of dolomite and ankerite rhombs and void-filling calcite mostly replaced by late Mg-calcite (Dall'Asta et al., 2022).

Inherited zircons can be observed in the fault zone. These zircons are affected by brittle deformation visible through the presence of fractures (Appendix C Fig. C.5A). Traces of dissolution on the surface such as pits are observed (Fig. C.5B). However, some zircons also show overgrowth on the crystal borders (Fig. C.5C). These overgrowths appear truncated on the border of the mineral indicating fracturing of the mineral postdating the overgrowth.

3.3.3. Core zone

The core zone is composed mostly of fine-grained white micas forming a black matrix corresponding to an indurated gouge, in which clasts of the damaged zone are reworked (Fig. IV.10A, B and D, Appendix C Fig. C.6). This gouge is composed of white micas and Ti/Fe oxides with a size below 10 μm (Dall'Asta et al., 2022). Reworked clasts of ultracataclasite are reworked in the core zone indicating early cementation prior to gouge formation (Fig. IV.10C). The black matrix (M2) is formed by progressive shearing of the cataclasite matrix (M1) leading to an important grain size decrease and illite formation. This deformation is correlated to a change of composition of the newly formed illites, from a more important muscovite component (Fig. IV.6C).

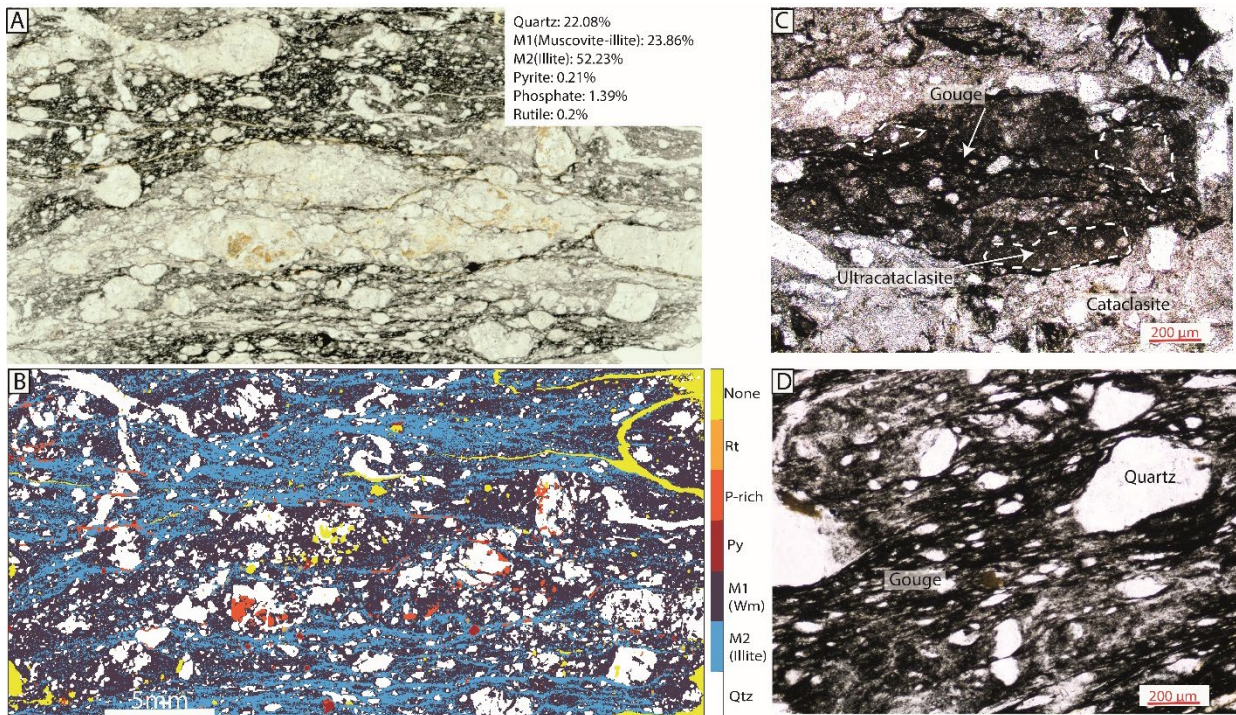


Figure IV.10: A- Optical image (PPL) of the gouge showing reworking of cataclasite in the gouge matrix. B- Corresponding phase map. C- Optical image (PPL) of the core zone showing clasts of cataclasite and ultracataclasite reworked in the gouge matrix. D- Optical image (PPL) of the gouge matrix with larger quartz grains and cataclasite clasts. Rt=Rutile, Py=Pyrite, Wm=White micas, Qtz=Quartz

In the core zone, a generation of quartz veins is post-dated by quartz-hyalophane veins parallel to the Y-plane of the gouge. They are larger than the quartz veins (up to cm-thick)). Elongated blocky hyalophane crystals are restricted to the border of the veins, while their centre is filled by coarse, quartz and hyalophane grains (Fig. IV.11A). Hyalophane has a composition between 10 and 30% of the celsian pole (Fig. IV.11B). A miscibility gap characteristic of low temperature precipitation (below 300°C, Essene et al., 2005) is also observed (Fig. IV.11B). Quartz-hyalophane veins crosscut the gouge foliation. However, the latter are fragmented, with quartz precipitation in the fractures, leading to formation of breccias along the vein border with small fragments reworked in the gouge (Fig. IV.11 E). This indicates that the veins were deformed after their emplacement.

Besides, there is also a relation between the amount of deformation and the size of the veins. The smallest veins are the most deformed, affected by strong fracturing and brecciation. In contrast, the larger veins (cm-thick) are only moderately deformed on their border. In the vicinity of the vein margins, the gouge matrix is strongly recrystallized with large white micas (> 100 μm long and 10-50 μm large) close to muscovite composition (Fig. IV.11D). Both muscovites and illites are Ba-rich (> 1 wt%).

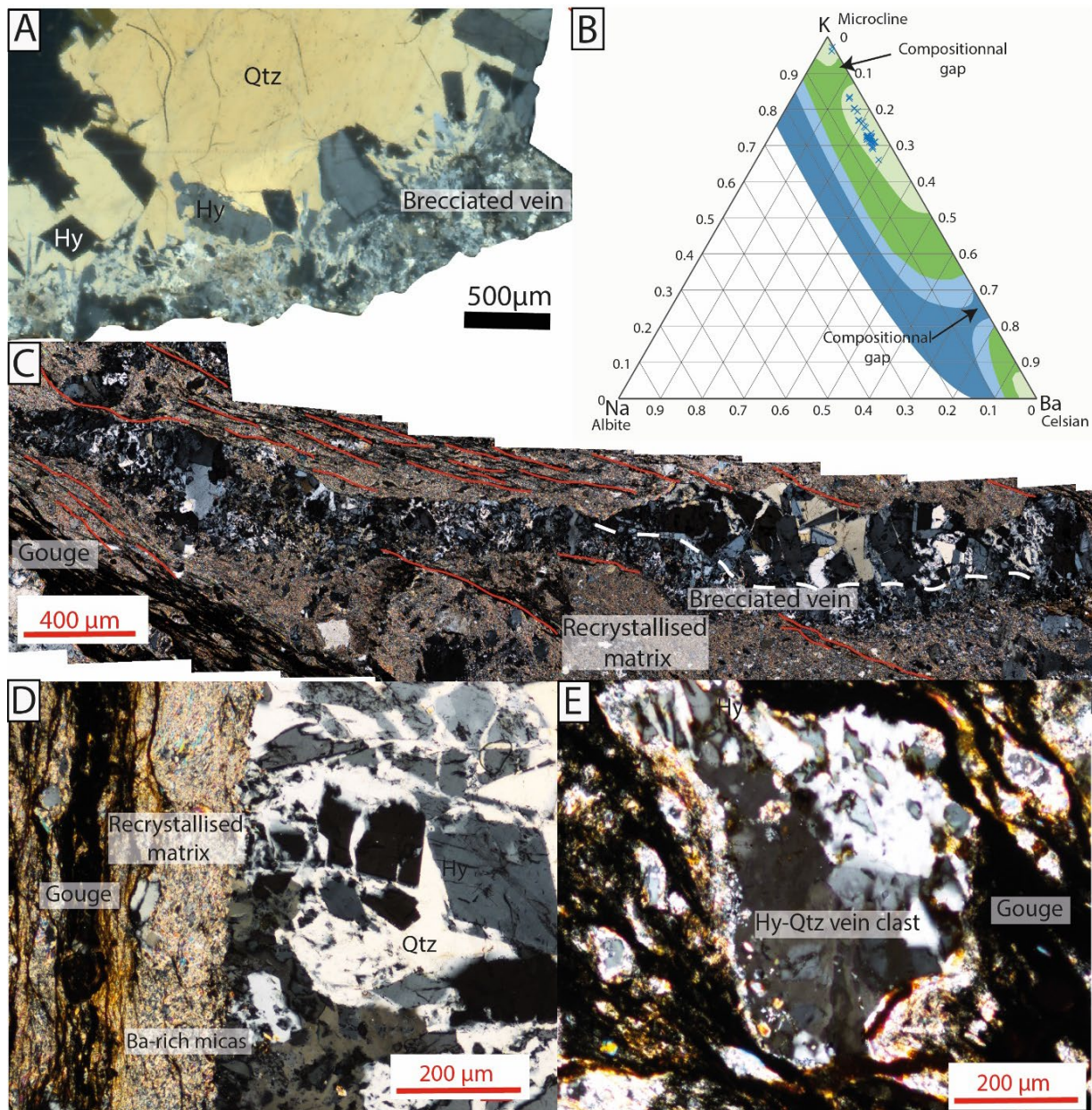


Figure IV.11: A- Thin section photograph (XPL) of the quartz-hyalophane veins. B- Composition of hyalophane in a ternary albite-microcline-celsian plot. The light green field corresponds the low-temperature hyalophane, the dark green field corresponds to the hyalophane composition for greenschist conditions, the light blue to lower amphibolite facies and dark blue to upper amphibolite facies (from Essene et al., 2005; Raith et al., 2014). C- Optical image (XPL) of a vein in the gouge showing the vein crosscutting the foliation but also being brecciated and significantly deformed. Note the recrystallized matrix around the vein. D- Optical image (XPL) of the border of the veins showing the transition from recrystallized matrix with Ba-rich white micas to the fine-grained gouge. E- Optical image (XPL) of reworked hyalophane-quartz veins clast in the gouge.

3.4. Bulk-rock chemistry

In the host rock, the main major elements are Si, Al, and K, with mean concentrations of 70, 14, and 5 wt% oxide (wt% ox.), respectively ($n = 4$). All other major elements have concentrations below 3 wt% ox. These concentrations are homogeneous between samples for all elements ($R < 0.5$) except for Mn ($R = 0.55$), Ca ($R = 1.4$) and for the LOI ($R = 0.6$) (Table 3). All trace elements have a mean concentration lower than 100 ppm, except Zr (109 ppm), Rb (198 ppm) and Ba (1310 ppm). These concentrations are heterogeneous between samples ($0.4 < R < 0.9$), with the noticeable exception of Mo ($R = 1.5$) (Table IV.4). Most REE have mean concentrations lower than 5 ppm, except La (20 ppm), Ce (41 ppm) and Nd (18 ppm) (Table 4). Such concentrations are homogeneous between samples ($R < 0.5$), except for Pr, Nd and Sm ($R = 0.6$) (Table 4).

In the outer damage zone, the main major elements are Si, Al, K with mean concentrations of 64.9, 14 and 6 wt% ox. respectively ($n=4$). All other elements have concentration below 3 wt% ox. except Fe (5.9 wt% ox.). These concentrations are homogeneous between samples Si, Al, Mn, Mg, Ti, P and heterogeneous for Fe, Na, Ca, K and for the LOI ($R=0.7$). Most of the trace elements have value below 100ppm except V (192 ppm), Zn (157 ppm), As (178 ppm), Rb (271 ppm), Zr (161 ppm) and Ba (935 ppm). These concentrations are heterogeneous to very heterogeneous except for Ge, Rb, Zr, Hf and U which are homogeneous. REE have concentrations below 5ppm except for La (28 ppm), Ce (62 ppm), Pr (7.4 ppm), Nd (27 ppm). These concentrations are heterogeneous between the samples ($0.5 < R < 1$).

In the inner damage zone, the main elements are Si, Al, K with concentrations of 64, 14 and 6 wt% ox. respectively ($n=9$). All other elements have concentrations below 4 wt%. These concentrations are homogeneous only for Si and Al. They are heterogeneous for Fe, Na, K and Ti and very heterogeneous for Mn, Mg, Ca, P and for the LOI. All trace elements have concentrations below 100ppm except for F (1516 ppm), Rb (275 ppm), Zr (188 ppm) and Ba (1568 ppm). The concentrations are homogeneous for Be, Ge, Rb, Cd, In, Sn, Ta and U, heterogeneous for V, Cr, Co, Ni, Sr, Y, Zr, Nb, Sb, Cs, Ba, Hf, Pb and Th. They are very heterogeneous for Cu, Zn, As, Mo, W. REE have concentration below 5 ppm for all elements except La (28ppm), Ce (60ppm), Pr (7ppm), Nd (27ppm). The concentrations are homogeneous for La and Lu and heterogeneous for the others.

In the core zone, the main elements correspond to Si, Al and K with concentrations of 63, 17 and 7 wt% ox. respectively ($n=6$). All the other elements have concentration below 2 ppm. The concentration is homogeneous for Si, Al, Mg, Ca, K as well as for the LOI. The concentration is heterogeneous for Fe, Na, Ti and very heterogeneous for P. For trace elements, the concentrations are below 100 ppm except for F (4182 ppm), V (147 ppm), Cr (103 ppm), Rb (334 ppm), Zr (283 ppm) and Ba (11118 ppm). The concentrations are homogeneous for Be, Ni, Ge, Rb, Cs and U, heterogeneous to very heterogeneous for the others. REE have concentration below 5ppm for all

Multiscale element transfer during crustal necking: the Mont-Blanc detachment fault

elements except La (35ppm), Ce (31ppm), Pr (8ppm), Nd (28ppm). The concentrations are homogeneous for all the elements.

	SiO ₂	Al ₂ O ₃	Fe ₂ O ₃	MnO	MgO	CaO	Na ₂ O	K ₂ O	TiO ₂	P ₂ O ₅	LOI	Total
	Host rock (n=4) Density=2.66											
<i>Average</i>	70.06	14.39	2.38	0.07	1.22	0.70	2.73	5.22	0.34	0.16	2.47	99.69
<i>SD (1σ)</i>	2.31	0.45	1.08	0.04	0.17	0.94	0.43	0.63	0.18	0.05	1.41	0.72
<i>Normalized spread</i>	0.04	0.04	0.50	0.55	0.17	1.40	0.17	0.12	0.59	0.24	0.61	0.01
	Outer damage zone (n=4) Density= 2.79											
<i>Average</i>	64.94	14.77	5.96	0.02	1.20	0.11	0.91	6.11	0.60	0.24	4.47	99.24
<i>SD (1σ)</i>	7.37	4.15	3.88	0.01	0.30	0.10	0.73	3.00	0.21	0.06	2.88	0.62
<i>Normalized spread</i>	0.13	0.30	0.62	0.39	0.30	0.84	0.91	0.58	0.37	0.21	0.72	0.01
	Inner damage zone (n=9) Density=2.85											
<i>Average</i>	64.63	14.97	3.52	0.08	1.91	1.74	1.24	6.38	0.57	0.18	4.31	99.35
<i>SD (1σ)</i>	8.79	4.02	2.08	0.06	1.58	3.16	0.81	2.65	0.21	0.12	3.76	0.51
<i>Normalized spread</i>	0.23	0.40	0.70	1.30	1.40	2.84	0.91	0.66	0.53	1.00	1.48	0.01
	Core zone (n=6) Density=2.84											
<i>Average</i>	63.34	17.48	2.88	0.00	1.84	0.06	0.12	7.14	0.97	0.04	4.79	98.63
<i>SD (1σ)</i>	4.27	1.92	1.47	0.00	0.47	0.01	0.09	0.54	0.50	0.09	1.46	2.26
<i>Normalized spread</i>	0.10	0.15	0.66		0.36	0.13	0.95	0.09	0.71	3.00	0.35	0.03

Table IV.3: Composition of the host rock, outer, inner damage zones and core zone in major elements (wt%). The standard deviation is given for 1σ. The normalized spread (R) allows to estimate the heterogeneity of the samples.

	F	Be	Sc	V	Cr	Co	Ni	Cu	Zn	Ga	Ge	As	Rb	Sr	Y	Zr	Nb	Mo	Cd	In	Sn	Sb	Cs	Ba	Hf	Ta	W	Pb	Bi	Th	U	
Host rock (n=4)																																
Average	955.0	2.7	7.0	29.4	37.1	4.3	15.1	11.5	63.6	15.7	1.3	11.6	197.6	81.8	19.2	109.4	10.6	0.2	0.1	0.1	6.5	2.2	10.8	1308.3	3.2	1.3	2.3	23.7	0.4	7.8	2.9	
SD (1σ)	799.0	0.9	2.7	10.5	11.7	2.0	7.8	6.9	44.8	6.2	0.1	5.7	24.2	32.3	7.9	59.4	6.2	0.3	0.1	0.0	0.4	0.1	1.6	640.3	1.7	0.5	1.3	11.5	0.3	4.2	1.1	
Normalized spread	0.6	0.4	0.4	0.4	0.3	0.5	0.6	0.7	0.8	0.4	0.1	0.5	0.1	0.5	0.4	0.6	0.7	1.5	0.7	0.2	0.1	0.0	0.2	0.6	0.6	0.4	0.6	0.5	0.9	0.6	0.4	
Outer damage zone (n=4)																																
Average		3.5	12.3	192.3	81.4	3.3	18.3	20.5	157.7	26.6	1.7	178.8	271.0	65.0	19.7	161.3	13.1	14.6	0.2	0.4	7.5	12.9	16.6	935.5	4.4	1.1	6.1	95.5	1.7	13.5	4.5	
SD (1σ)		1.4	5.5	234.3	41.6	2.2	8.6	13.1	142.5	8.0	0.3	189.8	97.5	48.6	12.2	51.0	4.7	27.3	0.2	0.7	4.4	8.2	9.0	483.6	1.6	0.3	3.2	94.5	1.8	10.7	1.2	
Normalized spread		0.5	0.6	1.3	0.5	0.6	0.6	0.6	1.1	0.3	0.2	1.2	0.4	0.7	0.7	0.4	0.5	1.9	1.1	1.7	0.6	0.7	0.6	0.6	0.4	0.5	0.6	1.1	1.2	1.0	0.3	
Inner damage zone (n=9)																																
Average	1434.0	3.1	10.5	73.6	68.7	6.3	23.4	30.5	46.7	28.8	1.8	32.3	275.3	54.0	18.4	188.5	11.4	3.1	0.1	0.1	5.0	8.2	16.8	1568.5	5.1	1.2	4.7	15.6	0.3	14.2	2.9	
SD (1σ)	75.5	0.8	6.0	42.5	30.0	3.5	10.7	24.4	33.4	21.5	0.2	25.4	69.0	31.3	8.6	74.2	5.0	2.9	0.0	0.0	1.3	4.7	7.4	714.4	1.8	0.4	4.6	7.8	0.2	7.2	0.6	
Normalized spread	0.45	0.4	0.8	0.8	0.6	0.8	0.6	1.2	1.0	1.3	0.3	1.3	0.4	0.8	0.7	0.6	0.7	1.2	0.4	0.2	0.4	0.9	0.7	0.7	0.7	0.5	0.4	1.6	0.7	1.1	0.8	0.3
Core zone (n=6)																																
Average	3300.0	8.4	14.9	147.0	103.6	3.6	21.8	22.1	55.4	20.1	2.0	40.3	334.5	67.2	11.4	283.5	15.2	1.8	0.1	0.0	13.1	11.4	24.0	11118.4	7.7	1.6	12.3	11.5	0.5	14.1	4.0	
SD (1σ)	902	2.2	6.1	68.0	49.2	2.4	5.9	16.3	44.3	9.5	0.3	22.6	46.3	94.9	3.5	138.8	9.2	1.0	0.1	0.0	4.3	3.9	5.9	16211.3	3.5	0.7	6.2	4.2	0.2	6.6	1.2	
Normalized spread	0.27	0.3	0.5	0.6	0.7	0.8	0.3	0.8	1.1	0.6	0.2	0.8	0.2	1.8	0.5	0.7	0.9	0.7	1.3	0.2	0.5	0.5	0.3	1.9	0.7	0.7	0.7	0.5	0.6	0.7	0.4	

Table IV.4: Composition of the host rock, outer, inner damaged zones and core zone in trace elements (ppm). The standard deviation is given for 1σ . The normalized spread (R) allows to estimate the heterogeneity of the samples.

	La	Ce	Pr	Nd	Sm	Eu	Gd	Tb	Dy	Ho	Er	Tm	Yb	Lu
	Host rock (n=4)													
<i>Average</i>	20.40	41.29	4.70	17.70	3.74	0.77	3.31	0.54	3.36	0.69	1.90	0.29	1.86	0.28
<i>SD (1σ)</i>	8.53	16.62	2.59	9.67	1.96	0.33	1.61	0.25	1.49	0.31	0.88	0.13	0.82	0.14
<i>Normalized spread</i>	0.45	0.44	0.61	0.60	0.57	0.48	0.51	0.48	0.45	0.44	0.44	0.46	0.46	0.48
	Outer damaged zone (n=4)													
<i>Average</i>	28.2	62.4	7.4	27.1	5.3	0.8	3.9	0.6	3.4	0.7	1.9	0.3	1.8	0.1
<i>SD (1σ)</i>	13.4	31.8	3.9	15.5	3.7	0.2	2.9	0.4	2.1	0.4	1.1	0.1	0.8	0.5
<i>Normalized spread</i>	0.5	0.6	0.6	0.6	0.8	0.3	0.8	0.7	0.6	0.7	0.7	0.6	0.5	0.26
	Inner damaged zone (n=9)													
<i>Average</i>	27.78	59.93	6.82	25.85	5.29	0.84	4.14	0.60	3.44	0.68	1.83	0.27	1.73	0.70
<i>SD (1σ)</i>	8.21	22.00	2.75	11.06		2.72	0.27	1.92	0.24	1.37	0.29	0.81	0.12	0.57
<i>Normalized spread</i>	0.43	0.55	0.65	0.68	0.79	0.47	0.71	0.59	0.51	0.62	0.68	0.67	0.60	0.24
	Core zone (n=6)													
<i>Average</i>	35.29	70.89	7.68	27.88	4.76	0.96	3.24	0.43	2.38	0.48	1.34	0.22	1.55	0.05
<i>SD (1σ)</i>	15.06	31.28	3.40	12.30	1.90	0.27	1.11	0.13	0.65	0.13	0.33	0.05	0.28	0.25
<i>Normalized spread</i>	0.5	0.5	0.5	0.5	0.5	0.4	0.5	0.4	0.4	0.4	0.4	0.3	0.3	0.3

Table IV.5: Composition of the host rock, outer, inner damaged zones and core zone in REE (ppm). The standard deviation is given for 1σ . The normalized spread (R) allows to estimate the heterogeneity of the samples.

Trace element concentrations normalized to the world average shale give ratio around 1 for most elements except for As, Mo, Sb, Cs, Ba and W which have ratios up to 10 in the fault rocks (damage and core zones) (Fig. IV.12A). Normalized REEs values also have a flat profile comprised between 1 and 0.1. The LREE values are higher in the fault rocks than in the host rock. In contrast, the HREE values are similar in the damaged zone and the host rock but decrease in the core zone. A negative anomaly in Eu is observed in the fault rock and in the host rock, with an Eu/Eu* ratio of 0.66 in the host rock, 0.54 in the inner and outer damaged zone and 0.7 in the core zone. Only the magmatic intrusion in the basement shows a positive Eu anomaly (Eu/Eu* = 2.8).

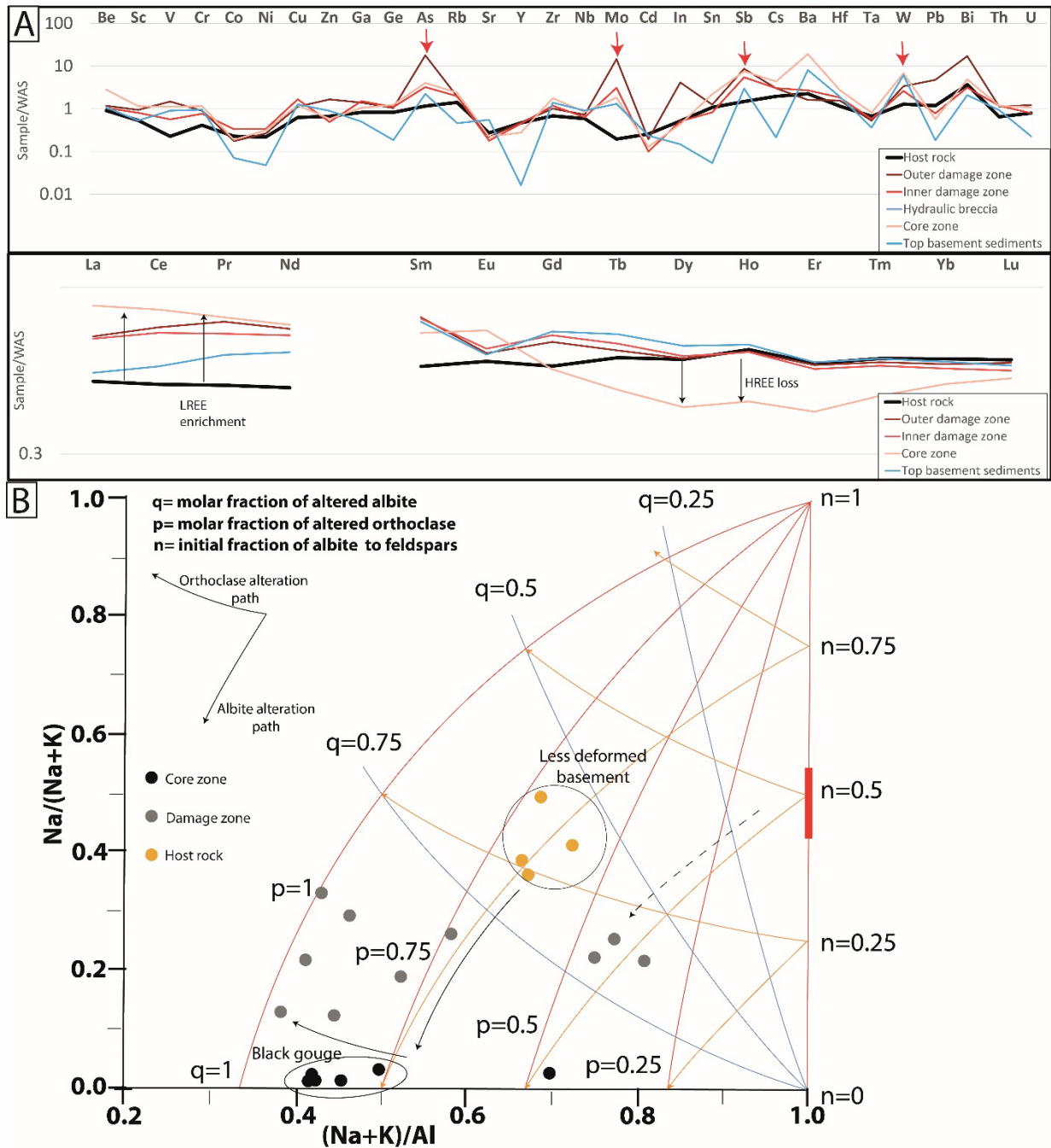


Figure IV.12: A-Trace and REE of host rock and fault rock normalized to World Average Shales (Wedepohl, 1971; Bau et al., 2018) as a proxy for the upper continental crust composition. B-Na/(Na+K) vs (Na+K)/Al plots of fault-rock compositions (Wibberley, 1999) showing progressive albite and orthoclase sericitization leading to formation of gouge.

3.5. Mass balance along the fault zone: bulk rock scale

3.5.1. Deformation induced hydration

The degree of alteration associated to deformation can be semi-quantified using the method of Wibberley and McCaig (2000) by plotting Na/(Na+K) vs (Na+K)/Al ratios for the different fault rock types (Fig. IV.12B). There is a progressive decrease of these ratio with deformation which is correlated to a loss Na and K compared to Al. In detail, the least deformed samples (host rock) have Na/(Na+K) ratios of 0.2 to 0.6, and (Na+K)/Al ratios of 0.6 to 0.8. For the most deformed sample

(gouge), the same ratios are close to 0 and of 0.4, respectively. These variations of composition highlight a general loss of Na and K of the rock associated to feldspar alteration. They are in complete accordance with petrographical observations.

3.5.2. Outer damage zone

In the damage zone, the main changes correspond to feldspar breakdown with related formation of white micas, and associated quartz and sulphide precipitation in the fractures (Fig. IV.7A and B).

For major elements (Fig. IV.13A, Appendix C Fig. C.7), the results of mass balance calculations are in relative agreement between the two methods (Zr and Al immobile elements (IE) and minimum mass change (MMC)). Taking Zr as the immobile element, a 35% loss of volume ($F_v = 0.65$) is calculated between the host rock and the outer damage zone. Taking Al as immobile give a loss of volume of 10% ($F_v=0.9$). Using the MMC method results in a gain of +1.5% ($F_v = 1.015$).

The results are detailed below for Zr immobile and the MMC due to the agreement between Al immobile and MMC. Corresponding element mass changes see a decrease of MnO (-100% for both methods) and CaO (-83% or -87%) for the IE/MMC methods respectively), an increase of TiO₂ (+21%/+90%), P₂O₅ (-1.6%/+54%), FeO (+70%/+166%) and LOI (+22%/+92%). The mass changes of Al₂O₃ (-30%/+10%), K₂O (-20%/+24%), MgO (32%/+5%) as well as SiO₂ (-37%/-1.52%) show significant discrepancy.

For trace elements, there is a good agreement between the two methods. Significant mass increase is obtained for some transition metals (Cu, W, Mo, Zn, As, Sb, W, Pb). There is significant decrease of alkaline-earth metals such as Ba, Sr, Y.

For REE, there is a slight increase for the LREE (but up to +70% for La and Ce), and a decrease for the HREE down to -30% for Tb, Dy, Ho, and Er.

Multiscale element transfer during crustal necking: the Mont-Blanc detachment fault

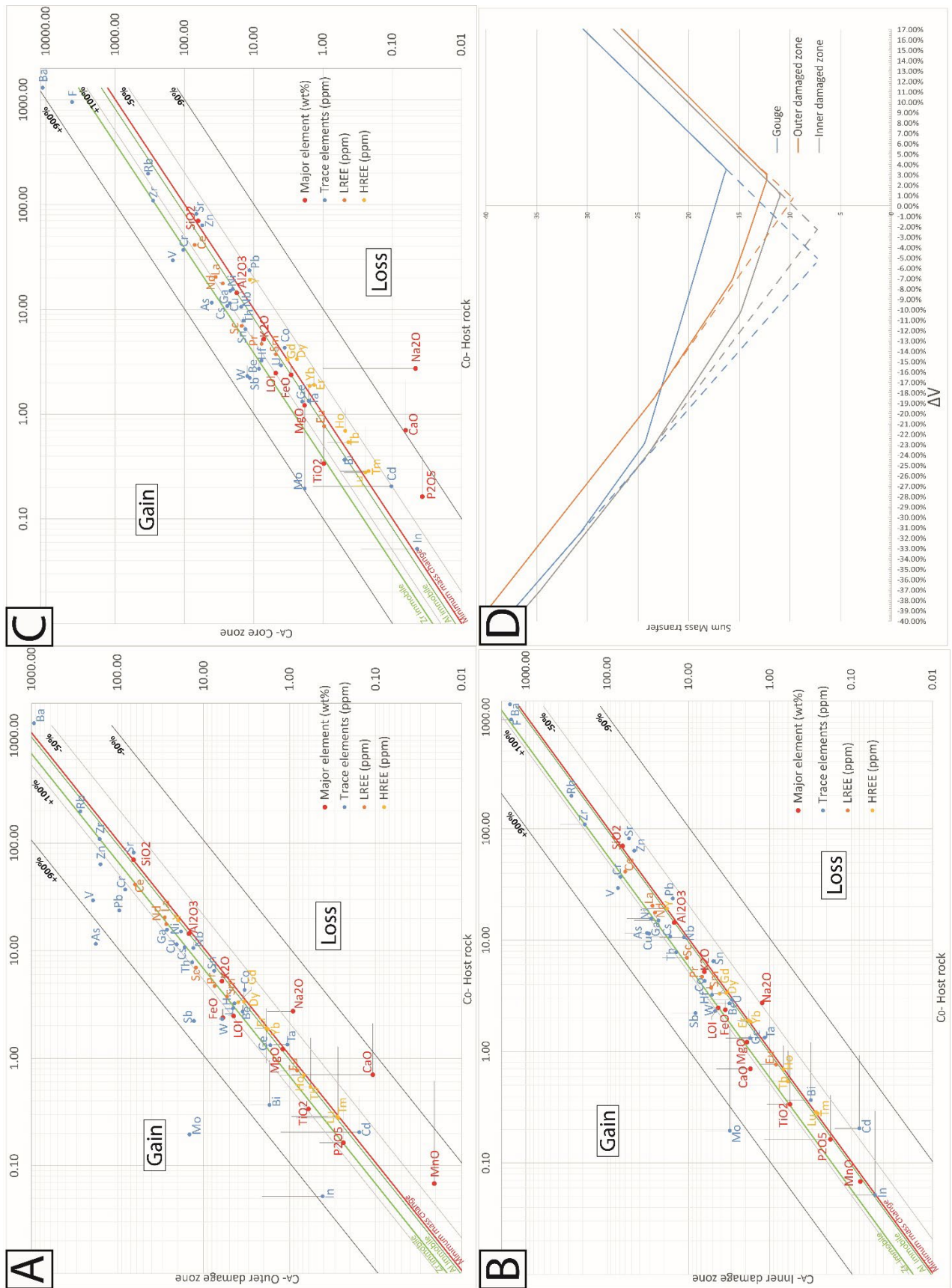


Figure IV.13: A, B, C: Log-log plots of the concentration of major, trace and rare-earth elements between the unaltered basement (CO) and the damaged rocks (CA) with A-outer damage zone, B- inner damage zone, C- core zone. The green straight lines are the isocons calculated using Zr and Al as the immobile elements (first method), and the red line is the one

calculated using the minimum mass change method. The black straight lines indicate mass change values as percentages. D-Sum of mass change vs volume change showing the minimum of mass change for each sample.

3.5.3. Inner damage zone

In the inner damage zone, feldspars are completely replaced by white micas, associated to important quartz comminution and quartz vein formation (Fig. IV.9A and B). Using Zr as the immobile element gives a corresponding loss of volume of -45% ($F_v = 0.55$) and using Al as immobile elements gives a loss of volume of 10% ($F_v=0.9$), whereas the MMC method results in only a slight decrease of +3.5% ($F_v = 0.965$, Fig. 14D), compared to the host rock.

The results of the Zr immobile element and MMC are presented below because of the good agreement between Al immobile and MMC methods. For major elements (Fig. IV.13B, Appendix C Fig. C.7), there is a large decrease of Na_2O (-73%/-53%, IE/MMC respectively), in contrast to the large increase in CaO (+43%/+155%). However, a discrepancy between the two methods arises for most other elements: Al_2O_3 (-39%/+7.57%), SiO_2 (-46%/-4%), MnO (-35%/+16%), MgO (-8%/+62%), TiO_2 (-2%/+73%), K_2O (-29%/+26%), FeO (-14%/+53%), and the LOI (+1.33%/+80 %).

For trace elements, both methods result in significant increase in transition metals (V, Cr, Cu, Mo, W), metals like Ge and Sb, alkaline earth such as Ba and non-metals such as As. In contrast, there is a large decrease in transition metals like Nb, Ta, Hf, Cd, metals like Zn, Ga, Sn, Pb and Bi and actinoids such as U and Th.

For the REE, an increase is visible for the LREE while the HREE remain immobile.

3.5.4. Core zone

The core zone is characterized by the presence of a gouge with a high phyllosilicate content and an important decrease of the grain size (Fig. IV.10A and B). The IE method (Zr) results in a very high loss of volume of -63% ($F_v = 0.2415$), in contrast to the MMC method, which results in a slight decrease of volume of -5% ($F_v = 0.95$, Fig. IV.13D), compared to the host rock. The IE method using Al immobile give a loss of volume of -23% ($F_v=0.77$). There is however no significant difference between the Al immobile and the MMC methods.

For major elements (Fig. IV.13C, Appendix C Fig. C.7), mass balance calculations show a large decrease of P_2O_5 (-91%/-77%, IE/ MMC respectively), Na_2O (-99%/-98%), and CaO (-96%/-90%), and an increase of TiO_2 (+10%/+ 191%). The results differ largely between the methods for K_2O (-47%/+38%), Al_2O_3 (-53%/+23%), MgO (-41%/+53%) and the LOI (-25%/+96%). Finally, for the IE method a total loss of -61 wt% is obtained, whereas for the MMC method a gain of +9 wt% is obtained, compared to the host rock.

For trace elements, there is an increase of F, Ba, As, V, and Mo, and a decrease of Pb, Zn, and Cd, for both methods. For the other trace elements, the behaviour depends on the method

considered. They appear depleted considering the IE method and enriched considering the MMC method.

For the REE, there is also a discrepancy between the methods. The IE method gives only a decrease in REE (LREE and HREE), whereas the MMC method results in an increase of LREE and a decrease of HREE (Fig. IV.13C)

3.6. Mass transfer associated to main mineralogical reactions

Petrographical observations show that deformation-assisted alteration of the basement host rock is controlled by 3 main reactions in the damage zone: feldspar sericitization (orthoclase to muscovite), biotite chloritization, and albite sericitization. The core zone is characterized by disappearance of chlorite and deformation induced of the cataclasite white micas into ultra- fine-grained white micas forming the dark matrix of the gouge.

In the following, the mass transfer associated to these reactions is presented based on EPMA chemical maps from the damage zone and the core zone. The phase compositions for mass balance calculation are extracted from the maps.

	<i>Min</i>	<i>SiO2</i>	<i>TiO2</i>	<i>Al2O3</i>	<i>FeO</i>	<i>MnO</i>	<i>MgO</i>	<i>CaO</i>	<i>Na2O</i>	<i>K2O</i>	<i>Ba</i>	<i>H2O</i>	<i>Density</i>
Biotite Alteration	Bt	38.1	4.4	22.1	16.8	0.3	5.9	0.1	0.1	5.3	0.8	6.1	3.1
	Chl	27.5	0.2	19.8	24.5	0.2	10.0	0.1	0.2	0.1	0.7	16.6	2.8
Orthoclase Alteration	Or	62.0	0.0	17.7	0.4	0.0	0.0	0.1	1.0	15.2	1.0	2.6	2.6
	Wm	49.9	0.0	28.4	2.1	0.0	1.3	0.0	0.0	12.1	1.2	3.8	2.8
Albite Alteration	Ab	64.7	0.6	19.3	1.2	0.0	0.1	0.1	9.1	4.0	0.1	0.8	2.6
	Wm	46.7	0.3	27.2	4.4	0.2	3.0	0.1	3.0	9.8	0.4	4.8	2.8
Gouge formation	Wm	50.4	0.0	29.4	1.2	0.1	1.5	0.2	0.0	10.3	0.5	6.2	2.8
	Ill	50.0	0.2	27.3	2.1	0.1	2.2	0.1	0.1	10.6	0.9	6.47	2.8

Table IV.4: Mineral composition (wt% ox.) extracted from the chemical maps. Bt=Biotite, Chl=Chlorite, Or=Orthoclase, Wm=White mica, Ab=Albite, Ill=Illite.

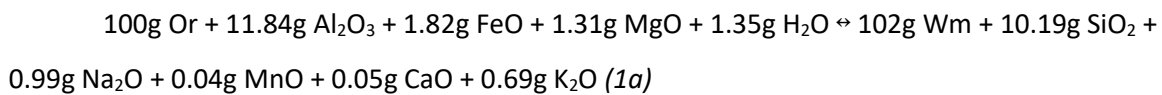
3.6.1. Orthoclase-muscovite alteration

One of the main mineralogical transformations is the replacement of orthoclase by white micas (sericitization). With the IE method (Al immobile), mass balance calculations (based on composition from Table IV.6) result in a significant volume increase of +57% ($F_v = +1.57$) associated to this reaction, whereas with the MMC method, a volume decrease of -4% ($F_v = 0.96$) is obtained

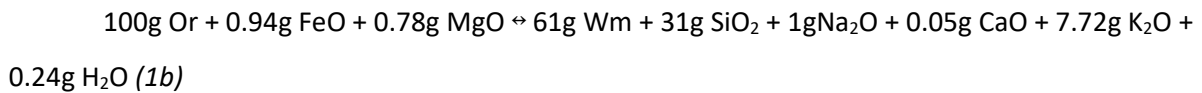
(Fig. IV.14A and B). The latter value is more consistent with petrographical evidence of a pseudomorphic reaction, added to a slight porosity increase (Fig. IV.7D).

Accordingly, for the analysed elements, considering the MMC method results in a large increase of Al₂O₃ (+74%). In both cases, the reaction is associated to a loss of mass for K₂O (-50%/-17% for the IE /MMC methods respectively), Na₂O (-97%/-95%), CaO (-74%/-57%), SiO₂ (-50%/16%) and MnO (-100%). A gain of mass is calculated for FeO (+264%/+509%). Moreover, no MgO is measured in the orthoclase and 1.27wt% is measured in the white micas indicating clear gains in Mg. However, the behaviour of BaO and the water content differs according to the methods considered (H₂O = -9%/+51% and BaO = 28%/+18%). The overall reaction leads to a gain of mass of +2.5 wt% with the MMC method, and a loss of -37 wt% with the IE one. The unrealistically high mass and volume loss calculated with the IE method, coupled to petrographical observations, strongly favours the MMC hypothesis.

Following mass balance calculations presented above, the overall mass balance reaction (for 100 g of initial orthoclase) can be written, considering isovolumic replacement (Equation 1a):



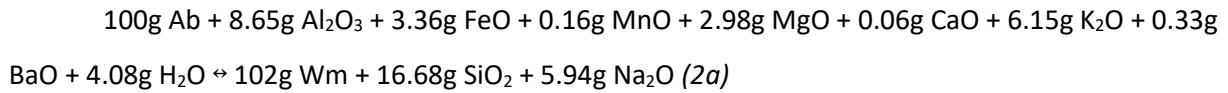
or alternatively, considering Al as immobile (Equation 1b):



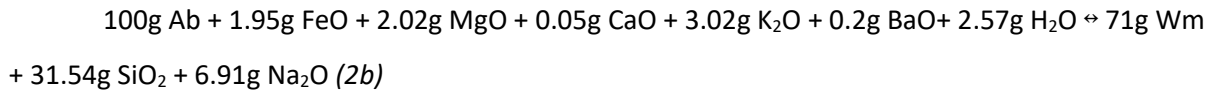
3.6.2. Albite-muscovite alteration

Similar to the orthoclase-to-muscovite reaction presented above, petrographical observations suggest that the alteration of albite into muscovite was pseudomorphic (Fig. IV.14C). This observation strongly differs with the large volume loss calculated using the IE method for this reaction (-37%; Fv = 0.67) (Fig. IV.14D). In contrast, the MMC method gives a change of volume of -5%, similar to the 5% porosity increase observed petrographically (Fig. IV.7E). Considering the MMC method, a significant gain of Al₂O₃ (+44%) is in turn obtained. Whatever the method chosen, this reaction is accompanied by gains of FeO (+163%/+282% for IE /MMC methods respectively), MnO (+777%/+1170%), K₂O (+76%/+155%), BaO (+171%/+293%) and H₂O (+313%/+498%), and by losses of SiO₂ (-48%/-25%) and Na₂O (-76%/-65%). Overall, the albite-to-muscovite reaction leads to a mass gain of 2.5 wt% for the MMC method, and a mass loss of -29 wt% for the IE one.

Considering the MMC method, the calculated mass balance reaction for the albite-to-muscovite transformation is (Equation 2a):



Considering Al as immobile (IE method), the reaction becomes (Equation 2b):

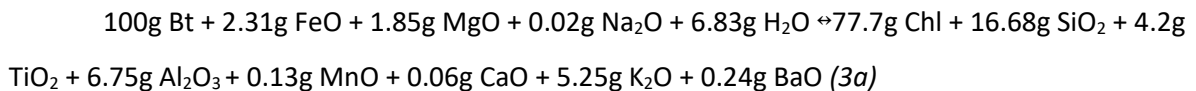


3.6.3. Biotite-Chlorite reaction

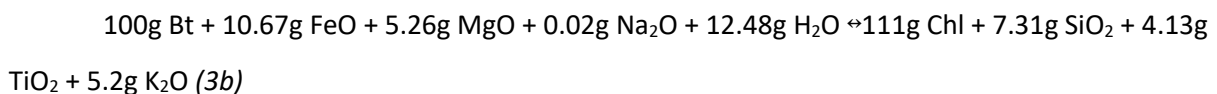
The biotite-to-chlorite reaction, which is associated to that of albite-to-muscovite, also appears petrographically as being pseudomorphic, as shown by the preservation of the cleavage and no evidence a significant volume change. The IE methods gives an increase of volume of +25% ($F_v = 1.25$), whereas the MMC gives a loss of volume of -2% ($F_v = 0.98$), as expected for a pseudomorphic reaction.

Mass balance calculations result in losses of SiO_2 (-19%/-36% for IE/ MMC methods respectively), TiO_2 (-100%), MnO (-22%/-39%), K_2O (-97%) and CaO (-34%/-48%), and in gains of FeO (+63%/+28%) MgO (+88%/+47%), Na_2O (+61%/+26%), BaO (+0.8%/-20%) and H_2O (+205%/+139%). Overall, the reaction leads to a loss of -12wt% for the MMC replacement, and a gain of 11 wt% for Al taken as immobile.

Considering the MMC method, the mass balance equation for biotite-chlorite alteration is (Equation 3a):



For the IE method, it becomes (Equation 3b):



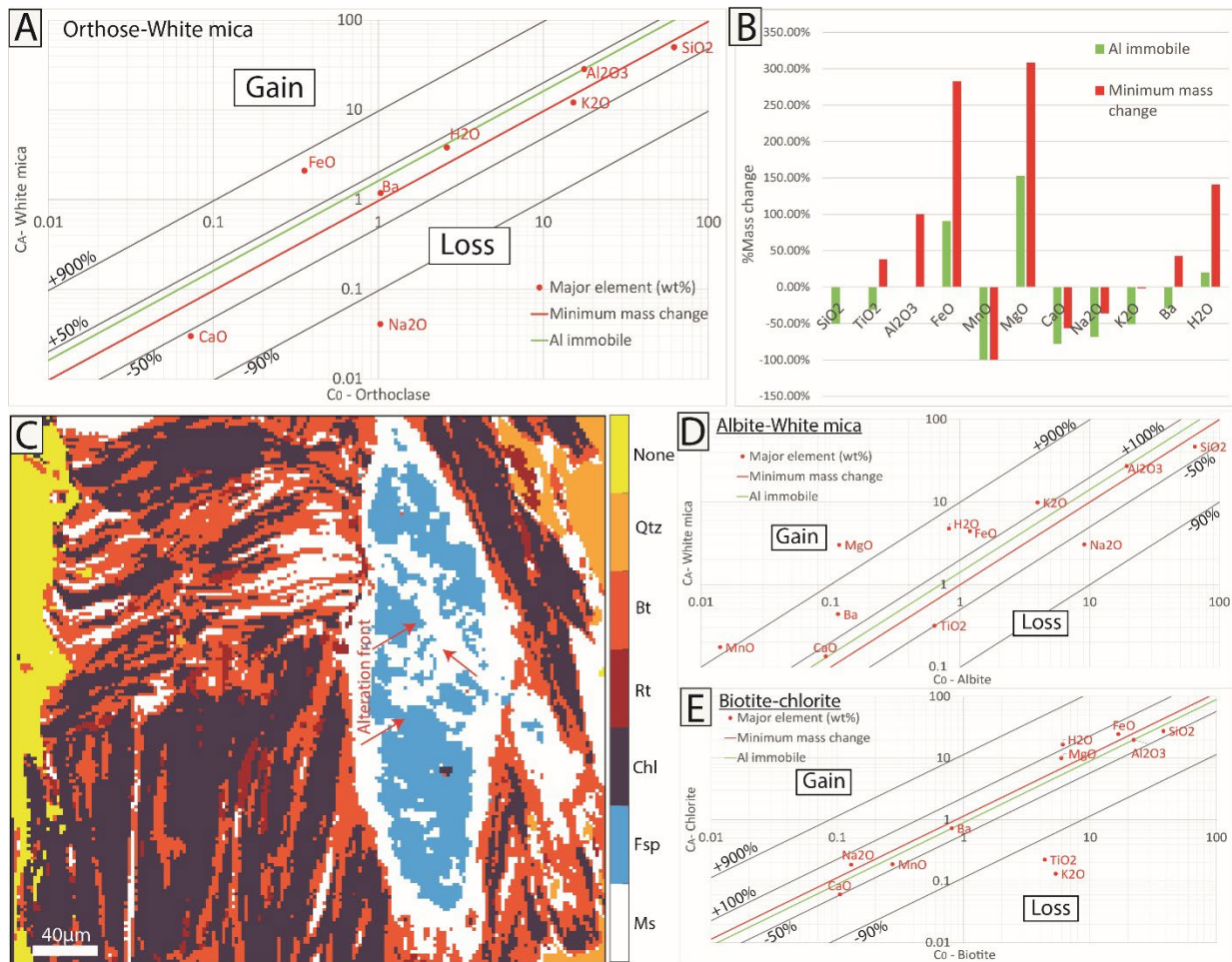
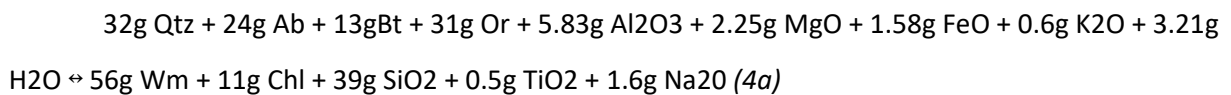


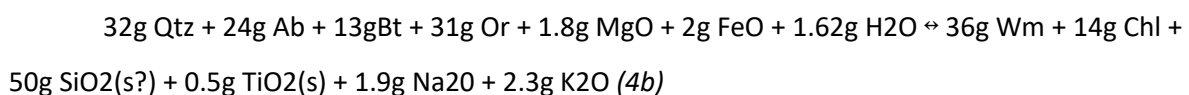
Figure IV.14: A- log-log plot of the concentration of major elements of the orthoclase and muscovite with isocons calculated using the IE (Al immobile) and the MMC methods. B- Histogram of the element mass change using the IE (Al immobile) and the MMC methods. C- Mineral map of the biotite/chlorite and albite/white micas alteration of the basement. D- Log-log plot of the concentrations of major element for the albite-muscovite alteration with isocons calculated using the IE (Al immobile) and the MMC method. E- Same as D but for the biotite-chlorite alteration reaction.

3.6.4. Coupled mass transfer

Knowing the phase proportions of the host rock (Fig. 6), it is possible to calculate the mass balance equation associated to complete basement alteration by combining equations (1), (2) and (3). For the MMC method, the corresponding equation is (Equation 4a):



Taking Al as immobile (IE method), the balance becomes (Equation 4b):



Therefore, considering the MMC method, the complete replacement of feldspars and biotite by muscovite and chlorite results in gains of Al, Mg, Fe, K and water, and losses of Ti, Si and Na. With the IE method, it results in gains of Mg, Fe and water and losses of Ti, Na, K, and Si.

3.6.1. Deformation induced reaction: Cataclasite to gouge transition

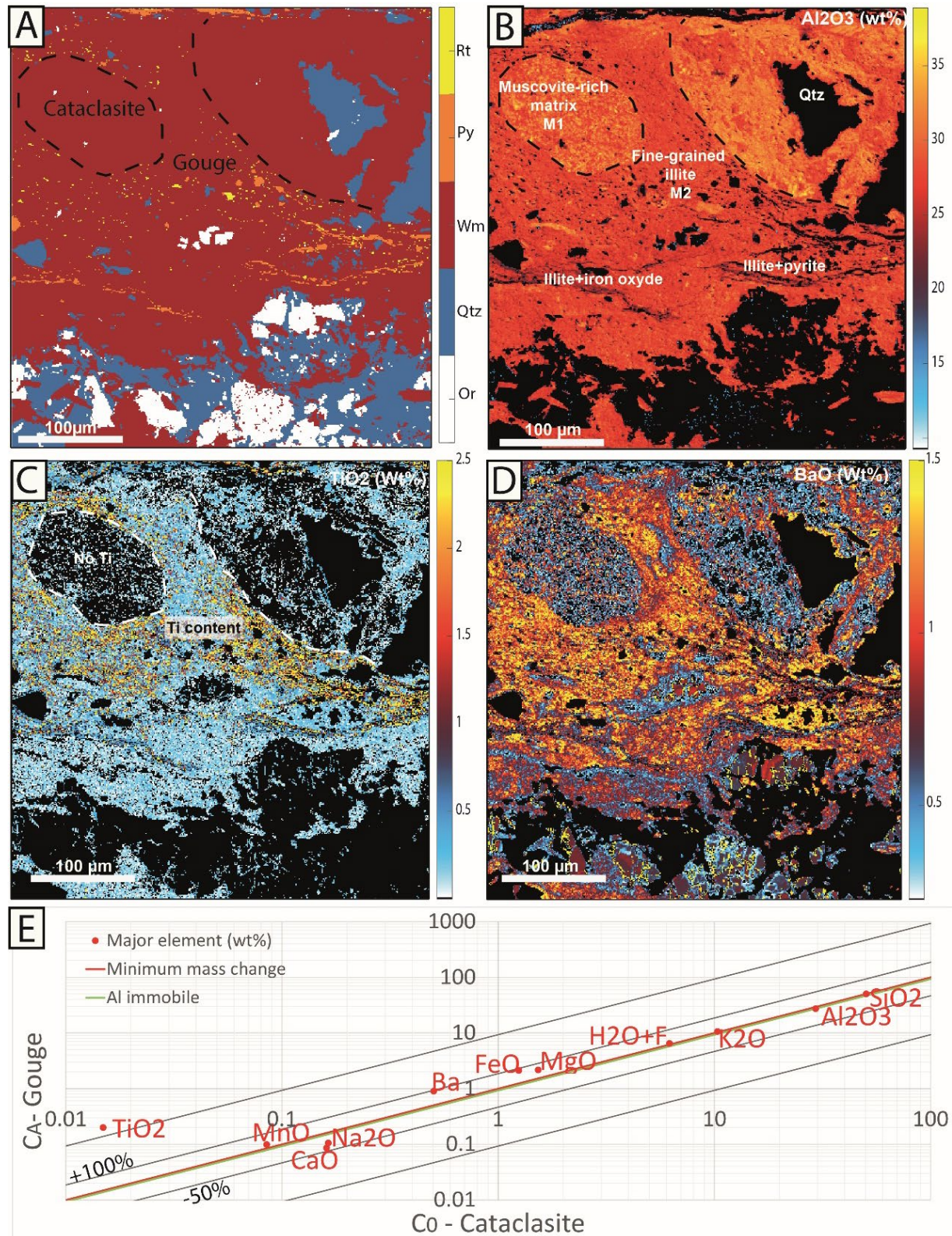


Figure IV.15: EPMA chemical map with associated mass balance calculation. A- Phase map of the gouge-cataclasite transition. Rt=Rutile, Py=Pyrite, Wm=White micas, Qtz=Quartz, Or=Orthoclase. B- Al_2O_3 map (in wt%) for the white mica phase. C- TiO_2 map for the white mica phase showing absence of TiO_2 in the cataclasite and presence of TiO_2 in the gouge matrix. D- BaO map for the white mica phase showing increase of concentration in the Ba in the gouge. E- Log-log plot of the

concentration of major elements in the cataclasite and the gouge with isocons calculated using the IE method (Al immobile) and the MMC method.

The shear induced transformation of the cataclasite matrix is associated to changes in composition. First, the concentration of F is higher in the gouge matrix up to 1.4 wt% in the illite. These mineralogical changes are associated to a significant increase of TiO₂ and BaO contents (Fig. IV.15C and D), passing from 0 to 2 wt (%) for TiO₂ and 0.5 to 2 wt (%) for BaO. Mass balance calculation between illite in the gouge and muscovite in the cataclasite give more information on the chemical variations using the MMC method ($F_v = 1.0595$) and the IE method (Al₂O₃ immobile; $F_v = 0.99$) (Fig. IV.15E). These very limited volume changes demonstrate that deformation was thus iso-volumic. Therefore, there is a good agreement between the two methods. There is an increase of BaO, FeO, MgO, MnO and TiO₂, a decrease of CaO and Na₂O, and minor changes of the water content. These changes are in good agreement with petrographical observations showing the presence of rutile and pyrite in the gouge matrix. In the gouge, the Ti increase (Fig. IV.15 C and E) is related to the presence of micro-rutile and to the incorporation of Ti in the illite (Appendix C Fig. C.5).

3.7. Fluid inclusions on veins along the fault zone

3.7.1. Quartz-vein from the damage zone

Fluid inclusions (average size of 7 μm) were found in the type 1 and type 2 quartz veins from the inner damage zone (Fig. IV.16C and D, Appendix C Tab. C.4). In the type 1 veins, primary, two-phase aqueous inclusions are parallel to the border of the crystals. They present freezing temperatures (T_f) of -51 to -53°C ($n = 18$). Only 2 melting temperatures (T_m) could be measured, with values ranging of -4 and -7 °C (average = -5.5°C; mode of -5/-6°C; Fig. IV.16B), which corresponds to a salinity of 11 wt% (NaCl equiv.). Similar salinities were estimated using Raman spectrometry ($n = 34$; 3 to 12 wt%, average = 7.7 wt%, mode = 8/9 wt%). Homogenization temperatures (T_h) range from 130 to 210°C ($n = 21$, average = $200 \pm 30^\circ\text{C}$, mode = 190/210°C; Fig. IV.16A). In the veins type 2, slightly bigger primary aqueous inclusions are parallel to the border of the veins (15 to 20 μm). Their freezing temperature (-48 to -55°C, $n = 18$) precludes the presence of CaCl₂. The eutectic temperature (T_e) was measured on 18 large inclusions (20 μm) give temperatures around -21.5°C to -23°C (Fig. IV.16F), indicating the predominance of NaCl with the possible presence of KCl (T_e of NaCl-KCl-H₂O at -22.9°C, Goldstein, 1994). The T_m measured on 18 inclusions larger than 10 μm give temperatures of -4.5 to -6.3°C (average = -5.7°C; mode = -5/-6°C; Fig. IV.17B), corresponding to a salinity of 11.5 ± 0.7 wt% NaCl-equiv. Values calculated from Raman analyses are relatively smaller ($n = 10$; 4 to 7 wt%; average = 5 wt%; mode = 5/6 wt%). T_h are comprised between 135 and 250°C ($n = 26$, average = $173 \pm 19^\circ\text{C}$, mode of 190-200°C; Fig. IV.16A). For both types of inclusions, Raman analysis of the gas bubbles revealed the absence of gas other than vapor.

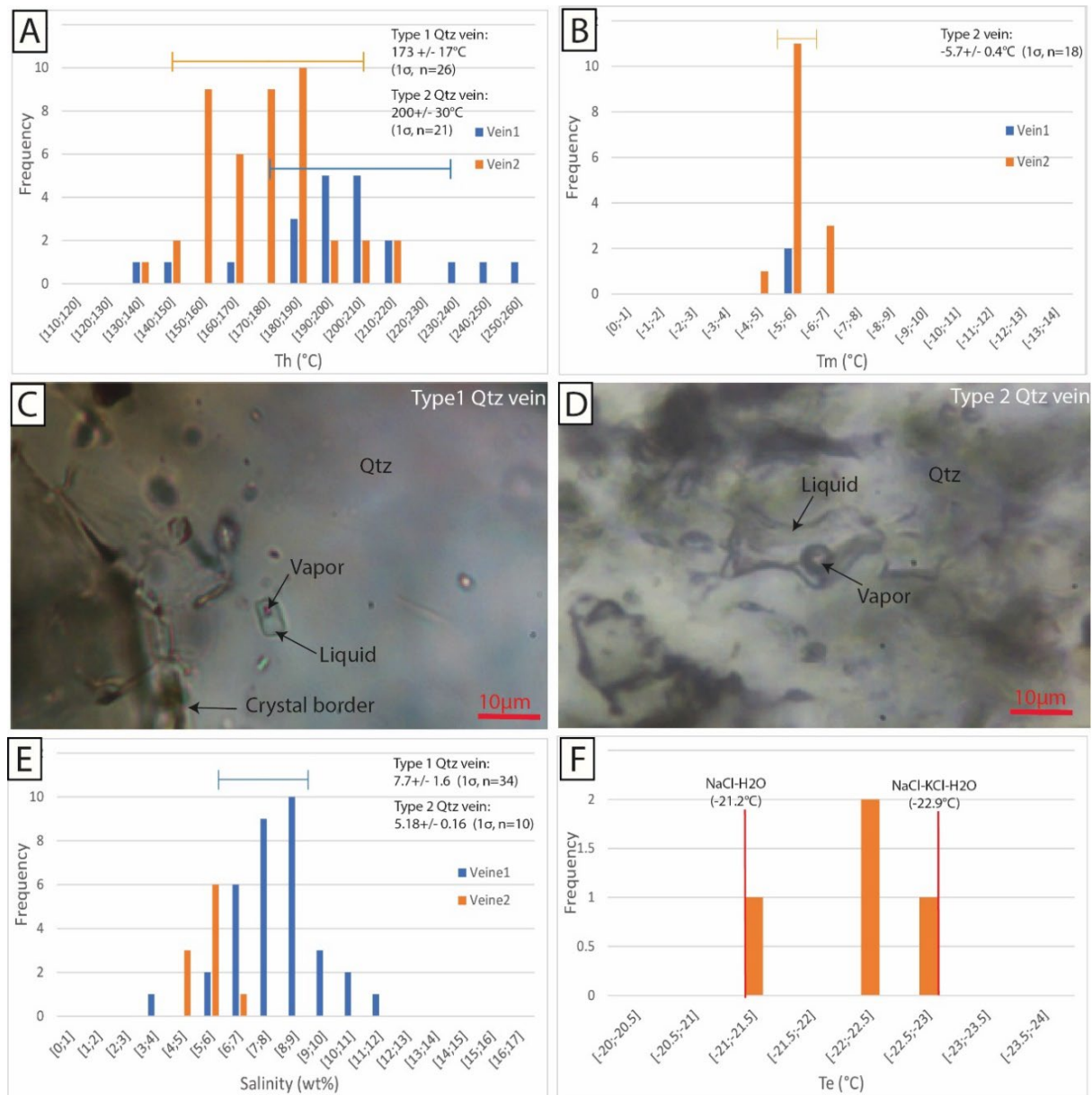


Figure IV.16: A- Histogram of the Th of fluid inclusions from quartz grains from the 2 generations of veins from the inner damage zone (average with 1σ uncertainty). B- Same as A but for the Tm. C- Optical image (PPL) of an inclusion from a type 1 quartz vein. D- Optical image (PPL) of an inclusion from a vein 2. E- Histogram of salinity (wt%) obtained with Raman spectrometry for the same 2 generations of veins. F- Histogram of Te measured for the larger inclusions in the type 2 quartz vein.

3.7.2. Qtz-Hy veins in the fault core

3.7.2.1. Fluid inclusions

In the quartz grains of the quartz-hyalophane veins, fluid inclusions are widespread (Appendix C Tab. C.5). Primary aqueous inclusions (5 to 10 μm) parallel to crystal or vein borders are crosscut by secondary aqueous inclusions. The primary inclusions are two-phase (liquid-vapor, Fig. IV.17C). Their Th range from 160 to 240°C (n = 40, average = 199 ± 14°C, mode = 200/210°C, Fig. IV.18A and Tab. C.5). The Tm range from -4.5 to -9.9°C (n = 21, average = -6.7, mode = -6/-7°C, Fig. IV.17B), corresponding to a salinity of 13.4 wt% NaCl-equiv. The salinity determined using Raman

spectrometry (n = 24) is of 9.4 ± 4.5 wt% with a mode of 9/10wt%. Eutectic temperatures (n = 8) are close to -21°C indicative of the NaCl-H₂O system.

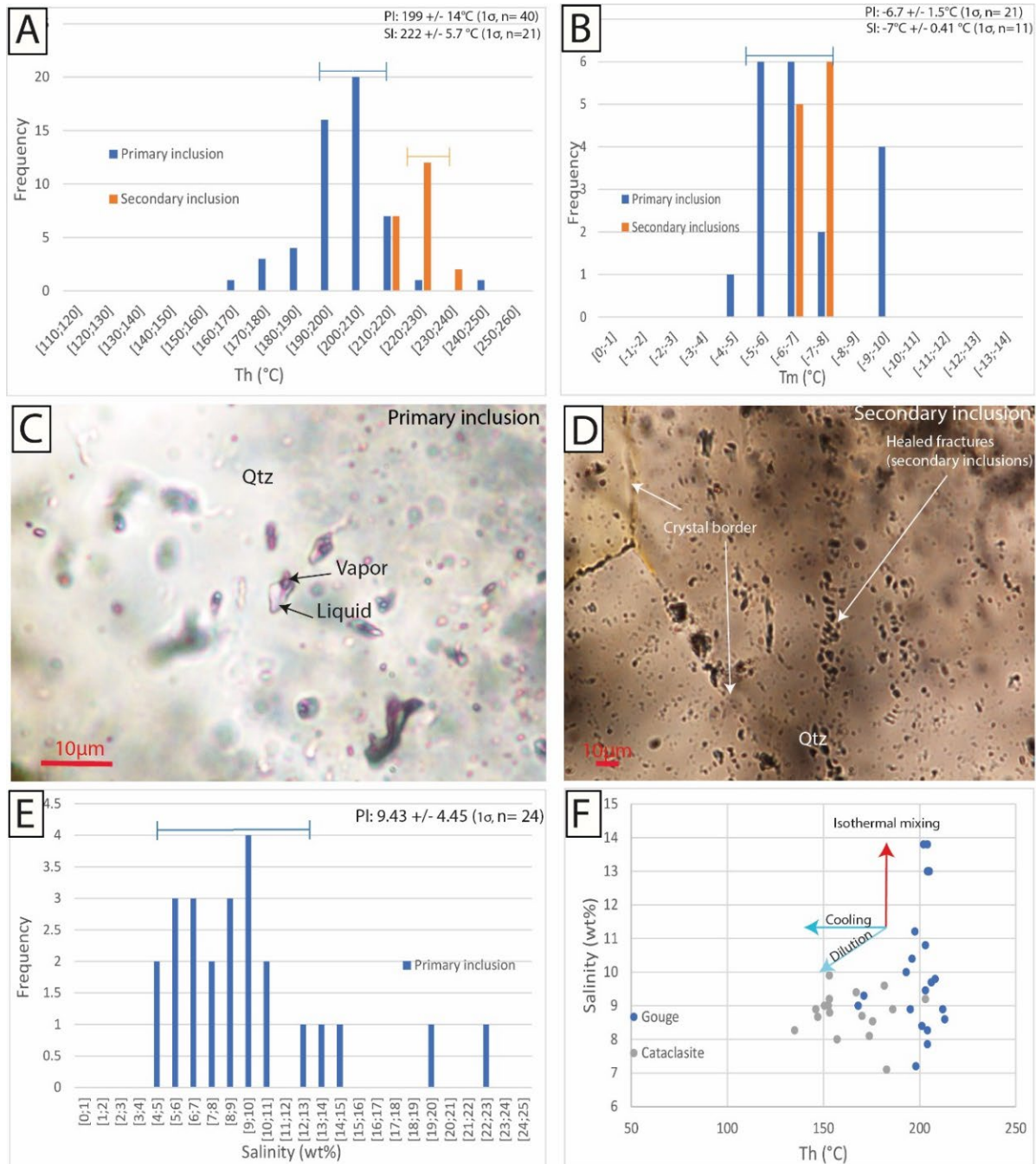


Figure IV.17: A- Histogram of the Th of primary and secondary fluid inclusions of vein-filling quartz grains from the core zone. B- Same as A but for Tm values. C- Optical images (PPL) of the primary inclusions. D- Optical image (PPL) of the secondary inclusions. E- Histogram of salinity (wt%) obtained with Raman spectrometry for the primary fluid inclusions. F- Th-salinity plot for the fluid inclusions from cataclasite and gouge.

Two-phase secondary inclusions correspond to healed fractures crosscutting the veins (Fig. IV.17D). Their Tf were measured between -40 and -52°C (n = 11), precluding at least the presence of CaCl₂. Their Tm are comprised between -6.6 and -7.6°C (n = 11; average = -7°C ; mode = $-7/-8^\circ\text{C}$; Fig.

IV.17B), whereas their Th range from 212 to 239°C (n= 21, average = 223 ± 6°C; mode = 220/230°; Fig. IV.17A).

Th-salinity plot (Fig. IV.17F) for the inner damage zone and the core zone shows a variation of the salinity for the same temperature in the gouge, while there is a slight change of salinity associated to temperature variation in the cataclasite.

3.8. Datation of the detachment fault

3.8.1. U-Pb datation of calcite in the damage zone

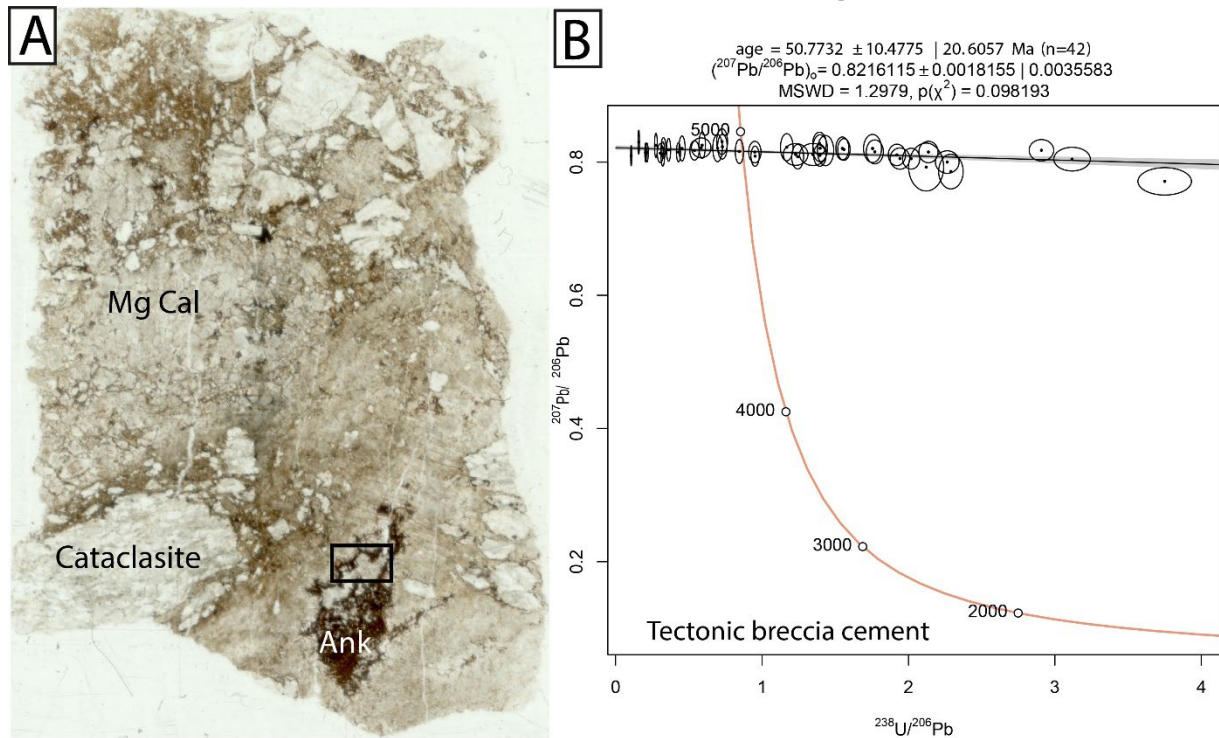


Figure IV.18: A- Microphotograph (PPL) of the fault breccia showing a dolomite-ankerite rhombs cemented by calcite overprinted by Mg calcite. The dating was performed on the calcite cement from the ankerite-dolostone primary texture. B- Tera-Wasserburg concordia graph showing the result of U-Pb dating on the calcite.

In the Mont-Blanc massif, calcite cement on tectonic breccias in the basement have been observed. This cement corresponds to fine-grained recrystallized Mg calcite. However, remnants of the initial cement are locally observed corresponding to large calcite crystals and dolomite rhombs associated ankerite (Fig. IV.18A). The space between the rhombs is filled by calcite. The calcite filling the spaces was dated giving an age of 50 ± 21 Ma. This corresponds to a really young age compared to the one expected (Fig. IV. 18B). However, this age is also older than the onset of convergence observed in the Mont-Blanc massif.

3.8.2. $^{40}\text{Ar}/^{39}\text{Ar}$ ages of hyalophanes in the core zone

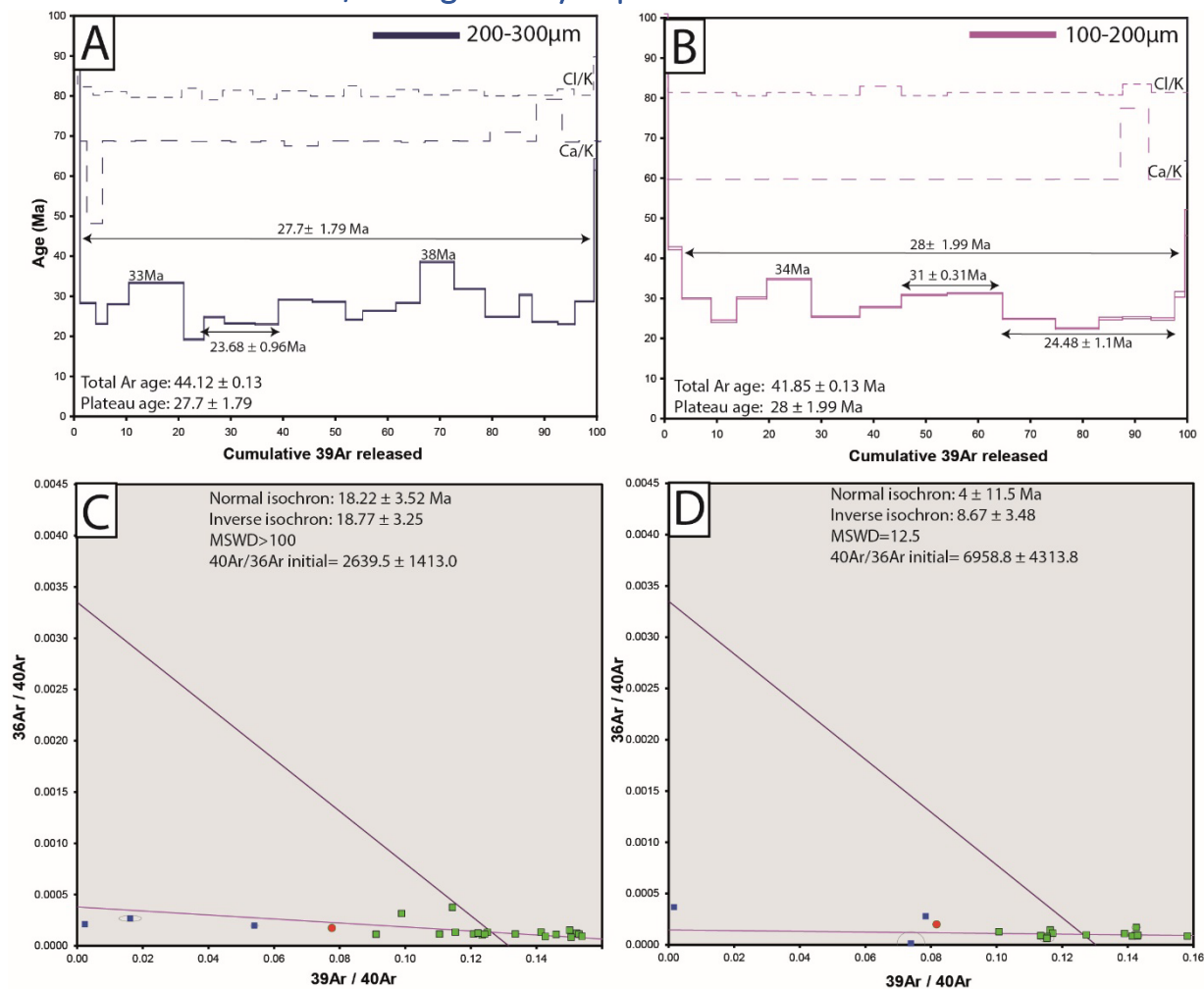


Figure IV.19: A- The $^{40}\text{Ar}/^{39}\text{Ar}$ step-release spectra for the fraction 100-200 μm . B- The $^{40}\text{Ar}/^{39}\text{Ar}$ step-release spectra for the fraction 200-300 μm . C- Isochron diagram for the fraction 100-200 μm . D- Isochron diagram for the fraction 200-300 μm .

Two size fractions (100-200 μm and 200-300 μm) of hyalophane have been measured for Ar-Ar dating (Table IV.3). The $^{40}\text{Ar}/^{39}\text{Ar}$ step release spectra does not show a clear plateau age (Fig. IV.18A and B). The first size fraction gives a plateau age of 27.7 ± 1.79 Ma with a minimum plateau age of 23.68 ± 0.96 Ma (Fig. IV.19A). The total Ar content gives an age of 44.12 ± 0.13 Ma. Changes in the Cl/K and Ca/K ratio are associated to decrepitation of inclusions during step heating. At around 10 and 70% Ar release, bumps are observed which are not correlated to changes of Cl/K and Ca/K indicating that they are not associated to Cl-rich inclusion decrepitation. The final heating stages are associated to an age of 197 Ma. The isochron graph ($^{36}\text{Ar}/^{40}\text{Ar}$ vs $^{39}\text{Ar}/^{40}\text{Ar}$; Fig. IV.19C) show poor correlations with a MSWD above 100. The normal and inverse isochron give an age of 18.22 ± 3.52 Ma and 18.77 ± 3.25 Ma respectively.

The second size fraction give a plateau age of 28 ± 1.99 Ma with a minimum plateau age of 24.48 ± 1.1 Ma (Fig. IV.19B). The total Ar gives an age of 41.85 ± 0.13 Ma. At around 20 and 40% of Ar release, bumps in the spectrum is observed correlated to the changes of K/Cl and Ca/K ratio

Multiscale element transfer during crustal necking: the Mont-Blanc detachment fault

associated to inclusions decrepitation. The isochron (Fig. IV.19D) diagram show a better correlation, still poor, with an MSWD of 12.5. The normal and inverse isochrone give an age of 4 ± 11.5 Ma and 8.67 ± 3.48 Ma respectively. The minimum plateau ages obtained are 23.68 ± 0.96 Ma and 24.48 ± 1.1 Ma for the two different fractions (Fig. IV.19A). Spikes with ages up to 14 Ma older than the minimum plateau ages are visible.

	40Ar/ 39K	SD (2 σ)	36Ar/ 40Ar	SD (2 σ)	39K/ 36Ar	SD (2 σ)	37Ca/ 39K	38Cl/ 39K	%39 Ar	Cumulative release	Age (Ma)	SD (2 σ)
<i>200-300μm</i>												
1	394.394 4	1.6217	0.0024	0.000 01	11.2516	0.0576	0.0268	0.0268	1.17	1.17	1064.22 5	3.308
2	7.7619	0.0243	0.1144	0.000 28	305.079 3	4.0062	0.0000	0.0000	2.99	4.16	28.296	0.088
3	6.3245	0.0287	0.1523	0.000 55	1228.41 35	82.5876	0.0054	0.0054	2.24	6.39	23.089	0.104
4	7.6792	0.0151	0.1251	0.000 18	945.268 9	30.6340	0.0034	0.0034	4.11	10.51	27.997	0.055
5	9.1591	0.0177	0.0989	0.000 16	313.444 2	2.3118	0.0023	0.0023	10.50	21.01	33.343	0.064
6	5.2630	0.0411	0.1811	0.001 23	1155.94 00	78.7806	0.0038	0.0038	3.86	24.87	19.235	0.150
7	6.7903	0.0407	0.1414	0.000 76	1057.13 60	57.7054	0.0000	0.0000	3.93	28.80	24.778	0.148
8	6.3555	0.0284	0.1501	0.000 58	980.024 5	40.3946	0.0000	0.0000	5.84	34.64	23.202	0.103
9	6.3137	0.0355	0.1530	0.000 77	1334.81 72	78.5681	0.0000	0.0000	4.48	39.12	23.050	0.129
10	7.9897	0.0164	0.1208	0.000 23	1039.65 74	21.1504	0.0006	0.0006	6.48	45.60	29.120	0.059
11	7.8449	0.0168	0.1235	0.000 24	1170.69 46	30.2177	0.0048	0.0048	6.34	51.94	28.596	0.061
12	6.6200	0.0251	0.1460	0.000 51	1298.64 80	55.1781	0.0032	0.0032	3.28	55.22	24.161	0.091
13	7.2279	0.0146	0.1335	0.000 25	1147.35 10	21.6467	0.0000	0.0000	6.39	61.61	26.364	0.053
14	7.7774	0.0206	0.1242	0.000 30	1082.94 57	30.3671	0.0000	0.0000	4.59	66.20	28.352	0.075
15	10.6016	0.0210	0.0911	0.000 17	798.585 1	16.7722	0.0031	0.0031	6.53	72.73	38.538	0.075
16	8.7418	0.0184	0.1105	0.000 21	957.021 1	22.0463	0.0055	0.0055	5.94	78.68	31.837	0.066
17	6.8148	0.0137	0.1427	0.000 27	1546.08 00	39.9015	0.0000	0.0000	6.48	85.16	24.867	0.050
18	8.3306	0.0405	0.1153	0.000 51	868.834 1	40.0633	0.0046	0.0046	2.46	87.62	30.352	0.146
19	6.4734	0.0168	0.1506	0.000 36	1786.02 26	68.0835	0.0000	0.0000	4.96	92.58	23.629	0.061
20	6.3129	0.0252	0.1539	0.000 56	1622.53 91	88.1595	0.0017	0.0017	3.24	95.82	23.047	0.092
21	7.8754	0.0257	0.1222	0.000 36	972.593 6	32.8406	0.0035	0.0035	3.68	99.50	28.706	0.093
22	17.4184	0.3948	0.0540	0.001 19	273.487 8	23.7190	0.0055	0.0055	0.46	99.95	62.892	1.401
23	56.9289	12.289 9	0.0162	0.003 49	60.4616	14.6132	0.3161	0.3161	0.05	100.00	197.927	40.47 3
<i>100-200μm</i>												
1	526.162 2	9.5191	0.0004	0.000 003	4.6054	0.0894	0.0821	0.0563	0.72	0.72	1315.47 7	16.90 9
2	11.6985	0.1053	0.0003	0.000 022	282.606 1	22.9334	0.0000	0.0000	2.61	3.33	42.510	0.378
3	8.2244	0.0461	0.0001	0.000 016	804.631 7	86.8900	0.0089	0.0000	5.58	8.92	29.990	0.167

4	6.6588	0.0799	0.0002	0.000 022	840.505 9	106.273 1	0.0083	0.0000	4.86	13.78	24.319	0.290
5	8.2515	0.0678	0.0001	0.000 015	1027.63 66	130.898 5	0.0000	0.0005	5.78	19.56	30.088	0.245
6	9.5507	0.0474	0.0001	0.000 009	791.847 9	54.2689	0.0006	0.0000	8.53	28.09	34.780	0.171
7	6.9573	0.0418	0.0001	0.000 011	1265.49 64	123.968 9	0.0000	0.0004	9.27	37.35	25.402	0.152
8	7.6245	0.0494	0.0001	0.000 012	1307.99 85	157.271 2	0.0026	0.0009	7.94	45.29	27.819	0.179
9	8.4580	0.0455	0.0001	0.000 010	1439.60 20	171.813 1	0.0032	0.0001	8.75	54.04	30.835	0.164
10	8.5809	0.0372	0.0001	0.000 008	1275.01 10	110.191 0	0.0007	0.0000	10.62	64.66	31.279	0.135
11	6.8170	0.0382	0.0001	0.000 010	1622.33 10	184.924 2	0.0040	0.0000	10.14	74.80	24.893	0.139
12	6.1608	0.0466	0.0001	0.000 014	1845.91 33	298.672 3	0.0000	0.0000	8.33	83.12	22.512	0.169
13	6.8393	0.0864	0.0001	0.000 023	1563.90 74	394.086 4	0.0000	0.0017	4.45	87.58	24.974	0.313
14	6.8934	0.0706	0.0001	0.000 018	1639.91 75	349.398 8	0.0001	0.0007	5.47	93.05	25.170	0.256
15	6.7989	0.0846	0.0001	0.000 022	1565.52 15	382.706 7	0.0000	0.0000	4.54	97.59	24.827	0.307
16	8.5053	0.1967	0.0001	0.000 041	1794.24 55	1151.08 30	0.0000	0.0000	1.96	99.55	31.005	0.711
17	13.4820	0.9013	0.0000	0.000 115	5762.55 53	51723.4 540	0.0000	0.0000	0.45	100.00	48.905	3.226

Table IV.5: Argon isotopic ratio for each heating stage associated to the calculated age

4. Discussion

4.1. Interpretation of the ages obtain along the detachment fault

1.1.1. U-Pb ages on calcite

The U-Pb age obtain of 50 ± 21 Ma and clearly older than the main alpine deformation in the Mont-Blanc between 20-30Ma. The occurrence of flysch deposits on the Mont-Blanc dated at 34Ma indicates an onset of tectonic burial younger than 34Ma. This means that these tectonic breccias age are unlikely related to the emplacement of the Penninic thrust. It is therefore not clear if this age corresponds to a partial reset of older calcite due to Alpine metamorphism, or if this age has a real geological significance and marks that of calcite precipitation.

The question of the temperature of opening and closure of U-Pb in calcite is not really well constrained. However, some observation and data concerning Pb diffusion can be used to constrain the problem of calcite opening in the Mont-Blanc massif.

Loss of Pb can be achieved through volume diffusion in calcite for temperature between 250 and 300°C (Cherniak, 1997). Beside, grain deformation and fluid infiltration can also alter the U/Pb ratio (Meinhold et al., 2020). Condition of ca. 330°C registered in the Col du Bonhomme implies that partial reset of the U/Pb ratio could have occurred. Indeed, calculations on the temperature of opening, reset and closing following the method of Gardés and Montel (2009) and based on the data of Pb diffusion from Cherniak, (1997) and using the prograde and retrograde gradients from Boutoux

et al., (2016) gives a T_{opening} of 238°C, a T_{reset} of 541°C and a T_{closure} of 421°C. For grains of 1 mm the T_{opening} is 330°C. Temperature in the Col du Bonhomme are above the opening temperature calculated meaning that partial reset is indeed possible. In addition, most of the cement appears recrystallised forming equigranular twinned calcite which indicates post-deposit transformations. Based on these elements it seems probable that these tectonic breccias are pre-Alpine submitted to partial reset during Alpine prograde metamorphism.

1.1.2. Age of the last event recorded along the fault: the hyalophane veins

Although hyalophanes had been recognized in the Western Alps (Legenbach ore deposits in the Gottard massif (Hofmann and Knill, 1996) and the Trou des Romain mine in the Mont-Blanc massif (Castello, 1977), this is the first age obtain for this mineral in the western Alps.

The $^{39}\text{Ar}/^{40}\text{Ar}$ age of hyalophane (ca. 27 Ma) fits with the timing of the emplacement of the Penninic unit, which is the earliest Alpine event in the ECM and marks the onset of maximum burial and heating in the Mont-Blanc massif (Boutoux et al., 2016). Therefore, the new age demonstrates that the gouge is undoubtedly pre-Alpine as the veins crosscut the gouge foliation. However, questions remain whether this age is geochronological (precipitation age) or thermochronological corresponding to the exhumation of the massif (Spikings and Popov, 2021). The thermal gradient during prograde alpine path is relatively important, up to 40°C/Ma followed by a stable temperature reached during ca. 10 Ma before exhumation and cooling (Boutoux et al., 2016).

Petrographical arguments tend to show that these hyalophanes are, indeed, pre-alpine. Reworking of the hyalophanes as clasts is observed in the sediments (Dall'Asta et al., 2022). These feldspars show the same euhedral shape as well as the same blue emission in cathodoluminescence (Dall'Asta et al., 2022) characteristic of hyalophanes (Yamauchi and Nishido, 2018). The presence of a miscibility gap for the hyalophane composition (Fig. IV.11B), the homogenization temperatures of cogenetic quartz ($T = 200^\circ\text{C}$) as well as the brittle deformation observed in the veins point toward a relatively low temperature of hyalophane precipitation and deformation ($T < 200^\circ\text{C}$).

Multiscale element transfer during crustal necking: the Mont-Blanc detachment fault

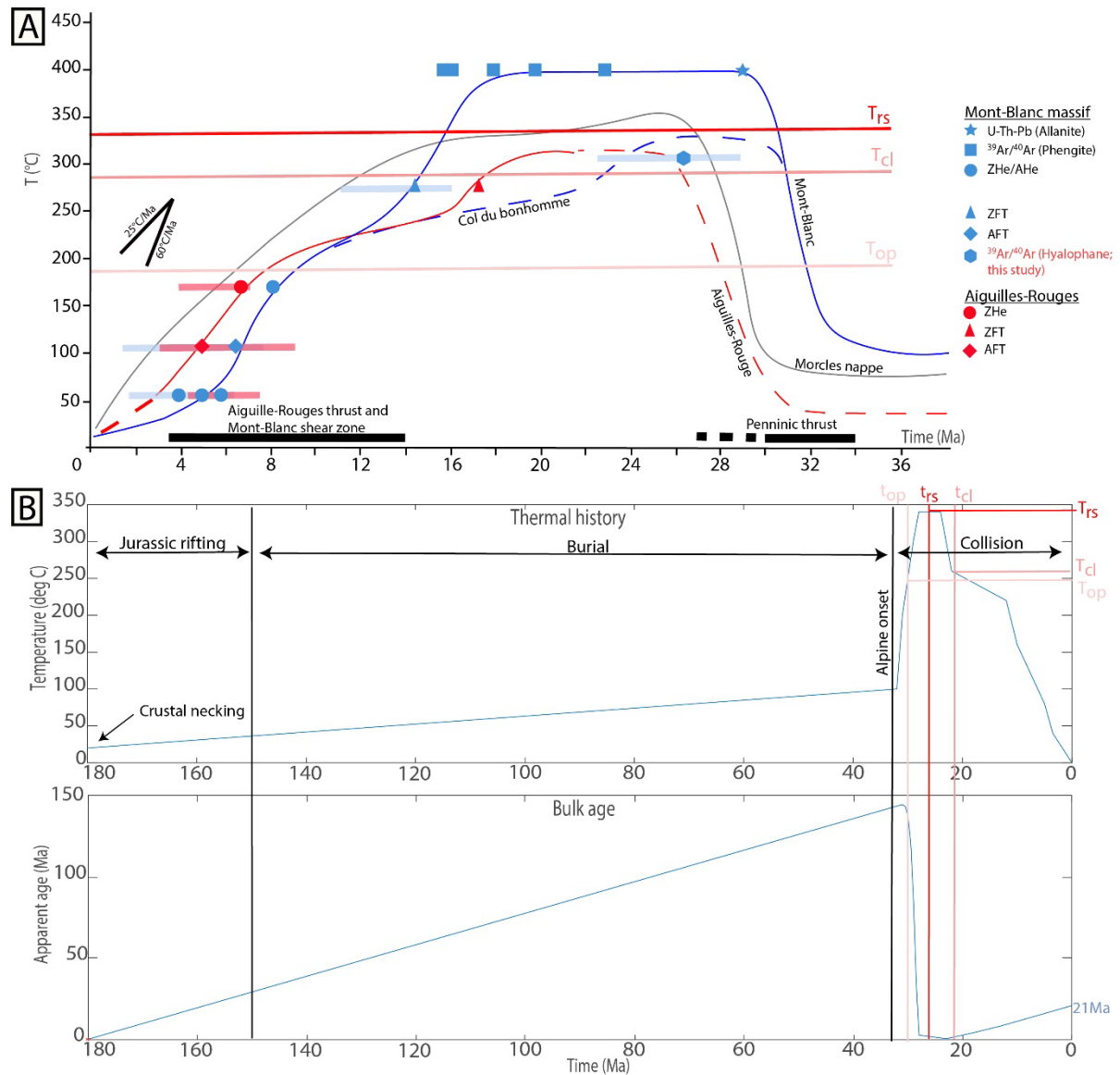


Figure IV.20: A- Thermal evolution of (i) the Mont-Blanc and Aiguilles-Rouge massifs (from Boutoux et al., (2016), based on age data from Leloup et al., 2005), Rolland et al., (2008), Glotzbach et al., (2008) and Cenki-Tok et al., (2014), and (ii) the Morcles nappe (from Kirschner et al., 1996). The thermal peak at 330°C is from RSCM data (Dall'Asta et al.2022). The hyalophane age is also indicated on the graph leading to a cooling age below T_{cl} around 20 to 25 Ma. B- Results of the DIFFARG modeling of a Jurassic feldspath submitted to the alpine thermal evolution from Boutoux et al., (2016). The pre-rift evolution which is not well constrained was chosen to be linear associated to burial under post-rift sediments. This shows a complete reset of the feldspar Ar/Ar age. The case scenarios with and without argon excess are represented.

It is well known that K-feldspars are affected by Ar modification through thermally-activated volume diffusion crystalline readjustment (Mussett, 1969) and fluid-rock interactions. Variscan feldspars in the Aar massif are reset through fluid rock interaction giving an Alpine age (Villa et al., 2000) crystal lattice readjustment and diffusion. Hydrothermal feldspars precipitating from aqueous solutions (e.g. adularia and hyalophane) have various degrees of Al/Si ordering depending on their growth and nucleation rate (Dong and Morrison, 1995), and are thus expected to be sensible to crystal lattice readjustment (De Pieri et al., 1977; Essene et al., 2005). Indeed, for such crystals, heating can lead to progressive ordering such as albite exsolution, as observed in the hyalophane

from the Mont-Blanc massif. Such reordering occurs at temperatures between 300 and 400°C (Teertstra et al., 1998). In addition, loss of Ar-Ar through diffusion for temperature around 200°C can lead to significant age rejuvenation depending on the duration of the heating stage (Mark et al., (2008), Franz et al., (2022)).

In this case, calculations of opening (T_{op}) and reset temperatures (T_{rs}) of a pre-Alpine feldspar using the method of Gardés and Montel (2009) gives a T_{op} of ~196°C and a T_{rs} of ~337°C for a grain size of 200 μm and a thermal gradient of 40°C/Ma (Table 7; Fig. IV.20A). The T_{rs} is similar to the maximum temperature recorded in the Col du Bonhomme area. Modelling of argon diffusion using the DIFFARG software (Wheeler, 1996) shows that Jurassic feldspar ages would be totally reset during prograde Alpine path (Fig. IV. 20B and C). To reach an age close to the Ar/Ar age measured on hyalophane (Fig. IV.19A), the onset of the retrograde path must be slightly earlier than that obtained by Boutoux et al., (2016). Moreover, the last Ar release steps give discordant pre-Alpine ages, which could be a sign of reset of pre-Alpine feldspars. In addition, the last Ar-release step gives an age of 197 Ma, which is close to the age of the Mont Blanc detachment determined from the syn-rift sediments (see Chapter 3).

<i>Diffusion coefficient ($\text{m}^2 \text{s}^{-1}$)</i>	<i>Activation energy (J)</i>	<i>Grain size (μm)</i>	<i>Heating gradient (°C/Ma)</i>	<i>Cooling gradient (°C/Ma)</i>
1.40E-06	180000	200	40	25
<i>T opening (°C)</i>	T reset (°C)	T closure (°C)		
196	337	287		

Table IV.6: Parameter used for calculating the temperature of opening, reset, closure following the procedure of Gardés and Montel (2009).

The possibility of Alpine ages associated to Ar excess might, however, not be excluded explaining therefore the pre-Alpine ages obtained. Nevertheless, these hyalophanes do not correspond to the classic Alpine clefts composed of Qtz-Chl-Cal-Ad and appear specific to the area of the Col du Bonhomme.

4.2. Mass balance calculations: evidence of an open system

4.2.1. Element redistribution during deformation

The detachment fault of the Col du Bonhomme affects the underlying basement over a thickness of ca. 30 m, defining the outer damage, inner damage and the core zones. Such an important thickness implies that large volumes of rocks have been the subject of major mineralogical transformations. Combined petrographical and chemical analyses show that during deformation, the chemical elements initially hosted in the mineral phases of the host rock have been redistributed to newly formed minerals in the damage and gouge zones.

This fault zone is associated to retrograde conditions in response to exhumation from sub-greenschist conditions to the surface. Indeed, the deformation started at temperatures between 200

and 300°C as evidenced by the absence of quartz plastic deformation and by the temperature of formation of the chlorite. Further, exhumation led to the formation of clay-rich gouges at temperature below 200°C.

Important basement hydration along the fault is associated first to albite replacement of orthoclase followed by feldspars and biotite breakdowns associated to chlorite and white mica formation in the damage zone. In the core zone, disappearance of chlorite as well as inherited apatite is visible.

In a previous study, Dall'Asta et al. (2022) showed that this early record of fault-related mineralogical transformations was likely largely preserved despite an Alpine thermal overprint that reached about 330°C. The latter resulted in partial recrystallization in the gouge, as seen by minor overgrowth of muscovites over illite (Dall'Asta et al., 2022). Except the quartz-hyalophane veins, which have an arguable origin as discussed above, no Alpine veins crosscut the fault zone, thereby indicating limited Alpine fluid circulation. The overall preservation of the pre-Alpine microstructures and parageneses suggests that the bulk composition of the basement and the fault rock was largely preserved, allowing for a confident interpretation of our mass balance calculations. The latter clearly demonstrate that significant gains and losses of elements from the system have occurred in the fault zone compared to the host rock. These gains and losses require that some elements have entered or left the system through a fluid phase, necessarily pointing to an open system at the scale of the studied zone during the activity of the detachment fault.

For major elements, mass balance calculation on the bulk fault rock samples gives gains of K, Ti, Fe, Mg as well as gain of water and loss of Na and Si. Loss of Ca is observed in the outer damage zone and core zone. Gains are visible in the inner damage zone due to the occurrence of calcite. For trace elements, general gain in Mo, Sb, W, V, U, Th, Zr, Hf is observed with loss of Cd. Ba shows a decrease in the outer damage zone and significant increase in the inner damage zone and core zone. Pb and Zn are gained in the outer damaged zone and lost in the inner damage zone and core zone. F shows important increase in the inner damage zone and core zone. For REEs there is a difference in behaviour between the HREEs and LREEs. There is a general gain in LREE while the HREE are immobile in the outer and inner damage zone and are lost in the core zone.

The mass balance calculations associated to the main reactions indicate that they were not achieved in a closed system. Complete replacement of biotite and feldspar by chlorite and white micas requires an external input of Mg and Fe as well as Al considering the MMC method highlighting the metasomatic character of these reactions. These reactions are associated to the release of Si, Na, Ca. The theoretical gain and loss obtained can be compared with the gain and loss from the most altered samples corresponding to the black gouge where no biotites and almost no feldspars are observed. Both mass balances based on IE and MMC methods show gains in Mg, Fe, Ti, K, Ba and loss

in Na and Ca. Gains in Al are also observed using the MMC method. This is similar with the calculation based on mineral mass balance except for K and Ba.

In the host rock, the trace elements are distributed between biotite, albite, orthoclase and apatite. Li, Rb, Cs, Tl, Sc, V, Cr, Ni, Nb are usually enriched in biotite (Bea et al., 1994; Neiva et al., 2002). This is observed at least for Rb and V in the μ XRF chemical maps (Appendix C Fig. C.1), while Ba and Pb are enriched in orthoclase. Apatite shows usually high concentrations in U, Th and REE (Bea et al., 1994) and in the Col du Bonhomme, high F concentration (Fluorapatite). The element gains are associated to uptake of these elements in neo-formed phases such as Fe oxides and sulphides, Ti-oxides, white micas and chlorite. For major elements, the gain of Mg is associated to the formation of chlorite and white micas, and the gain in Al and K is associated to that of white micas (Fig. IV.21). Gains of Ti are associated to the formation of Ti-oxide, mostly in the inner damage and core zones. Additionally, Ti is partially incorporated in white micas and Ti-oxides (rutile and anatase), but it is likely that most Ti in the core zone is related to the uptake of Ti by illite (appendix C Fig. C.8) through Ti substitution of Al (Dai et al., 2015). Moreover, Fe is hosted in newly formed iron sulphides, and mostly oxides (Fig. IV.21).

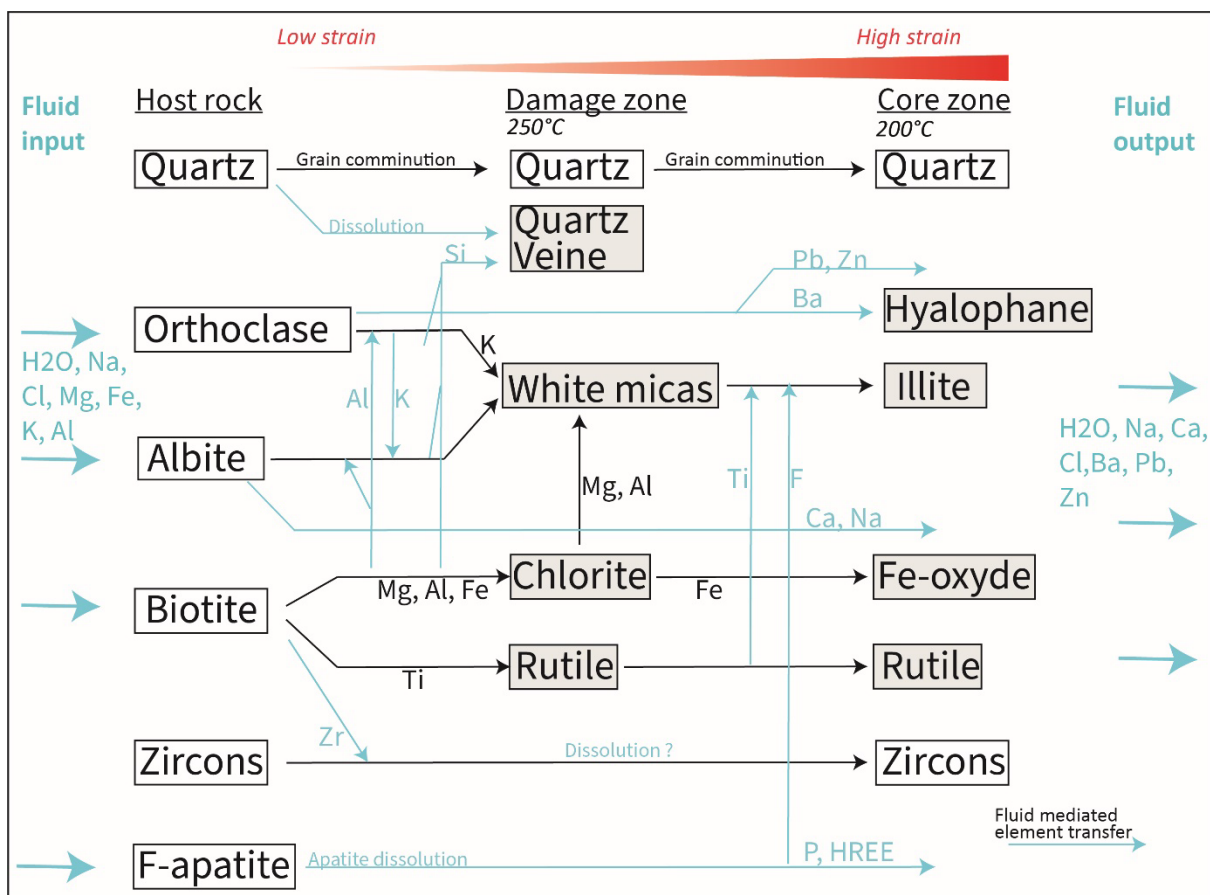


Figure IV.21: Schematic flow chart showing the mineral transformations and associated element transfers occurring in the detachment fault. The minerals in white correspond to primary phases from the host rock, while the minerals in grey correspond to secondary phases formed in the fault zone. The blue arrows correspond to element transfer in fluid while the black arrows correspond to mineralogical transformations.

Most trace element gains in transition metals such as Cu, Mo, W, Sn, Sb might be associated to the Fe-sulphides formed in the damage zone (Appendix C, Fig.C.1,2,3). V can be found associated to Ti in Ti-oxides and illites (Appendix C, Fig.C.2,3). Moreover, white micas can also incorporate significant amount of Sn and W (Neves, 1997). Ba and Rb are now found in white micas, illite and hyalophane (Ba). Rb is also found in Fe-oxides (Appendix C Fig. C.2). Regarding halogens, there is a large discrepancy between chlorine and fluorine in the fault rocks, with clear enrichment of fluorine in the inner damage zone ($F/Cl = 13$) and the core zone ($F/Cl = 50$). Part of this fluorine might be derived from F-apatite, which is observed in the host rock but not in the fault rock (Fig. IV.21). Indeed, the solubility of F-apatite increases under neutral to acidic conditions (Guidry and Mackenzie, 2003) enhancing their dissolution and thus the release of F. However, the increase of fluorine concentration in illite from the core zone (Fig. IV.21) indicates that it corresponds to a sink of excess fluorine originating from external fluids, through substitution of -OH by -F (Thomas et al., 1977; Pesquera et al., 1999). The concentration obtained in the illite is also consistent with other hydrothermal clays with high F content (Thomas et al., 1977; Segev, 1984). Loss of Pb and Zn in the inner damage zone and core zone are associated to the alteration of feldspars. These elements are not incorporated into white micas and are preferably released to the fluid phase.

4.2.2. Implications for mass balance calculation

The apparent simplicity of Gresens's equation (Gresens, 1967) masks important difficulties when it comes to the application to real samples. Indeed, the determination of the volume factor is difficult to assess. Postulating that some elements are immobile allows to relate any change in concentration to a change of volume. However, determining what elements are immobile is quite complex as it depends on various physico-chemical parameters. It is usually argued that the HFSE are immobile, especially Zr (Steyrer and Sturm, 2002).

The comparison between the two methods here highlight some significant differences especially for the core zone (Al immobile and MMC method vs Zr immobile). In both cases the models show a loss of water, Mg, Fe, Al and K compared to the host rock. The loss of water is counterintuitive as the core zone is dominated by hydrous phases such as white micas compared to the host rock. Besides, the large increase of white micas should lead to an increase in Al and K. Indeed, the complete alteration of the host rock (equation (4)) would lead on the contrary to a gain of Al, Mg, Fe, and K. On the other side, the minimum of mass change method gives more reliable results when compared to petrological observations. These observations raise doubts on the accuracy of the Zr immobile method.

The loss of volume obtained when assuming Zr immobile is important and results in up to 63% volume loss. This change of volume appears suspiciously important compared to what is expected. Indeed, the volume change in fault rocks depends on the competence between volume

decrease associated to porosity decrease because of grain size diminution and mechanical compaction (Song et al., 2017) and volume increase due to dilatancy (Marone and Scholz, 1989). During deformation, intense dilation in the damage zone can increase the volume, which at least compensates the change of volume due to grain size reduction (Reches and Dewers, 2005). In contrast, a decrease of volume (~15%) is expected in the core zone, mostly due to the decrease of porosity related particularly for important deformation. Mass balance along shear zone from low grade (Kerrich et al., 1977; Vocke et al., 1987) to high grade mylonites (Steyrer and Sturm, 2002) shows isovolumic to minor volume changes during deformation. Therefore, postulating Zr as immobile tends to overestimate the loss of volume and therefore the loss of mass. The mobility of Zr might not be controlled by zircons, which are resistant to alteration and deformation (Steyrer and Sturm, 2002) but might be controlled by other Zr-bearing phases such as biotite (Rubin et al., 1993). Minimizing the mass transfer is therefore preferred as it provides results in agreement with petrological observations.

This discrepancy between the Zr immobile and the MMC method raises the question of the mobility of this element in the fluid phase. For HFSE (Zr, Hf, Nb, Ta, Ti), the type of complexes they form in the aqueous phase is of prime importance for their mobility as dissolved elements. Indeed, they are commonly assumed as immobile in the fluid phase during mineral transformation reactions (MacLean and Kranidiotis, 1987). On the opposite, our mass-balance calculations strongly suggest their mobility as deformation proceeded, and as demonstrated by their significant increase in concentration in the gouge compared to the undeformed basement. Our findings concur with other observations of such mobility both in magmatic systems and hydrothermal systems from high temperature to diagenetic domains (Van Baalen, 1993; Rubin et al., 1993; Jiang et al., 2005, Rasmussen, 2005; Rapp et al., 2010). In detail, a link between mobility of HFSE and F content was observed in many geological environments (Bartley, 1986; Rubin et al., 1993; Gieré, 1990; Rasmussen, 2005). Indeed, the mobility of HFSE is sensitive to their speciation in the fluid phase (Van Baalen, 1993; Rubin et al., 1993). They form stronger complexes with F and OH than with Cl, in the form of HFSE \equiv F such as Zr and Ti-hexafluor complexes (Zr-TiF₆²⁻). These types of fluor complexes are stable up to pH < 6 at 200°C, for high F- and low Ca concentrations, preventing fluorite precipitation (Appendix C Fig. C.6A; Aja et al., 1995). As observed in the core zone, progressive uptake of F by illite in the gouge is related to an increase of Ti and Zr (see Appendix C Fig. C.6C), which might also be related to a decrease of activity of F⁻ in the fluid phase. In the case of the Mont-Blanc detachment fault, mobility of these elements was probably achieved at least along the fault zone from the damage zone to the core zone.

4.3. Paleo fluid characteristics

4.3.1. Fluid composition

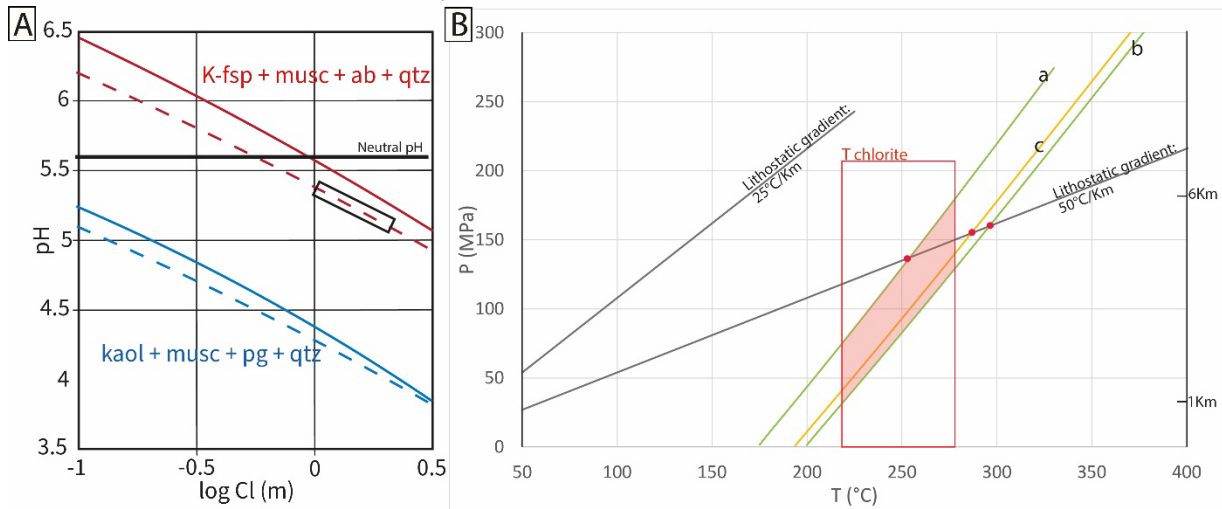


Figure IV.22: A- Estimation of pH in relation to chloride concentration in a Or-Mu-Ab-Qtz buffered system (Yardley, 2005) B- Temperature-pressure plot with calculated isochore (H₂O-NaCl; Bakker, 2018) corresponding to the different generations of inclusion observed in the cataclasite (a. isochore of vein1 and b. isochore of vein 2) and gouge (c.). The geothermal gradient of 50°C/km from numerical models of rifting (Chenin et al., 2020) and chlorite temperatures are indicated, giving a maximum pressure of formation for the inclusions.

The Th obtained for the fluid inclusions in the quartz veins from the inner damage zone and core zone is comprised between 170°C and 220°C for a salinity around 7 to 9 wt% equiv. NaCl, corresponding to brines. Thermobarometry on the fluid inclusions (Fig. IV.22B) was done assuming a maximum temperature for the fluid using calculated isochores from (Bakker, 2018). The maximum temperature reached by the fluid was determined using a theoretical geothermal gradient of 50°C/km (Chenin et al., 2020) and by using chlorite temperature estimates (250 ± 30°C). This gives a pressure of 30 to 170 MPa, corresponding to a maximum depth of emplacement of the veins between 6 and 1 km under lithostatic conditions. The upper range of pressure corresponds also to the temperature obtained under a lithostatic thermal gradient of 50°C/km. Tm-Th graph (Fig. IV.17F) shows that in the gouge, isothermal mixing is observed, while in the cataclasite cooling with possible surface dilution seems to occur.

Additional insights into fluid composition during deformation can be tentatively obtained from phase stability modelling. First, using the Cl concentration as estimated from the fluid inclusions and assuming that the chemical composition of the fluid was mostly buffered by interaction with major phases (Or-Mu-Qtz) along the core zone, a near neutral pH is obtained for a temperature of 250°C at a pressure of boiling water (Fig. IV.22A; Yardley, 2005) .

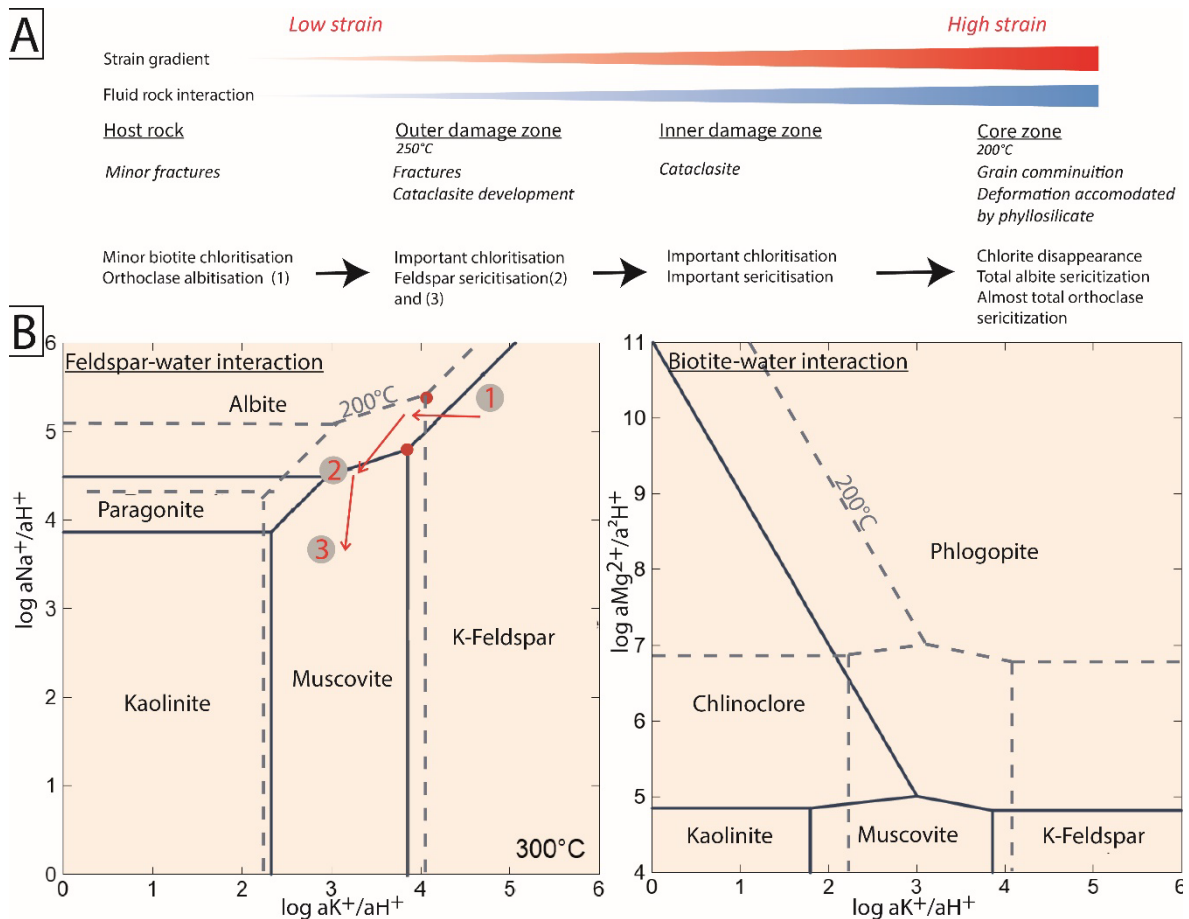


Figure IV.23: A- Alteration reactions associated to the strain evolution toward the core zone. B- Modelling of the stability of feldspar and biotite during fluid rock interaction for different temperatures compared with the mineralogical observations showing albitization (1) followed by sericitization (2) and (3) and disappearance of chlorite toward the core zone.

Second, the alteration along the fault differs in the inner, outer damage zone and in the core zone. In the outer damage zone orthoclase albitisation and biotite breakdown is visible. In the inner damage zone, feldspar and biotite breakdowns and replacement by white micas and chlorite in the damage zone is followed by disappearance of chlorite in the core zone (Fig. IV. 23A). In similar conditions ($T = 200\text{-}300^\circ\text{C}$, $P = 2$ kbar), the stability of the major phase in the host rock (albite, orthoclase, biotite) can be calculated according to the activity ratios $a\text{K}^+/\text{aH}^+$, aNa^+/aH^+ and $\text{aMg}^{2+}/\text{aH}^+$ in the fluid phase, still assuming equilibrium (Geochemist Benchmark ©, Fig. IV.23B). According to the model, temperature changes can strongly modify phase stability and thus fluid composition, whereas pressure has no significant impact. In that case, changes from albitisation to sericitization, which are observed in the fault could be simply explained by the progressive uptake of Na during albitization, changing the composition of the fluid during circulation in the basement. It is also worth noting the change of stability field (enlargement of muscovite field) with the decrease of temperature from 300°C to ca. 200°C . Therefore, change from albitisation to sericitization might be a combination of temperature drop and decrease of the activity Na in the fluid. Replacement of biotite to chlorite in the damage zone is followed by disappearance of chlorite in the core zone. The

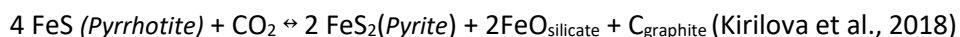
disappearance of chlorite and its replacement by muscovite in the core zone indicates the progressive destabilisation of biotite with increasing deformation. According to the model, a decrease of temperature leads to an important enlargement of the white mica stability field explaining the chlorite destabilisation at lower temperature.

4.3.2. Occurrence of graphite and its signification

The presence of graphite in the damage zone raises the question of the origin of the carbon and the conditions of its formation. These graphite-rich zones share similarities with pseudotachylites such as injection of dark material in the cataclastic host rock at the macroscale, and preservation of embayed clasts, sulphide droplets and microliths at the microscale (Kirkpatrick and Rowe, 2013). The dark grey matrix corresponds to the slip plane and might correspond to altered glass. However, there is no clear evidence for glass and/or melts conclusively proving the occurrence of pseudotachylites along the fault zone.

A spatial link between the low strain magmatic intrusions and the graphite rich veins appears from field observations. The high RSCM temperature could be associated to frictional heating up to 500°C occurring around aplitic bodies, which remained largely undeformed. These undeformed lowly altered bodies might correspond to strong patches along the fault zone associated to strain-hardening and possible shear heating (Collettini et al., 2019). Switch from cataclastic deformation to frictional melting is quite ubiquitous along fault planes (Magloughlin, 1989; Kirkpatrick and Rowe, 2013).

A first generation of graphite was followed by formation of illite-graphite mixture under cooling temperature (below 200°C-250°C) as observed through illite precipitation. The processes of graphite formation remain however unclear. Oxidation of sulphides is known to trigger reduction of CO₂ into graphite following a reaction similar to:



In addition, uptake of water due to the formation of hydrated phases under cooling temperatures could also lead to supersaturation with respect to C and precipitation of poorly ordered graphite as proposed by Rumble et al., (1986), Luque et al., (2009) and observed by Martz et al., (2017) in brittle basement faults in the Athabasca basin (Canada). Graphite associated to titanite in pseudotachylites was observed by Nakamura et al., (2018) and formed under similar conditions.

The presence of frictional melt along the Mont-Blanc remains unclear. However, it seems clear that graphite found in the Col du Bonhomme might have formed from precipitation of carbon-rich fluids during cooling of a carbonic fluid. The source of carbon can be derived from CO₂ from metamorphic fluids or from remobilization of carbon from the coal-rich Carboniferous basins found in the hangingwall of the Mont-Blanc detachment. It is therefore possible that initial fluid was NaCl (-

KCl)-H₂O-(CO₂), but that CO₂ was sequestered in the damage zone as graphite later reworked in the core zone.

4.3.3. Comparison with Alpine fluids

Alpine veins are composed of quartz (Poty et al., 1974; Marshall et al., 1998), quartz chlorite (Marshall et al., 1998) and quartz-chlorite-calcite-adularia mostly (Rossi and Rolland, 2014). Fluid inclusions show the presence of a NaCl-H₂O-CO₂ fluid (Poty et al., 1974; Marshall et al., 1998). The amount of CO₂ is variable, up to 14% of the inclusion volume at room temperature (Marshall et al., 1998). The Th obtained varies between 140 and 230°C for a salinity of 6 to 12%. The adularia are associated to calcite indicating the presence of dissolved Ca and CO₂ in the fluid. The change of fluid pH due to removal of CO₂ might have led to the precipitation of adularia as observed along the Alpine fault in New Zealand (Craw, 1997).

These veins show similarities with the vein in the detachment in terms of Th and salinity ranges, despite the lack of CO₂ in the detachment. However, the vein paragenesis is different. No calcite or chlorite is found associated to the veins along the detachment. Additionally, the hyalophanes were not reported elsewhere in the Mont-Blanc massif, which makes the veins along the detachment unique compared to the Alpine veins.

4.4. Implication of the Mont-Blanc detachment fault

4.4.1. Geochemical signature of a necking detachment fault

This study provides strong insights on fluid flow and composition along detachment faults during necking. In the present case, basement hydration started at ca. 250°C under sub-greenschist conditions, until exhumation to the surface. Metasomatic reactions under retrograde conditions associated to footwall exhumation led to element transfer along the fault. Large gains of K, Fe, Ti, Mg, Ba, F, As, V and loss of Si, Na, Ca, Pb, Zn indicate a strong mobility of these elements along the fault in fluids characterized by temperatures of 200°C and moderate salinity.

The origin of the external input of Fe, Mg, K and Al into the system is questionable as the fluid is supposed to be seawater. Fluid rock interactions associated to the downflow path of seawater-derived fluids is related to shift of the Mg/Ca ratio due to precipitation of calcite and anhydrite (Weinzierl et al., 2018) leading to a Mg-rich fluid and possibly enrichment in Fe. The source of Al is, however, not well constrained. Chloritization of biotite along the downflow path and in the host rock and outer damage zone without significant feldspar alteration might, however, provide Al to the fluid as well as K and Fe.

Redox conditions along the fault are difficult to evaluate. However, the occurrence of Fe-oxides intergrown with pyrite is highlighting oxidising conditions among the detachment faults. These conditions represent a favourable environment for base metal transport to the surface. Based on the

example of oceanic detachment faults, it has been advocated that oxidising conditions along detachment faults are related to large infiltration of seawater (Liao et al., 2022).

4.4.2. Fluid in necking domains

Examples of detachments associated to crustal necking in oblique margins have been reported in the Gulf of California (Los Cabos detachment fault; Geoffroy and Pronost, 2010; Bot et al., 2016). This Miocene detachment corresponds to an exhumed fault zone formed by a ductile shear zone overprinted by cataclastic sediments and overlaid by syn-rift sediments. Deformation was achieved under an unusually high thermal gradient. However, the characteristics of present-day and paleo fluids were not studied in detail, with the exception of evidence of K and Fe gains along the fault (Bot et al., 2016).

Only few studies focused on fluid circulation associated to the necking of the crust during rifting in fossil analogues. Analysis of cement and veins from pre-rift allochthonous blocks in the Adria fossil margin (Incerpi et al., 2019) show similarities with what is observed in the Mont-Blanc. Replacement and mineralization of the pre-rift cover was achieved through circulation of a hydrothermal fluid with a temperature of 120-150°C. A progressive change of fluid source during rifting has been observed associated to a decrease of $\delta^{18}\text{O}$ and increase in $\delta^{13}\text{C}$ between the Pliensbachian and the Toarcian, coeval to necking in the Mont-Blanc. Around the end of the Toarcian, a change of fluid source and composition is observed, as shown from a shift from calcite/dolomite vein to quartz vein precipitation. Sr, O and He isotopes point to a crustal source for these Si-rich fluids, which strongly interacted with silicate minerals.

Despite the lack of fossil necking detachment faults, many extensive detachment faults have been studied worldwide in different tectonic settings under different temperatures and with various host-rock lithologies. Four examples will be taken here as examples for comparison with the Mont-Blanc detachment fault: detachments from the hyperextended domain in the Alps, those from the Basin and Range, and from back-arc settings (Table IV.8).

Detachment faults from the hyperextended margins have been studied in detail in the central Alps (Err detachment; Manatschal, 1999, 2000; Pinto et al., 2015; Epin et al., 2017). They are associated to intense fluid circulation which led to strain softening through feldspar breakdown facilitating deformation (Manatschal, 1999), similarly to our observations in the Mont-Blanc (Dall'Asta et al., 2022). The alteration along the footwall corresponds to feldspar saussuritization (Ep+Chl) at temperature between 150 and 200 °C (Manatschal et al., 2000). Despite temperature ranges similar to the Mont-Blanc detachment, the type of metasomatic alteration (saussuritization vs sericitization) is different leading to different cataclasite and gouge compositions. Moreover, the circulation of fluids in the mantle led to enrichment in mantle-derived elements along the

continental detachment fault such as Ni, Cr, Cu, which is not observed in the Mont-Blanc detachment fault. However, loss of Na, Ca related to feldspar breakdown is also observed.

	<i>Tectonic setting</i>	<i>Host rock</i>	<i>Temperature of deformation</i>	<i>Type of alteration</i>	<i>Type of fluid</i>	<i>Element transfer</i>	<i>References</i>
<i>Err detachment (Switzerland)</i>	Hyperextended domain	Granite	Cataclasite: 200-150°C Gouge: 100-150°C	Saussuritization	H ₂ O	<u>Loss</u> : Ca, Na, Sr <u>Gain</u> : Ni, Cr, Cu	Manatschal et al., 2000
<i>Mont-Blanc detachment</i>	Necking domain	Gneiss	Th=170-220°C T _{chlorite} =200-250°C	Sericitization	H ₂ O-NaCl (-KCl)	<u>Gain</u> : K, Fe, Ti, Mg, Ba, F, As, V <u>Loss</u> : Si, Na, Ca, Pb, Zn	This study
<i>Bullard detachment (USA)</i>	Post-orogenic extension	Rhyolite	Th=290-310°C	K-metasomatism	H ₂ O-NaCl (-CO ₂)	<u>Loss</u> : Na, Ca, Mg, Sr, Pb, Zn	Roddy et al., 1988
<i>Snake range detachment (USA)</i>	Post-orogenic extension	Grano-diorite	Up to 400°C Th= 70-200°C	Saussuritization	C		McGrew, 1993; Losh, 1997; Gébelin et al., 2011; Carter et al., 2015;
<i>Boccheggiano detachment (Italy)</i>	Back-arc extension	Phyllites	Th=300°C	Sericitization Chloritization	H ₂ O-CO ₂ -NaCl	<u>Loss</u> : Na, Ca, Mg, Zn, U <u>Gain</u> : Ba, Rb, As	Rossetti et al., 2010

Table IV.7: Comparison between different continental detachment faults. The Th given corresponds to homogenization temperature of fluid inclusions in syn-kinematic veins.

Post-orogenic and back-arc extension are associated to volcanism and fluid temperatures up to 300 °C, i.e. slightly higher than what is observed in the Mont-Blanc fault (Roddy et al., 1988; Carter et al., 2015; Rossetti et al., 2010). Besides, CO₂ is present in most of the fluid inclusions (Roddy et al., 1988; Carter et al., 2015; Rossetti et al., 2010). The alteration of the basement corresponds to K-metasomatism and sericitization-chloritization. K-metasomatism occurs at moderate temperature (ca. 100°C), with K provided by the alteration of potassic volcanic rocks (Roddy et al., 1988). Systematic loss of Na and Ca is associated to plagioclase alteration and linked to loss of Pb and Zn. Gains in Ba, Rb and As are visible along the Boccheggiano fault (Rossetti et al., 2010), similarly to the Mont-Blanc fault. Despite different fluid compositions and temperatures, the mobile elements are largely similar between these detachments and the Mont-Blanc detachment. This finding highlights the major role played by feldspar breakdown in element mobility along detachment faults.

Finally, the Mont-Blanc detachment fault presents some specificity relatively to other detachment faults. It shares similar temperature ranges with detachments from the hyperextended domain. However, the elements mobilised are similar from continental detachment faults in back-arc

setting. The Mont-Blanc detachment may thus be representative of continental detachments under moderate temperatures in the absence of magmatic activity.

Conclusion

The Mont-Blanc detachment fault provides a new insight on fluid circulations associated to crustal necking. A hydration front, ca. 10 m thick, is visible around the fault zone characterized by significant mineralogical transformation associated to hydration. These metasomatic reactions in the fault correspond to biotite chloritization and feldspars sericitization in the damage zone under temperature of ca. 250°C and feldspars sericitization and chlorite destabilisation in the core under temperature below 150°C. They are triggered by the external input of a Mg and Fe-rich fluids along the fault leading to the release of Si, Na and Ca in the fluid phase.

Syn kinematic veins along the fault corresponds mostly to quartz veins and quartz-hyalophane veins. Dating of hyalophane in veins from the core zone give an age of 28 to 30 Ma, which corresponds to the age of the Alpine metamorphic peak in the Mont-Blanc massif. However, it remains unclear whereas the ages correspond to crystallisation ages or reset due to argon diffusion at lower greenschist conditions. Petrological evidence, however, supports the latter hypothesis. Fluid inclusion analysis in syn-kinematic veins provides more information on the type of fluid encountered along the fault. They give a homogenization temperature of 200°C for salinities of ca. 10 wt% in a H₂O-NaCl (-KCl) system. Thermobarometric constrains on the fluid inclusions provide an entrapment depth between 1 and 6 km. In addition, the occurrence of graphite with temperature of 450°C in the damage seems related to frictional melting and indicates the occurrence of a carbon rich fluid.

These metasomatic reactions are also responsible for trace elements mobility along the fault as observed through mass balance calculations. More specifically, gains of Ba, F, As, V and loss of Pb-Zn are observed in the damage and core zones, associated to loss of HREE in the core zone. Mobility of HFSE and especially Zr and Ti is also observed in the core zone, questioning their use as immobile elements in mass balance calculations. Such mobility was likely controlled by the presence of F along the fault zone.

The study of the Mont-Blanc detachment fault demonstrates that fluid circulation can occur during crustal necking using crustal faults as a pathway. This study complete the work of Incerpi et al., (2019) related to fluid circulation in the cover related to necking, confirming the occurrence of Si-rich fluids derived from the basement but also significant transfer of trace elements.

Chapter V- Preserved Jurassic Structures in the Northern Mont-Blanc massif (Val Ferret, Switzerland)



Dalle de l'Amône (Val Ferret, Switzerland)

« La nature n'a point fait l'homme pour ces hautes régions ; le froid et la rareté de l'air l'en écartant » (Horace Bénédicte de Saussure)

Foreword

The Mont-Blanc detachment fault was described in detail both in terms of structural and microstructural evolution and in terms of fluid associated to the fault. However, this work concerns only the southern Mont-Blanc massif.

The goal of this chapter is to see if the Mont-Blanc detachment fault can be prolonged northward. For this, observations on the basement-sedimentary interface were realized along the Val Ferret. In addition, new observations on the syn-rift cover as well as compilation of stratigraphic sections complement the observation on the top basement and allows a partial reconstruction of the basin evolution during Jurassic. These data are complemented by geochemical analysis of the basement and fault rocks identified in the Val Ferret. Finally, the Alpine thermal peak in the area was also constrained in the area using data from previous studies as well as new RSCM temperature in the cover. It appears that the Alpine temperature reached in the northern Mont-Blanc area is higher compared to its southern part. Besides, due to the tilting of this area at a high angle (ca. 70° to the SW), the outcrops are actually difficult to access. This makes the Jurassic evolution of the Val Ferret difficult to unravel. However, a rift-related model taking into account the tectonic and sedimentary evolution is proposed in the end of the chapter.

Introduction

The identification of the Mont-Blanc detachment fault and its characterization raise questions concerning the prolongation of the fault northward. It was proposed by Ribes et al. (2020) that the fault can be indeed prolonged to the north and that some remnants of the fault can be found in the Val Ferret area.

There, preserved Jurassic clastic sediments suggest that tectonic processes are similar to those described at the Col du Bonhomme. However, in detail, the situation is more complex. Indeed, two different clastic deposits are observed, an upper Liassic sandstone and a Lower Aalenian conglomerates. Furthermore, the occurrence of Carboniferous rhyolites at the contact with the granite, which is not observed in the southern Mont-Blanc massif, questioned the nature of this contact. This chapter presents sections through the basement-sediment interface as well as along the granite-rhyolite contact to characterize more precisely the nature of these contacts. New observations from the magmatic basement and the autochthonous cover are presented, in order to better constrain the pre-Alpine structural evolution of the northern Mont-Blanc massif.

Finally, a tentative rift-related model for the Val Ferret is proposed to reconcile sedimentary and tectonic observations. This model remains hypothetical, as more geochronological and structural constrains are needed.

1. Methodology

This work was realised based on field observations and structural measurements of the deformation in the basement and the cover. A total of 63 samples from the basement and the cover were collected and polished thin sections were realised (Table V.1). Petrographical characterisation was performed with a Nikon LV150ND optical microscope (LFCR, Pau, France). The biostratigraphic data associated to the sediments presented here can be found in the Appendix F.

Localisation	Coordinates	Number of samples	Type of contact
<i>Saillon</i>	46° 10' 11''N 7° 10' 48''	5	Syn-rift Sediment
<i>Combes des Fonds</i>	45° 55' 48''N 7° 05' 12''E	6	Rhyolite-sediment
<i>L'Amône</i>	45° 56' 31'' N 7° 05' 32''E	15	Rhyolite-Sediments
<i>Saleinaz</i>	45° 59' 08''N 7° 06' 37''E	4	Rhyolite-Sediments
<i>Breya</i>	46° 01' 14''N 7° 06' 00''E	11	Granite-Rhyolite (Fault zone)

<i>Catogne</i>	46° 03' 30"N 7° 06' 51"E		Gneiss-Rhyolite (Fault zone)
<i>Champex sur Lac</i>	46° 02' 26"N 7° 07' 02"E		Syn-rift sediments
<i>Col des planches (Mont-Chemin)</i>	46° 05' 07"N 7° 07' 25"E	19	Basement (Fault zone)
<i>Col des Planches</i>	46° 05' 30"N 7° 07' 18"E		Syn-rift sediments
<i>Trappiste mine (Mont-Chemin)</i>	46° 04' 49"N 7° 07' 34"E	3	Variscan mylonites Fluorite

Table V.1: Location of the different outcrops in the Val Ferret (+ Saillon)

Bulk rock analysis for major, trace and rare-earth elements were realized on 13 powdered samples from the Amône, Brea and Mont-Chemin area at the SARM (Service d'Analyse des Roches et Minéraux) in Nancy (France) using an ICP-OES for major elements and an ICP-MS for trace elements.

Raman spectroscopy on carbonaceous material (RSCM) was performed on 2 polished thin sections of carbon-rich limestones. A total of 23 Raman spectra were acquired with a Horiba Jobin-Yvon Labram II spectrometer coupled to a microscope, at the Institut des Sciences Moléculaires, Université de Bordeaux, France. Acquisitions parameters include a 514.5 nm argon laser, an extended scanning mode (500-2000 cm^{-1}) and an acquisition time of 30s. Spectra of the first-order region of carbonaceous material were processed using the Fityk software (Wojdyr, 2010). Each spectrum was fitted with 4 bands (D1, D2, D3, and the graphite band G) with Voigt profiles. The calibration of Beyssac et al. (2002), based on the parameter $R2 = D1/(G + D1 + D2)$ was used for estimating the maximum temperature reached in the cover.

2. Geological context

2.1. Localisation

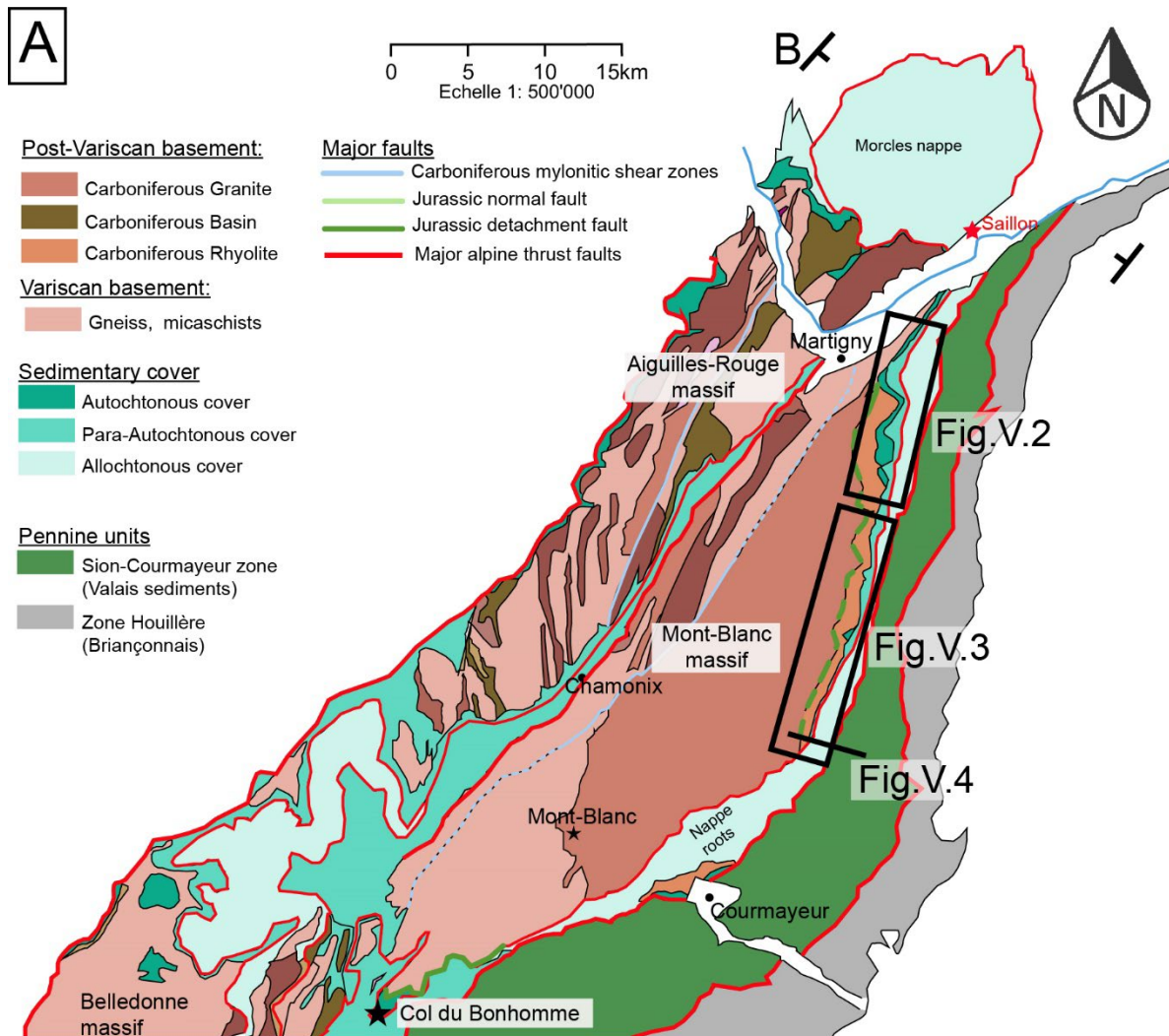


Figure V.1: Map of the Mont-Blanc showing the location of the Val Ferret.

The Val Ferret (Switzerland) corresponds to the northern part of the Mont-Blanc massif, bounded to the north by the Rhône Valley and Simplon-Rhône zone (Fig. V.1), and to the south by the Ferret pass leading to Italy. The western part of the Val Ferret is composed of the Mont-Blanc massif basement and autochthonous cover while the eastern part corresponds to the internal domain of the Sion-Courmayeur nappes.

The northern Mont-Blanc massif can be divided into two areas with different stratigraphic evolutions, the northern Val Ferret and the southern Val Ferret. The northern part of the valley (northern Val Ferret) is found between Vens and Champex Lac (Fig. V.2). It comprises the Mont-Chemin and Mt. Catogne while the southern part of the Val Ferret goes from Champex Lac until the Ferret pass (Fig. V.3).

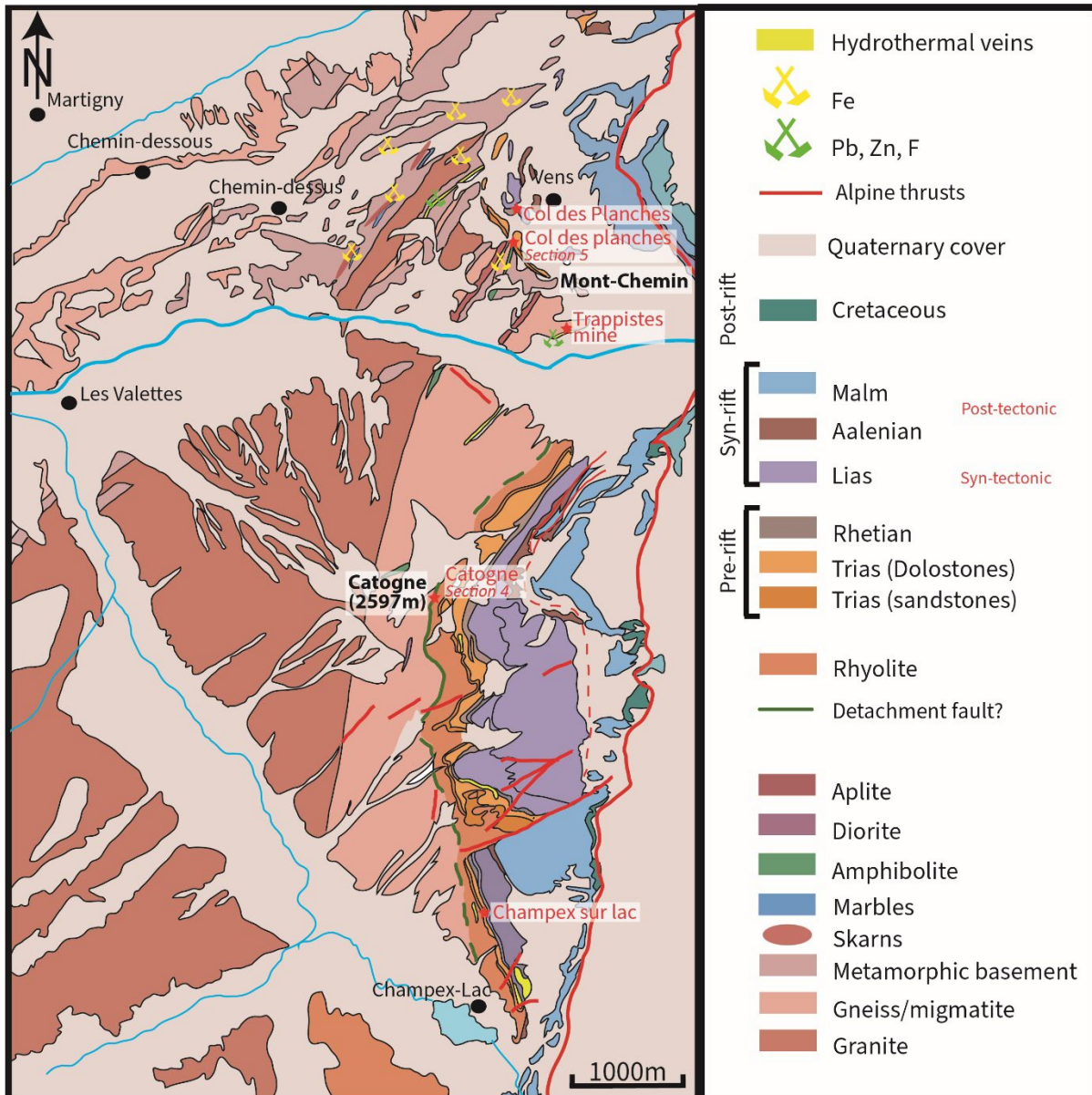


Figure V.2: Map of the north Val Ferret area showing the autochthonous cover of the Mont-Blanc (modified from Swisstopo). The Catogne is characterized by the presence of pre-rift cover over the basement disappearing southward. The position of the mines in this area is indicated.

The Catogne Mt. (Fig. V.2) is composed of the Mont-Blanc granites on its western side and of Variscan gneiss overlaid by Carboniferous rhyolites and autochthonous sedimentary cover on its eastern side. In the Variscan gneiss, lenses of Variscan amphibolites are observed. This autochthonous cover is overlaid by para-autochthonous cover associated to minor displacement and allochthonous cover associated to the Helvetic nappes. This sedimentary cover is dipping steeply (ca. 70°) towards the east which is associated to the rotation of the internal Mont-Blanc massif during Alpine exhumation (Leloup et al., 2005).

This area is characterized by an historic mining industry from the 14th century up to the 20th century. The main veins were discovered in the area of Mont-Chemin. Different types of ores were exploited (Ansermet, 1998a,b). The main exploitation was related to skarn-related magnetite to

Preserved Jurassic Structures in the Northern Mont-Blanc massif (Val Ferret, Switzerland)

produce iron (Ansermet, 1998a). Mining of silver-rich galena and fluorite was also realised during World War II with over 1500 tons of ores extracted (Chessex and Rivier, 1957).

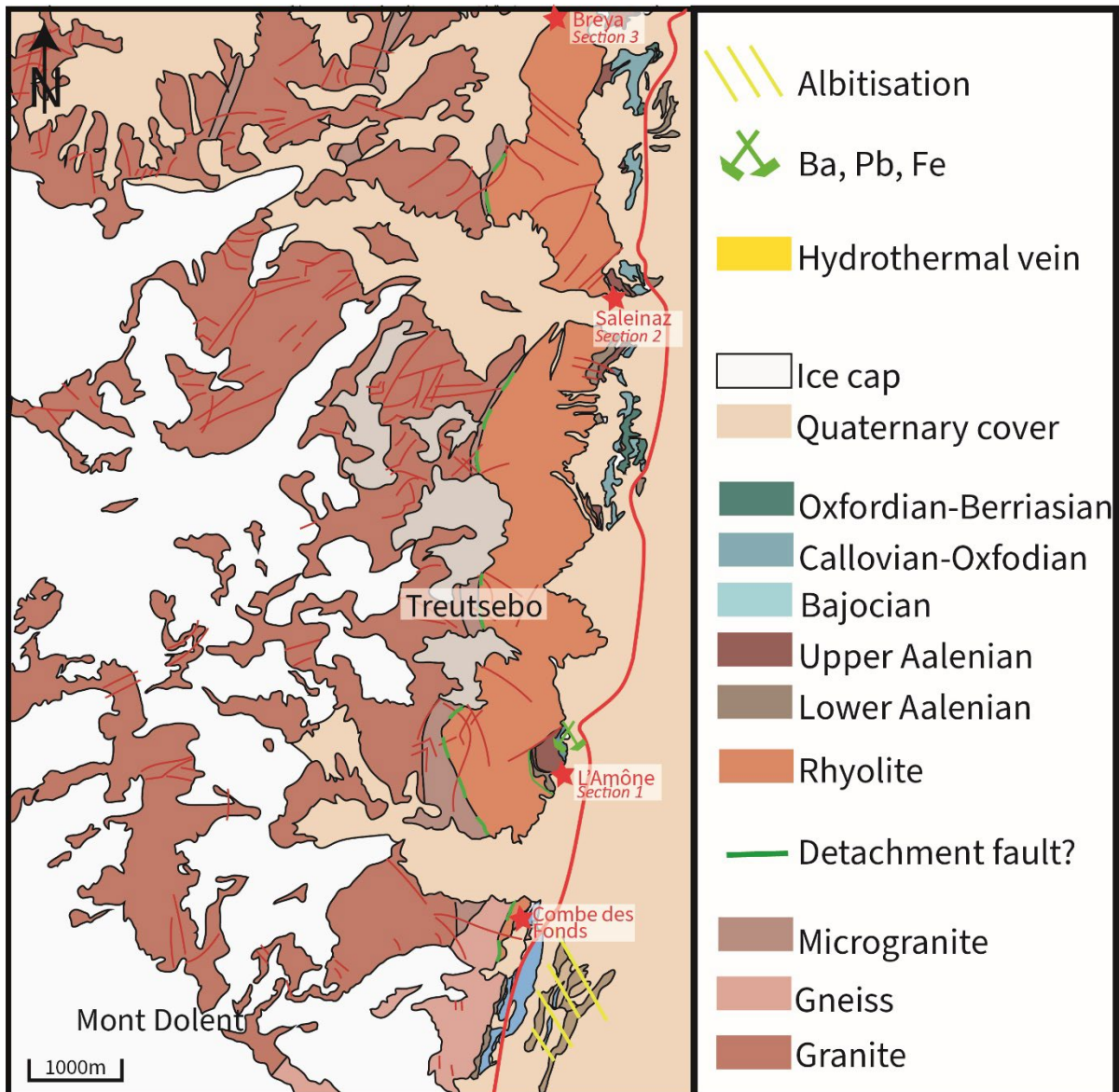


Figure V.3: Map of the southern Val Ferret showing the syn-rift cover lying above the basement.

In the south Val Ferret (Fig. V.3), two main changes can be noticed compared to the northern part of the valley. The first main characteristic is the absence of Triassic to Liassic cover. Indeed, the basement is overlaid by Aalenian sediments (Grasmück, 1961). Moreover, the area is characterized by significant rhyolitic formations over the granitic basement.

2.2. Alpine deformation

2.2.1. Alpine deformation

The massif is composed of basement overlaid by isoclinal autochthonous, para-autochthonous, and allochthonous Mesozoic units dipping steeply (ca. 70°) toward the east below the Penninic thrust.

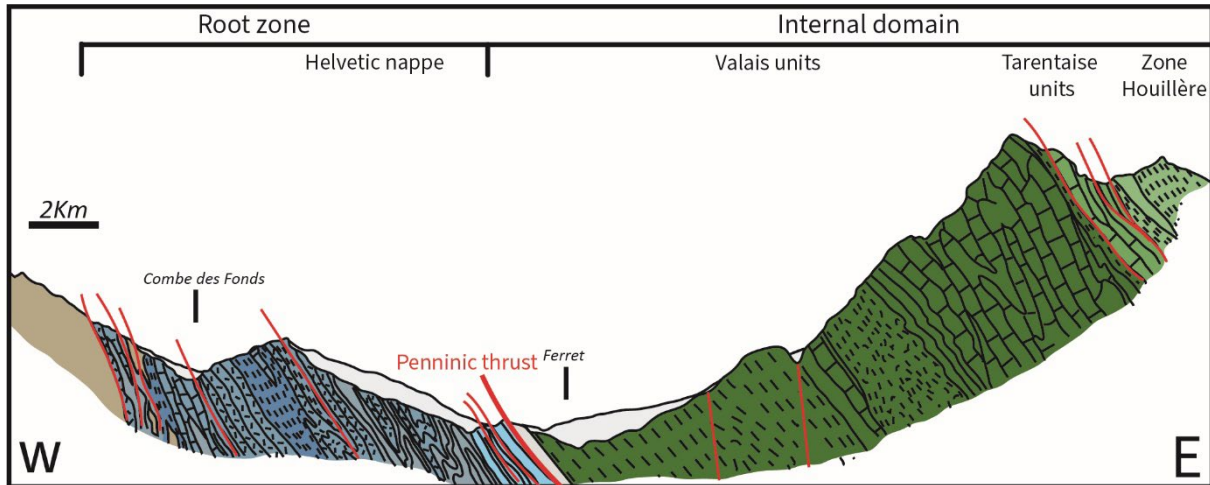


Figure V.4: Cross section of the Val Ferret in the Ferret Pass area showing the distal units (Helvetic nappes and Penninic nappes) thrust above the Mont-Blanc massif (Trümpy, 1954).

The main Alpine tectonic event recorded in the area is the thrusting of the internal nappes above the Mont-Blanc during the Oligocene (Egli et al., 2017). In between the internal domain and the Mont-Blanc massif, a series of allochthonous blocks with upper Jurassic sediments and a width of ca. 3 km correspond to the root of the Helvetic and Ultrahelvetic domains with a relatively constant NNE-SSW thrust direction (Fig. V.4). The autochthonous sedimentary cover is preserved below the base of the Helvetic thrust and shows minor Alpine deformation (Grasmück, 1961). Indeed, the Aalenian shales and Valanginian shales acted as a major decollement level for the Helvetic nappes (Trümpy, 1954; Grasmück, 1961). In the autochthonous cover, the S1 foliation is parallel to the S0 (Egli and Mancktelow, 2013). The para-autochthonous mid-Jurassic cover shows a progressive development of tight folds towards the base of the Helvetic nappes associated to the development of a S2 foliation (Egli and Mancktelow, 2013). Stretching lineations indicate a N120-150° transport direction (Egli and Mancktelow, 2013). However, toward the Ferret pass, strong Alpine deformation can be observed in the basement where decametric mylonitic slivers of basement are found in the sedimentary cover (Grasmück, 1961).

The internal Mont-Blanc massif was submitted to important rotation associated to the crustal stacking of the Mont-Blanc over the Aiguilles-Rouges (Leloup et al., 2005). Development of fractures affecting the cover and the basement are observed. NE-SW and NW-SE secondary faults affect the

basement with minor displacements (< 100 m). Besides, sets of fractures roughly NE-SW and NW-SE, and coated by chlorite, are clearly discernible.

2.2.2. P-T conditions

The thermal peak measured in the cover is higher in the Val Ferret than in the Col du Bonhomme area. Indeed, Raman spectra in the area give temperatures of $367\pm 35^{\circ}\text{C}$ in the area of l'Amône and $403\pm 35^{\circ}\text{C}$ in the Combe des Fonds (Table V.2, 3, 4). However, no RSCM data are available on the northern part of the Mont-Blanc massif (Catogne and Mont-Chemin). In the Mont-Chemin, stibiomelane-epidote-calcite-quartz veins give a temperature of formation between 360 and 430°C for a pressure of 2.5 to 5.2 Kbar (Marshall et al., 1998), which corresponds to similar temperatures than the ones obtained with RSCM further south.

Sample	Location	Lithologies	Coordinates	Nb of spectra	R1	R2	T (°C)	1σ (°C)	SD (95%)	SEM (95%)
Mb19c	Amône	Limestone	45°45'52.06"N 6°44'9.68"E	12	1.57	0.6	370	7.9	35 (4.49 σ)	6.34
Mb20c	Combe des Fonds	Bajocian limestone	45°45'51.37"N 6°44'7.22"E	11	1.73	0.53	403	7.76	35 (4.58 σ)	8.31

Table V.2: RSCM results from the Val Ferret. SD=Standard deviation and SEM= Standard Error of the Mean

In addition to these data, dark brown magmatic biotite is replaced by light brown biotite with rutile and green biotite as described by Bussy (1990) in the Mont-Blanc. This was also observed in the Aar massif and related to isotopic rejuvenation of the biotite (Dempster, 1986) during Alpine greenschist metamorphic overprint.

Sample: MB20c						
Spectrum	G position (cm ⁻¹)	G-FWHM	R1	R2	T (°C)	
1	1583	26	0.84	0.53	405	
2	1583	25	0.85	0.54	400	
3	1583	26	0.79	0.51	416	
4	1585	19	1.05	0.54	399	
5	1582	27	0.82	0.51	412	
6	1583	26	0.95	0.56	391	
7	1583	27	0.83	0.51	412	
8	1583	26	0.80	0.52	408	
9	1583	27	0.87	0.54	400	
10	1581	29	1.10	0.55	395	
11	1582	26	0.95	0.53	406	
Average	1582.82	25.82	0.89	0.53	404	
1σ	0.94	2.37	0.10	0.02	7.40	

Table V.3: RSCM data for each spectrum of sample MB20c

<i>Sample: MB19d</i>					
<i>Spectrum</i>	G position (cm-1)	G-FWHM	R1	R2	T (°C)
1	1594	39	1.93	0.64	357
2	1588	39	2.02	0.62	364
3	1585	34	1.64	0.61	371
4	1587	32	1.62	0.63	361
5	1589	26	1.29	0.62	365
6	1584	36	1.62	0.60	375
7	1583	26	1.51	0.59	379
8	1585	35	1.71	0.62	363
9	1585	34	1.51	0.59	379
10	1588	29	1.34	0.59	378
11	1581	29	1.25	0.60	375
12	1587	24	1.46	0.59	377
<i>Average</i>	1586.33	31.92	1.57	0.61	370
<i>1σ</i>	3.20	4.87	0.23	0.02	7.60

Table V.4: RSCM data for each spectrum of sample MB19d

3. Basement characterisation

3.1. Definition of basement type

3.1.1. Central and border granite

In the area, the main Mont-Blanc granite can be divided into a central porphyric granite (central granite) and lateral facies (border granite) showing equigranular textures and enriched in quartz (Fig. V.5A; Marro, 1987; Bussy, 1990). It is rather heterogeneous in composition. Various biotite and feldspar contents can be observed and are interpreted as mechanical segregation of grains in the magma (Bussy, 1990). Orthoclase minerals can form centimetric mega crystals with quartz and plagioclase inclusions. The plagioclase observed has a composition ranging from albite to oligoclase. Biotite represents around 5% of the modal composition in average (Bussy, 1990). Apatite and zircons inclusions as well as rutile needles are observed in the biotite. Hornblende partially replaced by biotite is also present (Bussy, 1990). This ferro-hornblende gives a crystallisation temperature of ca 760°C (Bussy, 1990) and a pressure of 3.8 Kbar based on tetrahedral Al (Marshall et al., 1997). Other secondary minerals such as zircon and allanite are also described. Mafic intrusions and mafic xenoliths (Fig. V.5A) can be observed locally. The border of the intrusion is composed of equigranular granites (Fig. V.5B and C) which appear more differentiated than the central granite (Bussy, 1990). Locally, biotite foliation is observed which indicates a syn-magmatic deformation (Fig. V.5D).



Figure V.5: A- Field photograph of the central granite appearing coarse grained with a porphyritic texture and mafic xenoliths. B and C- Border facies of the granite showing an equigranular texture as observed in the area of Brea. D- Microgranite with magmatic inherited texture such as biotite lineation.

The central granite is crosscut by microgranites and leucocratic granites which are characterized mainly by a homogeneous grain size repartition, smaller than in the granite. They have a composition almost similar to the granite with smaller amounts of biotite.

3.1.2. Pegmatite and schlieren

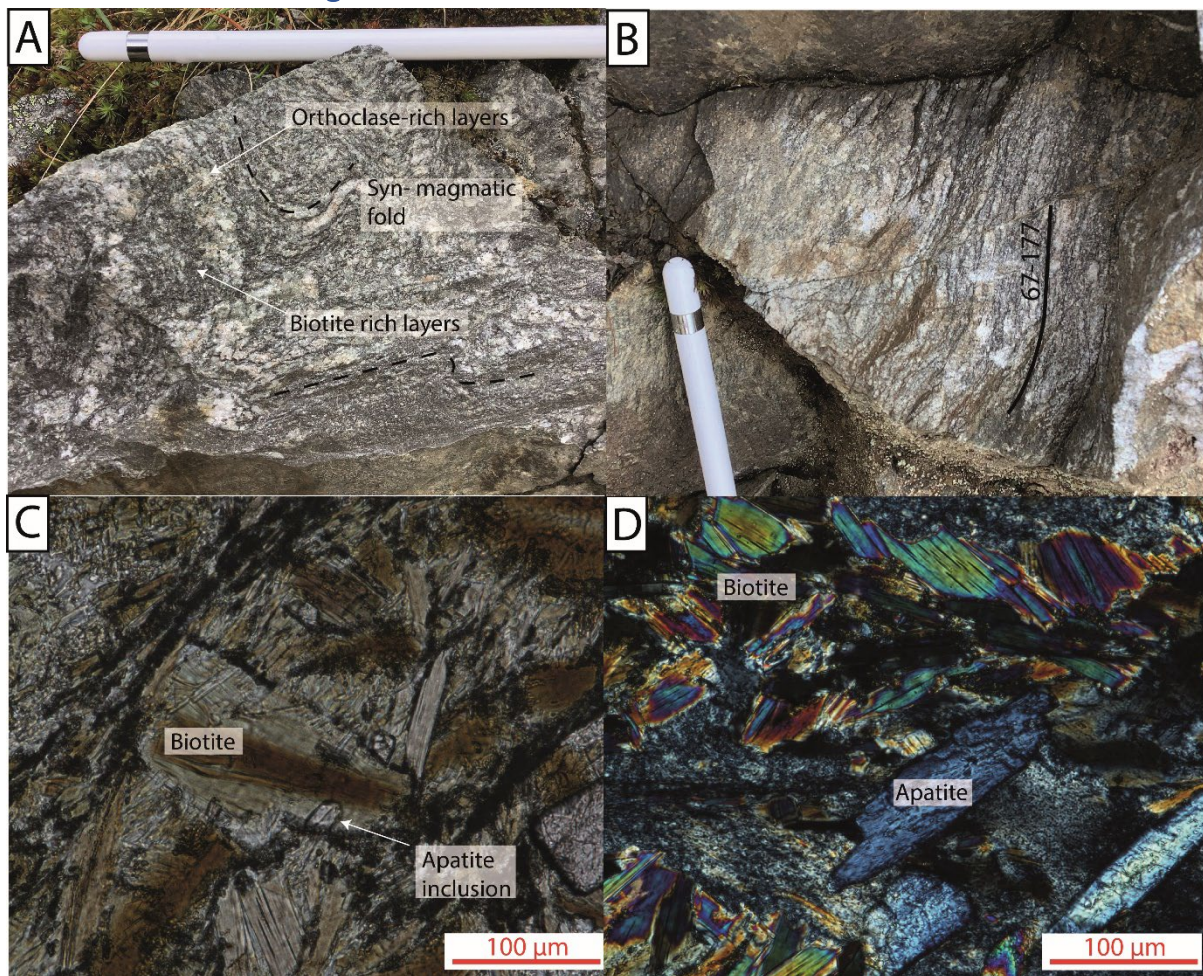


Figure V.6: A and B- Foliated magmatic rock with alternating black and with layers corresponding to schlieren. Syn-magmatic folds are visible. C- Optical microphotograph (PPL) of the black layers composed of biotite. Small apatite inclusion typical of magmatic biotite are present. D- Optical microphotograph (XPL) of the black, biotite-rich layers showing the presence of large apatite crystals associated with biotites.

Metric intrusions of coarse-grained granitic rocks are observed in the polymetamorphic basement. They are composed of millimetric plagioclase and orthoclase crystals mostly. The coarse-grained appearance of the rock is similar to pegmatites found along the main granitic intrusion.

Locally, foliated rocks composed of millimetric to centimetric dark layers affected by centimetric folds (Fig. V.6 A and B) are visible. The dark layers correspond to aggregates of large (> 100 µm), randomly oriented brown biotite and apatite (Fig. V.6C and D). These biotites have also small (10 µm) apatite inclusions and resemble to the magmatic biotite described in the main Mont-Blanc granite (Bussy, 1990). The white layers are composed of orthoclase mainly. This layered aspect with biotite aggregates is similar to textures such as schlieren described also in the Mont-Blanc by Bussy, (1990). Schlierens are concentrations of mafic minerals in magmatic intrusions associated to magmatic flow or crystal settling at the interface between layers with different viscosities (Ardill et al., 2020). Therefore, the micro-folds observed in the Mont-Blanc are probably syn-magmatic and related to magmatic flow leading to crystal sorting.

3.1.3. Carboniferous Rhyolite

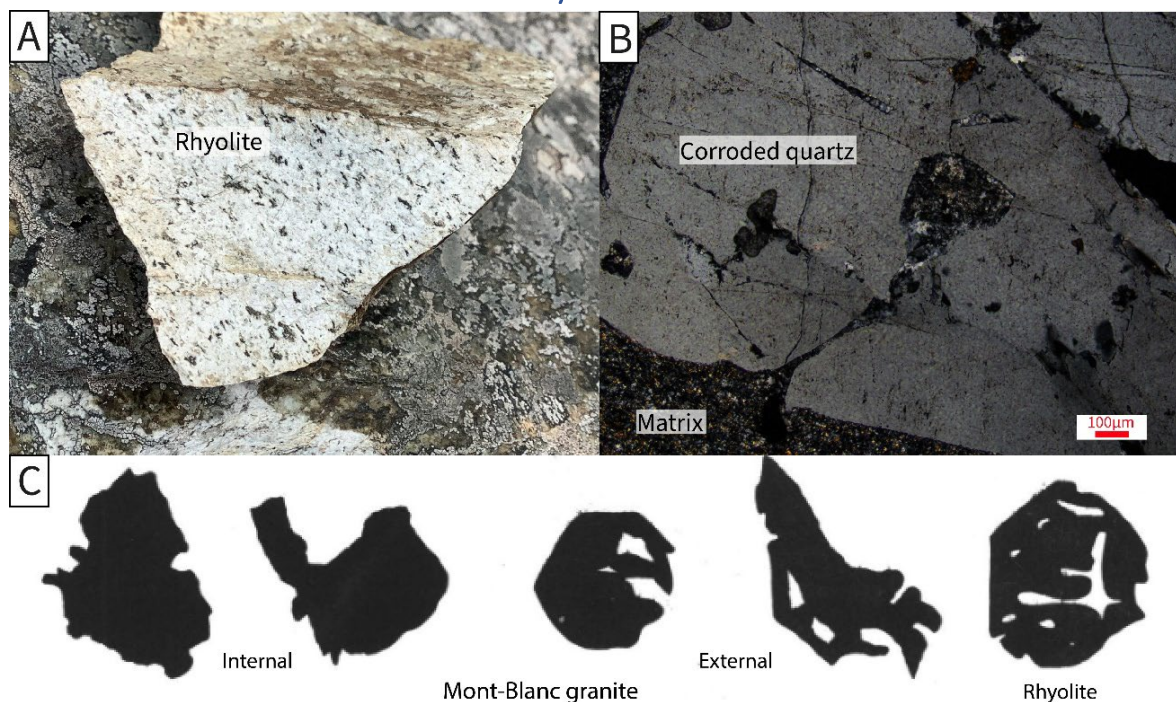


Figure V.7: A- Rhyolite from the Mont-Blanc showing dark biotite phenocrysts in a white matrix. B- Optical microphotograph (PPL) of a corroded quartz characteristic of rhyolites. C- Illustration of quartz shapes in the Mont-Blanc granites and rhyolites. Rhyolite are characterized by strongly corroded quartz (from Marro, 1987).

The granite is bordered by a rhyolite (Brea rhyolite) dated 307 ± 2 Ma (Capuzzo and Bussy, 2000). It can be observed from Champex until the Ferret pass. The rhyolite is white in most of the localities but can also appear reddish in the southern Val Ferret. Dark phenocrysts corresponding to biotites, and epidotes can be observed macroscopically (Fig. 7A). At the microscale, the rock is composed of millimetric corroded quartz grains, feldspars, and biotite in a fine-grained matrix of quartz, feldspars and white micas (Fig. 7B). This matrix appears recrystallized and strongly altered and might correspond to post-formational transformation of volcanic glass. However, no clear perlitic texture was identified.

Saussurization of the feldspars is also observed (Ep-Chl-Wm alteration) associated to epidote filling fractures. These epidotes appear dark green at microscale. The epidotes in the veins are relatively coarse-grained (100 μm), while epidotes associated to the alteration of feldspars are fine-grained (10 μm).

3.2. Composition of the magmatic basement

The Mont-Blanc granite corresponds to a granite to monzo-granite characterised by high-K and Fe content (Fig. V.8), as indicated by its high #Fe number (0.7-0.8). The Al/(Na+K) (A/NK) ratios are comprised between 0.9 and 1.42, and the Al/2Ca+Na+K (A/CNK) are ranging between 0.8 and 1.42, corresponding mostly to metaluminous rocks (Frost et al., 2001).

Preserved Jurassic Structures in the Northern Mont-Blanc massif (Val Ferret, Switzerland)

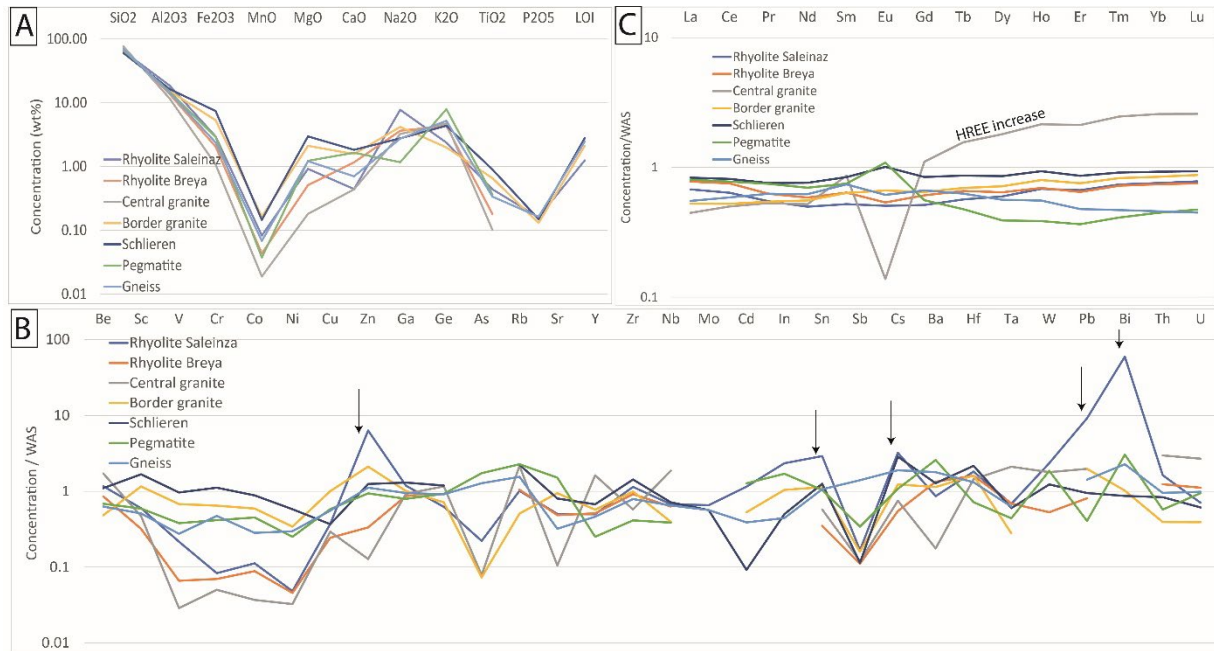


Figure V.8: A- Composition of the different basement samples of the Val Ferret in major elements. B- Composition in trace elements normalized to World Average Shales (WAS; Wedepohl, 1971). C- Composition in Rare Earth Elements normalized to WAS.

The composition in major elements is relatively homogeneous (Fig. V.8A). The border granite shows the highest concentration in FeO, MnO, MgO while the lowest concentrations are observed for the central granite. The Brea rhyolite is enriched in Na and K, while the pegmatite from the Col des Planches area shows the highest K content. The enrichment in Fe and Mg has been observed in the Mont-Blanc massif and in other Variscan granitoids, where it results from partial melting of a metasomatized mantle and reflects low crustal contamination (Bussy, 1990).

Trace elements show significant variations among the different samples (Fig. V.8B). The Mont-Blanc granite is depleted in Cr, V, Co, Ni and enriched in Rb, Hf, Ta, W, Pb and U compared to the other rocks. The increase of U in the Mont-Blanc granite is related to the refractory behaviour of this element leading to enrichment in silica melts (Friedrich et al., 1987; Cuney, 2014). The border granite has no clear enrichment in any elements, as was also observed by Bussy (1990). On the contrary, the Saleinaz rhyolites show significant enrichment in Pb, Zn and Bi.

The composition in Rare-Earth-Elements (REE) is more heterogeneous (Fig. V.8C). The normalization to the world shales representing the upper crust composition (Wedepohl, 1971) shows that the composition of the Mont-Blanc massif basement is similar to the composition of the upper crust. The diagram appears flat close to 1 except for the granite showing an increase on the Heavy Rare earth Element (HREE). This fractionation of HREE is not observed in highly differentiated rhyolites. The Eu anomaly varies strongly among the different basement samples (Fig. V.9B). Indeed, the Mont-Blanc granite shows a large negative anomaly ($Eu/Eu^*=0.09$) while the rhyolite samples shows only small Eu anomaly ($Eu/Eu^*=0.5-0.6$). Small positive anomalies are observed in the

microgranites ($Eu/Eu^*=1.07-1.14$). These variations in anomalies might reflect changes in the source (Norman et al., 1992) as well as changes in the degree of melt fractionation (Sawyer, 1987).

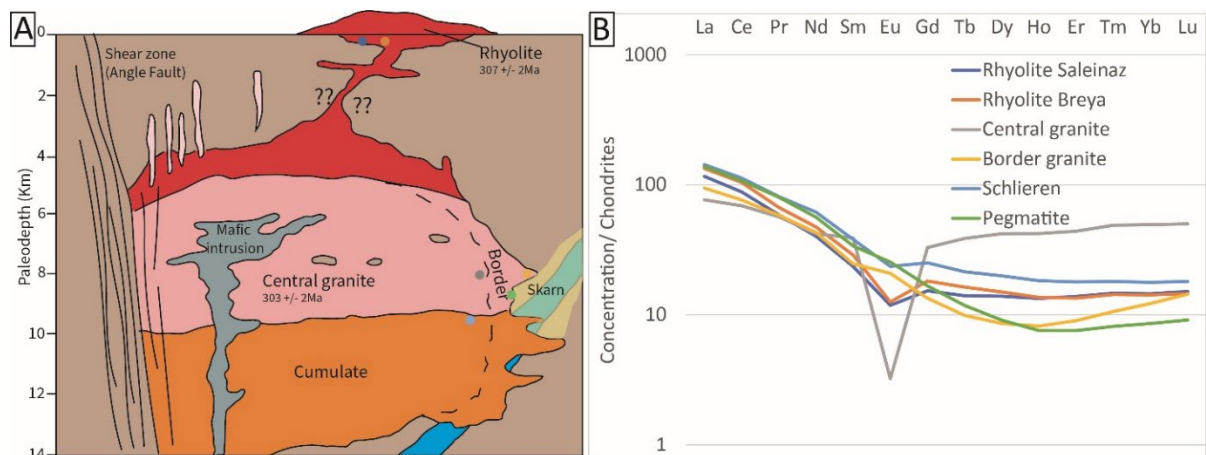


Figure V.9: A- Schematic view of the Mont-Blanc intrusion (modified from Bachmann and Bergantz, 2008) and its relation with Carboniferous shear zones. The points represent the position of the different samples. B- REE composition normalized to chondrites.

3.3. Scaling relation for the Mont-Blanc pluton size

The dimension of the Mont-Blanc granite can be deduced from the geological map. The lateral border of the granite is clearly defined which allows to calculate the length of the pluton. The homogeneous fission track ages along the NE-SW profile of the Mont-Blanc (Bergemann et al., 2019) indicates homogeneous exhumation. Therefore, the actual length of the granite corresponds to the initial length comprised between 25 and 30 km. The width of the intrusion is however more complex to obtain. Indeed, the exhumation of the external Mont-Blanc is different from the internal Mont-Blanc. In addition, the external part of the massif is affected by Alpine shear zones.

Scaling relations allow to extrapolate the thickness of the intrusion from the length of the intrusion (Cruden et al., 2017): $T = bL^a$ with T the thickness (m), L the length (m), b and a scaling factors. For plutons, they correspond to 1.08 ± 1.38 and 0.81 ± 0.12 respectively. This gives a thickness of the Mont-Blanc plutons of 14 to 16 km (Fig. V.9A).

The geobarometer of Johnson and Rutherford (1989) based on Al in hornblende gives a pressure of 3.8 Kbar for the Mont-Blanc granite, corresponding to a depth of ca. 12km (Marshall et al., 1997). This geobarometer gives a depth of emplacement similar to the pluton size estimated from scaling relations.

4. Autochthonous sedimentary cover

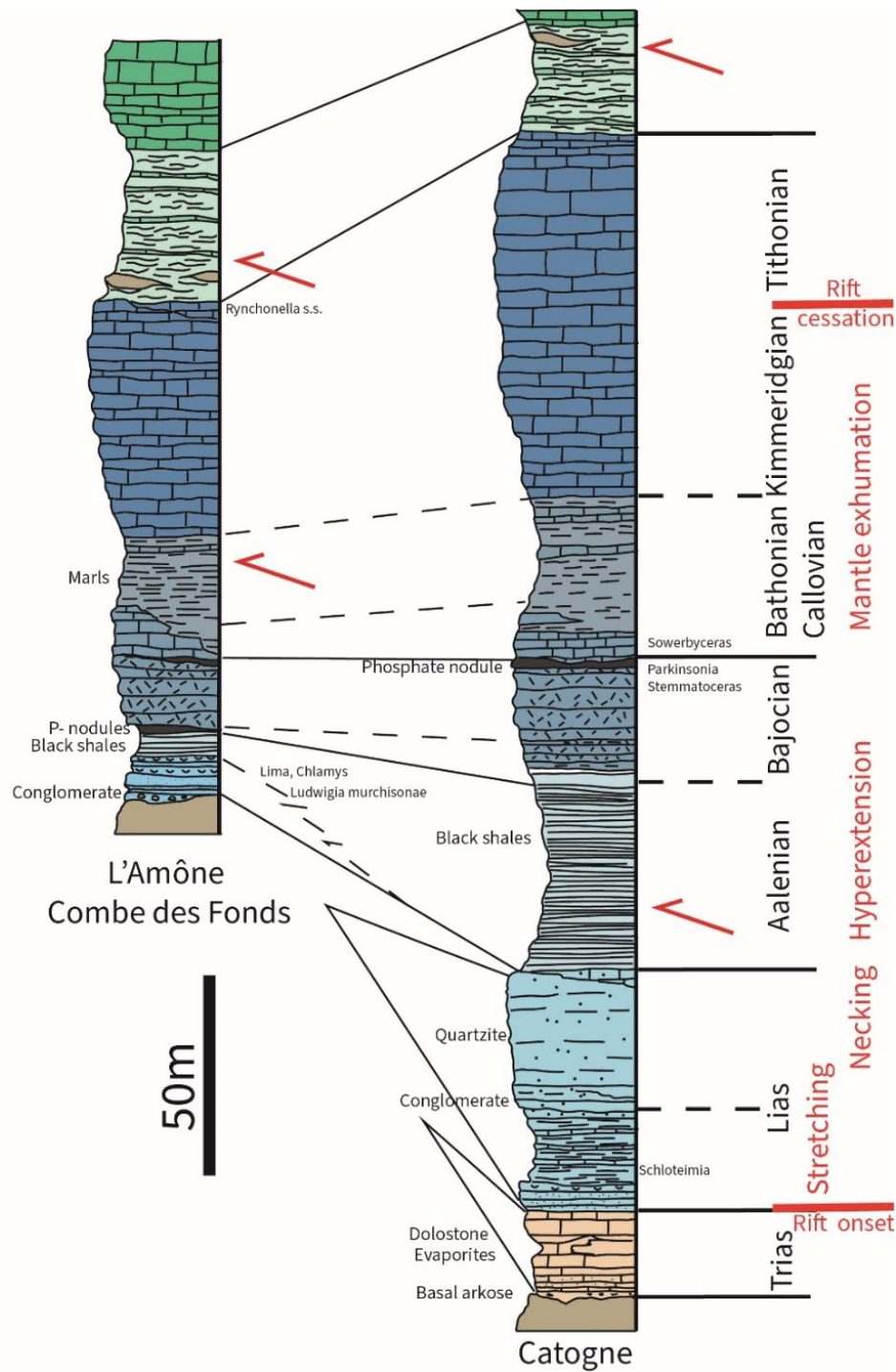


Figure V.10: Stratigraphic section (modified from Grasmück, 1961) from the south Val Ferret (L'Amône) and the north Val Ferret (Catogne) associated to the main rifting stages (from Ribes et al., 2019b, 2020).

An autochthonous cover is preserved in the Val Ferret above the basement (Trümpy, 1971; Grasmück, 1961). This cover corresponds in the Catogne Mt. (north Val Ferret) to Triassic pre-rift sediments overlaid by syn-rift Liasic limestones and sandstones coeval to the Grès Singuliers (Fig. V.10). The thick Aalenian shales overlying the sandstones form the base of the Helvetic nappes. The cover above the Aalenian shales corresponds to para-autochthonous and allochthonous units from

the Helvetic nappes. Toward the south, the basement is overlaid directly by lower Aalenian sandstones and siltstones and by Aalenian shales (Fig. V.11). The thickness of the Aalenian shales is progressively reduced toward the south leading to the absence of a decoupling level between the basement and mid-Jurassic sediments.

4.1. Pre-rift cover

The pre-rift cover is observed in the Catogne Mt and in the Mont-Chemin area. The Triassic series starts by an arkose (“basal arkose” of Grasmück, 1961) overlying the basement (Fig. V.11A). This layer is 2 to 4 meters thick. No sedimentary figures can be recognized at the base of the formation. This arkose shows moderate to no Alpine schistosity at all and is coarse-grained with centimetric clasts. Verrucano clasts (Carboniferous-Permian volcanism) can be clearly recognised indicating reworking of volcanic deposits. This arkose is characterized by the abundance of lithic clasts and feldspars. The lithic clasts can be monomineralic (quartz) or polymineralic (quartz + feldspar). The quartz shows clear signs of dynamic recrystallization indicating a metamorphic origin. No granitic fragments were recognized. The cement is mostly composed of sericite (recrystallized clays). Toward the top, dolomitic nodules were described (Grasmück, 1961) highlighting the progressive marine transgression above the basal arkose.

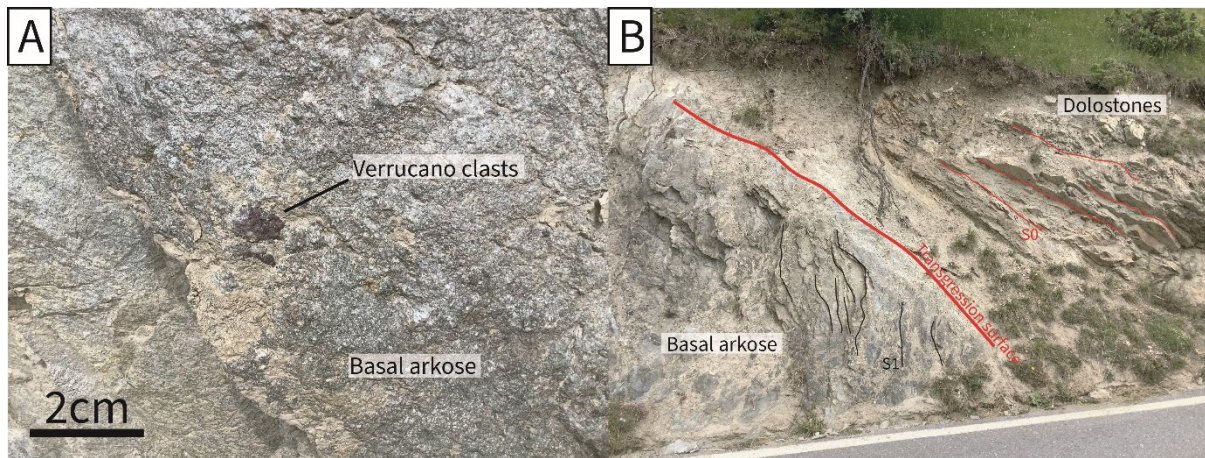


Figure V.11: Pre-rift cover in the Mont-Chemin area. A- Triassic basal arkose with rhyolitic clasts. B- Transition between basal arkose and the Triassic dolostones.

Dolostones, which overlie the Arkose, have a thickness of ca. 20 to 25 m (Grasmück, 1961) and comprise centimetric to metric beds without sedimentary figures (Fig. 11B). Centimetric shale intercalations are visible in-between the beds. Cornieule levels (former evaporite deposits) are also interlayered with the dolostone. They correspond to polygenic breccias with pluri-centimetric clasts of quartz veins reworked in the breccia.

4.2. Syn-rift cover

4.2.1. Syn-necking sediments

A clear change of sedimentation from carbonate- to clastic-dominated is observed during the Sinemurian. These clastic deposits are upper Sinemurian to Pliensbachian in age, coeval to the Grès Singuliers south of the Mont-Blanc massif (Ribes et al., 2020). These deposits have a thickness up to a 100 m to the north of the Catogne Mt. but are absent to its south. Their base is composed of polymictic breccias compositing basement and cover-derived centimetric clasts. Toward the south, the proportion of basement clasts is increasing (Grasmück, 1961). In addition, similarly to the Col du Bonhomme, basement clasts appear usually rounder than dolostones clasts.

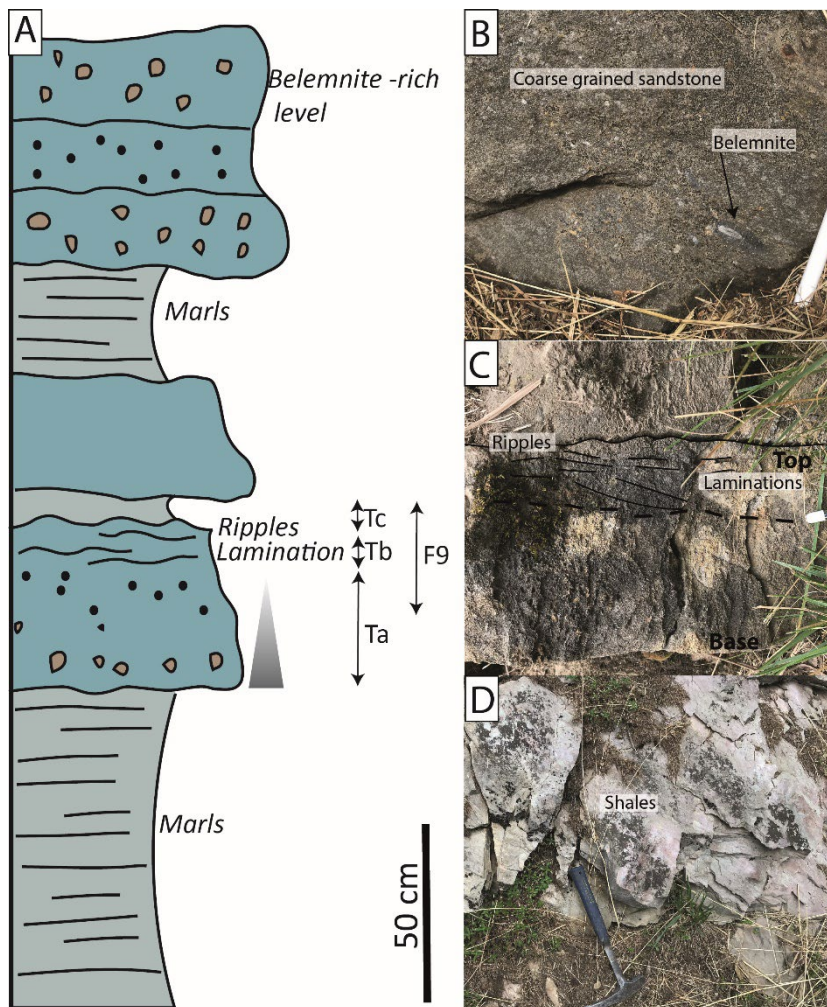


Figure V.12: A- Synthetic section drawn from field observations of the late Liassic shale- sandstones alternations from the Col de planches. Classification of turbidites from Bouma (1964) and Mutti (1992). B- Coarse-grained sandstones with belemnites. C- Top of a sandstone bed with laminations and ripples. D- Shales interlayered with the sandstones.

These breccias are overlaid by sandstones. These sandstones are formed by massive beds in the Catogne area while in the Mont-Chemin they correspond to an alternation of metric beds separated by shales. Some of the beds are coarse-grained with centimetric clasts, whereas others are fine-grained. Upward fining of the beds is locally observed (Fig. V.12). In the top of the fine-grained

beds, ripples and laminations can be seen (Fig. V.12). The presence of belemnites suggests open marine conditions (Fig. V.12). The outcrop conditions are relatively poor in this area making the mapping of these deposits impossible.

Further north, the Sinemurian to Pliensbachian cover from the Saillon area (corresponding to the northernmost Mont-Blanc cover; Fig. V.1) is preserved. It corresponds to Lower Sinemurian passing to thick Upper Sinemurian sandstone beds. It is overlaid by sandy limestones interlayered with marls. The marls layers are first thickening upward then fining before passing to Pliensbachian sandstones. The facies show open marine conditions, similar to the Upper Liassic sandstones from Mont-Chemin.

It appears that there is a deepening of the deposits between the Catogne and Saillon areas as observed by the increasing amount of marls and limestones toward the north (Saillon). The sediments derived from the Mont-Blanc massif were thus likely transported along strike of the margin (SW-NE) into this basinal area. The occurrence of upward fining beds (Ta of Bouma (1964)) with lamination (Tb of Bouma (1964)) followed by ripples (Tc of Bouma (1964) and F9a deposits of Mutti (1992)) share some characteristics with gravity flows such as turbidites (Shanmugam, 1997; Zavala and Arcuri, 2016). Therefore, the lateral transport of the sediments along the margin might have been achieved through such mechanism.

The Pliensbachian sandstones are pinching out toward the south of the Mt Catogne, around Champex. In this area, they correspond mostly to conglomerates reworking the dolostone cover and the basement. The matrix of the conglomerate is composed of coarse-grained arkose (Fig. V.13A). These conglomerates are similar to the basal conglomerates of the Col du Bonhomme. They are overlaid by coarse-grained sandstones with numerous basement clasts (Fig. V.13B). Further south, they disappear, and the basement is directly overlaid by Aalenian sediments.

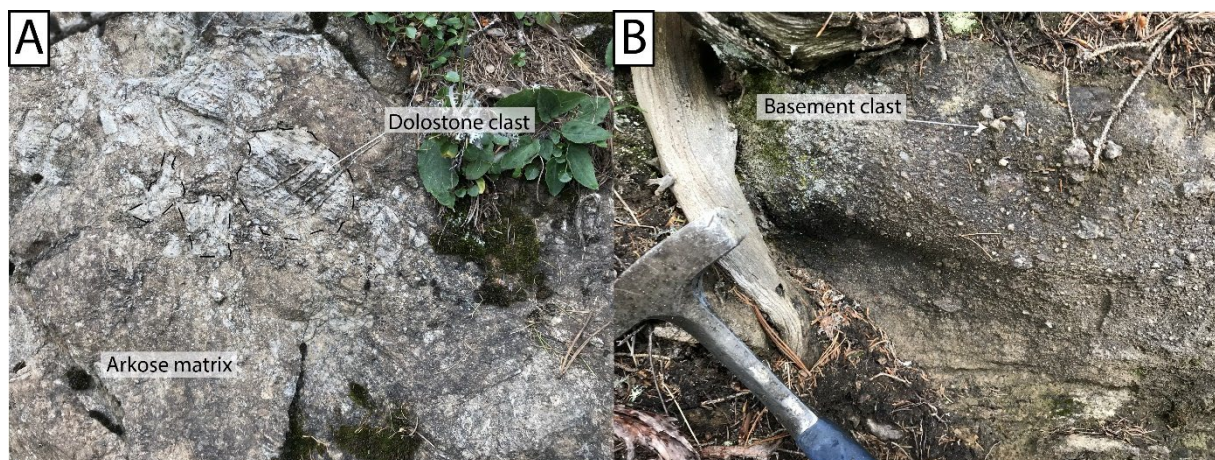


Figure V.13: A- Liassic conglomerates from the south Catogne massif showing decimetric clasts of dolostones reworked in the syn-rift sediments. B- Syn-rift sandstones with large basement clasts and fragments of quartz veins.

4.2.2. Post-tectonic sediments (Aalenian-Bajocian)

The main tectonic activity in the Mont-Blanc, as observed in the Col du Bonhomme area, occurred between the late Sinemurian and the Pliensbachian, before migration of the deformation toward the west associated to the hyperextension phase. Therefore, the middle to Upper Jurassic corresponds to syn-rift but post-necking sediments.

In the southern Val Ferret, the basement is overlaid directly by Aalenian sediments (transgressional conglomerate of Grasmück (1961)). They correspond to Lower Aalenian conglomerates and fine-grained sandstones. There is no occurrence of Liassic sediments which is surprising and raise the question of the post-tectonic evolution of the Val Ferret. The Upper Aalenian is characterized by the occurrence of phosphate nodules marking the presence of condensed levels associated to the progressive drowning of the massif. It is composed of black shales showing a developed Alpine schistosity (Fig. V. 14 B and C). The thickness of the shales is up to 200 m in Catogne and below 5 m in the southern Val Ferret. Abundant pyrite is found in these shales. This level is dated by *Graphoceras Concavum* ammonites (Grasmück, 1961).

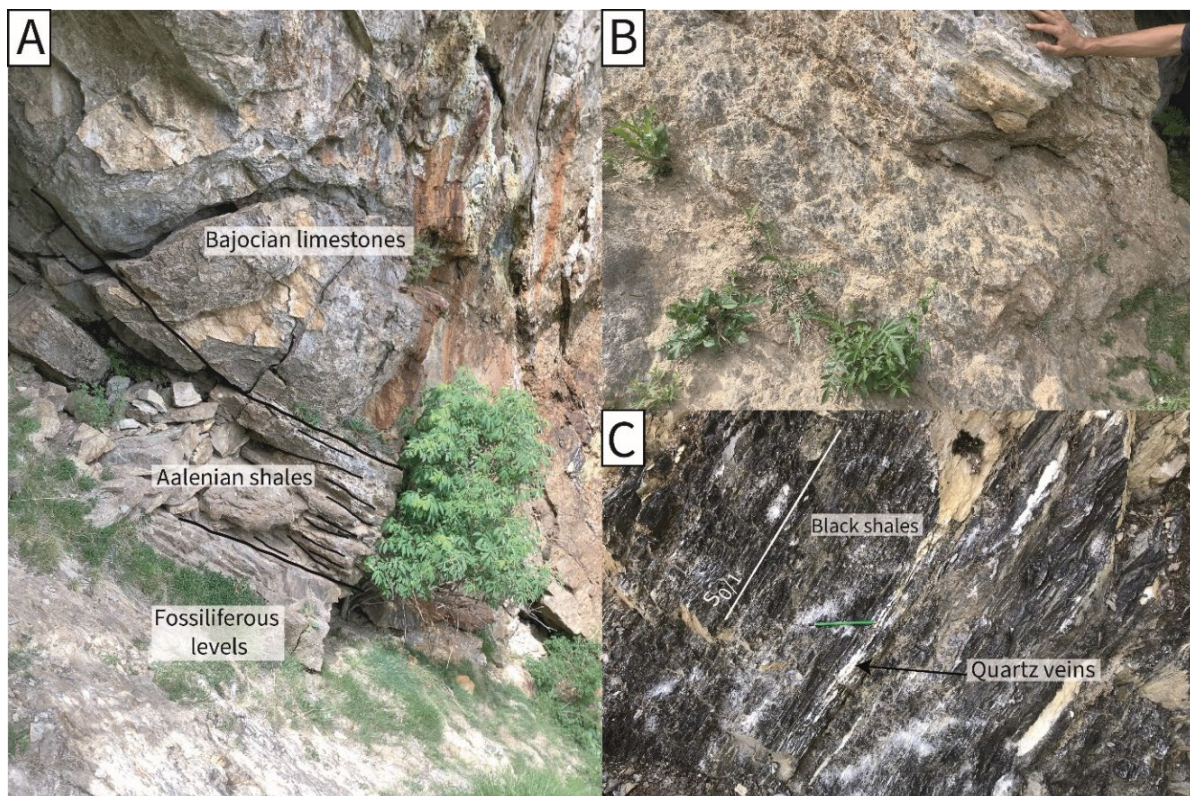


Figure V.14: A- Transition between fossiliferous Aalenian limestones to metric Aalenian shales level and Bajocian limestones. B- Mineralized black shales with yellowish sulphides alteration. C- Black shales with slaty cleavages and small quartz veins.

The black shales are overlaid by Bajocian echinoderm-rich limestones (Fig. V.14A). These limestones are strongly recrystallized especially in l'Amône, where they host ore deposits. The formation is overlaid by another condensation level, which is clearly visible in Champex but less

clearly marked in l'Amône. It also corresponds to a fossiliferous level precisely dated by ammonites *Parkinsonia Sowerbyceras* (Grasmück, 1961).

4.3. Post-rift sediments

Post-rift sediments are associated to the progressive drowning of the massif from the Bathonian to Callovian. They are found mostly in the para-autochthonous units. They correspond to nodular limestone and marl successions not dated precisely due to the lack of fossils (Grasmück, 1961). No indications of proximity with a landmass are visible.

Further south, after the Ferret pass, Albian sandstones have been described as lying directly above the basement (Compagnoni et al., 1964), which highlights two main features:

- The lateral discontinuity of the Jurassic cover along the massif. This discontinuity is also probable across the massif, between the external and internal massif, despite the lack of preservation of the cover;
- The long-term emersion of the Mont-Blanc.

5. Tectonized top basement

A series of sections through the sediment-basement interface and between the granite-rhyolite have been realised to better constrain the type of contacts observed in the northern Mont-Blanc massif.

5.1. South Val Ferret

5.1.1. L'Amône (section 1)

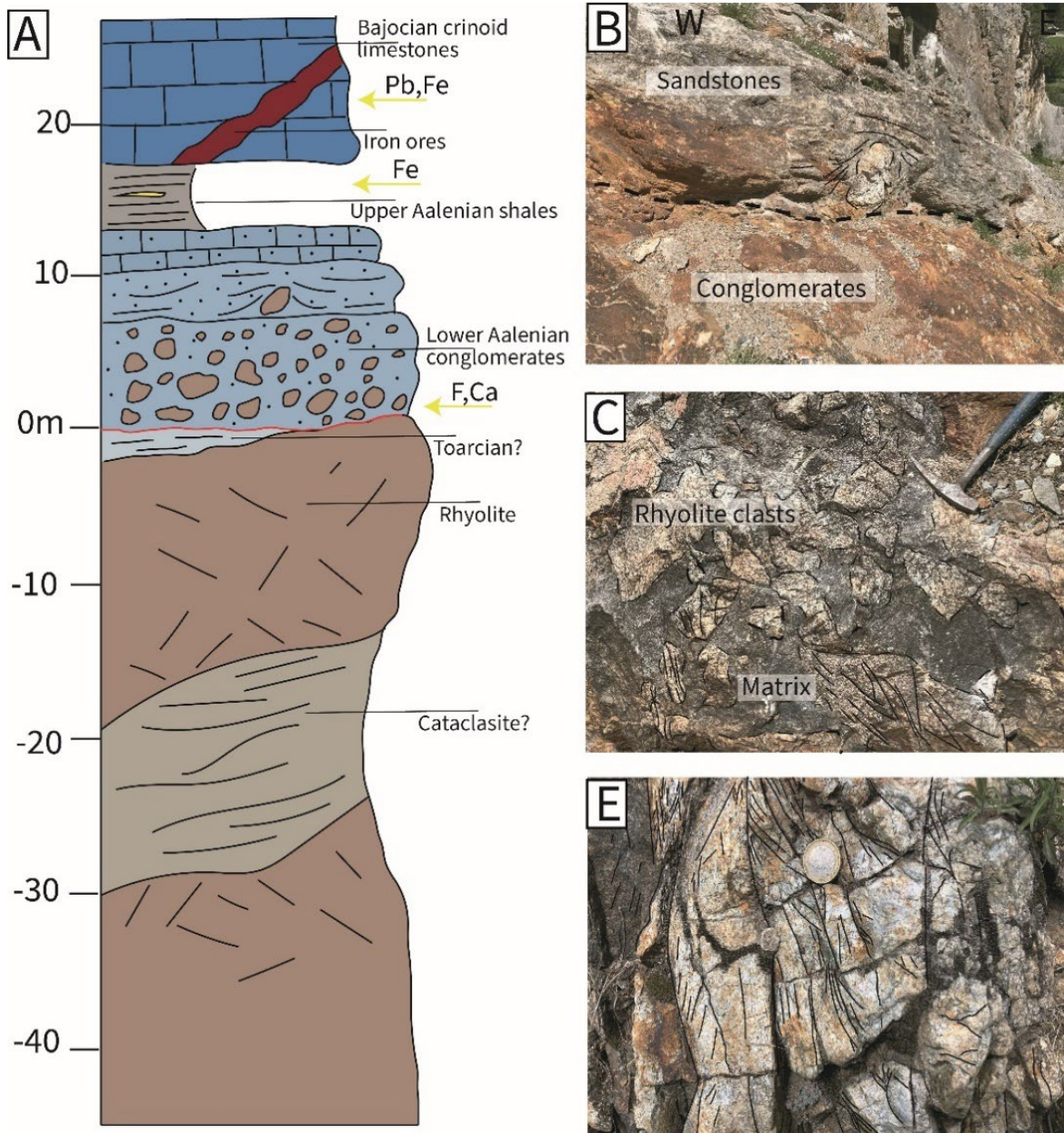


Figure V.15: A-Section (n°1) of the basement sediment-interface in l'Amône showing cataclasite affecting the basement and overlaid by Lower Aalenian conglomerates and sandstones. The arrows indicate the occurrence of mineralized sediments and ore deposits. B- Contact between the sandstone and the conglomerate showing large block sealed by the sandstone deposits. C- Breccias composed of clast of rhyolitic cataclasite. E-Cataclastic bands in the basement

5.1.1.1. Basement

The basement corresponds to whitish, strongly altered rhyolite. Locally, the rhyolite is strongly deformed (Fig.V.15). These zones correspond to sub-vertical meter-thick cataclasites developing a foliation and S/C structures. Toward the top basement, these cataclastic bands disappear but the basement is still affected by cataclastic deformation visible at microscale.

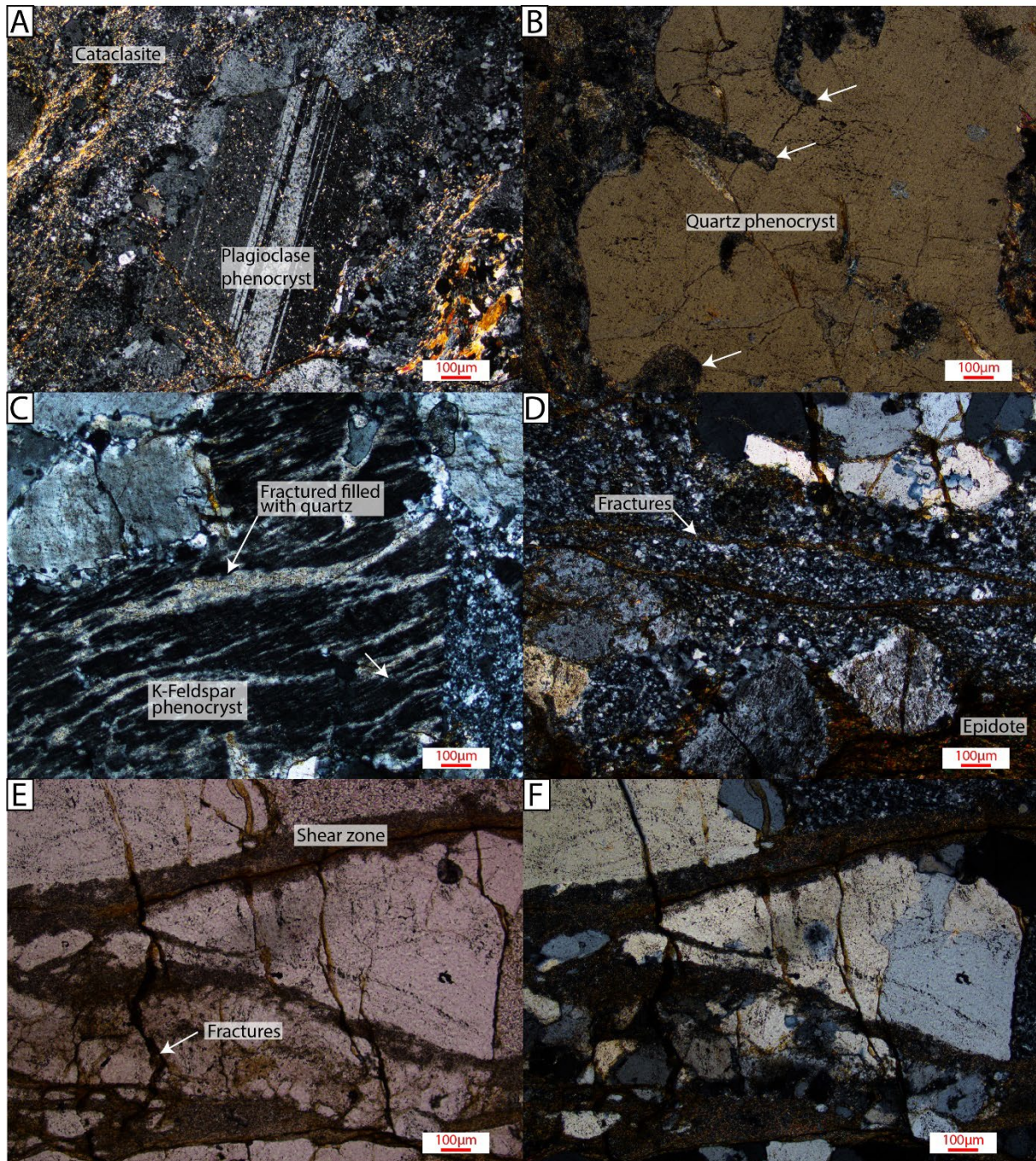


Figure V.16: A- Optical image (PPL) of a plagioclase phenocryst surrounded by cataclasite in the rhyolite matrix. B-Optical image (PPL) of a quartz phenocryst from the rhyolitic basement. C- Optical image (PPL) of a K-feldspar phenocryst crosscut by quartz filled fractures. D- Optical image of the recrystallized matrix of the rhyolite affected by fractures filled with epidote. E and F- Optical image (XPL and PPL resp.) of a shear zone composed of fine-grained epidote developing in the rhyolite.

At the microscale, the basement is composed of large quartz and plagioclase phenocrysts surrounded by a matrix of fine quartz grains (Fig. V.16 A and B). Although the amount of deformation varies, the whole section is affected by alteration and significant fractures. Important alteration of feldspars especially plagioclase is observed. This alteration corresponds to saussuritization (epidote-Chlorite-White micas). Sericitization is also observed mostly on K-feldspars. The primary texture of the rhyolite is overprinted by fractures developing mostly in the matrix and associated to the

formation of white micas and epidotes (Fig. V.16 A, D, E and F). The phenocrysts are also affected to a lesser extent by fractures (Fig. 16C). Small shear zones formed by ultra-fine-grained epidotes developed in the matrix. The anisotropy between the phenocrysts and the matrix seems to control the fractures development, which occurs preferentially in the matrix.

5.1.1.2. Sediment-Baseament contact

The top basement is marked by a less deformed rhyolite (deformation only visible at the microscale). A centimetre-thick level of dark limestone of unknown age is observed locally above the basement. This level might correspond to Toarcian condensed deposits although it has not been dated. Above, a massive conglomerate lies unconformably above the basement and the dark limestone. The contact between the conglomerates and the sediments is clearly primary and stratigraphic. Indeed, the matrix of the conglomerate is filling centimetric fractures in the basement (Fig. V.17A). This surface is however irregular and hard to map precisely. It appears as a series of metric depressions in the basement filled with decametric to metric blocks of rhyolite clasts.

5.1.1.3. Cover

The base of the cover is composed of rhyolite clasts similar to the rhyolite from the basement found just below. The clasts are centimetric to decametric and appear well rounded (Fig. V.17B). Indeed, while they seem to come from a local source, their shape indicates significant transport. These conglomerates have been interpreted as fan deposits derived from a nearby relief and deposited in a shoreface environment leading to reworking by wave vaning and progressive rounding of the blocks (Grasmück, 1961; Ribes et al., 2020). This hypothesis seems valid considering that the matrix of the conglomerate corresponds to a rhyolite arkose in a calcite cement probably derived from calcite mud in a marine environment. Moreover, ammonites have been found in this formation (Grasmück, 1961). These ammonites did not appear reworked from underlying sediments and indicate a Lower Aalenian age for the basal conglomerates. Clasts of rhyolitic cataclasite are observed at the base of the conglomerate (Fig. V.15C). It is worth noting that some clasts in the conglomerate show post-depositional fracturing with local centimetric displacement that are explained by Alpine deformation. In addition, coral fragments (*Isastrae*) are reworked in the conglomerates.

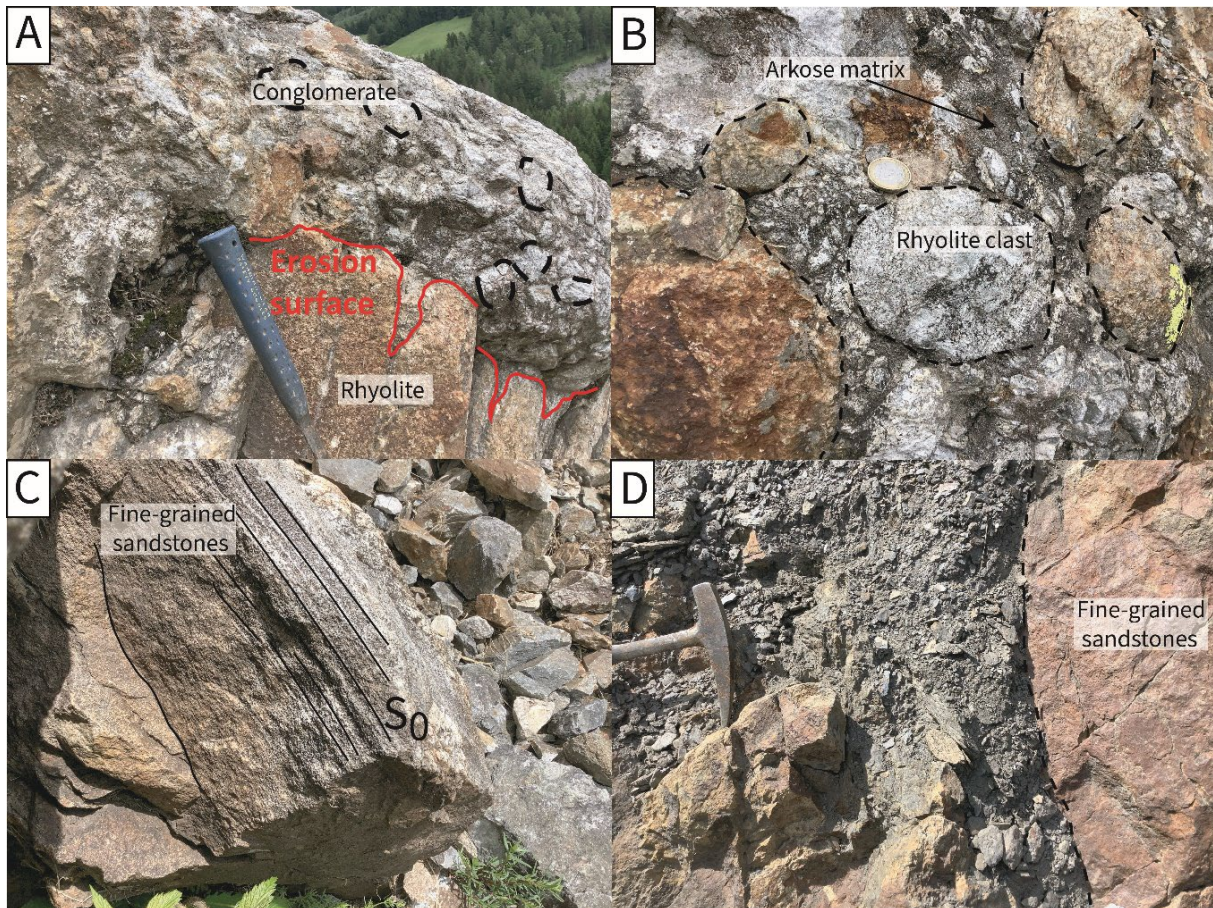


Figure V.17: A- Contact between the rhyolite and the Aalenian conglomerates. B- Decametric rhyolite rounded clasts in a sandstone matrix. C- Lower Aalenian sandstones showing fine-grained lamination. D- Contact between rhyolite and sandstones interlayered with shales in Saleinaz.

The conglomerate deposits are fining upward and pass to bioclastic sandstones (Fig. V.17C). At the base of the sandstones, decametric rhyolite blocks are locally observed, which are sealed by the sandstones indicating the persistence of a local relief with falling block in the sediments (Fig. V.15B). The overall decrease of coarse-grained sediments is associated with an increase of the content of calcite. The sandstones are overlaid by meter-thick sandy bioclastic limestones composed mostly of echinoderms, marking a progressive transgression over the conglomerates. They have been dated to the mid-Aalenian further north (Saleinaz) with ammonites (*Ludwigella nodata*; Grasmück, 1961). This transgression continued with deposition of a black shale. Its thickness is considerably reduced compared to the north of the Val Ferret and the south of the Mont-Blanc massif (Col du Bonhomme area). Above the Aalenian shales, fossiliferous Bajocian limestones are observed. They are locally lying directly over the basement, and in that case their base is coral-rich, indicating the occurrence of patch reefs over the basement.

5.1.1.4. Jurassic evolution of the l'Amône section

The section of l'Amône preserves remarkably well the transgressive conglomerates above the basement (Fig. V.18A). They are filling meter-thick depressions in the basement. The occurrence of

coarse conglomerates indicates the presence of a nearby relief responsible for the erosion of the rhyolitic basement. Remnants of pre-Aalenian sediments at the base of the conglomerate as well as reworking of the coral fragments in the conglomerates indicate a late uplift of this area reworking previous sedimentary deposits. The origin of this uplift is not well understood and will be discussed in the next chapter. These conglomerates are overlaid by marine sandstones and limestones indicating the progressive drowning of the area (Fig. 18B) from the middle to the upper Aalenian. This is associated with a decrease of the clastic input in the basin. This drowning is marked also by the deposits of upper Aalenian black shales. The occurrence of corals at the base of the limestones show that the black shales deposit was followed by a regressive phase during the Bajocian (Fig. 18C).

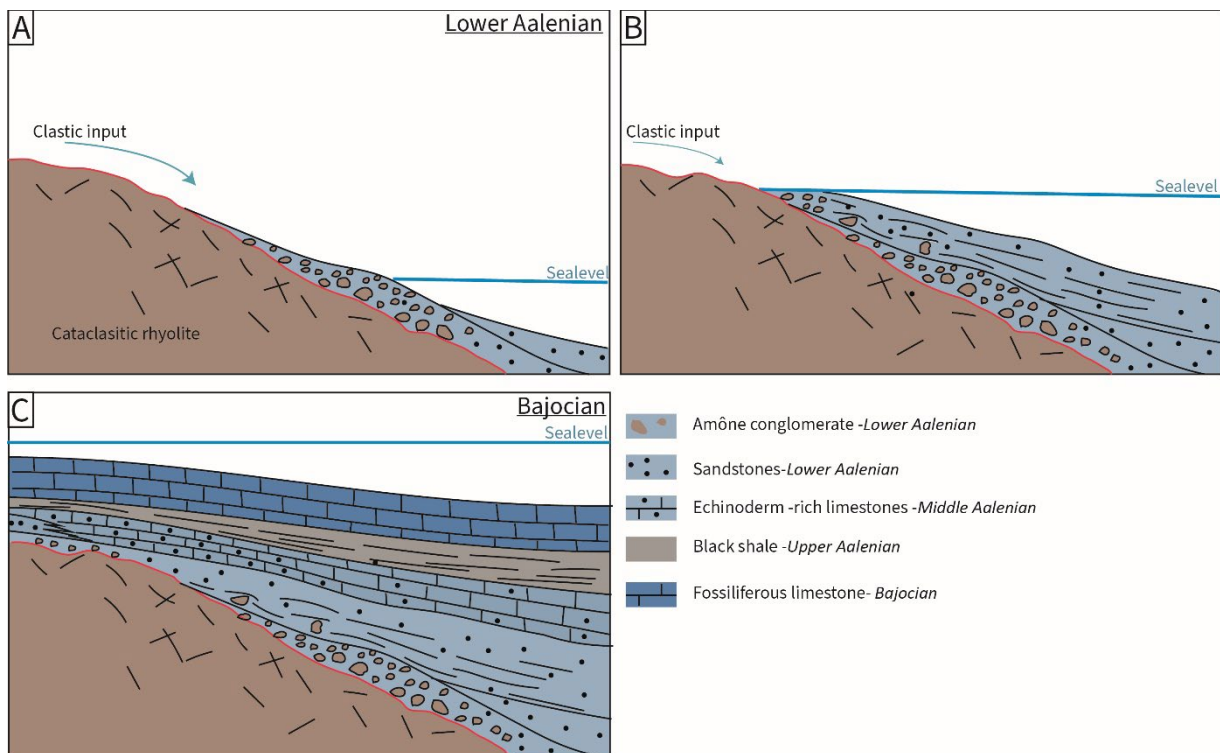


Figure V.18: A- Reconstitution of the area of l'Amône during Lower Aalenian with shoreface conglomerates over the basement highlighting the occurrence of a relief nearby. B- Progressive subsidence and smoothing of the relief led to the deposits of marine sandstone above the basement. C- Reconstitution during the Bajocian showing the transgression and progressive drowning of the area.

5.1.2. Saleinaz section (section 2)

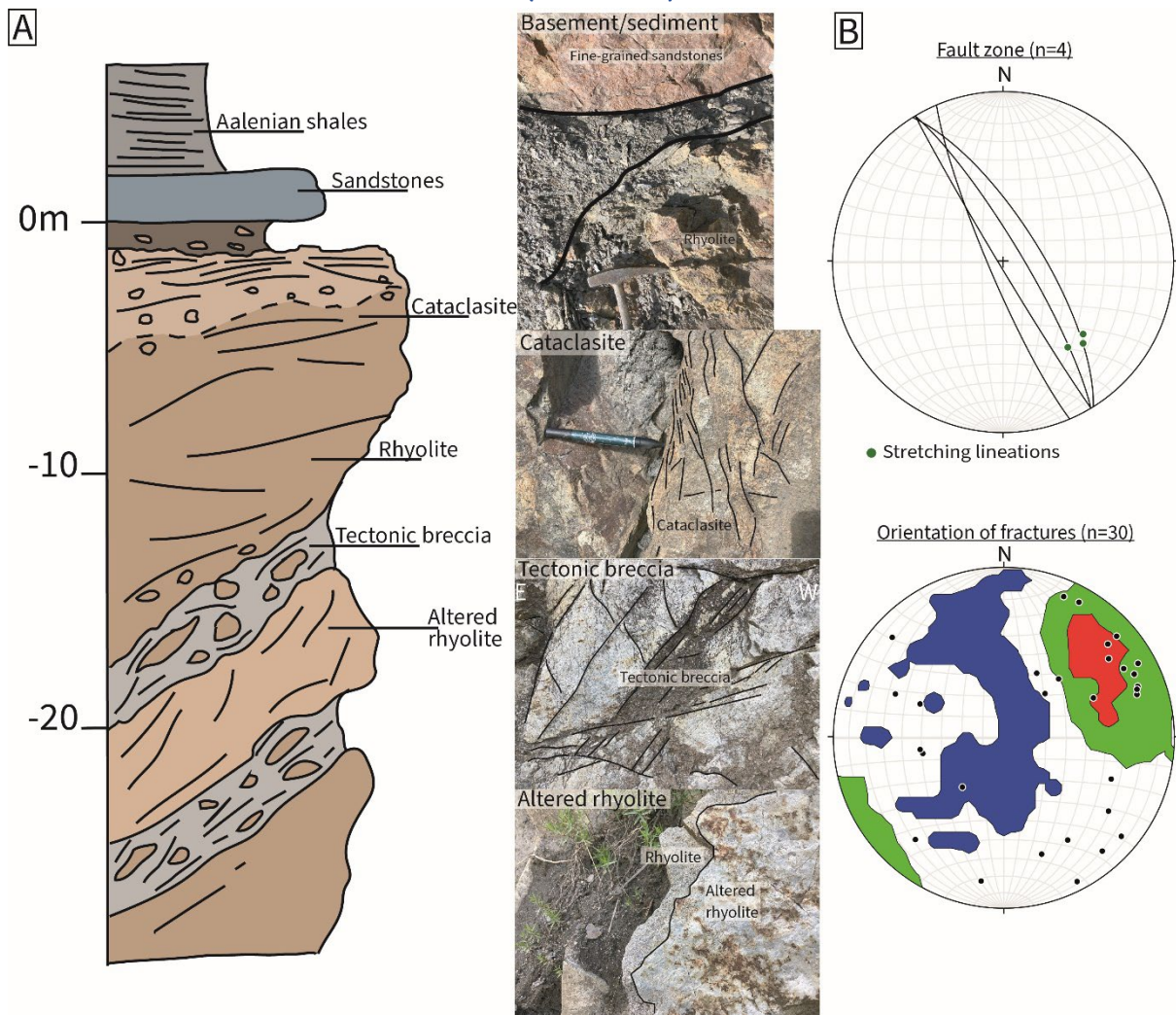


Figure V.19: A- Section of the sediment-rhyolite contact in Saleinaz. B- Orientation of cataclasite planes associated to stretching lineations and orientations of Alpine fractures in a stereogram (Wulf canevass; lower hemisphere).

5.1.2.1. Basement

The basement is composed of white rhyolite (Fig. V.19A). Toward the top, a progressive increase of deformation is observed. Sub-vertical tectonic breccias are also observed. They are composed of a strongly crushed and indurated dark matrix incorporating less deformed rhyolite clasts. Altered rhyolite form metric lenses in the tectonic breccia. They are whitish without any grains discernible. Closer to the top basement, cataclasites are present. At the basement/sediment contact, the basement is strongly deformed with widespread cataclasite visible. Stretching lineations on the cataclasite give a NW-SE direction on subvertical NW-SE fault planes corresponding to a strike slip movement (Fig. V. 19B).

At the microscale, the rhyolite appears relatively altered (Fig. V.20A and B). The matrix is recrystallized, and no trace of volcanic glass is visible. Perlites are observed indicating hydration of the matrix and possible devitrification processes (e.g., Davis and McPhie, 1996).

The deformation appears rather complex. It is localized along micrometric shear zones in the matrix of the rhyolite (Fig. V.20C). It is highlighted mostly by a decrease of the grain size (Fig. V.20D). Large feldspars and quartz are strongly fractured with clear displacement visible along the fractures. Plagioclase is affected by saussuritization (epidote + white micas). The cataclastic deformation is associated to important dilation with fractures filled with epidote (Fig. V.20A and B).

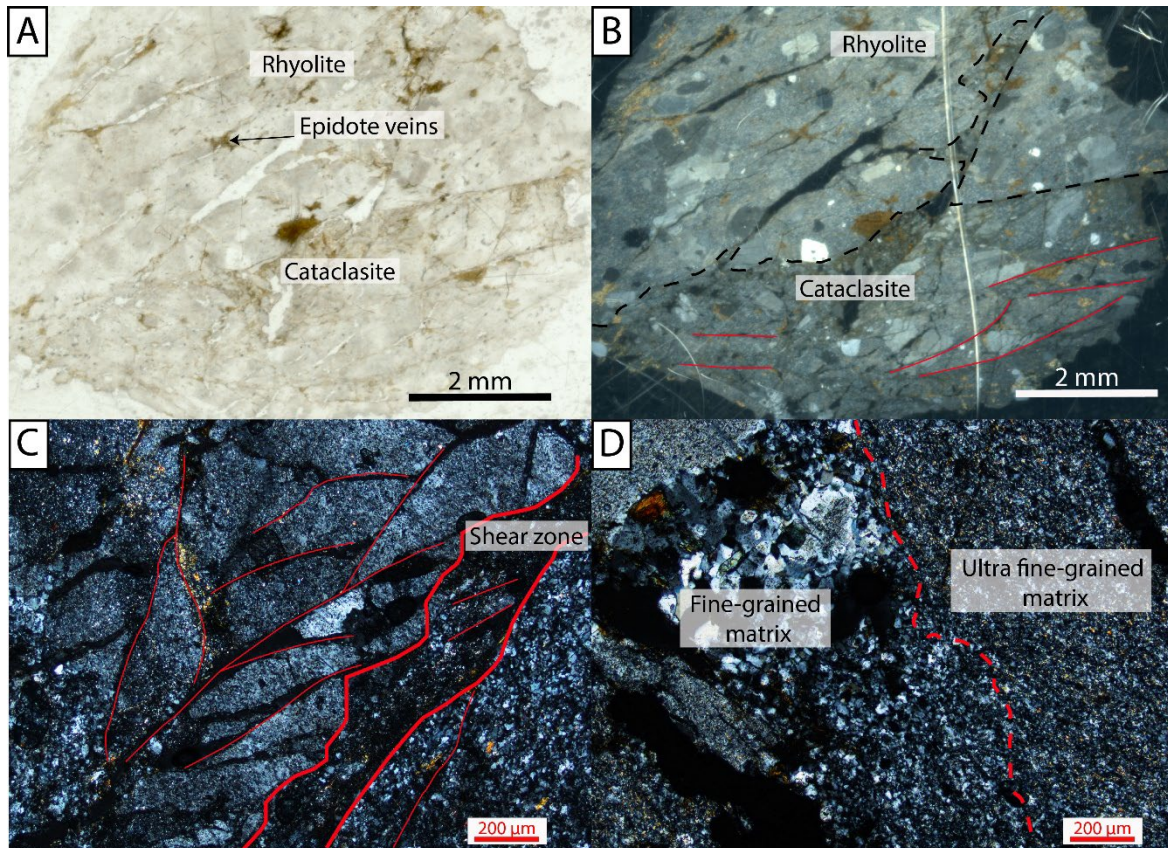


Figure V.20: A and B-Optical microphotograph (PPL and XPL) of cataclasite in rhyolite. C- Fractures in rhyolite associated to cataclastic deformation. Small shear zones are associated to strong comminution. D- Transition from fine-grained to ultra-fine-grained matrix associated to comminution.

5.1.2.2. Sediment-Baseament contact

The top basement surface, which is relatively irregular, is covered by a meter-thick shale level embedding fragments of the rhyolitic basement. This shale layer is overlaid by a meter-thick sandstone bed (Fig.17D). Additionally, a key element is the absence of deformation in the sandstone bed indicating that the deformation in the basement is pre-dating the sandstone deposition.

5.1.2.3. Cover

The sandstones are overlaid by around 60 m of Upper Aalenian black shales dated by ammonites (Appendix F; Grasmück, 1961). These black shales show a pervasive cleavage parallel to the bedding. It is overlaid by echinoderm limestones similar to the Bajocian limestones of l'Amône. Clasts of rhyolite have been recognized (Grasmück, 1961) in the limestones indicating the persistence of the topography during the Bajocian.

5.2. Brea section (section3)

The Brea peak (2373m) is found south of Champex where the best rhyolite outcrops are found giving its name to the rhyolite formation. The contact between the rhyolite and the Mont-Blanc granite has been mapped in this area (Marro, 1987). The nature of the contact between the granite and the rhyolite was, however, not clearly indicated.

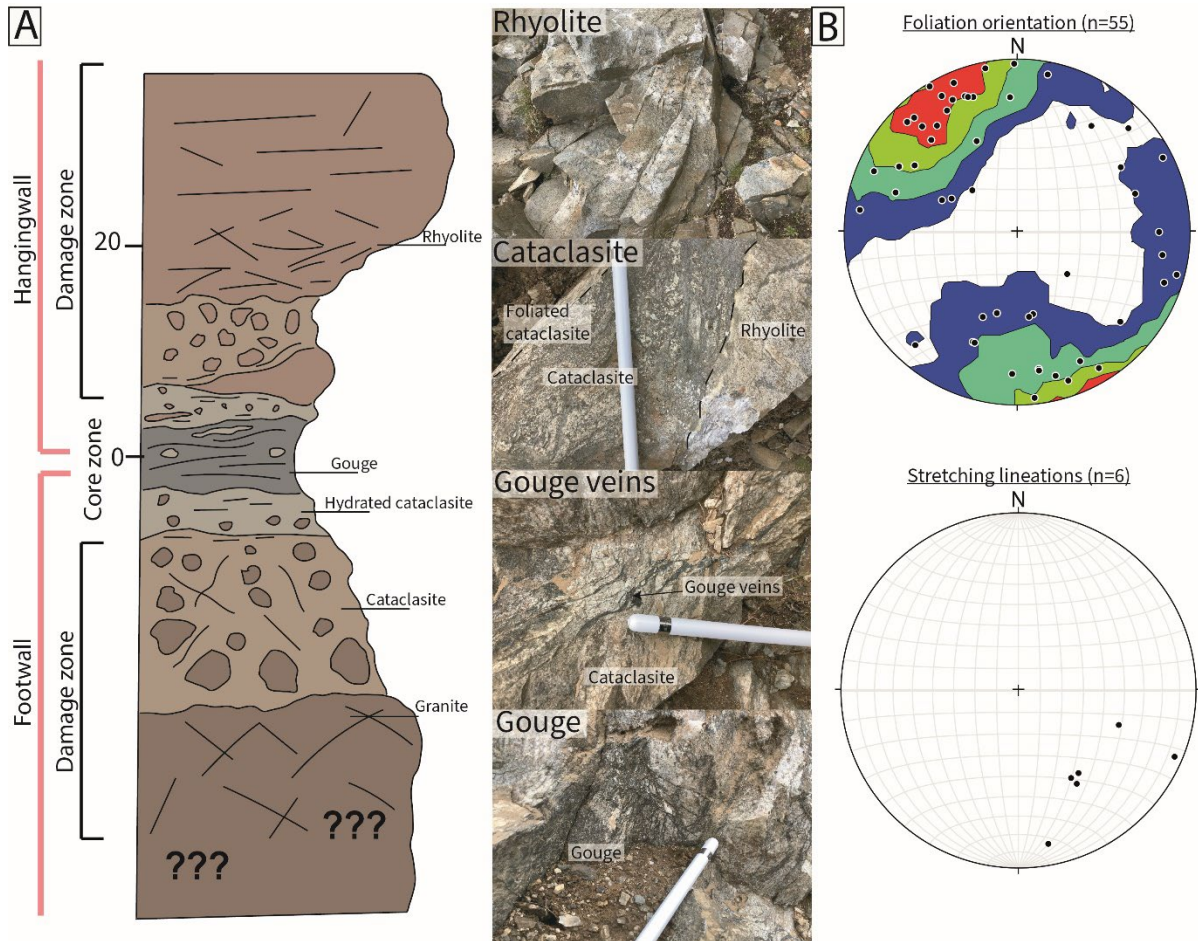


Figure V.21: A- Section of the fault zone between the rhyolite and granite from the Brea area. B- Poles of foliation orientation in the fault zone and stretching lineations associated to the fault zone in a stereogram (Wulf canevans; lower hemisphere).

The granite/rhyolite contact is clearly tectonic (Fig. 21A). Indeed, it is a fault zone ca. 40 m wide passing from a relatively intact granite (border granite and schlieren) to a cataclastic granite and rhyolite with centimetric levels of gouges reworking mostly clasts of rhyolite. The hangingwall of the fault is composed of rhyolite.

5.2.1. Damage zone

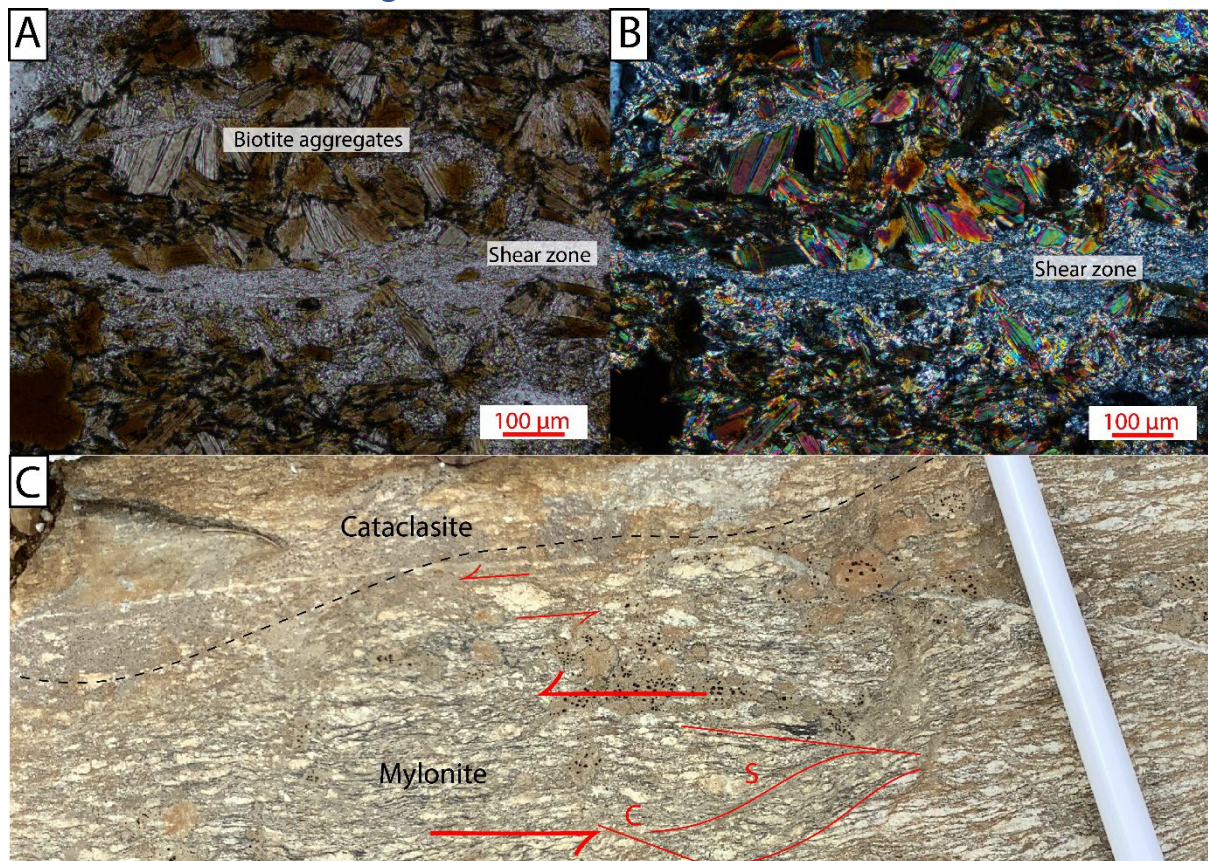


Figure V.22: A and B- Optical microphotograph (PPL and XPL) of schlieren overprinted by a micrometric shear zone. C- Mylonite in the damage zone overprinted by cataclastic deformation associated to loss of the S/C structures.

In the damage zone, the schlierens are affected by deformation pre-dating the syn- magmatic texture. The quartz-feldspar bands do not show significant dynamic recrystallization (Fig. V.22A and B). The feldspars appear strongly saussuritized. Primary biotite aggregates are affected by thin shear zones composed of fine grains white micas reworking biotite fragments. Quartz are also affected by dynamic recrystallization with bulging, corresponding to deformation at a temperature between 300°C to 400°C (Stipp et al., 2002).

The granite is also affected by mylonitic deformations. These mylonites show a sub-vertical N-S directed foliation with NW-SE sense of shear indicated by S/C structures and σ -clasts. This mylonites appear affected by strong alteration and cataclastic deformation overprinting the mylonitic foliation (Fig. V.22C). Toward the fault core, cataclasites are associated to strong alteration and a loss of any magmatic or mylonitic fabrics. The orientation of the cataclastic planes is roughly NW-SE. Stretching lineations give a NW-SE sense of shear (Fig. V.21B). Highly altered areas are greenish at the macroscopic scale. Closer to the granite-rhyolite contact, foliated cataclasites can be observed, associated to a localisation of the deformation. The feldspars are strongly altered and affected by important replacement by epidote. Epidotes are relatively coarse-grained with minerals up to 100 μm in size (Fig. V.23A). Clasts clearly derived from rhyolite can be observed (Fig. 23B). These quartz

are indeed characterized by important corroded gulfs (Marro, 1987). Indeed, equigranular millimetric quartz grains are observed associated to millimetric feldspars.

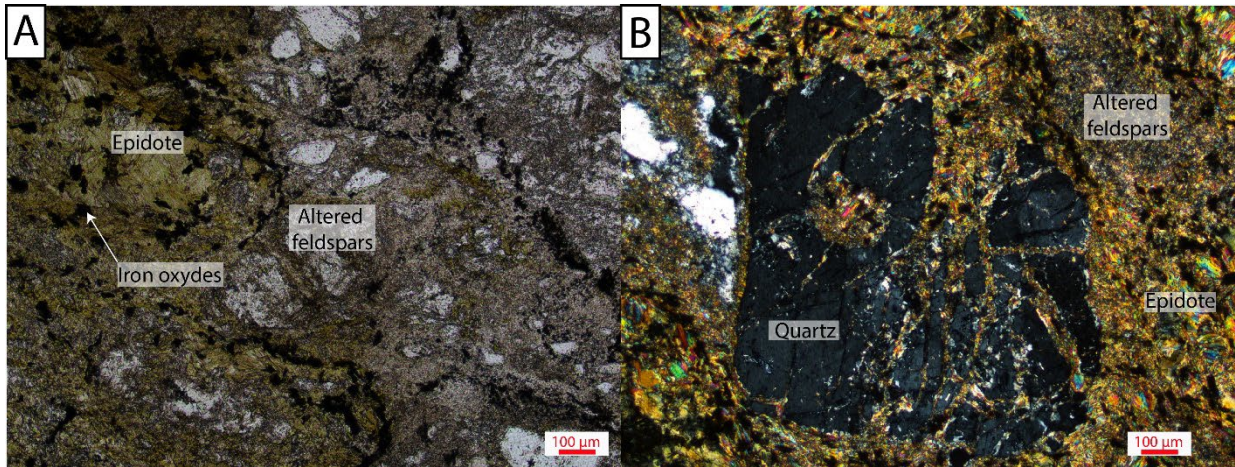


Figure V.23: A- Optical microphotograph (PPL) of cataclasite in granite associated to strong epidote neoformation. B- Optical microphotograph (PPL) of rhyolitic quartz found in the footwall damage zone.

5.2.2. Core zone

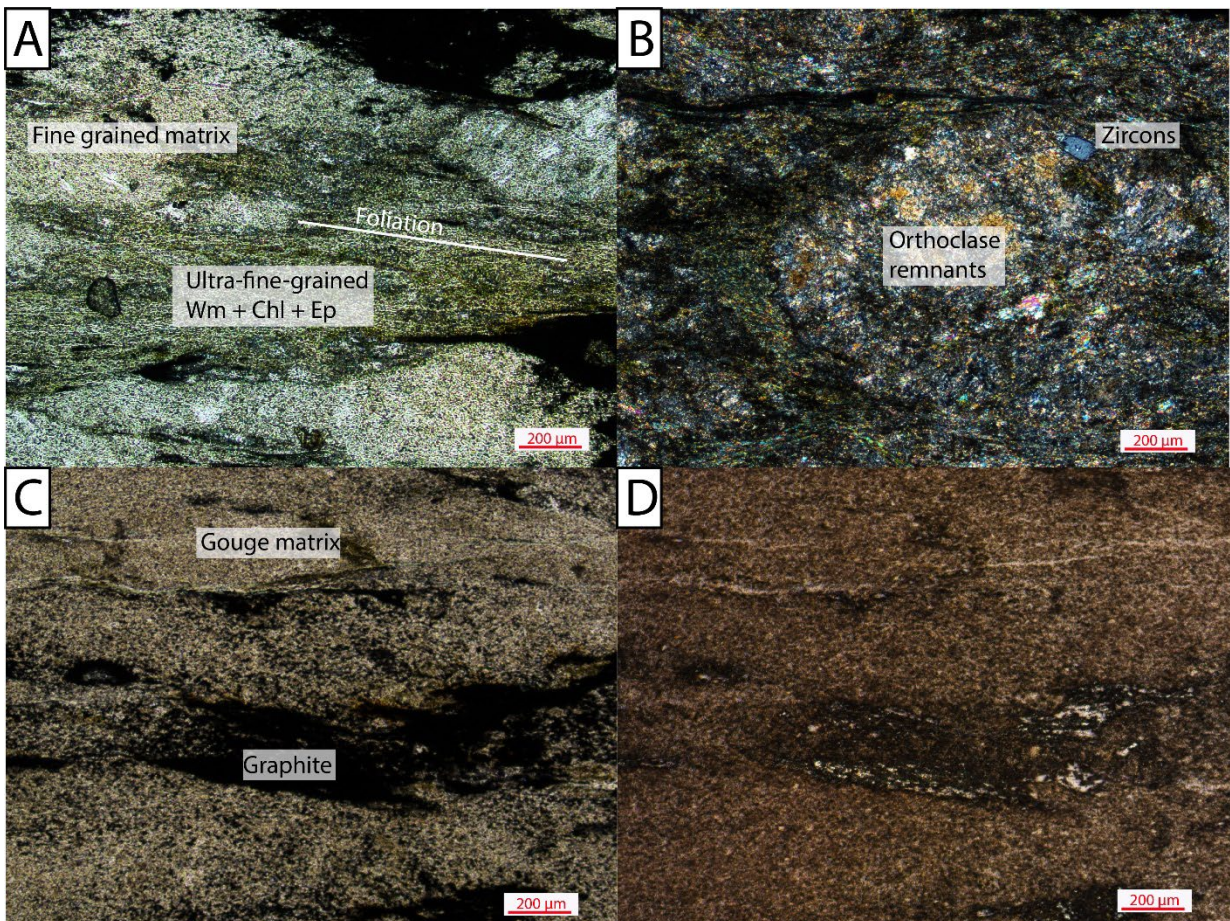


Figure V.24: A- Optical microphotograph (XPL) of the gouge composed of fine-grained white micas chlorite and epidote. B- Optical microphotograph (XPL) of remnants of orthoclase in the gouge. C and D- Optical microphotograph (PPL and reflected light) of the gouge showing darker area composed of graphite.

The core zone is characterized by 10-20 cm thick black indurated gouges. The gouges show a pervasive foliation dipping toward the east (63/108; dip/dip azimuth). Millimetric clasts and fragments of veins can be recognised on the gouge. Besides, in the cataclasite close to the fault core, centimetric thick dark levels correspond to small gouge levels. These centimetric gouge levels are organized “en-echelon” progressively forming larger gouge layers (10’s cm).

At microscopic scale, the gouge is composed of ultra-fine-grained phyllosilicates, mostly white micas, chlorite, and of epidote giving a greenish aspect of the section (Fig. V.24A). Only few remnants of feldspars and small quartz grains are visible (Fig. V.24B). Minor calcite is also observed replacing feldspars. Dark areas parallel to the foliation in the gouge matrix are formed by carbonaceous material (Fig. V.24C and D) similar to the one found in the Col du Bonhomme area. Veins are also found in the core zone. They correspond to millimetric and decimetric quartz veins.

5.2.3. Geochemical evolution

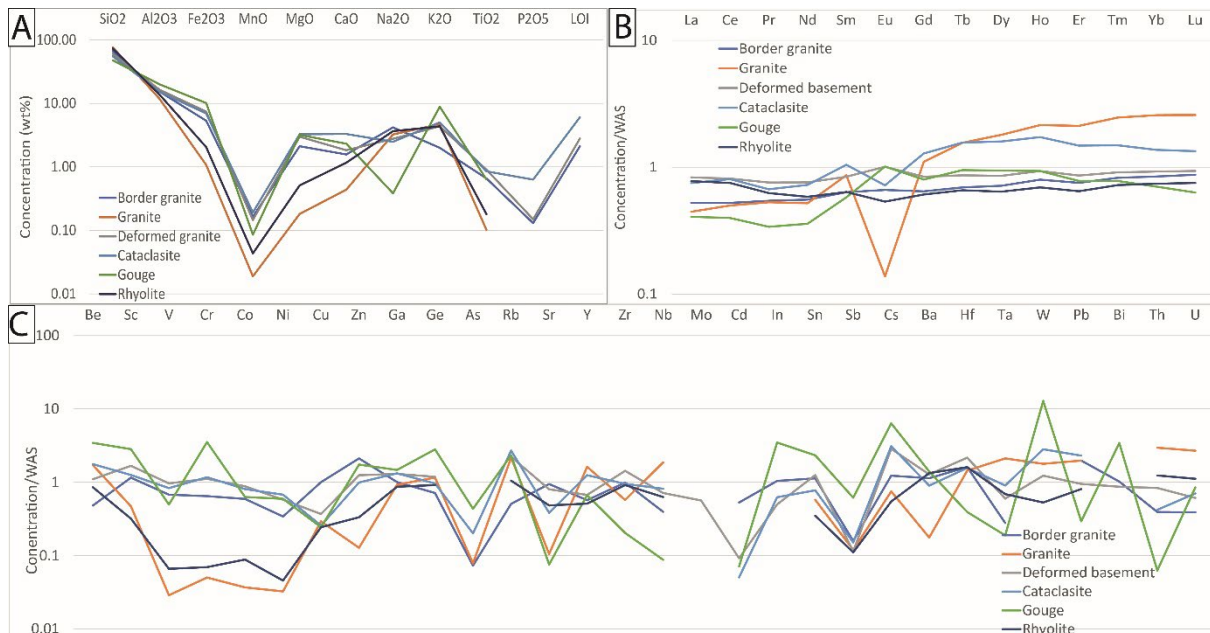


Figure V.25: A-Composition of the Brea fault zone in major elements. B- Composition of the fault zone in trace elements normalized to WAS. C- Composition of REE normalized to WAS.

The major elements (Fig. V.25A) show significant differences between the granite/ rhyolite samples and the other samples. Indeed, granite and rhyolite samples show lower concentration in FeO, MnO, MgO, CaO compared to fault rocks and the microgranite. Fault rocks are close to the composition of the border granite for FeO, MnO, MgO and CaO. Significant differences can be observed for Na₂O and K₂O in the gouge, compared to other samples, with an increase of K₂O and a decrease of Na₂O. This is similar to what was observed in the other gouge samples around the Mont-Blanc massif (Col du Bonhomme). It can be explained due to the plagioclase and orthoclase breakdown releasing K and Na and the formation of white micas incorporating K.

For trace elements (Fig. V.25B), there is again a clear difference between the granite/rhyolite samples and the other samples for Sc, V, Cr, Co, Ni, Cu. However, for the other elements there is a strong heterogeneity. Peaks in Ln, Cs, W, Bi are observed in the gouge associated to low concentration in Zr, Hf, Ta, Pb and Th.

For Rare Earth Elements (Fig. V.25C), the graph appears relatively flat except for the granite. A slight increase of HREE is visible for the gouge and cataclasite samples. The REE normalized to chondrites show negative Eu anomalies ($Eu/Eu^* = 0.7$ and 0.09) for all samples except the rhyolite which show no anomalies ($Eu/Eu^* = 0.94$).

5.3. Catogne section (section4)

The Catogne massif is found at the northern edge of the massif and is characterized by the presence of a Triassic cover above the basement.

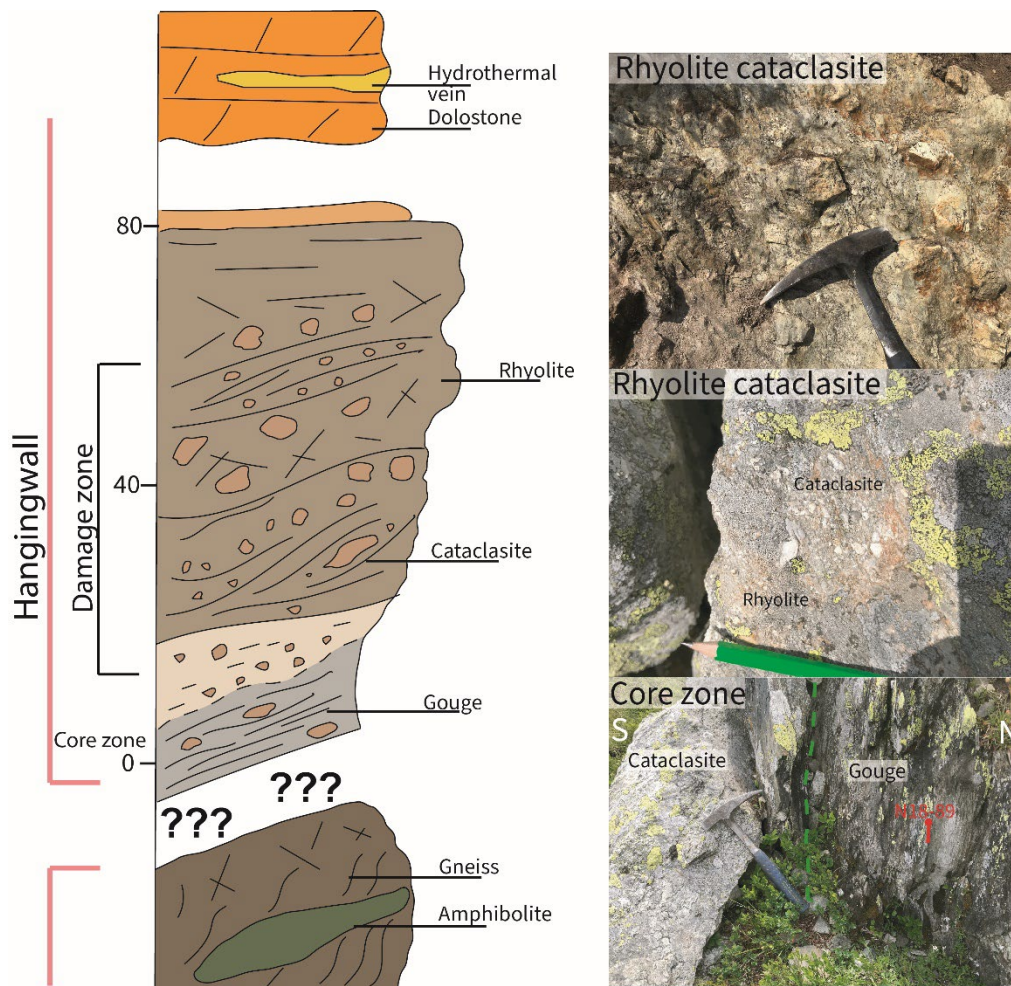


Figure V.26: Section of the basement-sediment interface showing a tectonic contact in the top basement overlaid by syn-rift sediments.

5.3.1. Basement

The basement of the Catogne massif corresponds to a Variscan gneiss with amphibolite lenses overlaid by Carboniferous rhyolites (Bussy et al., 2001; Von Raumer and Bussy, 2004). The

rhyolite is affected by cataclastic deformation. The cataclasite is made of relatively unaltered rhyolite fragments embedded in a strongly altered matrix. No clear dominant direction of the deformation is visible. Locally, highly foliated phyllosilicate-rich rocks are observed corresponding to indurated black gouge. This gouge is subvertical and oriented N-S. The transition with the Variscan gneiss is found in the cliff and cannot be observed unfortunately.

5.3.2. Cover

The contact between the sedimentary cover and the basement was not observed in the area of the Dent de Catogne where it is masked by the vegetation. However, in the peak of Catogne, the contact is visible and corresponds to a primary contact between the Triassic arkose and the rhyolite. The dolostone can be observed along the Catogne massif (Fig. V.26).

5.4. Mont-Chemin section (section5)

5.4.1. Fault zone description

Close to the Col des Planches, in the Mont-Chemin, the top tectonized basement is crosscut by a road leading to the exposure of a large shear zone which is ca. 60m wide.

5.4.2. Basement

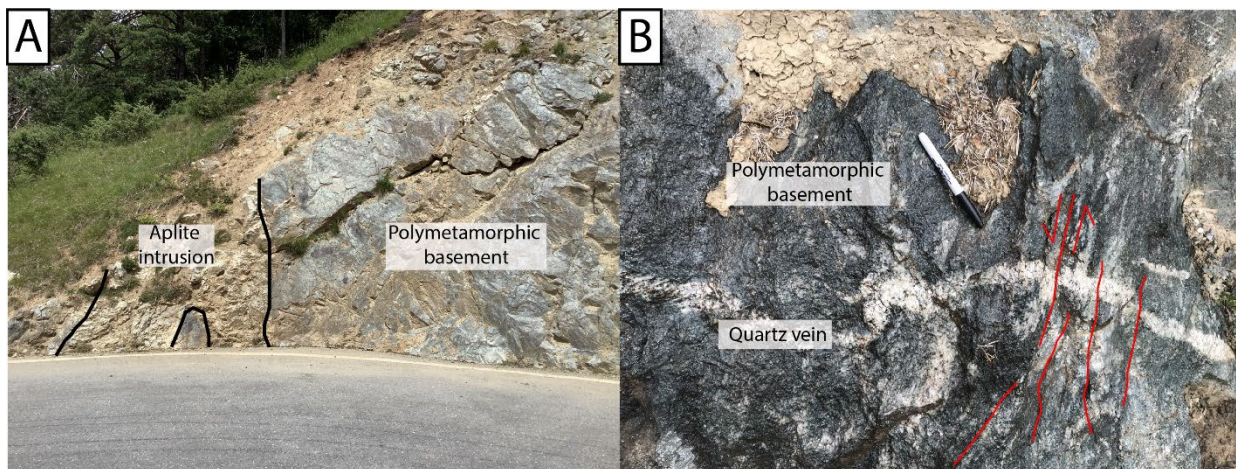


Figure V.27: A- Sub-vertical Variscan leucogranite intrusion in the polymetamorphic basement. B- Fractured veins in the polymetamorphic basement.

The basement corresponds to a Variscan gneiss intruded by subvertical, meter-thick aplite (Fig.V. 27A). These aplite intrusions are derived from the main Mont-Blanc granite. Smaller intrusions corresponding to pegmatite are also observed. Quartz veins associated to chalcopyrite are found in the polymetamorphic basement. These veins are affected by subsequent folding and fracturing associated to small displacement (Fig. V.27B). These deformations are possibly related to the surrounding fault zone. However, the age of the vein formation is unknown. They are clearly pre-Alpine probably associated to the Carboniferous intrusions.

5.4.3. Fault zone

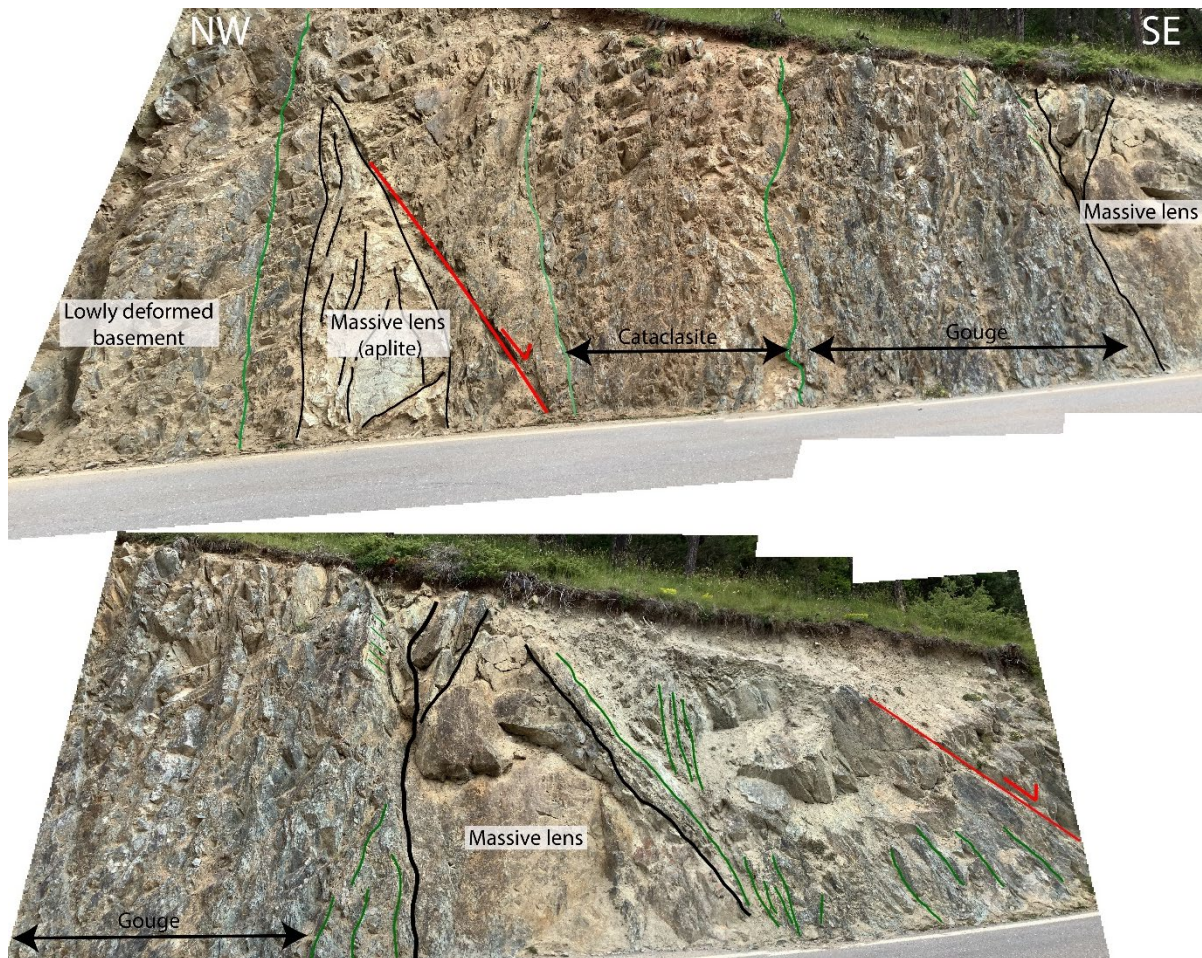


Figure V.28: Image merging of the fault zone in Mont-Chemin showing cataclasite from the damage zone passing to the gouge core zone and to the hanging wall damage zone. Note the presence of large undeformed massive basement lenses.

I.1.1.1 Damage zone and core zone

The basement is progressively affected by cataclastic deformation overprinting the initial fabric (Fig. V.28). The subvertical cataclastic planes are crosscut by secondary faults. The aplite lens is surrounded by a cataclastic zone up to 5 meter thick. They corresponds to an amalgamation of centimetre-thick shear zones where the deformation appears surrounding decimetric lenses of basement affected by minor deformation.

This passes to a zone of few meters of gouge defining the core zone (Fig. V.29C). The basement is affected by strong brittle deformation with centimetre-thick gouge layers surrounded by cataclasites. Large clasts of basement are reworked in the gouge. These clasts can be centimetric to millimetric. These gouge planes are also associated to slicken fibers composed mostly of chlorite defining clear stretching lineations (Fig. V.29A and B). Additionally, minor talc has been recognized along the gouge planes.

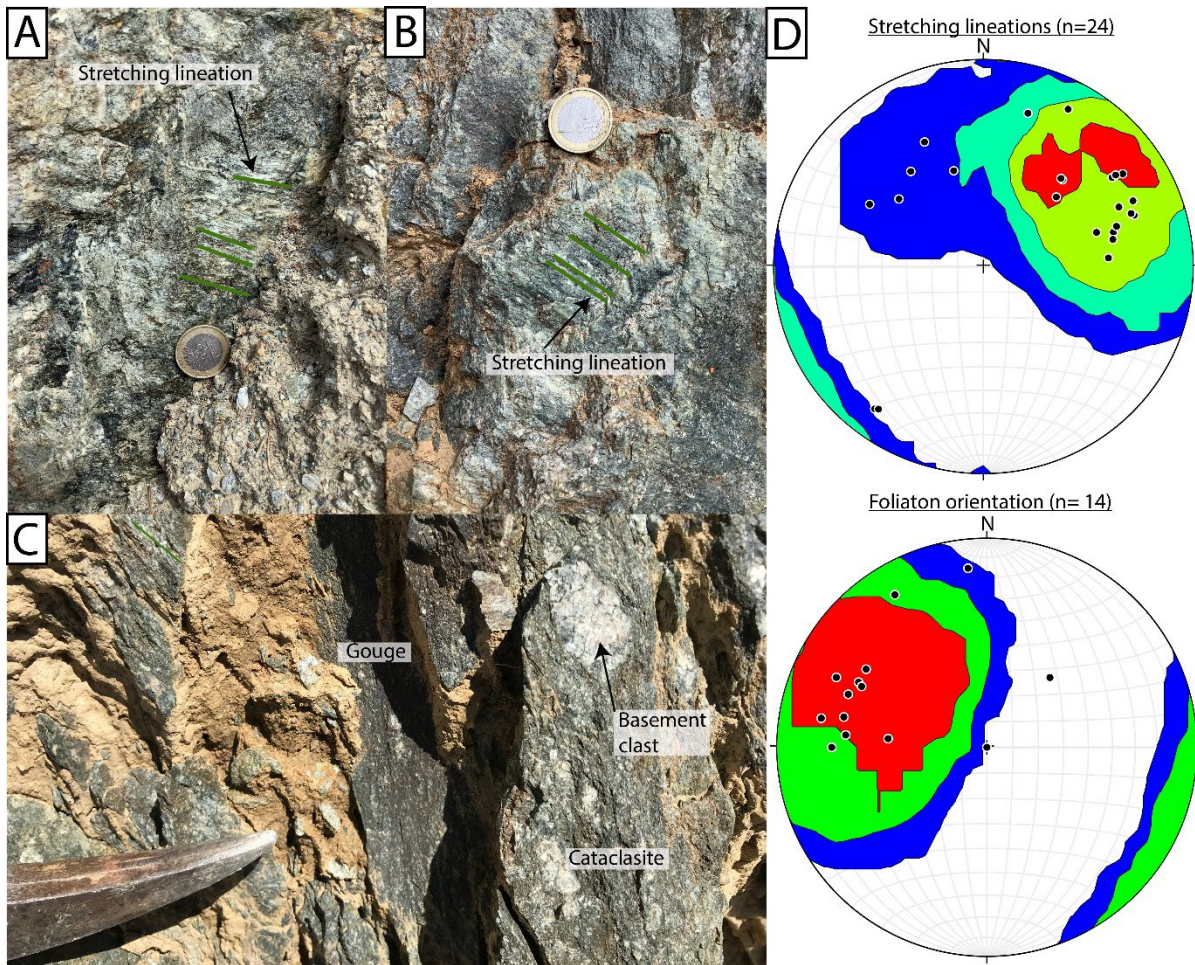


Figure V.29: A and B- Stretching lineations in the gouge. C- Gouge layers in contact with cataclasite reworking large basement clasts. D- Plot of the stretching lineation and of the gouge and cataclasite orientation in a stereogram (Wulff canevas).

Toward the left (Fig. V.28), the core zone is surrounded by a massive lens of undeformed basement corresponding to a Carboniferous magmatic intrusion. This passes to another meter-thick cataclasite zone with bands of strongly deformed basement surrounding lenses of lowly deformed basement. The size and spacing of these cataclastic bands progressively decrease away from the core zone.

The orientation of the cataclasite planes and gouge foliation is NE-SW. The stretching lineations in the gouge give a NE-SW top to the north sense of shear. This indicates normal sense of shear with a strike-slip component (Fig. V.29D).

At microscale, the cataclasite is composed of highly fractured basement showing significant grain comminution. The deformation is accommodated along cataclastic bands composed of ultracataclasite (Fig. V.30A). The matrix of these cataclasites and ultracataclasites is formed by fine-grained chlorite and epidote embedding clasts of basement. These cataclasites show clear YPR structures leading to NE-SW top to the north sense of shear (Fig. V.30A). The cataclastic bands corresponds to the Y and R planes accommodating most of the deformation.

The gouge is composed of an ultra-fine-grained matrix reworking clast of cataclasite (Fig. V.30B and C). S/CC' structures are visible in the gouge zone related to frictional-viscous flow. This gouge appears strongly recrystallized with overgrowths of white micas visible.

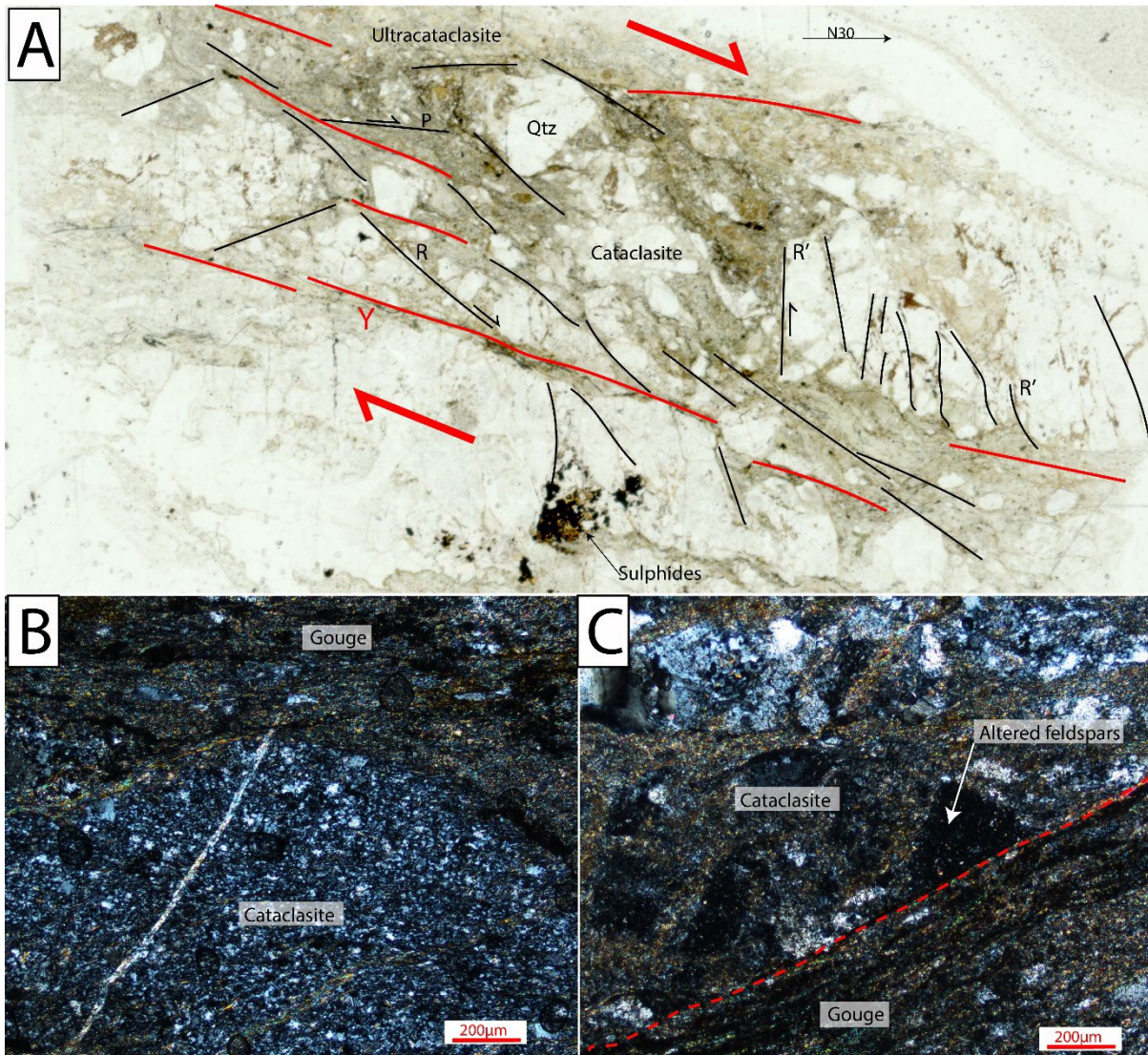


Figure V.30: A-Microphotograph (PPL) of cataclasite and ultracataclasite overprinting the basement. The microstructures indicates a NE-SW top to the north sense of shear. Y=Y-plane, R=Riedel plane, R'=Antithetic Riedel, P=P-plane. B-Microphotograph (XPL) of gouge reworking a large cataclasite clast. C- Microphotograph (XPL) of gouge overprinting the cataclasite. The gouge is composed of ultra-fine-grained phyllosilicates.

5.4.4. Cover

The undeformed basement is overlaid by the Triassic basal arkoses. This arkose appear undeformed and only affected by a vertical foliation. Dolostones (30/33) are lying above the arkose with a small angular unconformity and dipping. The Liasic cover corresponds to shale and sandstone alternations (40/105) corresponding to turbidites.

5.4.5. Geochemical evolution

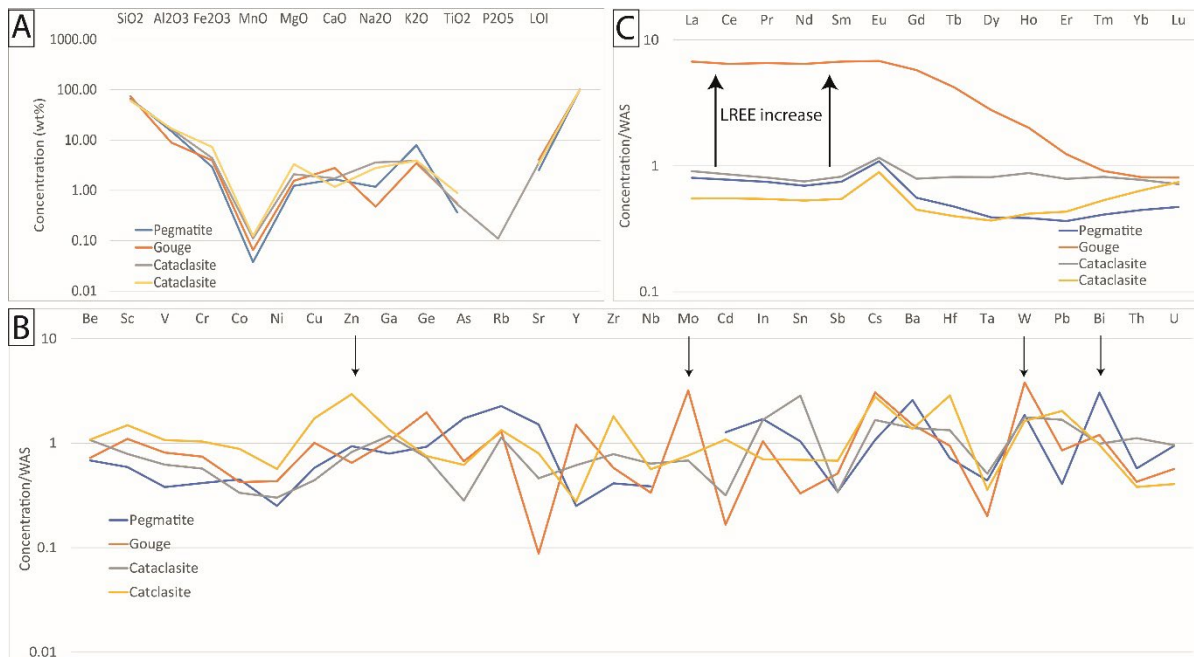


Figure V.31: A-Composition of the Mont-Chemin fault zone in major elements. B- Composition of the fault zone in trace elements normalized to WAS. C- Composition of REE normalized to WAS.

Major, trace and Rare-Earth Elements composition from the microgranite, the deformed basement and the gouge are compared. For the major elements (Fig. V.31A), there is an increase in FeO, MgO in the fault rocks compares to the basement. A decrease of K₂O is also observed. The content in Ca increases in the gouge which is correlated to the presence of calcite. A decrease in Na₂O is visible in the gouge while it increases in the deformed basement. The variations in K₂O and Na₂O are controlled by the feldspar breakdown.

Trace elements show important variabilities between the samples (Fig. V.31B). The deformed basement samples show increase in Zn, Pb, Cs. The gouge samples have peaks in Mo, W and Cs similarly to what is in the core zone from the Col du Bonhomme area.

The REE composition shows the clearest signal (Fig. V.31C). The basement shows a slight positive anomaly in Eu as shown in the previous section (Eu/Eu* = 1.07). The deformed basement samples also show a positive Eu anomaly (Eu/Eu* = 1.15) which is higher than in the basement. A negative anomaly is observed in the gouge samples (Eu/Eu* = 0.7). Slight enrichment in HREE is observed in the cataclasite compared to the basement. Besides, significant REE increase is observed in the gouge sample, mostly LREE. This increase in LREE is similar to what is observed in the core zone from the Col du Bonhomme.

6. Discussion: Rift-related model for the Val Ferret

6.1. Preservation of the detachment fault

Different types of tectonic contacts have been recognized in the Val Ferret area:

- Top tectonized basement covered by Lower Aalenian sediments;
- Intra basement tectonic contact juxtaposing the rhyolite with the granite

6.1.1. Basement faults

The first contact is the Brea fault juxtaposing the rhyolite with the granite. This contact is only clearly outcropping in one location, which makes its lateral extension difficult to map. The footwall of this fault is composed of granites passing to mylonites. The mylonites appear overprinted by cataclasite toward the fault core. Decimetric gouge levels are also observed. The hanging wall is composed of rhyolites. The tectonic juxtaposition of rhyolite over granites indicates an exhumation of the footwall granites. Indeed, the granite was emplaced at mid crustal conditions ($T = 300\text{-}400^{\circ}\text{C}$) while the rhyolite was at the surface covered by only a thin Triassic cover as observed at Catogne Mt. (Grasmück, 1961). Mylonites in the granitic footwall point to a deformation above 300°C passing to brittle deformations at temperature below 300°C , while the deformation in the hangingwall is only brittle. In addition, chlorite-epidotes alteration on cataclasites similar to what is observed in the Val Ferret have been observed along other detachment faults (e.g., Mormon point detachment and Amargosa detachment, USA) associated with temperatures ranging between 240 to 340°C (Haines et al., 2016). The age of the fault is unconstrained. No age determinations have been performed on this fault and no stratigraphic data constraining the age of the fault are available.

A prolongation of this fault zone might be observed in the northern Catogne massif. Indeed, a tectonized contact has been recognized between the rhyolite and the Variscan gneiss. This contact is composed of cataclasites and gouges. The outcrop conditions are, however, bad due to the topography of the area.

The third contact is found in the Mont-Chemin area. It corresponds to a large fault zone, which outcrops along a road. The footwall corresponds to Variscan polymetamorphic basement crosscut by pegmatites and aplite intrusions. The fault zone corresponds to cataclasites and gouges surrounding lenses of undeformed aplite. The hangingwall is composed of undeformed basement overlaid by Triassic pre-rift cover. The fault shows top to the northeast normal sense of shear with a strike slip component. This fault zone is crosscut by fracture planes with chlorite coating. The age of the fault zone is not constrained but it is post Variscan as it crosscut the Triassic paleo surface. It is, however, not possible to see if the contact is sealed by Jurassic syn-rift deposits.

6.1.2. Top tectonized basement

Top tectonized basement sealed by sediments are observed in the Val Ferret. They correspond to rhyolite cataclasites sealed by syn-rift sediments. These contacts can be observed mostly in the southern part of the Val Ferret (Amône, Saleinaz). Reworked clasts of rhyolite cataclasite are also visible in the conglomerates. This indicates a pre-Alpine age for the cataclastic deformation, which also corroborates the fact that the top basement sediments above the cataclasite appear undeformed. However, possible subsequent Alpine deformation might also be observed overprinting the pre-Alpine deformation. The sub-vertical cataclastic bands might indeed be associated to late brittle Alpine deformation similar to what is observed in the Aar massif (Rolland et al., 2009).

6.1.3. Fault interpretation

As mentioned above, the tectonic contact in the Mt. Catogne is possibly the continuation of the fault observed in the Brea area between the rhyolite and the Mont-Blanc granite. The relation between the other fault zone found in the Mont-Chemin area is however unclear. This fault is found at the proximity with the Alpine Simplon-Rhône strike slip fault and could be a part of this fault. If this was the case, all the syn-rift cover should be affected by deformation. However, no sign of the fault zone can be observed in the syn-rift sediments found upward of the fault along the road. This might be an indication of a pre-Alpine age for this contact. Moreover, recrystallization of the gouge matrix might indicate that the fault zone is pre-Alpine with recrystallization during prograde metamorphic overprint. The age of the fault therefore might be comprised between mid-Triassic and late Liassic. Restoration of the Pliensbachian sediments to the horizontal leads to a flattening of the Mont-Chemin fault zone fault as well (Fig. V.32). It is proposed that the Mont-Chemin/Brea fault corresponds to a major tectonic contact responsible for the granite exhumation.

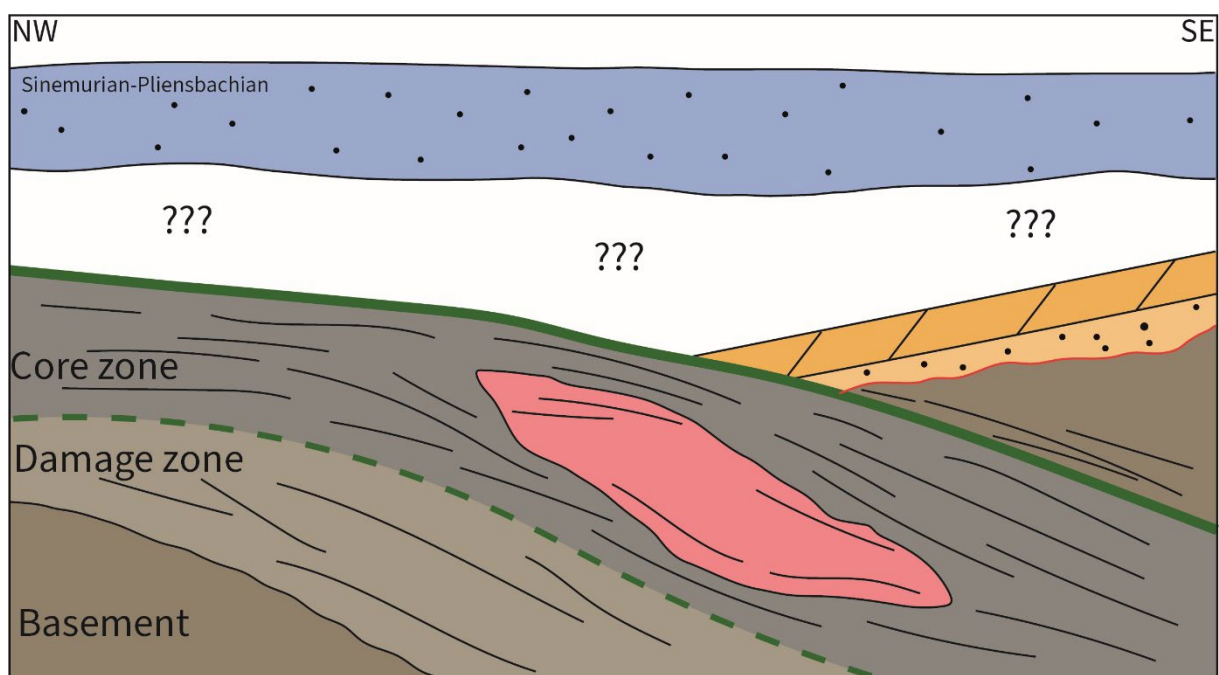


Figure V.32: Restoration of the Mont-Chemin fault zone back to its Late Liassic position achieved by the rotation of the Liassic sediments back to the horizontal

The top tectonized basement might correspond to secondary faults of Liassic age affecting the rhyolitic basement.

6.2. Tectono-stratigraphic evolution

The sedimentary evolution of supra-detachment basins is a key component to reconstruct the evolution of the fault. This evolution takes into account the change in facies composition and overall distribution of the sediments. It allows to constrain the evolution of the Mont-Blanc detachment fault in the southern Mont-Blanc massif (Ribes et al., 2020). However, the situation in the Val Ferret appears more complex. First, because of the difficulty to reach outcrops and secondly, the occurrence of rhyolite is adding more complexity because of the nature of the deformation in the rhyolitic bodies. However, some key features are worth mentioning.

As mentioned above, the north of the Val Ferret, in the Mt Catogne is characterized by the presence of pre-rift cover in stratigraphic contact with the basement. The pre-rift cover is overlaid by syn-rift sandstones, which are lying unconformably above the Triassic and lower Liassic sediments. The Mt. Catogne appears as a restricted basin pinching out to the south as noticed by Grasmück (1961).

The lateral termination of the basin is associated to the progressive disappearance of the pre-rift cover. The basement is directly overlaid by syn-rift sediments. The syn-rift sediments correspond to Pliensbachian sandstones in the southern edge of the Catogne Mt. and to lower Aalenian sandstones and conglomerates.

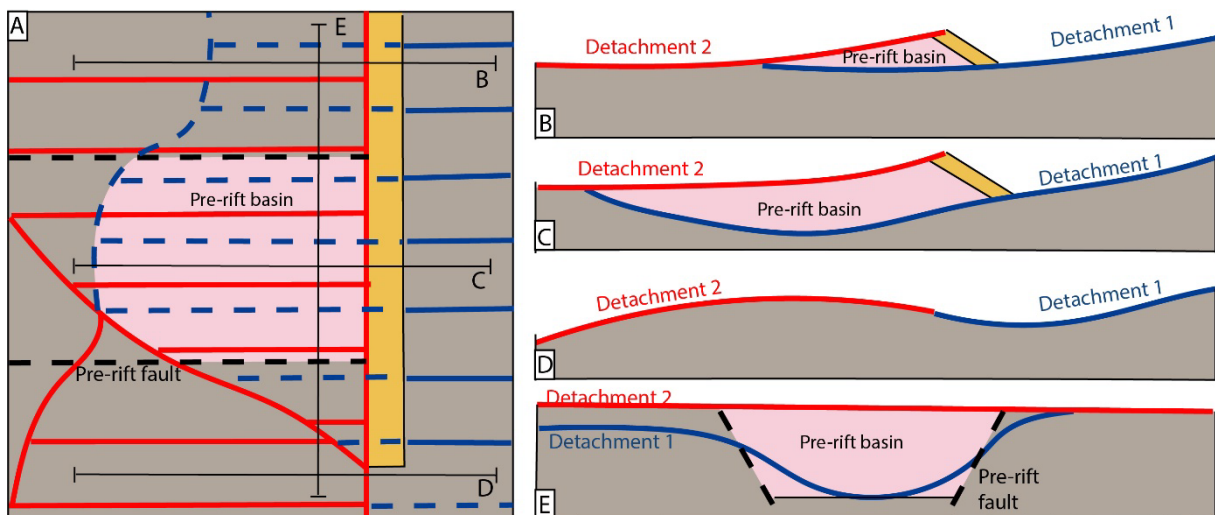
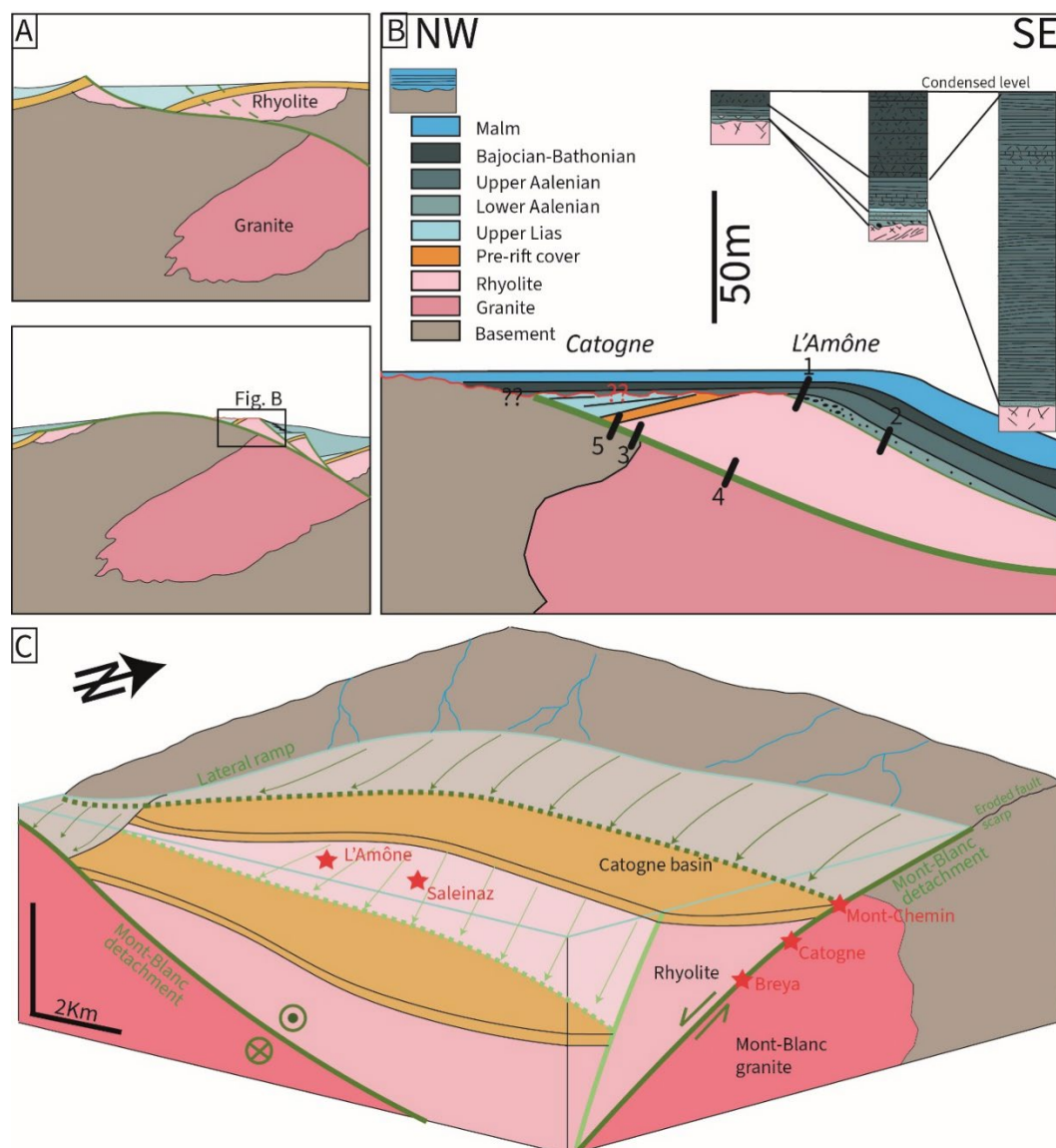


Figure V.33: Role of pre-rift basin on the detachment geometry (modified from Epin and Manatschal, 2018) A- Map view of the pre-rift (Permian) basin and the relation between the detachment fault and the basin. B, C and D- Sections perpendicular to the detachment direction showing the reactivation of the Permian basin and the formation of an allochthonous block of Permian. E- Section parallel to the detachment direction showing the relations between the detachment and the Permian faults.

This small “Catogne” basin is superimposed to rhyolitic deposits, which are ca. 20 km long between the Ferret Pass and the Mont-chemin. The influence of pre-rift basins on the subsequent deformation has been observed for both Jurassic rift-related (Epin and Manatschal, 2018) and Alpine convergent deformation (Fig. V.32). The impact of the Alpine deformation on the Carboniferous basin has been studied in the Verrucano basin (Pfiffner, 2014). It has been shown that the Alpine thrust passes at the base of the basin leading to a decoupling between the basin infill and the basement (Pfiffner, 2014). The basin margins acted as ramps and lateral ramps for the thrust. Similar processes have been advocated for extensional reactivation of Carboniferous basins. This has been studied in the Err detachment system (Central Alps, Switzerland; Epin and Manatschal, 2018). The detachment fault passes at the base of basin (Fig. V.33B, C, D). The secondary detachment fault crosscut the first one leading to the formation of an allochthonous block made of the Permian basin (Fig. V.33C). The Permian faults are usually too steep to be reactivated, therefore, the detachment fault formed lateral ramps cross cutting the basin margin (Fig. V.33E).



Preserved Jurassic Structures in the Northern Mont-Blanc massif (Val Ferret, Switzerland)

Figure V.34: A- Evolution of the detachment fault during Sinemurian and Aalenian associated to the Carboniferous rhyolites forming allochthonous blocks. B- Proposal of the stratigraphic architecture of the Val Ferret during Late Jurassic. The positions of the different sections are indicated. C- Block diagram of the Val Ferret during crustal necking (Pliensbachian) showing the inverted Carboniferous basin crosscut by secondary faults leading to the formation of allochthonous blocks. The southward termination of the basin leads to the formation of lateral ramps along the Mont-Blanc detachment fault.

A similar process might have occurred in the Mont-Blanc massif. Therefore, the rhyolite would form an allochthonous block bounded by two detachment faults (Fig. V.34A). The lower fault corresponds to the granite rhyolite contact which accommodated large displacement especially in the footwall, which corresponds to deeper crustal levels put in contact with shallower crustal levels. The Catogne basin registered the first step of deformation with the initiation of the Mont-Blanc detachment. The activation of the secondary faults is related to exhumation of the rhyolites (Fig. V.34B). This is followed by subsidence associated to the progressive downing of the Mont-Blanc followed by the progradation of carbonate platforms. The Val Ferret might correspond to the lateral ramp marking the termination of the Carboniferous basin, which is associated to a change of the detachment direction. Deformation is accommodated by a strike slip deformation (Fig. V.34C).

A late Toarcian/Aalenian uplift is visible in l'Amône providing a clastic source for the transgressive conglomerates (Fig. V.34B). This uplift is also visible in the "Catogne basin". Indeed, the Liassic sediments seem to be affected by an unconformity with the overlying Aalenian shales. Indeed, the shales are lying above the Toarcian sediments to the north and over the Pliensbachian sediments to the south of the Catogne massif (Grasmück, 1961).

Analogues of allochthonous blocks on necking detachment faults can be found along the Norwegian margin (Osmundsen and Péron-Pinvidic, 2018). They correspond to crustal blocks lying over an abandoned detachment fault and forming small basin filled with syn-rifts sediments on their top. The intersection between the initial faults and the newer fault segment is usually marked by a bend (K for knick) in the detachment shape (Fig. V.35). The configuration of the Catogne basin reminds these small basins possibly associated to allochthonous blocks.

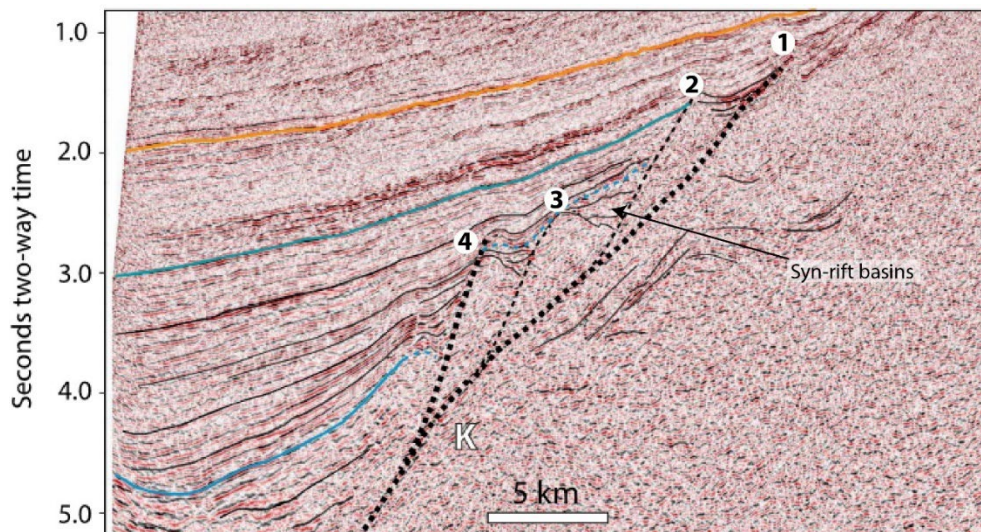
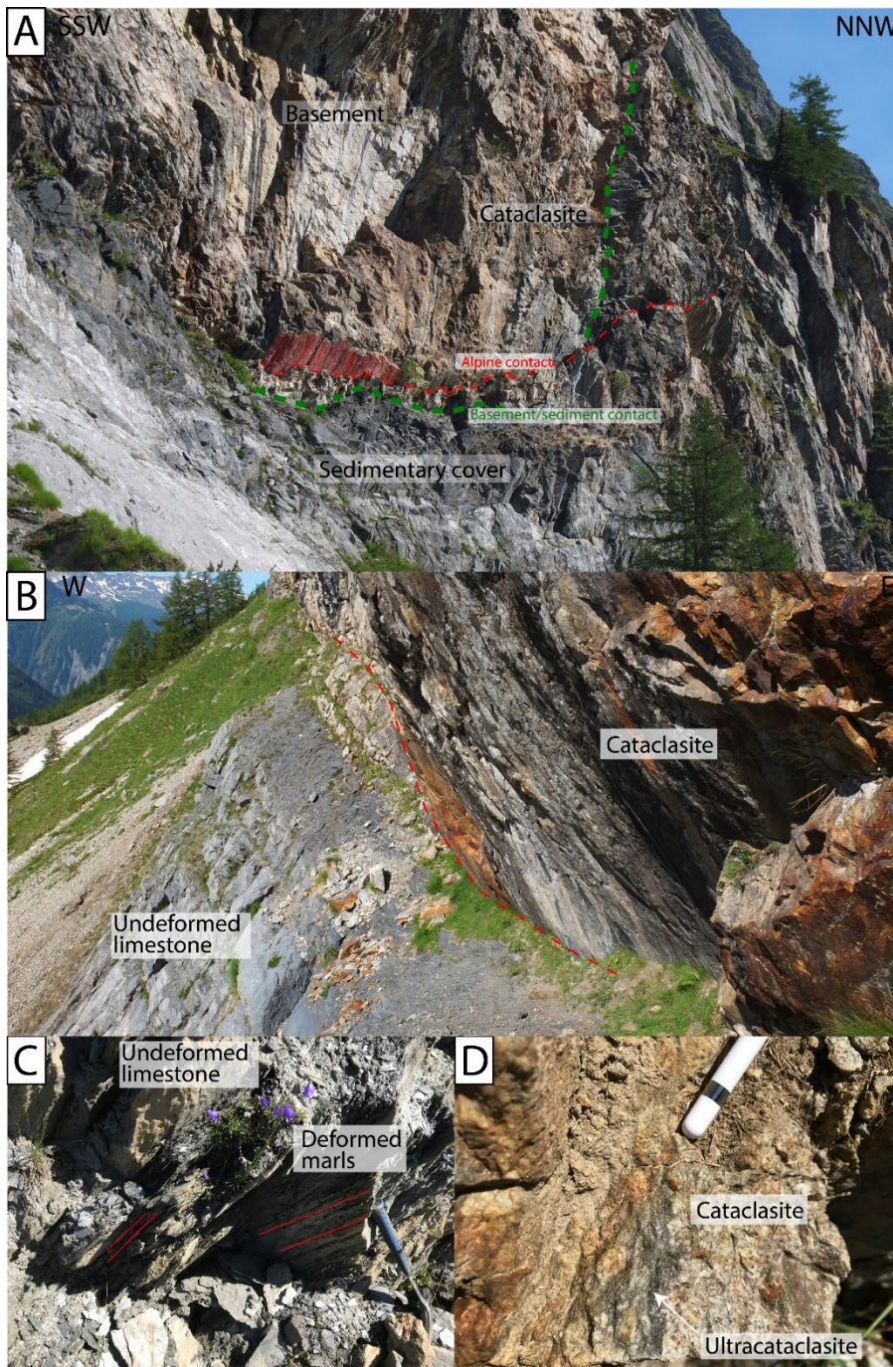


Figure V.35: Seismic example of allochthonous blocks above a necking detachment fault (1) in the Norwegian margin (modified from Osmundsen and Péron-Pinvidic, 2018). This fault is incised by another detachment fault (4) which is responsible for crustal-mantle coupling. Small syn-rift basins are observed associated to the the allochthonous blocks.

6.3. Connexion with the Southern Mont-Blanc detachment fault

Possible remnants of detachment faults have been observed in the Val Ferret. However, the connection with the southern detachment fault in the Col du Bonhomme is not well defined. The hypothesis is that it corresponds to the same fault segment. The only difference would be the occurrence of allochthonous blocks in the Val Ferret associated to the existence of a rhyolitic basin. The allochthonous blocks pinch out toward the Ferret Pass. The missing segment connecting the northern and southern Mont-Blanc detachment faults corresponds to the Courmayeur area (Fig. V.35).



Preserved Jurassic Structures in the Northern Mont-Blanc massif (Val Ferret, Switzerland)

Figure V.36: A- Image of the Mont-Blanc back thrust showing an Alpine fault cross-cutting the basement/sediment interface (credit from J.F. Giene and C.Ribes). B-Closer view at the contact between the basement and the overturned sediments (credit from J.F. Giene and C.Ribes). C- Focus on the cover showing undeformed limestones associated to deformed marls showing developed foliation. D- Cataclasite associated to the Mont-Blanc back-thrust.

The basement/sediment interface appears strongly deformed in the area of Courmayeur. The sedimentary cover is overturned and mylonitic deformation associated to the Mont-Blanc back thrust is observed (Guermani and Pennacchioni, 1998). Cataclastic top basement is crosscut by mylonitic shear zones. The mylonitic shear zones reworked clasts of cataclasite and quartz adularia veins possibly contemporaneous of cataclasite formation. However, the Alpine fault seems to crosscut the basement-sediment interface (Fig. V.36A and B). Therefore, the cataclasites at the interface are pre-dating the Alpine fault. Moreover, the sediments in the hanging wall appear overturned and much less deformed (Fig. V.36C). The deformation appears localised on the marl levels where a foliation sub-parallel to the stratification is observed (Fig. V.36D). Therefore, brittle deformation corresponds to a precursor to plastic deformation. Butler (1985) proposed that this basement-cover contact corresponds to a Jurassic normal fault overturned during Alpine orogenesis and cross cut by Alpine faults. Ribes et al., (2020) associated the cataclastic deformation to the Mont-Blanc detachment fault crosscut by later Alpine mylonites. This would correspond to the missing link between the southern and the northern Mont-Blanc detachment fault (Fig. V.37).

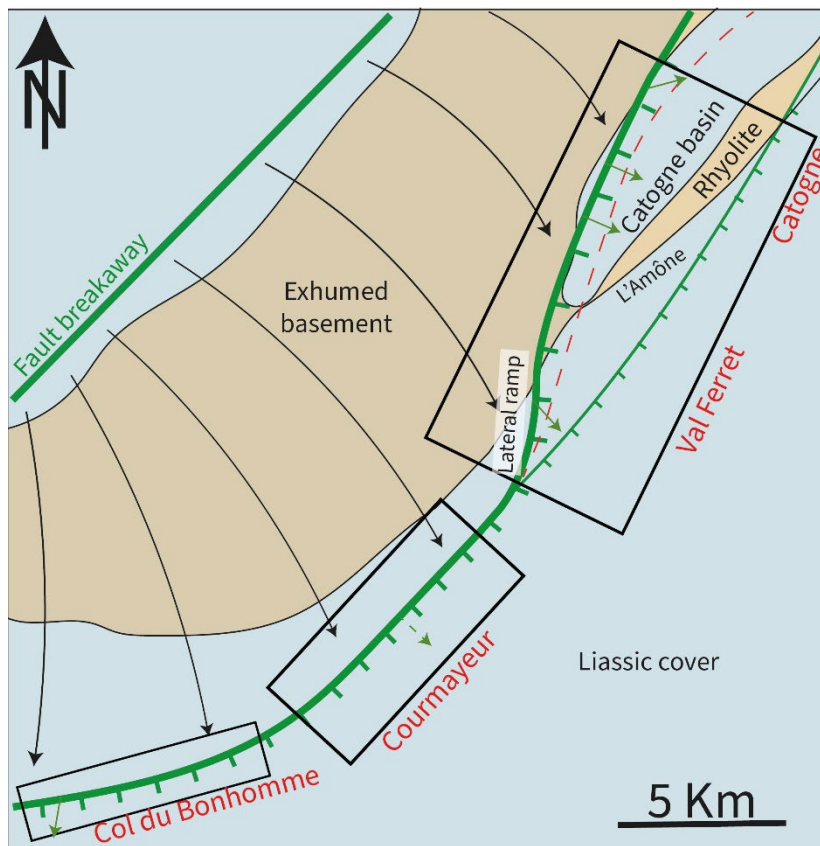


Figure V.37: Connection between the northern and southern Mont-Blanc detachment fault through the Courmayeur area. Stretching lineations associated to fault are indicated with the arrows.

Conclusion

The northern part of the Mont-Blanc massif presents differences to the southern part. In terms of basement composition, the Mont-Blanc granite has a composition clearly different from the gneiss observed in the south. This obvious observation has, however, a significant impact on the type of alteration observed in the basement. The occurrence of saussuritization of plagioclase is widespread while only sporadic in the gneiss where sericitization is the main process. This is mostly due to the more Ca-rich plagioclase found in the granite and rhyolite. Enrichment in REE, Pb, Zn is also observed especially in the main granite. Concerning the stratigraphic evolution, whereas Liassic sandstones are observed in this section of the Mont-Blanc, the main characteristic is the occurrence of Aalenian conglomerates and sandstones above the basement. Section from the top basement indicates stratigraphic contact between the cover and the basement, which appears affected by pre-Alpine cataclastic deformation. The section from the granite-rhyolite interface also indicates the occurrence of an undated tectonic contact.

A rift-related model based on the stratigraphic observation and the occurrence of tectonic contact is proposed. In this model, the rhyolite corresponds to an allochthonous block over the exhumed granite. The formation of this allochthone led to the isolation of the Catogne basin. A later uplift event during the Aalenian seems to occur leading to the formation of the conglomerates above the rhyolite.

Chapter VI- Large-scale evolution of the Jurassic necking domain of the Alpine Tethys



View of the Lemman Lake (Prealps, Switzerland)

« Tout le monde veut vivre au sommet de la montagne, sans soupçonner que le vrai bonheur est dans la manière de gravir la pente. » (Gabriel Garcia Marquez)

Foreword

The transition between the proximal domain (External Mont-Blanc) and the necking domain (Internal Mont-Blanc) as well as the evolution along strike of the necking remains relatively unconstrained. The syn-rift stratigraphic evolution across the proximal and necking domain in the Alps provides a glimpse of the syn- to post-rift evolution of the necking domain.

This chapter presents a compilation of sedimentary sections from the Aar, Aiguilles-Rouges, and Mont-Blanc cover as well as sections from the Helvetic and Ultrahelvetic nappes. The correlation of these sections and the reconstruction of eustatic variations allows to reconstruct the large-scale evolution of the necking domain.

Introduction

The Helvetic shelf (cover of the Mont-Blanc and Aar massif) shows a relatively complex facies evolution both in time and space. The main characteristic is the occurrence of carbonate-rich Dauphinois facies until the Sinemurian and of the clastic-rich Helvetic facies during the Sinemurian and Pliensbachian (Epard, 1989; Loup, 1992).

The preserved early to middle Jurassic sedimentary cover surrounding the massif offers an overview of the facies evolution and sedimentary architecture related to crustal necking. The preservation of the distal as well as the more proximal units allows to reconstruct the proximal to distal transition of the European margin. The main questions concern the timing and extension of clastic sediments in the basin in response to basement uplift and the duration of the post-rift subsidence and drowning of the massif.

1. Methodology

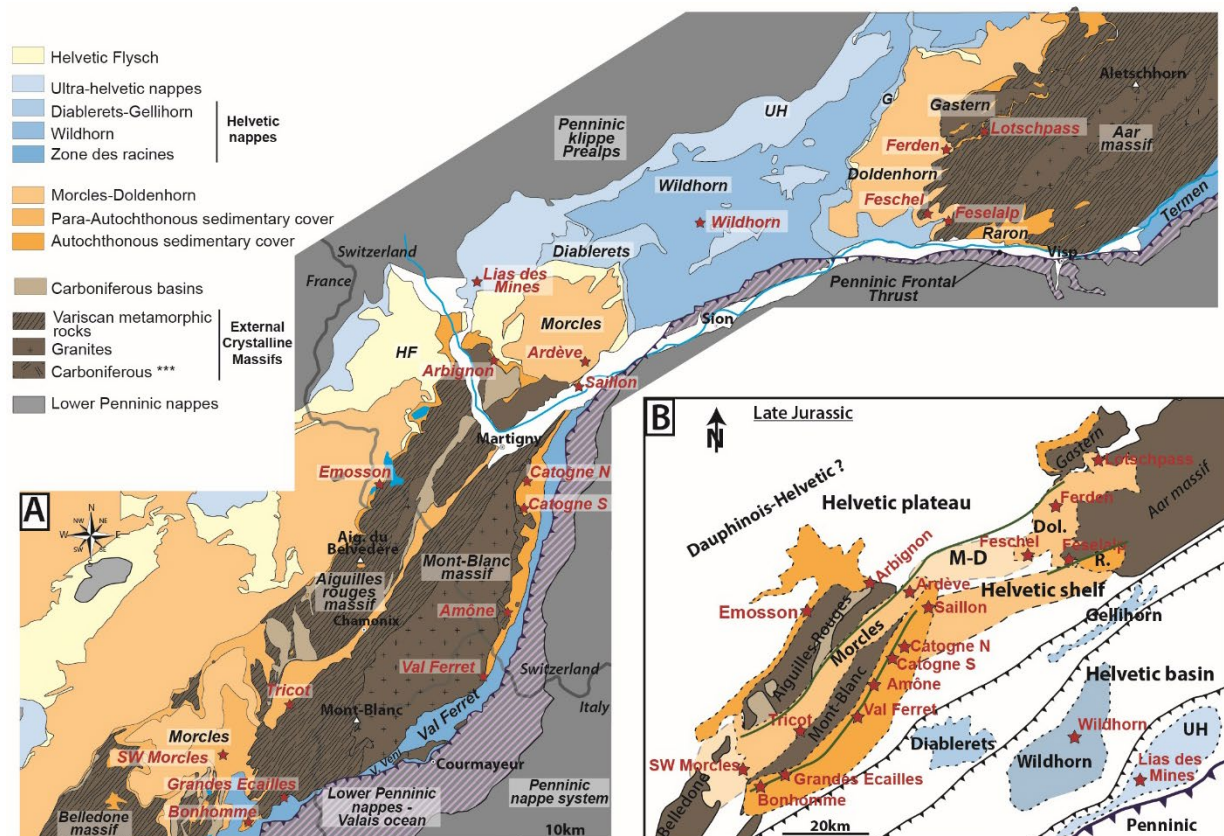


Figure VI.1: A- Map of the External Crystalline Massifs (ECM) from the north Belledonne to the Aar massif highlighting the location of the autochthonous and allochthonous sedimentary cover (modified from Ribes et al., 2020). The location of the sedimentary sections used is indicated on the map as red stars. B- Palinspatic reconstruction of the Belledonne-Aar domain during the late Jurassic (modified from Ribes et al., 2020). M-D = Morcles Doldenhorn, Dol. = Doldenhorn.

The sedimentary evolution of the necking domain was determined using sedimentary sections of the autochthonous and allochthonous cover from the Aiguilles-Rouges massif, Aar massif, Mont-Blanc massif as well as the Morcles and Helvetic nappes (Fig. VI.1A). The goal is to decipher the evolution across (NW-SE profile) and along the margin (NE-SW profiles). The different tectonic units were replaced in their paleogeographic position (Fig. VI.1B) according to the palinspatic reconstruction of Trümpy (1980), Burkhard, (1988) and Pfiffner et al., (2011). The sections provided in this chapter come from bibliography compilation for the Aar, Aiguilles-Rouges and Morcles domain and personal observations from the Mont-Blanc cover and Ultrahelvetic domain (Table VI.1). The correlations are based on the biostratigraphic ages of the different formations when available and by facies analogy where no biostratigraphic data are available. Biostratigraphic data used for these correlations have been compiled in the bibliography and are presented in the Appendix F.

The area can be divided into the Helvetic plateau, Helvetic shelf and Helvetic basin (Fig. VI.1B; Wildi et al., 1989). The Helvetic plateau corresponds to the area from the Jura to the Aiguilles-rouges massif. The Helvetic shelf corresponds to the area between the Aiguilles-Rouges massif and the Mont-Blanc and includes the Morcles basin (Fig. VI.1B). The Helvetic basin corresponds to the area above the Mont-Blanc/Aar massif and composed the distal Wildhorn and Ultrahelvetic units (Fig. VI.1B). Most of the sections presented here are from the Helvetic shelf and basin.

In addition to compaction related to burial, tectonic deformation led to significant changes of sediment thickness. In some sections of the Morcles nappe, where the deformation has been analysed in detail (Huggenberger, 1985), it was shown that the initial sedimentary thickness can be doubled from present-day thickness. However, the data on the amount of deformation are scarce. In this work, the sections have been used to obtain a first order idea of the facies evolution and were not decompacted. The subsidence evolution of the Helvetic shelf has been studied in detail by Wildi et al., (1989) and Loup (1992) and provides a better understanding of the evolution of the margin.

Section	Coordinates	References
Amône	45°56'31"N/7°05'31"E	<i>Grasmück, (1961), Ribes et al., (2020), this study</i>
Arbignon	46°11'15.54"N/7°4'0.89"E	<i>Trümpy (1945), Badoux (1971), Badoux et al., (1971), Badoux (1972), Masson et al., (1980), Loup (1992)</i>
Ardève	46°11'33N/7°12'17"E	<i>Loup (1992)</i>
Tête des Fours	45°43'50"N/6°41'47"E	<i>Landry (1976), Eltchaninoff (1980), Epard (1989), Ribes et al., (2020), this study</i>
Catogne N	46°4'17"N/7°7'38"E	<i>Grasmück (1961), this study</i>
Catogne S	46°01'39"N/7°7'20"E	<i>Grasmück (1961), this study</i>
Emosson	46°02'57.5"N/6°53'07"E	<i>Epard (1989), Wizevich et al. (2019)</i>
Ferden	46°24'13"N/7°42'49"E	<i>Lugeon (1905), Collet (1947), Baer (1959), Schläppi (1980),</i>

		<i>Hügi et al., (1998), Loup (1992)</i>
Feselalp	46°19'56"N/7°43'33"E	<i>Loup (1992)</i>
Grandes-Ecailles	45°45'36"N/6°48'57"E	<i>Antoine et al. (1975, 1971)</i>
Lotschpass	46°24'56"N/7°42'52"E	<i>Collet (1947), Schläppi (1980), Loup (1992)</i>
SW Morcles		<i>Epard (1989)</i>
Saillon	46°10'10"N/7°10'53"E	<i>Lugeon (1929), Badoux (1972), Loup (1992), this study</i>
Tricot	45°50'52"N/6°46'05"E	<i>Epard (1986)</i>
Ultrahelvetic Lias des Mines	46°17'11"N/7°02'51"E	<i>Trümpy (1951), this study</i>
Val Ferret (Italy)		<i>Compagnoni et al., (1964)</i>
Wildhorn		<i>Cardello (2013), based on map estimation of the thickness</i>

Table VI.1: Sections of the early Jurassic to Mid Jurassic cover between the Belledonne and Aar massifs

2. Evolution across the necking domain (NW-SE correlation)

2.1. The Aiguilles-Rouges cover

2.1.1. Emosson section

In the Aiguilles-Rouges massif autochthonous Triassic cover can be found over the basement (Fig. VI.1). It is composed of the basal arkose overlaid by Triassic sandstones and dolostones marking the initiation of the mid-Triassic transgression above the basement. The basal arkose is not dated and might be Permian to Triassic in age. The Triassic sandstones on the other side have been dated due to the presence of Archosaurian footprints observed in the area (Demathieu and Weidmann, 1982). These sandstones correspond in fact to non-marine playa lake deposits (Wizevich et al., 2019). The presence of the footprints is highlighting the existence a several kilometre long archosaur route (Cavin and Piuze, 2020). This structure corresponds to the termination of the Vindelician high which is a topographic high connecting the Bohemian massif to the Massif Central and inherited from the Eastern Variscan Shear zone (Ballèvre et al., 2018).

2.1.2. Au d'Arbignon synform

The Au d'Arbignon synform forms the autochthonous to para-autochthonous cover of the Aiguilles-Rouges massif (Fig. VI.1) and found at the base of the Morcles nappes (Badoux et al., 1971). It corresponds to the northern margin of the Morcles-Doldenhorn basin (Trümpy, 1945). The cover is composed of lower Liasic marls corresponding to the Dauphinois facies. The Upper Sinemurian is marked by the increase of clastic input in the basin and the formation of sandstones followed by Pliensbachian sand-rich limestones. Bajocian limestones lay unconformably over the basement, pre-rift to syn-rift sediments (Loup, 1992). This situation is similar to what is described in Pormenaz

(Aiguilles-Rouges massif), where late Jurassic to early Cretaceous limestones are lying above the Carboniferous sediments and also Triassic sandstones.

This tends to show that the border of the Aiguilles-Rouges massif was uplifted between the Pliensbachian and the Bajocian before progressive subsidence and deposition of Bajocian shales. This uplift will be discussed more in detail in this chapter.

2.2. SW Morcles nappe

The Morcles nappe (Fig. VI.1) is characterized by a thick Liassic series corresponding mostly of the alternation of marls and limestones. The significant deformation associated to folding of the cover makes difficult the estimate of the initial thickness of the layer (Epard, 1989). The Lower Liasic Tierce Fm. is estimated at ca. 150 m (Epard, 1989). A change of sedimentation is observed during the upper Sinemurian, which is marked by an increase of the quartz and echinoderms content. The Pliensbachian is characterized by the abundance of echinoderms and the arrival of sandstones interlayered with limestones and marls corresponding the Mt Joly Fm, with a thickness estimated at ca. 100m. This is followed by a thick Toarcian marl formation (Mt. Rosset Fm.) up to 200 m thick, followed by Aalenian black shales except in the southern part of the basin, where the black shales begin in the Upper Toarcian (Epard, 1989). The transition between the marls and the shales is abrupt in the basin with the exception south of the basin where interlayered marls and shales have been described (Epard, 1989).

The main feature of the Morcles basin is the increase of clastic input during the upper Sinemurian to Pliensbachian similarly to the Au d'Arbignon synform. This is related to the first occurrence of a local source during the Sinemurian. It is followed by a transgression leading to deepening of the basin with deposits of Toarcian marls and Aalenian black shales. The black shales appear slightly diachronous in the basin, being upper Toarcian to Aalenian in age (Epard, 1990).

2.3. The Mont-Blanc cover

2.3.1. External Mont-Blanc: Tricot section

The cover of the External Crystalline Massif (Fig. VI.1) is preserved only on the Mt. Tricot (Paréjas, 1922; Epard, 1986). A basal arkose has been described lying above the basement and overlaid by Triassic dolostones. The presence of evaporites interlayered with the dolostones led to decollement of the cover above these evaporites. Therefore, the late Triassic to early Liasic cover is affected by folding forming para-autochthonous nappes. The Liassic cover is largely reduced compared to the Morcles basin indicating pinching of the cover toward the Mont-Blanc (Epard, 1986).

2.3.2. Internal Mont-Blanc: L'Amône section

The cover in the internal Mont-Blanc massif is composed of late Liasic to lower Aalenian sediments lying directly above the basement and pre-rift sediments. The section of L'Amône is formed actually of Lower Aalenian conglomerates (Grasmück, 1961) to fine-grained sandstones derived from the underlying rhyolitic basement and transgressed by a meter-thick black shale layer. The black shales are overlaid by echinoderm-rich Bajocian limestones (see also Chapter V).

2.4. Distal Mont-Blanc cover (Wildorn nappe)

The distal Mont-Blanc cover is found in the Helvetic nappes and detached above the underlying basement through evaporite decollement levels. The cover is relatively well preserved in the Wildhorn nappe found in between the Diableret and the Ultra-Helvetic nappes (Fig. VI.1). In a Jurassic paleogeographic reconstruction of the margin, the Wildhorn domain is located at ca. 20 to 40 km of the internal Mont-Blanc (Burkhard, 1988; Pfiffner et al., 2011). It corresponds to a thick Liasic cover up to 500 m which was strongly modified by Alpine deformation. The early Lias appears relatively similar to the Early Lias from the Morcles nappes, with alternation of marls and limestones (Cardello and Mancktelow, 2014). Late Liasic sediments are however different from the more proximal domains, since they correspond to shales without strong detrital input. They are overlaid by Aalenian shales and by limestones to sandy limestones. The Bajocian corresponds to a succession of marls and sandy limestones. Crinoids are observed to the top of the series, similar to the Bajocian cover of the Mont-Blanc (L'Amône).

2.5. Ultrahelvetic domain

The Ultrahelvetic nappes can be found below the Penninic thrust and correspond to the most distal sediments of the margin (Fig. VI.1), preserved before reaching the exhumed mantle domain found in the Penninic units. In a paleogeographic reconstruction it can be found at a distance of ca. 60 km from the Mont-Blanc massif (Fig. 1; Butler, 1985; Burkhard, 1988). The massive evaporites found at the base of the units acted as a decollement level between the cover and the basement. The stratigraphic succession is well preserved in the area of Bex (Switzerland). It starts with preserved Triassic dolostones overlaid by thin layers of sandstones possibly Rhaetian in age, overlaid by Hettangian fossiliferous limestones interlayered with shales corresponding to shoreface sediments (Trümpy, 1951). The Sinemurian is formed by strongly indurated marly and sandy limestones. The Upper Sinemurian is marked by the appearance of echinoderms and sponges associated to levels rich in brachiopods (Trümpy, 1951). The Pliensbachian is characterized by siliceous limestones rich in sponges and echinoderms with also fine-grained detrital quartz. The Upper Pliensbachian is composed of a series of thick marls followed by Toarcian marls. The thickness

of the Aalenian shales is not well constrained due to strong Alpine deformation but estimated at hundreds of meters at minimum.

The conditions of sedimentation varied strongly during the Lias. Indeed, the Hettangian and Sinemurian deposits are similar to the facies in the Morcles nappes and associated to a progressive deepening from shore face sediments to sediments deposited under a water depth up to 200 m. The Sinemurian is marked by the initiation of the clastic input with increase of shale content. The clastic input increases during the Pliensbachian. The upper Pliensbachian and Toarcian are characterized by deep water conditions with bathyal sedimentation (Trümpy, 1951).

2.6. Correlation across the margin

The correlation across the margin show a global increase of the sedimentary cover thickness toward the SE corresponding to the distal part of the margin (Fig. VI.2). An important increase of sediment thickness is visible from the Pliensbachian, with thick deposits formed during Aalenian. The northern part of the section corresponds to the Morcles basin. The increase of sediment thickness from the Sinemurian marks the onset of tectonic activity of the basin (Epard, 1990). The subsidence rate in the Helvetic shelf obtained by Wildi et al. (1989) shows a low subsidence rate during the early Lias and an increase between 200 and 190 Ma. This is coeval with the main activity on the Ornon fault in the Belledonne massif (Chevalier, 2002).

However, a major topographic high corresponding to the Mont-Blanc massif is clearly visible (Fig. VI.2). On the external part, the Liassic units are pinching out indicating the termination of the Morcles basin. However, due to the alpine deformation, the geometry of the syn-rift deposits above the pre-rift cover (e.g., onlapping or wedging) cannot be distinguished. The internal Mont-Blanc is characterized by the absence of the Liassic cover in the Val Ferret and the presence of Aalenian conglomerates, observed nowhere else. Bajocian echinoderm-rich limestones are observed in the Aiguilles-Rouges massifs and in the internal Mont-Blanc as well as in the Wildhorn units. This raises the question of the lateral extension of these Bajocian limestones above the Morcles basin and the Mont-Blanc.

The apparition of clastic inputs during the Upper Sinemurian and Pliensbachian in the different basins surrounding the Mont-Blanc massif is one of the key characteristics of the syn-rift sedimentation in the area defining the "helvetic facies" in opposition to the marly "Dauphinois facies" (Franchi et al., 1908; Barf  ty and Mouterde, 1980). The occurrence of detrital input is correlated to the emersion of the Mont-Blanc. Indeed, the clastic input is diminishing away from the massif with only fine quartz grains observed in the Ultrahelvetic (Trümpy, 1951).

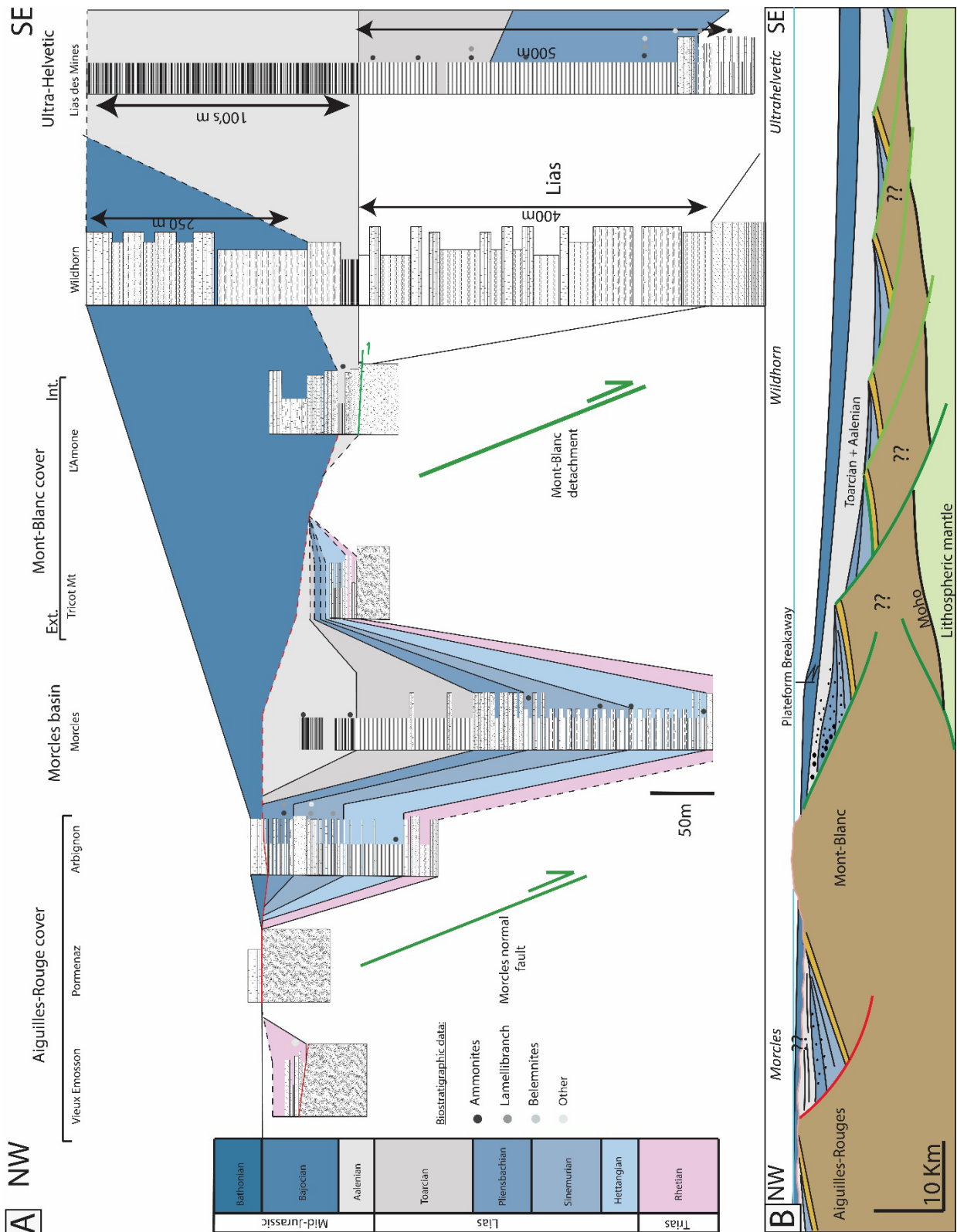


Figure VI.2: A-Correlation of the sections across the margin from the Aiguilles-Rouge to the Ultrahelvetics domain. B-Reconstitution of the margin during Bajocian associated to the syn-rift sedimentary cover (vertical exaggeration of cover thickness).

3. Evolution along the necking domain (SW-NE correlation)

3.1. Aar massif border

3.1.1. Ferden

The area of the Torrenthorn corresponds to the cover of the External Aar massif at the extremity of the Morcles-Doldenhorn basins (Fig. VI.1). The Triassic and Liasic covers are autochthonous to para-autochthonous while the middle and upper Jurassic covers are detached above the Aalenian shales, corresponding to allochthonous units (Loup, 1992).

The Triassic cover is formed by a basal arkose lying above the basement. Thickness variations reflect small topographic changes. The arkose is overlaid by evaporites and few meters of dolostones deposits associated to a tidal environment (Loup, 1992). The dolostones pass to marls and quartzite corresponding to the Rhaetian. The Hettangian deposits are formed by marl-limestone alternation. The Lower Sinemurian is marked by the apparition of *Gryphae sp.* (*Ostrea*). A significant change occurred during the Upper Sinemurian with the increase of the quartz content. The base corresponds to marls passing progressively to massive sandstones with a total of ca. 30 m. The Lower Pliensbachian is composed of siliceous limestones with a thickness of 30 m. The Upper Pliensbachian is composed of a 40 m-thick sandstone formation. The base of the formation marks the transition between the limestones and sandy limestones passing the calcareous sandstones. Microconglomeratic levels consisting of dolostones, and basement clasts are recognized. The sandstones are also coarse-grained. The lithoclasts are derived from the metamorphic basement and dolostones from the pre-rift cover. Echinoderm fragments are also observed in the sandstone. The sandstones are overlaid by echinoderm-rich limestones from the Toarcian.

3.1.2. Lotschpass

The Lotschpass corresponds to series of tectonic slivers pinched between the Gastern and the Aar massif (Fig. VI.1). These tectonic slivers formed by a reduced Liasic cover forming the termination of the Doldenhorn basin. The age of the formations were determined by comparison of facies with the Torrenthorn area (Loup, 1992). The pre-rift cover preserved in that area is the Triassic dolostone overlaid by marls and quartzite levels corresponding possibly to Rhaetian and Hettangian ages. These levels are overlaid by the *Gryphae* limestones attributed to the Lower Sinemurian, followed by sandstones alternating with marls that thicken upsection. This corresponds to the upper Sinemurian and Pliensbachian formations. The Toarcian sediments correspond to echinoderm-rich limestones (Loup, 1992).

3.1.3. Feschel-Feselalp

The area of Feschel-Feselalp can be found on the border of the Aar massif and forms a SW-NE syncline in the Aar massif (Fig. VI.1; Loup, 1992). The first work on this area was realized by Lugeon (1910) and Baer (1959). This area corresponds to the cover of the internal Aar massif (Baer, 1959; Masson et al., 1980). The Liasic cover is autochthonous over the basement while the Late Jurassic and Cretaceous to Tertiary cover can be found in the para-autochthonous units overlying the Aar basement.

No biostratigraphic dating were realised on this area, therefore the age of the formations was obtained by correlation using the Triassic dolostones and the Aalenian black shales as key levels to constrain the ages (Loup, 1992). The Triassic cover corresponds to a basal arkose over the basement overlaid by dolostones. These dolostones are affected by important thickness variations, from 1 m to 50 m thick (Loup, 1992), with breccias found in the top of the formation. They are overlaid by few meters of marls and shales.

Two types of Liasic cover are observed. In the Feschel area, 20 to 30 m of siliceous limestones are visible, with the apparition of echinoderms and an increase of the quartz content toward the top. In the area of Feselalp, 2 km south of Feschel, the base of the Lias is marked by the occurrence of meter-thick sandstone beds and fossil-rich limestones. At the base a conglomerate with rounded dolostone clasts and gneiss is exposed. This is followed by 20 to 30 meters of sandy limestones to calcareous sandstones with microconglomeratic levels. The carbonate-dominated one corresponds to a platform environment. However, the occurrence of the top Trias unconformity associated to reworking of the Triassic cover and the basement are traces of a tectonic activity on the Aar massif extremity. The occurrence of echinoderms associated to the clastic input might indicate a Sinemurian to Pliensbachian age. It is plausible that the carbonate-dominated cover corresponds to the lower Lias units absent (erosion?) further south.

3.1.4. Interpretation

Both the external and internal borders of the Aar massif show clastic input from the Upper Sinemurian and tectonic activity associated to erosional unconformity at the base of the Upper Liasic sediments. (Baer, 1959) proposed an uplift of the area during the Upper Sinemurian to explain the occurrence of a clastic source.

3.2. Morcle nappe (Ardèche)

The section of Ardèche corresponds to the Liassic core of the Morcles nappe and can be found in the northern part of the Rhône valley (Fig. VI.1). This section is well known for the numerous structural and microstructural studies realised in relation with the Morcles nappe and its deformation (e.g., Masson et al., 1980; Huggenberger, 1985; Ramsay, 1981,1989). Stratigraphic work

was realised by Badoux et al., (1971), Badoux (1972), Epard (1990) and Loup (1992). The formation were dated by comparison with the Federnthorn and Torenthorn section in the Aar massif (Loup, 1992).

The base of the formation corresponds to 20 m of dolostones, and marls attributed to the upper Triassic. Above these formations, bioclastic limestones attributed to Rhetian can be observed. They are overlaid by Hettangian calcareous marls showing significant tectonic overprint with a stretching up to 375% (Badoux, 1963) and compaction of 33% (Ramsay and Huber, 1983). They are overlaid by *Gryphae* limestone from the Lower Sinemurian with occurrence of clastic sediments toward the top. The upper Sinemurian is marked by the occurrence of sandstones. The base of these sandstones corresponds to ca. 5 m of massive sandstones before passing to ca. 40 m of marls/sandstones. Benthic foraminifera have been described by Loup (1992). The top of this formation corresponds to a condensed level before passing to Pliensbachian marls and limestones marked by the occurrences of belemnites. The Toarcian is marked by the occurrence of echinoderm-rich limestones.

3.3. The Mont-Blanc cover

3.3.1. Saillon

The section in Saillon (Fig. VI.1) was recognized by Favre et al., (1883) and dated by comparison of facies with the Aar cover (Lugeon, 1929). The main problem was the origin of the Saillon unit. Indeed, two hypotheses were strongly discussed. The first one was to attach the Saillon unit to the inverse limb of the Morcles nappe (Antal, 1971) while the second hypothesis attached this same unit to the autochthonous Mont-Blanc cover (Badoux, 1971). Finally, Masson (1988) proposed to attach the Saillon unit to the internal Mont-Blanc cover detached from the basement by the Poya strike slip fault (related to the Simplon-Rhône fault).

The Saillon cover corresponds to the Liasic cover of the internal Mont-Blanc and was described in detail by (Loup, 1992). The base corresponds to marls with minor echinoderm fragments and quartz grains. This is overlaid by ca. 20 m of *Gryphaea* bearing limestones associated to the Lower Sinemurian. Remnant of sponges have been described by Loup (1992). The upper Sinemurian corresponds to 20 meters of sandstones. The base corresponds to alternation of sandstone beds and limestones passing progressively to thick sandstone beds with centimetre thick shale levels. The sandstones are also coarsening upward. A transgression level with phosphatic nodules is visible on the top. This is followed by 100 m of sandy limestones and siliceous shales from the lower Pliensbachian with abundant HCS indicating a storm-dominated lower offshore environment. It is overlaid by upper Pliensbachian sandstones (Loup, 1992). The base of the sandstones is formed by individualised small bed separated by small shale levels. These shale levels disappear toward the top.

This unit clearly highlights the beginning of clastic input in the basin during upper Sinemurian. These two sandstone deposits, Upper Sinemurian and Upper Pliensbachian in age, are similar to those observed in the Aar massif but not recognized in the Mont-Blanc massif. This difference is explained by Loup (1992) as the result of transgression during the Lower Pliensbachian, which would block the clastic sediment toward the continent.

3.3.2. Catogne

The Catogne (Fig. VI.1) corresponds to a monoclinical serie dipping toward the east and corresponding the Triassic and Liassic autochthonous cover below the Aalenian shales. This cover corresponds to the basal Triassic arkose overlying the rhyolite (see Chapter V). It is overlaid by the Triassic dolostones and Hettangian marls (dated by *Schlotheimia angulata* ammonites; Grasmück, 1961). Above this formation are found sandy bioclastic limestones dated as lower Sinemurian (*Entolium cf. hehli*; Grasmück, 1961). To the north of the Catogne area, Pliensbachian sandstones are found lying over Hettangian deposits, whereas to the south unconformably over Hettangian and Triassic deposits. The base of the sandstones corresponds to microconglomeratic levels reworking the pre-rift cover followed by massive sandstone beds with only few shale levels. Toward the top, the sandstones are fine-grained. The top of the formation is formed by large sigmoidal structures interpreted as a tidal bar (Loup, 1992). These sandstones are overlaid in the north by Toarcian limestones and Aalenian shales and in the south by Aalenian shales only.

3.3.3. Val Ferret

Toward the south, in the Val Ferret (l'Amône and Italian Val Ferret, Fig.VI.1) the Liassic sediments disappear, and the basement is directly overlaid by Aalenian conglomerates as observed in l'Amône which have been described in the previous section. After the Ferret pass, Albian sediments have been described lying over the basement (Compagnoni et al., 1964). This indicates that the Mont-Blanc massif remained a topographic high at least until the Albian.

3.3.4. Tête des Fours et Grandes Ecailles

The internal southern Mont-Blanc massif goes from the Col du Bonhomme to the Seigne pass where an autochthonous sedimentary cover can be observed (Fig. VI.1).

In the Tête des Fours area, massive Pliensbachian sandstones, the Grès Singuliers, are outcropping (Landry,1976; Eltchaninoff, 1980; Epard, 1989). They are lying unconformably above Hettangian calcschists, Triassic dolostones and the exhumed basement (see chapters II to IV). The base of these Grès Singuliers is composed of conglomerates reworking the pre-rift cover and the basement. The basement clasts are rounded and characteristic of shore face sediments. They are overlaid by coarse-grained sandstones with cross stratification observed. The sandstones are more fine-grained toward the top (Dall'asta, 2019). Bundle sequences are present in the Grès Singuliers

indicating a lower tidal environment (Tape et al., 2003). Large sigmoidal beds with bioturbations in the top of the formation were finally described and interpreted as tidal bars (Ribes et al., 2020). A small conglomeratic level is observed and might correspond to a transgression surface. The Grès Singuliers are overlaid by Aalenian black shales. The occurrence of this transgression surface associated to interlayered shales and sandstones (Meyer, 2002) indicates that this contact is stratigraphic. However, significant Alpine deformation is visible in the Aalenian shales.

In the Grandes Ecailles area, the basement is covered by meter-thick conglomerates and sandstones (Antoine et al., 1975). Above, black shales could be associated to the Aalenian shales. Therefore, the sandstones above the basement can be correlated with the Grès Singuliers.

3.3.5. Interpretation

The cover of the Mont-Blanc massif is characterized by the presence of massive syn-rift sandstones and conglomerates from the Upper Sinemurian up to the Aalenian. These syn-rift sandstone deposits are lying uncomfortably above the pre-rift cover and exhumed basement. These clastic deposits are interpreted as the result of the uplift of the massif started during the Upper Sinemurian (Grasmück, 1961; Ribes et al., 2020), and leading to the formation of the “Mont-Blanc island” (Trümpy, 1949). The proximal facies correspond to the shoreface conglomerates while the Saillon units represent more fine-grained distal deposits in an upper to lower offshore environment. The top of the Pliensbachian sandstones show a tidal dominated environment along the Mont-Blanc, from the Catogne to the southern Mont-Blanc massif.

3.4. Correlation along the margin (NE-SW profile)

3.4.1. Correlation along the Morcles-Doldenhorn basin

The existence of the Morcles-Doldenhorn basin between the Aar massif and the external Belledonne massif is attested by sediment thickening during from the Sinemurian to the Aalenian (Fig. VI.3). Beginning of basin formation is observed during the Hettangian. The Upper Lias is characterized by the increase of quartz content which is associated to the Mont-Blanc and Aar uplift. Most of the subsidence is observed during the Toarcian with depositions of marls.

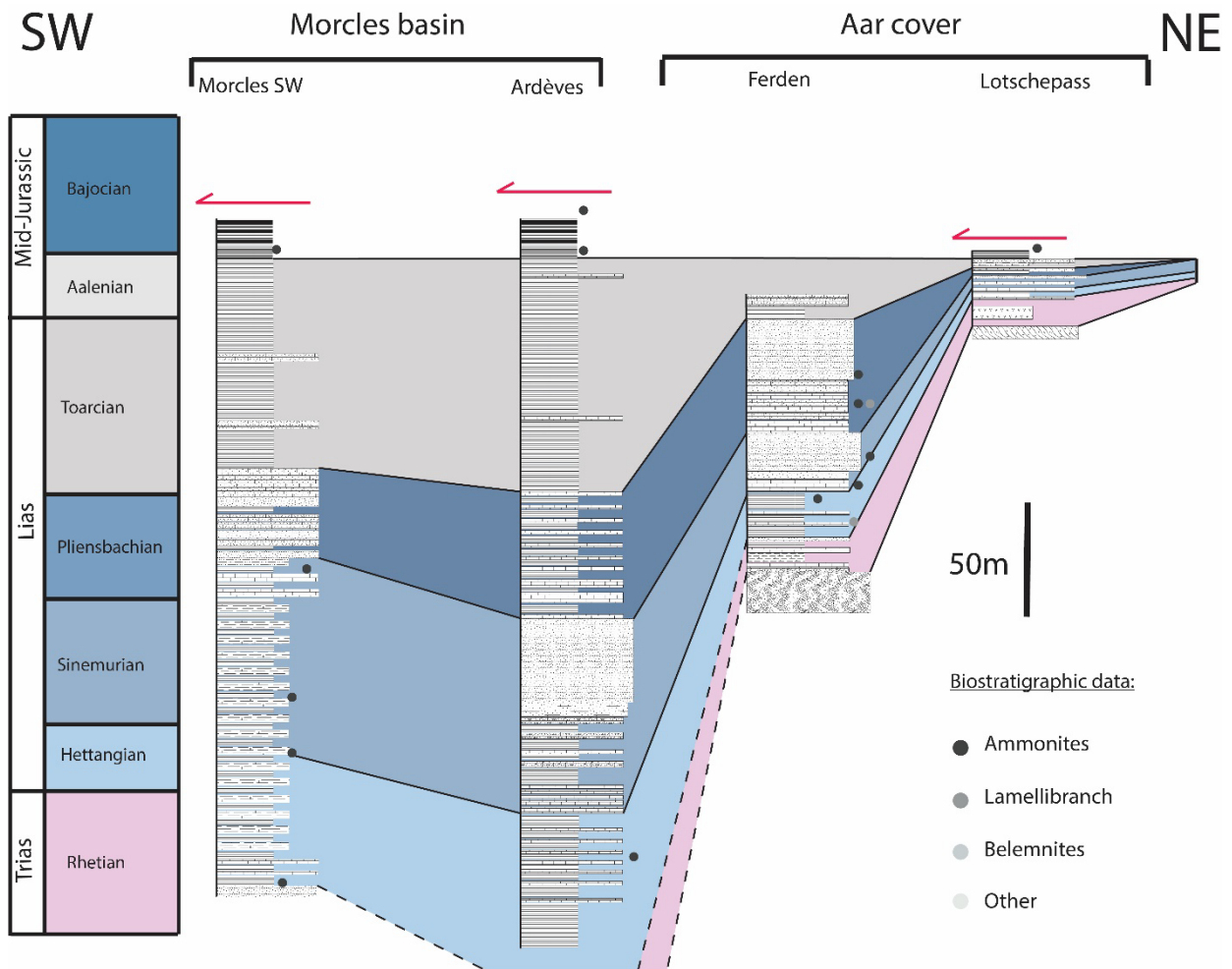


Figure VI.3: Correlation of the section along the Morcles-Doldenhorn basin using the Aalenian as a datum.

3.4.2. Correlation across the necking domain

Correlations along the necking domain highlight the occurrence of two topographic highs (Aar and Mont-Blanc) separated by a basin area (Fig. VI.4).

The Aar and Mont-Blanc massifs correspond to topographic highs that emerged during the upper Sinemurian. In between the massifs, a depression is observed focusing sediments derived from the Aar and Mont-Blanc. However, the connection between the Morcles-Doldenhorn basin is unclear because of the poor preservation. The Aalenian shale deposits around the Mont-Blanc are discontinuous. Indeed, they clearly pinch out toward the centre of the massif where they disappear. The Albian unconformity of the Italian Val Ferret appears to be a culminating point indicating that the Mont-Blanc remained emerged for up to 60 Ma after the necking stage. Moreover, the clastic input appears also long lived, from the Upper Sinemurian to the Aalenian. The Upper Pliensbachian is associated to the development of tidal currents at least in the internal Mont-Blanc.

Large-scale evolution of the Jurassic necking domain of the Alpine Tethys

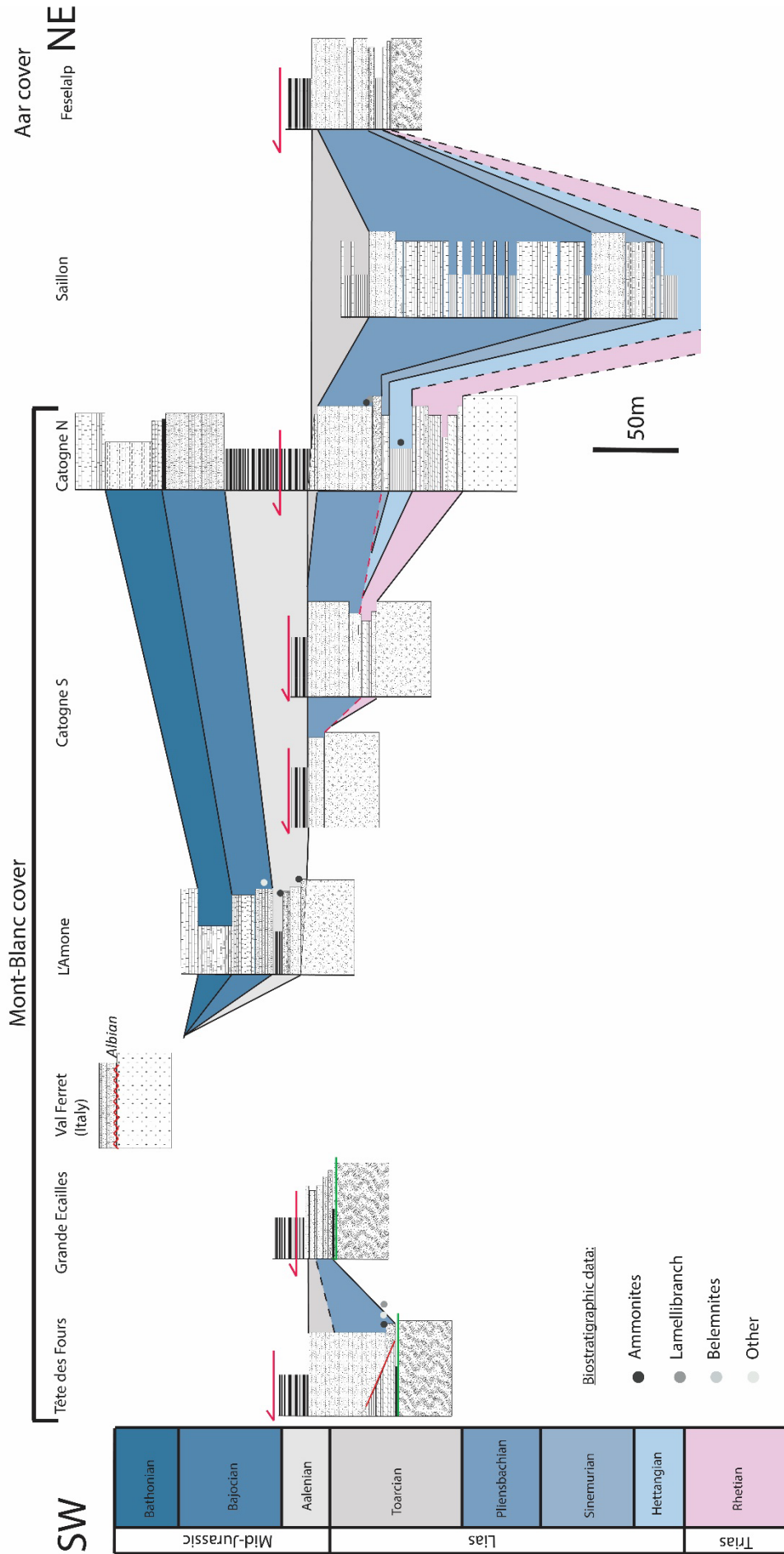


Figure VI.4: Correlation of the margin along the necking domain from the Aar to the southern Mont-Blanc massif using the base of Aalenian for datum

4. Eustatic evolution of the margin

Local eustatic variations of the different areas of the margin have been compared to the large scale eustatic variations from Hardenbol et al. (1998). The sections have been also compared to the evolution of the Jura platform (Fig. VI.5). The Late Triassic to Early Liasic transgression is observed in all the sections. The end of the transgression is highlighted by the transition from mud-dominated lower offshore facies to storm-dominated upper offshore facies (Loup, 1992). This corresponds to the Si3 surface from Hardenbol et al., (1998). The regression is associated to the arrival of sandstones during the Late Sinemurian.

The top Sinemurian condensed level observed in the Arbignon and Ardèche sections indicates a transgression in the Morcles-Doldenhorn basin, which does not correlate with global eustatic variations (Fig. VI.5). This transgression is not clearly marked in the Morcles basin to the south but is observed in the Doldenhorn basin to the north.

The Pliensbachian transgression/regression cycles (Pi3 to Pi6) can be observed in some areas such as the Torrenthorn and the Mont-Blanc (Fig. VI.5). Indeed, this lower Pliensbachian transgression is an explanation for the two clastic pulses observed in the upper Sinemurian and upper Pliensbachian in the basins. According to Loup (1992) they correspond to two High Stand System tracts, while the lower Sinemurian led to the formation of Transgression System Tract blocking the clastic sediments toward the continent. In the southern Mont-Blanc, the progressive fining of the sandstones with bundle development followed by coarsening might also reflect this transgression/regression cycle. These cycles are visible only in the most proximal sections (shoreface to upper offshore facies).

The top Pliensbachien transgression (Pi8) is recorded in the Aar and Mont-Blanc massifs as well as in the Morcles basin (Fig. VI.5). However, the regression of the upper Toarcian and lower Aalenian observed in the proximal Jura domain is not observed in the Helvetic domain. Indeed, Aalenian is marked by black shales indicating continuous transgression or at least no change of water depth. The change from marls to black shales appears abrupt and is slightly diachronous throughout the basin.

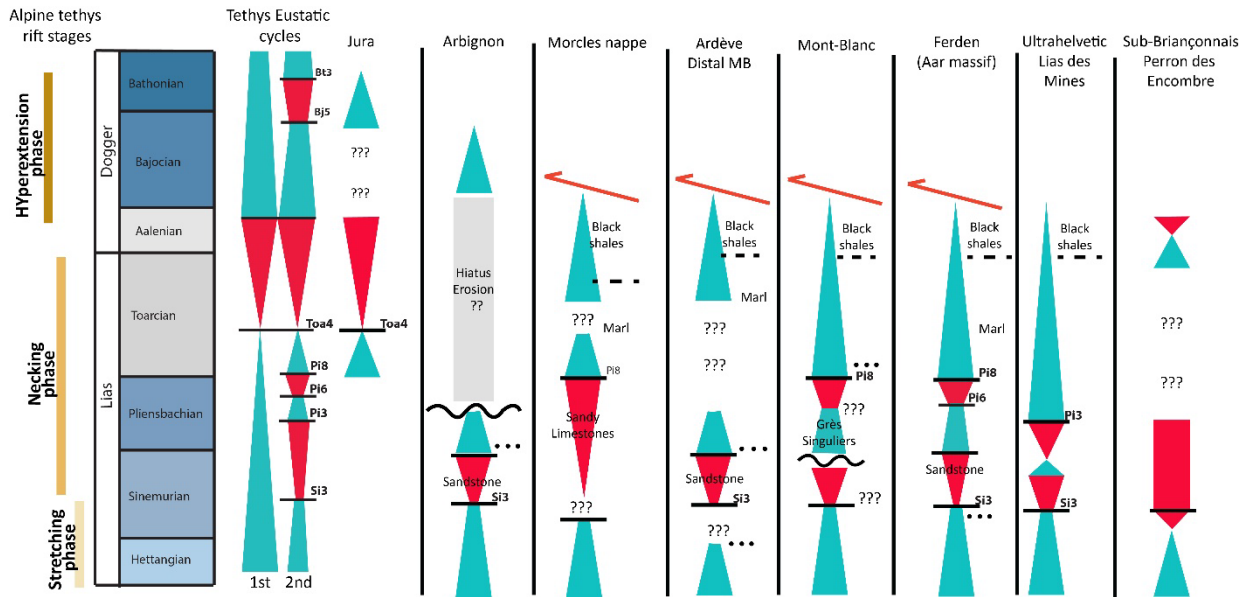


Figure VI.5: Eustatic variations of the Helvetic margin compared to the large scale eustatic variations of the Tethys from Hardenbol et al., 1998. The most striking feature is the Aalenian transgression which is not recorded in the proximal domain (e.g., Jura domain), and which indicates strong tectonic subsidence.

The Aalenian transgression clearly does not correspond to large scale eustatic variations at least during the lower Aalenian. It thus reflects the tectonic subsidence of the whole margin. This transgression occurred earlier in the most distal part of the margin (e.g., Ultrahelvetico domain), starting during the Pliensbachian, related to the oceanward migration of deformation associated to the hyperextension.

Comparison of the eustatic cycles of the two margins of the Valais basin (Helvetic domain and Sub-Briançonnais) have been proposed by Loreau et al., (1995). There are similarities between the cycles registered in the Helvetic domain and in the Sub-Briançonnais for the Hettangian and the lower Sinemurian (Loreau et al., 1995). In contrast, the evolution during the Pliensbachian differs between the Helvetic domain and the Penninic units, marking the beginning of an individualisation associated to the Valais opening. The Toarcian-Aalenian subsidence is however observed throughout the entire area. However, the Late Aalenian of the sub-Briançonnais is marked by a regression not observed in the Helvetic domain.

5. Palaeogeographical reconstruction of the necking domain

5.1. Helvetic / Dauphinois facies

Two main Jurassic facies are described in the Western Alps, the Dauphinois facies and the Helvetic facies. The Dauphinois facies is characterized by the abundance of limestones to marls deposits (Franchi et al., 1908), while the Helvetic facies is characterized by the occurrence of clastic deposits derived from the Mont-Blanc and Aar Massifs. The Dauphinois facies can be recognized in

the Morcles basin forming the Lower Liasic deposits similar to the formation recognized in the Bourg d'Oisans half graben further south (Chevalier, 2002; Epard, 1989). The Upper Lias is composed of an alternation of limestones and sandy limestones that does not correspond to the Dauphinois facies *sensu stricto*.

The Helvetic facies corresponds to the sandstones observed in autochthonous cover of the Aar and Mont-Blanc massifs (Trümpy, 1971). The isopach map (Fig. VI.6) of the Lias facies highlights the peculiar position of the Mont-Blanc forming an island surrounded by basinal area. A clear thickness increase is visible toward the SE. The Aar massif corresponds to a second emerged area but its extension to the north and north-east is not constrained. The area between the Aar and Mont-Blanc was not preserved. It therefore impossible to know if the clastic deposits from the Mont-Blanc and Aar were connected.

Two main directions of sedimentary transport are visible. The NW-SE direction enables transport of sediments toward the future distal domain while the NE-SW direction led to sediment transport along the margin.

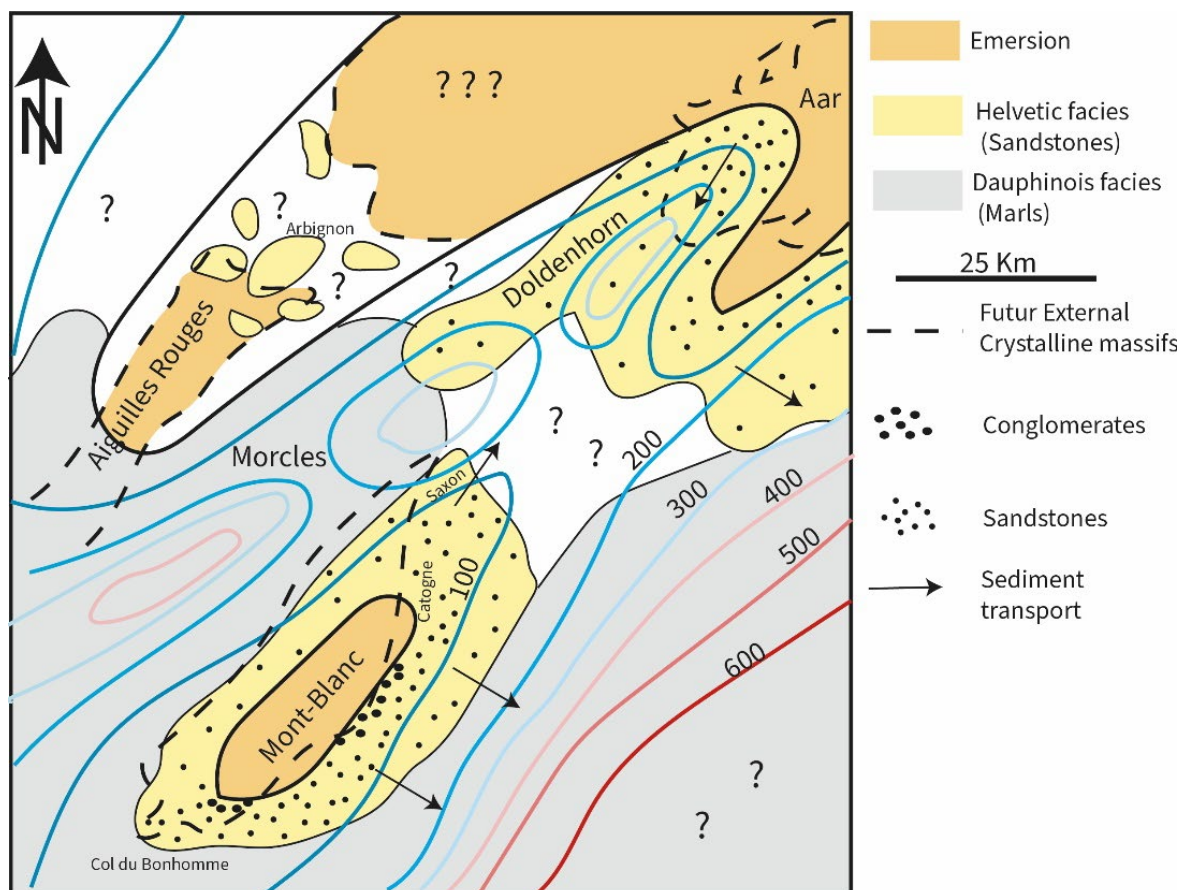


Figure VI.6: Repartition of the Helvetic and Dauphinois facies around the Mont-Blanc and Aar massif (Trümpy, 1971). The isopach line of the Liasic sediments are from (Loup, 1992).

5.2. Paleogeographic evolution

5.2.1. Hettangian to Sinemurian

During the Early Lias, the western Alpine realm corresponded to an epicontinental sea, dominated by carbonate sediments. From the Late Trias to the Early Hettangian, N-S to NW-SE minor extension occurred as recognized in the Bourg d'Oisans half-graben (Gillcrist, 1988; Chevalier, 2002).

The Early Sinemurian is characterized by the development of half graben basins filled with marls to limestones (Dauphinois facies). This highlights the absence of connection with any continental sources. During the Late Sinemurian (Fig. VI.7A), the occurrence of sandy limestones is a proxy for the initiation of the Mont-Blanc basement uplift. There was also the appearance of widespread echinoderm-rich limestones (mostly crinoids) which highlight the development of crinoid meadows in the basin margins.

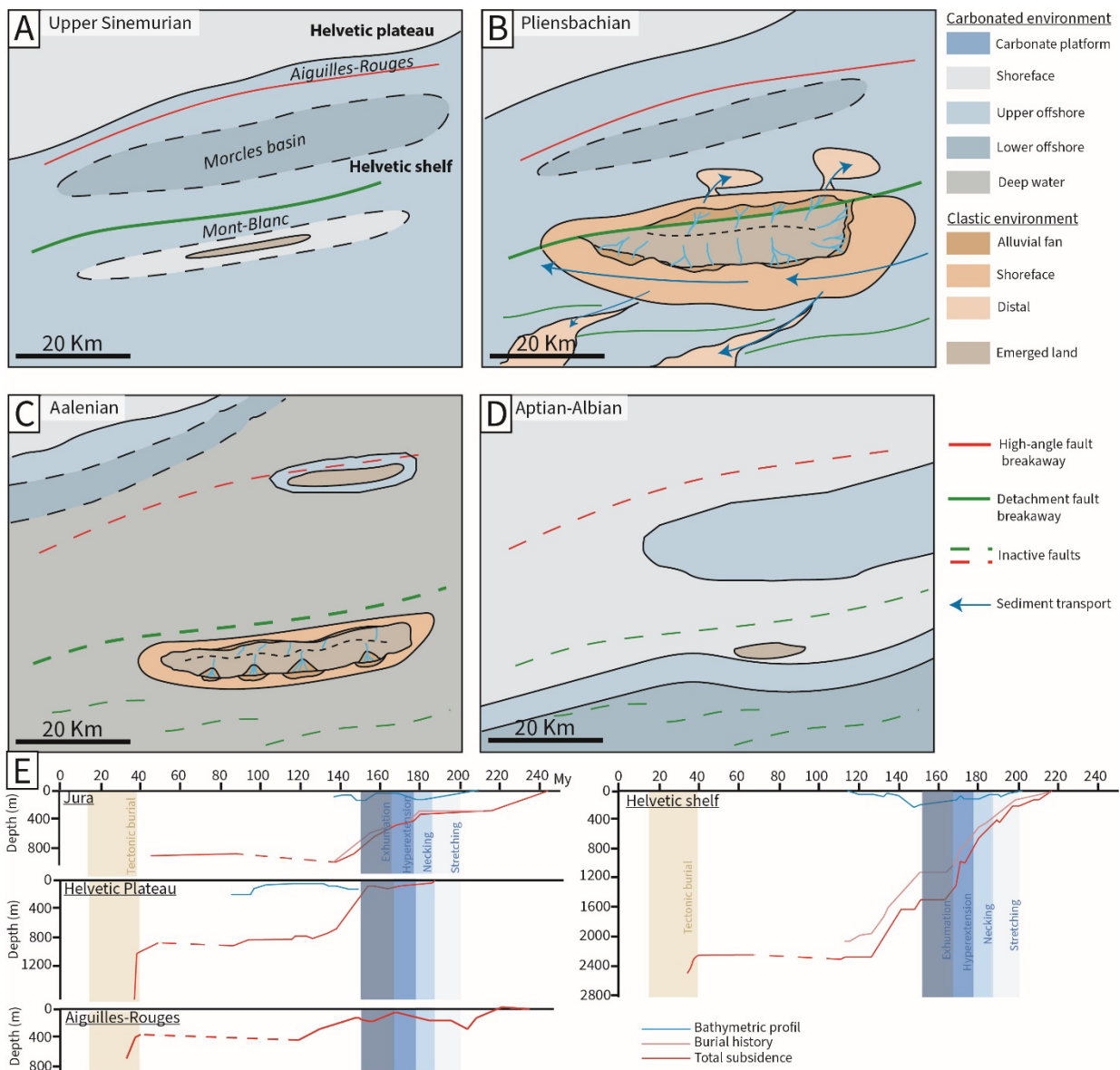


Figure VI.7: A- Paleogeographic reconstruction of the Mont-Blanc area during the Sinemurian. Subsidence in the Morcles basin is observed while topographic uplift is starting in the Mont-Blanc. B- Reconstruction during the Pliensbachian showing

the emersion of the “Mont-Blanc Island” associated to important clastic deposits around the Mont-Blanc. Sediments are exported toward the distal Ultrahelvetetic domain. C- Reconstruction during the Aalenian showing the progressive transgression on the basement. Clastic deposits are restricted to the Mont-Blanc. Uplift is also observed in the Aiguilles-Rouges massif. D- Reconstruction during the Lower Cretaceous showing progradation of the carbonate platforms. Only a small portion of the Mont-Blanc remained emerged. E- Burial history for the base of the base of the Mesozoic sediments (from Wildi et al., 1989) for the Jura platform, the Helvetic plateau, the Aiguilles-Rouges massif and the Helvetic shelf.

5.2.2. Pliensbachian-Toarcian

The Pliensbachian is characterized by important clastic deposits around the Mont-Blanc massif (Fig. VI.7B). They highlight the presence of the “Mont-Blanc Island” providing sediments to the surrounding basins. The comparison of similar structures such as the Los Cabos detachment indicates how the drainage network might have looked like on these types of structures. The rivers are parallel to each other and also parallel to the stretching directions with a regular spacing of 4 to 6 km (Bot et al., 2016). This repartition is controlled by the fault corrugation forming megamullions.

Significant subsidence in the distal domain (Ultrahelvetetic) was associated to progressive migration of the deformation (Fig. VI.7E). The presence of detrital input in the Ultrahelvetetic indicates a connection between the Mont-Blanc and Aar sedimentary system. The export of the sediment in the distal part of the rift was achieved through gravitational flow leading to progressive fining of the sediments. The presence of vegetal fragments in the Ultrahelvetetic sediments observed by Trümpy, (1951) is a sign of the proximity with emerged lands (Mont-Blanc and Aar massif). Strong tidal currents are visible along the Mont-Blanc leading to lateral reworking of the sediment. The development of relatively narrow seaways led to high bed shear stress due to tidal flow constriction (Mitchell et al., 2011). These strong tidal currents seemed to appear during the late Pliensbachian, when the conditions seemed the most favourable. An increase of subsidence is visible also in the proximal domain (Jura) from 180 Ma onwards.

The Toarcian is characterized by thick marl deposits in the basin associated locally with crinoid-rich limestones. The Toarcian is however present locally in the Mont-Blanc and Aar cover where it is mostly composed of echinoderm-rich limestones. The absence of clastic deposits in the Mont-Blanc nor in the basins indicates that most of the topography might have been already flattened. Fragment of corals (*Isastrae*; Grasmück, 1961) have also been found, indicating the development of reef locally over the Mont-Blanc basement.

5.2.3. Post tectonic evolution (Aalenian to Bajocian)

During the Aalenian, most of the deformation migrated to the distal domain where crustal thinning related to hyperextension was occurring associated to thick shale deposits (Fig. VI.3 and 7C). However, uplift was taking place in the Helvetic shelf mostly around the Aiguilles-Rouges massif. This uplift seems to have occurred during the Aalenian. Besides that, the Lower Aalenian of the Mont-Blanc massif corresponds to massive shoreface conglomerates passing to sandstones. This indicates a

rejuvenation of the topography in the Mont-Blanc. This late Toarcian/Aalenian uplift is not well explained yet. Several hypotheses can be formulated to explain this event. The first one is the activity of a large fault west of the Mont-Blanc, which would lead to the uplift of the necking and proximal domains. This fault could correspond to the outer necking fault (see chapter II 2.3.1) as observed by Osmundsen and Péron-Pinvidic, (2018) in Norway, and associated to the onset of hyperextension. Secondly, post-rift uplift of the passive margin can occur because of the isostatic readjustment due to lithospheric thickening of the distal margin associated to thinning in the proximal domain (Leroy et al., 2008) or because of mantle dynamic topography (Hauptert et al., 2016; Hoggard et al., 2016; Müller et al., 2018). These margin uplifts occur several tens of Ma after lithospheric breakup, which is not the case in the Helvetic domain. However, uplift contemporaneous of the hyperextension in Gulf of Suez have been observed in the rift shoulder (Omar et al., 1989) and interpreted as the consequence of the development of small convection cells in the mantle (Steckler, 1985). These types of large-scale mantle activity lead to anomalous uplift on the proximal domain which can be easily detected (Hauptert, 2015). Additionally, basement deformation occurring after the onset of oceanic accretion and continental break up has been observed in the Gulf of California (Geoffroy and Pronost, 2010) indicating unexplained long lived tectonic activity on rifted margins . These different hypotheses might explain the Aalenian basement uplift of the whole section of the margin.

The massif was progressively drowned, which is visible through the deposits of black shales over the shoreface deposits. The thickness of the Aalenian shales is highly variable around the Mont-Blanc, indicating progressive transgression above the exhumed basement. The transition from marls to black shales is slightly diachronous in the basin.

5.2.4. Post-rift evolution

The post-rift history was characterized first by a plateau in the subsidence during mantle exhumation in the Helvetic shelf and an increase of subsidence between 150 and 140 Ma associated to the onset of seafloor spreading in the Liguro-Piemont basin and Valais basin indicating subsidence of the whole margin (Fig. VI.7E; Wildi et al., 1989). This was also coeval to the acceleration of rift spreading velocity up to 22 cm/yr in the Liguro-Piemont basin (Le Breton et al., 2021). This was followed by an important decrease of the subsidence from 140-130 Ma (Fig. VI.7E; Wildi et al., 1989).

The Early to Middle Cretaceous was characterized by progressive progradation of carbonate platforms in the basin. The Urgonian platform has been recognized as patch reefs in the Wildhorn nappe (Föllmi and Gainon, 2008) indicating shallow marine conditions below the External Crystalline massif. Only a small portion of the Mont-Blanc remained emerged at least until the Albian (Fig. VI.7D, Compagnoni et al., 1964).

Conclusion

The evolution of the Helvetic domain was marked by the emersion of the Mont-Blanc massif during the Upper Sinemurian, changing the type of sedimentary infill of the basin from carbonate-dominated to clastic-dominated and defining the Helvetic facies. This event was relatively short-lived from Upper Sinemurian to Pliensbachian followed by Toarcian transgression. The Aalenian was characterized by the progressive drowning of the emerged massif. However, lower Aalenian was marked by local rejuvenation of the topography associated to strong subsidence in the distal part of the margin.

Chapter VII- Linking ore deposits to crustal necking: Insight from the Western Alps

Nicolas Dall'Asta^{*1}, Gianreto Manatschal², Guilhem Hoareau¹

¹ Université de Pau et des Pays de l'Adour, E2S UPPA, CNRS, LFCR-France

² Université de Strasbourg, CNRS, ITES UMR 7063, Strasbourg F-67084, France



Mineralisations in limestone (Val Ferret, Switzerland)

« La montagne et l'eau finiront par se rencontrer. » (Proverbe chinois)

Foreword

This chapter synthesise the observations on the fluid circulation along the Mont-Blanc detachment faults with the stratigraphic evolution and the occurrences of pre-Alpine ore deposits to propose a model for fluid circulation and ore deposits on necking domains. The goal is to constrain the type of deposits associated to crustal necking and precise the possible downward and upward fluid pathway in the crust. The ore deposits are discussed in terms of mineral systems combining large-scale considerations associated to the fertility of the basement and the thermal gradient, with basement tectonic architecture and considerations about the nature of the fluid interacting and the conditions for metal extraction the local conditions necessary for ore deposit at the surface. Finally, the evolution of the fluid and ore deposits from stretching to mantle exhumation is detailed indicating changes of fluid content and temperature as well as changes of ore types.

This chapter is written in the form of a short synthetic article providing the basis for understanding fluid circulation in necking domains.

Introduction

Rift systems are closely linked to hydrothermal circulations and ore deposits (Pirajno and Cawood, 2009). However, many questions remain on the way fluid flow and mineralisations interact in time and space during rifting. Understanding these complexities create opportunities to explore successfully for ore deposits in rift systems. Here we focus on ore deposits that form during crustal and lithospheric necking, corresponding to the moment when the crust and lithosphere are dramatically thinned, representing a key event within the life cycle of a rift-system (Sutra and Manatschal, 2012). This event is associated with elevated thermal gradient, and uplift. The key questions addressed in this paper are what are: (i) the type of elements transferred during necking, (ii) the mechanisms driving the fluid flow and its pathways, as well as (iii) the conditions controlling ore deposition.

At present, many studies focus on hydrothermal systems and element transfer at Mid Ocean Ridges (MORs; Boschi et al., 2006; McCaig and Harris, 2012; Schroeder et al., 2015) or extensional systems linked to intracontinental rifting or orogenic collapse (Tiercelin et al., 1993; Shelton et al., 2019; Wiest et al., 2019). In contrast, almost nothing is known about fluid circulation and ore deposition related to crustal necking. The main reason is the lack of well described fossil analogues. Although former studies identified hydrothermal activity with a crustal signature in the pre- and syn-rift cover sequences of necking domains (Incerpi et al., 2020), the mechanisms of fluid flow such as the processes triggering fluid advection along pathways and related element transfer at necking zones has not yet been clearly identified and investigated.

The discovery of a fossil necking domain in the External Crystalline Massifs (ECM) and more specifically at the Mont-Blanc massif in the Western Alps (Ribes et al., 2020; Dall'Asta et al., 2022; Dall'Asta et al., in prep) allows to describe for the first-time fluid flow, element transfer and ore deposits linked to crustal and lithospheric necking. These results, added to previous ones obtained from numerical models, present-day and fossil examples of necking zones and related hydrothermal activity, are used to propose a play element approach for ore deposits linked to crustal necking.

1. What is crustal necking?

Crustal necking corresponds to the process that controls crustal thinning from initial crustal thickness (30 ± 5 km) to less than 10 km (Péron-Pinvidic et al., 2017). It is associated to strain localisation and progressive coupling between brittle layers in the crust and the mantle lithosphere (Sutra and Manatschal, 2012; Sutra et al., 2013). It occurs after an initial stage of distributed decoupled rifting (stretching phase) and terminates when the crust is fully embrittled and faults can penetrate and exhume the mantle (hyperextended stage). This necking phase has been studied quite

extensively both using seismic data of present-day rifted margins (Osmundsen and Ebbing, 2008; Osmundsen and Redfield, 2011; Osmundsen and Péron-Pinvidic, 2018; Chao, 2021; Muñoz-Barrera et al., 2020; Muñoz-Barrera et al., 2021) and numerical modelling (Chenin et al., 2018, 2019b, 2020; Petri et al., 2019). However, much less is known about the tectono-stratigraphic evolution and the fluid circulations linked to necking, which is due to the lack of natural analogues. Mohn et al. (2012) were among the first to describe a fossil example of a necking system exposed in the Grosina-Campo nappe in the Alpes in N-Italy. These authors showed that necking is linked with a transition from a distributed rift system with high-angle normal faults accommodating minor displacements, to the formation of low-angle, long offset extensional detachment faults forming the major bounding faults accommodating major displacement (Fig. VII.1A and B). This strain localisation is interpreted to occur when the strongest layer controlling the overall strength of the lithosphere yields, and subsequent deformation focus upon the future rupture zone. For a typical Western European lithosphere, composed of a brittle upper crust, a ductile middle crust and a mafic lower crust and a strong, thermally equilibrated mantle lithosphere (Petri et al., 2019; Mouthereau et al., 2021), crustal necking is interpreted to occur above the location where the mantle lithosphere yields, and appears to be achieved by two sets of conjugated master faults in the brittle upper and the lower crusts that are separated by a ductile middle crust (Mohn et al., 2012; Chenin et al., 2018, 2020). Frictional strain in the necking domain is short lived and occurs during crustal necking. The deformation along major basin bounding faults ceases while deformation migrates toward the more distal part of the margin (Fig. VII.1B; Petri et al., 2019). Overall, the necking phase appears to be short-lived (less than 8 Ma; Chenin et al., 2020), representing a transient state followed by subsequent deformation in the distal part of the margin. Necking is accompanied by a complex isostatic evolution, where initial short uplift is followed by fast subsidence of the whole future distal margin. This is manifested by deep marine sediments overlying shallow marine to subaerial early syn-rift sediments.

The architecture of these faults is variable and is controlled by the crustal rheology as well as the thermal, structural and compositional state inherited from the orogenic event pre-dating the rifting (Osmundsen and Péron-Pinvidic, 2018; Manatschal et al., 2021). The main detachment faults related to necking-flatten towards the surface-(e.g., rolling hinge model; Wernicke and Axen, 1988; Lavier and Buck, 2002) and form dome shape structure (Ribes et al., 2020). The exhumation of the footwall across such a downward concave fault is expected to generate a transition from an extensional (outer part of the hinge) to a compressional domain within the footwall (Fig. VII.1A) during exhumation at the seafloor (Sandiford et al., 2021).

The mechanical failure of the upper lithospheric mantle is associated to the rising of the asthenosphere that is at the origin of the increasing thermal gradient within the domain undergoing necking (Chenin et al., 2020). This leads to an increase of the temperature at the Moho by up to

100°C and to a diffusive thermal gradient that can be 60°C/km or higher in the central part of the rift during necking (Chenin et al., 2020). The necking domain corresponds to the juxtaposition of a hotter hanging wall block, also referred to as keystone (e.g., H-Block of Lavier and Manatschal, 2006) against a cooler crust in its footwall. As a consequence, necking zones do not only show the transient presence of a strong vertical, but also of a lateral thermal gradient. The associated isostatic rebound and thermal support leads to an uplift and subaerial exposure of the necking domain (Chenin et al. 2019).

In general terms, fluid circulations are triggered by high thermal and pressure gradients and the occurrence of brittle fault zones that, altogether favour the establishment of fluid circulations. Faults are indeed natural pathways as they generate an increase of permeability due to important fracturing and dilation during deformation (Sibson, 1990, 2000; Manatschal et al., 2000; Taillefer et al., 2017). Previous studies (KTB drilling; Müller et al., 1997) tend to show that the upper crust is saturated in fluids of various origins, which can be mobilized during tectonic events. Fluids can also derive from surface water (seawater/meteoric water) or have an internal origin due to dehydration/ devolatilization processes and degassing (Yardley and Bodnar, 2014).

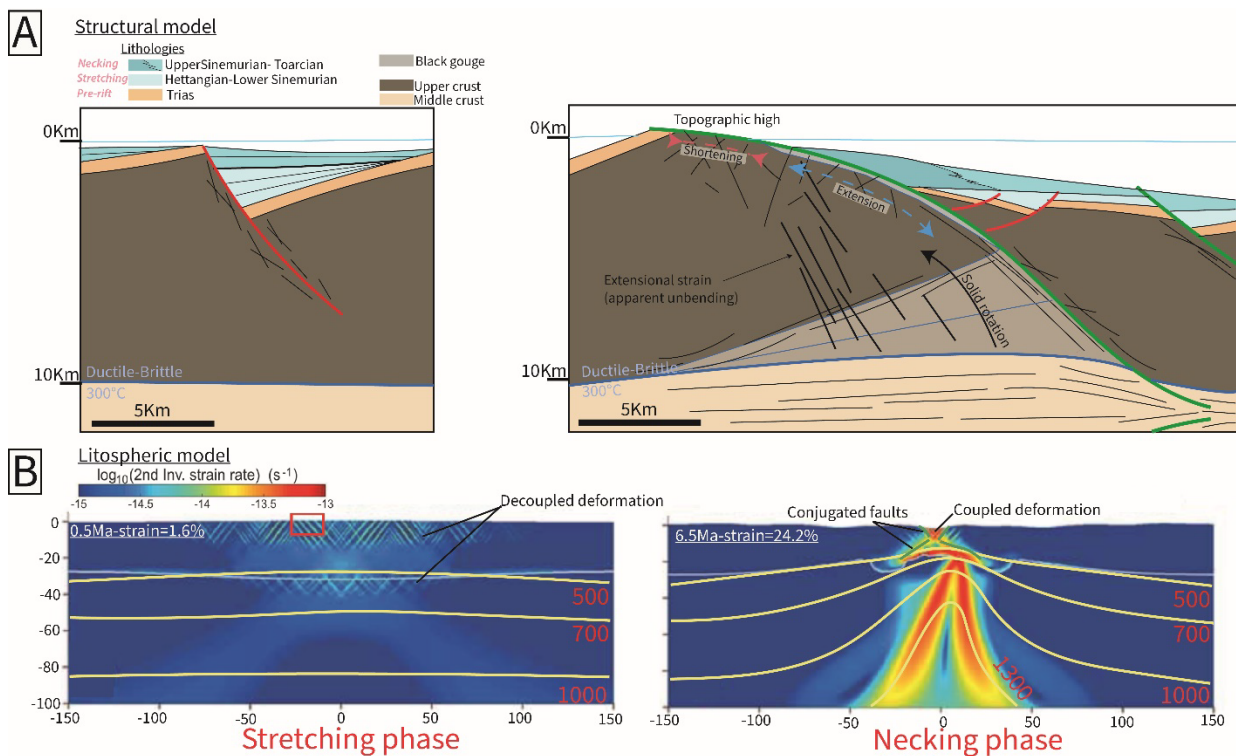


Figure VII.1: A- Structural model for the stretching phase and the necking phase. The stretching phase is associated to high angle normal fault bounding half grabens. The crustal necking is associated to large offset detachment faults leading to important topographic uplift. B- Numerical model showing the strain in the lithosphere during the stretching phase and the necking phase. The isotherms are also indicated showing increase of temperature during crustal necking (from (Chenin et al., 2020)).

2. The Case study of the External crystalline massifs

2.1. Preserved necking domain in the Mont-Blanc massif

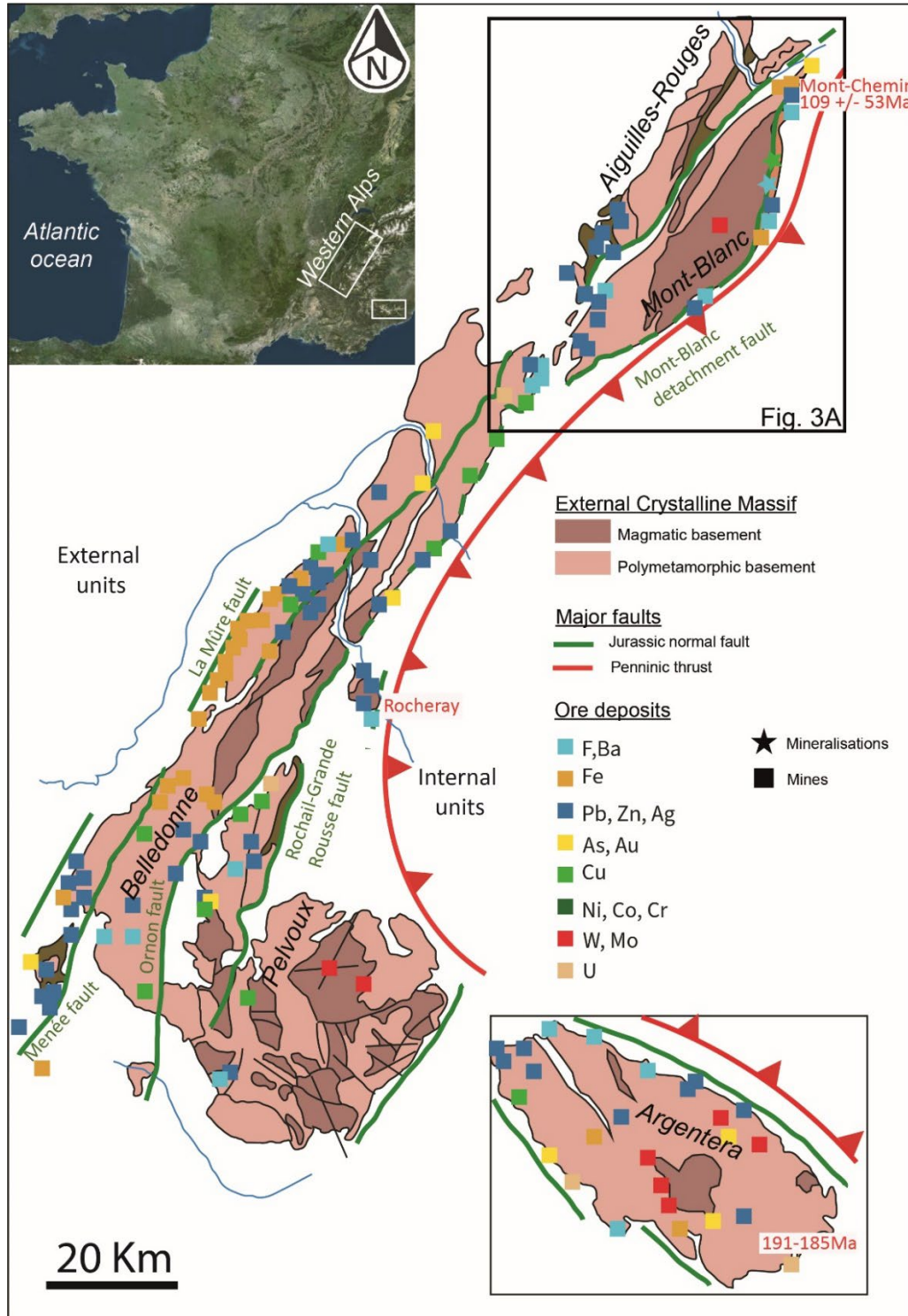


Figure VII.2: Map of the External Crystalline Massifs with location of the different mines indicated (based on BRGM, 1984; Ochoa Alencastre and Chenevoy, 1979; Sivade and Thibieroz, 1989; Nögler et al., 1995; Dorignaux, 2017). There is a clear alignment of the mines along the Jurassic faults (from Lemoine and Trümpy, 1987; Ribes et al., 2020; Dall'Asta et al., 2022). Some of these ore deposits were dated giving a pre alpine age. Uranium deposits in the Argentera Massif give a Late Sinemurian to Pliensbachian age coeval with crustal necking in the Alps (Geffroy et al., 1964).

The Mont-Blanc massif is part of the ECM in the Western Alps and is located at the transition between the highly metamorphosed internal domains (Penninic nappes) and the weakly metamorphosed external domains (Dauphinois nappes) of the Western Alps (Fig VII.2).

It was recognized as part of the former necking domain of the European Tethyan margin (Mohn et al., 2014) formed during Early to Middle Jurassic rifting (201 to 152 Ma; Ribes et al., 2019a). The preserved syn-necking cover corresponds to Pliensbachian to Aalenian conglomerates and sandstones (e.g., Grès Singuliers; Ribes et al., 2020). These sandstones seal locally a tectonized top basement formed of cataclasites and gouges (Dall’Asta et al., 2022). Thus, the absence of Triassic pre-rift sediments at the exception of allochthons in the internal Mont-Blanc is not due to erosion only, but the result of tectonic crustal exhumation during necking along extensional detachment faults (Ribes et al., 2020). Remnants of evaporites at the base of pre-rift extensional allochthons highlight the presence of salt and their importance as a decoupling level during extension (Epin and Manatschal, 2018).

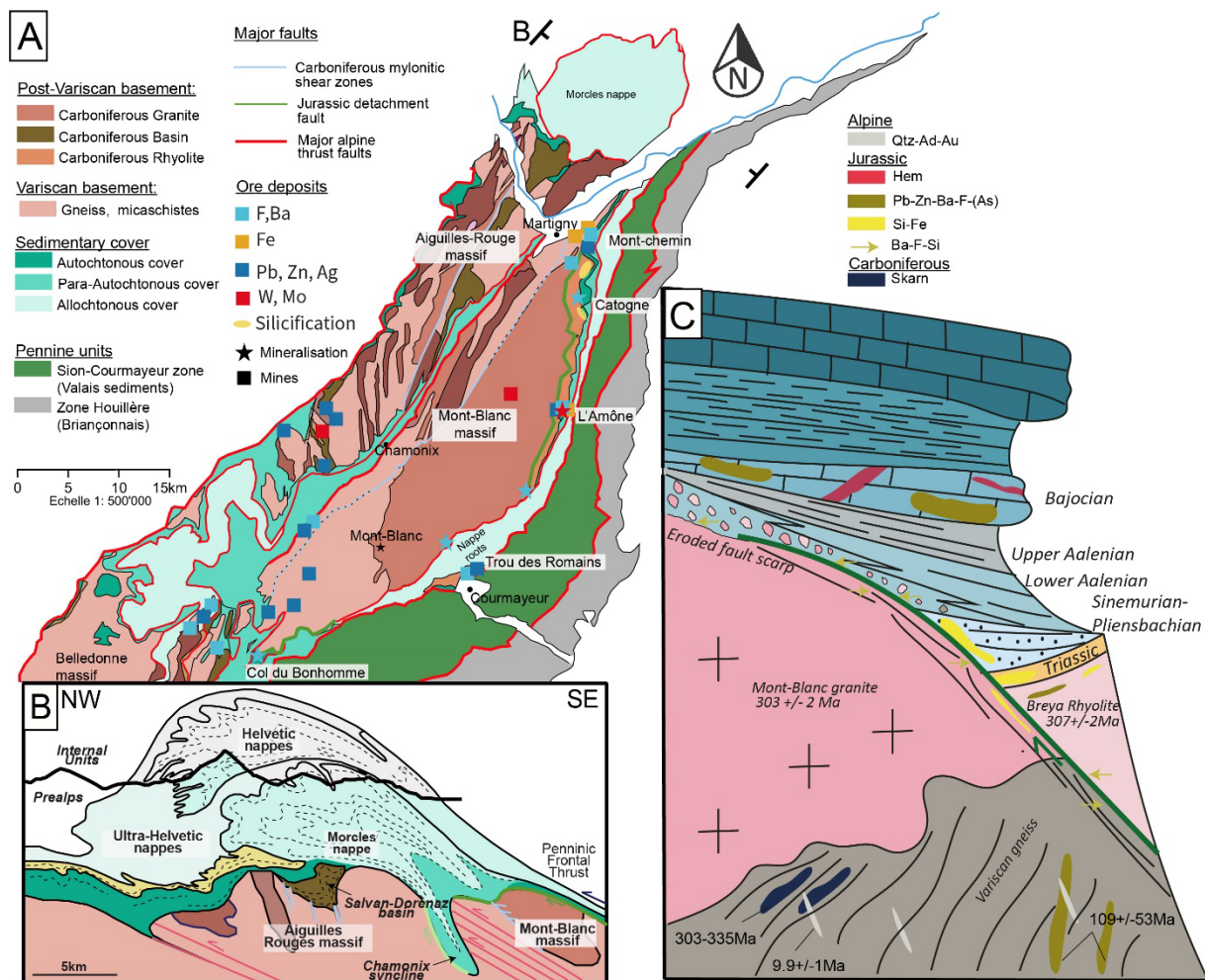


Figure VII.3: A- Map of the Mont-Blanc massif showing the different basement lithologies. Most of the cover around the Mont-Blanc is para-autochthonous or allochthonous detached above the Aalenian shales. However autochthonous cover is preserved in the internal Mont-Blanc massif. Mines are also indicated on the map (from Tagini, 1951; Chessex and Rivier

1957; Costa and Troilo, 2013; Dorignaux, 2017; Rys, 2020). B- Section of the Mont-Blanc and Aiguilles-Rouges massifs showing the relation between the Carboniferous shear zone, the Jurassic normal fault and the Alpine shear zone (modified from Escher et al., 1993). The Morcles basin correspond to the extruded cover of a half-graben. The Helvetic nappes corresponds to distal sediments thrust over the necking domain. C- Simplified section of the basement showing the relation between the Mont-Blanc detachment fault, the syn-rift to post-rift sediments and the different mineralisations. Qtz = quartz, Hem=Hematite, Ad=Adularia, Au = gold

2.2. Pre-Alpine mineralisations

Ore deposits along the ECM are preferentially localized along Jurassic rift structures such as high-angle normal faults (Ornon, Menée, La Mûre; Lemoine and Trümpy, 1987) and detachment fault linked to exhumation (Mont-Blanc detachment fault; Ribes et al., 2020; Dall'Asta et al., 2022). This indicates a major role of the tectonic basement-sediment interface for ore mineralizations (Fig. VII.2). Among the deposits recognized to pre-date Alpine orogeny, some have been referred to be related to Jurassic rift activity (e.g., Menée Fault (Lemoine et al., 1982), Rocheray (Sivade and Thibieroz, 1989)) and in some cases the mineralization could be dated at 191-185 Ma, i.e., to be linked to necking as is the case for U deposits in the Argentera massif (see Fig. VII.2; Geffroy et al., 1964).

In the internal Mont-Blanc massif ore deposits are common (Fig. VII.3A) and occur in the Trou des Romains (Costa and Troilo, 2013), l'Amône (Schmidt, 1902; Tagini, 1951), Mont-Chemin (Schmidt, 1920; Chessex and Rivier, 1957; Grasmück, 1961). They correspond to F-Ba-Zn-Pb mineralisations found all along the internal Mont-Blanc, either in the basement (Mine des Trappeur, Mont-Chemin; Chessex and Rivier, 1957) or in the Triassic to mid-Jurassic cover (l'Amône (Tagini, 1951), Catogne (Grasmück, 1961), Trou des Romains (Costa and Troilo, 2013)).

In the Mont-Blanc basement, they appear as meter-thick veins with the border composed of quartz, fluorite and baryte and the core composed of galena and fluorite (Mont-Chemin, Fig. VII.3A). The veins containing the ore deposits are sub-parallel to the Variscan foliation, suggesting a structural control. The fluorite in this area is generally whitish and highly affected by cataclastic deformation. It was dated at 109 ± 53 Ma (Sm-Nd; Nägler et al., 1995) and interpreted as post Variscan and pre Alpine with a partial Alpine reset. The mineralisations also affected the Triassic cover, when present, and the Mid-Jurassic carbonates (Fig. VII.3C). The basement-sediment interface is significantly mineralised with the notable presence of calcite and fluorite in the northern Mont-Blanc massif (l'Amône and Catogne). In l'Amône (Fig. VII.3A), the cement of the Jurassic sandstones corresponds to calcite, but fluorite was also described (Duparc and Pearce, 1898). Ore deposits are visible as lenses in the Aalenian shales and Bajocian limestones, sub-parallel to the stratification and composed of quartz, calcite, fluorite baryte with Pb-Zn-Fe sulphides and As sulfosalt (Rys, 2020). Massive silicification also affects mostly the early Liassic sediments (Grasmück, 1961), especially at the southern extremity of the Catogne area (Fig. VII.3A).

2.3. Fluid circulation along necking detachment faults

The access to a preserved detachment faults system in the Mont-Blanc massif allows to investigate conditions of fluid rock interaction and element transfer during crustal necking (Dall'Asta et al., in prep.). The main mineral reactions observed along the fault are the breakdown of biotite, albite and orthoclase, and the formation of chlorite and white micas, a process that increases in intensity from the damage zone toward the fault core (core zone). The latter corresponds to a gouge composed mostly of illite and clasts reworking the damage zone (Fig. VII.4A). It is characterized by the absence of biotite and chlorite, and remnants of albite and orthoclase. Feldspar breakdown was associated first to albitisation of orthoclase before complete sericitization of albite. This change from albitization to sericitization is likely related to a change of fluid composition, in particular through the release of K, and/or to a decrease of temperature during exhumation (Fig. VII.4B).

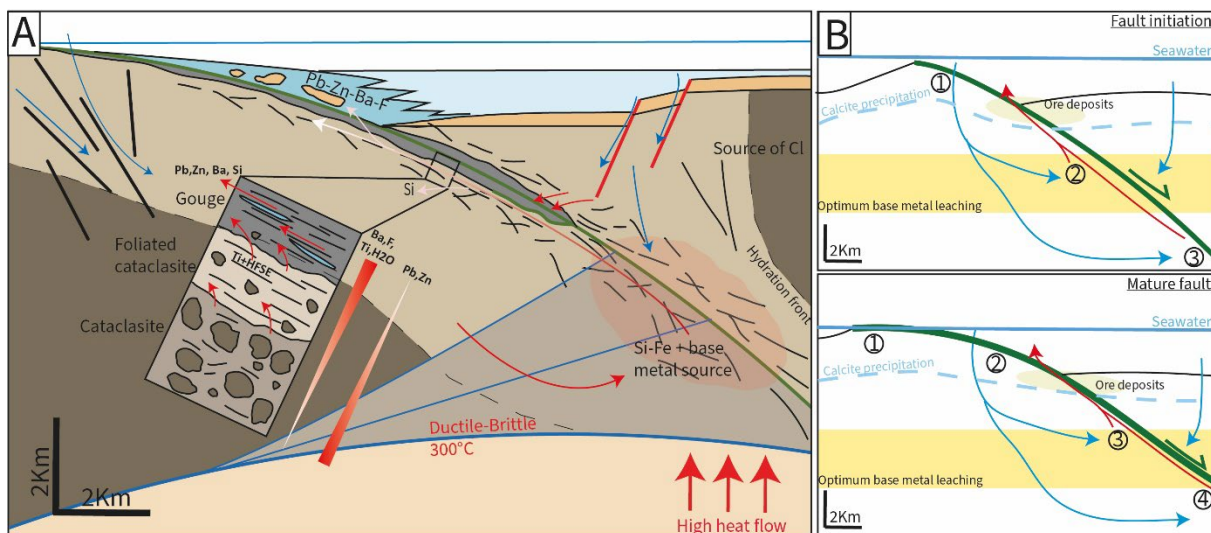


Figure VII.4: A- Sketch of a detachment fault with proposed fluid pathway indicated, based on observation from the Mont-Blanc massif. The downward path of the fluid occurs through crustal fractures in the footwall and faults in the hangingwall associated to calcite precipitation at temperature up to 150°C. The upward path is the detachment fault. Metals are leached from the basement at temperature around 250°C. B- Evolution of the detachment fault showing progressive exhumation. The optimum metal leaching area corresponds to temperatures of around 200 to 250°C. The footwall during exhumation passes from the metal leaching area to the zone of ore formation.

Fluid inclusions in quartz veins from the damage zone and the core zone give a minimum fluid entrapment temperature of 200°C for a salinity ranging from 5 to 20 wt% with an average of 10 wt% (Dall'Asta et al., soumis). The fluid composition is of the NaCl-H₂O type with minor content of K₂O. The fluid composition and temperature are similar to those observed in epithermal deposits (Wilkinson, 2001). Besides, chlorite thermometry gives a temperature of basement alteration of ca. 250°C (Fig. 3). The estimation of pH using Cl content in the K-Fsp-Mu-Ab-Qtz buffered system (Yardley, 2005) is around 5.7, which is near neutral at a temperature of ca. 250°C.

The deformation is associated to metasomatic reactions along the fault zone. External fluids are associated to biotite and feldspar breakdown, and the formation of chlorite and white micas

under temperature of ca. 250°C (Dall'Asta et al., in prep.). This is related to important release of Si, Na, Ca, Pb, Zn and gains of K, Fe, Ti, Mg, Ba, F, As, V and water in an open chemical system. Since the solubility of Si depends on the temperature (Stefánsson, 2001), late precipitation of quartz is interpreted to be achieved from cooling rising fluids. Significant mobility of Ba, F and Ti is also indicated by their significant enrichment in the core zone compared to the unaltered basement.

Trace elements show also important variations with important increase of As, Sb, Mo in the fault rocks, which highlight their strong mobility. A loss of Pb and Zn is visible in the core zone, correlated to feldspar breakdown. The mobility of trace elements is then controlled by the metasomatic alteration of feldspars and biotites. Overall, the mobile elements involved in the mineral reactions highlight a crustal signature.

2.4. Link between detachment fluid circulation and ore deposits

The timing and type of elements mobilised along the necking detachment fault raises the question of the link between the emplacement of ore deposits and the necking process. Detachment faulting led to exhumation of the footwall (basement) and therefore of the source of the metals enriched in the ore mineralisations. In the Mont-Blanc massif, sealing of this exhumed footwall by Pliensbachian sediments gives good temporal constraints on the minimum age of basement leaching, which is late Triassic to Lower Jurassic. The detachment faults may have provided pathways, and the necking process the necessary thermal gradient to trigger fluid flow and significant mobilization of elements in the crust.

Mobile elements along the detachment fault (Si, Fe, Ba, Pb, Zn, F, As, Sb) are similar to the elements enriched in the ore deposits and testify of a crustal signature as observed through the flat shale normalized REE pattern (Dall'asta et al., in prep.). More specifically, the decrease in Pb and Zn in the fault zone is correlated to their increase in the sedimentary cover as ore lenses. This highlights the likely link between element transfer along detachment faults and in the overlying cover. Such link strongly suggests that the fault may have acted as a conduit for the fluids up into the cover (Fig. VII.4A and B).

3. Discussion

3.1. Fluid migration in the basement and in the cover

One of the main questions related to hydrothermal systems is how fluids migrate downward (Gleeson et al., 2003; Cathles and Adams, 2005). Buoyancy-driven downward percolation of dense brines within the upper crust was advocated for different hydrothermal systems worldwide (Munoz et al., 1999). However, permeable pathways are necessary for deep fluid penetration (McCaig, 1988; Magri et al., 2010). Geoffroy and Dorbath (2008) showed that percolation of fluid is facilitated by

brittle fracturing and dilation associated with fault systems (Sandiford et al., 2021). This was also advocated for intracontinental hydrothermal systems (e.g, Aquitanian basin; Boiron et al., 2002). During crustal necking, deformation related to exhumation of crustal rocks through the hinge of downward concave detachment faults creates fractures and dilatation likely favouring significant fluid penetration. Pathways for fluids may also be created along high-angle faults within the hanging wall of such detachment faults (Fig. VII.5A).

The large-scale Mont Blanc detachment fault (Fig. 5) may have provided a fluid pathway toward the surface and connected reservoirs with various fluid pressures to the surface (Sibson, 2019). Along this necking related detachment fault, fluid flow was discontinuous as documented by different generations of veins in the fault rocks. It is likely that the core zone played the role of an impermeable barrier. Important silicification as observed along the fault progressively sealed the fault, disabling further fluid flow due to decrease in permeability (Dall'Asta et al., 2022). In such cases, high permeability can be maintained only during fault activity (e.g., dynamic permeability) when new fractures and dilatation occurs (Curewitz and Karson, 1997, Cox, 2005).

The mechanism of fluid circulation in the cover are different and related to stratigraphic architecture of the basin such as variation of sediment thickness and the occurrence of impermeable barriers such as black shales. In the case of the necking domain of the Mont-Blanc area, following the necking phase, fluids from the deeper distal part of the margin can move back(up)wards along the basement/cover contact into the necking domain. The thick black shales deposited in the hyperextended domain probably acted as an impermeable barrier. The fluid was likely to circulate along the basement-cover interface driven by pressure gradient toward topographic highs (i.e., Boiron et al., 2010), which may explain the occurrence of mineralisations along this interface. These types of circulation highlight the role of seal cover, which might drive the fluid toward the continent (Boiron et al., 2010; Rodríguez et al., 2021). Therefore, ore deposits in the necking domain might not be restricted, temporally, to the time of crustal necking but may also postdate necking, driven by the overall tectono-stratigraphic architecture of the margin.

3.2. Fluid composition and metal leaching

Progressive heating of downward convecting seawater is associated to precipitation of calcite, celadonite, anhydrite and chlorite for temperature as low as 20°C (Weinzierl et al., 2018). Precipitation of these phases would modify the initial fluid composition and might lead to fracture sealing by mineral precipitation if no new fractures form to enable further fluid percolation (Hedenquist and Henley, 1985)

A key question for element mobility is the location and nature of the metal source (Groves et al., 2022). The ore deposits in the Mont-Blanc massif include elements with crustal affinity, which

cannot be derived solely from seawater. Fluid rock interactions during fault activity led to biotite and feldspar breakdown, which released major and trace elements that were in part leached by the fluid, at temperature of ca. 250°C (Dallasta et al., in prep.). This temperature is consistent with that of metal leaching obtained from other areas with Pb-Zn mineralisations (Leach et al., 2005). The high thermal gradient reached during crustal necking may allow important metal extraction from the crust, under relatively shallow depth (ca. 5 km for a gradient of 50°C/km; Figs. 4 and 5A). The upper crust is compositionally heterogeneous, with variable potential to act as a source for elements. Magmatic rocks can be responsible for the enrichment of some elements (Ba, Pb, Zn, U, REE) due to magmatic fractionation leading to geochemical inheritance, which is followed by remobilisation during rifting as observed for U deposits (Cathelineau et al., 1990). As an example, the Mont Blanc granite is enriched in REE and Pb, Zn, Ba, U as well as Ca compared the host rocks. These higher concentrations might be an explanation for the localisation of the Pb-Zn ore deposits close to the Mont-Blanc granite. Element transfer from the basement to the cover might therefore be a long term, and sometimes polyphase process, which for the Mont-Blanc example may have taken at least 120 Myr between a first concentration through magmatic fractionation during Variscan times and subsequent hydrothermal remobilisation of various elements during Jurassic rifting.

The mobility of elements in the fluids is controlled by various state parameters, such as temperature and pressure as well as pH-Eh conditions and the presence of ligands especially necessary for Pb-Zn mobility, such as Cl that will form soluble complexes with metals under a wide range of conditions (Cathelineau et al., 2021). Fluids along the detachment faults show moderate salinity, providing the Cl that favoured Pb and Zn solubility. This fluid was likely derived from seawater or basinal brines with moderate salinity. The presence of pre-rift evaporites around the Mont-Blanc massif could also have provided high salinity brines into the basement. However, some elements, which appear relatively mobile (HFSE-Ti), are more prompt to form complexes with -OH and -F, the latter being strongly enriched in the Mont-Blanc detachment fault. As the main source of F could not be seawater (ca. 1 ppm of F; Stumm and Morgan, 2012), this element may have been provided through fluid-rock interaction by F-apatite leaching (disappearance of apatite in the core zone of the detachment). For transport of significant amount of metals such as Pb and Zn, the absence of sulphur and/or oxidising conditions are required throughout the circulation of the fluids in the cover (Leach et al., 2005; Emsbo, 2009; McCuaig et al., 2018). The presence of Fe-oxides along the Mont-Blanc detachment fault tend to show unfavourable conditions for precipitation of massive sulphides and therefore metal transport along the fault. Metal solubility decreases with decreasing temperature, and increases with decreasing pressure (Hemley and Hunt, 1992). These two effects tend to compensate each other which enable large-scale transport of these elements from the crust

to the cover (Hemley and Hunt, 1992). Besides, these authors postulated that the upward metal transport along faults may occur in a near adiabatic way.

The last point concerns the source of the sulphurs necessary for sulphides formation. The sulphur might be derived from mixing with surface-derived fluids such as seawater or brines, or from bacterial reduction of sulphate in the organic rich shales deposited during subsidence of the necking domain (Beales, 1975, Emsbo, 2009).

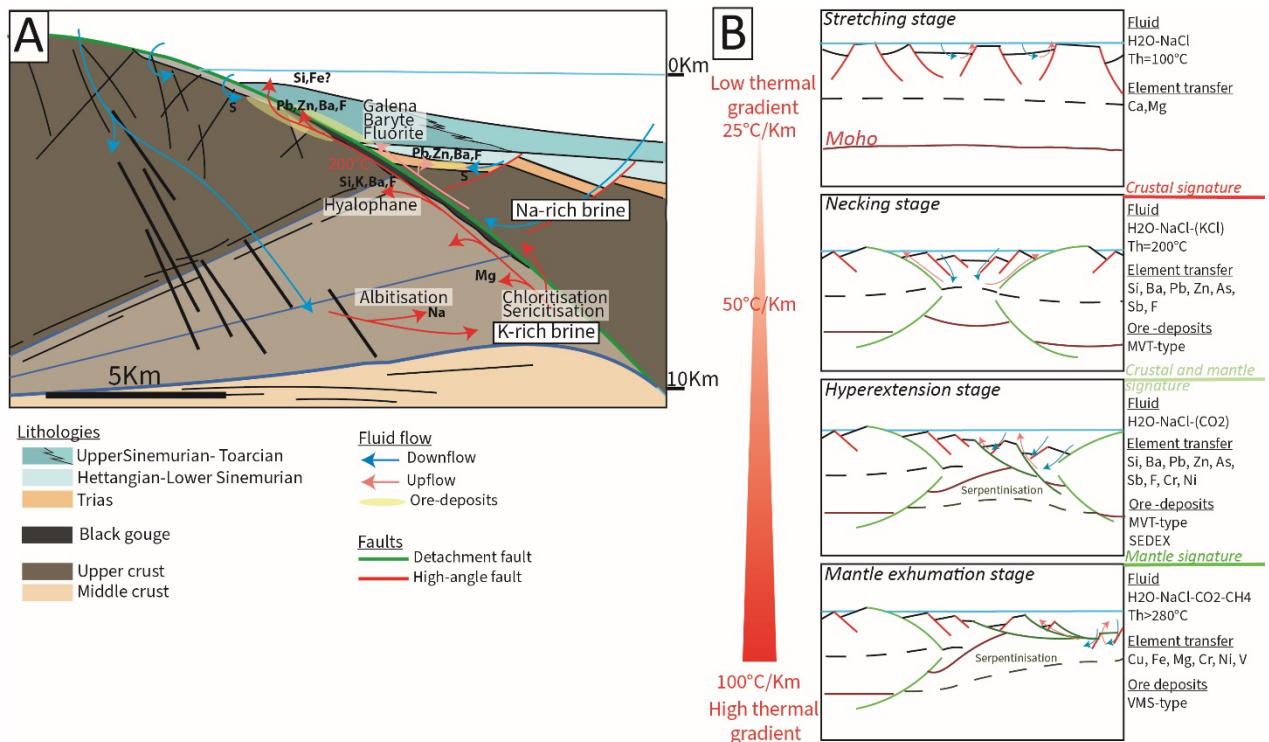


Figure VII.5: A- Fluid circulation and element transfer associated to crustal necking based on the example of the Mont-Blanc. At higher temperature, albitisation occurs followed by sericitization and chloritization. Metal-rich brines move upward along the fault leading to formation of ore deposits in the cover. The core zone (gouge) is acting as an impermeable barrier. B- Evolution of the hydrothermal system and fluid signature during rifting. Stretching phase from Hips et al., 2016; Chenin et al., 2020; Barale et al., 2021. The data for the necking stage are from Incerpi et al., 2017; Chenin et al., 2020 and Dall'Asta et al. in prep. The data for the hyperextended stage are from Manatschal et al., 2000; Lescoutre et al., (2019), Saspiturry et al., 2020. Data from the exhumation stage are from Pinto et al., 2015; Quesnel et al., 2019; Coltat et al., 2019, 2021; Nteme Mukonzo et al., 2021.

3.3. Predictability of ore deposition in the necking domain

The concept of mineral systems (McCuaig and Hronsky, 2014) enables to take into account the tectonic, stratigraphic and thermal evolution as well as the nature of the source, and the properties of the fluid to better understand the effective mineralizing process (Fig. VII.5B).

Deposition of metals is a process in which the metal bearing fluid is discharged from its metallic content due to change in physico-chemical conditions during fluid rock interactions (Anderson, 1975; Leach et al., 2005). Two types of deposits are found in the Mont-Blanc massif and its surrounding area, which highlight different processes of deposition (basement-hosted and sediment hosted deposits). The first type are the mineralisations found in the basement. They were

likely triggered by precipitation in a cooling fluid, possibly by mixing with cold surface water, as observed for Pb-Zn basement-hosted deposits in the Rhine graben (Fusswinkel et al., 2013) or in the Parisian basin (Lenoir, 2022). Similar processes might have occurred in the Mont-Blanc responsible for precipitation of fluorine associated with REE-rich Pb-Zn sulphides.

The second type are sediment-hosted mineralisations (MVT and SEDEX deposits). In the Mont-Blanc massif, deposition of Pb-Zn sulphides, iron-oxides with various baryte and fluorine contents occurred mostly in carbonates (Grasmück, 1961; Rys, 2020). It was postulated that these mineralisations were emplaced through carbonate replacement due to hot brine circulation (Rys, 2020). They show affinities with carbonate-hosted deposits such as MVT, except for iron minerals (pyrite / magnetite; Rys, 2020). Ore deposition was likely favoured by pH-buffering of the fluids by carbonate dissolution and sulphide precipitation (Liu et al., 2017). Therefore, the presence of carbonate platforms appears as an important factor for the emplacement of syn-rift MVT-type deposits in this segment of the margin (Leach et al., 2005). It is expected that the topographic uplift associated to detachment faults can locally favour shallow marine conditions necessary for the platforms to develop.

However in the distal part of the basin, when metal-bearing fluids reach seafloor syn-sedimentary stratiform deposits form in response to mixing with cold seawater through active fault reaching seafloor (Sangster, 2018). Depending on the redox state of the water controlled by the H_2S/O_2 buffer (Emsbo, 2009), sulphides similar to SEDEX-type deposits or oxides can form. In the Western Alps, anoxic conditions are observed in the distal margins associated to restricted basins (Ribes et al., 2019c) and possibly in the necking domain in relation to black shales deposits. Oxide deposits (Fe-Mn) are also observed in the European distal margin (Pfeifer et al., 1988).

Preservation of the necking domain was variable along strike during Alpine reactivation. Studies in the fossil Cretaceous Pyrenean-Biscay hyperextended basins show preservation of the necking domain at the extremities of the rift segments (Lescoutre and Manatschal, 2020; Cadenas et al., 2021) when different basins overlap leading to thrust shortcut (Lescoutre and Manatschal, 2020b) and passive transport of relatively undeformed remnants of the margin. This enables to predict the area of the margin preserved in the collisional orogen. Besides, in fossil-rifted margins, the former necking domain is submitted to metamorphism, which will have an impact on pre-orogenic deposits and must be considered in the mineral system. In the Mont-Blanc massif, the rifted margin was submitted to low greenschist to greenschist facies while further north, in the Aar-Gotthard massif the metamorphism can reach 600°C. At lower temperature such as in the Mont-Blanc massif, the deposits are affected by cataclastic deformation and recrystallisation as well as partial isotopic reset at least for fluorine (Nägler et al., 1995), while in the Aar massif, pre Alpine ore deposits are affected

by partial sulphide melting at ca. 520°C (Hofmann and Knill, 1996; Frost et al., 2002) leading to the concentration of Tl, As and Sb in the sulphidic melt and subsequently in sulphosalt.

Conclusion

Crustal necking is a major event during rifting both in terms of tectonic and fluid evolution. It appears as a suitable environment for significant fluid circulations. Fossil analogues such as the Mont-Blanc example provides strong clues for significant hydrothermal circulation during necking. Large detachment faults act as a conduit connecting different geochemical reservoirs to the surface leading to significant metal leaching and transport to the surface. The fluids are finally responsible for ore deposition in the cover. This attempt to link tectonic, structural, and sedimentological data to fluid circulation raises many questions concerning the downward fluid path. Much remains to be done in order to confirm the results and compare with other fossil necking domains. One of the final questions requiring a larger corpus of fossil analogues concerns the size of the ore deposits. Is crustal necking able to generate giant ore deposits?

Chapter VIII- Discussion, perspectives, and conclusions



View of the Mont-Blanc massif (Val Veny, Italy)

« Dieu dort dans le minéral, rêve dans le végétal, s'éveille dans l'animal, pense et aime dans l'homme. » (Père Monié)

Foreword

This last chapter will discuss the different aspects of the Mont-Blanc fossil necking domain described in this manuscript. The first part will synthesise the different results obtained and will discuss what could be done to further constrain the lateral extent of the Mont-Blanc detachment fault and the fluid circulation along the Mont-Blanc detachment fault.

The second part will discuss the characteristics of the necking domain based on field observation and present-day necking domain. More specifically, the fault geometry, the kinematic and the stratigraphic signature of crustal necking are discussed. An important point concerning the distinction between an unconformity and a tectonized top basement is raised.

The third part concerns the reactivation of the necking and its preservation during subsequent collision. The impact of the mechanical stratigraphy is discussed using the example of the Helvetic nappes. Different types of reactivations associated to different types of fault geometry as observed along the ECM are also detailed. Finally, the evolution of the necking domain during progressive shortening is described using the example of the Belledonne, Mont-Blanc and Aar massif, which experienced different amounts of shortening.

The fourth part concerns the fluid circulations recorded during crustal necking. The behaviour of the different ore deposits during a Wilson cycle is described here using the example of post-Variscan, Jurassic and Alpine deposits. Finally, the necking mineral system is described. More specifically, a compilation of possible necking related deposits in fossil margins worldwide is provided highlighting the possible importance of crustal necking for ore deposits.

1. Recognition of the Mont-Blanc detachment fault

1.1. Southern Mont-Blanc massif

1.1.1. Recognition of the detachment fault

The existence of a detachment fault was first proposed by Ribes et al., (2020) in the Col du Bonhomme area in relation with syn-rift sandstones. The careful examination of this contact revealed that it corresponds to a tectonized top basement sealed by Jurassic sediment. This tectonized top basement is made of cataclasites to foliate cataclasites with locale preservation of fault gouges. The first sedimentary deposits overlaing the tectonized basement corresponds to bioclastic crinoid-rich mud filling cracks in the basement and overlaid by the Grès Singuliers. The age of the crinoid-rich sediments is, compared to the other dated crinoid-deposits supposed to be Late Sinemurian which represents a minimum age for the tectonic surface. This portion of the fault remained under water and was probably not emerged to the surface.

The recognition of the detachment fault is, however, not simple. First of all, detachment faults are usually extremely heterogeneous (Smith et al., 2007; Collettini, 2011). The fault core, as observed on other detachment faults, appears extremely heterogeneous as well, and composed of foliated cataclasite and lenses of gouge, which are not continuous. These detachment faults can also be cross-cut by syn-to post-tectonic high-angle normal faults (Smith et al., (2007), Webber et al., (2022)), which may have been the case in the Mont-Blanc. Moreover, the preservation of detachment surfaces is complex, and they are easily reactivated by later compressional phases. The exhumation above sealevel also leads to its reworking and erosion, which might erase part of the structural record. As observed on oceanic core complexes, the detachment is partially covered by sediments and rubbles and the fault rocks are preserved only locally (Escartín et al., 2017). It is therefore expected that the detachment fault is only preserved locally in the Mont-Blanc area.

1.1.2. Fluid circulation along the fault

The fluid has been studied using chemical maps, mass balance calculations and fluid inclusion analysis. Mass transfer appears controlled mostly by the biotite and feldspar breakdown leading to gain in K, Fe, Ti, Mg, Ba, F, As, V and loss in Si, Na, Ca, Pb, and Zn. The fluid corresponds to H₂O-NaCl (-K₂O) brines with a salinity of 7 to 9 wt% equiv. NaCl and homogenization temperatures between 170 and 200°C. No other data constraining the temperature of formation of quartz are available. The temperature associated to fluid alteration is given by chlorite. This temperature up to 250°C might represent the maximum temperature reached by the fluid along the fault. The depth of entrapment is therefore estimated at a maximum of 5 to 7 Km. The other possible method to constrain the

temperature of quartz formation such as Ti in quartz (Wark and Watson, 2006) cannot be used for temperatures below 400°C.

Isotopic analysis such as $\delta^2\text{H}$ and $\delta^{18}\text{O}$ on white micas were avoided because of the possible re-equilibration of the isotopic signatures under lower greenschist conditions. Oxygen isotopic signature is preserved at lower temperature ca. 250°C in Alpine opicalcite as proposed by Coltat et al. (2019) and further discussed in Coltat et al. (2021). However, the highest temperature reached in the Mont-Blanc and the fine-grained nature of the white mica led to more doubt concerning the preservation of the pre-Alpine signal. However, $\delta^{18}\text{O}$ on the quartz veins could be considered in a future study.

The occurrence of graphite in the cataclasite is not really understood. The temperature of ca. 450°C, which are higher than the Alpine peak in this area, is puzzling. In analogy to other graphite deposit in cataclasite and based on some observations, it is proposed that this graphite precipitated from cooling of a carbon-saturated fluid in response to frictional heating or frictional melting. Beside, graphitization of gouge is a common process along fault zones (Kuo et al., 2014), where it is usually associated to coseismic slip and shear heating. The source of carbon is not well understood either. To better constrain the origin of this graphite further work is needed. First, $\delta^{13}\text{C}$ isotopic analysis can provide better constrains on the origin of the graphite. Second, RSCM data acquired across the graphite plane can also help to better constrain the temperature evolution throughout these planes following the same method than Moris-Muttoni et al., (2022).

1.1.3. The problem of dating a pre-Alpine detachment in the Mont-Blanc massif

The dating of the detachment fault is based on the relation between the fault and the cover. Indeed, the occurrence of deformation between the basement and the pre-rift cover and the upper Sinemurian sealing of the fault gives a Liassic age to the fault. The occurrence of Sinemurian-Pliensbachian syn-rift sandstones as a response to basement uplift further constrain this age. However, geochronological dating did not match this “stratigraphic” age. Indeed, U-Pb ages have been tentatively obtained on calcite minerals (see Chapter IV and Appendix D). Calcite likely formed through recrystallisation of Triassic evaporites gave an age of 120 ± 37 Ma, which must be considered cautiously given its very low U and Pb contents. Dating of calcite cement in tectonic breccias along the detachment fault gave a more reliable, but poorly precise age of 48.3 ± 21 Ma. These ages do not correspond to any major tectonic event. It has been postulated that a thermal event occurred in the Valais basin at ca. 109 Ma as observed through zircon overgrowth (Beltrando et al., 2007a) and based on RSCM data on the cover (Célini et al., 2022). The second age corresponds to the Alpine stage. This age predates by ca. 15 Ma the thrusting of the internal domain over the Mont-Blanc (Cardello et al.,

2019). Therefore, is it unclear whether this age corresponds to a specific tectonic event or if it corresponds to a partial reset of the U-Pb in calcite during peak metamorphism.

Ar-Ar dating on hyalophanes from the gouge veins provided an age of about 24 Ma (23.68 ± 0.96 Ma and 24.48 ± 1.1 Ma). This age is consistent with the peak metamorphism observed in the Mont-Blanc. However, it is in contradiction with some observations made in this area. The Qtz-Hy veins crosscut the gouge foliation but are also reworked in the gouge, suggesting a syn-gouge age. In fact, similar vein clasts have been observed in the syn-rift sandstones as clasts. Modelling of Ar diffusion for Jurassic feldspar with a size of $200 \mu\text{m}$ (which is the size of the fraction dated) indicates that total reset is expected for pre-Alpine minerals. These results tend to favour the pre-Alpine origin of the hyalophane. However, it is not possible to conclude definitively yet. The age obtained during the final heating stage of 197 Ma might point toward a pre-Alpine age for these hyalophanes. A way to go further would be to date detrital feldspars (including adularia / hyalophane) from the Pliensbachian sandstones (which are obviously older than the Pliensbachian) and see what age is obtained.

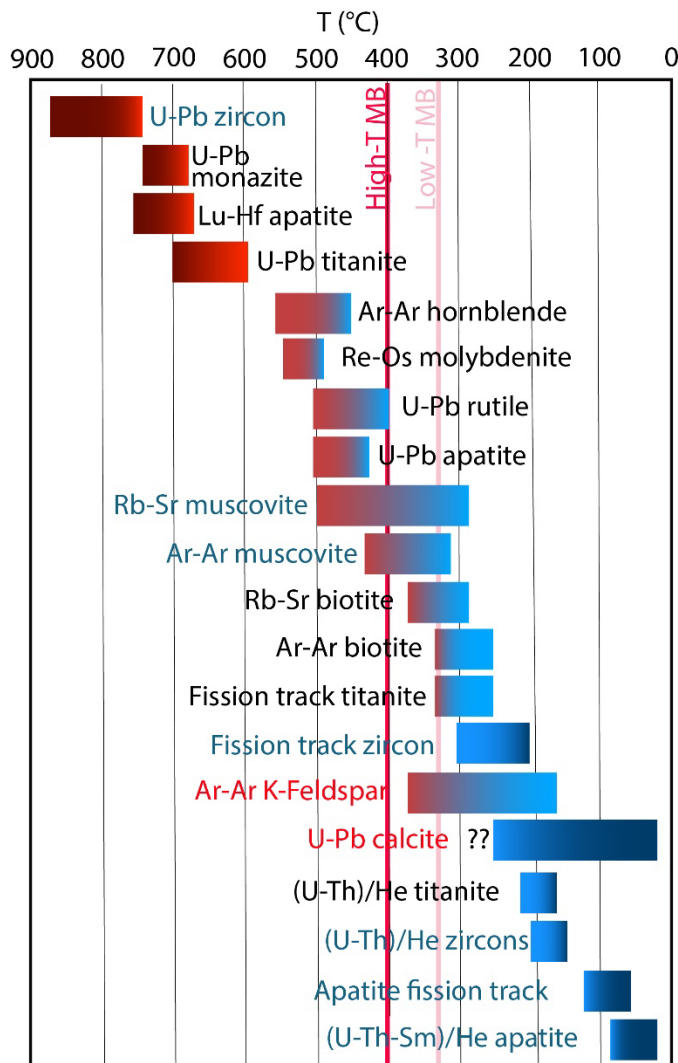


Figure VIII.1: Temperature sensitivity of different thermochronological systems (modified from Doepke, 2017). The lowest and highest Alpine temperature recorded in the Mont-Blanc are indicated (High-T MB and Low-T MB). The method written in

Discussion, perspectives, and conclusions

red correspond to dating realised in the Col du Bonhomme and presented here. The method written in blue correspond to methods used in the Mont-Blanc (U-Pb on zircon (Bussy et al., 2001), Rb-Sr on muscovite (Leutwein et al., 1970), Ar-Ar on muscovite (Leloup et al., 2005 and Rolland et al., 2008), Fission track on zircon (Glotzbach et al., 2008), ZHe (Boutoux et al., 2016), AHe (Glotzbach et al., 2008 and Boutoux et al., 2016)).

Dating of pre-Alpine low-temperature event in the Alps seems complex due to partial to total reset of most of the geochronological and thermochronological systems (Fig. VIII.1) during Alpine metamorphism. However, some approaches, which were not tested yet, remain such as U-Pb on titanite and apatite as well as U-Pb on rutile. The main problem is the size of these syn-kinematic phases, which are very small (< 10 µm usually) in the studied samples, and therefore not suitable for dating.

1.2. Northern Mont-Blanc

1.2.1. Recognition of detachment fault

Both tectonized top basement and fault located between the granite and rhyolite have been recognized. In the outcrops of tectonized top basement, clasts of cataclastic rhyolite have been observed indicating that the deformation was pre-Alpine. However, no gouge could be recognized. In addition, this basement is also overprinted by late Alpine brittle deformation. In the outcrops showing the contact between the granite and rhyolite, the contact is composed of mylonites passing to cataclasites and gouges forming the core zone. In the hanging wall formed by the rhyolite, only cataclasite was recognized. This fault is, however, undated. The syn-rift architecture in this area unravels a more complex rift-related evolution than the southern part. The occurrence of Aalenian conglomerates over the basement indicates a lower Aalenian uplift of the area, post-dating the deposition of the Sinemurian-Pliensbachian syn-rift sandstones.

It is proposed that the rhyolite formed an allochthonous block soled by detachment faults. The basal fault would correspond to the main fault observed at the contact between the granite and the rhyolite, while the upper fault would correspond to a fault crosscutting the rhyolite. This secondary fault would be a minor fault, which did not accommodate the major displacement. Actually, this fault would have been partially eroded during lower Aalenian. This interpretation tries to reconcile the complex sedimentary evolution and the structural observations made along the Val Ferret. However, this preliminary work should be backed up by more observations. The structure of the Val Ferret with the steeply dipping sedimentary cover makes the contact extremely hard to follow along strike.

1.2.2. Geochemical characterization

The content in major elements of the Mont-Blanc magmatic rocks is relatively homogeneous which is also the case of REE. The only main difference is related to the high content of HREE in the Mont-Blanc granite. These rock shows variability in the trace element content especially for Pb, Zn which are enriched in the rhyolite. Sc, Cr, Ni, V and As show a strong variability in the composition

between the samples. The variability of Th and U have been noticed by Bussy, (1990) and associated to syn-to post-magmatic remobilisation of these elements by fluids. In general term, it is relatively hard to assess if this variability is controlled by magmatic processes or later fluid remobilisation.

The fault zones are characterized by a significant decrease of Na and gain of K associated to feldspar alteration. The trace and REE compositions are variable but an increase of HREE can be observed in the gouge and cataclasite samples.

Despite the amount information known at this moment, more work should be carried out on in this area. The first one corresponds to further dating of the contacts. Based on observations from the southern part of the massif, and due to the higher thermal peak in this part of the massif, geochronology should focus on U-Pb on apatite and rutile. On the other hand, dating of epidote can also be realised. These age determinations should focus on the coarse-grained and fine-grained epidote to see if these two types of epidotes yield the same age, or if they provide different ages as observed in the Aar massif (Peverelli et al., 2022). Moreover, further characterisation of the mineral composition using the same approach than in the southern Mont-Blanc should be realised to better understand the chemical evolution during alteration and deformation.

2. Tectono-sedimentary evolution of the necking domain

2.1. Structural evolution of the necking domain

2.1.1. Architecture of detachment faults related to crustal necking

Crustal necking is a transient state related to localisation of the deformation in response to upper lithosphere rupture (Chenin et al., 2019b). During necking, an important amount of strain is accommodated by few faults, resulting in the exhumation of deep levels of the basement and significant crustal thinning. Different fault geometries according to the pre-rift rheology are expected. In any cases fault rotation is expected in response to fault unroofing and increased thermal support. In theory, weak crust will show strong decoupling between the upper and lower crust and is related to the formation of Core Complex-type structures (Osmundsen and Péron-Pinvidic, 2018) defined as an arched exhumed fault (Whitney et al., 2013). The denomination Metamorphic Core Complex (MCC) is restricted to core complexes leading to the exhumation of high-grade rocks from the middle to lower crust, which is not always the case for necking domains. These core complexes have been described in present-day margins such as the Norwegian margin (e.g., Gossa High; Osmundsen and Ebbing, 2008; Osmundsen and Péron-Pinvidic, 2018), the Angola margin (Unternehr et al., 2010), the Bay of Biscay margin (Jammes et al., 2010; Cadenas et al., 2021), and the South Australian margin (Ribes et al., 2020).

One of the striking features is the presence of a pre-rift cover above the exhumed basement. They represent parts of the hanging wall cover detached from the underlying basement. The main explanation for these sedimentary allochthons is the presence of evaporitic cover acting as a decollement level. Thick evaporites can lead to complete decoupling of the supra salt cover and the basement until the evaporite layer is completely delaminated above the detachment.

2.1.2. Petrographical and thermal evolution of the detachment fault

In the Col du Bonhomme, the exhumed basement corresponds to a complex tectonic surface formed by the exhumed core zone of the fault and the damage zone in its footwall. The damage zone was formed due to temperatures around 250°C under brittle conditions with significant strain softening associated to phyllosilicate formation. Localization of the deformation in the core zone at shallower depth led to the formation of a black gouge. They are characterized by important grain comminution and high phyllosilicate content, mostly white micas. The lack of plastic deformation (e.g., mylonites) observed around the Mont-Blanc might be explained by the portion of exhumed upper crustal basement.

The detachment in the northern part of the massif shows some differences from the Col du Bonhomme. Indeed, mylonites in the footwall have been clearly identified in the Breya fault zone. These mylonites are reworked in the core zone. The core zone is composed of white micas, epidote and chlorite giving a greenish colour to the gouge at microscale. These differences of composition are probably related to the difference of composition of the host rock enriched in Fe, Mg, Ca compared to the gneiss from the Col du Bonhomme. This might indeed explain the occurrence of chlorite and epidotes.

Other example of detachment faults and necking detachment faults exists in the Alps, especially in the Central Alps. In the fossil necking domain of the northern Adria margin, remnants of the exhumed detachment fault are observed (Campo-Grosina detachment fault; Mohn et al., 2012). It is composed of a tectonized top basement overlaid by allochthonous pre-rift cover. This tectonized top basement is formed by cataclasite and gouges. Minor mylonites are also visible reworked in the gouge. Moreover, the brittle-ductile transition formed under greenschist conditions (e.g., Eita shear zone; Mohn et al., 2012) have been exhumed in response to the Campo-Grosina detachment fault. This example is the only other example of a necking detachment fault in the Alps.

Detachment faults associated to hyperextension and mantle exhumation have been studied in detail in the Central Alps (Manatschal, 1999). These fault zones are composed of green cataclasites in the damage zone and black indurated gouge in the core zone. Green cataclasites are formed during fluid assisted deformation related to saussuritization of feldspars under temperature below 300°C

(Manatschal, 1999). The gouge is composed of white micas, chlorite neo-formed albite and fine-grained quartz. The main mechanism of deformation in the gouges appears to be frictional viscous flow leading to the formation of S-C microstructures (Manatschal, 1999). The induration of the gouge appears pre-Alpine as shown by reworking of the gouge in the sediments (Masini et al., 2011). This is associated to Si-rich fluids leading to quartz precipitation.

2.1.3. Kinematic evolution

The Mont Blanc detachment fault shows progressive rotation of the stretching direction along strike. In the Val Ferret, the few stretching lineations preserved are NW-SE while toward the south, the stretching lineations are N-S. This rotation is interpreted to be related to the presence of a transfer zone associated to a linkage of faults between the proximal and necking domains. The detachment fault is also crosscut by high-angle normal faults with 2 different directions, parallel and perpendicular to the detachment strike direction. These faults crosscut the basement and the pre-rift allochthons, and therefore appear to be a post-kinematic relative to the detachment fault (e.g., Webber et al., 2022). Moreover, some of these faults might be syn-Aalenian. It is also interesting to note that the N-S directed sediment transport (Ribes et al., 2020; Dall'Asta, 2019) at the base of the Grès Singuliers is parallel to the stretching direction, which might indicate a link between sediment transport and deformation possibly through the formation of basement corrugations (as observed in the Gulf of California by Bot et al., (2016).

Present-day margins provide insights of what could have been the Mont-Blanc necking domain. Necking detachment faults appear to change direction along strike where it progressively passes into a high-angle normal fault rooting in the proximal domain (Osmundsen and Péron-Pinvidic, 2018). Secondary normal faults cross-cutting the largest faults are also observed with various orientations (Muñoz-Barrera et al., 2020), similarly to what is observed in the Mont-Blanc. Necking domains present a complexity that is not observed in oceanic core complexes, where for instance stretching remains parallel along strike and the strike axis of the detachment is parallel to the ridge axis (Escartín et al., 2017). Transfer zones are also not observed in oceanic core complexes. These differences reflect a fundamental difference between necking detachments and oceanic core complexes. In necking domains, part of the answer come from the fact that basin segmentation starts during crustal necking with the formation of transfer zones mostly through reactivation of inherited structures (Nirrengarten et al., 2018). The difference of extension rates in the basin are accommodated by diffuse transfer zones leading to complex fault geometries along strike. These transfer zones can be accommodated by strike slip faults or by continuous fault depending on the offset between the two fault segments. On the contrary, during formation of an oceanic core complex, the transfer zones are well localized on transform faults and the extension rates remain

roughly constant between the transfer faults leading to parallel stretching direction between to transfer zones (e.g., Mid Atlantic ridge; Escartín et al., 2008).

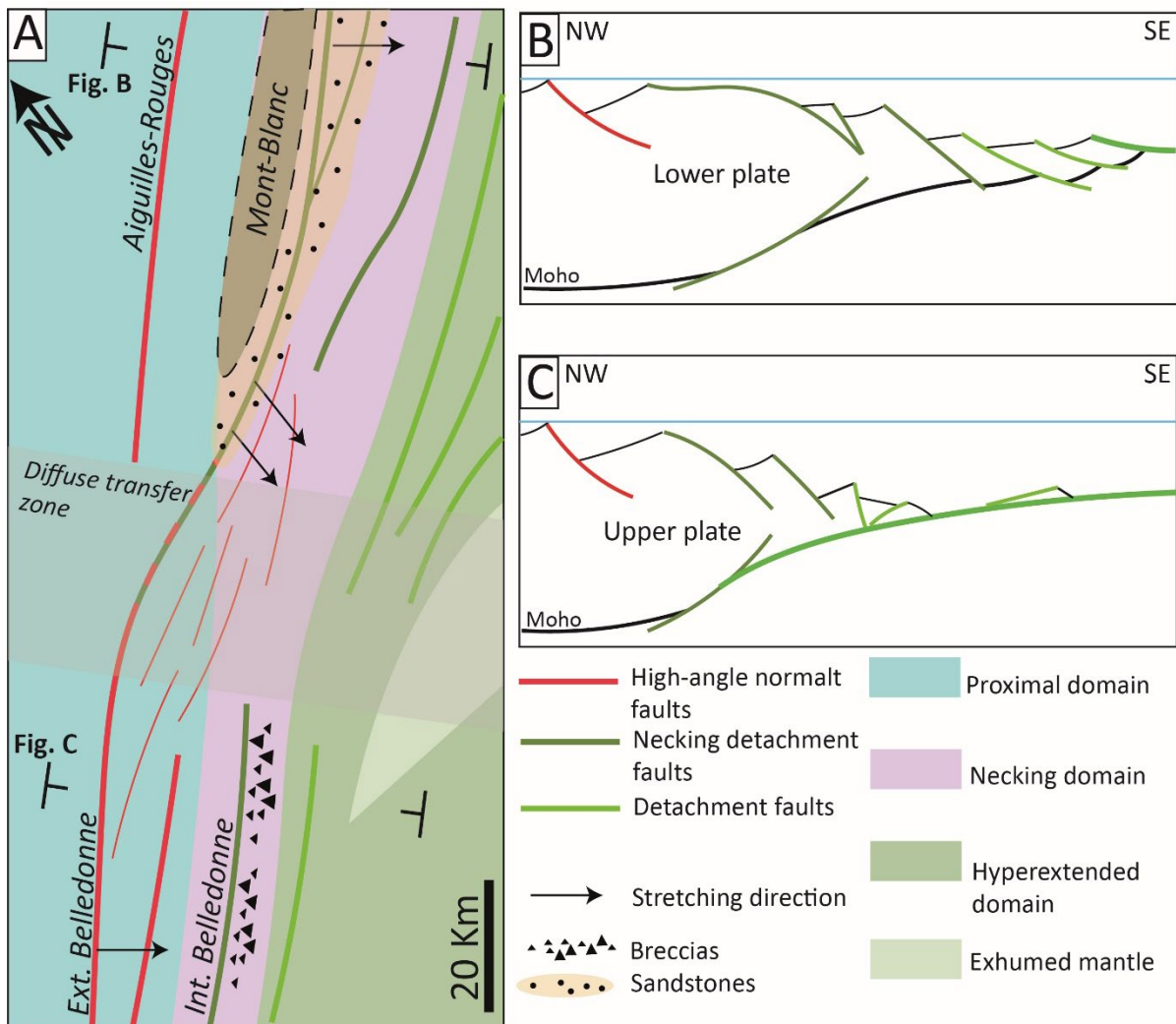


Figure VIII.2: A- Model for the Mont-Blanc Belledonne transfer zone showing switch in the rift polarity between the upper and lower plates. B- Section of the lower plate in the Mont-Blanc massif. C- Section of the upper plate in the Belledonne massif.

It was proposed that the Mont-Blanc/Belledonne transition corresponds to a diffuse transfer zone which would explain the change of kinematics in the Southern Mont-Blanc massif (Fig. VIII.2A; Ribes et al., 2019a). This would also explain the change of margin architecture between the internal Mont-Blanc detachment fault with the characteristic Grès Singuliers syn-rift deposits, and the internal Belledonne mega-fault scarp with the Moûtier syn-rift breccias as emphasized by Ribes et al., 2019a. This change may be explained by a change of margin polarity with the Mont-Blanc forming part of the lower plate and the Belledonne part of the upper plate (Fig. VIII.2A and B). The localisation of the transfer zone in this area might be related to the presence of inherited Variscan structures such as the Pormenaz Carboniferous basin (Epard, 1990). Moreover, there is a change in the nature of the basement between the Mont-Blanc massif composed of migmatite and Variscan gneiss intruded by the granite and the Belledonne massif composed mostly of micaschists (Von

Raumer et al., 1993). This might highlight the role of compositional and structural inheritance in partitioning of the deformation.

2.1.4. Stratigraphic signature of necking

Crustal necking is related to significant topographic uplift associated to a characteristic stratigraphic response. Syn-necking deposits are characterized by three main features:

- A basal unconformity between the basement/pre-rift and the syn-rift deposits. This unconformity has different origins. 1- It can be an erosional unconformity as observed between the Grès Singuliers and the pre-rift cover. This erosion can be sub-aerial or basal erosion related to high energy flows (Fig. VIII.3A); 2- The unconformity can be related to a tectonic surface. This is the case for the contact between the basement and the Grès Singuliers (Fig. VIII.3B); 3- The unconformity can be a combination of tectonics and erosion (Fig. VIII.3C).
- The presence of clastic deposits highlighting the presence of a topographic high (Fig. VIII.3D). These deposits are usually shallow marine to continental at the base and marine at the top. The dispersion of the sediments is achieved through density flow across the basin axis and tidal currents along the basin.
- A transgression above the syn-rift deposits marking the onset thermal subsidence in the necking domain and the initiation of the hyperextension stage located in the future distal domain (Fig. VIII.3D).

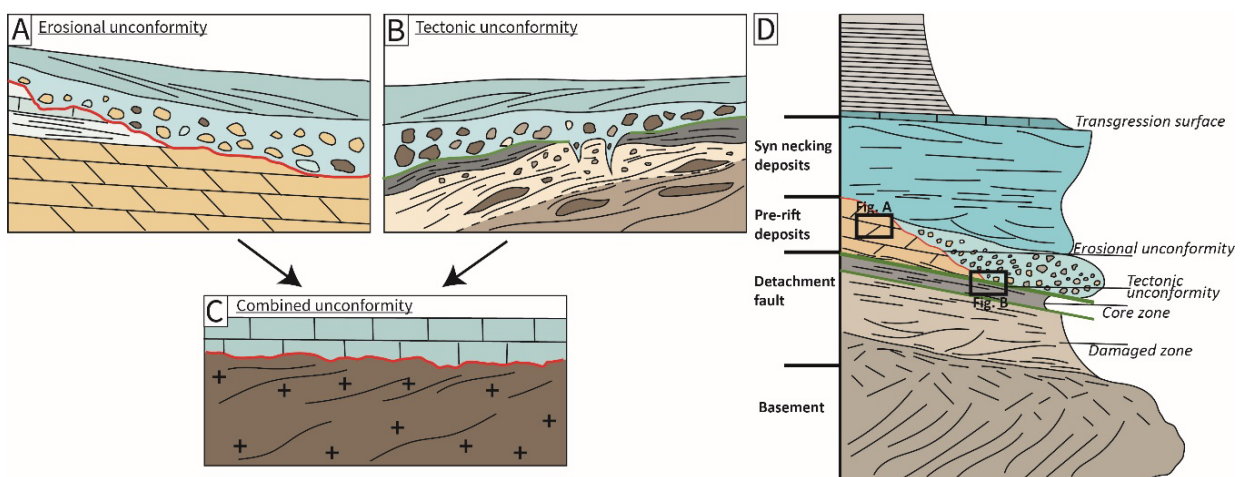


Figure VIII.3: A- Erosional unconformity with the pre-rift truncated and overlaid by syn-rift deposits. B- Tectonic unconformity showing an exhumed fault plane sealed by syn-rift sediments. C- Exhumed detachment fault affected by strong erosion erasing most of the fault remnants. D- Section of the contact between the syn-rift sandstones and the exhumed basement

Discussion, perspectives, and conclusions

This corresponds to the stratigraphic signature of crustal necking as defined in the Western Alps. This stratigraphic signature is also observed in the southern Adria margin (Gozzano–Inverio–Arona) where Pliensbachian to Toarcian clastic sediments are also present, coeval to detachment activity (Beltrando et al., 2015, Decarlis et al., 2017a). They are deposited above karstified pre-rift sediments marking a sub-aerial exposure corresponding to the necking unconformity.

This signature is particularly visible in the Alpine Tethys because the margin is disconnected from any continental sources. The closest continental source corresponds to the Massif Central and the Bohemian massif (Thierry, 2000). The sedimentation is only carbonated which makes the Upper Sinemurian-Pliensbachian sandstones only more striking.

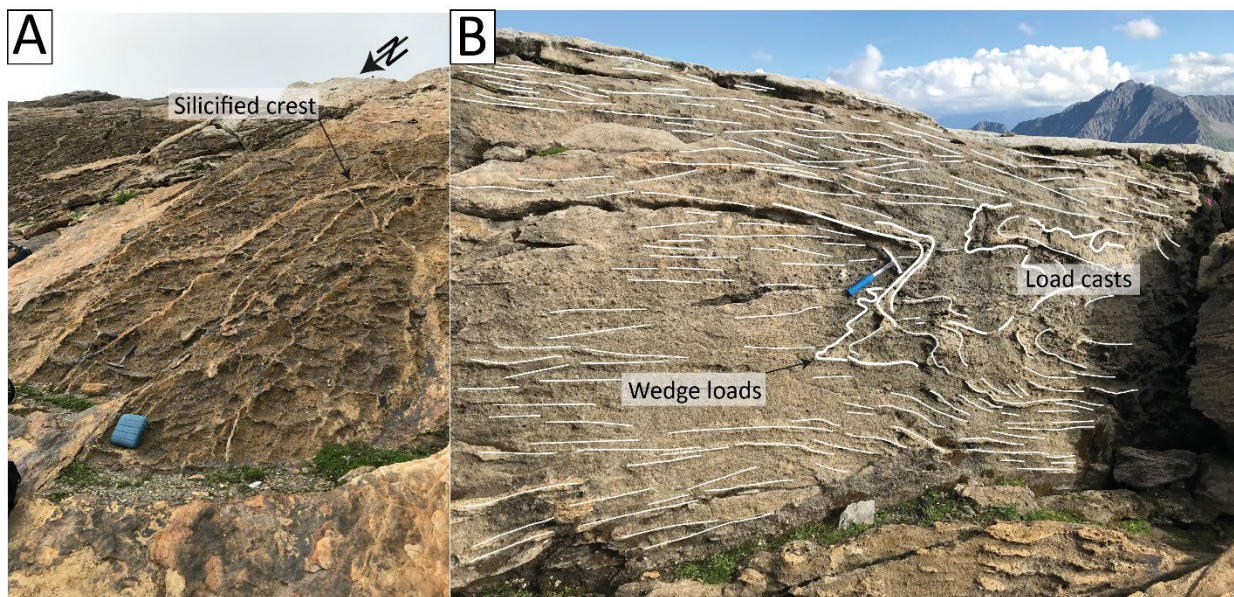


Figure VIII.4: A- Top view of the beds showing silicified wedge load forming a polygonal network of crests. B- Cross section of the beds showing load casts and soft-sediment deformation structures such as folds.

The last important feature is the occurrence of seismite deposits as observed in the Grès Singuliers (Ribes et al., 2020). Sub-horizontal view of the beds shows the presence of silicified crests forming a polygonal network (Fig. VIII.4A) with a preferential N-S direction. These crests are interpreted as cracks or wedge loads filled by silicified sediments preserving this peculiar morphology. Cross section of the seismite beds show the presence of soft-sediment deformation structure such as load casts and folds (Fig. VIII.4B). These structures are formed due to liquefaction of the sediments as response to an earthquake. The different morphologies are due to various fluid content in the sediments. Wedge loads are formed under low fluid content while load casts are formed under higher fluid content (Wizevich et al., 2016; Shanmugam, 2016). This is a sedimentary record of the tectonic activity in the area during Pliensbachian. The occurrence of load casts might also be the occurrence of earthquake with a $M_w > 4.5$ and possibly up to 7 (Atkinson et al., 1984; Rodríguez-Pascua et al., 2000; van Loon et al., 2016) associated to fault with a length of minimum 2-3 km (Zoback and Gorelick, 2012).

2.2. Recognition of necking detachment faults

2.2.1. Fossil rifted margins

The recognition of these type of tectonic unconformities is the key for recognizing and characterizing detachment faults related to necking. The age of the first sediment gives a minimum age of exhumation. However, the exhumed detachment fault is usually overprinted by erosion and therefore, the remnants of the detachment fault are erased. However, misinterpretation of the detachment fault as a simple erosion surface can lead to large underestimation of the amount of basement exhumation. Additionally, the amount of crustal thinning and extension during rifting can be also largely underestimated changing the overall tectonic interpretation of the studied area.

2.2.2. Present-day rifted margins

Detachment faults are sub-horizontal and overlaid by the sedimentary cover which on seismic section is hard to distinguish from a non-tectonic top basement. The shallower part of the detachment fault might be eroded which can lead to misinterpretation of the total offset of the fault. Few key observations can, however, suggest the presence of a detachment fault or of an eroded fault scarp.

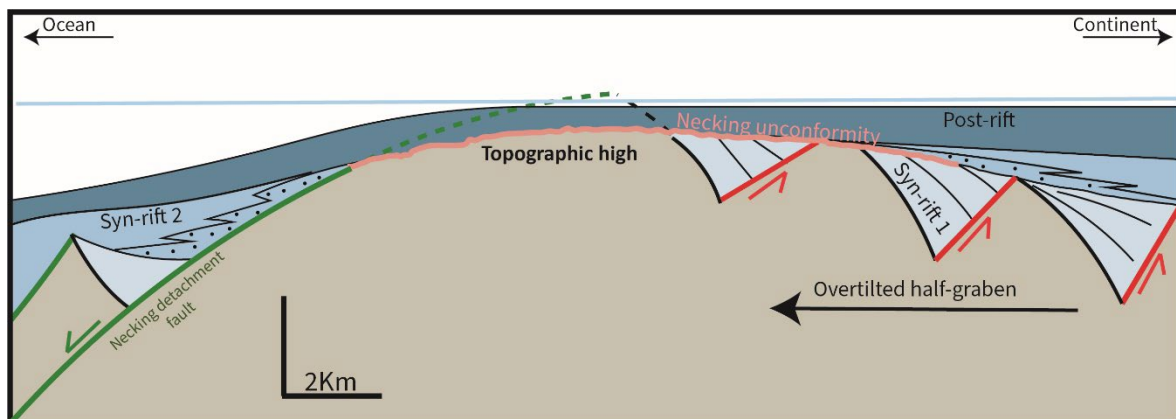


Figure VIII.5: Schematic view of the necking domain showing the truncated necking detachment fault associated to over tilted basins.

The presence of overtilted basins surrounding a topography can be an indication of the presence a large-scale detachment fault resulting in basement uplift (Fig. VIII.5). These overtilted basins are affected by a large-scale erosion level corresponding to the necking unconformity.

3. Preservation of the necking domain in orogens

3.1. Alpine overprint on the pre-Alpine structures

3.1.1. The importance of the mechanical stratigraphy

The architecture of the sedimentary cover exerts a strong control on the nappe geometry. Indeed, the position of the decollement level controls the position of the flat and ramp of the thrusts. Also, the ratio (n) of mechanically weak to strong layers controls the style of deformation. Low ratio leads to harmonic folding while high ratio lead to disharmonic folding and thrusting (Pfiffner, 1993). The main decollement level in the Helvetic domain corresponds to the Triassic evaporitic layer and the Middle Jurassic corresponding to Aalenian shales and Bajocian schists (Pfiffner, 1993).

The Dauphinois facies in the Morcles basin led to a low n ratio and the formation of polyharmonic folds (Ramsay, 1981). However, the Helvetic nappes are characterized by disharmonic folds (Ramsay, 1981) associated to a higher n ratio (Pfiffner, 1993). As mentioned before, the Aalenian shale cover is not continuous across the Mont-Blanc massif. The termination of the Aalenian shale led to the impossibility of thrusts to propagate across the Mont-Blanc along the same level. Therefore, the thrust had to propagate along ramps in the upper Jurassic and Cretaceous cover (Fig. VIII.5). In addition, the base of the nappe is detached from the basement over evaporites mostly as observed in the Ultrahelvetic nappe (Trümpy, 1951).

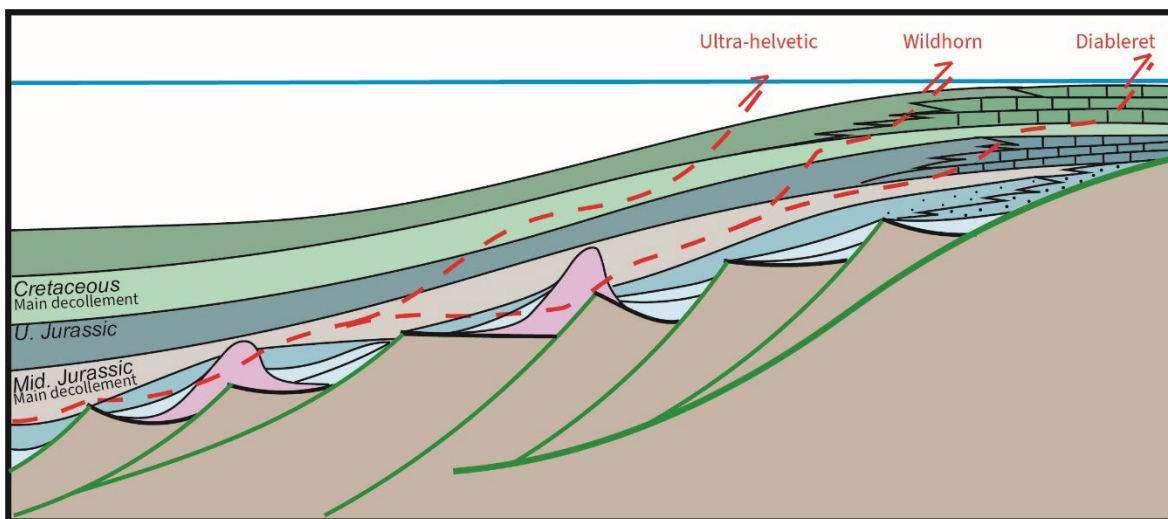


Figure VIII.6: Impact of the mechanical stratigraphy on the nappe geometry. Thinning of the Aalenian shales toward the Mont-Blanc led to the formation of a ramp in the Upper Jurassic.

Since the Sinemurian, the Mont-Blanc is separating two different basins with different subsidence histories. Indeed, the north western side of the Mont-Blanc corresponds to the Morcles basin which remained a mud-dominated half-graben basin throughout all the rift history, while the south eastern part of the Mont-Blanc corresponds to the distal rift margin with a relatively thick

cover associated to important subsidence (Fig. VIII.6). The architecture of the sedimentary cover explains the first order geometry of the nappes around the Mont-Blanc massif.

3.1.1.1. Impact of Alpine deformation on the detachment fault

Inversion corresponds to the closure of a rift basin. It is achieved through fault reactivation in contraction if the fault is favourably orientated. If the fault is not well oriented, inversion occurs through footwall deformation with short-cut faults or back rotation of the fault (Bonini et al., 2012).

3.1.1.2. Impact of the obliquity on the preservation

The presence of a transfer zone has an impact on the margin inversion and controls the preservation of rift segments (Lescoutre and Manatschal, 2020b). This might be the case of the southern Mont-Blanc and northern Belledonne massif (Fig. VIII.7). The shortening seems to be accommodated in the transfer zone by small thrusts oblique to the main thrust with a strong strike-slip component (Joye, 1989). They form nappe imbrications as observed in the area between the Mont-Blanc and the Belledonne (Fig. VIII. 7A). These nappes may correspond to the inversion of small half-grabens (e.g., Sallestet syncline; Epard, 1990) oblique to the main extension direction (Butler, 1985) as a result of the transfer zone. As well, following this interpretation part of the shortening is accommodated by a strike-slip fault system. The propagation of the deformation toward the continent leads to shortcuts in the transfer zone. Meanwhile, reactivation of the transfer zone leads to strong Alpine overprint, the basins bounding the faults appears relatively well preserved. Thrust shortcuts lead to passive transport of the rift fault on the thrust nappe preserving pre-alpine contacts.

3.1.1.3. Half-Graben inversion

Closure of half-graben basins is responsible for the extrusion of the syn-rift cover as observed in the Morcles basin (Kiss et al., 2020) and in the Bourg d'Oisan basin of the Western Alps. Bellahsen et al., (2012) proposed that shear zones in the hanging wall are responsible for shortening of the basin with the high-angle normal faults forming a buttress responsible for the cover extrusion. The cover is characterized by the formation of poly-harmonic folds and development of important foliation parallel to the normal fault (Fig. VIII.6B).

3.1.1.4. Basin Inversion by short-cut faults

Short-cuts of normal faults allow preservation of a portion of the pre-Alpine contacts transported passively above the thrust. These geometries appear ideal for preservation of detachment faults even on strongly deformed area such as the Mont-Blanc (Fig. VIII.7C).

In the Col du Bonhomme area, the detachment fault is folded and transported passively on a thrust nappe. No signs of reactivation of the basement/ sediment interface are observed, all the

kinematic markers on the detachment faults pointing to a different direction from the Alpine direction. The Alpine deformation is clearly accommodated in the top of the syn-rift cover close to the base of the Helvetic nappe. However, overprint of the detachment by Alpine deformation can be observed with foliation crosscutting the detachment and the base of the sedimentary cover at the base of the Helvetic nappes. This occurs when the decoupling level and the syn-rift cover is too thin to accommodate all the Alpine deformation related to thrust emplacement.

3.1.1.5. Basin inversion by fault rotation and reactivation

As mentioned before (Chapter V, 5.3), the Mont-Blanc back thrust might correspond to the Mont-Blanc detachment fault overprinted by an Alpine thrust (Butler, 1985, Ribes et al., 2020). In this case, the detachment was overturned during Mont-Blanc exhumation and crosscut by sub-vertical Alpine shear zones (Fig. VIII.7D). The formation of the mylonites may have been controlled by the inherited cataclastic fabric (e.g., Guermani and Pennacchioni, 1998). This would provide an example of reactivation of the detachment fault during Alpine deformation.

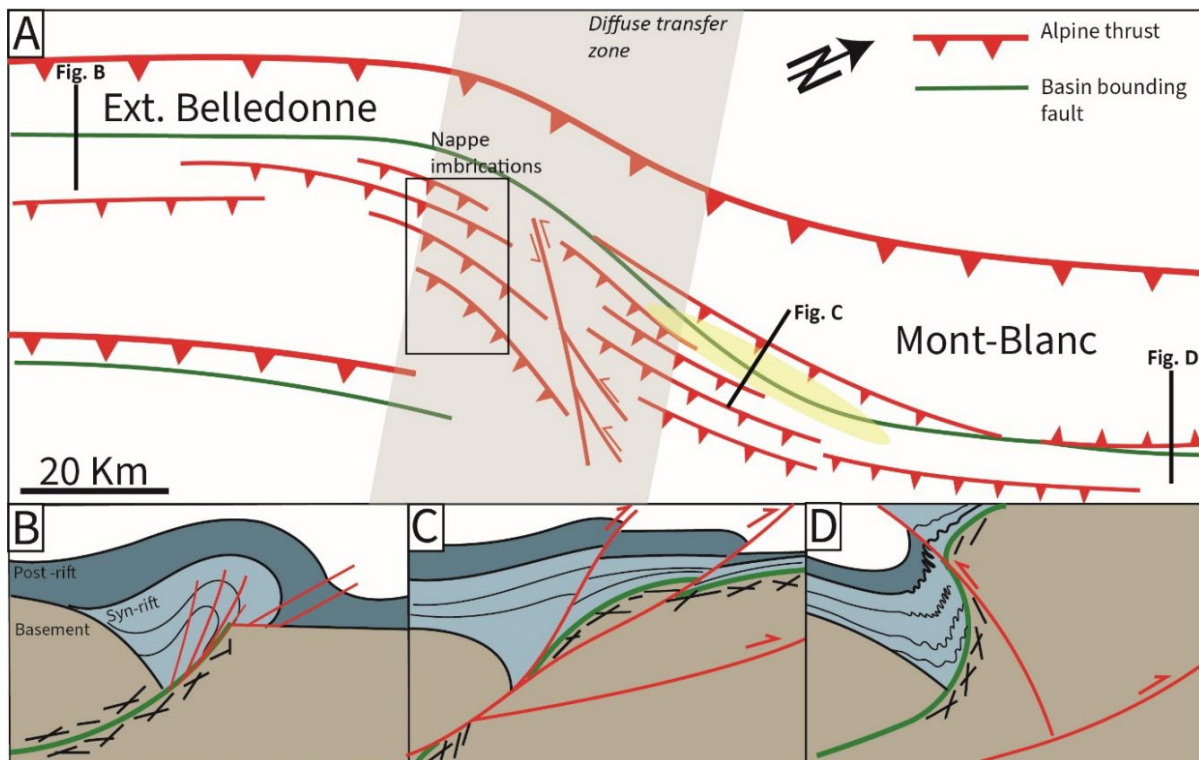


Figure VIII.7: A- Map showing the geometry of the main thrusts associated to the reactivation of the transfer zone (based on Gourlay, 1982 and Epard, 1990). B- Cross section showing the inversion of a half-graben basin with the extrusion of the sedimentary cover. C- inversion of the detachment fault in the transfer zone with shortcuts leading to the preservation of the pre-Alpine contacts. D- Overturned detachment fault crosscut by back thrust leading to overprint of the pre-Alpine contact (modified from Grocott and McCaffrey, 2017).

3.2. Thermal imprint on the detachment fault

The temperature increase in the collisional prism is due to tectonic burial but also to local anomalies along shear zones (Maino et al., 2015; Decarlis et al., 2017b). The high temperatures along shear zones are due to shear heating associated to fluid flow and are spatially restricted to the fault.

In the Mont-Blanc massif, an important burial gradient of 60°C/Ma is observed, indicating fast burial of the massif under the internal nappes during the Oligocene (Boutoux et al., 2016). Lower greenschist conditions were reached during Alpine thermal peak. This raises the question of the preservation of the low temperature pre-Alpine fabric under these conditions. It appeared that it affects mostly the low temperature clay minerals in the core zone and calcite in the cover and in the fault. White micas were affected by recrystallization and progressive transformation into muscovite, while calcite was affected by significant twinning and recrystallization.

This thermal imprint is also responsible for large argon release from the K-rich phase such as white micas and feldspars leading to age reset during prograde path (Ballentine et al., 1994). The ages recorded correspond to the cooling of the massif below the closure temperature of 200 to 250°C for white micas and feldspars. Besides, partial recrystallization of the clay in the core zone may have led to isotopic reset of stable isotopes such as oxygen or hydrogen.

3.3. Evolution of the necking domain during collision

3.3.1. Decoupling levels

Rifted margin inversion will re-use decoupling levels inherited from the rifting phase, and which would correspond to:

- The exhumed mantle domain formed by low friction serpentinised mantle (Lescoutre and Manatschal, 2020b; Auzemery et al., 2022);
- The ductile middle crust in the proximal domain decoupling the upper and lower crust (Miró et al., 2021; Manatschal et al., 2021);
- Decollement levels in the cover corresponding to evaporites remnants or thick shale deposits controlled by the architecture of the margin (Ducoux et al., 2021)

The exhumed mantle domain and the proximal domain are characterized by decollement levels which are not observed in the brittle hyperextended domain (Manatschal et al., 2021).

3.3.2. Margin evolution during collision

Generally speaking, the initiation of subduction in magma-poor margins appears to be controlled by the presence of serpentinised exhumed mantle which will lead to under thrusting of the oceanic domain below the rifted margin (Auzemery et al., 2022). This is followed by the formation of an accretionary prism thrust above the hyper extended domain. The Coulomb prism is controlled by the friction of the sedimentary decollement level (Dahlen et al., 1984). In the western

Alps, the migration of the deformation toward the continent led to the formation of ramps in the shallow water carbonate platforms above the necking domain (Pfiffner, 1993). This led to the burial of the hyperextended domain and necking domain below the accretionary prism, associated to an increase of the temperature. This was responsible for the metamorphic peak observed in the External Crystalline Massifs with up to 350°C reached at the base of the sedimentary cover (Bellanger et al., 2015; Boutoux et al., 2016; Girault et al., 2020).

A progressive re-thickening of the crust and the transition from thin to thick-skin deformation is therefore expected (Tavani et al., 2021). The consequence of the tectonic burial is a progressive change from brittle to plastic deformation in the whole crust (Fig. VIII.8). As observed in the Western Alps, this is responsible for thermal softening of the crust and self-consistent shear zone generation (Jaquet et al., 2018). The spacing of the shear zones between 30 and 50 km appears controlled by the depth of the upper-lower crust boundary (Dotare et al., 2016; Jaquet et al., 2018). However, pre-orogenic variations of this boundary are observed in rifted margins, which could have an impact on the Alpine shear zones in the case of the Alps.

Formation of these crustal shear zones with decollement in the middle crust were responsible for important shortening of the upper crust, as observed in the ECM with the Mont-Blanc shear zone and the Belledonne/Aiguilles-Rouge basal thrust (Leloup et al., 2005; Bellahsen et al., 2014). The thrusting of the necking domain above the proximal domain led to a rotation and steepening of the internal part (Fig. VIII.8). As observed in the ECORS profile, it can appear overturned at depth in response to the exhumation and tightening of the orogenic prism (Thouvenot et al., 1996; Mohn et al., 2014).

Meanwhile, underthrusting of the hyperextended crust below the necking domain is achieved forming the Alpine root (Mohn et al., 2014). Similar mechanisms have been observed in the Taiwan Southern range (McIntosh et al., 2013). The increased shortening might be responsible for the exhumation of metamorphic units (Fig.8; Tavani et al., 2021). This is actually observed in the Aar-Gothard massif where amphibolite-facies units derived from the European margin have been exhumed and thrust above the necking domain (e.g., the Adula nappe; Galster et al., 2012).

The specific crustal architecture found in the necking domain clearly plays a role in the architecture of the orogen as observed in many collisional prisms (e.g., the Appennine, Oman, Taiwan; Tavani et al., 2021). The fossil necking domain is systematically found at the transition between the internal and external domain of the orogens. The transition from a thick to a thin crust acts as buttress during collision focusing the deformation on this domain (Mohn et al., 2014). It has a clear impact on the localisation of the main decoupling level as well.

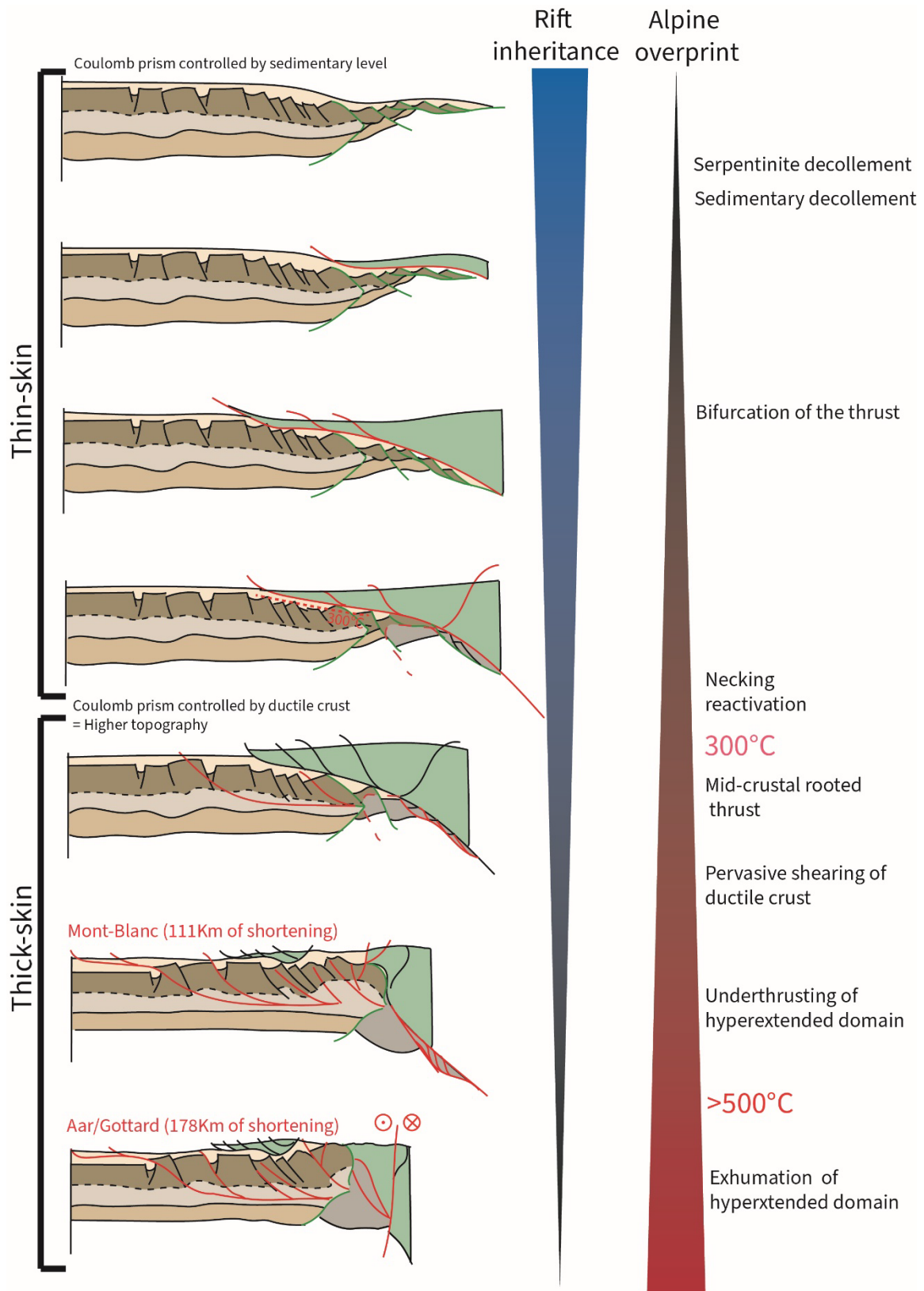


Figure VIII.8: Proposal of evolution of the necking domain during compression (based on Tavani et al., 2021). The temperature indicated corresponds to the temperature reached by the necking domain. The shortening in the Mont-Blanc and Aar are from Rosenverg et al., 2021.

4. Fluid evolution in rifted margins

4.1. Fluid circulation along necking detachment fault

Fluid circulations have been studied in detail in the distal part of the margin. The hydrothermal circulation and geochemical signature of crustal necking remained a keystone in the evolution of fluid circulations throughout rifting.

4.1.1. Fluid properties

The fluids circulating along the detachment fault show a moderate salinity and moderate temperatures. The fluid is H₂O-NaCl dominated with also KCl present. The main question is the source of the fluid. The moderate salinity and the absence of gas suggest seawater and sedimentary brines as being the main sources. Indeed, meteoric water are characterized by low salinity, while metamorphic and magmatic fluids are characterized by the presence of gas such as CO₂ (Yardley and Bodnar, 2014). In addition, no magmatic activity is recorded around the Mont-Blanc during the Liassic rifting. The epicontinental context of the rifting is favourable for significant seawater percolation into the basement as well (Incerpi et al., 2019).

4.1.2. Fluid/rock interaction

Significant fluid-rock interactions can occur during the downward pathway of the fluid associated to heating. Indeed, over-saturation of different minerals can occur related to progressive increase of temperature (Weinzierl et al., 2018). However, evidence of the downward pathway is not well preserved in the Mont-Blanc massif. Large calcite veins with infills such as reddish clays are observed in the top Pelvoux cataclastic basement at the base of the Jurassic cover (Appendix D) and might correspond to a witness of the downward flow missing in the Mont-Blanc massif.

Along the detachment, strong hydration of the basement was observed along the detachment fault representing the upward pathway of the fluid. This indicates significant fluid-rock interaction. The main reactions are associated to feldspar and biotite breakdown. These reactions are controlled by the temperature and fluid composition. As the fluid evolved through fluid rock interaction, a change in the alteration reaction can be observed. Albitization of the feldspars is controlled by the concentration of Na and K in the water. For biotite breakdown and chlorite stability, the reaction is controlled by the concentration of Fe and Mg in the water. High-Mg concentration and low-K concentration led to the transformation of biotite into chlorite. A decrease of Mg may have led to muscovite replacement. However, this type of reaction is also strongly dependent on the temperature.

Metasomatic reactions leading to feldspar and biotite breakdowns were responsible for release of base metals such as Pb, Zn, As, Sb. Besides, release of F and Ba is observed with strong increase of

these elements in the core zone. These elements highlight a specific geochemical signature for crustal necking.

4.2. Ore deposits

4.2.1. Basement-hosted mineralisations

Pb-Zn-F-Ba mineralisations are found in the basement as meter-thick veins in the footwall of the detachment faults, possibly as filling of fractures forming during footwall rotation. They likely form as the result of fluid mixing between hydrothermal fluids and surface, triggering precipitation of fluorine (Richardson and Holland, 1979). Precipitation of fluorine favoured by fluid cooling and mixing would lead to a decrease of the activity of fluorine in water and to precipitation of REE-rich phases (allanite; Dorignaux, 2017).

4.2.2. Sediment-hosted ore deposits

Hydrothermal fluids reaching the sedimentary cover are submitted to different processes leading to the formation of ore deposits. For example, cooling and fluid mixing can lead to sulphide precipitation (Zhang et al., 2021). Different types of ore deposits are observed across the necking domain from the topographic high to the basin area.

MVT-type deposits are observed in carbonate platforms of the necking domain. The location of these platforms is controlled by the topographic high created during crustal necking. The ore deposits may occur when the basement-derived fluids reached the carbonate platforms leading to replacement of carbonates through dissolution-precipitation mechanisms (Rys, 2020). The deposition is likely triggered by pH buffering of the fluids reacting with carbonates. Lowering of pH might indeed enables sulphides precipitation (Zhang et al., 2021). However, the provenance of sulphur is not well constrained.

SEDEX type deposits can be recognized in the basin areas where fluids can reach the surface under anoxic conditions (Sangster, 2018). The key component is the presence of organic-rich shales. Indeed, organic matter provides sulphides through bacterial sulphate reduction, leading to ore precipitation (Emsbo, 2009). General anoxic conditions in the basement appears favourable for organic matter preservation and ore deposit formation over long periods (Emsbo, 2009; Sangster, 2018). SEDEX are not observed in the Western Alps but are common in rifted margins. Moreover syn-sedimentary Fe-Mn oxides deposits are observed in the Western Alps indicating seafloor oxidising conditions (Pfeifer et al., 1988).

4.3. Ore deposits throughout the Wilson cycle

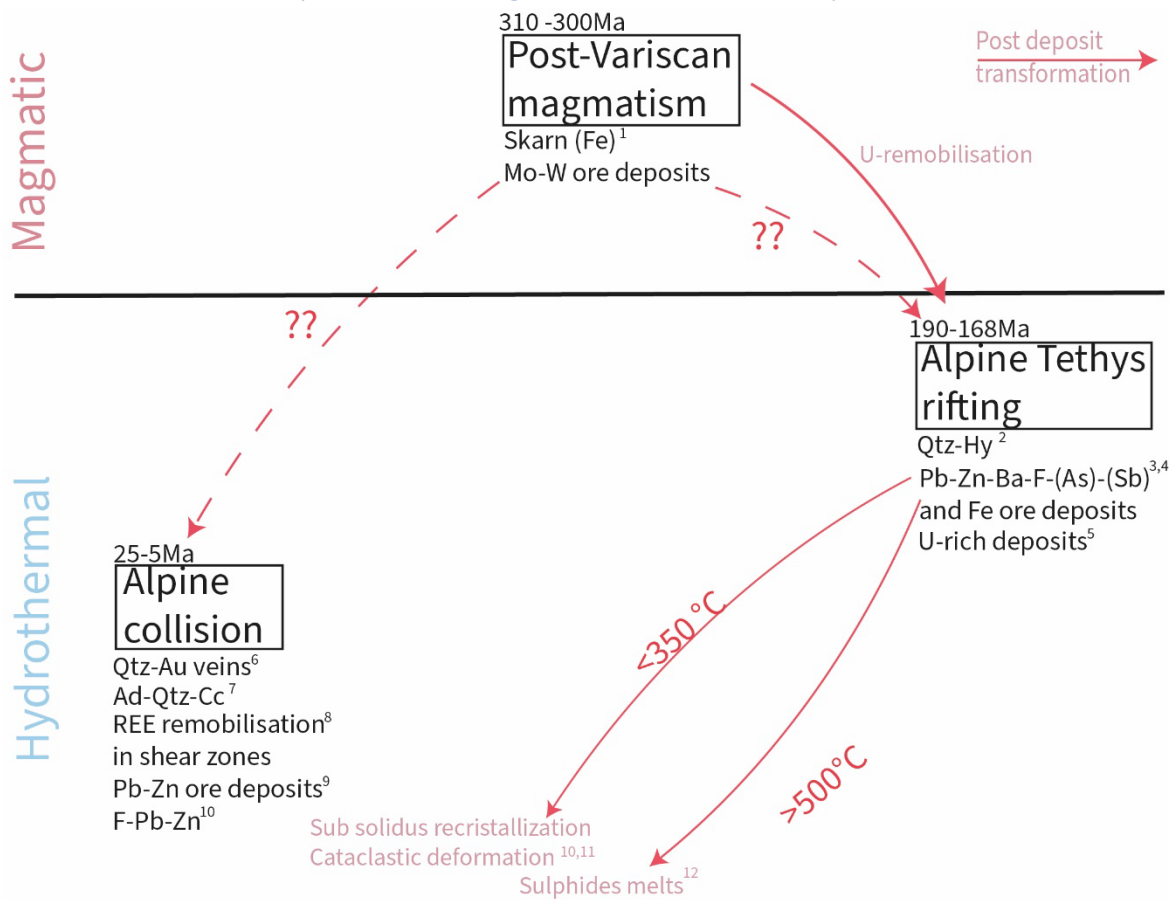


Figure VIII.9: Conceptual model of the relation between the Variscan, rift-related and Alpine ore deposits in the External Crystalline Massifs. Post-Variscan magmatism is responsible for the concentration of some metals in the upper crust, which are remobilized in later tectonic events. The Jurassic deposits are affected by Alpine deformation and metamorphism leading to strong overprint. 1- Marshall et al., 1997; 2-Dall'Asta et al., 2022 ; 3-Rys, 2020; 4-Dorignaux, 2017; 5-Geffroy et al., 1964; 6-Marshall et al., 1998 ; 7-Rossi and Rolland, 2014; 8-Rolland et al., 2003; 9-Polliand and Moritz, 1999; 10-Ochoa Alencastre and Chenevoy, 1979; 11-Chessex and Rivier, 1957; 12-Hofmann, 1994.

The External Crystalline Massifs record a Wilson cycle with the Variscan orogeny followed by post-Variscan Carboniferous extension, Jurassic rifting, and Alpine orogeny. Preservation of the ore deposits and veins associated to the different tectonic events highlight the possible remobilisation of ore deposits during later tectonic events.

Variscan ore deposits are associated to hematite deposits associated to skarn and Mo-W deposits (Fig. VIII.9). In addition, magmatic differentiation led to the concentration of some elements such as Pb-Zn and U in the granites. The Jurassic rifting phase is characterized by the important mobilisation of Pb-Zn-Ba-F as well as U-deposits. The source of metals corresponds to the enriched Carboniferous magmatic intrusions (Fig. VIII.9).

Different types of ore deposits are associated to the Alpine collisions. Since they correspond to the last event, they are better constrained than the pre-Alpine deposition events. Pb-Zn ore deposits are observed. Moreover, REE remobilisation is observed along shear zones affecting the Carboniferous granites (e.g., the Mont-Blanc massif). Mineralized fissures known as Alpine clefts are

formed by quartz, calcite and adularia mostly (Rossi and Rolland, 2014). Furthermore, in the northern part of the Mont-Blanc massif, gold bearing quartz veins are present (Marshall et al., 1998a). The ore deposits are affected by deformation and metamorphic transformation related to the Alpine orogeny (Fig. VIII.9). Cataclastic deformation and recrystallisation are described in Pb-Zn-F deposits in the ECM (Chessex and Rivier, 1957). Increase of temperature can lead to sulphide melts which modify drastically the ore deposits as observed in the Gottard massif (Hofmann and Knill, 1996). This occurs mostly in As-Sb rich deposits with lower melting temperature (Frost et al., 2002). The stockwork of metal was emplaced during the rifting but the ore deposits is composed mainly of neoformed Alpine sulphides (Hofmann and Knill, 1996).

Deposit reworking during subsequent tectonic events lead to strong modification of the initial ore deposits. These modifications can occur in an open system leading to changes in the overall composition of the ores, or in a closed system related to a modification of the paragenesis without changes of the composition (Frost et al., 2002). These modifications can alter partially to completely the initial texture of the ore deposits as well as the isotopic records (e.g., Sm-Nd ages of the fluorite deposits; Nägler et al., 1995).

4.4. The concept of mineral system applied to crustal necking

4.4.1. Definition of mineral system

The mineral system approach is an holistic method integrating the different features necessary of ore deposits: *“source(s) of the mineralizing fluids and transporting ligands, source(s) of ore components, a migration pathway for the fluids, an energy source and thermal gradients to drive fluid flow, a mechanical and structural focusing mechanism at the trap site, and chemical or physical traps for mineralization”* (McCuaig and Hronsky, 2014).

The emplacement of ore deposits depends on processes at different scales (Fig. VIII.10). The source of metals and fluids is dependent on regional processes. The nature of the basement at large scale must be considered to have a reliable view of the type of elements potentially mobilized in the fluid. The tectonic setting controls the fluid pathway and is related to the crustal architecture in the area. The process triggering ore deposits are occurring at the scale of several hundred meters to the micro scale, being controlled by pressure, temperature, and chemical gradients.

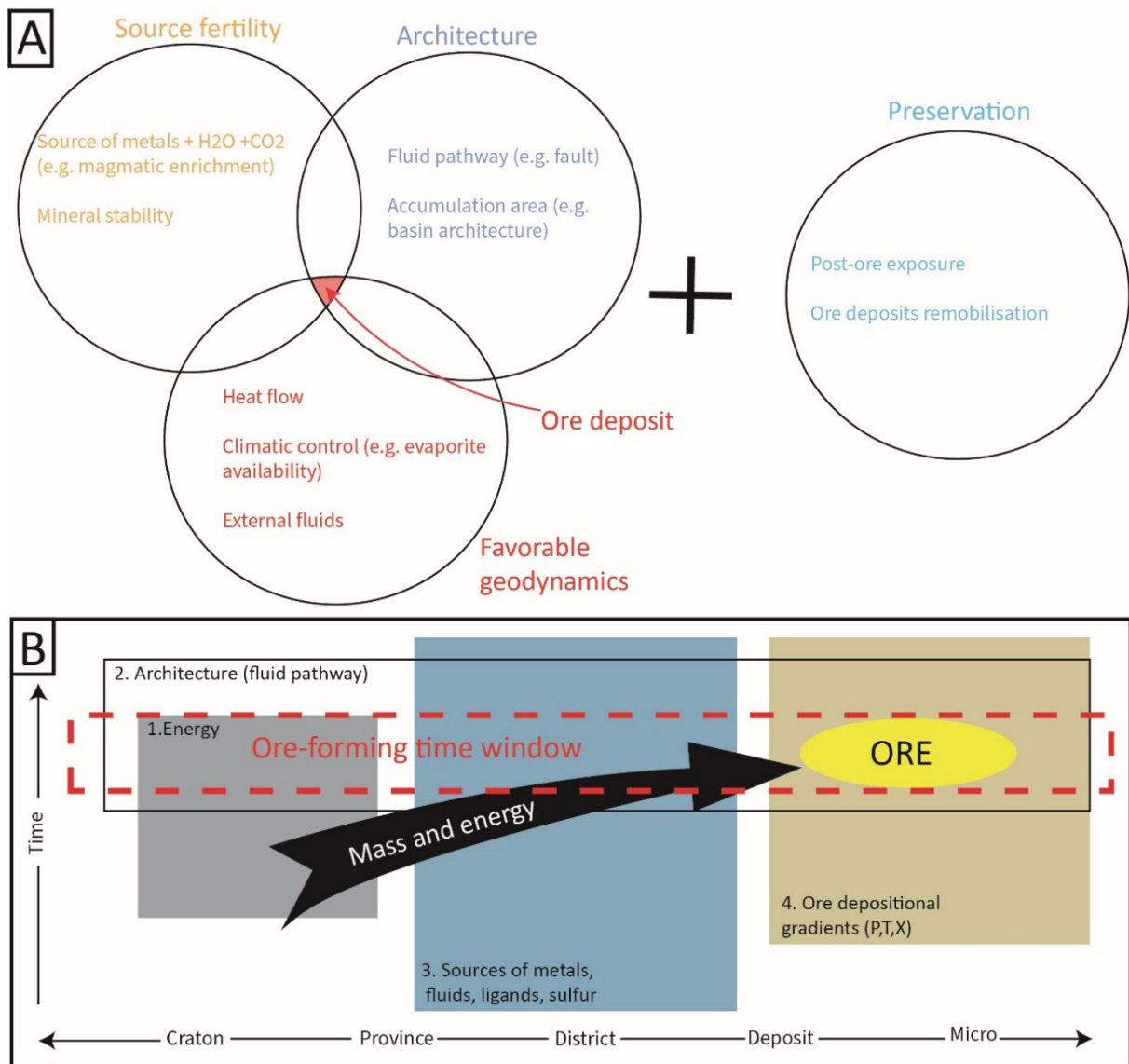


Figure VIII.10: A- Conceptual sketch of the mineral system according to McCuaig and Hronsky (2014) B- Conceptual sketch of the mineral system according to Dulfer et al., (2016) highlighting the different space and time scales associated to ore deposits.

4.4.2. Necking mineral system

The necking mineral system can be decomposed into 4 parts, source fertility, geodynamics, architecture and preservation of the ore deposit (Fig.VIII.11).

The favourable geodynamics would correspond to the increase of temperature related to the asthenosphere uplift leading to gradient up to 50°C/km (Fig.VIII.11). This provides a source of energy for base metal extraction from the basement and for hydrothermal systems. This favourable geodynamics corresponds to the availability of seawater and evaporite providing fluids and ligands to base metal for solubilisation and transport.

The source fertility corresponds to the ability of the basement to provide significant amounts of metals to the fluid phase (Fig. VIII.11). Crustal necking occurs, by definition, in the continental crust, which is highly heterogeneous in composition. Therefore, the fertility will depend on the local

pre-rift history and must be evaluated locally. For the Mont-Blanc area, the basement is characterized by significant post-Variscan magmatism leading to local enrichment in some elements such as Pb, Zn, F, REE, U. Conjointly, the releasing of the metals is also controlled by the stability of the metal-bearing minerals. In the case of the Mont-Blanc, the instability of the feldspars and biotite under retrograde, fluid-rich conditions led to important release of the metals in the fluids.

The architecture corresponds to the geometry of the necking domain. Indeed, the large necking detachment faults provide a pathway of the fluids up the surface (Fig. VIII.11). Minor normal faults affecting the hangingwall and footwall deformation can provide a pathway for descending fluids. The architecture can also integrate the cover architecture with the thick shale levels forming an impermeable barrier. Moreover, the topographic high related to necking and surrounded by basins can guide the fluid flow at the basement-cover interface up to the surface. The cover controls also the ore-deposits. The position of the carbonate platforms is a key element to predict the position of ore deposits in necking domains.

Necking system:

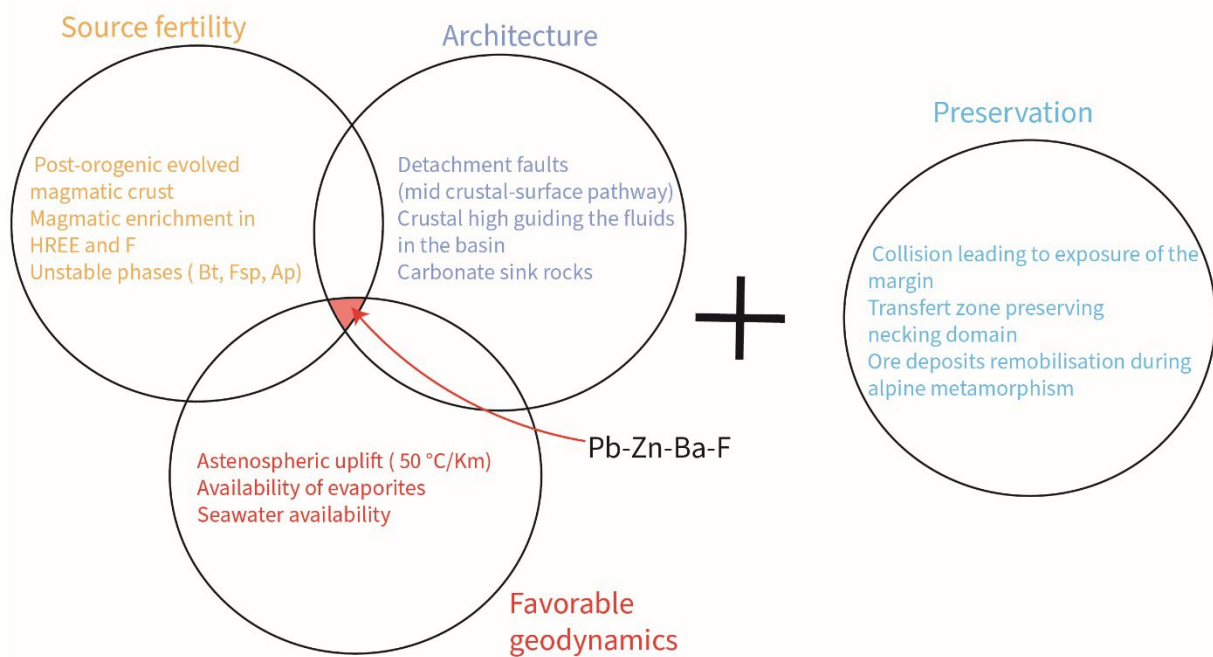


Figure VIII.11: Concept of mineral system applied to crustal necking domain.

Crustal necking is a transient process through time therefore the mineral system evolves through time, especially in terms of architecture. Syn-tectonic fluids circulating along the active detachment fault will lead to ore deposits in the basement and in the pre to syn-tectonic cover. The cessation of fault activity can lead to the progressive cementation of the fault. However, distal faults can be associated to strong hydrothermal circulations. Depending on the cover thickness in the distal area, pressure gradients can lead to a migration of the fluid along the basement-cover interface guided by

the necking domain topographic high leading to deposits in the post-tectonic carbonates of the necking domain.

The last parameter corresponds to the preservation of the ore deposits in fossil-rifted margins and their exposure. The exposure of the fossil margin depends on the total amount of shortening but also vary along strike. A larger section of the necking domain is exposed when larger shortening occurs. However, this leads also to strong deformation and metamorphism of the ore deposits. Sulphide melting can occur at conditions as low as 300°C, depending on the composition (Frost et al., 2002). Sulphur melting concentrates specific metals in the melts such as the Ag, As, Bi, Hg, Se, Sb, Sn, Tl or Te which can improve the recovery of metals in the Pb-Zn deposits (Vokes, 1969; Frost et al., 2002; Sangster, 2020).

4.5. A model of evolution of the geochemical signature of the rifting through time

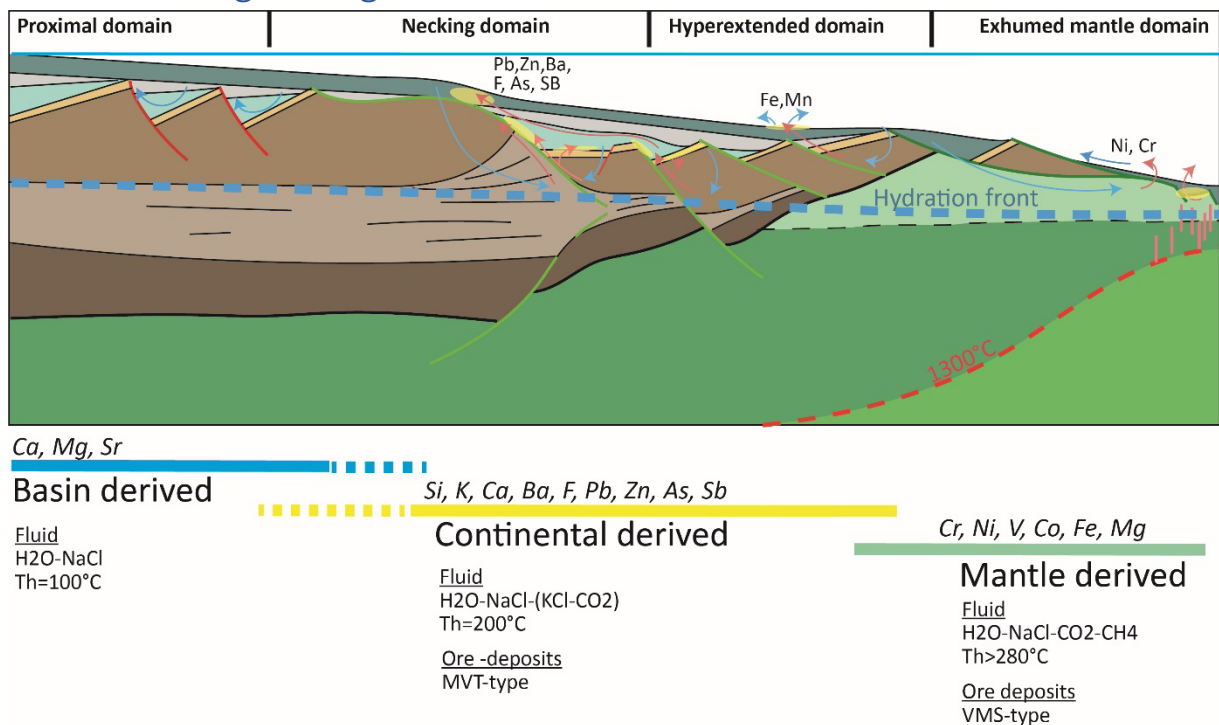


Figure VIII.12: Evolution of rift-related fluids in a magma-poor margin from the proximal to the exhumed mantle.

The geochemical evolution of a magma poor-rifted margin can be reconstructed using the example of the Alpine Tethys. The onset of crustal necking is marked by an increase in temperature which marks the moment where condition for significant metal extraction is reached, following the penetration of brines in the basement under high heat flow. The geochemical signature associated of crustal necking is the release of Si, K, Ca, Ba, F, Pb, Zn and to gains in As and Sb along the fault and associated to the formation of MVT (Fig. VIII.12).

The impact of the basement-derived fluids on the sediments at the basin scale is hard to assess. Strong silicification of the sediments as observed in the internal Mont-Blanc points to

Discussion, perspectives, and conclusions

Figure VIII.13: A- Graph of the critical raw material according to the supply risk and economic importance (from Blengini et al., 2020). The yellow circle indicates material present in necking domains, and green circles material observed in exhumed mantle domains. B- Evolution of the zinc and lead known resources through time (from Sverdrup et al., 2019). The graph presents the total known resources divided in rich, high, low and ultra-low according to the ore grade. The red line corresponds to the supposed peak in the known resources.

Long-term sustainability of metal is critical for societies. Copper, zinc, and lead are some of the most used metals in industry in terms of volume (Sverdrup et al., 2019). Assessment of these resource were proposed by Sverdrup et al., (2019) for copper, zinc, and lead, Sverdrup and Ragnarsdottir (2016) for Platinoid Group Metals (PGM) and Sverdrup (2016) for lithium. They indicate the decrease of these resources between 2000 and 2050, along with an increase of market price associated to resource scarcity (Sverdrup and Olafsdottir, 2020). Critical resource, after the definition of Blengini et al., (2020), corresponds to resources of economic importance facing supply risk because of resource scarcity and/or geopolitical tensions. Some of the elements in this list are facing strong supply risk. The resources with no economic importance or showing no supply risk corresponds to the non-critical raw materials.

In this perspective, prospection of new resources might be a part of the solution. Some of the critical materials such as baryte, antimonium and cobalt can be found in rifted margins and fossil rifted margins (Fig. VIII. 13A). Some of the resources found in necking domains such as Pb, Zn could face tension on the market due to increased demand and resource scarcity (Fig. VIII.13B). Therefore, the next question related to necking domains concerns the size of the ore deposits and their economic potential. The ore deposits likely related to crustal necking in the Alps are relatively small (up to 350000 t) and were exploited only during a short period of time. This questions, therefore, of the ability of crustal necking to produce large deposits:

- Is crustal necking capable of forming giant ore deposits?
- What type of deposits?

These questions are hard to answer because of the lack of datasets. Indeed, most of present-day necking domains have been drilled for oil and gas discoveries, in context usually unfavourable for metal transport (McCuaig et al., 2018). In addition, few data are available concerning wells in necking domains. For fossil domains, the problem is similar. Few examples of fossil rifted margins have been identified worldwide and fewer work has been done on the ore deposits related to necking.

Discussion, perspectives, and conclusions

	Location	Age	Type	Elements	Magmatic activity	Size	Ore grade (Pb+Zn)	References
<i>Lady Loretta</i>	Australia	Mid-Proterozoic	SEDEX	Ag, Pb, Zn	Syn-rift felsic intrusions	8300000	26.80%	(Loudon et al., 1975)
<i>Century</i>	Australia	Mid-Proterozoic	SEDEX	Ag, Pb, Zn	Syn-rift felsic intrusions	105000000	13.85%	(NS Energy, 2022) (Mining Data online, 2022a)
<i>Mc Arthur</i>	Australia	Mid-Proterozoic	SEDEX	Ag, Pb, Zn	Syn-rift felsic intrusions	194000000	13%	(Mukherjee and Large, 2017)
<i>Broken hill</i>	Australia	Mid-Proterozoic	BHT (M)	Ag, Pb, Zn		280000000	19%	(Walters et al., 1996)
<i>H.Y.C</i>	Australia	Mid-Proterozoic	SEDEX (M)	Ag, Pb, Zn		227000000	13%	(Logan et al., 1990)
<i>Silver King</i>	Australia			Ag, Pb, Zn		700000	12.50%	(Mining Data online, 2022a)
<i>Faro</i>	Canada	Cambrian	SEDEX	Pb, Zn		63000000	9.1%	Cooper, 1975)
<i>Pend Oreille</i>	Canada	Cambro-ordovician	MVT	Pb, Zn		2400000	8%	(Mining Data online, 2022b)
<i>Meggen</i>	Germany	Devonian	SEDEX	Ag, Pb, Zn		50000000	8%	(Krebs, 1981)
<i>Jabal Dhaylan</i>	Saudi Arabia	Mid-Miocene	MVT	Zn, Pb, Cu, Ag		300 000	6.29%	(Hayes, 2001)
<i>Rabigh</i>	Saudi Arabia			Ba, Mn, Zn		40000	6.60%	(El Aref and Amstutz, 1983)
<i>Um Gheig</i>	Egypt	Miocene	Sediment hosted	Pb, Zn		2000000	12.00%	(El Aref and Amstutz, 1983)
<i>Elba</i>	Egypt	Mid-Miocene	Sediment - basement hosted	Mn		40000	74.00%	(Basta and Saleeb, 1971),
<i>Wadi Araba</i>	Egypt					4000	20.00%	El Aref and Amstutz, 1983)
<i>Um Greifat</i>	Egypt	Mid-Miocene		Mn, Zn, Fe, Ba, U				(Afify et al., 2020)
<i>El Reocin</i>	Spain	Early Cretaceous	MVT	Pb, Zn		30000000	12.30%	(Velasco et al., 1994)
<i>San Jose</i>	Spain	Early Cretaceous	MVT			??	13.00%	(Variscan mine, 2022)
<i>Troya</i>	Spain	Early Cretaceous	MVT	Pb, Zn, Cu, Fe		3500000	14.10%	(Fernández-Martínez and Velasco, 1996)
<i>Matienzo</i>	Spain	Early Cretaceous	MVT	Ag, Pb, Zn		??	5.40%	
<i>Montroc</i>	Spain	Early Cretaceous	MVT	F, Ba, Cu		2000000	??	
<i>La Florida</i>	Spain	Early Cretaceous	MVT			1500000	5.10%	(Essalhi, 2009)
<i>Nantuel</i>	France	Early Jurassic?	Basement hosted	Pb, Zn, F	Triassic intrusions	300000	4.00%	(Ochoa Alencastre and Chenevoy, 1979), (BRGM, 1984), (Sivade and Thibieroz, 1989)
<i>Rocheray</i>	France				Triassic intrusions	150000	6.60%	(Ochoa Alencastre and Chenevoy, 1979), (BRGM, 1984), (Sivade and Thibieroz, 1989)
<i>Rocheray</i>	France	Early Jurassic?	Basement hosted	Pb, Zn, F	Triassic intrusions	350000	3.00%	(Ochoa Alencastre and Chenevoy, 1979), (BRGM, 1984), (Sivade and Thibieroz, 1989)
<i>Rocheray</i>	France			F		350000	60.00%	(Ochoa Alencastre and Chenevoy, 1979), (BRGM, 1984), (Sivade and Thibieroz, 1989)

Discussion, perspectives, and conclusions

<i>Rocheray</i>	France			Pb, Zn, F		150000	5.20%	(Ochoa Alencastre and Chenevoy, 1979), (BRGM, 1984), (Sivade and Thibieroz, 1989)
<i>Sainte-Marie du Fouilly</i>	France	???	Basement-hosted	Pb,Zn, Sb,As		130000	6%	(BRGM, 1984)
<i>L'Amône</i>	Switzerland	Bajocian?	MVT	Pb, Zn, Fe		2000	2.70%	(Rys, 2020)
<i>Mont-chemin</i>	Switzerland	Early Jurassic?	Basement hosted	F, Ba, Pb, Zn		300000	50.00%	(Nägler et al., 1995), (Dorignaux, 2017)
<i>Lengenbach</i>	Switzerland	Early Jurassic?	Sediment hosted (M)	Pb, As, Tl				(Hofmann and Knill, 1996), (Hofmann, 1994)

Table VIII.1: Compilation of ore deposits in fossil-rifted margins and present-day rifted margins providing the type, age, and size of the deposits. The (M) associated to the type of ore deposits means that this deposit has been submitted to metamorphism.

Using data worldwide of Pb, Zn, Mn and Ba deposits, a compilation of possibly necking related ore deposits is proposed here (Table VIII.1). This compilation is not complete and only preliminary, but it ranges from the Alpine deposits to super giant deposits from Cambrian to Miocene in age. They are formed of MVT-deposits and SEDEX deposits clastic deposits, basement-hosted deposits, and sediment-hosted oxide deposits.

Deposits from the NW American Cordillera (Alaska, Canada) correspond to remnants of the Cambrian to Devonian Palaeozoic magma-poor rifted margins. The ore deposits from Australia are related to the opening of the Mt Isa-McArthur basin system (ca. 1800 Ma) followed by an orogenic phase inverting the basin. The Cretaceous ore deposits in Cantabria, Spain (Velasco et al., 1994) correspond to syn-rift ore deposits from the inverted Bay of Biscay margin. They are found in an area corresponding, in fact, to the paleo necking domain (e.g., Santander block; Miró et al., 2021). The deposits found around the Red Sea are Miocene syn-rift ore deposits. They are located along the coast line and roughly aligned, parallel to the main rift-related faults (Dadet et al., 1970). Their localisation correspond to the necking domain of the Red Sea margin (Stockli and Bosworth, 2019).

Discussion, perspectives, and conclusions

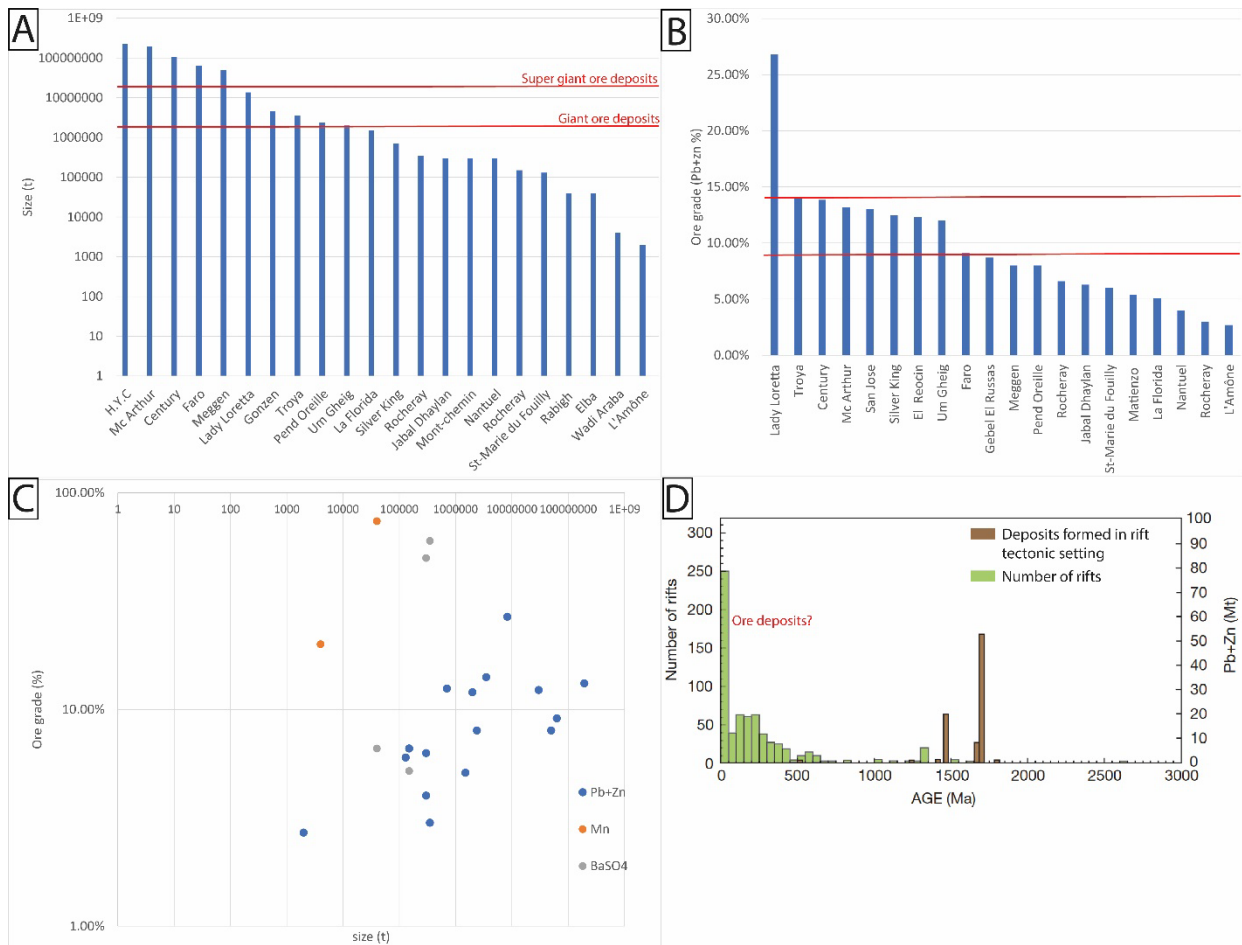


Figure VIII.14: A- Size (in tons) of some Pb-Zn deposits found in necking domains. B- Ore-grade (%) of some Pb-Zn deposits found in necking domains. C- Ore grade vs size graph of Pb-Zn, baryte and Mn-oxide from necking domains. D- Proportion of rift and rift-related Pb-Zn deposits through Earth history (from Leach et al., 2010).

Large scale deposits seem to be possible in the necking domain. They correspond mostly to SEDEX-type deposits under anoxic conditions (Emsbo, 2009) with size above 10 Mt and ore grades above 10% (Fig. VIII.14A,B and C). These super-giant deposits have Palaeozoic and Proterozoic ages mostly. Indeed, it was noticed by Leach et al., (2010) that most of the rifts from Mesozoic to present-day are not associated to Pb-Zn deposits (Fig. VIII.14D). It is unclear if this lack of deposits younger than 1000Ma is due to the to the underestimation of Pb-Zn deposits during Mesozoic and Tertiary period because of a lack of knowledge concerning present-day margins or because of more favourable conditions before 1000 Ma.

Oxide deposits are also associated to crustal necking as observed in the Red Sea. Fe-Mn-Zn polymetallic deposits are found in syn-rift Miocene limestones (Basta and Saleeb, 1971; El Aref and Amstutz, 1983; Afify et al., 2020) representing a modest size (up to 40000 t; Fig. VIII. 14). These deposits are mostly found in the Egyptian margin where no rift volcanic intrusion have been recognized (Stockli and Bosworth, 2019).

Discussion, perspectives, and conclusions

These partial results emphasize the role played by crustal necking in magma poor margins in the generation of ore deposits. Indeed, crustal necking might be able to trigger the formation of large Pb-Zn deposits. The increase of temperature associated to asthenosphere uplift might be sufficient to maintain strong hydrothermal circulations without magmatic input. The Selwyn basin described lately as part of a fossil magma-poor margin (Beranek, 2017) is the place where the largest Pb-Zn SEDEX deposits were found. Obviously, syn-necking magmatic intrusion (e.g., South China Sea; Chao et al., 2021) would facilitate crustal scale transfers of some elements and enhance hydrothermal circulation due to the higher thermal gradient. Focus on the processes of ore accumulations in amagmatic rifted margins would provide a better insight.

Perspectives and Conclusion

The recognition of a fossil necking domain in the Mont-Blanc massif provides an opportunity to better understand the tectono-sedimentary evolution and fluid circulation during crustal necking. The relation between the sedimentary cover and the exhumed detachment fault gives an upper Sinemurian age for the contact.

Generally speaking, crustal necking is associated to migration of the syn-rift depot centre toward the distal part. The necking domain corresponds, also, to the breakaway of post-rift carbonate platforms. As observed in the Western Alps, due to the architecture of the margin with a thinned to ultra-thinned crust in the distal domain and a thick continental crust in the proximal domain, the fossil necking domain is likely to be found at the transition between the external and internal part of the orogen.

The example of the Mont-Blanc detachment faults shows that the fluid circulations along the fault lead to element mobility with gain of K, Fe, Ti, Mg, Ba, F, As, V along the fault and loss in Si, Na, Ca, Pb, Zn. The fluids are composed of H₂O-NaCl (-K₂O) brines with a salinity of 7 to 9 wt% equiv. NaCl and homogenization temperature between 170 and 200°C. A maximum depth of entrapment of the inclusions is estimated between 5 and 7 km with an initial fluid temperature up to 250°C. Occurrence of graphite possibly associated to pseudotachylites are visible along the fault.

The recognition of other fossil necking domains would provide more constrains in the fluid evolution. The identification of the syn- to post-rift stratigraphic architecture at the transition between the external and internal domain of the orogen, might help to localise the necking domains in orogens. One of the characteristics of crustal necking is the occurrence of clastic deposits in response to basement uplift associated to detachment faulting. These types of contacts can be found at the interface between the basement and the cover. Examples of fossil necking domains have been proposed in Oman (Ducoux et al., 2022), in the Pyrenees (Tugend et al., 2015) as well as in the Taiwan belt and in the Apennines (Tavani et al., 2021). The recognition of other fossil necking

Discussion, perspectives, and conclusions

domains would lead to a more representative view of the fluid circulation during crustal necking. One of the main tasks would be to identify syn-rift ore deposits in other fossil necking domains to confirm or infirm the observation from the Alpine necking domain.

General Conclusion



View of the Mont-Blanc from la Ville des Glaciers (Mont-Blanc massif, France)

Conclusion (En)

This work provides an insight on the tectono-stratigraphic evolution and fluid circulation in a fossil necking domain preserved in the Mont-Blanc massif. This study started by the recognition of a Jurassic detachment fault preserved in the southern part of the Mont-Blanc massif, which is a key observation for understanding the pre-Alpine evolution of the Mont-Blanc. This fault is characterized by cataclasites and locally fault gouges overlaid by pre- and syn-rift sediments. Fluid assisted deformation led to the formation of cataclasites under temperatures of ca. 250°C and progressive localisation of the deformation on the fault core leading to fault gouge formation. The P-T-t evolution remains, however, unconstrained due to the lack of direct information on the pressure evolution. Reasonable assumption on the thermal gradient (30 to 50°C/km) would lead to an exhumation of ca. 5 to 10 km.

The examination of the contact in the Col du Bonhomme shows that both stratigraphic and tectonic contacts are found between the exhumed basement and the sediments. Locally, remnants of pre-rift cover can be found lying above the exhumed basement. This contact appears tectonic. The occurrence of traces of evaporites in the form of anhydrite inclusions in quartz at the base of the pre-rift allochthons indicates the occurrence of evaporites which might have acted as potential a decoupling level between the pre-rift and the basement. This indicates that the fault must be younger than the upper Triassic dolostones from the pre-rift cover. The contact between the syn-rift cover and the basement, however, is stratigraphic, sealing the exhumed fault. The first sediment over the basement corresponds to Upper Sinemurian crinoid-rich bioclastic mud overlaid by Sinemurian to Pliensbachian sandstones reworking fault rocks. The age of the first sediments over the detachment associated to the occurrence of sandstones point toward a Sinemurian to Pliensbachian age for the detachment activity.

Analysis of fluid circulations and element transfer along the fault indicates gain of K, Fe, Ti, Mg, Ba, F, As, V along the fault and loss in Si, Na, Ca, Pb, Zn associated to H₂O-NaCl (-K₂O) brines with a salinity of 7 to 9 wt% equiv. NaCl and homogenization temperature between 170 and 200°C. Besides, relative mobility of HFSE associated to F enrichment is observed. This raises the question of the use of these elements as immobile elements for mass balance calculation.

The source of the fluid may be seawater penetrating the basement along secondary faults and through fractures in the basement. The interactions between an external fluid and the rocks led to biotite and feldspars breakdown as well as apatite dissolution. Feldspar alteration corresponds to a first phase of albitisation of orthoclase before sericitization of both albite and orthoclase. Biotite is affected by chlorite replacement coeval to albite alteration. These reactions are responsible for the

General Conclusion

element transfer observed along the fault. Warm fluid then migrated upward along the fault until the surface. It is proposed here that there is a genetic link between the fluid circulation observed along the detachment fault and the pre-Alpine ore deposits observed in the internal Mont-Blanc cover. These deposits correspond to Pb-Zn-Ba-F mineralisations possibly derived from basement leaching along the detachment fault.

The preservation of a fossil detachment fault in the Col du Bonhomme and its relationship with the syn-rift cover provides a new insight on syn-necking evolution. The exhumation of the basement related to the necking detachment fault is responsible for the formation of a topographic high forming the “Mont-Blanc Island”. This island was the source of clastic sediments found in the neighbouring basins between Upper Sinemurian and Aalenian. The observations in the northern part of the massif tend to show that the detachment fault can be prolonged until the northern termination of the Mont-Blanc massif. During Toarcian a decrease of the clastic input in the basins marks the progressive decrease of tectonic activity. An uplift of the Mont-Blanc and the Aiguilles-Rouges during Upper Toarcian/Lower Aalenian is observed. This uplift of the proximal and necking domains might mark the onset of hyperextension in the distal margin. Post-rift subsidence is marked by the progradation of the carbonate platform over the necking domain. However, it appears that the Mont-Blanc remained partially emerged until Albian. However, many unknowns remain on the architecture of the European margin especially concerning the distal part of the margin. The exact length and architecture of the hyperextended domain remains poorly constrained. This has implication on the paleo-reconstruction and restoration of the margin.

This study documents one of the first example of a fossil necking domain preserving both the cover and the necking detachment fault complementing the work done on present-day necking domains and numerical modelling of crustal necking. The observations from the Mont-Blanc corroborate prediction from numerical models such as the important topographic uplift. It also raises the question of the occurrence and importance of ore deposits in crustal necking zones. This question cannot be answered using the example of the Mont-Blanc alone. The identification of other fossil necking domain and their associated ore deposits is the next to understand ore deposits associated to necking. Promising examples such as the fossil Oman margin or the Pyrenees could provide more constrains on fluid and ore deposits during this key process that is crustal necking. Another promising area is the Red Sea margins and especially the western margin where the necking zone is nowadays outcropping and associated to different types of ore deposits.

More than 200 years after the first work of Saussure (1779) on the Mont-Blanc, this massif remains at the centre of the scientific debate providing new observations concerning its rift evolution. Despite all the previous studies done on this massif, it appears that not all of its secrets have been unravelled yet for the enjoyment of future geologists.

Conclusion (Fr)

Ce travail donne un premier aperçu de l'évolution tectono-stratigraphique ainsi que des circulations fluides associées à l'amincissement crustal. Le premier point clé est la caractérisation du détachement jurassique préservé au sud du massif du Mont-Blanc (Col du Bonhomme). Ce détachement est en effet important pour comprendre l'évolution préalpine du Mont-Blanc. Cette faille est caractérisée par la présence de cataclasite et gouges scellées par des sédiments pré- et syn-rift. La déformation associée aux circulations fluides est responsable de la formation de cataclasite à des températures de 250°C puis à la formation de gouge dans le cœur de la faille. L'évolution P-T reste cependant peu contrainte à cause du manque de données sur la pression. Une hypothèse raisonnable sur le gradient géothermique (30 à 50°C/km) donne une exhumation du socle de 5 à 10 km.

L'examen du détachement (Col du Bonhomme) montre que les sédiments pré-rifts sont en contact tectonique. La présence d'inclusions d'anhydrite dans les quartz à la base des sédiments pré-rift permet de supposer la présence d'un niveau d'évaporite ayant joué le rôle de niveau de décollement entre les sédiments pré-rift et le socle. Cela indique également que ce détachement est postérieur aux dépôts des dolomies triasique supérieur. Les sédiments syn-rifts sont en contact stratigraphiques avec le socle et également avec les sédiments pré-rifts. En effet, les premiers dépôts sur le socle correspondent à une boue bioclastique composé d'entroques de crinoïdes probablement d'âge Sinémurien supérieur et surmonté de grès Sinémurien supérieur à Pliensbachien remaniant les roches de failles. L'âge des premiers dépôts sur les détachements associés à l'apparition de grès syn-rift permet de proposer un âge Sinémurien-Pliensbachien pour l'activité de la faille.

L'analyse des circulations fluides et des transferts d'éléments le long de la faille indique des gains en K, Fe, Ti, Mg, Ba, F, As, V dans les roches de failles et des pertes de Si, Na, Ca, Pb, Zn associés à des fluides composés de H₂O-NaCl (-K₂O) avec une salinité de 7 à 9 wt% equiv. NaCl et une température d'homogénéisation entre 170 et 200°C. De plus, la mobilité des HFSE associée à des enrichissements en F est observée. Cela soulève le problème de l'utilisation de ces éléments comme immobiles pour le calcul de bilans de masse.

La source des fluides est probablement l'eau de mer pénétrant dans le socle le long de failles secondaires et le long de fractures dans le socle. L'interaction entre le fluide et le socle est responsable de la déstabilisation des biotites et feldspaths ainsi que la dissolution des apatites. En détail, l'altération des feldspaths se fait en deux temps avec une première phase d'albitisation des orthoses suivis de la séricitisation des albites et orthoses. La biotite est remplacée par de la chlorite. Ces réactions sont responsables de transferts d'éléments le long de la faille. Un lien génétique est

proposé entre les circulations de fluides le long de la faille et les minéralisations préalpines observé dans le massif du Mont-Blanc. Ces dépôts correspondent à des minéralisations Pb-Zn-Ba-F potentiellement associés au lessivage des métaux dans le socle le long du détachement.

La préservation du détachement fossile et sa relation avec les sédiments syn-rifts donne un aperçu nouveau de l'évolution d'un domaine d'amincissement. L'exhumation du socle est responsable de la formation d'un haut topographique ou « île du Mont-Blanc ». Cette « île » est la source des dépôts clastiques dans les bassins adjacents au Mont-Blanc entre le Sinémurien et l'Aalénien. Les observations réalisées dans la partie nord du massif tendent à montrer que le détachement se prolonge vers le nord du massif. Les observations sédimentaires dans cette zone permettent de contraindre plus précisément l'évolution stratigraphique durant le rifting. Des grès d'âge Sinémurien à Pliensbachien sont observés similaires aux Grès Singuliers du Col du Bonhomme. Durant le Toarcien, une diminution des apports clastiques est observée et associée à une diminution de l'activité tectonique. Une remontée de la marge est visible durant le Toarcien supérieur et l'Aalénien inférieur. Cette remontée de la partie proximale et du domaine d'amincissement marque le début de l'hyperextension dans la partie distale. La subsidence post-rift est associée à la progradation de plateformes carbonatées par-dessus domaine d'amincissement crustal. Néanmoins, le Mont-Blanc apparaît partiellement émergé jusqu'à l'Albien. De nombreuses inconnues demeurent concernant l'architecture de la partie distale de la marge. La longueur exacte de la marge hyper étirée demeure incertaine.

Ce travail présente un des premiers exemples de domaine d'amincissement préservant à la fois la couverture et le socle associé à une faille de détachement. Il permet de compléter le travail réalisé sur des marges actuelles et à partir de modèle numérique. Les observations sur le Mont-Blanc corroborent la prédiction des modèles numériques sur la création de hauts topographiques durant l'amincissement crustal. Il soulève aussi la question des minéralisations associées à la phase de rifting. La reconnaissance d'autres marges fossiles est le prochain pas afin de caractériser les types de minéralisations associés à cet événement. Des exemples prometteurs comme les marges fossiles en Oman ou les Pyrénées pourraient permettre de mieux contraindre les circulations fluides et minéralisations liées à l'amincissement crustal. Une autre zone prometteuse correspond aux marges passives de la mer Rouge et particulièrement la marge ouest ou la zone d'amincissement crustal affleure et est associé à divers types de minéralisations syn-rift.

Plus de 200 ans après le travail de Saussure (1779) sur le Mont-Blanc, ce massif reste au centre des débats scientifiques notamment associé aux processus de rifting. Malgré tous les travaux déjà réalisés sur cette zone, il semble que le Mont-Blanc n'a pas encore livré tous ces secrets pour le plus grand bonheur des futures générations de géologues.

References

- Afify, A.M., Sanz-Montero, M.E., Osman, R.A., 2020. Zinc-bearing ferromanganese mineralization in a rift-marginal carbonate platform, Red Sea, Egypt: Reconstruction of an epigenetic-supergenic system. *Ore Geology Reviews* 127, 103837.
- Agard, P., 2021. Subduction of oceanic lithosphere in the Alps: Selective and archetypal from (slow-spreading) oceans. *Earth-Science Reviews* 214, 103517.
<https://doi.org/10.1016/j.earscirev.2021.103517>
- Agard, P., Handy, M.R., 2021. Ocean subduction dynamics in the Alps. *Elements: An International Magazine of Mineralogy, Geochemistry, and Petrology* 17, 9–16.
- Airaghi, L., Bellahsen, N., Dubacq, B., Chew, D., Rosenberg, C., Janots, E., Waldner, M., Magnin, V., 2020. Pre-orogenic upper crustal softening by lower greenschist facies metamorphic reactions in granites of the central Pyrenees. *Journal of Metamorphic Geology* 38, 183–204.
- Aja, S.U., Wood, S.A., Williams-Jones, A.E., 1995. The aqueous geochemistry of Zr and the solubility of some Zr-bearing minerals. *Applied Geochemistry* 10, 603–620.
[https://doi.org/10.1016/0883-2927\(95\)00026-7](https://doi.org/10.1016/0883-2927(95)00026-7)
- Alves, T.M., Moita, C., Sandnes, F., Cunha, T., Monteiro, J.H., Pinheiro, L.M., 2006. Mesozoic–Cenozoic evolution of North Atlantic continental-slope basins: The Peniche basin, western Iberian margin. *AAPG Bulletin* 90, 31–60. <https://doi.org/10.1306/08110504138>
- Ampferer, O., Hammer, W., 1911. Geologischer Querschnitt durch die Ostalpen vom Allgäu zum Gardasee. *Jahrbuch der Kaiserlich-Königlichen Geologischen Reichsanstalt* 61, 532–710.
- An, L.-J., Sammis, C.G., 1994. Particle size distribution of cataclastic fault materials from Southern California: A 3-D study. *pure and applied geophysics* 143, 203–227.
<https://doi.org/10.1007/BF00874329>
- Andersen, T., Burke, E.A.J., Austrheim, H., 1989. Nitrogen-bearing, aqueous fluid inclusions in some eclogites from the Western Gneiss Region of the Norwegian Caledonides. *Contributions to Mineralogy and Petrology* 103, 153–165.
- Anderson, E.M., 1905. The dynamics of faulting. *Transactions of the Edinburgh Geological Society* 8, 387. <https://doi.org/10.1144/transed.8.3.387>
- Anderson, G.M., 1975. Precipitation of Mississippi Valley-type ores. *Economic Geology* 70, 937–942.
<https://doi.org/10.2113/gsecongeo.70.5.937>

References

- Angrand, P., Mouthereau, F., 2021. Evolution of the Alpine orogenic belts in the Western Mediterranean region as resolved by the kinematics of the Europe-Africa diffuse plate boundary. *Bulletin de la Société Géologique de France* 192, 42. <https://doi.org/10.1051/bsgf/2021031>
- Ansermet, S., 1998a. Les mines de fer : description des travaux. *Minaria Helvetica* b, 17–25.
- Ansermet, S., 1998b. Les mines de plomb argentifère et de fluorine du Mont Chemin. *Minaria Helvetica* b, 26–35.
- Antal, J.-W., 1971. The structure of the core of the nappe de Morcles. Université de Lausanne.
- Antoine, P., 1971. La zone des brèches de Tarentaise entre Bourg-Saint-Maurice (vallée de l'Isère) et la frontière italo-suisse. Université de Grenoble.
- Antoine, P., Pairis, J.-L., Pairis, B., 1975. Quelques observations nouvelles sur la structure de la couverture sédimentaire interne du massif du Mont-Blanc, entre le col Ferret (frontière italo-suisse) et la Tête des Fours (Savoie, France). *Géologie Alpine*.
- Ardill, K.E., Paterson, S.R., Stanback, J., Alasino, P.H., King, J.J., Crosbie, S.E., 2020. Schlieren-bound magmatic structures record crystal flow-sorting in dynamic upper-crustal magma-mush chambers. *Frontiers in Earth Science* 190.
- Argand, E., 1924. La tectonique de l'Asie in 13th International Geological Congress. Brussels.
- Argand, E., 1916. Sur l'arc des Alpes occidentales. G. Bridel.
- Arndt, N.T., Fontboté, L., Hedenquist, J.W., Kesler, S.E., Thompson, J.F., Wood, D.G., 2017. Future global mineral resources. *Geochemical Perspectives* 6, 1–171.
- Arthaud, F., Matte, P., 1977. Late Paleozoic strike-slip faulting in southern Europe and northern Africa: Result of a right-lateral shear zone between the Appalachians and the Urals. *Geological Society of America Bulletin* 88, 1305–1320.
- Atkinson, G.M., Finn, W.D.L., Charlwood, R.G., 1984. Simple Computation of Liquefaction Probability for Seismic Hazard Applications. *Earthquake Spectra* 1, 107–123. <https://doi.org/10.1193/1.1585259>
- Aubouin, J., 1961. Propos sur les geosynclinaux. *Bulletin de la Société Géologique de France* S7-III, 629–711. <https://doi.org/10.2113/gssgfbull.S7-III.7.629>

References

- Auzemery, A., Yamato, P., Duretz, T., Willingshofer, E., Matenco, L., Porkoláb, K., 2022. Influence of magma-poor versus magma-rich passive margins on subduction initiation. *Gondwana Research* 103, 172–186. <https://doi.org/10.1016/j.gr.2021.11.012>
- Axen, G.J., 2004. 3. Mechanics of low-angle normal faults, in: *Rheology and Deformation of the Lithosphere at Continental Margins*. Columbia University Press, pp. 46–91.
- Axen, G.J., 1993. Ramp-flat detachment faulting and low-angle normal reactivation of the Tule Springs thrust, southern Nevada. *GSA Bulletin* 105, 1076–1090. [https://doi.org/10.1130/0016-7606\(1993\)105<1076:RFDFA>2.3.CO;2](https://doi.org/10.1130/0016-7606(1993)105<1076:RFDFA>2.3.CO;2)
- Axen, G.J., Hartley, J.M., 1997. Field tests of rolling hinges: Existence, mechanical types, and implications for extensional tectonics. *Journal of Geophysical Research: Solid Earth* 102, 20515–20537.
- B**achmann, O., Bergantz, G., 2008. The Magma Reservoirs That Feed Supereruptions. *Elements* 4, 17–21. <https://doi.org/10.2113/GSELEMENTS.4.1.17>
- Badoux, B., 1972. Tectonique de la Nappe de Morcles entre Rhône et Lizerne. *Matér. Carte géol. Suisse (n.s.)* 143.
- Badoux, H., 1971. Notice explicative de la carte géologique au 1:25'000, feuille 1305 Dt de Morcles. *Comm. géol. suisse*.
- Badoux, H., 1963. Les bélemnites trançonnées de Leytrons. *Bull Soc Vaud Sci Nat* 68, 15–239.
- Badoux, H., Burri, M., Ga, J.H., Krummenacher, D., LouP, G., Sublet, P., 1971. Atlas géologique de la Suisse au 1: 25'000, feuille 1305 Dt de Mordes. *Comm. géol. suisse*.
- Badoux, H., Homewood, P., 1978. Le soubassement de la nappe du Niesen dans la région du Sépey (Alpes vaudoises). *Verlag nicht ermittelbar*.
- Baer, A., 1959. L'extrémité occidentale du massif de l'Aar. *Bull. Soc. neuchât. Sei. nat.* 82.
- Bagby, W.C., Berger, Byron R., 1985. Geologic Characteristics of Sediment-Hosted, Disseminated Precious-Metal Deposits in the Western United States, in: Berger, B. R., Bethke, P.M. (Eds.), *Geology and Geochemistry of Epithermal Systems*. Society of Economic Geologists, p. 0. <https://doi.org/10.5382/Rev.02.08>

References

- Bakker, R.J., 2018. AqSo_NaCl: Computer program to calculate pTVx properties in the H₂O-NaCl fluid system applied to fluid inclusion research and pore fluid calculation. *Computers & geosciences* 115, 122–133.
- Ballentine, C.J., Mazurek, M., Gautschi, A., 1994. Thermal constraints on crustal rare gas release and migration: Evidence from Alpine fluid inclusions. *Geochimica et Cosmochimica Acta* 58, 4333–4348. [https://doi.org/10.1016/0016-7037\(94\)90337-9](https://doi.org/10.1016/0016-7037(94)90337-9)
- Ballèvre, M., Manzotti, P., Dal Piaz, G.V., 2018. Pre-Alpine (Variscan) Inheritance: A Key for the Location of the Future Valaisan Basin (Western Alps). *Tectonics* 37, 786–817. <https://doi.org/10.1002/2017TC004633>
- Barale, L., Bertok, C., d’Atri, A., Mantovani, A., Martire, L., Agostini, S., Bernasconi, S.M., Gerdes, A., Ferrando, S., 2021. Syn-rift hydrothermal circulation in the Mesozoic carbonates of the western Adriatic continental palaeomargin (Western Southalpine Domain, NW Italy). *Basin Research* 33, 3045–3076.
- Barfety, J.C., 1985. Le Jurassique dauphinois entre Durance et Rhône: étude stratigraphique et géodynamique; évolution d’une portion de la marge nord téthysienne (Alpes occidentales françaises). Université Scientifique et Médicale de Grenoble.
- Barfety, J.-C., Gidon, M., 1984. Un exemple de sédimentation sur un abrupt de faille fossile. *Revue de Géologie Dynamique et de Géographie Physique* 25, 267–276.
- Barféty, J.-C., Mouterde, R., 1980. Evolution des faciès du Jurassique dans la zone dauphinoise du Mont Blanc au Pelvoux (Alpes occidentales). *Bull. Soc. géol. France* 557–565.
- Barféty, J.-C., Mouterde, R., 1978. Présence d’Hettangien fossilifère dans le massif du Mont-Joly (Megève, Haute-Savoie). Implications stratigraphiques et conséquences structurales. *C. R. Acad. Sci. Paris* 113–116.
- Barr, D., 1987. Structural/stratigraphic models for extensional basins of half-graben type. *Journal of Structural Geology* 9, 491–500. [https://doi.org/10.1016/0191-8141\(87\)90124-6](https://doi.org/10.1016/0191-8141(87)90124-6)
- Bartley, J.M., 1986. Evaluation of REE mobility in low-grade metabasalts using mass-balance calculations. *Norsk geologisk tidsskrift* 66, 145–152.
- Bartley, J.M., Glazner, A.F., 1985. Hydrothermal systems and Tertiary low-angle normal faulting in the southwestern United States. *Geology* 13, 562–564. [https://doi.org/10.1130/0091-7613\(1985\)13<562:HSATLN>2.0.CO;2](https://doi.org/10.1130/0091-7613(1985)13<562:HSATLN>2.0.CO;2)
- Basile, C., 2015. Transform continental margins — part 1: Concepts and models. *Tectonophysics* 661, 1–10. <https://doi.org/10.1016/j.tecto.2015.08.034>

References

- Basta, E.Z., Saleeb, W.S., 1971. Elba manganese ores and their origin, South-eastern Desert, U.A.R. *Mineralogical Magazine* 38, 235–244. <https://doi.org/10.1180/minmag.1971.038.294.13>
- Battaglia, S., 2004. Variations in the chemical composition of illite from five geothermal fields: a possible geothermometer. *Clay Minerals* 39, 501–510.
- Bau, M., Schmidt, K., Pack, A., Bendel, V., Kraemer, D., 2018. The European Shale: An improved data set for normalisation of rare earth element and yttrium concentrations in environmental and biological samples from Europe. *Applied Geochemistry* 90, 142–149.
- Baud, A., Masson, H., Septfontaine, M., 1977. Karsts et paléotectoniques jurassiques du domaine Briançonnais des Préalpes. *Symposium sur la sédimentation jurassique ouest-européenne*, Paris.
- Baud, A., Megard-Galli, J., 1975. Evolution d'un bassin carbonaté du domaine alpin durant la phase pré-océanique: cycles et séquences dans le Trias de la zone Briançonnaise des Alpes occidentales et des Préalpes. *Verlag nicht ermittelbar*.
- Bauville, A., Schmalholz, S.M., 2015. Transition from thin- to thick-skinned tectonics and consequences for nappe formation: Numerical simulations and applications to the Helvetic nappe system, Switzerland. *Tectonophysics* 665, 101–117. <https://doi.org/10.1016/j.tecto.2015.09.030>
- Bayrakci, G., Minshull, T.A., Sawyer, D.S., Reston, T.J., Klaeschen, D., Papenberg, C., Ranero, C., Bull, J.M., Davy, R.G., Shillington, D.J., 2016. Fault-controlled hydration of the upper mantle during continental rifting. *Nature Geoscience* 9, 384–388.
- Bea, F., Pereira, M.D., Stroh, A., 1994. Mineral/leucosome trace-element partitioning in a peraluminous migmatite (a laser ablation-ICP-MS study). *Chemical Geology* 117, 291–312. [https://doi.org/10.1016/0009-2541\(94\)90133-3](https://doi.org/10.1016/0009-2541(94)90133-3)
- Beales, F.W., 1975. Precipitation mechanisms for Mississippi Valley-type ore deposits. *Economic Geology* 70, 943–948. <https://doi.org/10.2113/gsecongeo.70.5.943>
- Bebout, G.E., Penniston-Dorland, S.C., 2016. Fluid and mass transfer at subduction interfaces—The field metamorphic record. *Lithos* 240–243, 228–258. <https://doi.org/10.1016/j.lithos.2015.10.007>
- Bellahsen, N., Bayet, L., Denele, Y., Waldner, M., Airaghi, L., Rosenberg, C., Dubacq, B., Mouthereau, F., Bernet, M., Pik, R., Lahfid, A., Vacherat, A., 2019. Shortening of the axial zone, pyrenees: Shortening sequence, upper crustal mylonites and crustal strength. *Tectonophysics* 766, 433–452. <https://doi.org/10.1016/j.tecto.2019.06.002>

References

- Bellahsen, N., Jolivet, L., Lacombe, O., Bellanger, M., Boutoux, A., Garcia, S., Mouthereau, F., Le Pourhiet, L., Gumiaux, C., 2012. Mechanisms of margin inversion in the external Western Alps: Implications for crustal rheology. *Tectonophysics* 560, 62–83.
- Bellahsen, N., Mouthereau, F., Boutoux, A., Bellanger, M., Lacombe, O., Jolivet, L., Rolland, Y., 2014. Collision kinematics in the western external Alps. *Tectonics* 33, 1055–1088. <https://doi.org/10.1002/2013TC003453>
- Bellanger, M., Augier, R., Bellahsen, N., Jolivet, L., Monié, P., Baudin, T., Beysac, O., 2015. Shortening of the European Dauphinois margin (Oisans Massif, Western Alps): New insights from RSCM maximum temperature estimates and $^{40}\text{Ar}/^{39}\text{Ar}$ in situ dating. *Journal of Geodynamics* 83, 37–64. <https://doi.org/10.1016/j.jog.2014.09.004>
- Belliere, J., 1988. On the age of mylonites within the Mont Blanc massif. *Geodinamica Acta* 2, 13–16.
- Beltrando, M., Frasca, G., Compagnoni, R., Vitale-Brovarone, A., 2012. The Valaisan controversy revisited: Multi-stage folding of a Mesozoic hyper-extended margin in the Petit St. Bernard pass area (Western Alps). *Tectonophysics* 579, 17–36. <https://doi.org/10.1016/j.tecto.2012.02.010>
- Beltrando, M., Hermann, J., Lister, G., Compagnoni, R., 2007a. On the evolution of orogens: Pressure cycles and deformation mode switches. *Earth and Planetary Science Letters* 256, 372–388.
- Beltrando, M., Rubatto, D., Compagnoni, R., Lister, G., 2007b. Was the Valaisan basin floored by oceanic crust? Evidence of Permian magmatism in the Versoyen Unit (Valaisan domain, NW Alps). *Ophioliti* 32, 85–99.
- Beltrando, M., Stockli, D.F., Decarlis, A., Manatschal, G., 2015. A crustal-scale view at rift localization along the fossil Adriatic margin of the Alpine Tethys preserved in NW Italy. *Tectonics* 34, 1927–1951. <https://doi.org/10.1002/2015TC003973>
- Benioff, H., 1949. SEISMIC EVIDENCE FOR THE FAULT ORIGIN OF OCEANIC DEEPS. *GSA Bulletin* 60, 1837–1856. [https://doi.org/10.1130/0016-7606\(1949\)60\[1837:SEFTFO\]2.0.CO;2](https://doi.org/10.1130/0016-7606(1949)60[1837:SEFTFO]2.0.CO;2)
- Beranek, L.P., 2017. A magma-poor rift model for the Cordilleran margin of western North America. *Geology* 45, 1115–1118. <https://doi.org/10.1130/G39265.1>
- Bergemann, C.A., Gnos, E., Whitehouse, M.J., 2019. Insights into the tectonic history of the Western Alps through dating of fissure monazite in the Mont Blanc and Aiguilles Rouges Massifs. *Tectonophysics* 750, 203–212.
- Berger, A., Herwegh, M., 2019. Cockade structures as a paleo-earthquake proxy in upper crustal hydrothermal systems. *Scientific reports* 9, 1–9.

References

- Bernoulli, D., Caron, C., Homewood, P., 1979. Evolution of continental margins in the Alps. *SCHWEIZ. MINERAL. PETROGR. MITT.* 165–170.
- Bernoulli, D., Manatschal, G., Desmurs, L., Müntener, O., 2003. Where did Gustav Steinmann see the trinity? Back to the roots of an Alpine ophiolite concept, in: Dilek, Y., Newcomb, S. (Eds.), *Ophiolite Concept and the Evolution of Geological Thought*. Geological Society of America, p. 0. <https://doi.org/10.1130/0-8137-2373-6.93>
- Bertotti, G., 1990. Early Mesozoic extension and Alpine tectonics in the western Southern Alps: The geology of the area between Lugano and Menaggio (Lombardy, Northern Italy). *ETH Zurich*.
- Bertotti, G., Picotti, V., Bernoulli, D., Castellarin, A., 1993. From rifting to drifting: tectonic evolution of the South-Alpine upper crust from the Triassic to the Early Cretaceous. *Sedimentary Geology* 86, 53–76. [https://doi.org/10.1016/0037-0738\(93\)90133-P](https://doi.org/10.1016/0037-0738(93)90133-P)
- Bertrand, M., 1884. Rapports de structure des Alpes de Glaris et du bassin houiller du Nord. *Bull. Soc. geol. France*. 3, 318–330.
- Beysac, O., Goffé, B., Chopin, C., Rouzaud, J.N., 2002. Raman spectra of carbonaceous material in metasediments: a new geothermometer. *Journal of Metamorphic Geology* 20, 859–871. <https://doi.org/10.1046/j.1525-1314.2002.00408.x>
- Blengini, G.A., El Latunussa, C., Eynard, U., Torres de Matos, C., Wittmer, D., Georgitzikis, K., Pavel, C., Carrara, S., Mancini, L., Unguru, M., Blagoeva, D., Mathieux, F., Pennington, D., 2020. Study on the EU's list of Critical Raw Materials (2020). *European Commission*.
- Boccaletti, M., ELTER, P., Guazzone, G., 1971. Plate Tectonic Models for the Development of the Western Alps and Northern Apennines. *Nature Physical Science* 234, 108–111. <https://doi.org/10.1038/physci234108a0>
- Boillot, G., 2012. Des marges continentales atlantiques aux chaînes plissées: les recherches françaises entre 1967 et 2000.
- Boillot, G., Recq, M., Winterer, E.L., Meyer, A.W., Applegate, J., Baltuck, M., Bergen, J.A., Comas, M.C., Davies, T.A., Dunham, K., Evans, C.A., Girardeau, J., Goldberg, G., Haggerty, J., Jansa, L.F., Johnson, J.A., Kasahara, J., Loreau, J.P., Luna-Sierra, E., Moullade, M., Ogg, J., Sarti, M., Thurow, J., Williamson, M., 1987. Tectonic denudation of the upper mantle along passive margins: a model based on drilling results (ODP leg 103, western Galicia margin, Spain). *Tectonophysics* 132, 335–342. [https://doi.org/10.1016/0040-1951\(87\)90352-0](https://doi.org/10.1016/0040-1951(87)90352-0)
- Boiron, M.C., Cathelineau, M., Banks, D.A., Buschaert, S., Fourcade, S., Coulibaly, Y., Michelot, J.L., Boyce, A., 2002. Fluid transfers at a basement/cover interface: Part II. Large-scale introduction of chlorine into the basement by Mesozoic basinal brines. *Chemical Geology* 192, 121–140.

References

- Boiron, M.-C., Cathelineau, M., Richard, A., 2010. Fluid flows and metal deposition near basement/cover unconformity: lessons and analogies from Pb–Zn–F–Ba systems for the understanding of Proterozoic U deposits. *Geofluids* 10, 270–292.
- Bond, G.C., Kominz, M.A., 1988. Evolution of thought on passive continental margins from the origin of geosynclinal theory (~1860) to the present. *GSA Bulletin* 100, 1909–1933. [https://doi.org/10.1130/0016-7606\(1988\)100<1909:EOTOPC>2.3.CO;2](https://doi.org/10.1130/0016-7606(1988)100<1909:EOTOPC>2.3.CO;2)
- Bonini, M., Sani, F., Antonielli, B., 2012. Basin inversion and contractional reactivation of inherited normal faults: A review based on previous and new experimental models. *Tectonophysics* 522–523, 55–88. <https://doi.org/10.1016/j.tecto.2011.11.014>
- Bonnemains, D., Escartín, J., Mével, C., Andreani, M., Verlaquet, A., 2017. Pervasive silicification and hanging wall overplating along the 13°20'N oceanic detachment fault (Mid-Atlantic Ridge). *Geochemistry, Geophysics, Geosystems* 18, 2028–2053. <https://doi.org/10.1002/2017GC006846>
- Borsi, L., Schärer, U., Gaggero, L., Crispini, L., 1996. Age, origin and geodynamic significance of plagiogranites in Iherzolites and gabbros of the Piedmont-Ligurian ocean basin. *Earth and Planetary Science Letters* 140, 227–241. [https://doi.org/10.1016/0012-821X\(96\)00034-9](https://doi.org/10.1016/0012-821X(96)00034-9)
- Bos, B., Peach, C.J., Spiers, C.J., 2000. Frictional-viscous flow of simulated fault gouge caused by the combined effects of phyllosilicates and pressure solution. *Tectonophysics* 327, 173–194. [https://doi.org/10.1016/S0040-1951\(00\)00168-2](https://doi.org/10.1016/S0040-1951(00)00168-2)
- Bos, B., Spiers, C.J., 2002. Frictional-viscous flow of phyllosilicate-bearing fault rock: Microphysical model and implications for crustal strength profiles. *Journal of Geophysical Research: Solid Earth* 107, ECV 1-1. <https://doi.org/10.1029/2001JB000301>
- Boschi, C., Früh-Green, G.L., Delacour, A., Karson, J.A., Kelley, D.S., 2006. Mass transfer and fluid flow during detachment faulting and development of an oceanic core complex, Atlantis Massif (MAR 30 N). *Geochemistry, Geophysics, Geosystems* 7.
- Bot, A., Geoffroy, L., Authemayou, C., Bellon, H., Graindorge, D., Pik, R., 2016. Miocene detachment faulting predating EPR propagation: Southern Baja California. *Tectonics* 35, 1153–1176.
- Boullier, A.-M., Fujimoto, K., Ohtani, T., Roman-Ross, G., Lewin, É., Ito, H., Pezard, P., Ildefonse, B., 2004. Textural evidence for recent co-seismic circulation of fluids in the Nojima fault zone, Awaji island, Japan. *Tectonophysics* 378, 165–181. <https://doi.org/10.1016/j.tecto.2003.09.006>

References

- Boulton, C., Davies, T., McSaveney, M., 2009. The frictional strength of granular fault gouge: application of theory to the mechanics of low-angle normal faults. Geological Society, London, Special Publications 321, 9. <https://doi.org/10.1144/SP321.2>
- Bouma, A., 1964. Turbidites, in: *Developments in Sedimentology*. Elsevier, pp. 247–256.
- Bourdelle, F., Cathelineau, M., 2015. Low-temperature chlorite geothermometry: a graphical representation based on a T–R₂–Si diagram. *European Journal of Mineralogy* 27, 617–626.
- Bousquet, R., Goffé, B., Vidal, O., Oberhänsli, R., Patriat, M., 2002. The tectono-metamorphic history of the Valaisan domain from the Western to the Central Alps: New constraints on the evolution of the Alps. *GSA Bulletin* 114, 207–225. [https://doi.org/10.1130/0016-7606\(2002\)114<0207:TTMHOT>2.0.CO;2](https://doi.org/10.1130/0016-7606(2002)114<0207:TTMHOT>2.0.CO;2)
- Bousquet, R., Oberhänsli, R., Goffé, B., Wiederkehr, M., Koller, F., Schmid, S.M., Schuster, R., Engi, M., Berger, A., Martinotti, G., 2008. Metamorphism of metasediments at the scale of an orogen: a key to the Tertiary geodynamic evolution of the Alps. Geological Society, London, Special Publications 298, 393–411.
- Boutoux, A., Bellahsen, N., Nanni, U., Pik, R., Verlaquet, A., Rolland, Y., Lacombe, O., 2016. Thermal and structural evolution of the external Western Alps: Insights from (U–Th–Sm)/He thermochronology and RSCM thermometry in the Aiguilles Rouges/Mont Blanc massifs. *Tectonophysics* 683, 109–123.
- Braathen, A., Osmundsen, P.T., Gabrielsen, R.H., 2004. Dynamic development of fault rocks in a crustal-scale detachment: An example from western Norway. *Tectonics* 23. <https://doi.org/10.1029/2003TC001558>
- BRGM, 1984. Les gisements de Pb-Zn français (No. 2), Ressources minières françaises. Bureau de recherche géologique et minière.
- Brune, S., 2018. Forces within continental and oceanic rifts: Numerical modeling elucidates the impact of asthenospheric flow on surface stress. *Geology* 46, 191–192.
- Buck, W.R., 1993. Effect of lithospheric thickness on the formation of high- and low-angle normal faults. *Geology* 21, 933–936. [https://doi.org/10.1130/0091-7613\(1993\)021<0933:EOLTOT>2.3.CO;2](https://doi.org/10.1130/0091-7613(1993)021<0933:EOLTOT>2.3.CO;2)
- Buck, W.R., Martinez, F., Steckler, M.S., Cochran, J.R., 1988. Thermal consequences of lithospheric extension: Pure and simple. *Tectonics* 7, 213–234. <https://doi.org/10.1029/TC007i002p00213>

References

- Bullard, E., Everett, J.E., Gilbert Smith, A., 1965. The fit of the continents around the Atlantic. *Philosophical Transactions of the Royal Society of London. Series A, Mathematical and Physical Sciences* 258, 41–51.
- Burg, J.-P., van den Driessche, J., Brun, J.-P., 1994. Syn-to post-thickening extension in the Variscan Belt of Western Europe: modes and structural consequences. *Géologie de la France* 33–51.
- Burke, K., Dewey, J.F., Kidd, W.S.F., 1977. World distribution of sutures — the sites of former oceans. *Tectonophysics* 40, 69–99. [https://doi.org/10.1016/0040-1951\(77\)90030-0](https://doi.org/10.1016/0040-1951(77)90030-0)
- Burkhard, M., 1988. L’Helvétique de la bordure occidentale du massif de l’Aar (évolution tectonique et métamorphique). *Eclogae Geologicae Helvetiae* 63–114.
- Bussy, F., 1990. Pétrogenèse des enclaves microgrenues associées aux granitoïdes calco-alcalins: exemple des massifs varisque du Mont Blanc (Alpes occidentales) et miocène du Monte Capanne (Ile d’Elbe, Italie).
- Bussy, F., Hernandez, J., Von Raumer, J., 2001. Bimodal magmatism as a consequence of the post-collisional readjustment of the thickened Variscan continental lithosphere (Aiguilles Rouges-Mont Blanc Massifs, Western Alps). *SPECIAL PAPERS-GEOLOGICAL SOCIETY OF AMERICA* 221–234.
- Butler, R.W., 2017. Basement–cover tectonics, structural inheritance and deformation migration in the outer parts of orogenic belts: a view from the western Alps. *Geological Society of America, Memoirs* 213, 55–74.
- Butler, R.W.H., 1989. The influence of pre-existing basin structure on thrust system evolution in the Western Alps. *Geological Society, London, Special Publications* 44, 105. <https://doi.org/10.1144/GSL.SP.1989.044.01.07>
- Butler, R.W.H., 1986. Thrust tectonics, deep structure and crustal subduction in the Alps and Himalayas. *Journal of the Geological Society* 143, 857. <https://doi.org/10.1144/gsjgs.143.6.0857>
- Butler, R.W.H., 1985. The restoration of thrust systems and displacement continuity around the Mont Blanc massif, NW external Alpine thrust belt. *Journal of Structural Geology* 7, 569–582. [https://doi.org/10.1016/0191-8141\(85\)90029-X](https://doi.org/10.1016/0191-8141(85)90029-X)
- Buxtorf, A., 1907. Profile durch das nordschweizerische Juragebirge, der Kettenjura als “gefaltete Abscherungdecke” aufgefasst. Bericht über die 30ste Versammlung des Oberrheinischen Vereinigung zu Lindau 29–38.
- Byerlee, J., 1978. Friction of rocks, in: *Rock Friction and Earthquake Prediction*. Springer, pp. 615–626.

- Cadenas, P., Fernández-Viejo, G., Pulgar, J.A., Tugend, J., Manatschal, G., Minshull, T.A., 2018. Constraints Imposed by Rift Inheritance on the Compressional Reactivation of a Hyperextended Margin: Mapping Rift Domains in the North Iberian Margin and in the Cantabrian Mountains. *Tectonics* 37, 758–785. <https://doi.org/10.1002/2016TC004454>
- Cadenas, P., Lescoutre, R., Manatschal, G., Fernández-Viejo, G., 2021. The role of extensional detachment systems in thinning the crust and exhuming granulites: analogies between the offshore Le Danois High and the onshore Labourd Massif in the Biscay/ Pyrenean rifts. *BSGF - Earth Sciences Bulletin Special Issue Orogen lifecycle: learnings and perspectives from Pyrenees, Western Mediterranean and analogues*.
- Caine, J.S., Evans, J.P., Forster, C.B., 1996. Fault zone architecture and permeability structure. *Geology* 24, 1025–1028. [https://doi.org/10.1130/0091-7613\(1996\)024<1025:FZAAPS>2.3.CO;2](https://doi.org/10.1130/0091-7613(1996)024<1025:FZAAPS>2.3.CO;2)
- Cannat, M., Fontaine, F., Escartin, J., 2010. Serpentinization and associated hydrogen and methane fluxes at slow spreading ridges. *American Geophysical Union*.
- Cannat, M., Mevel, C., Maia, M., Deplus, C., Durand, C., Gente, P., Agrinier, P., Belarouchi, A., Dubuisson, G., Humler, E., Reynolds, J., 1995. Thin crust, ultramafic exposures, and rugged faulting patterns at the Mid-Atlantic Ridge (22°–24°N). *Geology* 23, 49–52. [https://doi.org/10.1130/0091-7613\(1995\)023<0049:TCUEAR>2.3.CO;2](https://doi.org/10.1130/0091-7613(1995)023<0049:TCUEAR>2.3.CO;2)
- Capdevila, R., Boillot, G., Lepvrier, C., Malod, J.A., Mascle, G., 1980. METAMORPHIC AND PLUTONIC ROCKS FROM THE LE-DANOIS BANK (NORTH IBERIAN MARGIN). *COMPTES RENDUS HEBDOMADAIRES DES SEANCES DE L ACADEMIE DES SCIENCES SERIE D* 291, 317–+.
- Capuzzo, N., Bussy, F., 2000. High-precision dating and origin of synsedimentary volcanism in the Late Carboniferous Salvan-Dorénaz basin (Aiguilles-Rouges Massif, Western Alps). *Schweizerische Mineralogische und Petrographische Mitteilungen* 80, 147–167.
- Capuzzo, N., Handler, R., Neubauer, F., Wetzel, A., 2003. Post-collisional rapid exhumation and erosion during continental sedimentation: the example of the late Variscan Salvan-Dorénaz basin (Western Alps). *International Journal of Earth Sciences* 92, 364–379.
- Cardello, G.L., 2013. The Rawil depression: its structural history from Cretaceous to Neogene. *ETH Zurich*.
- Cardello, G.L., Di Vincenzo, G., Giorgetti, G., Zwingmann, H., Mancktelow, N., 2019. Initiation and development of the Pennine Basal Thrust (Swiss Alps): a structural and geochronological study of an exhumed megathrust. *Journal of Structural Geology* 126, 338–356.

References

- Cardello, G.L., Mancktelow, N.S., 2014. Cretaceous syn-sedimentary faulting in the Wildhorn Nappe (SW Switzerland). *Swiss Journal of Geosciences* 107, 223–250.
<https://doi.org/10.1007/s00015-014-0166-8>
- Carter, M.J., Siebenaller, L., Teyssier, C., 2015. Orientation, composition, and entrapment conditions of fluid inclusions in the footwall of the northern Snake Range detachment, Nevada. *Journal of Structural Geology* 81, 106–124. <https://doi.org/10.1016/j.jsg.2015.11.001>
- Castello, P., 1977. Lo lalofane e gli altri minerali del giacimento piombo-baritico del Trou des Romains, (Courmayeur, Valle d’Aosta). *Rivista Mineralogica Italiana*, Milano 8.
- Cathelineau, M., 1988. Cation site occupancy in chlorites and illites as a function of temperature. *Clay minerals* 23, 471–485.
- Cathelineau, M., Boiron, M.C., Holliger, P., Poty, B., 1990. Metallogensis of the French part of the Variscan orogen. Part II: Time-space relationships between U, Au and Sn–W ore deposition and geodynamic events — mineralogical and U–Pb data. *Tectonophysics* 177, 59–79.
[https://doi.org/10.1016/0040-1951\(90\)90274-C](https://doi.org/10.1016/0040-1951(90)90274-C)
- Cathelineau, M., Boiron, M.-C., Jakomulski, H., 2021. Triassic evaporites: a vast reservoir of brines mobilized successively during rifting and thrusting in the Pyrenees. *Journal of the Geological Society* 178.
- Cathles, L.M., III, Adams, J.J., 2005. Fluid Flow and Petroleum and Mineral Resources in the Upper (<20-km) Continental Crust, in: Hedenquist, J.W., Thompson, J.F.H., Goldfarb, R.J., Richards, J.P. (Eds.), *One Hundredth Anniversary Volume*. Society of Economic Geologists, p. 0.
<https://doi.org/10.5382/AV100.05>
- Caumon, M.-C., Dubessy, J., Robert, P., Tarantola, A., 2013. Fused-silica capillary capsules (FSCCs) as reference synthetic aqueous fluid inclusions to determine chlorinity by Raman spectroscopy. *European Journal of Mineralogy* 25, 755–763.
- Caumon, M.-C., Tarantola, A., Mosser-Ruck, R., 2015. Raman spectra of water in fluid inclusions: I. Effect of host mineral birefringence on salinity measurement. *Journal of Raman Spectroscopy* 46, 969–976.
- Cavin, L., Piuze, A., 2020. A several-kilometer-long archosaur route in the triassic of the swiss alps. *Frontiers in Earth Science* 8, 4.
- Célini, N., Mouthereau, F., Lahfid, A., Gout, C., Callot, J.-P., 2022. Rift thermal inheritance in the SW Alps (France): insights from RSCM thermometry and 1D thermal numerical modelling. *EGU sphere* 1–18.

References

- Cenki-Tok, B., Darling, J.R., Rolland, Y., Dhuime, B., Storey, C.D., 2014. Direct dating of mid-crustal shear zones with synkinematic allanite: new in situ U-Th-Pb geochronological approaches applied to the Mont Blanc massif. *Terra Nova* 26, 29–37. <https://doi.org/10.1111/ter.12066>
- Centrella, S., Beaudoin, N.E., Derluyn, H., Motte, G., Hoareau, G., Lanari, P., Piccoli, F., Pecheyran, C., Callot, J.P., 2021. Micro-scale chemical and physical patterns in an interface of hydrothermal dolomitization reveals the governing transport mechanisms in nature: Case of the Layens anticline, Pyrenees, France. *Sedimentology* 68, 834–854.
- Chao, P., 2021. Tectono-sedimentary and magmatic evolution of rifting and early seafloor spreading in the NW propagator of the South China Sea. *Strasbourg*.
- Chao, P., Manatschal, G., Chenin, P., Ren, J., Zhang, C., Pang, X., Zheng, J., Yang, L., Kuznir, N., 2021. The tectono-stratigraphic and magmatic evolution of conjugate rifted margins: Insights from the NW South China Sea. *Journal of Geodynamics* 148, 101877. <https://doi.org/10.1016/j.jog.2021.101877>
- Chelle-Michou, C., McCarthy, A., Moyen, J.-F., Cawood, P.A., Capitanio, F.A., 2022. Make subductions diverse again. *Earth-Science Reviews* 226, 103966. <https://doi.org/10.1016/j.earscirev.2022.103966>
- Chenin, P., Manatschal, G., Ghienne, J.-F., Chao, P., 2022. The syn-rift tectono-stratigraphic record of rifted margins (Part II): A new model to break through the proximal/distal interpretation frontier. *Basin Research* 34, 489–532.
- Chenin, P., Schmalholz, S.M., Manatschal, G., Duretz, T., 2020. Impact of crust–mantle mechanical coupling on the topographic and thermal evolutions during the necking phase of ‘magma-poor’ and ‘sediment-starved’ rift systems: A numerical modeling study. *Tectonophysics* 786, 228472. <https://doi.org/10.1016/j.tecto.2020.228472>
- Chenin, P., Jammes, S., Lavier, L.L., Manatschal, G., Picazo, S., Müntener, O., Karner, G.D., Figueredo, P.H., Johnson, C., 2019a. Impact of mafic underplating and mantle depletion on subsequent rifting: a numerical modeling study. *Tectonics* 38, 2185–2207.
- Chenin, P., Manatschal, G., Decarlis, A., Schmalholz, S.M., Duretz, T., Beltrando, M., 2019b. Emersion of Distal Domains in Advanced Stages of Continental Rifting Explained by Asynchronous Crust and Mantle Necking. *Geochemistry, Geophysics, Geosystems* 20, 3821–3840. <https://doi.org/10.1029/2019GC008357>
- Chenin, P., Picazo, S., Jammes, S., Manatschal, G., Müntener, O., Karner, G., 2019c. Potential role of lithospheric mantle composition in the Wilson cycle: a North Atlantic perspective. *Geological Society, London, Special Publications* 470, 157–172.

References

- Chenin, P., Schmalholz, S.M., Manatschal, G., Karner, G.D., 2018. Necking of the Lithosphere: A Reappraisal of Basic Concepts With Thermo-Mechanical Numerical Modeling. *Journal of Geophysical Research: Solid Earth* 123, 5279–5299. <https://doi.org/10.1029/2017JB014155>
- Chenin, P., Manatschal, G., Picazo, S., Müntener, O., Karner, G., Johnson, C., Ulrich, M., 2017. Influence of the architecture of magma-poor hyperextended rifted margins on orogens produced by the closure of narrow versus wide oceans. *Geosphere* 13, 559–576. <https://doi.org/10.1130/GES01363.1>
- Chenin, P., 2016. Unravelling the impact of inheritance on the Wilson Cycle: A combined mapping and numerical modelling approach applied to the North Atlantic rift system. Strasbourg.
- Cherniak, D.J., 1997. An experimental study of strontium and lead diffusion in calcite, and implications for carbonate diagenesis and metamorphism. *Geochimica et Cosmochimica Acta* 61, 4173–4179. [https://doi.org/10.1016/S0016-7037\(97\)00236-6](https://doi.org/10.1016/S0016-7037(97)00236-6)
- Chessex, R., 1959. La géologie de la haute vallée d'Abondance, Haute-Savoie (France). *Eclogae Geologicae Helvetiae*.
- Chessex, R., Rivier, F., 1957. Le gisement des Trappistes près de Sembrancher (Valais). *Bulletin de La Murithienne* 25–49.
- Chevalier, F., 2002. Vitesse et cyclicité de fonctionnement des failles normales de rift: implication sur le remplissage stratigraphique des bassins et sur les modalités d'extension d'une marge passive fossile: application au demi-graben liasique de Bourg-d'Oisans (Alpes occidentales, France). Université de Bourgogne.
- Chevalier, F., Guiraud, M., Garcia, J.-P., Dommergues, J.-L., Quesne, D., Allemand, P., Dumont, T., 2003. Calculating the long-term displacement rates of a normal fault from the high-resolution stratigraphic record (early Tethyan rifting, French Alps). *Terra Nova* 15, 410–416.
- Chew, D.M., Petrus, J.A., Kamber, B.S., 2014. U–Pb LA–ICPMS dating using accessory mineral standards with variable common Pb. *Chemical Geology* 363, 185–199.
- Chopin, C., 1984. Coesite and pure pyrope in high-grade blueschists of the Western Alps: a first record and some consequences. *Contributions to Mineralogy and Petrology* 86, 107–118.
- Choubert, B., 1935. Recherches sur la genèse des chaînes paléozoïques et antécambriennes. *Rev. Géogr. phys. Géol. dyn* 8, 5–50.

References

- Christie-Blick, N., Anders, M.H., Wills, S., Walker, C.D., Renik, B., 2007. Observations from the Basin and Range Province (western United States) pertinent to the interpretation of regional detachment faults. *Geological Society, London, Special Publications* 282, 421–441.
- Claesson, L., Skelton, A., Graham, C., Dietl, C., Mörrth, M., Torssander, P., Kockum, I., 2004. Hydrogeochemical changes before and after a major earthquake. *Geology* 32, 641–644. <https://doi.org/10.1130/G20542.1>
- Clark, C., James, P., 2003. Hydrothermal brecciation due to fluid pressure fluctuations: examples from the Olary Domain, South Australia. *Tectonophysics* 366, 187–206. [https://doi.org/10.1016/S0040-1951\(03\)00095-7](https://doi.org/10.1016/S0040-1951(03)00095-7)
- Clerc, C., Lagabrielle, Y., Labaume, P., Ringenbach, J.-C., Vauchez, A., Nalpas, T., Bousquet, R., Ballard, J.-F., Lahfid, A., Fourcade, S., 2016. Basement – Cover decoupling and progressive exhumation of metamorphic sediments at hot rifted margin. Insights from the Northeastern Pyrenean analog. *Tectonophysics* 686, 82–97. <https://doi.org/10.1016/j.tecto.2016.07.022>
- Clinton, D., 2011. Mont-Chemin Au-Ag property, Marécottes U property and Siviez U-Cu property (No. NI-43-101).
- Collart, J., 1973. La zone des brèches de Tarentaise entre Montgirod et le vallon du Cornet d'Arêches (au Nord de Moûtiers), Savoie-Alpes françaises. Université Scientifique et Médicale de Grenoble.
- Collet, L.-W., 1947. Les Ammonites du Lias dans le Ferdenrothom (Nappe de Morcles, Lôtschental). *Eclogae Geologicae Helveticae* 1–6.
- Collettini, C., 2011. The mechanical paradox of low-angle normal faults: Current understanding and open questions. *Tectonophysics* 510, 253–268.
- Collettini, C., Tesei, T., Scuderi, M.M., Carpenter, B.M., Viti, C., 2019. Beyond Byerlee friction, weak faults and implications for slip behavior. *Earth and Planetary Science Letters* 519, 245–263. <https://doi.org/10.1016/j.epsl.2019.05.011>
- Collettini, C., Viti, C., Smith, S.A.F., Holdsworth, R.E., 2009. Development of interconnected talc networks and weakening of continental low-angle normal faults. *Geology* 37, 567–570. <https://doi.org/10.1130/G25645A.1>
- Colombo, F., Ghiglione, G., Compagnoni, R., 1993. Relitti di porfidi granitici a xenoliti granulitici nelle migmatiti dell'Argentera (Alpi Marittime). *Plinius* 10, 113–116.

References

- Coltat, R., Boulvais, P., Branquet, Y., Collot, J., Epin, M.E., Manatschal, G., 2019. Syntectonic carbonation during symagmatic mantle exhumation at an ocean-continent transition. *Geology* 47, 183–186. <https://doi.org/10.1130/G45530.1>
- Coltat, R., Boulvais, P., Branquet, Y., Poujol, M., Gautier, P., Manatschal, G., 2021. Discussion to “Oxygen isotope in ophicalcites: an ever-lasting controversy?” *International Journal of Earth Sciences* 110, 1117–1121.
- Coltat, R., Boulvais, P., Riegler, T., Pelleter, E., Branquet, Y., 2021. Element distribution in the root zone of ultramafic-hosted black smoker-like systems: Constraints from an Alpine analog. *Chemical Geology* 559, 119916. <https://doi.org/10.1016/j.chemgeo.2020.119916>
- Compagnoni, R., Sturani, C., Elter, G., 1964. Segnalazione di Albiano fossilifero nel tratto valdostano della zona delfinese-elvetica. *Accademia Nazionale dei Lincei*.
- Cooper, M., 1975. Exploration evaluation “Anvil group” - Anvil mining district, Yukon Territory. (No. ARMC019530). Energy, Mines and Resources Property.
- Costa, E., Troilo, F., 2013. Materiali di interesse gemmologico dalla Valle d’Aosta. *REV. VALDÔTAINE HIST. NAT.* 67, 5–28.
- Costa, S., Caby, R., 2001. Evolution of the Ligurian Tethys in the Western Alps: Sm/Nd and U/Pb geochronology and rare-earth element geochemistry of the Montgenèvre ophiolite (France). *Chemical Geology* 175, 449–466. [https://doi.org/10.1016/S0009-2541\(00\)00334-X](https://doi.org/10.1016/S0009-2541(00)00334-X)
- Coward, M.P., 1986. Heterogeneous stretching, simple shear and basin development. *Earth and Planetary Science Letters* 80, 325–336. [https://doi.org/10.1016/0012-821X\(86\)90114-7](https://doi.org/10.1016/0012-821X(86)90114-7)
- Cox, S.F., 2005. Coupling between Deformation, Fluid Pressures, and Fluid Flow in Ore-Producing Hydrothermal Systems at Depth in the Crust, in: Hedenquist, J.W., Thompson, J.F.H., Goldfarb, R.J., Richards, J.P. (Eds.), *One Hundredth Anniversary Volume. Society of Economic Geologists*, p. 0. <https://doi.org/10.5382/AV100.04>
- Craw, D., 1997. Fluid inclusion evidence for geothermal structure beneath the Southern Alps, New Zealand. *New Zealand Journal of Geology and Geophysics* 40, 43–52.
- Cruden, A.R., McCaffrey, K.J., Bungler, A.P., 2017. Geometric scaling of tabular igneous intrusions: Implications for emplacement and growth, in: *Physical Geology of Shallow Magmatic Systems*. Springer, pp. 11–38.
- Cuney, M., 2014. Felsic magmatism and uranium deposits. *Bulletin de la Société Géologique de France* 185, 75–92. <https://doi.org/10.2113/gssgfbull.185.2.75>

References

- Curewitz, D., Karson, J.A., 1997. Structural settings of hydrothermal outflow: Fracture permeability maintained by fault propagation and interaction. *Journal of Volcanology and Geothermal Research* 79, 149–168. [https://doi.org/10.1016/S0377-0273\(97\)00027-9](https://doi.org/10.1016/S0377-0273(97)00027-9)
- Dadet, P., Marchesseau, J., Millon, R., Motti, E., Schürmann, H.M.E., 1970. Mineral Occurrences Related to Stratigraphy and Tectonics in Tertiary Sediments near Umm Lajj, Eastern Red Sea Area, Saudi Arabia. *Philosophical Transactions for the Royal Society of London. Series A, Mathematical and Physical Sciences* 99–106.
- Dahlen, F.A., Suppe, J., Davis, D., 1984. Mechanics of fold-and-thrust belts and accretionary wedges: Cohesive Coulomb theory. *Journal of Geophysical Research: Solid Earth* 89, 10087–10101.
- Dai, S., Li, T., Jiang, Y., Ward, C.R., Hower, J.C., Sun, J., Liu, J., Song, H., Wei, J., Li, Q., 2015. Mineralogical and geochemical compositions of the Pennsylvanian coal in the Hailiushu Mine, Daqingshan Coalfield, Inner Mongolia, China: Implications of sediment-source region and acid hydrothermal solutions. *International Journal of Coal Geology* 137, 92–110.
- Dall’Asta, N., Hoareau, G., Manatschal, G., Centrella, S., Denèle, Y., Ribes, C., Kalifi, A., 2022. Structural and petrological characteristics of a Jurassic detachment fault from the Mont-Blanc massif (Col du Bonhomme area, France). *Journal of Structural Geology* 104593. <https://doi.org/10.1016/j.jsg.2022.104593>
- Dall’Asta, N., 2019. Sedimentary systems associated with the necking of continental crust during rifting: the example of the ‘Grès Singulier’ Formation (Mont-Blanc massif, Western Alps) (Master dissertation). Université de Strasbourg.
- Daly, R.A., 1942. *The Floor of the Ocean*. University of North Carolina Press, Chapel Hill.
- Dana, J.D., 1873. On some results of the earth’s contraction from cooling including a discussion of the origin of mountains and the nature of the earth’s interior. *Am J Sci* s3-5, 423. <https://doi.org/10.2475/ajs.s3-5.30.423>
- Davies, J., von Blanckenburg, F., 1995. Slab breakoff: A model of lithosphere detachment and its test in the magmatism and deformation of collisional orogens. *Earth and Planetary Science Letters* 129, 85–102. [https://doi.org/10.1016/0012-821X\(94\)00237-S](https://doi.org/10.1016/0012-821X(94)00237-S)
- Davis, B.K., McPhie, J., 1996. Spherulites, quench fractures and relict perlite in a Late Devonian rhyolite dyke, Queensland, Australia. *Journal of Volcanology and Geothermal Research* 71, 1–11. [https://doi.org/10.1016/0377-0273\(95\)00063-1](https://doi.org/10.1016/0377-0273(95)00063-1)
- Davis, G.H., Reynolds, S.J., Kluth, C.F., 2011. *Structural geology of rocks and regions*. John Wiley & Sons.

References

- de Beaumont, L.É., 1829. Recherches sur quelques-unes des révolutions de la surface du globe. *Annales des Sciences Naturelles* 284–417.
- de Beaumont, L.É., Brongniart, A., 1828. Notice sur un gisement de végétaux fossiles et de Bélemnites, situé à Petit-Coeur près Moutiers, en Tarentaise. Crochard.
- De Charpal, O., Guennoc, P., Montadert, L., Roberts, D.G., 1978. Rifting, crustal attenuation and subsidence in the Bay of Biscay. *Nature* 275, 706–711.
- De Graciansky, P.-C., Roberts, D.G., Tricart, P., 2010. The Western Alps, from rift to passive margin to orogenic belt: an integrated geoscience overview. Elsevier.
- De Pieri, R., Quarenzi, S., Hall, K.M., 1977. Refinement of the structures of low and high hyalophanes. *Acta Crystallographica Section B: Structural Crystallography and Crystal Chemistry* 33, 3073–3076.
- De Wever, P., Danelian, T., Durand-Delga, M., Cordey, F., Kito, N., 1987. Datations des radiolarites post-ophiolitiques de Corse alpine à l'aide des Radiolaires. *CR Acad. Sci. Paris* 305, 893–900.
- Debelmas, J., Lemoine, M., 1970. The western Alps: palaeogeography and structure. *Earth-Science Reviews* 6, 221–256.
- Debon, F., Lemmet, M., 1999. Evolution of Mg/Fe Ratios in Late Variscan Plutonic Rocks from the External Crystalline Massifs of the Alps (France, Italy, Switzerland). *Journal of Petrology* 40, 1151–1185. <https://doi.org/10.1093/petroj/40.7.1151>
- Debret, B., Beunon, H., Mattielli, N., Andreani, M., Ribeiro da Costa, I., Escartin, J., 2018. Ore component mobility, transport and mineralization at mid-oceanic ridges: A stable isotopes (Zn, Cu and Fe) study of the Rainbow massif (Mid-Atlantic Ridge 36°14'N). *Earth and Planetary Science Letters* 503, 170–180. <https://doi.org/10.1016/j.epsl.2018.09.009>
- Decarlis, A., Beltrando, M., Manatschal, G., Ferrando, S., Carosi, R., 2017a. Architecture of the Distal Piedmont-Ligurian Rifted Margin in NW Italy: Hints for a Flip of the Rift System Polarity. *Tectonics* 36, 2388–2406. <https://doi.org/10.1002/2017TC004561>
- Decarlis, A., Fellin, M.G., Maino, M., Ferrando, S., Manatschal, G., Gaggero, L., Seno, S., Stuart, F.M., Beltrando, M., 2017b. Tectono-thermal Evolution of a Distal Rifted Margin: Constraints From the Calizzano Massif (Prepiedmont-Briançonnais Domain, Ligurian Alps). *Tectonics* 36, 3209–3228.
- Decrausaz, T., Müntener, O., Manzotti, P., Lafay, R., Spandler, C., 2021. Fossil oceanic core complexes in the Alps. New field, geochemical and isotopic constraints from the Tethyan Aiguilles

References

- Rouges Ophiolite (Val d'Hérens, Western Alps, Switzerland). *Swiss Journal of Geosciences* 114, 1–27.
- Delaloye, M., Bertrand, J., 1976. Datation par la méthode K-Ar de diverses ophiolites du flysch des Gets (Haute-Savoie, France). *Eclogae Geologicae Helvetiae* 69, 335–341.
- Demathieu, G., Weidmann, M., 1982. Les empreintes de pas de reptiles dans le Trias du Vieux Emosson. *Eclogae Geologicae Helvetiae* 721–757.
- Dempster, T.J., 1986. Isotope systematics in minerals: biotite rejuvenation and exchange during Alpine metamorphism. *Earth and Planetary Science Letters* 78, 355–367. [https://doi.org/10.1016/0012-821X\(86\)90003-8](https://doi.org/10.1016/0012-821X(86)90003-8)
- Desmurs, L., Müntener, O., Manatschal, G., 2002. Onset of magmatic accretion within a magma-poor rifted margin: a case study from the Platta ocean-continent transition, eastern Switzerland. *Contributions to Mineralogy and Petrology* 144, 365–382.
- Dewey, J.F., Burke, K., 1974. Hot Spots and Continental Break-up: Implications for Collisional Orogeny. *Geology* 2, 57–60. [https://doi.org/10.1130/0091-7613\(1974\)2<57:HSACBI>2.0.CO;2](https://doi.org/10.1130/0091-7613(1974)2<57:HSACBI>2.0.CO;2)
- Dewey, John.F., Pitman, Walter.C.I., Ryan, W.B.F., Bonnin, J., 1973. Plate Tectonics and the Evolution of the Alpine System. *GSA Bulletin* 84, 3137–3180. [https://doi.org/10.1130/0016-7606\(1973\)84<3137:PTATEO>2.0.CO;2](https://doi.org/10.1130/0016-7606(1973)84<3137:PTATEO>2.0.CO;2)
- Dietz, R.S., 1961. Continent and ocean basin evolution by spreading of the sea floor. *Nature* 190, 854–857.
- Ding, K., Seyfried, W.E., Zhang, Z., Tivey, M.K., Von Damm, K.L., Bradley, A.M., 2005. The in situ pH of hydrothermal fluids at mid-ocean ridges. *Earth and Planetary Science Letters* 237, 167–174. <https://doi.org/10.1016/j.epsl.2005.04.041>
- Doepke, D., 2017. Modelling the Thermal History of Onshore Ireland, Britain and Its Offshore Basins Using Low-temperature Thermochronology. Trinity College Dublin.
- Dogliani, C., Dagostino, N., Mariotti, G., 1998. Normal faulting vs regional subsidence and sedimentation rate. *Marine and Petroleum Geology* 15, 737–750. [https://doi.org/10.1016/S0264-8172\(98\)00052-X](https://doi.org/10.1016/S0264-8172(98)00052-X)
- Dong, G., Morrison, G.W., 1995. Adularia in epithermal veins, Queensland: morphology, structural state and origin. *Mineralium Deposita* 30, 11–19.
- Doré, T., Lundin, E., 2015. RESEARCH FOCUS: Hyperextended continental margins—Knowns and unknowns. *Geology* 43, 95–96. <https://doi.org/10.1130/focus012015.1>

References

- Dorignaux, D., 2017. Genèse et minéralogie d'un filon à fluorite riche en terres rares en bordure septentrionale du massif du Mont-Blanc (Mont Chemin, Valais, Suisse).
- Dotare, T., Yamada, Y., Adam, J., Hori, T., Sakaguchi, H., 2016. Initiation of a thrust fault revealed by analog experiments. *Tectonophysics* 684, 148–156.
<https://doi.org/10.1016/j.tecto.2015.12.023>
- Dresen, G., 1991. Stress distribution and the orientation of Riedel shears. *Tectonophysics* 188, 239–247. [https://doi.org/10.1016/0040-1951\(91\)90458-5](https://doi.org/10.1016/0040-1951(91)90458-5)
- Driscoll, N.W., Hogg, J.R., Christie-Blick, N., Karner, G.D., 1995. Extensional tectonics in the Jeanne d'Arc Basin, offshore Newfoundland: implications for the timing of break-up between Grand Banks and Iberia. Geological Society, London, Special Publications 90, 1.
<https://doi.org/10.1144/GSL.SP.1995.090.01.01>
- Drost, K., Chew, D., Petrus, J.A., Scholze, F., Woodhead, J.D., Schneider, J.W., Harper, D.A., 2018. An image mapping approach to U-Pb LA-ICP-MS carbonate dating and applications to direct dating of carbonate sedimentation. *Geochemistry, Geophysics, Geosystems* 19, 4631–4648.
- Du Toit, A.L., 1937. *Our wandering continents: an hypothesis of continental drifting*. Oliver and Boyd.
- Dubessy, J., Lhomme, T., Boiron, M.-C., Rull, F., 2002. Determination of chlorinity in aqueous fluids using Raman spectroscopy of the stretching band of water at room temperature: application to fluid inclusions. *Applied spectroscopy* 56, 99–106.
- Ducoux, M., Jolivet, L., Cagnard, F., Baudin, T., 2021. Basement-cover decoupling during the inversion of a hyperextended basin: Insights from the Eastern Pyrenees. *Tectonics* 40, e2020TC006512.
- Ducoux, M., Jolivet, L., Callot, J.-P., Aubourg, C., Masini, E., Lahfid, A., Homonnay, E., Cagnard, F., Gumiaux, C., Baudin, T., 2019. The Nappe des Marbres unit of the Basque-Cantabrian Basin: the tectono-thermal evolution of a fossil hyperextended rift basin. *Tectonics* 38, 3881–3915.
- Ducoux, M., Masini, E., Scharf, A., Calassou, S., 2022. The Neotethyan Arabian necking zone exposed at the SE Oman mountains: field evidence and consequences. *Copernicus Meetings*.
- Dulfer, H., Milligan, P.R., Coghlan, R., Czarnota, K., Hight, L.M., Champion, D.C., Skirrow, R.G., 2016. Potential for intrusion-hosted Ni-Cu-PGE sulfide deposits in Australia: a continental-scale analysis of mineral system prospectivity. *Geoscience Australia*.
- Dumas, J.-P., 1964. *Contribution à l'étude géologique et minière de la vallée du Bon Nant (Haute-Savoie)* (Dipl. études sup. Géol. (DES)). Université de Grenoble.

References

- Dumont, T., Lemoine, M., Tricart, P., 1984. Pérennité de la sédimentation pélagique du Jurassique supérieur jusque dans le crétacé supérieur au-dessus de la croûte océanique téthysienne ligure: la série supra-ophiolitique du lac des Cordes (zone piémontaise des Alpes occidentales au SE de Briançon). *Comptes-rendus des séances de l'Académie des sciences. Série 2, Mécanique-physique, chimie, sciences de l'univers, sciences de la terre* 299, 1069–1072.
- Duparc, L., Pearce, F., 1898. Sur le poudingue de l'Amône (Mont-Blanc). *C. R. Acad. Sci.*, 126.
- Duretz, T., Petri, B., Mohn, G., Schmalholz, S.M., Schenker, F.L., Müntener, O., 2016. The importance of structural softening for the evolution and architecture of passive margins. *Scientific Reports* 6, 38704. <https://doi.org/10.1038/srep38704>
- Eberl, D.D., Srodon, J., Lee, M., Nadeau, P.H., Northrop, H.R., 1987a. Sericite from the Silverton Caldera, Colorado; correlation among structure, composition, origin, and particle thickness. *American Mineralogist* 72, 914–934.
- Egli, D., Mancktelow, N., 2013. The structural history of the Mont Blanc massif with regard to models for its recent exhumation. *Swiss journal of geosciences* 106, 469–489.
- Egli, D., Mancktelow, N., Spikings, R., 2017. Constraints from $^{40}\text{Ar}/^{39}\text{Ar}$ geochronology on the timing of Alpine shear zones in the Mont Blanc-Aiguilles Rouges region of the European Alps. *Tectonics* 36, 730–748. <https://doi.org/10.1002/2016TC004450>
- El Aref, M.M., Amstutz, G.C., 1983. Lead-zinc deposits along the Red Sea coast of Egypt. New observations and genetic models on the occurrences of Um Geigh, Wizr, Essel and Zug El Bohar. *Monograph series on mineral deposits* 1–103.
- Eltchaninoff, C., 1980. Etude géologique entre Belledonne et Mont Blanc. La terminaison méridionale du massif du Mont Blanc et les terrains de son enveloppe. Université Paris VI, Paris.
- Eltchaninoff, C., Triboulet, S., 1980. Étude Géologique entre Belledonne et Mont Blanc. Livre synthétique Travaux du Département de Géotectonique de l'Université Pierre et Marie Curie aParis 1–54.
- Eltchaninoff-Lancelot, C., Triboulet, S., Doudoux, B., Fudral, S., Rampoux, J.-P., Tardy, M., 1982. Stratigraphie et tectonique des unités delphino-helvetiques comprises entre Mont-Blanc et Belledonne (Savoie-Alpes occidentales); Implications régionales. *Bulletin de la Société géologique de France* 7, 817–830.
- Elter, G., 1971. Schistes lustrés et ophiolites de la zone piémontaise entre Orco et Doire Baltée (Alpes Graies). Hypothèses sur l'origine des ophiolites. *Géologie Alpine* 47, 147–169.

References

- Elter, G., Elter, P., Alpi, C. nazionale delle ricerche (Italia) C. nazionale per lo studio geologico e petrografico delle, 1965. Carta geologica della regione del Piccolo S. Bernardo (versante italiano): note illustrative. Società cooperativa tipografica.
- Emsbo, P., 2009. Geologic criteria for the assessment of sedimentary exhalative (sedex) Zn-Pb-Ag deposits. US Geological Survey open-file report 1209, 21.
- Epard, J.L., 1990. La nappe de Morcles au sud-ouest du Mont-Blanc. Université de Lausanne.
- Epard, J.-L., 1989. Triassic and Lias stratigraphy of the Dauphinoise zone between Belledonne, Aiguilles-Rouges and Mont Blanc. Bulletin de la Societe Vaudoise des Sciences Naturelles 79, 301–338.
- Epard, J.-L., 1986. Le contact entre le socle du Mont-Blanc et la zone de Chamonix: implications tectoniques. Bull. Soc. vaud. Sci. nat 225–245.
- Epin, M.-E., 2017. Evolution morpho-tectonique et magmatique polyphasée des marges ultra-distales pauvres en magma: la transition océan-continent fossile de l'Err et de la Platta (SE Suisse) et comparaison avec des analogues actuels. Strasbourg.
- Epin, M.-E., Manatschal, G., 2018. Three-Dimensional Architecture, Structural Evolution, and Role of Inheritance Controlling Detachment Faulting at a Hyperextended Distal Margin: The Example of the Err Detachment System (SE Switzerland). *Tectonics* 37, 4494–4514. <https://doi.org/10.1029/2018TC005125>
- Epin, M.-E., Manatschal, G., Amann, M., 2017. Defining diagnostic criteria to describe the role of rift inheritance in collisional orogens: the case of the Err-Platta nappes (Switzerland). *Swiss Journal of Geosciences* 110, 419–438.
- Escartín, J., Mével, C., Petersen, S., Bonnemains, D., Cannat, M., Andreani, M., Augustin, N., Bezos, A., Chavagnac, V., Choi, Y., Godard, M., Haaga, K., Hamelin, C., Ildefonse, B., Jamieson, J., John, B., Leleu, T., MacLeod, C.J., Massot-Campos, M., Nomikou, P., Olive, J.A., Paquet, M., Rommevaux, C., Rothenbeck, M., Steinfuhrer, A., Tominaga, M., Triebe, L., Campos, R., Gracias, N., Garcia, R., 2017. Tectonic structure, evolution, and the nature of oceanic core complexes and their detachment fault zones (13°20'N and 13°30'N, Mid Atlantic Ridge). *Geochemistry, Geophysics, Geosystems* 18, 1451–1482. <https://doi.org/10.1002/2016GC006775>
- Escartín, J., Smith, D.K., Cann, J., Schouten, H., Langmuir, C.H., Escrig, S., 2008. Central role of detachment faults in accretion of slow-spreading oceanic lithosphere. *Nature* 455, 790–794.
- Escher, A., Masson, H., Steck, A., 1993a. Nappe geometry in the Western Swiss Alps. *Journal of Structural Geology* 15, 501–509. [https://doi.org/10.1016/0191-8141\(93\)90144-Y](https://doi.org/10.1016/0191-8141(93)90144-Y)

References

- Esput, N., Angrand, P., Teixell, A., Labaume, P., Ford, M., de Saint Blanquat, M., Chevrot, S., 2019. Crustal-scale balanced cross-section and restorations of the Central Pyrenean belt (Nestes-Cinca transect): Highlighting the structural control of Variscan belt and Permian-Mesozoic rift systems on mountain building. *Tectonophysics* 764, 25–45.
- Essalhi, M., 2009. Application de l'étude du magnétisme des roches à la compréhension des gisements: Traçage des paléocirculations (expérimentation et cas des minéralisations de La Florida, Espagne); Structuration et histoire de l'altération des amas sulfurés (cas des chapeaux de fer de la Province Pyriteuse Sud Ibérique, Espagne). Université d'Orléans.
- Essene, E.J., Claflin, C.L., Giorgetti, G., Mata, P.M., Peacor, D.R., Árkai, P., Rathmell, M.A., 2005. Two-, three- and four-feldspar assemblages with hyalophane and celsian : implications for phase equilibria in $\text{BaAl}_2\text{Si}_2\text{O}_8$ — $\text{CaAl}_2\text{Si}_2\text{O}_8$ — $\text{NaAlSi}_3\text{O}_8$ — KAlSi_3O_8 **Contribution No. 518 from the Mineralogical Laboratory, Department of Geological Sciences, The University of Michigan 48109–1063. *European Journal of Mineralogy* 17, 515–535. <https://doi.org/10.1127/0935-1221/2005/0017-0515>
- Evans, B.W., Hattori, K., Baronnet, A., 2013. Serpentinite: What, Why, Where? *Elements* 9, 99–106. <https://doi.org/10.2113/gselements.9.2.99>
- Evans, J.P., Chester, F.M., 1995. Fluid-rock interaction in faults of the San Andreas system: Inferences from San Gabriel fault rock geochemistry and microstructures. *Journal of Geophysical Research: Solid Earth* 100, 13007–13020. <https://doi.org/10.1029/94JB02625>
- Evans, J.P., Forster, C.B., Goddard, J.V., 1997. Permeability of fault-related rocks, and implications for hydraulic structure of fault zones. *Journal of Structural Geology* 19, 1393–1404. [https://doi.org/10.1016/S0191-8141\(97\)00057-6](https://doi.org/10.1016/S0191-8141(97)00057-6)
- Fagereng, Å., Toy, V.G., 2011. Geology of the earthquake source: an introduction. Geological Society, London, Special Publications 359, 1. <https://doi.org/10.1144/SP359.1>
- Faulkner, D.R., Sanchez-Roa, C., Boulton, C., Den Hartog, S.A.M., 2018. Pore fluid pressure development in compacting fault gouge in theory, experiments, and nature. *Journal of Geophysical Research: Solid Earth* 123, 226–241.
- Faure, M., 1995. Late orogenic carboniferous extensions in the Variscan French Massif Central. *Tectonics* 14, 132–153.
- Faure, M., Leloix, C., Roig, J.-Y., 1997. L'Evolution polycyclique de la chaîne hercynienne. *Bulletin de la Société Géologique de France* 168, 695–705.

References

- Favre, E., Renevier, E., Ischier, M.G., Gerlach, H., 1883. Feuille 17 de l'Atlas géologique de la Suisse au 1:100'000.
- Favre, P., Stampfli, G.M., 1992. From rifting to passive margin: the examples of the Red Sea, Central Atlantic and Alpine Tethys. *Tectonophysics* 215, 69–97. [https://doi.org/10.1016/0040-1951\(92\)90075-H](https://doi.org/10.1016/0040-1951(92)90075-H)
- Féraud, G., Ruffet, G., Stephan, J.F., Lapierre, H., Delgado, E., Popoff, M., 1995. Nouvelles données géochronologiques sur le volcanisme paléogène des Alpes occidentales: existence d'un événement magmatif breh généralisé, in: *Magmatisme Dans Le Sud-Est de La France*. Presented at the Séance spé. de la Soc. géol. de France et de l'Assoc. des géologues du SE, p. 38.
- Fernández-Martínez, J., Velasco, E., 1996. The Troya Zn-Pb Carbonate-Hosted Sedex Deposit, Northern Spain, in: Sangster, D.F. (Ed.), *Carbonate-Hosted Lead-Zinc Deposits: 75th Anniversary Volume*. Society of Economic Geologists, p. 0. <https://doi.org/10.5382/SP.04.27>
- Ferrando, S., Rubatto, D., Lombardo, B., Compagnoni, R., 2007. High-pressure–high-temperature Variscan metamorphism in the Western Alps: petrological constraints from the Laghi del Frisson omphacite granulites (Argentera Massif, Italy), in: *Geoitalia 2007, Sesto Forum Italiano Di Scienze Della Terra*. FIST, pp. 158–158.
- Ferry, J.M., 1979. Reaction mechanisms, physical conditions, and mass transfer during hydrothermal alteration of mica and feldspar in granitic rocks from south-central Maine, USA. *Contributions to Mineralogy and Petrology* 68, 125–139. <https://doi.org/10.1007/BF00371895>
- Fitz Gerald, J.D., Stünitz, H., 1993. Deformation of granitoids at low metamorphic grade. I: Reactions and grain size reduction. *Tectonophysics* 221, 269–297. [https://doi.org/10.1016/0040-1951\(93\)90163-E](https://doi.org/10.1016/0040-1951(93)90163-E)
- Föllmi, K.B., Gainon, F., 2008. Demise of the northern Tethyan Urogenian carbonate platform and subsequent transition towards pelagic conditions: The sedimentary record of the Col de la Plaine Morte area, central Switzerland. *Sedimentary Geology* 205, 142–159. <https://doi.org/10.1016/j.sedgeo.2008.02.005>
- Ford, M., Duchêne, S., Gasquet, D., Vanderhaeghe, O., 2004. Coupling of internal and external orogenic processes in the western Alps, in: *Réun. Sci. Terre*.
- Ford, M., Rohais, S., Williams, E.A., Bourlange, S., Jousset, D., Backert, N., Malartre, F., 2013. Tectono-sedimentary evolution of the western Corinth rift (Central Greece). *Basin Research*,.
- Forsyth, D.W., 1992. Finite extension and low-angle normal faulting. *Geology* 20, 27–30. [https://doi.org/10.1130/0091-7613\(1992\)020<0027:FEALAN>2.3.CO;2](https://doi.org/10.1130/0091-7613(1992)020<0027:FEALAN>2.3.CO;2)

References

- Fossen, H., 2016. Structural geology. Cambridge university press.
- Franchi, S., Kilian, W., Lory, P., 1908. Sur les rapports des Schistes lustrés avec les faciès dauphinois et briançonnais du Lias. Bull. Carte Géol. France, XVIII, 119 (1907-1908) 135–141.
- Franke, D., 2013. Rifting, lithosphere breakup and volcanism: Comparison of magma-poor and volcanic rifted margins. *Marine and Petroleum Geology* 43, 63–87.
<https://doi.org/10.1016/j.marpetgeo.2012.11.003>
- Franz, G., Sudo, M., Khomenko, V., 2022. 40 Ar/39 Ar dating of a hydrothermal pegmatitic buddingtonite–muscovite assemblage from Volyn, Ukraine. *European Journal of Mineralogy* 34, 7–18.
- Frezzotti, M.L., Tecce, F., Casagli, A., 2012. Raman spectroscopy for fluid inclusion analysis. *Journal of Geochemical Exploration* 112, 1–20.
- Fricke, H.C., Wickham, S.M., O’Neil, J.R., 1992. Oxygen and hydrogen isotope evidence for meteoric water infiltration during mylonitization and uplift in the Ruby Mountains-East Humboldt Range core complex, Nevada. *Contributions to Mineralogy and Petrology* 111, 203–221.
<https://doi.org/10.1007/BF00348952>
- Friedrich, M., Cuney, M., Poty, B., 1987. Uranium geochemistry in peraluminous leucogranites. *Uranium* 3, 353–385.
- Frisch, W., 1979. Tectonic progradation and plate tectonic evolution of the Alps. *Tectonophysics* 60, 121–139. [https://doi.org/10.1016/0040-1951\(79\)90155-0](https://doi.org/10.1016/0040-1951(79)90155-0)
- Froitzheim, N., Eberli, G., 1990. Extensional detachment faulting in the evolution of a Tethys passive continental margin, Eastern Alps, Switzerland. *GSA Bulletin* 102, 1297–1308.
[https://doi.org/10.1130/0016-7606\(1990\)102<1297:EDFITE>2.3.CO;2](https://doi.org/10.1130/0016-7606(1990)102<1297:EDFITE>2.3.CO;2)
- Froitzheim, N., Pleuger, J., Nagel, T.J., 2006. Extraction faults. *Journal of Structural Geology* 28, 1388–1395. <https://doi.org/10.1016/j.jsg.2006.05.002>
- Frost, B.R., Barn, C.G., Collins, W.J., Arculus, R.J., Ellis, D.J., Frost, C.D., 2001. A Geochemical Classification for Granitic Rocks. *Journal of Petrology* 42, 2033–2048.
<https://doi.org/10.1093/petrology/42.11.2033>
- Frost, B.R., Mavrogenes, J.A., Tomkins, A.G., 2002. Partial melting of sulfide ore deposits during medium-and high-grade metamorphism. *The Canadian Mineralogist* 40, 1–18.

References

- Fügenschuh, B., Froitzheim, N., Capdevila, R., Boillot, G., 2003. Offshore granulites from the Bay of Biscay margins: fission tracks constrain a Proterozoic to Tertiary thermal history. *Terra Nova* 15, 337–342. <https://doi.org/10.1046/j.1365-3121.2003.00502.x>
- Fusswinkel, T., Wagner, T., Wälle, M., Wenzel, T., Heinrich, C.A., Markl, G., 2013. Fluid mixing forms basement-hosted Pb-Zn deposits: Insight from metal and halogen geochemistry of individual fluid inclusions. *Geology* 41, 679–682. <https://doi.org/10.1130/G34092.1>
- G**alster, F., Cavargna-Sani, M., Epard, J.-L., Masson, H., 2012. New stratigraphic data from the Lower Penninic between the Adula nappe and the Gotthard massif and consequences for the tectonics and the paleogeography of the Central Alps. *Tectonophysics* 579, 37–55. <https://doi.org/10.1016/j.tecto.2012.05.029>
- Gardés, E., Montel, J.-M., 2009. Opening and resetting temperatures in heating geochronological systems. *Contributions to Mineralogy and Petrology* 158, 185–195.
- Garzanti, E., Radeff, G., Malusà, M.G., 2018. Slab breakoff: A critical appraisal of a geological theory as applied in space and time. *Earth-Science Reviews* 177, 303–319. <https://doi.org/10.1016/j.earscirev.2017.11.012>
- Gawthorpe, R.L., Leeder, M.R., Kranis, H., Skourtsos, E., Andrews, J.E., Henstra, G.A., Mack, G.H., Muravchik, M., Turner, J.A., Stamatakis, M., 2018. Tectono-sedimentary evolution of the Plio-Pleistocene Corinth rift, Greece. *Basin Research*,.
- Gébelin, A., Mulch, A., Teyssier, C., Heizler, M., Vennemann, T., Seaton, N.C., 2011. Oligo-Miocene extensional tectonics and fluid flow across the Northern Snake Range detachment system, Nevada. *Tectonics* 30.
- Geffroy, J., Lenoble, A., Vernet, J., 1964. Age et particularités minéralogiques de la minéralisation à pechblende de la galerie de la Gordolasque (AM). *CR Acad. Sci. Paris D* 258, 994–997.
- Genier, F., Bussy, F., Epard, J.-L., Baumgartner, L., 2008. Water-assisted migmatization of metagraywackes in a Variscan shear zone, Aiguilles-Rouges massif, western Alps. *Lithos* 102, 575–597. <https://doi.org/10.1016/j.lithos.2007.07.024>
- Geoffroy, L., Dorbath, C., 2008. Deep downward fluid percolation driven by localized crust dilatation in Iceland. *Geophysical research letters* 35.
- Geoffroy, L., Pronost, J., 2010. Late Pliocene to Early Quaternary extensional detachment in the La Paz–El Cabo area (Baja California Sur, Mexico): implications on the opening of the Gulf of California and the mechanics of oblique rifting. *Terra Nova* 22, 64–69.

References

- Gieré, R., 1990. Hydrothermal mobility of Ti, Zr and REE: examples from the Bergell and Adamello contact aureoles (Italy). *Terra Nova* 2, 60–67. <https://doi.org/10.1111/j.1365-3121.1990.tb00037.x>
- Gillcrist, J.R., 1988. Mesozoic basin development and structural inversion in the external Franch Alps. Imperial college London.
- Girault, J.B., Bellahsen, N., Boutoux, A., Rosenberg, C.L., Nanni, U., Verlaguet, A., Beyssac, O., 2020. The 3-D Thermal Structure of the Helvetic Nappes of the European Alps: Implications for Collisional Processes. *Tectonics* 39, e2018TC005334. <https://doi.org/10.1029/2018TC005334>
- Gleeson, S.A., Yardley, B.D., Munz, I.A., Boyce, A.J., 2003. Infiltration of basinal fluids into high-grade basement, South Norway: sources and behaviour of waters and brines. *Geofluids* 3, 33–48.
- Glotzbach, C., Reinecker, J., Danišík, M., Rahn, M., Frisch, W., Spiegel, C., 2008. Neogene exhumation history of the Mont Blanc massif, western Alps. *Tectonics* 27. <https://doi.org/10.1029/2008TC002257>
- Goguel, J., 1948. Introduction à l'étude mécanique des déformations de l'écorce terrestre. Min. de l'Industrie et du Commerce.
- Gholamrezaie, E., Scheck-Wenderoth, M., Sippel, J., Strecker, M.R., 2018. Variability of the geothermal gradient across two differently aged magma-rich continental rifted margins of the Atlantic Ocean: the Southwest African and the Norwegian margins. *Solid Earth* 9, 139–158. <https://doi.org/10.5194/se-9-139-2018>
- Goldfarb, R.J., Groves, D.I., Gardoll, S., 2001. Orogenic gold and geologic time: a global synthesis. *Ore Geology Reviews* 18, 1–75. [https://doi.org/10.1016/S0169-1368\(01\)00016-6](https://doi.org/10.1016/S0169-1368(01)00016-6)
- Goldstein, H.R., 1994. Systematics of fluid inclusions in diagenetic minerals. *SEPM short course* 31, 199.
- Goldstein, R.H., Samson, I., Anderson, A., Marshall, D., 2003. Petrographic analysis of fluid inclusions. *Fluid inclusions: Analysis and interpretation* 32, 9–53.
- Gómez-Romeu, J., Kuszniir, N., Roberts, A., Manatschal, G., 2020. Measurements of the extension required for crustal breakup on the magma-poor Iberia-Newfoundland conjugate margins. *Marine and Petroleum Geology* 118, 104403. <https://doi.org/10.1016/j.marpetgeo.2020.104403>
- Gouiza, M., Naliboff, J., 2021. Rheological inheritance controls the formation of segmented rifted margins in cratonic lithosphere. *Nature communications* 12, 1–9.

References

- Grant, J.A., 1986. The isocon diagram; a simple solution to Gresens' equation for metasomatic alteration. *Economic Geology* 81, 1976–1982. <https://doi.org/10.2113/gsecongeo.81.8.1976>
- Grasemann, B., Mancktelow, N.S., 1993. Two-dimensional thermal modelling of normal faulting: the Simplon Fault Zone, Central Alps, Switzerland. *Tectonophysics* 225, 155–165. [https://doi.org/10.1016/0040-1951\(93\)90277-Q](https://doi.org/10.1016/0040-1951(93)90277-Q)
- Grasmück, K.P., 1961. Die helvetischen Sedimente am Nordostrand des Mont Blanc-Massivs (zwischen Sembrancher und dem Col Ferret). ETH Zurich.
- Gresens, R.L., 1967. Composition-volume relationships of metasomatism. *Chemical Geology* 2, 47–65. [https://doi.org/10.1016/0009-2541\(67\)90004-6](https://doi.org/10.1016/0009-2541(67)90004-6)
- Griggs, D.T., Handin, J., 1960. Rock deformation. Wiley Online Library.
- Grocott, J., McCaffrey, K.J., 2017. Basin evolution and destruction in an Early Proterozoic continental margin: the Rinkian fold–thrust belt of central West Greenland. *Journal of the Geological Society* 174, 453–467.
- Groves, D.I., Santosh, M., Müller, D., Zhang, L., Deng, J., Yang, L.-Q., Wang, Q.-F., 2022. Mineral systems: Their advantages in terms of developing holistic genetic models and for target generation in global mineral exploration. *Geosystems and Geoenvironment* 1, 100001. <https://doi.org/10.1016/j.geogeo.2021.09.001>
- Guellec, S., Mugnier, J.-L., Tardy, M., Roure, F., 1990. Neogene evolution of the western Alpine foreland in the light of ECORS data and balanced cross-section. *Mémoires de la Société géologique de France (1833)* 156, 165–184.
- Guermani, A., Pennacchioni, G., 1998a. Brittle precursors of plastic deformation in a granite: an example from the Mont Blanc massif (Helvetic, western Alps). *Journal of Structural Geology* 20, 135–148. [https://doi.org/10.1016/S0191-8141\(97\)00080-1](https://doi.org/10.1016/S0191-8141(97)00080-1)
- Guidry, M.W., Mackenzie, F.T., 2003. Experimental study of igneous and sedimentary apatite dissolution: Control of pH, distance from equilibrium, and temperature on dissolution rates. *Geochimica et Cosmochimica Acta* 67, 2949–2963. [https://doi.org/10.1016/S0016-7037\(03\)00265-5](https://doi.org/10.1016/S0016-7037(03)00265-5)
- Haas, H., 1885. Etude monographique et critique des brachiopodes rhétiens et jurassiques des Alpes vaudoises. *Mém. soc. pal. suisse*,.
- Haines, S., Lynch, E., Mulch, A., Valley, J.W., van der Pluijm, B., 2016. Meteoric fluid infiltration in crustal-scale normal fault systems as indicated by $\delta^{18}\text{O}$ and $\delta^2\text{H}$ geochemistry and $^{40}\text{Ar}/^{39}\text{Ar}$ dating of neofomed clays in brittle fault rocks. *Lithosphere* 8, 587–600.

References

- Hall, J., 1882. Contributions to the geological history of the American continent. Salem Press.
- Handy, M.R., Ustaszewski, K., Kissling, E., 2015. Reconstructing the Alps–Carpathians–Dinarides as a key to understanding switches in subduction polarity, slab gaps and surface motion. *International Journal of Earth Sciences* 104, 1–26.
- Handy, M.R., M. Schmid, S., Bousquet, R., Kissling, E., Bernoulli, D., 2010. Reconciling plate-tectonic reconstructions of Alpine Tethys with the geological–geophysical record of spreading and subduction in the Alps. *Earth-Science Reviews* 102, 121–158.
<https://doi.org/10.1016/j.earscirev.2010.06.002>
- Handy, M.R., 1987. The structure, age and kinematics of the Pogallo Fault Zone; Southern Alps, northwestern Italy. *Eclogae Geologicae Helvetiae* 80, 593–632.
- Hardenbol, J.A.N., Thierry, J., Farley, M.B., Jacquin, T., De Graciansky, P.-C., Vail, P.R., 1998. Mesozoic and Cenozoic sequence chronostratigraphic framework of European basins.
- Harris, P.T., Macmillan-Lawler, M., Rupp, J., Baker, E.K., 2014. Geomorphology of the oceans. *Marine Geology* 352, 4–24.
- Hart, N.R., Stockli, D.F., Lavier, L.L., Hayman, N.W., 2017. Thermal evolution of a hyperextended rift basin, Mauléon Basin, western Pyrenees. *Tectonics* 36, 1103–1128.
- Haug, E., 1900. Les géosynclinaux et les aires continentales: contribution à l'étude des transgressions et des regressions marines. Au siège de la Société géologique de France.
- Hauptert, I., 2015. Etude des hauts et bas topographiques dans les marges profondes de type « upper plate » : Exemple des unités du Briançonnais et du Prépiémontais dans les Alpes et comparaison avec des analogues modernes. Institut de Physique du Globe de Strasbourg, Strasbourg.
- Hauptert, I., Manatschal, G., Decarlis, A., Unternehr, P., 2016. Upper-plate magma-poor rifted margins: Stratigraphic architecture and structural evolution. *Marine and Petroleum Geology* 69, 241–261. <https://doi.org/10.1016/j.marpetgeo.2015.10.020>
- Hawkesworth, C.J., Waters, D.J., Bickle, M.J., 1975. Plate tectonics in the Eastern Alps. *Earth and Planetary Science Letters* 24, 405–413. [https://doi.org/10.1016/0012-821X\(75\)90147-8](https://doi.org/10.1016/0012-821X(75)90147-8)
- Hayes, T.S., 2001. Jabal Dhaylan district, Saudi Arabia: Salt-related carbonate-hosted zinc-lead deposits formed in the Red Sea early passive margin. *Mineral Deposits at the Beginning of the 21st Century* 137.

References

- Hedenquist, J.W., Henley, R.W., 1985. Hydrothermal eruptions in the Waiotapu geothermal system, New Zealand; their origin, associated breccias, and relation to precious metal mineralization. *Economic Geology* 80, 1640–1668. <https://doi.org/10.2113/gsecongeo.80.6.1640>
- Heezen, B.C., Tharp, M., 1965. Tectonic fabric of the Atlantic and Indian Oceans and continental drift. *Philosophical transactions of the Royal Society of London. Series A, Mathematical and Physical Sciences* 258, 90–106.
- Heim, A., 1918. Das Gewicht der Berge. *Jahrbuch des Schweizer Alpenclub* 53, 179–201.
- Heirtzler, J.R., Dickson, G.O., Herron, E.M., Pitman III, W.C., Le Pichon, X., 1968. Marine magnetic anomalies, geomagnetic field reversals, and motions of the ocean floor and continents. *Journal of Geophysical Research* 73, 2119–2136.
- Helwig, J., 1976. Shortening of continental crust in orogenic belts and plate tectonics. *Nature* 260, 768–770.
- Hemley, J.J., Hunt, J.P., 1992. Hydrothermal ore-forming processes in the light of studies in rock-buffered systems; II, Some general geologic applications. *Economic Geology* 87, 23–43.
- Hendry, H.E., 1972. Breccias deposited by mass flow in the Breccia Nappe of the French pre-Alps. *Sedimentology* 18, 277–292.
- Herrington, R.J., Brown, D., 2011. The Generation and Preservation of Mineral Deposits in Arc–Continent Collision Environments, in: *Arc-Continent Collision*. Springer, pp. 145–159.
- Herviou, C., Agard, P., Plunder, A., Mendes, K., Verlaquet, A., Deldicque, D., Cubas, N., 2022. Subducted fragments of the Liguro-Piemont ocean, Western Alps: Spatial correlations and offscraping mechanisms during subduction. *Tectonophysics* 827, 229267. <https://doi.org/10.1016/j.tecto.2022.229267>
- Herwegh, M., Berger, A., Glotzbach, C., Wangenheim, C., Mock, S., Wehrens, P., Baumberger, R., Egli, D., Kissling, E., 2020. Late stages of continent-continent collision: Timing, kinematic evolution, and exhumation of the Northern rim (Aar Massif) of the Alps. *Earth-science reviews* 200, 102959.
- Herwegh, M., Pfiffner, O.A., 2005a. Tectono-metamorphic evolution of a nappe stack: A case study of the Swiss Alps. *Tectonophysics* 404, 55–76. <https://doi.org/10.1016/j.tecto.2005.05.002>
- Hess, H.H., Engel, A.E.J., James, H.L., Leonard, B.F., 1962. History of ocean basins.
- Hetényi, G., Molinari, I., Clinton, J., Bokelmann, G., Bondár, I., Crawford, W.C., Dessa, J.-X., Doubre, C., Friederich, W., Fuchs, F., 2018. The AlpArray seismic network: a large-scale European experiment to image the Alpine orogen. *Surveys in geophysics* 39, 1009–1033.

References

- Hill, C.A., Polyak, V.J., Asmerom, Y., P. Provencio, P., 2016. Constraints on a Late Cretaceous uplift, denudation, and incision of the Grand Canyon region, southwestern Colorado Plateau, USA, from U-Pb dating of lacustrine limestone. *Tectonics* 35, 896–906.
- Hips, K., Haas, J., Győri, O., 2016. Hydrothermal dolomitization of basinal deposits controlled by a synsedimentary fault system in Triassic extensional setting, Hungary. *International Journal of Earth Sciences* 105, 1215–1231.
- Hoareau, G., Claverie, F., Pecheyran, C., Paroissin, C., Grignard, P.-A., Motte, G., Chailan, O., Girard, J.-P., 2021. Direct U–Pb dating of carbonates from micron-scale femtosecond laser ablation inductively coupled plasma mass spectrometry images using robust regression. *Geochronology* 3, 67–87. <https://doi.org/10.5194/gchron-3-67-2021>
- Hochscheid, F., Coltat, R., Ulrich, M., Munoz, M., Manatschal, G., Boulvais, P., 2022. The Sr isotope geochemistry of oceanic ultramafic-hosted mineralizations. *Ore Geology Reviews* 104824.
- Hofmann, B.A., Knill, M.D., 1996. Geochemistry and genesis of the Lengenbach Pb-Zn-As-Tl-Ba-mineralisation, Binn Valley, Switzerland. *Mineralium Deposita* 31, 319–339. <https://doi.org/10.1007/BF02280795>
- Hofmann, B.A., 1994. Formation of a sulfide melt during Alpine metamorphism of the Lengenbach polymetallic sulfide mineralization, Binntal, Switzerland. *Mineralium Deposita* 29, 439–442.
- Hoggard, M.J., White, N., Al-Attar, D., 2016. Global dynamic topography observations reveal limited influence of large-scale mantle flow. *Nature Geoscience* 9, 456–463.
- Holland, T.J.B., Powell, R., 2006. Mineral activity–composition relations and petrological calculations involving cation equipartition in multisite minerals: a logical inconsistency. *Journal of Metamorphic Geology* 24, 851–861.
- Holland, T.J.B., Powell, R., 1998. An internally consistent thermodynamic data set for phases of petrological interest. *Journal of metamorphic Geology* 16, 309–343.
- Horstwood, M.S., Košler, J., Gehrels, G., Jackson, S.E., McLean, N.M., Paton, C., Pearson, N.J., Sircombe, K., Sylvester, P., Vermeesch, P., 2016. Community-derived standards for LA-ICP-MS U-(Th-) Pb geochronology–Uncertainty propagation, age interpretation and data reporting. *Geostandards and Geoanalytical Research* 40, 311–332.
- Hou, Z., Cook, N.J., 2009. Metallogensis of the Tibetan collisional orogen: A review and introduction to the special issue. *Ore Geology Reviews* 36, 2–24. <https://doi.org/10.1016/j.oregeorev.2009.05.001>

References

- Huggenberger, P., 1985. Faltenmodelle und Verformungsverteilung in Deckenstrukturen am Beispiel der Morcles-Decke (Helvetikum der Westschweiz). ETH Zurich.
- Hügi, Th., Ledermann, H., Schläppi, E., 1998. Feuille Lotschental : notice explicative. Comm. géol. Suisse.
- Huismans, R., Beaumont, C., 2011. Depth-dependent extension, two-stage breakup and cratonic underplating at rifted margins. *Nature* 473, 74–78.
- Huismans, R.S., Beaumont, C., 2003. Symmetric and asymmetric lithospheric extension: Relative effects of frictional-plastic and viscous strain softening. *Journal of Geophysical Research: Solid Earth* 108.
- Hunziker, J.C., Desmons, J., Hurford, A.J., 1992. Thirty-two years of geochronological work in the Central and Western Alps: A review on seven maps, *Mémoires de Géologie* (Lausanne). Lausanne.
- Ikari, M.J., Marone, C., Saffer, D.M., 2011. On the relation between fault strength and frictional stability. *Geology* 39, 83–86. <https://doi.org/10.1130/G31416.1>
- Imber, J., Holdsworth, R.E., Smith, S.A.F., Jefferies, S.P., Collettini, C., 2008. Frictional-viscous flow, seismicity and the geology of weak faults: a review and future directions. *Geological Society, London, Special Publications* 299, 151–173.
- Incerpi, N., Martire, L., Manatschal, G., Bernasconi, S.M., 2017. Evidence of hydrothermal fluid flow in a hyperextended rifted margin: the case study of the Err nappe (SE Switzerland). *Swiss Journal of Geosciences* 110, 439–456. <https://doi.org/10.1007/s00015-016-0235-2>
- Incerpi, N., Martire, L., Manatschal, G., Bernasconi, S.M., Gerdes, A., Czuppon, G., Palcsu, L., Karner, G.D., Johnson, C.A., Figueredo, P.H., 2019. Hydrothermal fluid flow associated to the extensional evolution of the Adriatic rifted margin: Insights from the pre- to post-rift sedimentary sequence (SE Switzerland, N ITALY). *Basin Research* n/a. <https://doi.org/10.1111/bre.12370>
- Inoue, A., Meunier, A., Patrier-Mas, P., Rigault, C., Beaufort, D., Vieillard, P., 2009. Application of chemical geothermometry to low-temperature trioctahedral chlorites. *Clays and Clay Minerals* 57, 371–382.
- Izquierdo-Llavall, E., Menant, A., Aubourg, C., Callot, J.-P., Hoareau, G., Camps, P., Péré, E., Lahfid, A., 2020. Preorogenic folds and syn-orogenic basement tilts in an inverted hyperextended margin: The Northern Pyrenees case study. *Tectonics* 39, e2019TC005719.

References

- Jammes, S., Huismans, R.S., 2012. Structural styles of mountain building: Controls of lithospheric rheologic stratification and extensional inheritance. *Journal of Geophysical Research: Solid Earth* 117. <https://doi.org/10.1029/2012JB009376>
- Jammes, S., Manatschal, G., Lavier, L., 2010. Interaction between prerift salt and detachment faulting in hyperextended rift systems: The example of the Parentis and Mauléon basins (Bay of Biscay and western Pyrenees). *AAPG Bulletin* 94, 957–975. <https://doi.org/10.1306/12090909116>
- Jaquet, Y., Duretz, T., Grujic, D., Masson, H., Schmalholz, S.M., 2018. Formation of orogenic wedges and crustal shear zones by thermal softening, associated topographic evolution and application to natural orogens. *Tectonophysics* 746, 512–529.
- Jeanbourquin, P., Burri, M., 1991. Les métasédiments du Pennique inférieur dans la région de Brigue-Simplon. Lithostratigraphie, structure et contexte géodynamique dans le bassin valaisan. *Eclogae Geologicae Helveticae* 84, 463–481.
- Jefferies, S.P., Holdsworth, R.E., Shimamoto, T., Takagi, H., Lloyd, G.E., Spiers, C.J., 2006a. Origin and mechanical significance of foliated cataclastic rocks in the cores of crustal-scale faults: Examples from the Median Tectonic Line, Japan. *Journal of Geophysical Research: Solid Earth* 111.
- Jefferies, S.P., Holdsworth, R.E., Wibberley, C.A.J., Shimamoto, T., Spiers, C.J., Niemeijer, A.R., Lloyd, G.E., 2006b. The nature and importance of phyllonite development in crustal-scale fault cores: an example from the Median Tectonic Line, Japan. *Journal of Structural Geology* 28, 220–235.
- Jiang, S.-Y., Wang, R.-C., Xu, X.-S., Zhao, K.-D., 2005. Mobility of high field strength elements (HFSE) in magmatic-, metamorphic-, and submarine-hydrothermal systems. *Physics and Chemistry of the Earth, Parts A/B/C* 30, 1020–1029.
- Johnson, M.C., Rutherford, M.J., 1989. Experimental calibration of the aluminum-in-hornblende geobarometer with application to Long Valley caldera (California) volcanic rocks. *Geology* 17, 837–841. [https://doi.org/10.1130/0091-7613\(1989\)017<0837:ECOTAI>2.3.CO;2](https://doi.org/10.1130/0091-7613(1989)017<0837:ECOTAI>2.3.CO;2)
- Jourdon, A., Le Pourhiet, L., Mouthereau, F., Masini, E., 2019. Role of rift maturity on the architecture and shortening distribution in mountain belts. *Earth and Planetary Science Letters* 512, 89–99. <https://doi.org/10.1016/j.epsl.2019.01.057>
- Jowett, E.C., 1991. Fitting Iron and Magnesium into the hydrothermal chlorite geothermometer. In *Proceedings of the GAC/MAC/SEG Joint Annual Meeting, Toronto, ON, Canada, 27–29 May 1991*

References

- Joye, J.B., 1989. L'évolution pression-température-déformation dans le massif des Aiguilles Rouges, massif externe alpin.
- Kaczmarek, M.-A., Müntener, O., Rubatto, D., 2008. Trace element chemistry and U–Pb dating of zircons from oceanic gabbros and their relationship with whole rock composition (Lanzo, Italian Alps). *Contributions to Mineralogy and Petrology* 155, 295–312.
- Kalifi, A., Leloup, P.H., Sorrel, P., Galy, A., Demory, F., Spina, V., Huet, B., Quillévéré, F., Ricciardi, F., Michoux, D., Lecacheur, K., Grime, R., Pittet, B., Rubino, J.-L., 2021. Chronology of thrust propagation from an updated tectono-sedimentary framework of the Miocene molasse (western Alps). *Solid Earth* 12, 2735–2771. <https://doi.org/10.5194/se-12-2735-2021>
- Keith, S.B., Reynolds, S.J., 1980. Geochemistry of Cordilleran metamorphic core complexes. Cordilleran metamorphic core complexes and their uranium favorability: US Department of Energy Open-File Report GJBX-256 (80) 321.
- Kerrich, R., Allison, I., Barnett, R.L., Moss, S., Starkey, J., 1980. Microstructural and chemical transformations accompanying deformation of granite in a shear zone at Miéville, Switzerland; with implications for stress corrosion cracking and superplastic flow. *Contributions to Mineralogy and Petrology* 73, 221–242. <https://doi.org/10.1007/BF00381442>
- Kerrich, R., Fyfe, W.S., German, B.E., Allison, I., 1977. Local modification of rock chemistry by deformation. *Contributions to Mineralogy and Petrology* 65, 183–190.
- Kerrich, R., Goldfarb, R., Groves, D., Garwin, S., Jia, Y., 2000. The characteristics, origins, and geodynamic settings of supergiant gold metallogenic provinces. *Science in China Series D: Earth Sciences* 43, 1–68.
- Kessel, R., Schmidt, M.W., Ulmer, P., Pettke, T., 2005. Trace element signature of subduction-zone fluids, melts and supercritical liquids at 120–180 km depth. *Nature* 437, 724–727.
- Kirilova, M., Toy, V.G., Timms, N., Halfpenny, A., Menzies, C., Craw, D., Beyssac, O., Sutherland, R., Townend, J., Boulton, C., 2018. Textural changes of graphitic carbon by tectonic and hydrothermal processes in an active plate boundary fault zone, Alpine Fault, New Zealand. Geological Society, London, Special Publications 453, 205–223.
- Kirkpatrick, J.D., Rowe, C.D., 2013. Disappearing ink: How pseudotachylytes are lost from the rock record. *Journal of Structural Geology* 52, 183–198. <https://doi.org/10.1016/j.jsg.2013.03.003>
- Kirschner, D.L., Cosca, M.A., Masson, H., Hunziker, J.C., 1996. Staircase $^{40}\text{Ar}/^{39}\text{Ar}$ spectra of fine-grained white mica: Timing and duration of deformation and empirical constraints on argon diffusion. *Geology* 24, 747–750. [https://doi.org/10.1130/0091-7613\(1996\)024<0747:SAASOF>2.3.CO;2](https://doi.org/10.1130/0091-7613(1996)024<0747:SAASOF>2.3.CO;2)

References

- Kiss, D., Duretz, T., Schmalholz, S.M., 2020. Tectonic inheritance controls nappe detachment, transport and stacking in the Helvetic nappe system, Switzerland: insights from thermomechanical simulations. *Solid Earth* 11, 287–305. <https://doi.org/10.5194/se-11-287-2020>
- Klee, J., Chabani, A., Ledésert, B.A., Potel, S., Hébert, R.L., Trullenque, G., 2021. Fluid-rock interactions in a paleo-geothermal reservoir (Noble Hills Granite, California, USA). part 2: the influence of fracturing on granite alteration processes and fluid circulation at low to moderate regional strain. *Geosciences* 11, 433.
- Klein, F., Le Roux, V., 2020. Quantifying the volume increase and chemical exchange during serpentinization. *Geology* 48, 552–556. <https://doi.org/10.1130/G47289.1>
- Klemperer, S.L., 1988. Crustal thinning and nature of extension in the northern North Sea from deep seismic reflection profiling. *Tectonics* 7, 803–821. <https://doi.org/10.1029/TC007i004p00803>
- Kopf, A., 2001. Permeability variation across an active low-angle detachment fault, western Woodlark Basin (ODP Leg 180), and its implication for fault activation. Geological Society, London, Special Publications 186, 23–41.
- Koppers, A.A.P., 2002. ArAR CALC—software for Ar. Ar age.
- Kranidiotis, P., MacLean, W.H., 1987. Systematics of chlorite alteration at the Phelps Dodge massive sulfide deposit, Matagami, Quebec. *Economic geology* 82, 1898–1911.
- Krebs, W., 1981. The geology of the Meggen ore deposit, in: *Regional and Specific Deposits*. Elsevier, pp. 509–549.
- Kuehnbaum, R.M., 2011. TECHNICAL REPORT ON THE MONT CHEMIN GOLD-SILVER PROPERTY, CANTON VALAIS, SWITZERLAND FOR URANIA RESOURCES LTD. Watt, Griffis and McOuat, Toronto, Canada.
- Kuo, L.-W., Li, H., Smith, S.A.F., Di Toro, G., Suppe, J., Song, S.-R., Nielsen, S., Sheu, H.-S., Si, J., 2014. Gouge graphitization and dynamic fault weakening during the 2008 Mw 7.9 Wenchuan earthquake. *Geology* 42, 47–50. <https://doi.org/10.1130/G34862.1>
- Kurz, W., Fritz, H., 2003. Tectonometamorphic evolution of the Austroalpine Nappe Complex in the central Eastern Alps—consequences for the Eo-Alpine evolution of the Eastern Alps. *International Geology Review* 45, 1100–1127.

References

- Labaume, P., Teixell, A., 2020. Evolution of salt structures of the Pyrenean rift (Chaînons Béarnais, France): From hyper-extension to tectonic inversion. *Tectonophysics* 785, 228451.
- Lacassin, R., Tapponnier, P., Bourjot, L., 1990. Culminations anticlinales d'échelle crustale et imbrication de la lithosphère dans les Alpes, apports du profil ECORS-CROP. *Comptes rendus de l'Académie des sciences. Série 2, Mécanique, Physique, Chimie, Sciences de l'univers, Sciences de la Terre* 310, 807–814.
- Lacombe, O., Bellahsen, N., 2016. Thick-skinned tectonics and basement-involved fold–thrust belts: insights from selected Cenozoic orogens. *Geological Magazine* 153, 763–810.
<https://doi.org/10.1017/S0016756816000078>
- Lagabrielle, Y., 1987. Les ophiolites: marqueurs de l'histoire tectonique des domaines océaniques: le cas des Alpes franco-italiennes (Queyras, Piémont): comparaison avec les ophiolites d'Antalya (Turquie) et du Coast Range de Californie. Brest.
- Lagabrielle, Y., Asti, R., Fourcade, S., Corre, B., Labaume, P., Uzel, J., Clerc, C., Lafay, R., Picazo, S., 2019. Mantle exhumation at magma-poor passive continental margins. Part II: Tectonic and metasomatic evolution of large-displacement detachment faults preserved in a fossil distal margin domain (Saraillé lherzolites, northwestern Pyrenees, France) Exhumation du manteau au pied des marges passives pauvres en magma. Partie 2: Évolution tectonique et métasomatique des failles de détachement à fort déplacement dans le domaine distal fossile (lherzolites du Saraillé, Pyrénées NW, France). *Bulletin de la Société géologique de France* 190.
- Lagabrielle, Y., Brovarone, A.V., Ildefonse, B., 2015. Fossil oceanic core complexes recognized in the blueschist metaophiolites of Western Alps and Corsica. *Earth-Science Reviews* 141, 1–26.
- Lagabrielle, Y., Labaume, P., de Saint Blanquat, M., 2010a. Mantle exhumation, crustal denudation, and gravity tectonics during Cretaceous rifting in the Pyrenean realm (SW Europe): Insights from the geological setting of the lherzolite bodies. *Tectonics* 29.
- Lanari, P., Vho, A., Bovay, T., Airaghi, L., Centrella, S., 2019. Quantitative compositional mapping of mineral phases by electron probe micro-analyser. *Geological Society, London, Special Publications* 478, 39–63.
- Lanari, P., Vidal, O., De Andrade, V., Dubacq, B., Lewin, E., Grosch, E.G., Schwartz, S., 2014. XMapTools: A MATLAB®-based program for electron microprobe X-ray image processing and geothermobarometry. *Computers & Geosciences* 62, 227–240.
- Landry, P., 1976. Contribution à l'étude géologique de la région de Roselend (Savoie). Univ. Grenoble, Grenoble.

References

- Langmuir, D., 1978. Uranium solution-mineral equilibria at low temperatures with applications to sedimentary ore deposits. *Geochimica et Cosmochimica Acta* 42, 547–569.
- Latin, D., White, N., 1990. Generating melt during lithospheric extension: Pure shear vs. simple shear. *Geology* 18, 327–331. [https://doi.org/10.1130/0091-7613\(1990\)018<0327:GMDLEP>2.3.CO;2](https://doi.org/10.1130/0091-7613(1990)018<0327:GMDLEP>2.3.CO;2)
- Lavier, L.L., Manatschal, G., 2006. A mechanism to thin the continental lithosphere at magma-poor margins. *Nature* 440, 324–328. <https://doi.org/10.1038/nature04608>
- Lavier, L.L., Buck, W.R., 2002. Half graben versus large-offset low-angle normal fault: Importance of keeping cool during normal faulting. *Journal of Geophysical Research: Solid Earth* 107, ETG 8-1. <https://doi.org/10.1029/2001JB000513>
- Lavier, L.L., Buck, W.R., Poliakov, A.N.B., 2000. Factors controlling normal fault offset in an ideal brittle layer. *Journal of Geophysical Research: Solid Earth* 105, 23431–23442. <https://doi.org/10.1029/2000JB900108>
- Le Breton, E., Brune, S., Ustaszewski, K., Zahirovic, S., Seton, M., Müller, R.D., 2021. Kinematics and extent of the Piemonte–Liguria Basin—implications for subduction processes in the Alps. *Solid Earth* 12, 885–913.
- Le Pichon, X., Heirtzler, J.R., 1968. Magnetic anomalies in the Indian Ocean and sea-floor spreading. *Journal of Geophysical Research* 73, 2101–2117.
- Le Pichon, X., Sibuet, J.-C., Francheteau, J., 1977. The fit of the continents around the North Atlantic Ocean**Contribution No. 470 of the Département Scientifique, Centre Océanologique de Bretagne. *Tectonophysics* 38, 169–209. [https://doi.org/10.1016/0040-1951\(77\)90210-4](https://doi.org/10.1016/0040-1951(77)90210-4)
- Le Pourhiet, L., Huet, B., Traore, N., 2014. Links between long-term and short-term rheology of the lithosphere: Insights from strike-slip fault modelling. *Tectonophysics* 631, 146–159.
- Le Pourhiet, L., May, D.A., Huille, L., Watremez, L., Leroy, S., 2017. A genetic link between transform and hyper-extended margins. *Earth and Planetary Science Letters* 465, 184–192.
- Leach, David.L., Bradley, D.C., Huston, D., Pisarevsky, S.A., Taylor, R.D., Gardoll, S.J., 2010. Sediment-Hosted Lead-Zinc Deposits in Earth History. *Economic Geology* 105, 593–625. <https://doi.org/10.2113/gsecongeo.105.3.593>
- Leach, D.L., Sangster, D.F., Kelley, K.D., Large, R.R., Garven, G., Allen, C.R., Gutzmer, J., Walters, S., 2005. Sediment-hosted lead-zinc deposits: A global perspective. *Economic Geology* 100, 561–607.

References

- Lee, J.-Y., Marti, K., Severinghaus, J.P., Kawamura, K., Yoo, H.-S., Lee, J.B., Kim, J.S., 2006. A redetermination of the isotopic abundances of atmospheric Ar. *Geochimica et Cosmochimica Acta* 70, 4507–4512.
- Leeder, M.R., Gawthorpe, R.L., 1987. Sedimentary models for extensional tilt-block/half-graben basins. Geological Society, London, Special Publications 28, 139.
<https://doi.org/10.1144/GSL.SP.1987.028.01.11>
- Leloup, P.-H., Arnaud, N., Sobel, E.R., Lacassin, R., 2005. Alpine thermal and structural evolution of the highest external crystalline massif: The Mont Blanc. *Tectonics* 24.
- Lemoine, M., 2006. Une science en crise au milieu du XXe siècle, la géodynamique: des géosynclinaux aux océans disparus. *Travaux du Comité français d’Histoire de la Géologie* 3, 129–165.
- Lemoine, M., Arnaud-Vanneau, A., Arnaud, H., Letolle, R., Mevel, C., Thieuloy, J.P., 1982. Indices possibles de paleo-hydrothermalisme sous-marin dans le Jurassique et le Cretace des Alpes occidentales (ocean tethysien et sa marge continentale europeenne); essai d’inventaire. *Bulletin de la Société Géologique de France S7-XXIV*, 641–647.
<https://doi.org/10.2113/gssgfbull.S7-XXIV.3.641>
- Lemoine, M., Bas, T., Arnaud-Vanneau, A., Arnaud, H., Dumont, T., Gidon, M., Bourbon, M., de Graciansky, P.-C., Rudkiewicz, J.-L., Megard-Galli, J., Tricart, P., 1986. The continental margin of the Mesozoic Tethys in the Western Alps. *Marine and Petroleum Geology* 3, 179–199.
[https://doi.org/10.1016/0264-8172\(86\)90044-9](https://doi.org/10.1016/0264-8172(86)90044-9)
- Lemoine, M., Dardeau, G., Delpech, P.Y., Dumont, T., de Graciansky, P.C., 1989. Extension Jurassique et failles transformantes jurassiques dans les Alpes occidentales. *C. R. Acad. Sci.* 1711–1716.
- Lemoine, M., Gidon, M., Barfety, J.-C., 1981. Les massifs cristallins externes des Alpes occidentales: d’anciens blocs basculés nés au Lias lors du rifting téthysien. *Comptes rendus des séances de l’Académie des sciences* 2, 917–920.
- Lemoine, M., Tricart, P., 1986. Les Schistes lustrés piémontais des Alpes occidentales: approche stratigraphique, structurale et sédimentologique. *Eclogae Geologicae Helvetiae* 79, 271–294.
- Lemoine, M., Trümpy, R., 1987. Pre-oceanic rifting in the Alps. *Tectonophysics* 133, 305–320.
- Lenoir, L., 2022. Interactions fluide-roche à l’origine des gisements à F-Ba à l’interface socle-couverture sédimentaire du sud-est du Bassin de Paris. Université Paris-Saclay.
- Leroy, M., Gueydan, F., Dauteuil, O., 2008. Uplift and strength evolution of passive margins inferred from 2-D conductive modelling. *Geophysical Journal International* 172, 464–476.

References

- Lescoutre, R., Manatschal, G., 2020a. Role of rift-inheritance and segmentation for orogenic evolution: example from the Pyrenean-Cantabrian system Rôle de l'héritage associé au rift et à sa segmentation pour l'évolution orogénique: exemple du système pyrénéo-cantabrique. *Bulletin de la Société Géologique de France* 191.
- Lescoutre, R., Manatschal, G., 2020b. Role of rift-inheritance and segmentation for orogenic evolution: example from the Pyrenean-Cantabrian system Rôle de l'héritage associé au rift et à sa segmentation pour l'évolution orogénique: exemple du système pyrénéo-cantabrique. *Bulletin de la Société Géologique de France* 191.
- Lescoutre, R., Tugend, J., Brune, S., Masini, E., Manatschal, G., 2019. Thermal Evolution of Asymmetric Hyperextended Magma-Poor Rift Systems: Results From Numerical Modeling and Pyrenean Field Observations. *Geochemistry, Geophysics, Geosystems* 20, 4567–4587. <https://doi.org/10.1029/2019GC008600>
- Leutwein, F., Poty, B., Sonet, J., Zimmerman, J.-J., 1970. Age des cavités à cristaux du granite du Mont-Blanc. *C. R. Acad. Sci.*, 156–158.
- Levell, B., Argent, J., Doré, A.G., Fraser, S., 2010. Passive margins: overview. Geological Society, London, *Petroleum Geology Conference series* 7, 823. <https://doi.org/10.1144/0070823>
- Liao, S., Tao, C., Jamieson, J.W., Liu, J., Zhu, C., Barriga, F.J.A.S., Li, W., Liang, J., Yang, W., Zhou, J., Deng, X., Yu, J., 2022. Oxidizing fluids associated with detachment hosted hydrothermal systems: Example from the Suye hydrothermal field on the ultraslow-spreading Southwest Indian Ridge. *Geochimica et Cosmochimica Acta* 328, 19–36. <https://doi.org/10.1016/j.gca.2022.04.025>
- Liati, A., Froitzheim, N., Fanning, C.M., 2005. Jurassic ophiolites within the Valais domain of the Western and Central Alps: geochronological evidence for re-rifting of oceanic crust. *Contributions to Mineralogy and Petrology* 149, 446–461. <https://doi.org/10.1007/s00410-005-0658-7>
- Lister, G.S., Etheridge, M.A., Symonds, P.A., 1991. Detachment models for the formation of passive continental margins. *Tectonics* 10, 1038–1064. <https://doi.org/10.1029/90TC01007>
- Lister, G.S., Etheridge, M.A., Symonds, P.A., 1986. Detachment faulting and the evolution of passive continental margins. *Geology* 14, 246–250. [https://doi.org/10.1130/0091-7613\(1986\)14<246:DFATEO>2.0.CO;2](https://doi.org/10.1130/0091-7613(1986)14<246:DFATEO>2.0.CO;2)
- Liu, X., Xing, H., Zhang, D., 2017. Influences of Hydraulic Fracturing on Fluid Flow and Mineralization at the Vein-Type Tungsten Deposits in Southern China. *Geofluids* 2017, 4673421. <https://doi.org/10.1155/2017/4673421>

References

- Lockner, D.A., Byerlee, J.D., Kuksenko, V., Ponomarev, A., Sidorin, A., 1991. Quasi-static fault growth and shear fracture energy in granite. *Nature* 350, 39–42. <https://doi.org/10.1038/350039a0>
- Lockner, D.A., Morrow, C., Moore, D., Hickman, S., 2011. Low strength of deep San Andreas fault gouge from SAFOD core. *Nature* 472, 82–85.
- Logan, R.G., Murray, W.J., Williams, N., 1990. Hyc silver-lead-zinc deposit, McArthur River. *Geology of the mineral deposits of Australia and Papua New Guinea* 1, 907–911.
- Lombardo, B., Rubatto, D., Castelli, D., 2002. Ion microprobe U-Pb dating of zircon from a Monviso metaplagiognite: implications for the evolution of the Piedmont-Liguria Tethys in the Western Alps. *Ophioliti* 27, 109–117.
- Long, K.R., 1992. Preliminary descriptive deposit model for detachment-fault related mineralization, in: Bliss, J. (Ed.), *Developments in Mineral Deposit Modeling*, U.S. Geological Survey Bulletin.
- Loprieno, A., Bousquet, R., Bucher, S., Ceriani, S., Dalla Torre, F.H., Fügenschuh, B., Schmid, S.M., 2011. The Valais units in Savoy (France): a key area for understanding the palaeogeography and the tectonic evolution of the Western Alps. *International Journal of Earth Sciences* 100, 963–992. <https://doi.org/10.1007/s00531-010-0595-1>
- Loreau, J.-P., Gely, J.-P., Rampnoux, J.-P., 1995. Cycles stratigraphiques dans les séries alpines du Lias et de l'Aalénien de part et d'autre du Front pennique (Savoie, France) : contrôle tectonique et rapport avec l'eustatisme. *Eclogae Geologicae Helveticae* 88, 529–551. <https://doi.org/doi.org/10.5169/seals-167686>
- Losh, S., 1997. Stable isotope and modeling studies of fluid-rock interaction associated with the Snake Range and Mormon Peak detachment faults, Nevada. *Geological Society of America Bulletin* 109, 300–323.
- Loudon, A.G., Lee, M.K., Dowling, J.F., Bourn, R., 1975. Lady Loretta silver-lead-zinc deposit. *Economic Geology of Australia and Papua New Guinea* 1, 377–382.
- Loup, B.F.R., 1992. Evolution de la partie septentrionale du domaine helvétique en Suisse occidentale au Trias et au Lias : contrôle par subsidence thermique et variations du niveau marin. Université de Genève, Genève.
- Lu, Y., Stehly, L., Brossier, R., Paul, A., AlpArray Working Group, 2020. Imaging Alpine crust using ambient noise wave-equation tomography. *Geophysical Journal International* 222, 69–85. <https://doi.org/10.1093/gji/ggaa145>
- Lu, Y., Stehly, L., Paul, A., AlpArray Working Group, 2018. High-resolution surface wave tomography of the European crust and uppermost mantle from ambient seismic noise. *Geophysical Journal International* 214, 1136–1150. <https://doi.org/10.1093/gji/ggy188>

References

- Lugeon, M., 1929. Géologie de Saillon (Valais). *Eclogae Geologicae Helvetiae* 22.
- Lugeon, M., 1910. Carte géologique des hautes-alpes calcaires entre la Licerne et la Kander: 1: 50.000.
- Lugeon, M., 1905. Deuxième communication préliminaire sur la géologie de la région comprise entre le Sanetsch et la Kander (Valais-Berne). *Eclogae Geologicae Helvetiae* 421–433.
- Lugeon, M., 1902. Les grandes nappes de recouvrement des Alpes du Chablais et de la Suisse. *Bull. Soc. Géol. France*. 4, 723-.
- Lugeon, M., Argand, E., 1905. Sur les grandes nappes de recouvrement de la zone du Piémont. *C. R. Acad. Sci. Paris*.
- Luque, F.J., Ortega, L., Barrenechea, J.F., Millward, D., Beyssac, O., Huizenga, J.M., 2009. Deposition of highly crystalline graphite from moderate-temperature fluids. *Geology* 37, 275–278.
- M**acchiavelli, C., Vergés, J., Schettino, A., Fernández, M., Turco, E., Casciello, E., Torne, M., Pierantoni, P.P., Tunini, L., 2017. A new southern North Atlantic isochron map: Insights into the drift of the Iberian plate since the Late Cretaceous. *Journal of Geophysical Research: Solid Earth* 122, 9603–9626.
- MacLean, W.H., Kranidiotis, P., 1987. Immobile elements as monitors of mass transfer in hydrothermal alteration; Phelps Dodge massive sulfide deposit, Matagami, Quebec. *Economic Geology* 82, 951–962. <https://doi.org/10.2113/gsecongeo.82.4.951>
- Magloughlin, J.F., 1989. The nature and significance of pseudotachylite from the Nason terrane, North Cascade Mountains, Washington. *Journal of Structural Geology* 11, 907–917. [https://doi.org/10.1016/0191-8141\(89\)90107-7](https://doi.org/10.1016/0191-8141(89)90107-7)
- Magri, F., Akar, T., Gemici, U., Pekdeger, A., 2010. Deep geothermal groundwater flow in the Seferihisar–Bağçova area, Turkey: results from transient numerical simulations of coupled fluid flow and heat transport processes. *Geofluids* 10, 388–405.
- Maino, M., Casini, L., Ceriani, A., Decarlis, A., Di Giulio, A., Seno, S., Setti, M., Stuart, F.M., 2015. Dating shallow thrusts with zircon (U-Th)/He thermochronometry—The shear heating connection. *Geology* 43, 495–498. <https://doi.org/10.1130/G36492.1>
- Maldonado, M., Carmona, M.C., Uriz, M.J., Cruzado, A., 1999. Decline in Mesozoic reef-building sponges explained by silicon limitation. *Nature* 401, 785–788.

References

- Malusà, M.G., Guillot, S., Zhao, L., Paul, A., Solarino, S., Dumont, T., Schwartz, S., Aubert, C., Baccheschi, P., Eva, E., 2021. The deep structure of the Alps based on the CIFALPS seismic experiment: A synthesis. *Geochemistry, Geophysics, Geosystems* 22, e2020GC009466.
- Malusà, M.G., Faccenna, C., Garzanti, E., Polino, R., 2011a. Divergence in subduction zones and exhumation of high pressure rocks (Eocene Western Alps). *Earth and Planetary Science Letters* 310, 21–32. <https://doi.org/10.1016/j.epsl.2011.08.002>
- Malusà, M.G., Villa, I.M., Vezzoli, G., Garzanti, E., 2011b. Detrital geochronology of unroofing magmatic complexes and the slow erosion of Oligocene volcanoes in the Alps. *Earth and Planetary Science Letters* 301, 324–336. <https://doi.org/10.1016/j.epsl.2010.11.019>
- Malusà, M.G., Philippot, P., Zattin, M., Martin, S., 2006. Late stages of exhumation constrained by structural, fluid inclusion and fission track analyses (Sesia–Lanzo unit, Western European Alps). *Earth and Planetary Science Letters* 243, 565–580. <https://doi.org/10.1016/j.epsl.2005.12.030>
- Manatschal, G., Chenin, P., Lescoutre, R., Miró, J., Cadenas, P., Saspiturry, N., Masini, E., Chevrot, S., Ford, M., Jolivet, L., 2021. The role of inheritance in forming rifts and rifted margins and building collisional orogens: a Biscay-Pyrenean perspective. *BSGF-Earth Sciences Bulletin* 192, 55.
- Manatschal, G., Lavier, L., Chenin, P., 2015. The role of inheritance in structuring hyperextended rift systems: Some considerations based on observations and numerical modeling. *Gondwana Research* 27, 140–164. <https://doi.org/10.1016/j.gr.2014.08.006>
- Manatschal, G., Sauter, D., Karpoff, A.M., Masini, E., Mohn, G., Lagabrielle, Y., 2011. The Chenaillet Ophiolite in the French/Italian Alps: An ancient analogue for an Oceanic Core Complex? *Lithos* 124, 169–184. <https://doi.org/10.1016/j.lithos.2010.10.017>
- Manatschal, G., 2004. New models for evolution of magma-poor rifted margins based on a review of data and concepts from West Iberia and the Alps. *International Journal of Earth Sciences* 93, 432–466.
- Manatschal, G., Froitzheim, N., Rubenach, M., Turrin, B.D., 2001. The role of detachment faulting in the formation of an ocean-continent transition: insights from the Iberia Abyssal Plain. *Geological Society, London, Special Publications* 187, 405. <https://doi.org/10.1144/GSL.SP.2001.187.01.20>
- Manatschal, G., Marquer, D., Früh-Green, G.L., 2000. Channelized fluid flow and mass transfer along a rift-related detachment fault (Eastern Alps, southeast Switzerland). *GSA Bulletin* 112, 21–33. [https://doi.org/10.1130/0016-7606\(2000\)112<21:CFFAMT>2.0.CO;2](https://doi.org/10.1130/0016-7606(2000)112<21:CFFAMT>2.0.CO;2)

References

- Manatschal, G., 1999. Fluid- and reaction-assisted low-angle normal faulting: evidence from rift-related brittle fault rocks in the Alps (Err Nappe, eastern Switzerland). *Journal of Structural Geology* 21, 777–793. [https://doi.org/10.1016/S0191-8141\(99\)00069-3](https://doi.org/10.1016/S0191-8141(99)00069-3)
- Mancktelow, N.S., Pavlis, T.L., 1994. Fold-fault relationships in low-angle detachment systems. *Tectonics* 13, 668–685. <https://doi.org/10.1029/93TC03489>
- Mann, P., Gahagan, L., Gordon, M.B., 2003. Tectonic setting of the world's giant oil and gas fields.
- Mark, D.F., Kelley, S.P., Lee, M.R., Parnell, J., Sherlock, S.C., Brown, D.J., 2008. Ar–Ar dating of authigenic K-feldspar: Quantitative modelling of radiogenic argon-loss through subgrain boundary networks. *Geochimica et Cosmochimica Acta* 72, 2695–2710. <https://doi.org/10.1016/j.gca.2008.03.018>
- Marone, C., Scholz, C.H., 1989. Particle-size distribution and microstructures within simulated fault gouge. *Journal of Structural Geology* 11, 799–814. [https://doi.org/10.1016/0191-8141\(89\)90099-0](https://doi.org/10.1016/0191-8141(89)90099-0)
- Marro, C., 1987. Histoire des granitoides du Mont Blanc en Suisse. *Bulletin de la Société Fribourgeoise des Sciences Naturelles* 76, 73–128.
- Marshall, D., Kirschner, D., Bussy, F., 1997. A Variscan pressure-temperature-time path for the NE Mont Blanc massif. *Contributions to Mineralogy and Petrology* 126, 416–428.
- Marshall, D., Meisser, N., Taylor, R.P., 1998a. Fluid inclusion, stable isotope and Ar–Ar evidence for the age and origin of gold-bearing quartz veins at Mont Chemin, Switzerland. *Mineralogy and Petrology* 62, 147–165.
- Marshall, Daniel, Pfeifer, H.-R., Hunziker, J.C., Kirschner, D., 1998b. A pressure-temperature-time path for the NE Mont-Blanc massif; fluid-inclusion, isotopic and thermobarometric evidence. *European Journal of Mineralogy* 10, 1227–1240.
- Martz, P., Cathelineau, M., Mercadier, J., Boiron, M.-C., Jaguin, J., Tarantola, A., Demacon, M., Gerbeaud, O., Quirt, D., Doney, A., Ledru, P., 2017. C-O-H-N fluids circulations and graphite precipitation in reactivated Hudsonian shear zones during basement uplift of the Wollaston-Mudjatik Transition Zone: Example of the Cigar Lake U deposit. *Lithos* 294–295, 222–245. <https://doi.org/10.1016/j.lithos.2017.10.001>
- Masini, E., Manatschal, G., Tugend, J., Mohn, G., Flament, J.-M., 2014. The tectono-sedimentary evolution of a hyper-extended rift basin: the example of the Arzacq–Mauléon rift system (Western Pyrenees, SW France). *International Journal of Earth Sciences* 103, 1569–1596. <https://doi.org/10.1007/s00531-014-1023-8>

References

- Masini, E., Manatschal, G., Mohn, G., Unternehr, P., 2012. Anatomy and tectono-sedimentary evolution of a rift-related detachment system: The example of the Err detachment (central Alps, SE Switzerland). *GSA Bulletin* 124, 1535–1551. <https://doi.org/10.1130/B30557.1>
- Masini, E., Manatschal, G., Mohn, G., Ghienne, J.-F., Lafont, F., 2011. The tectono-sedimentary evolution of a supra-detachment rift basin at a deep-water magma-poor rifted margin: the example of the Samedan Basin preserved in the Err nappe in SE Switzerland. *Basin Research*,
- Massaad, M., 1973. Pétrographie de quelques shales de l'Aalénien de l'Helvétique et de l'Ultraschiste. *Bull. Soc. vaud. Sci. nat* 373–383.
- Masson, H., 1988. Les décrochements de la vallée du Rhône. *Abstr. 2ème Symp. NFP, Sion* 20.
- Masson, H., Herb, R., Steck, A., 1980. Helvetic Alps of Western Switzerland, excursion no. I, in: *Geology of Switzerland- a Guide Book, Part B: Geological Excursions, Comm. Géol. Suisse. Wepf, Basel*.
- Masson, H., 1976. Un siècle de géologie des Préalpes : de la découverte des nappes à la recherche de leur dynamique. *Eclogae Geologicae Helveticae* 69, 527–575. <https://doi.org/doi.org/10.5169/seals-164526>
- Mazzini, A., Etiope, G., 2017. Mud volcanism: An updated review. *Earth-Science Reviews* 168, 81–112. <https://doi.org/10.1016/j.earscirev.2017.03.001>
- McAleer, R.J., Bish, D.L., Kunk, M.J., Sicard, K.R., Valley, P.M., Walsh, G.J., Wathen, B.A., Wintsch, R.P., 2017. Reaction softening by dissolution–precipitation creep in a retrograde greenschist facies ductile shear zone, New Hampshire, USA. *Journal of Metamorphic Geology* 35, 95–119.
- McCaig, A.M., Harris, M., 2012. Hydrothermal circulation and the dike-gabbro transition in the detachment mode of slow seafloor spreading. *Geology* 40, 367–370. <https://doi.org/10.1130/G32789.1>
- McCaig, A.M., 1988. Deep fluid circulation in fault zones. *Geology* 16, 867–870.
- McCarthy, A., Tugend, J., Mohn, G., Candiotti, L., Chelle-Michou, C., Arculus, R., Schmalholz, S.M., Müntener, O., 2020. A case of Ampferer-type subduction and consequences for the Alps and the Pyrenees. *American Journal of Science* 320, 313–372.
- McCarthy, A., Chelle-Michou, C., Müntener, O., Arculus, R., Blundy, J., 2018. Subduction initiation without magmatism: The case of the missing Alpine magmatic arc. *Geology* 46, 1059–1062. <https://doi.org/10.1130/G45366.1>

References

- McCollom, T.M., Bach, W., 2009. Thermodynamic constraints on hydrogen generation during serpentinization of ultramafic rocks. *Geochimica et Cosmochimica Acta* 73, 856–875.
- McCuaig, T., Scarselli, S., O'Connor, T., Busuttill, S., McCormack, N., 2018. The power of a systems approach to mineral and petroleum exploration in sedimentary basins. *Metals, minerals, and society* 21, 39–62.
- McCuaig, T.C., Hronsky, J.M., 2014. The mineral system concept: the key to exploration targeting.
- McGrew, A.J., 1993. The origin and evolution of the southern Snake Range décollement, east central Nevada. *Tectonics* 12, 21–34.
- McIntosh, K., van Avendonk, H., Lavier, L., Lester, W.R., Eakin, D., Wu, F., Liu, C.-S., Lee, C.-S., 2013. Inversion of a hyper-extended rifted margin in the southern Central Range of Taiwan. *Geology* 41, 871–874. <https://doi.org/10.1130/G34402.1>
- McKenzie, D., 1978. Some remarks on the development of sedimentary basins. *Earth and Planetary Science Letters* 40, 25–32. [https://doi.org/10.1016/0012-821X\(78\)90071-7](https://doi.org/10.1016/0012-821X(78)90071-7)
- Meiller, C., 2013. Etude cristallographique de solutions solides de minéraux argileux. Impact de la déshydratation des smectites sur les surpressions dans les bassins sédimentaires. Université Pierre et Marie Curie-Paris VI.
- Meinhold, G., Roberts, N.M., Arslan, A., Jensen, S., Ebbestad, J.O.R., Högström, A.E., Høyberget, M., Agić, H., Palacios, T., Taylor, W.L., 2020. U–Pb dating of calcite in ancient carbonates for age estimates of syn-to post-depositional processes: a case study from the upper Ediacaran strata of Finnmark, Arctic Norway. *Geological Magazine* 157, 1367–1372.
- Meister, C., Loup, B., 1989. Les gisements d'ammonites liasiques (Hettangien à Pliensbachien) du Ferdenrothorn (Valais, Suisse) : analyses paléontologique, biostratigraphique et aspects lithostratigraphiques. *Eclogae Geologicae Helvetiae* 1003–1041.
- Melosh, H.J., 1979. Acoustic fluidization: A new geologic process? *Journal of Geophysical Research: Solid Earth* 84, 7513–7520. <https://doi.org/10.1029/JB084iB13p07513>
- Ménard, G., Molnar, P., Platt, J.P., 1991. Budget of crustal shortening and subduction of continental crust in the Alps. *Tectonics* 10, 231–244.
- Menard, G., Thouvenot, F., 1984. Ecaillage de la lithosphère européenne sous les Alpes Occidentales; arguments gravimétriques et sismiques liés à l'anomalie d'Ivrea. *Bulletin de la Société Géologique de France* S7-XXVI, 875–884. <https://doi.org/10.2113/gssgfbull.S7-XXVI.5.875>

References

- Ménot, R.-P., Peucat, J.J., Scarenzi, D., Piboule, M., 1988. 496 My age of plagiogranites in the Chamrousse ophiolite complex (external crystalline massifs in the French Alps): evidence of a Lower Paleozoic oceanization. *Earth and Planetary Science Letters* 88, 82–92.
- Merriman, R.J., 1999. Patterns of low-grade metamorphism in metapelitic rocks. *Low-grade metamorphism* 60–107.
- Meunier, A., Velde, B., Velde, B., 2004. *Illite: Origins, evolution and metamorphism*. Springer Science & Business Media.
- Meyer, S., 2002. Etude géologique de la couverture mésozoïque para-autochtone du Mt-Blanc et des unités helvétiques au sud-ouest du Mt-Blanc. Institut de Géologie et Paléontologie, Université de Lausanne.
- Miller, S.A., 2013. Chapter 1 - The Role of Fluids in Tectonic and Earthquake Processes, in: Dmowska, R. (Ed.), *Advances in Geophysics*. Elsevier, pp. 1–46. <https://doi.org/10.1016/B978-0-12-380940-7.00001-9>
- Mining Data online, 2022a. Century mine. URL <https://miningdataonline.com/property/287/Century-Mine.aspx>
- Mining Data online, 2022b. Pend Oreille. Mining data online. URL <https://miningdataonline.com/property/208/Pend-Oreille-Mine.aspx>
- Miró, J., Manatschal, G., Cadenas, P., Muñoz, J.A., 2021. Reactivation of a hyperextended rift system: The Basque–Cantabrian Pyrenees case. *Basin Research* 33, 3077–3101.
- Mitchell, A.J., Allison, P.A., Gorman, G.J., Piggott, M.D., Pain, C.C., 2011. Tidal circulation in an ancient epicontinental sea: The Early Jurassic Laurasian Seaway. *Geology* 39, 207–210. <https://doi.org/10.1130/G31496.1>
- Mock, S., Herwegh, M., 2017. Tectonics of the central Swiss Molasse Basin: Post-Miocene transition to incipient thick-skinned tectonics? *Tectonics* 36, 1699–1723. <https://doi.org/10.1002/2017TC004584>
- Mohn, G., Manatschal, G., Beltrando, M., Hauptert, I., 2014. The role of rift-inherited hyper-extension in Alpine-type orogens. *Terra Nova* 26, 347–353. <https://doi.org/10.1111/ter.12104>
- Mohn, G., Manatschal, G., Beltrando, M., Masini, E., Kusznir, N., 2012. Necking of continental crust in magma-poor rifted margins: Evidence from the fossil Alpine Tethys margins. *Tectonics* 31. <https://doi.org/10.1029/2011TC002961>
- Mohn, G., Manatschal, G., Masini, E., Müntener, O., 2011. Rift-related inheritance in orogens: a case study from the Austroalpine nappes in Central Alps (SE-Switzerland and N-Italy).

References

- International Journal of Earth Sciences 100, 937–961. <https://doi.org/10.1007/s00531-010-0630-2>
- Mohn, G., Manatschal, G., Müntener, O., Beltrando, M., Masini, E., 2010. Unravelling the interaction between tectonic and sedimentary processes during lithospheric thinning in the Alpine Tethys margins. *International Journal of Earth Sciences* 99, 75–101.
- Moine, B., Fortune, J.P., Moreau, P., Viguiier, F., 1989. Comparative mineralogy, geochemistry, and conditions of formation of two metasomatic talc and chlorite deposits; Trimouns (Pyrenees, France) and Rabenwald (Eastern Alps, Austria). *Economic Geology* 84, 1398–1416. <https://doi.org/10.2113/gsecongeo.84.5.1398>
- Montadert, L., Roberts, D.G., Auffret, G.A., Bock, W., DuPeuble, P.A., Hailwood, E.A., Harrison, W., Kagami, H., Lumsden, D.N., Muller, C., 1977. Rifting and subsidence on passive continental margins in the North East Atlantic. *Nature* 268, 305–309.
- Monzawa, N., Otsuki, K., 2003. Comminution and fluidization of granular fault materials: implications for fault slip behavior. *Tectonophysics* 367, 127–143. [https://doi.org/10.1016/S0040-1951\(03\)00133-1](https://doi.org/10.1016/S0040-1951(03)00133-1)
- Moore, D.E., Lockner, D.A., Hickman, S., 2016. Hydrothermal frictional strengths of rock and mineral samples relevant to the creeping section of the San Andreas Fault. *Journal of Structural Geology* 89, 153–167. <https://doi.org/10.1016/j.jsg.2016.06.005>
- Moris-Muttoni, B., Raimbourg, H., Augier, R., Champallier, R., Le Trong, E., 2022. The impact of melt versus mechanical wear on the formation of pseudotachylyte veins in accretionary complexes. *Scientific reports* 12, 1–12.
- Morrison, J., Anderson, J.L., 1998. Footwall Refrigeration Along a Detachment Fault: Implications for the Thermal Evolution of Core Complexes. *Science* 279, 63. <https://doi.org/10.1126/science.279.5347.63>
- Morrow, C.A., Moore, D.E., Lockner, D.A., 2000. The effect of mineral bond strength and adsorbed water on fault gouge frictional strength. *Geophysical Research Letters* 27, 815–818. <https://doi.org/10.1029/1999GL008401>
- Motus, M., Nardin, E., Mouthereau, F., Denèle, Y., 2022. Evolution of rift-related cover-basement decoupling revealed by 5 brecciation processes in the eastern Pyrenees. *BSGF - Earth Sciences Bulletin*.
- Mouthereau, F., Angrand, P., Jourdon, A., Ternois, S., Fillon, C., Calassou, S., Chevrot, S., Ford, M., Jolivet, L., Manatschal, G., Masini, E., Thion, I., Vidal, O., Baudin, T., 2021. Cenozoic mountain building and topographic evolution in Western Europe: impact of billions of years

References

- of lithosphere evolution and plate kinematics. *Bulletin de la Société Géologique de France* 192, 56. <https://doi.org/10.1051/bsgf/2021040>
- Mugnier, J.-L., Guellec, S., Menard, G., Roure, F., Tardy, M., Vialon, P., 1990. A crustal scale balanced cross-section through the external Alps deduced from the ECORS profile. *Mémoires de la Société géologique de France (1833)* 156, 203–216.
- Mukherjee, I., Large, R., 2017. Application of pyrite trace element chemistry to exploration for SEDEX style Zn-Pb deposits: McArthur Basin, Northern Territory, Australia. *Ore Geology Reviews* 81, 1249–1270. <https://doi.org/10.1016/j.oregeorev.2016.08.004>
- Müller, P., Weise, S.M., Althaus, E., Bach, W., Behr, H.J., Borchardt, R., Bräuer, K., Drescher, J., Erzinger, J., Faber, E., 1997. Paleofluids and recent fluids in the upper continental crust: Results from the German Continental Deep Drilling Program (KTB). *Journal of Geophysical Research: Solid Earth* 102, 18233–18254.
- Müller, R., Petter Ngstuen, J., Eide, F., Lie, H., 2005. Late Permian to Triassic basin infill history and palaeogeography of the Mid-Norwegian shelf—East Greenland region, in: Wandås, B.T.G., Nystuen, J.P., Eide, E., Gradstein, F. (Eds.), *Norwegian Petroleum Society Special Publications*. Elsevier, pp. 165–189. [https://doi.org/10.1016/S0928-8937\(05\)80048-7](https://doi.org/10.1016/S0928-8937(05)80048-7)
- Müller, R.D., Hassan, R., Gurnis, M., Flament, N., Williams, S.E., 2018. Dynamic topography of passive continental margins and their hinterlands since the Cretaceous. *Gondwana Research* 53, 225–251. <https://doi.org/10.1016/j.gr.2017.04.028>
- Munoz, M., De Andrade, V., Vidal, O., Lewin, E., Pascarelli, S., Susini, J., 2006. Redox and speciation micromapping using dispersive X-ray absorption spectroscopy: Application to iron in chlorite mineral of a metamorphic rock thin section. *Geochemistry, Geophysics, Geosystems* 7.
- Munoz, M., Boyce, A.J., Courjault-Rade, P., Fallick, A.E., Tollon, F., 1999. Continental basinal origin of ore fluids from southwestern Massif Central fluorite veins (Albigeois, France): evidence from fluid inclusion and stable isotope analyses. *Applied Geochemistry* 14, 447–458.
- Muñoz-Barrera, J.M., Rotevatn, A., Gawthorpe, R., Henstra, G., Kristensen, T.B., 2021. Supradetachment basins in necking domains of rifted margins: insights from the Norwegian Sea. *Basin Research*.
- Muñoz-Barrera, J.M., Rotevatn, A., Gawthorpe, R.L., Henstra, G.A., Kristensen, T.B., 2020. The role of structural inheritance in the development of high-displacement crustal faults in the necking domain of rifted margins: The Klakk Fault Complex, Frøya High, offshore mid-Norway. *Journal of Structural Geology* 140, 104163.
- Mussett, A.E., 1969. Diffusion measurements and the potassium-argon method of dating. *Geophysical Journal International* 18, 257–303.

References

- Mutter, J.C., Buck, W.R., Zehnder, C.M., 1988. Convective partial melting: 1. A model for the formation of thick basaltic sequences during the initiation of spreading. *Journal of Geophysical Research: Solid Earth* 93, 1031–1048.
- Mutter, J.C., Larson, R.L., 1989. Extension of the Exmouth Plateau, offshore northwestern Australia: Deep seismic reflection/refraction evidence for simple and pure shear mechanisms. *Geology* 17, 15–18. [https://doi.org/10.1130/0091-7613\(1989\)017<0015:EOTEPO>2.3.CO;2](https://doi.org/10.1130/0091-7613(1989)017<0015:EOTEPO>2.3.CO;2)
- Mutti, E., 1992. Turbidite Sandstones. AGIP—Istituto di Geologia Università di Parma.
- Nägler, Th.F., Pettke, Th., Marshall, D., 1995. Initial isotopic heterogeneity and secondary disturbance of the Sm-Nd system in fluorites and fluid inclusions: A study on mesothermal veins from the central and western Swiss Alps. *Chemical Geology* 125, 241–248. [https://doi.org/10.1016/0009-2541\(95\)00091-Y](https://doi.org/10.1016/0009-2541(95)00091-Y)
- Nakamura, Y., Oohashi, K., Toyoshima, T., Satish-Kumar, M., Akai, J., 2015. Strain-induced amorphization of graphite in fault zones of the Hidaka metamorphic belt, Hokkaido, Japan. *Journal of Structural Geology* 72, 142–161. <https://doi.org/10.1016/j.jsg.2014.10.012>
- Nakamura, Y., Toyoshima, T., Satish-Kumar, M., 2018. Microstructure and geochemical signatures of metasedimentary origin pseudotachylyte: Implications for fluid activity during paleoseismicity. *Tectonophysics* 745, 170–182. <https://doi.org/10.1016/j.tecto.2018.07.010>
- Nance, R.D., Murphy, J.B., Santosh, M., 2014. The supercontinent cycle: A retrospective essay. *Gondwana Research* 25, 4–29. <https://doi.org/10.1016/j.gr.2012.12.026>
- Neiva, A.M.R., Silva, M., Gomes, M.E.P., Campos, T.F.C., 2002. Geochemistry of coexisting biotite and muscovite of Portuguese peraluminous granitic differentiation series. *Geochemistry* 62, 197–215.
- Nemčok, M., 2016. Introduction to hydrocarbons in rift and passive margin settings, in: *Rift and Passive Margins*. Cambridge University Press.
- Neves, L.J.P.F., 1997. Trace element content and partitioning between biotite and muscovite of granitic rocks; a study in the Viseu region (central Portugal). *European Journal of Mineralogy* 9, 849–857.
- Nibourel, L., Berger, A., Egli, D., Heuberger, S., Herwegh, M., 2021. Structural and thermal evolution of the eastern Aar Massif: insights from structural field work and Raman thermometry. *Swiss journal of geosciences* 114, 1–43.

References

- Nicolas, A., Polino, R., Hirn, A., Nicolich, Rinald., 1990. ECORS-CROP traverse and deep structure of the western Alps: a synthesis. *Mem. Soc. Geol. Fr* 156, 15–27.
- Nirrengarten, M., Manatschal, G., Tugend, J., Kuzsnir, N., Sauter, D., 2018. Kinematic evolution of the southern North Atlantic: Implications for the formation of hyperextended rift systems. *Tectonics* 37, 89–118.
- Nirrengarten, M., Manatschal, G., Yuan, X.P., Kuzsnir, N.J., Maillot, B., 2016. Application of the critical Coulomb wedge theory to hyper-extended, magma-poor rifted margins. *Earth and Planetary Science Letters* 442, 121–132. <https://doi.org/10.1016/j.epsl.2016.03.004>
- Nissen, S.S., Hayes, D.E., Bochu, Y., Zeng, W., Chen, Y., Nu, X., 1995. Gravity, heat flow, and seismic constraints on the processes of crustal extension: Northern margin of the South China Sea. *Journal of Geophysical Research: Solid Earth* 100, 22447–22483.
- Norman, M.D., Leeman, W.P., Mertzman, S.A., 1992. Granites and rhyolites from the northwestern USA: temporal variation in magmatic processes and relations to tectonic setting. *Earth and Environmental Science Transactions of the Royal Society of Edinburgh* 83, 71–81.
- NS Energy, 2022. Century mine. URL <https://www.nsenergybusiness.com/projects/century-zinc-mine-australia/>
- Nteme Mukonzo, J., Boiron, M.-C., Lagabrielle, Y., Cathelineau, M., Quesnel, B., 2021. Fluid–rock interactions along detachment faults during continental rifting and mantle exhumation: the case of the Urdach Iherzolite body (North Pyrenees). *Journal of the Geological Society* 178, jgs2020-116. <https://doi.org/10.1144/jgs2020-116>
- Ochoa Alencastre, A., Chenevoy, M., 1979. Etude gîtologique des minéralisations fluorées du massif de Rocheray, Savoie - Alpes françaises externes. Université Claude Bernard - Lyon I.
- Oliver, J., Isacks, B., 1967. Deep earthquake zones, anomalous structures in the upper mantle, and the lithosphere. *Journal of Geophysical Research (1896-1977)* 72, 4259–4275. <https://doi.org/10.1029/JZ072i016p04259>
- Oliver, N.H., McLellan, J.G., Hobbs, B.E., Cleverly, J.S., Ord, A., Feltrin, L., 2006. Numerical models of extensional deformation, heat transfer, and fluid flow across basement-cover interfaces during basin-related mineralization. *Economic Geology* 101, 1–31.
- Omar, G.I., Steckler, M.S., Buck, W.R., Kohn, B.P., 1989. Fission-track analysis of basement apatites at the western margin of the Gulf of Suez rift, Egypt: evidence for synchronicity of uplift and subsidence. *Earth and Planetary Science Letters* 94, 316–328. [https://doi.org/10.1016/0012-821X\(89\)90149-0](https://doi.org/10.1016/0012-821X(89)90149-0)

References

- Osmundsen, P.T., Péron-Pinvidic, G., 2018. Crustal-Scale Fault Interaction at Rifted Margins and the Formation of Domain-Bounding Breakaway Complexes: Insights From Offshore Norway. *Tectonics* 37, 935–964. <https://doi.org/10.1002/2017TC004792>
- Osmundsen, P.T., Redfield, T.F., 2011. Crustal taper and topography at passive continental margins. *Terra Nova* 23, 349–361. <https://doi.org/10.1111/j.1365-3121.2011.01014.x>
- Osmundsen, P.T., Ebbing, J., 2008. Styles of extension offshore mid-Norway and implications for mechanisms of crustal thinning at passive margins. *Tectonics* 27.
- Otsuki, K., 1998. An empirical evolution law of fractal size frequency of fault population and its similarity law. *Geophysical Research Letters* 25, 671–674. <https://doi.org/10.1029/98GL00380>
- P**antet, A., Epard, J.-L., Masson, H., 2020. Mimicking Alpine thrusts by passive deformation of synsedimentary normal faults: a record of the Jurassic extension of the European margin (Mont Fort nappe, Pennine Alps). *Swiss Journal of Geosciences* 113, 13. <https://doi.org/10.1186/s00015-020-00366-2>
- Paquette, J.-L., Menot, R.-P., Peucat, J.-J., 1989. REE, SmNd and UPb zircon study of eclogites from the Alpine External Massifs (Western Alps): evidence for crustal contamination. *Earth and Planetary Science Letters* 96, 181–198. [https://doi.org/10.1016/0012-821X\(89\)90131-3](https://doi.org/10.1016/0012-821X(89)90131-3)
- Paréjas, E., 1925. La tectonique du Mont Joly (Haute-Savoie). *Eclogae Geologicae Helvetiae* 419–503.
- Paréjas, E., 1922. Géologie de la zone de Chamonix comprise entre le Mont-Blanc et les Aiguilles-Rouges. *Mém. Soc. Phys. Hist. nat. Genève* 373–442.
- Paréjas, E., 1920. La partie sud-ouest du synclinal de Chamonix. *C. R. Soc. Phys. Hist. nat. Genève* 58–60.
- Parneix, J.C., Beaufort, D., Dudoignon, P., Meunier, A., 1985. Biotite chloritization process in hydrothermally altered granites. *Chemical Geology* 51, 89–101.
- Parnell-Turner, R., Escartin, J., Olive, J.-A., Smith, D.K., Petersen, S., 2018. Genesis of corrugated fault surfaces by strain localization recorded at oceanic detachments. *Earth and Planetary Science Letters* 498, 116–128.
- Parry, W.T., Downey, L.M., 1982. Geochemistry of Hydrothermal Chlorite Replacing Igneous Biotite. *Clays and Clay Minerals* 30, 81–90. <https://doi.org/10.1346/CCMN.1982.0300201>

References

- Parsons, T., Thompson, G.A., 1993. Does magmatism influence low-angle normal faulting? *Geology* 21, 247–250. [https://doi.org/10.1130/0091-7613\(1993\)021<0247:DMILAN>2.3.CO;2](https://doi.org/10.1130/0091-7613(1993)021<0247:DMILAN>2.3.CO;2)
- Paton, C., Hellstrom, J., Paul, B., Woodhead, J., Hergt, J., 2011. Iolite: Freeware for the visualisation and processing of mass spectrometric data. *Journal of Analytical Atomic Spectrometry* 26, 2508–2518.
- Patten, C.G.C., Coltat, R., Junge, M., Peillod, A., Ulrich, M., Manatschal, G., Kolb, J., 2022. Ultramafic-hosted volcanogenic massive sulfide deposits: an overlooked sub-class of VMS deposit forming in complex tectonic environments. *Earth-Science Reviews* 224, 103891. <https://doi.org/10.1016/j.earscirev.2021.103891>
- Pec, M., Stünitz, H., Heilbronner, R., Drury, M., de Capitani, C., 2012. Origin of pseudotachylites in slow creep experiments. *Earth and Planetary Science Letters* 355–356, 299–310. <https://doi.org/10.1016/j.epsl.2012.09.004>
- Péron-Pinvidic, G., Manatschal, G., 2019. Rifted margins: State of the art and future challenges. *Frontiers in Earth Science* 218.
- Péron-Pinvidic, G., Manatschal, G., Masini, E., Sutra, E., Flament, J.M., Hauptert, I., Unternehr, P., 2017. Unravelling the along-strike variability of the Angola–Gabon rifted margin: a mapping approach. *Geological Society, London, Special Publications* 438, 49–76.
- Péron-Pinvidic, G., Manatschal, G., Osmundsen, P.T., 2013. Structural comparison of archetypal Atlantic rifted margins: A review of observations and concepts. *Marine and Petroleum Geology* 43, 21–47. <https://doi.org/10.1016/j.marpetgeo.2013.02.002>
- Péron-Pinvidic, G., Manatschal, G., Osmundsen, P.T., 2013. Structural comparison of archetypal Atlantic rifted margins: A review of observations and concepts. *Marine and Petroleum Geology* 43, 21–47. <https://doi.org/10.1016/j.marpetgeo.2013.02.002>
- Persem, M., 2022. Tracing geochemical signals in the Early and Middle Jurassic syn-rift sedimentary record of the European Alpine Tethys margin. *Université de Strasbourg, Université de Strasbourg*.
- Pesquera, A., Torres-Ruiz, J., Gil-Crespo, P.P., Velilla, N., 1999. Chemistry and genetic implications of tourmaline and Li-F-Cs micas from the Valdeflores area (Cáceres, Spain). *American Mineralogist* 84, 55–69.
- Petri, B., Duretz, T., Mohn, G., Schmalholz, S.M., Karner, G.D., Müntener, O., 2019. Thinning mechanisms of heterogeneous continental lithosphere. *Earth and Planetary Science Letters* 512, 147–162. <https://doi.org/10.1016/j.epsl.2019.02.007>

References

- Peveerelli, V., Berger, A., Mulch, A., Pettke, T., Piccoli, F., Herwegh, M., 2022. Epidote U-Pb geochronology and H isotope geochemistry trace pre-orogenic hydration of midcrustal granitoids. *Geology* 50, 1073–1077. <https://doi.org/10.1130/G50028.1>
- Pfeifer, H.-R., Oberhänsli, H., Epprecht, W., 1988. Geochemical evidence for a synsedimentary hydrothermal origin of Jurassic iron-manganese deposits at Gonzen (Sargans, Helvetic Alps, Switzerland). *Marine Geology* 84, 257–272. [https://doi.org/10.1016/0025-3227\(88\)90105-3](https://doi.org/10.1016/0025-3227(88)90105-3)
- Pfiffner, O.A., 2014. *Geology of the Alps*. John Wiley & Sons.
- Pfiffner, O.A., 1993. The structure of the Helvetic nappes and its relation to the mechanical stratigraphy. *Journal of Structural Geology* 15, 511–521. [https://doi.org/10.1016/0191-8141\(93\)90145-Z](https://doi.org/10.1016/0191-8141(93)90145-Z)
- Pfiffner, O.A., Ramsay, J.G., Schmid, S.M., 2011. Structural map of the Helvetic Zone of the Swiss Alps. Geological special map 1.
- Philippe, Y., 1994. Transfer zone in the Southern Jura thrust belt (Eastern France): Geometry, development, and comparison with analogue modeling experiments, in: *Hydrocarbon and Petroleum Geology of France*. Springer, pp. 327–346.
- Philippot, P., Chevallier, P., Chopin, C., Dubessy, J., 1995. Fluid composition and evolution in coesite-bearing rocks (Dora-Maira massif, Western Alps): implications for element recycling during subduction. *Contributions to Mineralogy and Petrology* 121, 29–44.
- Pinto, V.H.G., Manatschal, G., Karpoff, A.M., Viana, A., 2015. Tracing mantle-reacted fluids in magma-poor rifted margins: The example of Alpine Tethyan rifted margins. *Geochemistry, Geophysics, Geosystems* 16, 3271–3308.
- Pinto, V.H., 2014. Linking tectonic evolution with fluid history in hyperextended rifted margins: examples from the fossil Alpine and Pyrenean rift systems, and the present-day Iberia rifted margin. *Strasbourg*.
- Pirajno, F., Cawood, P.A., 2009. *Hydrothermal processes and mineral systems*. Springer.
- Pirard, C., Hermann, J., 2015. Focused fluid transfer through the mantle above subduction zones. *Geology* 43, 915–918. <https://doi.org/10.1130/G37026.1>
- Piromallo, C., Faccenna, C., 2004. How deep can we find the traces of Alpine subduction? *Geophysical Research Letters* 31.
- Plümper, O., Botan, A., Los, C., Liu, Y., Malthe-Sørensen, A., Jamtveit, B., 2017. Fluid-driven metamorphism of the continental crust governed by nanoscale fluid flow. *Nature Geoscience* 10, 685–690. <https://doi.org/10.1038/ngeo3009>

References

- Polliand, M., Moritz, R., 1999. Basement-hosted quartz-barite sulfide veins in the French Alps; a record of alpine tectonic fluid expulsion in the external crystalline massifs; structural, fluid inclusion, and isotope (S and Sr) evidences. *Economic Geology* 94, 37–56.
- Potdevin, J.-L., Marquer, D., 1987. Quantitative methods for the estimation of mass transfers by fluids in deformed metamorphic rocks. *Journal of Metamorphic Geology* 5, 193–206. <https://doi.org/10.1080/09853111.1987.11105138>
- Poty, B.P., Stalder, H.A., Weisbrod, A.M., 1974. Fluid inclusions studies in quartz from fissures of Western and Central Alps. *SCHWEIZ. MINERAL PETROGR. MITT.*
- Poulet, T., Lesueur, M., Kelka, U., 2021. Dynamic modelling of overprinted low-permeability fault cores and surrounding damage zones as lower dimensional interfaces for multiphysics simulations. *Computers & Geosciences* 150, 104719.
- Prigent, C., Guillot, S., Agard, P., Lemarchand, D., Soret, M., Ulrich, M., 2018. Transfer of subduction fluids into the deforming mantle wedge during nascent subduction: Evidence from trace elements and boron isotopes (Semail ophiolite, Oman). *Earth and Planetary Science Letters* 484, 213–228. <https://doi.org/10.1016/j.epsl.2017.12.008>
- Q**uesnel, B., Boiron, M.-C., Cathelineau, M., Truche, L., Rigaudier, T., Bardoux, G., Agrinier, P., de Saint Blanquat, M., Masini, E., Gaucher, E.C., 2019. Nature and Origin of Mineralizing Fluids in Hyperextensional Systems: The Case of Cretaceous Mg Metasomatism in the Pyrenees. *Geofluids* 2019, 7213050. <https://doi.org/10.1155/2019/7213050>
- R**aith, M.M., Devaraju, T.C., Spiering, B., 2014. Paragenesis and chemical characteristics of the celcian–hyalophane–K-feldspar series and associated Ba–Cr micas in barite-bearing strata of the Mesoarchean Ghattihosahalli Belt, Western Dharwar Craton, South India. *Mineralogy and Petrology* 108, 153–176.
- Ramsay, J.G., 1989. Fold and fault geometry in the western Helvetic nappes of Switzerland and France and its implication for the evolution of the arc of the western Alps. Geological Society, London, Special Publications 45, 33. <https://doi.org/10.1144/GSL.SP.1989.045.01.02>
- Ramsay, J.G., Huber, M.I., 1983. The techniques of modern structural geology: strain analyses. Course
- Ramsay, J.G., 1981. Tectonics of the Helvetic Nappes. Geological Society, London, Special Publications 9, 293. <https://doi.org/10.1144/GSL.SP.1981.009.01.26>
- Ramsay, J.G., 1980. The crack–seal mechanism of rock deformation. *Nature* 284, 135–139.

References

- Ranero, C.R., Pérez-Gussinyé, M., 2010. Sequential faulting explains the asymmetry and extension discrepancy of conjugate margins. *Nature* 468, 294–299.
- Rapp, J.F., Klemme, S., Butler, I.B., Harley, S.L., 2010. Extremely high solubility of rutile in chloride and fluoride-bearing metamorphic fluids: An experimental investigation. *Geology* 38, 323–326. <https://doi.org/10.1130/G30753.1>
- Rasband, W.S., 1997. ImageJ. Bethesda, MD.
- Rasmussen, B., 2005. Zircon growth in very low grade metasedimentary rocks: evidence for zirconium mobility at ~ 250 C. *Contributions to Mineralogy and Petrology* 150, 146–155.
- Reches, Z., Dewers, T.A., 2005. Gouge formation by dynamic pulverization during earthquake rupture. *Earth and Planetary Science Letters* 235, 361–374.
- Renevier, E., 1890. Monographie géologique des Hautes-Alpes vaudoises. Mat. Carte géol. Suisse.
- Renevier, E., 1852. La géologie des Alpes vaudoises. Bull. Soc. vaud. Sc. nat.
- Renne, P.R., Balco, G., Ludwig, K.R., Mundil, R., Min, K., 2011. Response to the comment by WH Schwarz et al. on “Joint determination of ^{40}K decay constants and $^{40}\text{Ar}^*/^{40}\text{K}$ for the Fish Canyon sanidine standard, and improved accuracy for $^{40}\text{Ar}/^{39}\text{Ar}$ geochronology” by PR Renne et al.(2010). *Geochimica et Cosmochimica Acta* 75, 5097–5100.
- Reston, T., 2020. On the rotation and frictional lock-up of normal faults: Explaining the dip distribution of normal fault earthquakes and resolving the low-angle normal fault paradox. *Tectonophysics* 790, 228550. <https://doi.org/10.1016/j.tecto.2020.228550>
- Reston, T.J., 2009. The structure, evolution and symmetry of the magma-poor rifted margins of the North and Central Atlantic: A synthesis. *Tectonophysics* 468, 6–27. <https://doi.org/10.1016/j.tecto.2008.09.002>
- Reston, T.J., 2005. Polyphase faulting during the development of the west Galicia rifted margin. *Earth and Planetary Science Letters* 237, 561–576. <https://doi.org/10.1016/j.epsl.2005.06.019>
- Reston, T.J., Krawczyk, C.M., Klaeschen, D., 1996. The S reflector west of Galicia (Spain): Evidence from prestack depth migration for detachment faulting during continental breakup. *Journal of Geophysical Research: Solid Earth* 101, 8075–8091.
- Reston, T.J., McDermott, K.G., 2011. Successive detachment faults and mantle unroofing at magma-poor rifted margins. *Geology* 39, 1071–1074. <https://doi.org/10.1130/G32428.1>

References

- Rey, P., Burg, J.-P., Casey, M., 1997. The Scandinavian Caledonides and their relationship to the Variscan belt. *Geological Society, London, Special Publications* 121, 179–200.
- Ribes, C., Ghienne, J.-F., Manatschal, G., Dall'Asta, N., Stockli, D.F., Galster, F., Gillard, M., Karner, G.D., 2020. The Grès Singuliers of the Mont Blanc region (France and Switzerland): stratigraphic response to rifting and crustal necking in the Alpine Tethys. *International Journal of Earth Sciences* 109, 2325–2352. <https://doi.org/10.1007/s00531-020-01902-z>
- Ribes, C., Ghienne, J.-F., Manatschal, G., Decarlis, A., Karner, G.D., Figueredo, P.H., Johnson, C.A., 2019a. Long-lived mega fault-scarps and related breccias at distal rifted margins: insights from present-day and fossil analogues. *Journal of the Geological Society* 176, 801. <https://doi.org/10.1144/jgs2018-181>
- Ribes, C., Manatschal, G., Ghienne, J.-F., Karner, G.D., Johnson, C.A., Figueredo, P.H., Incerpi, N., Epin, M.-E., 2019b. The syn-rift stratigraphic record across a fossil hyper-extended rifted margin: the example of the northwestern Adriatic margin exposed in the Central Alps. *International Journal of Earth Sciences* 108, 2071–2095. <https://doi.org/10.1007/s00531-019-01750-6>
- Ribes, C., Petri, B., Ghienne, J.-F., Manatschal, G., Galster, F., Karner, G.D., Figueredo, P.H., Johnson, C.A., Karpoff, A.-M., 2019c. Tectono-sedimentary evolution of a fossil ocean-continent transition: Tasna nappe, central Alps (SE Switzerland). *GSA Bulletin*. <https://doi.org/10.1130/B35310.1>
- Richardson, C.K., Holland, H.D., 1979. Fluorite deposition in hydrothermal systems. *Geochimica et Cosmochimica Acta* 43, 1327–1335.
- Rietbrock, A., Tiberi, C., Scherbaum, F., Lyon-Caen, H., 1996. Seismic slip on a low angle normal fault in the Gulf of Corinth: Evidence from high-resolution cluster analysis of microearthquakes. *Geophysical Research Letters* 23, 1817–1820.
- Ritter, E., 1897. La bordure sud-ouest du Mont-Blanc (les plis couchés du Mont-Joly et de ses attaches). *Bull. Serv. Carte géol. France* 1–232.
- Roberts, N.M., Rasbury, E.T., Parrish, R.R., Smith, C.J., Horstwood, M.S., Condon, D.J., 2017. A calcite reference material for LA-ICP-MS U-Pb geochronology. *Geochemistry, Geophysics, Geosystems* 18, 2807–2814.
- Roddy, M.S., Reynolds, S.J., Smith, B.M., Ruiz, J., 1988. K-metasomatism and detachment-related mineralization, Harcuvar Mountains, Arizona. *GSA Bulletin* 100, 1627–1639. [https://doi.org/10.1130/0016-7606\(1988\)100<1627:KMADRM>2.3.CO;2](https://doi.org/10.1130/0016-7606(1988)100<1627:KMADRM>2.3.CO;2)
- Rodríguez, A., Weis, P., Magnall, J.M., Gleeson, S.A., 2021. Hydrodynamic constraints on ore formation by basin-scale fluid flow at continental margins: Modelling Zn metallogenesis in the Devonian Selwyn Basin. *Geochemistry, Geophysics, Geosystems* 22, e2020GC009453.

References

- Rodríguez-Pascua, M.A., Calvo, J.P., De Vicente, G., Gomez Gras, D., 2000. Seismites in lacustrine sediments of the Prebetic Zone, SE Spain, and their use as indicators of earthquake magnitudes during the Late Miocene. *Sedimentary Geology* 135, 117–135.
- Rolland, Y., Cox, S.F., Corsini, M., 2009. Constraining deformation stages in brittle–ductile shear zones from combined field mapping and $^{40}\text{Ar}/^{39}\text{Ar}$ dating: The structural evolution of the Grimsel Pass area (Aar Massif, Swiss Alps). *Journal of Structural Geology* 31, 1377–1394. <https://doi.org/10.1016/j.jsg.2009.08.003>
- Rolland, Y., Rossi, M., Cox, S.F., Corsini, M., Mancktelow, N., Pennacchioni, G., Fornari, M., Boullier, A.-M., 2008. $^{40}\text{Ar}/^{39}\text{Ar}$ dating of synkinematic white mica: insights from fluid-rock reaction in low-grade shear zones (Mont Blanc Massif) and constraints on timing of deformation in the NW external Alps. *Geological Society, London, Special Publications* 299, 293–315.
- Rolland, Y., Cox, S., Boullier, A.-M., Pennacchioni, G., Mancktelow, N., 2003. Rare earth and trace element mobility in mid-crustal shear zones: insights from the Mont Blanc Massif (Western Alps). *Earth and Planetary Science Letters* 214, 203–219. [https://doi.org/10.1016/S0012-821X\(03\)00372-8](https://doi.org/10.1016/S0012-821X(03)00372-8)
- Rosenbaum, G., Lister, G.S., 2005. The Western Alps from the Jurassic to Oligocene: spatio-temporal constraints and evolutionary reconstructions. *Earth-Science Reviews* 69, 281–306.
- Rosenberg, C.L., Bellahsen, N., Rabaute, A., Girault, J.B., 2021. Distribution, style, amount of collisional shortening, and their link to Barrovian metamorphism in the European Alps. *Earth-Science Reviews* 103774. <https://doi.org/10.1016/j.earscirev.2021.103774>
- Rosenberg, P.E., 2002. The nature, formation, and stability of end-member illite: A hypothesis. *American Mineralogist* 87, 103–107.
- Rossetti, F., Aldega, L., Tecce, F., Balsamo, F., Billi, A., Brilli, M., 2010. Fluid flow within the damage zone of the Boccheggiano extensional fault (Larderello–Travale geothermal field, central Italy): structures, alteration and implications for hydrothermal mineralization in extensional settings. *Geological Magazine* 148, 558–579. <https://doi.org/10.1017/S001675681000097X>
- Rossi, M., Rolland, Y., 2014. Stable isotope and Ar/Ar evidence of prolonged multiscale fluid flow during exhumation of orogenic crust: Example from the Mont Blanc and Aar Massifs (NW Alps). *Tectonics* 33, 1681–1709. <https://doi.org/10.1002/2013TC003438>
- Rossi, P., Cocherie, A., Fanning, C.M., Ternet, Y., 2003. Datation U-Pb sur zircons des dolérites tholéitiques pyrénéennes (ophites) à la limite Trias–Jurassique et relations avec les tufs volcaniques dits « infra-liasiques » nord-pyrénéens. *Comptes Rendus Geoscience* 335, 1071–1080. <https://doi.org/10.1016/j.crte.2003.09.011>

References

- Roure, F., Choukroune, P., Polino, R., 1996. Deep seismic reflection data and new insights on the bulk geometry of mountain ranges. *Comptes rendus de l'Académie des sciences. Série 2. Sciences de la terre et des planètes* 322, 345–359.
- Roux, M., Bourseau, J.-P., Bas, T., Dumont, T., de Graciansky, P.-C., Lemoine, M., Rudkiewicz, J.-L., 1988. Bathymetric evolution of the Tethyan margin in the western Alps (data from stalked crinoids): a reappraisal of eustatism problems during the Jurassic. *Bulletin de la Société géologique de France, série 8*, 633–41.
- Rubin, J.N., Henry, C.D., Price, J.G., 1993. The mobility of zirconium and other “immobile” elements during hydrothermal alteration. *Chemical Geology* 110, 29–47.
[https://doi.org/10.1016/0009-2541\(93\)90246-F](https://doi.org/10.1016/0009-2541(93)90246-F)
- Rumble, D., III, Duke, E.F., Hoering, T.L., 1986. Hydrothermal graphite in New Hampshire: Evidence of carbon mobility during regional metamorphism. *Geology* 14, 452–455.
[https://doi.org/10.1130/0091-7613\(1986\)14<452:HGINHE>2.0.CO;2](https://doi.org/10.1130/0091-7613(1986)14<452:HGINHE>2.0.CO;2)
- Rys, A., 2020. Les minéralisations Pb-Zn-Cu-Ba du Val Ferret, Valais, Suisse.
- Salomon, E., Rotevatn, A., Kristensen, T.B., Grundvåg, S.-A., Henstra, G.A., Meckler, A.N., Albert, R., Gerdes, A., 2020. Fault-controlled fluid circulation and diagenesis along basin-bounding fault systems in rifts—insights from the East Greenland rift system. *Solid Earth* 11, 1987–2013.
- Sandiford, D., Brune, S., Glerum, A., Naliboff, J., Whittaker, J.M., 2021. Kinematics of footwall exhumation at oceanic detachment faults: solid-block rotation and apparent unbending. *Geochemistry, Geophysics, Geosystems* 22, e2021GC009681.
- Sangster, D.F., 2020. Evidence that Broken Hill-type Pb-Zn deposits are metamorphosed SEDEX deposits. *Mineralium Deposita* 55, 1263–1270.
- Sangster, D.F., 2018. Toward an integrated genetic model for vent-distal SEDEX deposits. *Mineralium Deposita* 53, 509–527.
- Sapin, F., Ringenbach, J.-C., Clerc, C., 2021. Rifted margins classification and forcing parameters. *Scientific Reports* 11, 8199. <https://doi.org/10.1038/s41598-021-87648-3>
- Saspiturry, N., Issautier, B., Razin, P., Andrieu, S., Lasseur, E., Allanic, C., Serrano, O., Baudin, T., cochelin, B., 2021. Review of the syn-rift to early post-rift depositional systems of the Cretaceous Mauléon rift: sedimentary record of continental crust hyperextension and mantle denudation (Western Pyrenees). *Bulletin de la Société Géologique de France*.
- Saspiturry, N., Lahfid, A., Baudin, T., Guillou-Frottier, L., Razin, P., Issautier, B., Le Bayon, B., Serrano, O., Lagabrielle, Y., Corre, B., 2020. Paleogeothermal gradients across an inverted

References

- hyperextended rift system: Example of the Mauléon Fossil Rift (Western Pyrenees). *Tectonics* 39, e2020TC006206.
- Saussure, H.B.D., 1779. *Voyages dans les Alpes*. Fauche, Neuchâtel.
- Sawyer, D.S., 1987. The Role of Partial Melting and Fractional Crystallization in Determining Discordant Migmatite Leucosome Compositions. *Journal of Petrology* 28, 445–473. <https://doi.org/10.1093/petrology/28.3.445>
- Scambelluri, M., Philippot, P., 2001. Deep fluids in subduction zones. *Lithos* 55, 213–227. [https://doi.org/10.1016/S0024-4937\(00\)00046-3](https://doi.org/10.1016/S0024-4937(00)00046-3)
- Schaer, J.-P., 2011. Swiss and Alpine geologists between two tectonic revolutions. Part 2: From drifting continents towards plate tectonics. *Swiss Journal of Geosciences* 104, 507–536.
- Schaer, J.-P., 2010. Swiss and Alpine geologists between two tectonic revolutions. Part 1: from the discovery of nappes to the hypothesis of continental drift. *Swiss Journal of Geosciences* 103, 503–522. <https://doi.org/10.1007/s00015-010-0037-x>
- Schaltegger, U., Abrecht, J., Corfu, F., 2003. The Ordovician orogeny in the Alpine basement: constraints from geochronology and geochemistry in the Aar Massif (Central Alps). *Swiss Bulletin of Mineralogy and Petrology* 83, 183–239.
- Schaltegger, U., Nowak, A., Ulianov, A., Fisher, C.M., Gerdes, A., Spikings, R., Whitehouse, M.J., Bindeman, I., Hanchar, J.M., Duff, J., Vervoort, J.D., Sheldrake, T., Caricchi, L., Brack, P., Müntener, O., 2019. Zircon Petrochronology and $^{40}\text{Ar}/^{39}\text{Ar}$ Thermochronology of the Adamello Intrusive Suite, N. Italy: Monitoring the Growth and Decay of an Incrementally Assembled Magmatic System. *Journal of Petrology* 60, 701–722. <https://doi.org/10.1093/petrology/egz010>
- Schardt, H., 1907. Les vues modernes sur la tectonique et l'origine de la chaîne des Alpes. *Arch. Sci. phys. nat* 4, 356–385 et 483–496.
- Schardt, H., 1900. Encore les régions exotiques. Réplique aux attaques de M. Emile Haug. *Bulletin de la Société Vaudoise de Sciences Naturelles* 36, 147–169.
- Schardt, H., 1898. Les régions exotiques du versant N des Alpes suisses. *Bulletin de la Société Vaudoise de Sciences Naturelles* 34, 114–219.
- Schardt, H., 1893. Sur l'origine des Pré-alpes romandes. *Archives des Sciences physiques et Naturelles de Genève* 30, 570–583.

References

- Schläppi, E., 1980. Geologische und tektonische Entwicklung der Doldenhomdecke und zugehöriger Elemente. Univ. Bern.
- Schmid, S.M., Fügenschuh, B., Kissling, E., Schuster, R., 2004. Tectonic map and overall architecture of the Alpine orogen. *Eclogae Geologicae Helvetiae* 97, 93–117.
- Schmid, S.M., Kissling, E., 2000. The arc of the western Alps in the light of geophysical data on deep crustal structure. *Tectonics* 19, 62–85.
- Schmid, S.M., Zingg, A., Handy, M., 1987. The kinematics of movements along the Insubric Line and the emplacement of the Ivrea Zone. *Tectonophysics* 135, 47–66.
[https://doi.org/10.1016/0040-1951\(87\)90151-X](https://doi.org/10.1016/0040-1951(87)90151-X)
- Schmidt, C., 1920. Texte explicatif de la carte des gisements des matières premières minérales de la Suisse : 1 : 500000 : I. Charbons : Asphalte, Pétrole, Gaz naturels, Schistes bitumineux : II. Sels. : III. Minerais. Edition française.
- Schmidt, C., 1902. Die Bleiglanz – und Eisenerzlagerstätten im Val d’Entremont un Val de Ferrex (La galène et les gisements de minerai de fer dans le Val D’entremont et le Val Ferret).
- Scholz, C.H., 1990. *The mechanics of earthquakes and faulting*. Cambridge university press.
- Scholz, C.H., 1989. Mechanics of faulting. *Annual Review of Earth and Planetary Sciences* 17, 309–334.
- Schroeder, T., Bach, W., Jöns, N., Jöns, S., Monien, P., Klügel, A., 2015. Fluid circulation and carbonate vein precipitation in the footwall of an oceanic core complex, Ocean Drilling Program Site 175, Mid-Atlantic Ridge. *Geochemistry, geophysics, geosystems* 16, 3716–3732.
- Searle, M.P., 2010. Low-angle normal faults in the compressional Himalayan orogen; Evidence from the Annapurna–Dhaulagiri Himalaya, Nepal. *Geosphere* 6, 296–315.
<https://doi.org/10.1130/GES00549.1>
- Segev, A., 1984. Gibbsite mineralization and its genetic implication for the Um Bogma manganese deposit, southwestern Sinai. *Mineralium Deposita* 19, 54–62.
- Septfontaine, M., Lombard, A., 1976. Le Jurassique des Préalpes médianes dans le SW du Chablais (Haute-Savoie, France) : cadre tectonique et lithostratigraphique. *Eclogae Geologicae Helvetiae* 69, 425–460. <https://doi.org/doi.org/10.5169/seals-164518>
- Shanmugam, G., 2016. The seismite problem. *Journal of Palaeogeography* 5, 318–362.
<https://doi.org/10.1016/j.jop.2016.06.002>

References

- Shanmugam, G., 1997. The Bouma Sequence and the turbidite mind set. *Earth-Science Reviews* 42, 201–229. [https://doi.org/10.1016/S0012-8252\(97\)81858-2](https://doi.org/10.1016/S0012-8252(97)81858-2)
- Shelton, K.L., Hendry, J.P., Gregg, J.M., Truesdale, J.P., Somerville, I.D., 2019. Fluid circulation and fault-and fracture-related diagenesis in Mississippian syn-rift carbonate rocks on the northeast margin of the Metalliferous Dublin Basin, Ireland. *Journal of Sedimentary Research* 89, 508–536.
- Shepard, F.P., Goldberg, E.D., Inman, D.L., 1963. *Submarine geology*. Harper & Row New York.
- Sibson, R.H., 2019. Arterial faults and their role in mineralizing systems. *Geoscience Frontiers* 10, 2093–2100. <https://doi.org/10.1016/j.gsf.2019.01.007>
- Sibson, R.H., 2014. Earthquake rupturing in fluid-overpressured crust: how common? *Pure and Applied Geophysics* 171, 2867–2885.
- Sibson, R.H., 2000. Fluid involvement in normal faulting. *Journal of Geodynamics* 29, 469–499.
- Sibson, R.H., 1996. Structural permeability of fluid-driven fault-fracture meshes. *Journal of Structural Geology* 18, 1031–1042. [https://doi.org/10.1016/0191-8141\(96\)00032-6](https://doi.org/10.1016/0191-8141(96)00032-6)
- Sibson, R.H., 1992. Implications of fault-valve behaviour for rupture nucleation and recurrence. *Tectonophysics* 211, 283–293. [https://doi.org/10.1016/0040-1951\(92\)90065-E](https://doi.org/10.1016/0040-1951(92)90065-E)
- Sibson, R.H., 1990. Conditions for fault-valve behaviour. *Geological Society, London, Special Publications* 54, 15–28.
- Sibson, R.H., 1986. Earthquakes and Rock Deformation in Crustal Fault Zones. *Annu. Rev. Earth Planet. Sci.* 14, 149–175. <https://doi.org/10.1146/annurev.ea.14.050186.001053>
- Simon-Labric, T., Rolland, Y., Dumont, T., Heymes, T., Authemayou, C., Corsini, M., Fornari, M., 2009. ⁴⁰Ar/³⁹Ar dating of Penninic Front tectonic displacement (W Alps) during the Lower Oligocene (31–34 Ma). *Terra Nova* 21, 127–136.
- Sindern, S., Meyer, F.M., Lögering, M.J., Kolb, J., Vennemann, T., Schwarzbauer, J., 2012. Fluid evolution at the Variscan front in the vicinity of the Aachen thrust. *International Journal of Earth Sciences* 101, 87–108.
- Sivade, M.A., Thibieroz, J., 1989. Les filons et stratiformes à fluorine, blende, galène, barytine du Grand Chatelard (massifs cristallins externes, Savoie) : relations, rôle de la distension liasique, remobilisation alpine. *Université Pierre et Marie Curie - Paris VI*.

References

- Smith, S.A.F., Holdsworth, R.E., Collettini, C., Imber, J., 2007. Using footwall structures to constrain the evolution of low-angle normal faults. *Journal of the Geological Society* 164, 1187–1191.
- Song, S.J., Choo, C.O., Chang, C.J., Jang, Y.D., 2017. A microstructural study of the fault gouge in the granite, Yangbuk, Gyeongju, southeastern Korea, with implications for multiple faulting. *Geosciences Journal* 21, 1–19.
- Spencer, J.E., Chase, C.G., 1989. Role of crustal flexure in initiation of low-angle normal faults and implications for structural evolution of the Basin and Range province. *Journal of Geophysical Research: Solid Earth* 94, 1765–1775.
- Spencer, J.E., Reynolds, S.J., 1989. Middle Tertiary tectonics of Arizona and adjacent areas. *Geologic evolution of Arizona: Arizona Geological Society Digest* 17, 539–574.
- Spencer, J.E., Welty, J.W., 1986. Possible controls of base- and precious-metal mineralization associated with Tertiary detachment faults in the lower Colorado River trough, Arizona and California. *Geology* 14, 195–198. [https://doi.org/10.1130/0091-7613\(1986\)14<195:PCOBAP>2.0.CO;2](https://doi.org/10.1130/0091-7613(1986)14<195:PCOBAP>2.0.CO;2)
- Spikings, R.A., Popov, D.V., 2021. Thermochronology of alkali feldspar and muscovite at $T > 150^{\circ}$ C using the $40\text{Ar}/39\text{Ar}$ method: a review. *Minerals* 11, 1025.
- Spring, L., Reymond, B., Masson, H., Steck, A., 1992. La nappe du Lebendum entre Alte Kaserne et le Val Cairasca (massif du Simplon): Nouvelles observations et interprétations. *Eclogae Geologicae Helveticae* 85, 85–104.
- Stampfli, G.M., 1993. Le Briançonnais, terrain exotique dans les Alpes? *Eclogae Geologicae Helveticae* 86, 1–45. <https://doi.org/doi.org/10.5169/seals-167234>
- Stampfli, G.M., Hochard, C., 2009. Plate tectonics of the Alpine realm. Geological Society, London, Special Publications 327, 89. <https://doi.org/10.1144/SP327.6>
- Stampfli, G.M., Marthaler, M., 1990. Divergent and convergent margins in the North-Western Alps confrontation to actualistic models. *Geodynamica Acta* 4, 159–184.
- Stampfli, G.M., Mosar, J., Favre, P., Pilleveit, A., Vannay, J.-C., 2001. Permo-Mesozoic evolution of the western Tethys realm: the Neo-Tethys East Mediterranean basin connection. *Mémoires du Muséum national d'histoire naturelle (1993)* 186, 51–108.
- Stampfli, G.M., Mosar, J., Marquer, D., Marchant, R., Baudin, T., Borel, G., 1998. Subduction and obduction processes in the Swiss Alps. *Tectonophysics* 296, 159–204. [https://doi.org/10.1016/S0040-1951\(98\)00142-5](https://doi.org/10.1016/S0040-1951(98)00142-5)

References

- Steck, A., 2008. Tectonics of the Simplon massif and Lepontine gneiss dome: deformation structures due to collision between the underthrusting European plate and the Adriatic indenter. *Swiss Journal of Geosciences* 101, 515–546.
- Steckler, M.S., 1985. Uplift and extension at the Gulf of Suez: indications of induced mantle convection. *Nature* 317, 135–139.
- Stefánsson, A., 2001. Dissolution of primary minerals of basalt in natural waters: I. Calculation of mineral solubilities from 0°C to 350°C. *Chemical Geology* 172, 225–250.
[https://doi.org/10.1016/S0009-2541\(00\)00263-1](https://doi.org/10.1016/S0009-2541(00)00263-1)
- Steinmann, G., 1905. Die Schardtsche Überfaltungstheorie und die geologische Bedeutung der Tiefseeabsätze und der ophiolitischen Massengesteine. *Berichte der Naturforschende Gesellschaft, Freiburg im Breisgau* 16, 18–67.
- Steyrer, H.P., Sturm, R., 2002. Stability of zircon in a low-grade ultramylonite and its utility for chemical mass balancing: the shear zone at Miéville, Switzerland. *Chemical Geology* 187, 1–19. [https://doi.org/10.1016/S0009-2541\(02\)00010-4](https://doi.org/10.1016/S0009-2541(02)00010-4)
- Stipp, M., StuÈnitz, H., Heilbronner, R., Schmid, S.M., 2002. The eastern Tonale fault zone: a ‘natural laboratory’ for crystal plastic deformation of quartz over a temperature range from 250 to 700 C. *Journal of structural geology* 24, 1861–1884.
- Stockli, D.F., Bosworth, W., 2019. Timing of extensional faulting along the Magma-Poor Central and Northern Red Sea rift margin—Transition from regional extension to necking along a hyperextended rifted margin, in: *Geological Setting, Palaeoenvironment and Archaeology of the Red Sea*. Springer, pp. 81–111.
- Stumm, W., Morgan, J.J., 2012. *Aquatic chemistry: chemical equilibria and rates in natural waters*. John Wiley & Sons.
- Suess, E., 2014. Marine cold seeps and their manifestations: geological control, biogeochemical criteria and environmental conditions. *International Journal of Earth Sciences* 103, 1889–1916.
- Suess, E., 1904. *The face of the Earth, Volume 1* (Translation from 1884 [Sollas, HBC, ed.]). Oxford, England, Oxford University Press.
- Sutra, E., Manatschal, G., 2012. How does the continental crust thin in a hyperextended rifted margin? Insights from the Iberia margin. *Geology* 40, 139–142.
<https://doi.org/10.1130/G32786.1>

References

- Sutra, E., Manatschal, G., Mohn, G., Unternehr, P., 2013. Quantification and restoration of extensional deformation along the Western Iberia and Newfoundland rifted margins. *Geochemistry, Geophysics, Geosystems* 14, 2575–2597.
- Svensen, H., Jamtveit, B., Yardley, B., Engvik, A.K., Austrheim, H., Broman, C., 1999. Lead and bromine enrichment in eclogite-facies fluids: Extreme fractionation during lower-crustal hydration. *Geology* 27, 467–470. [https://doi.org/10.1130/0091-7613\(1999\)027<0467:LABELIE>2.3.CO;2](https://doi.org/10.1130/0091-7613(1999)027<0467:LABELIE>2.3.CO;2)
- Sverdrup, H.U., 2016. Modelling global extraction, supply, price and depletion of the extractable geological resources with the LITHIUM model. *Resources, Conservation and Recycling* 114, 112–129. <https://doi.org/10.1016/j.resconrec.2016.07.002>
- Sverdrup, H.U., Olafsdottir, A.H., 2020. Conceptualization and parameterization of the market price mechanism in the WORLD6 model for metals, materials, and fossil fuels. *Mineral Economics* 33, 285–310.
- Sverdrup, H.U., Olafsdottir, A.H., Ragnarsdottir, K.V., 2019. On the long-term sustainability of copper, zinc and lead supply, using a system dynamics model. *Resources, Conservation & Recycling: X* 4, 100007. <https://doi.org/10.1016/j.rcrx.2019.100007>
- Sverdrup, H.U., Ragnarsdottir, K.V., 2016. A system dynamics model for platinum group metal supply, market price, depletion of extractable amounts, ore grade, recycling and stocks-in-use. *Resources, Conservation and Recycling* 114, 130–152. <https://doi.org/10.1016/j.resconrec.2016.07.011>
- Sverjensky, D.A., 1986. Genesis of Mississippi Valley-type lead-zinc desposits. *Annual Review of Earth and Planetary Sciences* 14, 177–199.
- T**agini, B., 1951. Etude métallogénique du gisement de l'Amône (Val Ferret) (Travail de diplôme). Lausanne.
- Taillefer, A., Soliva, R., Guillou-Frottier, L., Le Goff, E., Martin, G., Seranne, M., 2017. Fault-Related Controls on Upward Hydrothermal Flow: An Integrated Geological Study of the Têt Fault System, Eastern Pyrénées (France). *Geofluids* 2017, 8190109. <https://doi.org/10.1155/2017/8190109>
- Tape, C.H., Cowan, C.A., Runkel, A.C., 2003. Tidal-Bundle Sequences in the Jordan Sandstone (Upper Cambrian), Southeastern Minnesota, U.S.A.: Evidence for Tides Along Inboard Shorelines of the Sauk Epicontinental Sea. *Journal of Sedimentary Research* 73, 354–366. <https://doi.org/10.1306/091602730354>
- Tavani, S., Granado, P., Corradetti, A., Camanni, G., Vignaroli, G., Manatschal, G., Mazzoli, S., Muñoz, J.A., Parente, M., 2021. Rift inheritance controls the switch from thin-to thick-skinned

References

- thrusting and basal décollement re-localization at the subduction-to-collision transition. *GSA Bulletin*.
- Teertstra, D.K., Cerny, P., Hawthorne, F.C., 1998. Rubidium feldspars in granitic pegmatites. *The Canadian Mineralogist* 36, 483–496.
- Tembe, S., Lockner, D.A., Wong, T.-F., 2010. Effect of clay content and mineralogy on frictional sliding behavior of simulated gouges: Binary and ternary mixtures of quartz, illite, and montmorillonite. *Journal of Geophysical Research: Solid Earth* 115. <https://doi.org/10.1029/2009JB006383>
- Termier, P., 1922. *A la Gloire de la Terre*, Nouvelle Librairie nationale. ed. Paris.
- Tesei, T., Harbord, C.W.A., De Paola, N., Collettini, C., Viti, C., 2018. Friction of mineralogically controlled serpentinites and implications for fault weakness. *Journal of Geophysical Research: Solid Earth* 123, 6976–6991.
- Thierry, J., 2000. Late Sinemurian (193–191 Ma). *Peri-tethys Paleogeographical Atlas: Paris, CCGM/GGMW/Paris* 49–59.
- Thomas, J., Glass, H.D., White, W.A., Trandell, R.M., 1977. Fluoride content of clay minerals and argillaceous earth materials. *Clays and Clay Minerals* 25, 278–284.
- Thouvenot, F., Senechal, G., Truffert, C., Guellec, S., 1996. Comparison between two techniques of line-drawing migration (ray-tracing and common tangent method). *MEMOIRES-SOCIETE GEOLOGIQUE DE FRANCE* 53–60.
- Tiercelin, J.-J., Pflumio, C., Castrec, M., Boulégué, J., Gente, P., Rolet, J., Coussement, C., Stetter, K.O., Huber, R., Buku, S., 1993. Hydrothermal vents in Lake Tanganyika, East African, Rift system. *Geology* 21, 499–502.
- Tillberg, M., Drake, H., Zack, T., Kooijman, E., Whitehouse, M.J., Åström, M.E., 2020. In situ Rb-Sr dating of slickenfibres in deep crystalline basement faults. *Scientific reports* 10, 1–13.
- Triboulet, S., 1980. *Etude géologique entre Belledonne et Mont Blanc. La terminaison septentrionale du massif de Belledonne et les terrains de son enveloppe*. Université Paris VI, Paris.
- Tricart, P., De Graciansky, P., Lemoine, M., 2000. *De l’océan à la chaîne de montagnes: tectonique des plaques dans les Alpes*. Gordon and Breach.

References

- Trümpy, R., 2001. Why plate tectonics was not invented in the Alps. *International Journal of Earth Sciences* 90, 477–483. <https://doi.org/10.1007/s005310000175>
- Trümpy, R., 1980. *Geology of Switzerland: a guide-book*. Geologische Kommission. Wepf & Co. Publishers, Basel.
- Trümpy, R., 1975. Penninic-Austroalpine boundary in the Swiss Alps: a presumed former continental margin and its problems. *American Journal of Science* 275, 209–238.
- Trümpy, R., 1971. Sur le Jurassique de la zone Helvétique en Suisse. *Annales of the Geological Institute of Hungary* 54, 370–382.
- Trümpy, R., 1954. La zone de Sion-Courmayeur dans le haut Val Ferret valaisan. *Eclogae Geologicae Helvetiae* 47.
- Trümpy, R., 1951. Le Lias de la Nappe de Bex (Préalpes internes) dans la Basse Gryonne. *Bulletin de la Société Vaudoise de Sciences Naturelles* 161–182.
- Trümpy, R., 1949. Der Lias der Glarner Alpen. *Denkschr. schweiz. natf. Ges.* 79.
- Trümpy, R., 1945. Le Lias autochtone d'Arbignon, Groupe de la Dent de Morcles. *Eclogae Geologicae Helvetiae* 421–429.
- Tugend, J., Gillard, M., Manatschal, G., Nirrengarten, M., Harkin, C., Epin, M.-E., Sauter, D., Autin, J., Kuszniir, N., Mcdermott, K., 2020. Reappraisal of the magma-rich versus magma-poor rifted margin archetypes. *Geological Society, London, Special Publications* 476, 23–47.
- Tugend, J., Manatschal, G., Kuszniir, N.J., Masini, E., 2015. Characterizing and identifying structural domains at rifted continental margins: application to the Bay of Biscay margins and its Western Pyrenean fossil remnants. *Geological Society, London, Special Publications* 413, 171. <https://doi.org/10.1144/SP413.3>
- Tugend, J., Manatschal, G., Kuszniir, N.J., Masini, E., Mohn, G., Thion, I., 2014. Formation and deformation of hyperextended rift systems: Insights from rift domain mapping in the Bay of Biscay-Pyrenees. *Tectonics* 33, 1239–1276. <https://doi.org/10.1002/2014TC003529>
- Tullis, J., Yund, R.A., 1985. Dynamic recrystallization of feldspar: A mechanism for ductile shear zone formation. *Geology* 13, 238–241.
- Urich, M., Muñoz, M., Guillot, S., Cathelineau, M., Picard, C., Quesnel, B., Boulvais, P., Couteau, C., 2014. Dissolution–precipitation processes governing the carbonation and silicification of the

References

- serpentinite sole of the New Caledonia ophiolite. *Contributions to Mineralogy and Petrology* 167, 1–19.
- Unternehr, P., Péron-Pinvidic, G., Manatschal, G., Sutra, E., 2010. Hyper-extended crust in the South Atlantic: in search of a model. *Petroleum Geoscience* 16, 207–215.
<https://doi.org/10.1144/1354-079309-904>
- Van Baalen, M.R., 1993. Titanium mobility in metamorphic systems: a review. *Chemical Geology* 110, 233–249. [https://doi.org/10.1016/0009-2541\(93\)90256-I](https://doi.org/10.1016/0009-2541(93)90256-I)
- van Hinsbergen, D.J.J., Torsvik, T.H., Schmid, S.M., Mañenco, L.C., Maffione, M., Vissers, R.L.M., Gürer, D., Spakman, W., 2020. Orogenic architecture of the Mediterranean region and kinematic reconstruction of its tectonic evolution since the Triassic. *Gondwana Research* 81, 79–229. <https://doi.org/10.1016/j.gr.2019.07.009>
- van Loon, A.J. (Tom), Pisarska-Jamroży, M., Nartišs, M., Krievāns, M., Soms, J., 2016. Seismites resulting from high-frequency, high-magnitude earthquakes in Latvia caused by Late Glacial glacio-isostatic uplift. *Journal of Palaeogeography* 5, 363–380.
<https://doi.org/10.1016/j.jop.2016.05.002>
- Vanardois, J., Roger, F., Trap, P., Goncalves, P., Lanari, P., Paquette, J.-L., Marquer, D., Cagnard, F., Le Bayon, B., Melleton, J., 2022. Exhumation of deep continental crust in a transpressive regime: The example of Variscan eclogites from the Aiguilles-Rouges massif (Western Alps). *Journal of Metamorphic Geology*.
- Vance, D., Little, S.H., 2019. The History, Relevance, and Applications of the Periodic System in Geochemistry. *The Periodic Table I: Historical Development and Essential Features*.
- Variscan mine, 2022. EXPANSION OF HIGH-GRADE ZINC MINERALISATION AT THE SAN JOSE MINE.
- Vatin, N., aumaitre, R., Buffet, G., 1974. La spilitisation dans le massif des Écrins-Pelvoux Un cortège intrusif et effusif dolérito-spilitique. *Géologie Alpine* 50, 153–194.
- Vatin-Pérignon, N., Juteau, T., Le Fort, P., 1972. Les filons du massif du Pelvoux. *Géologie Alpine* 48, 207–227.
- Velasco, F., Herrero, J.M., Gil, P.P., Alvarez, L., Yusta, I., 1994. Mississippi Valley-type, sedex, and iron deposits in Lower Cretaceous rocks of the Basque-Cantabrian Basin, northern Spain, in: *Sediment-Hosted Zn-Pb Ores*. Springer, pp. 246–270.
- Velde, B., 1985. Clay minerals.

References

- Venturelli, G., Thorpe, R.S., Dal Piaz, G.V., Del Moro, A., Potts, P.J., 1984. Petrogenesis of calc-alkaline, shoshonitic and associated ultrapotassic Oligocene volcanic rocks from the Northwestern Alps, Italy. *Contributions to Mineralogy and Petrology* 86, 209–220.
- Vermeesch, P., 2018. IsoplotR: A free and open toolbox for geochronology. *Geoscience Frontiers* 9, 1479–1493.
- Villa, I.M., Hermann, J., Müntener, O., Trommsdorff, V., 2000. ³⁹Ar–⁴⁰Ar dating of multiply zoned amphibole generations (Malenco, Italian Alps). *Contributions to Mineralogy and Petrology* 140, 363–381.
- Vine, F.J., 1966. Spreading of the Ocean Floor: New Evidence: Magnetic anomalies may record histories of the ocean basins and Earth's magnetic field for 2× 10⁸ years. *Science* 154, 1405–1415.
- Vocke, R.D., Hanson, G.N., Grünenfelder, M., 1987. Rare earth element mobility in the Roffna Gneiss, Switzerland. *Contributions to Mineralogy and Petrology* 95, 145–154.
- Voggenreiter, W., Hötzl, H., Jado, A.R., 1988. Red Sea related history of extension and magmatism in the Jizan area (Southwest Saudi Arabia): indication for simple-shear during early Red Sea rifting. *Geologische Rundschau* 77, 257–274. <https://doi.org/10.1007/BF01848688>
- Vokes, F.M., 1969. A review of the metamorphism of sulphide deposits. *Earth-Science Reviews* 5, 99–143. [https://doi.org/10.1016/0012-8252\(69\)90080-4](https://doi.org/10.1016/0012-8252(69)90080-4)
- von Blanckenburg, F., Davies, J.H., 1995. Slab breakoff: a model for syncollisional magmatism and tectonics in the Alps. *Tectonics* 14, 120–131.
- Von Fellenberg, E., 1893. Geologische Beschreibung des westlichen Theils des Aarmassivs, enthalten auf dem nördlich der Rhône gelegenen Theile des Blattes XVIII der Dufour-Karte. *Matér. Carte géol. Suisse*.
- von Raumer, J.F., Bussy, F., Stampfli, G.M., 2009. The Variscan evolution in the External massifs of the Alps and place in their Variscan framework. *Comptes Rendus Geoscience* 341, 239–252.
- von Raumer, J.F., Stampfli, G.M., 2008. The birth of the Rheic Ocean — Early Palaeozoic subsidence patterns and subsequent tectonic plate scenarios. *Tectonophysics* 461, 9–20. <https://doi.org/10.1016/j.tecto.2008.04.012>
- Von Raumer, J.F., Bussy, F., 2004. Mont Blanc and Aiguilles Rouges; geology of their polymetamorphic basement (External massifs, Western Alps, France-Switzerland).
- Von Raumer, J.F., Stampfli, G., Borel, G., Bussy, F., 2002. Organization of pre-Variscan basement areas at the north-Gondwanan margin. *International Journal of Earth Sciences* 91, 35–52.

References

Von Raumer, J.F., Ménot, R.P., Abrecht, J., Biino, G., 1993. The Pre-Alpine evolution of the External massifs, in: *Pre-Mesozoic Geology in the Alps*. Springer, pp. 221–240.

Wadati, K., 1935. On the activity of deep focus earthquakes and in the Japan Island and neighbourhoods. *Geophys. Mag.* 8, 305–325.

Wagner, F.H., Johnson, R.A., 2006. Coupled basin evolution and late-stage metamorphic core complex exhumation in the southern Basin and Range Province, southeastern Arizona. *Tectonophysics* 420, 141–160. <https://doi.org/10.1016/j.tecto.2006.01.012>

Wagner, M., Kissling, E., Husen, S., 2012. Combining controlled-source seismology and local earthquake tomography to derive a 3-D crustal model of the western Alpine region. *Geophysical Journal International* 191, 789–802. <https://doi.org/10.1111/j.1365-246X.2012.05655.x>

Wallis, D., Lloyd, G.E., Phillips, R.J., Parsons, A.J., Walshaw, R.D., 2015. Low effective fault strength due to frictional-viscous flow in phyllonites, Karakoram Fault Zone, NW India. *Journal of Structural Geology* 77, 45–61. <https://doi.org/10.1016/j.jsg.2015.05.010>

Walters, S.J., Pontgratz, J., Davidson, G., 1996. An overview of Broken Hill type deposits. *New developments in Broken Hill type deposits. CODES Spec. Publ* 1, 1–10.

Wang, Y.-Y., Xiao, Y., 2018. Fluid-controlled element transport and mineralization in subduction zones. *Solid Earth Sciences* 3, 87–104. <https://doi.org/10.1016/j.sesci.2018.06.003>

Wark, D.A., Watson, E.B., 2006. TitaniQ: a titanium-in-quartz geothermometer. *Contributions to Mineralogy and Petrology* 152, 743–754.

Warr, L.N., Cox, S., 2001. Clay mineral transformations and weakening mechanisms along the Alpine Fault, New Zealand. *Geological Society, London, Special Publications* 186, 85. <https://doi.org/10.1144/GSL.SP.2001.186.01.06>

Webber, S., Little, T.A., Boulton, C., Biemiller, J., Mizera, M., 2022. Regional-scale low-angle normal fault friction and cohesion constrained from Mohr-Coulomb models of active and abandoned range-front faults in Papua New Guinea. *Journal of Geophysical Research: Solid Earth*.

Wedepohl, K.H., 1971. Environmental influences on the chemical composition of shales and clays. *Physics and Chemistry of the Earth* 8, 307–333.

Wegener, A., 1922. *Die entstehung der kontinente und ozeane*, 5th ed. F. Vieweg & sohn.

References

- Weidman, M., 1972. Le front de la Breche du Chablais dans le secteur de Saint-Jean-d'Aulph (Haute-Savoie). *Géologie Alpine* 48, 229–246.
- Weinzierl, C.G., Regelous, M., Haase, K.M., Bach, W., Böhm, F., Garbe-Schönberg, D., Sun, Y.D., Joachimski, M.M., Krumm, S., 2018. Cretaceous seawater and hydrothermal fluid compositions recorded in abiogenic carbonates from the Troodos Ophiolite, Cyprus. *Chemical Geology* 494, 43–55. <https://doi.org/10.1016/j.chemgeo.2018.07.014>
- Wernicke, B., Axen, G.J., 1988. On the role of isostasy in the evolution of normal fault systems. *Geology* 16, 848–851. [https://doi.org/10.1130/0091-7613\(1988\)016<0848:OTROII>2.3.CO;2](https://doi.org/10.1130/0091-7613(1988)016<0848:OTROII>2.3.CO;2)
- Wernicke, B., 1981. Low-angle normal faults in the Basin and Range Province: nappe tectonics in an extending orogen. *Nature* 291, 645–648.
- Wheeler, J., 1996. DIFFARG: a program for simulating argon diffusion profiles in minerals. *Computers & Geosciences* 22, 919–929.
- White, R.S., McKenzie, D., 1989. Magmatism at rift zones: the generation of volcanic continental margins and flood basalts. *Journal of Geophysical Research: Solid Earth* 94, 7685–7729.
- White, R.S., Spence, G.D., Fowler, S.R., McKenzie, D.P., Westbrook, G.K., Bowen, A.N., 1987. Magmatism at rifted continental margins. *Nature* 330, 439–444. <https://doi.org/10.1038/330439a0>
- Whitmarsh, R.B., Manatschal, G., Minshull, T.A., 2001a. Evolution of magma-poor continental margins from rifting to seafloor spreading. *Nature* 413, 150–154.
- Whitmarsh, R.B., Minshull, T.A., Russell, S.M., Dean, S.M., Loudon, K.E., Chian, D., 2001b. The role of syn-rift magmatism in the rift-to-drift evolution of the West Iberia continental margin: geophysical observations, in: Wilson, R.C.L., Whitmarsh, R.B., Taylor, B., Froitzheim, N. (Eds.), *Non-Volcanic Rifting of Continental Margins: A Comparison of Evidence from Land and Sea*. Geological Society of London, p. 0. <https://doi.org/10.1144/GSL.SP.2001.187.01.06>
- Whitney, D.L., Teyssier, C., Rey, P., Buck, W.R., 2013. Continental and oceanic core complexes. *GSA Bulletin* 125, 273–298. <https://doi.org/10.1130/B30754.1>
- Wibberley, C.A.J., 2005. Initiation of basement thrust detachments by fault-zone reaction weakening. Geological Society, London, Special Publications 245, 347. <https://doi.org/10.1144/GSL.SP.2005.245.01.17>
- Wibberley, C.A.J., Shimamoto, T., 2003. Internal structure and permeability of major strike-slip fault zones: the Median Tectonic Line in Mie Prefecture, Southwest Japan. *Journal of Structural Geology* 25, 59–78.

References

- Wibberley, C.A.J., McCaig, A.M., 2000. Quantifying orthoclase and albite muscovitisation sequences in fault zones. *Chemical Geology* 165, 181–196. [https://doi.org/10.1016/S0009-2541\(99\)00170-9](https://doi.org/10.1016/S0009-2541(99)00170-9)
- Wibberley, C.A.J., 1999. Are feldspar-to-mica reactions necessarily reaction-softening processes in fault zones? *Journal of Structural Geology* 21, 1219–1227. [https://doi.org/10.1016/S0191-8141\(99\)00019-X](https://doi.org/10.1016/S0191-8141(99)00019-X)
- Wiest, J.D., Osmundsen, P.T., Jacobs, J., Fossen, H., 2019. Deep crustal flow within postorogenic metamorphic core complexes: insights from the southern Western Gneiss Region of Norway. *Tectonics* 38, 4267–4289.
- Wildi, W., Funk, H., Loup, B.F.R., Amato, E., Huggenberger, P., 1989. Mesozoic subsidence history of the European marginal shelves of the alpine Tethys (Helvetic realm, Swiss Plateau and Jura). *Eclogae Geologicae Helveticae* 82, 817–840.
- Wilkinson, J.J., 2001. Fluid inclusions in hydrothermal ore deposits. *Lithos* 55, 229–272.
- Wills, S., Buck, W.R., 1997. Stress-field rotation and rooted detachment faults: A Coulomb failure analysis. *Journal of Geophysical Research: Solid Earth* 102, 20503–20514. <https://doi.org/10.1029/97JB01512>
- Wilson, J.T., 1968. Static or mobile earth: the current scientific revolution. *Proceedings of the American Philosophical Society* 112, 309–320.
- Wilson, J.T., 1966. Did the Atlantic Close and then Re-Open? *Nature* 211, 676–681. <https://doi.org/10.1038/211676a0>
- Wilson, R.W., Houseman, G.A., Buitter, S.J.H., McCaffrey, K.J.W., Doré, A.G., 2019. Fifty years of the Wilson Cycle concept in plate tectonics: an overview. *Geological Society, London, Special Publications* 470, 1. <https://doi.org/10.1144/SP470-2019-58>
- Wintsch, R.P., Christoffersen, R., Kronenberg, A.K., 1995. Fluid-rock reaction weakening of fault zones. *Journal of Geophysical Research: Solid Earth* 100, 13021–13032. <https://doi.org/10.1029/94JB02622>
- Wizevich, M.C., Ahern, J., Meyer, C.A., 2019. The Triassic of southwestern Switzerland – Marine or non-marine, that is the question! *Palaeogeography, Palaeoclimatology, Palaeoecology* 514, 577–592. <https://doi.org/10.1016/j.palaeo.2018.11.016>

References

- Wizevich, M.C., Simpson, E.L., Hilbert-Wolf, H.L., Tindall, S.E., 2016. Development of large-scale seismites in Upper Cretaceous fluvial sandstones in a fault-proximal setting. *Sedimentology* 63, 1719–1738. <https://doi.org/10.1111/sed.12283>
- Wojdyr, M., 2010. Fityk: a general-purpose peak fitting program. *Journal of Applied Crystallography* 43, 1126–1128.
- Woodcock, N.H., Dickson, J.A.D., Tarasewicz, J.P.T., 2007. Transient permeability and reseat hardening in fault zones: evidence from dilation breccia textures. Geological Society, London, Special Publications 270, 43–53.
- Woodhead, J.D., Hergt, J.M., 2001. Strontium, neodymium and lead isotope analyses of NIST glass certified reference materials: SRM 610, 612, 614. *Geostandards Newsletter* 25, 261–266.
- X**iao, H.-B., Dahlen, F.A., Suppe, J., 1991. Mechanics of extensional wedges. *Journal of Geophysical Research: Solid Earth* 96, 10301–10318.
- Y**amauchi, Y., Nishido, H., 2018. Temperature effects on cathodoluminescence of Ba-feldspar, in: AGU Fall Meeting Abstracts. pp. MR21B-0064.
- Yardley, B.W., Bodnar, R.J., 2014. Fluids in the continental crust. *Geochemical Perspectives* 3, 1–2.
- Yardley, B.W.D., 2005. 100th Anniversary Special Paper: Metal Concentrations in Crustal Fluids and Their Relationship to Ore Formation. *Economic Geology* 100, 613–632. <https://doi.org/10.2113/gsecongeo.100.4.613>
- Yin, A., 1989. Origin of regional, rooted low-angle normal faults: A mechanical model and its tectonic implications. *Tectonics* 8, 469–482. <https://doi.org/10.1029/TC008i003p00469>
- Yin, A., Dunn, J.F., 1992. Structural and stratigraphic development of the Whipple-Chemehuevi detachment fault system, southeastern California: Implications for the geometrical evolution of domal and basal low-angle normal faults. *Geological Society of America Bulletin* 104, 659–674.
- Z**appettini, E.O., Rubinstein, N., Crosta, S., Segal, S.J., 2017. Intracontinental rift-related deposits: A review of key models. *Ore Geology Reviews* 89, 594–608. <https://doi.org/10.1016/j.oregeorev.2017.06.019>

References

- Zavala, C., Arcuri, M., 2016. Intrabasinal and extrabasinal turbidites: Origin and distinctive characteristics. *Sedimentary Geology* 337, 36–54.
<https://doi.org/10.1016/j.sedgeo.2016.03.008>
- Zellmer, G.F., Edmonds, M., Straub, S.M., 2015. Volatiles in subduction zone magmatism. Geological Society, London, Special Publications 410, 1–17.
- Zhang, M., Salje, E.K., Redfern, S.A., Bismayer, U., Groat, L.A., 2013. Intermediate structures in radiation damaged titanite (CaTiSiO₅): a Raman spectroscopic study. *Journal of Physics: Condensed Matter* 25, 115402.
- Zhang, Y., Han, R., Ding, X., Wang, Y., Wei, P., 2021. Precipitation reaction mechanisms of mineral deposits simulated with a fluid mixing model. *Geofluids* 2021.
- Zhang, H., Hou, Z., Rolland, Y., Santosh, M., 2022. The cold and hot collisional orogens: Thermal regimes and metallogeny of the Alpine versus Himalayan-Tibetan belts. *Ore Geology Reviews* 141, 104671. <https://doi.org/10.1016/j.oregeorev.2021.104671>
- Zhao, L., Paul, A., Guillot, S., Solarino, S., Malusà, M.G., Zheng, T., Aubert, C., Salimbeni, S., Dumont, T., Schwartz, S., Zhu, R., Wang, Q., 2015. First seismic evidence for continental subduction beneath the Western Alps. *Geology* 43, 815–818. <https://doi.org/10.1130/G36833.1>
- Zhao, Y., Ren, J., Pang, X., Yang, L., Zheng, J., 2018. Structural style, formation of low angle normal fault and its controls on the evolution of Baiyun Rift, northern margin of the South China Sea. *Marine and Petroleum Geology* 89, 687–700.
<https://doi.org/10.1016/j.marpetgeo.2017.11.001>
- Zhu, W., Allison, K.L., Dunham, E.M., Yang, Y., 2020. Fault valving and pore pressure evolution in simulations of earthquake sequences and aseismic slip. *Nature Communications* 11, 4833.
<https://doi.org/10.1038/s41467-020-18598-z>
- Zoback, M.D., Gorelick, S.M., 2012. Earthquake triggering and large-scale geologic storage of carbon dioxide. *Proceedings of the National Academy of Sciences* 109, 10164–10168.
- Zwaan, F., Chenin, P., Erratt, D., Manatschal, G., Schreurs, G., 2022. Competition between 3D structural inheritance and kinematics during rifting: Insights from analogue models. *Basin Research* 34, 824–854.



Appendix

Appendix A Why large offset detachment faults are mechanically possible?

Introduction

Low angle normal fault (LANF) or detachment faults are faults dipping at shallow angle and accommodating large offsets (m's). While impossible in theory according to the Andersonian theory of faulting, they have been described worldwide in different tectonic environment from rifting and back arc extension to orogen and orogenic collapse. Two type of detachment faults have been in fact described. The first one corresponds to high-angle faults rotation due to isostatic uplift (Wernicke and Axen, 1988) while the second type corresponds to true detachment fault starting at a shallow angle.

In this appendix, a review of the mechanism responsible for detachment formation are presented from fault rotation and stress misorientation to fault weakening. The mechanism of deformation along extensional fault are also presented in more detail. Finally, a discussion on the evolution of extensional fault during rifting is proposed.

1. An modelling approach

1.1. The Anderson theory for steep normal fault

Faulting envisaged as brittle fracture (mode II and III) can be understood using the simple Coulomb-criteria (see (Scholz, 1989)):

$\tau = C_o + \mu\sigma_n$ (1) with σ_n the normal stress on the surface, τ the shear stress, C_o the cohesion of the material and μ the coefficient of internal friction

This equation links the shear stress with the normal stress necessary for failure in the brittle regime. This criterion represented in the Mohr space (σ_n - τ) corresponds to a straight line with a slope μ and the intercept C_o (Fig. A.1).

Why large offset detachment faults are mechanically possible?

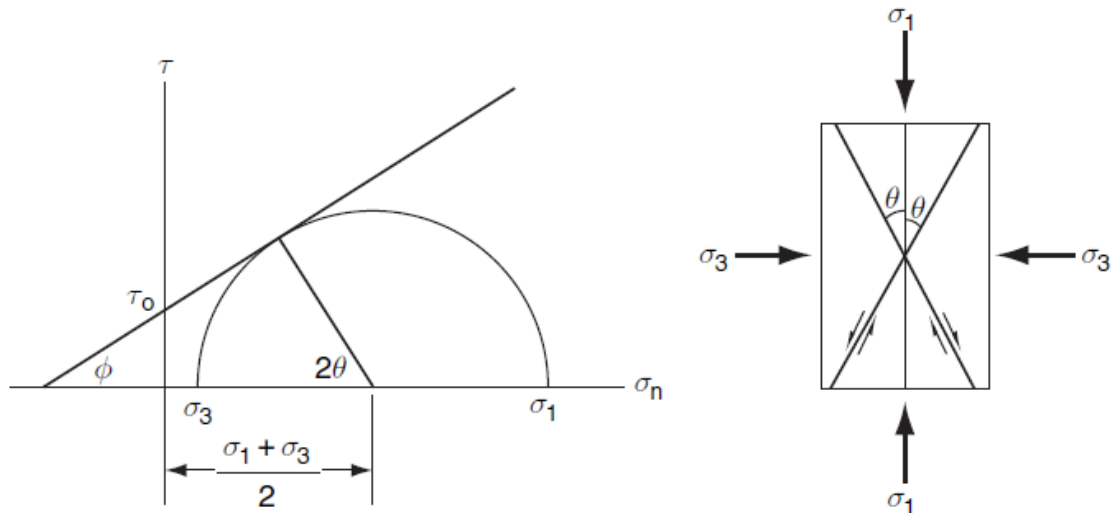


Fig. A.1: Relation between σ_1 and the shear zone and its representation on the Mohr space with the Coulomb criterion (Scholz, 1989).

The failure occurs when the Mohr circle touch the Coulomb curve. For average value of $\mu = 0.6$, it occurs at an angle $\theta = 45^\circ - \frac{\varphi}{2} = 30^\circ$ (2) with $\varphi = \tan^{-1} \mu$

The angle between the principal axis of the stress σ_1 and the fault plane must be 30° . For σ_1 horizontal (compression), the fault dip would be 30° . For σ_1 vertical, the fault dip would be 60° (Anderson, 1905). Another way to calculate this is to find the dip angle that would minimize the regional stress needed to overcome the friction. In the calculation by Forsyth (1992), the regional stress is horizontal but divergent (pointing in opposite direction like a tractive stress) and the vertical stress is only the weight of the rocks:

$$\sigma_R = \sigma_t = \frac{\mu \rho g \frac{H}{2} + C}{\mu \sin^2 \theta + \sin \theta \cos \theta} \quad (3)$$

with σ_R the regional extensive stress, H the thickness of the brittle layer, ρ the volumic mass

The minimum is reached around 60° even if it is a broad minimum which mean a wider dip angle distribution than 60° .

Why large offset detachment faults are mechanically possible?

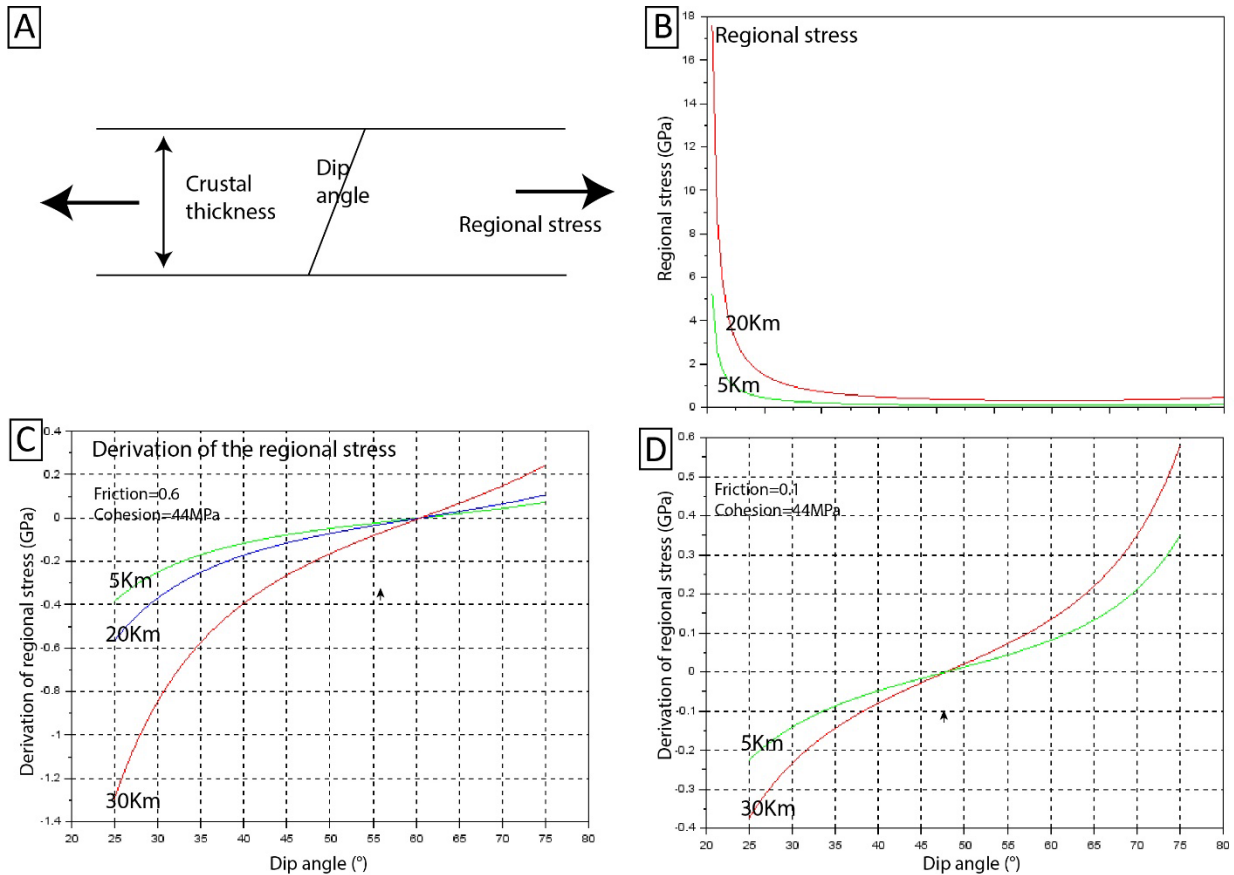


Fig. A.2: Representation of the regional stress according to the equation (3). The derivation of the stress with ϑ was represented to show for what angle the regional stress is minimal (when the derivation equals 0) which occurs for $\vartheta = 60^\circ$.

The graphic shows the influence of the dip angle and the thickness of the crust on the regional stress. For a certain crustal thickness, the rupture will occur at the dip angle corresponding to the minimum in the regional stress. The regional stress function of the dip angle for a thickness of 5 and 20 km are represented in the Fig. A.2. The stress decreases slowly from 90° to reach a minimum between 40 and 70° . There is an important increase of the stress below 10° . However, the minimum is hard to see. The derivation of the equation (3) is represented in the Fig. A.2C and permits to see the stress minimum required for fault activation. It occurs at 60° for a cohesion of 0.6 which is in total agreement with the theory of Anderson. For a friction of 0.1 the minimum occurs at a dip angle of 52° . There is no influence of the crustal thickness on the regional stress minimum. The important factor there is the friction.

Petrophysical experiments with uniaxial press show result agreeing with this theoretical prediction. (Lockner et al., 1991) localised the acoustic emissions from the fracture development throughout deformation (Fig. A.3). They show that during elastic deformation the fractures developed homogeneously on the sample but when the failure is reached, there is a localisation of the fracture along a single shear band with an angle of 30° respect to σ_1 .

Why large offset detachment faults are mechanically possible?

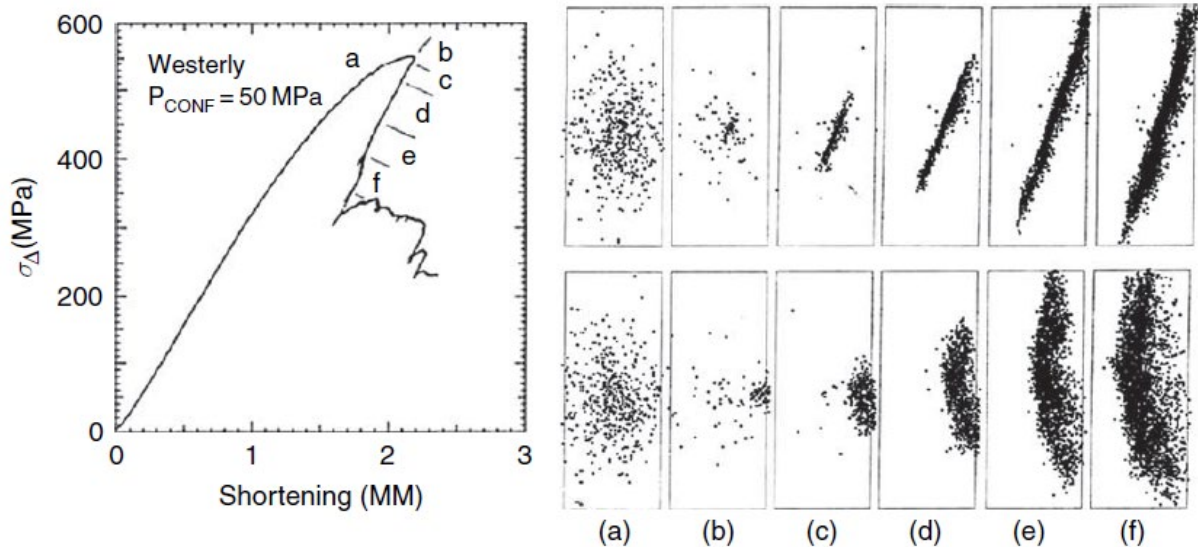


Fig. A.3: Graph representing the stress applied and the shortening measured (experience at constant strain rate). The stress reach a peak at 550MPa. After the peak a large drop of pressure is notice indicating failure of the rock. The figures a to f show the different stages of deformation from an homogeneous deformation through a localised deformation on shear plane after the failure (Lockner et al., 1991).

1.2. Large offset faults

1.2.1. The importance of the flexure

Detachment faults are faults with a dip angle of 30° which is in apparent contradiction with Anderson theory of faulting. However, the existence of this detachment faults is attested worldwide and in a large variety of tectonic settings. How then is it possible to have low angle large offset normal fault?

Before presenting the different models of detachment fault, let examine the simple equations more in details. The equation (3) for describing the whole crustal deformation is too simple as it considers only the friction as a factor to overcome for the deformation to take place. The vertical displacement of the hanging wall and footwall means that they move from the equilibrium level. Therefore, the gravitational potential energy needs to be considered. The hanging wall and the footwall can be considered as elastic plates free to move close to the fault and fixed far from it. As a consequence, the plate bends in response to gravity, distributing the work required for vertical displacements between elastic strain energy associated with bending and potential energy associated with displacement from the equilibrium level (Forsyth, 1992):

$$\sigma_R = \sigma_t + \frac{(E(\rho_e g H_e)^3 / 3(1 - \nu^2))^{0.25} \Delta x \tan^2 \theta}{4H} \quad (4)$$

with E is the Young modulus, ν is the Poisson coefficient, ρ_e is the effective density, H_e is the effective elastic thickness, Δx horizontal offset of the fault

Why large offset detachment faults are mechanically possible?

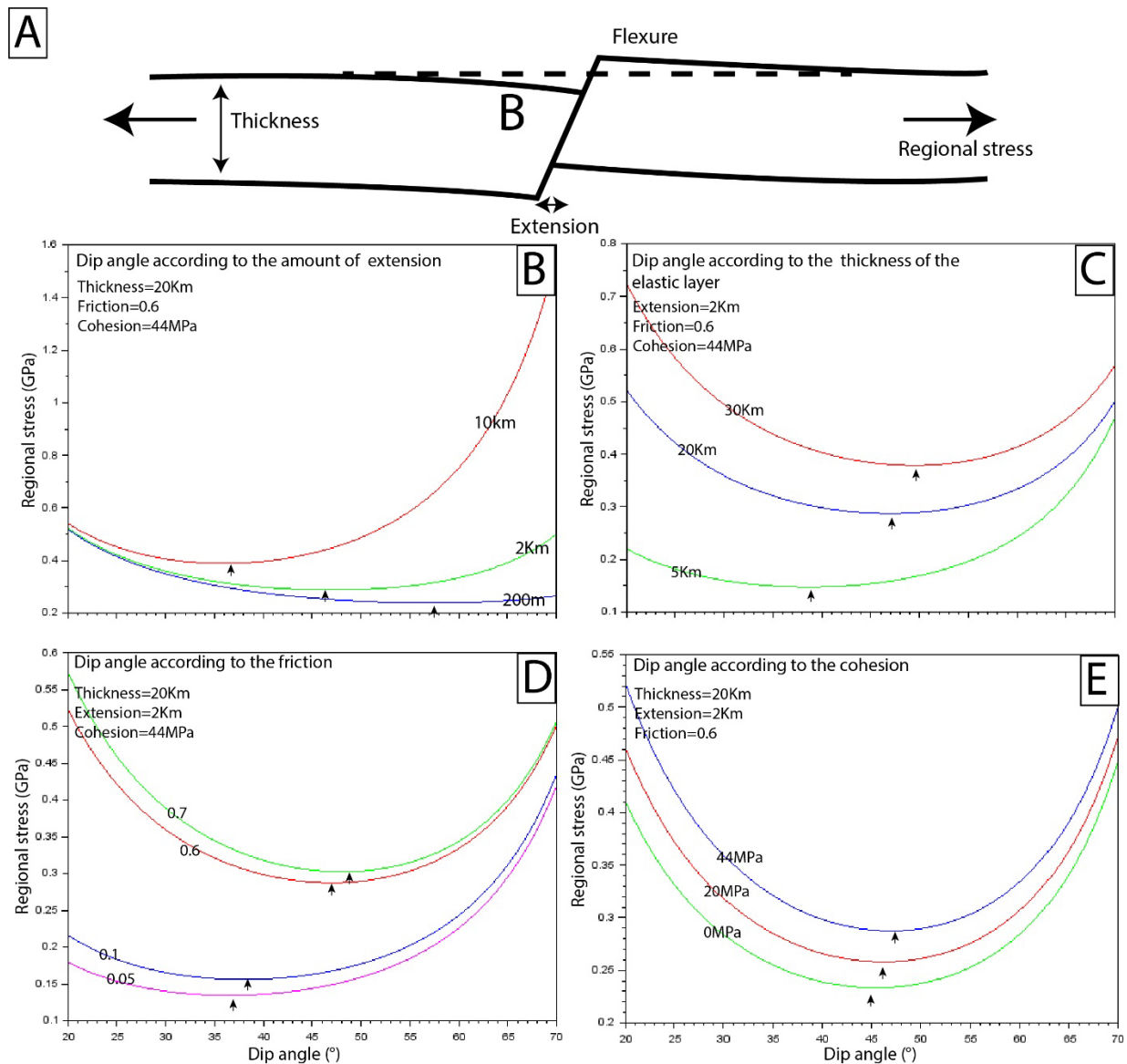


Fig. A.4: Representation of the regional stress from the equation (4). Different parameters are used to see how the optimal angle varies. The arrows indicate the optimal angle (minimum stress). The fault must be flat for having important extension. The most important parameters are the friction and the crust thickness.

The optimum dip angle would correspond the minimum regional stress for a given Δx . The result of (Forsyth, 1992) give interesting results. For small amount of displacement, the optimum angle is 57° . After 2 km of displacement, the optimum dip angle is 47° and after 10 km it is 37° . If the fault is steep, important horizontal displacement means important vertical displacement. Therefore, important movement on a steep fault require more work than displacement on a flat fault with less vertical offset. According to this model, large offset normal fault must be flat fault. Other parameters are important factors controlling the dip angle. The first one is the crustal thickness. The thinner the crust is the flatter the fault will be. The second parameter is the friction. A low friction makes the movement on the fault easier. Low friction faults are flatter than high friction fault (Fig. A.5). There is not only a change of the dip angle, but the minimum of stress also decreases (around 0.34 GPa for a

Why large offset detachment faults are mechanically possible?

friction of 0.7 and 0.15 for a friction of 0.05). The last parameter is the cohesion. It does not have an impact on the dip angle but obviously on the minimum stress that decreases with the loss of cohesion.

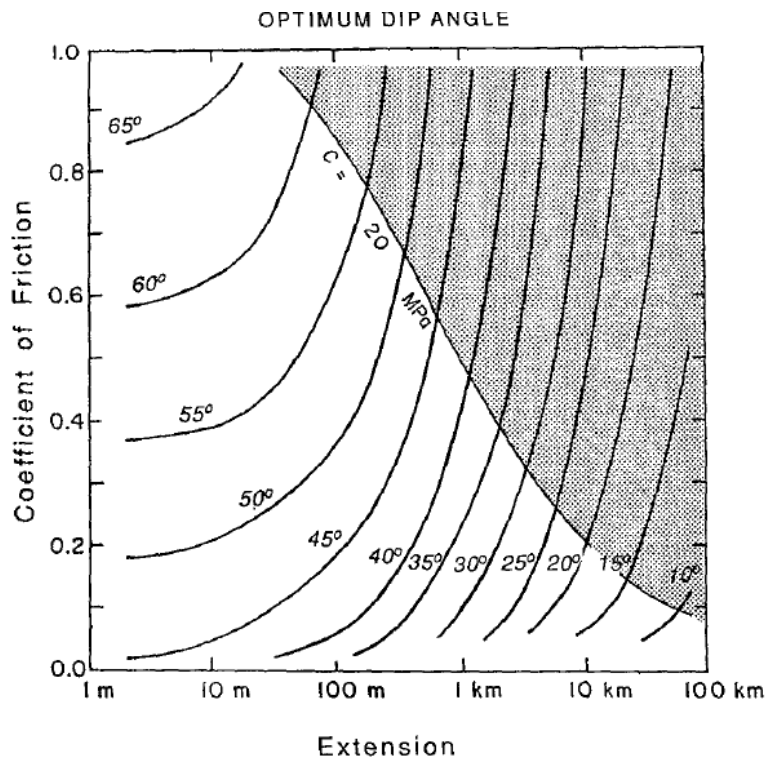


Fig. A.5: Representation of the optimum dip angle according to the friction and extension (Forsyth, 1992). It appears clearly that for important displacement (kilometric) the friction must be low and the angle low either.

Why is it in some cases easier to continue the deformation on the same fault instead of creating a new one?

For larger offset, the flattening of the fault is not the only parameter as mentioned above. The friction coefficient μ must decrease too. The model shows that for having 10 km of offset, the dip angle must be less than 20° and the friction coefficient must be less than 0.2. As indicated in Fig. A.4, the large offsets are possible only if there is a decrease of the friction or fault weakening. In the equation (3), the effective elastic thickness is also a key component. The thickest the plate the more important the work linked to elastic strain from the flexure and the gravitational potential energy so it would be less favourable for large offset fault. It would be more favourable then to create a new fault than continuing the deformation on the same fault even with flattening. To summarize this more analytical approach of the normal fault development, the deformation initiates on a steep normal fault. However, a steep normal fault must flatten and have a decrease of the friction coefficient to be able to generate important displacement. If these conditions are not met, the deformation will be transferred to a new steep normal fault. Large offset faults must be flat with a thin elastic layer.

1.3. The role of fault weakening and advective thinning: Numerical models

The previous models are using the approximation of the a thin plate with a pre-existing slip surface which as mentioned by Lavier et al., (2000) do not explain the weakening of the layer leading to the fault. Using numerical models, Lavier et al., (2000) understood the impacts of different factors on the fault geometry and behaviour. They used a non-associated plastic flow rule to calculate the plastic strain. The rupture occurs when the yield stress given by the Mohr-Coulomb condition is reached. At that moment, the cohesion is decreased to simulate the weakening according to the equation:

$$C(\varepsilon) = C(0)[1 - \left(\frac{\varepsilon}{\varepsilon_c}\right)] \quad (5)$$

The loss of cohesion is proportional to the strain. When the strain $\varepsilon = \varepsilon_c$, the cohesion $C = 0$.

The parameters fixed for the model are (see Lavier et al., 2000):

- The elastic thickness H
- The friction μ
- The initial cohesion
- The limit strain ε_c
- $\Delta C_0/\varepsilon$ which is the rate of cohesion loss with the strain.

To understand the results, it is important to keep in mind the different forces in competition and their evolution with increasing offset. The first one ΔF_w is the force linked to the cohesion loss of the fault:

$$\Delta F_w = C(0)H \left(\gamma + (1 - \gamma) \frac{\Delta x}{\Delta x_c} \right) \quad \text{if } \Delta x < \Delta x_c \quad (6)$$

$$\Delta F_w = C(0)H(\gamma - 1) \quad \text{if } \Delta x > \Delta x_c \quad (7)$$

From these to equation it is possible to see that ΔF_w decreases with the offset until it $\Delta x = \Delta x_c$. After that point it remains constant.

The second force is the gravitational force linked to the resistance to the bending and to the topographic building: $\Delta F_B = AH^2(1 - e^{-B\Delta x/H})$ (8).

The most important parameter in this expression is the thickness H which appears both in the coefficient AH^2 and in the exponential. The thickest the layer is and the more important the gravitational force will be which is therefore not surprising.

Why large offset detachment faults are mechanically possible?

The last force is $\Delta F = \Delta F_B + \Delta F_w$ (9) which is the combination of the weakening force and the gravitational force.

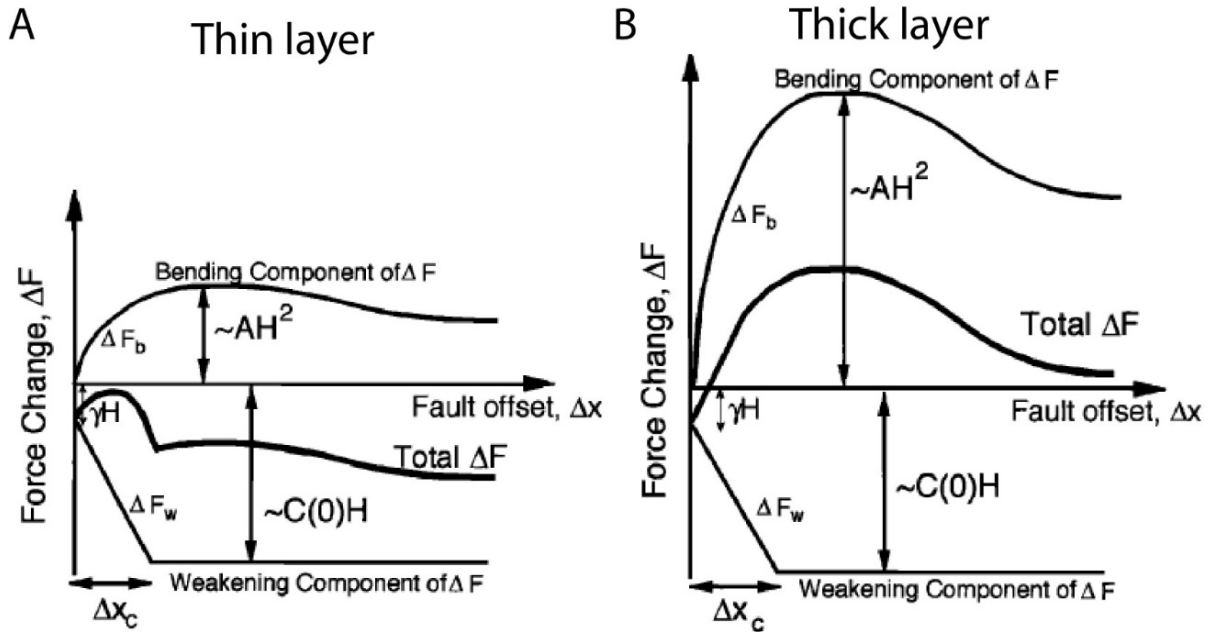


Fig. A.6: Graph showing the competence between the faults weakening and the bending component for a thin layer (A) and a thick layer (B) (from Lavier and Buck, 2002).

For small offset what is controlling the development of the fault is the competition between the bending force and the fault weakening (Fig. A.6). Two factors are important, the thickness H which is linked to the bending force and the characteristic offset Δx_c . For small Δx_c , the rate of cohesion loss is faster, and the fault weakening wins against the bending force. For larger offset, the main parameter is the thickness H . For thick layers, the bending force is too important, and it is easier to create a new fault than continuing the deformation on the same one. For thin layers, the weakening of the fault is enough to enable further deformation on the same fault.

Why large offset detachment faults are mechanically possible?

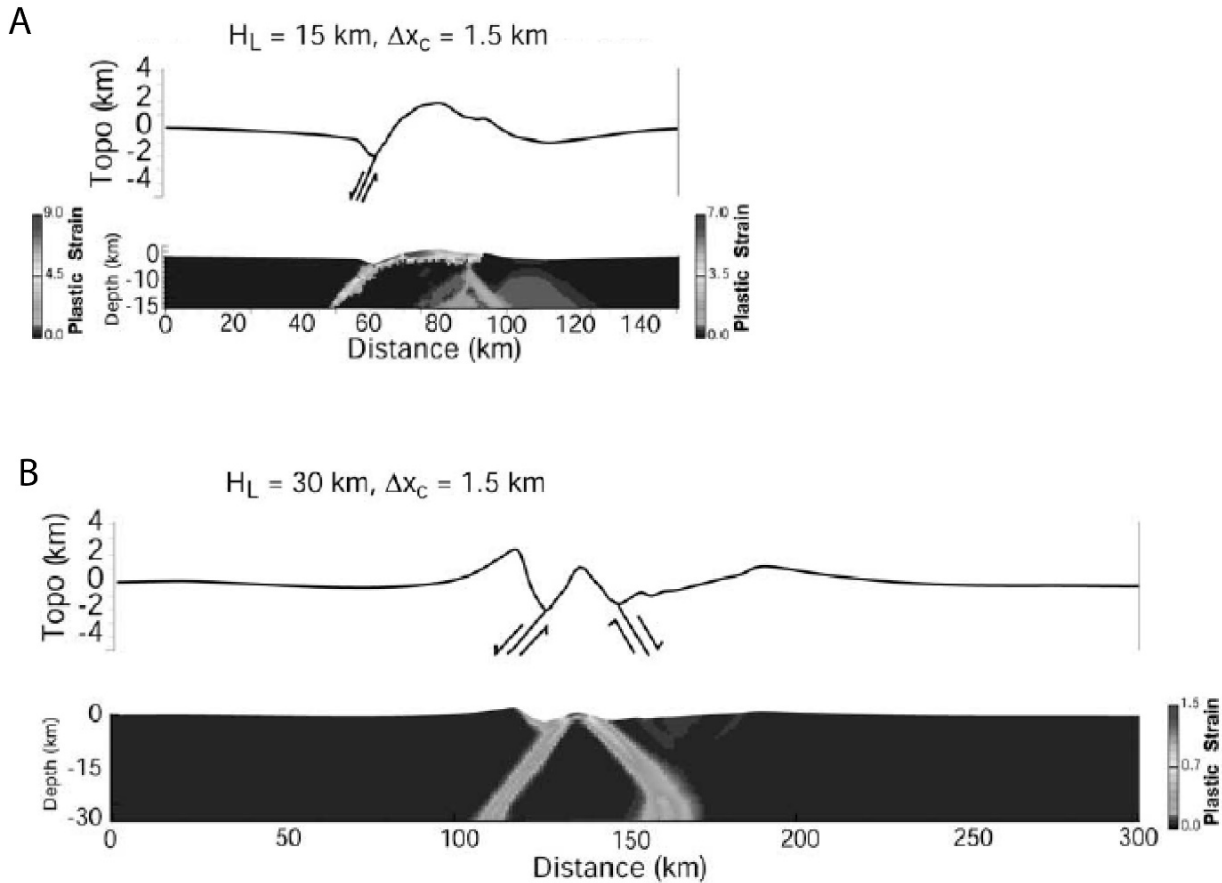


Fig. A.7: Numerical models of rifting (the deformation is centered in the middle of the model)(from Lavier and Buck, 2002. A- Thin layer (15Km) generating a core complex structure B- Thick layer generating an half-graben structure (30Km)

The model A (Fig. A. 7A) show a single fault with a convex geometry. It is dipping with an angle of 60° under the surface and it is flat above the surface. This geometry is a core complex geometry. The model B (Fig. A.7B) shows 2 antithetic faults with a dip angle of 60°. There is a transition from a core complex geometry to a graben geometry for a thickness between 15 km and 30 km. Lavier et al., (2000) propose a core complex geometry for a thickness below 22 km and with Δx_c between 1 and 4 km. In a second paper (Lavier and Buck, 2002), they introduced the concept of advective thinning. Above the fault due to the movement of the hanging wall respect to the footwall, the plate is locally thinned. The thickness is: $H = H_L - \Delta H$ (10).

This decrease of the thickness has therefore an impact on the fault weakening and the gravitational component (see equations 6 and 7). There is also a thermal impact, the fault inducing a deformation of the isotherms. This advective thinning has an influence on the weakening of the fault (ΔF_w; Fig. A.8). The bending component is not affected because the bending occurs on a larger segment of the plate than the one affected by the advective thinning. The weakening is therefore too small to compete against the bending force. It is easier to create a new fault than continuing the deformation on the same one. To explain the large offset faults observed, Lavier and Buck (2002) added hydrothermal cooling to the model to counteract the effect of the advective thinning. Fluid

Why large offset detachment faults are mechanically possible?

circulations along the fault can enable more cooling than thermal diffusion alone. According to these models, if the plate is too thick, the bending component is strong and therefore it is easier to make new fault than continuing the deformation on the same one. For a thinner plate, large offset faults are possible only with hydrothermal cooling.

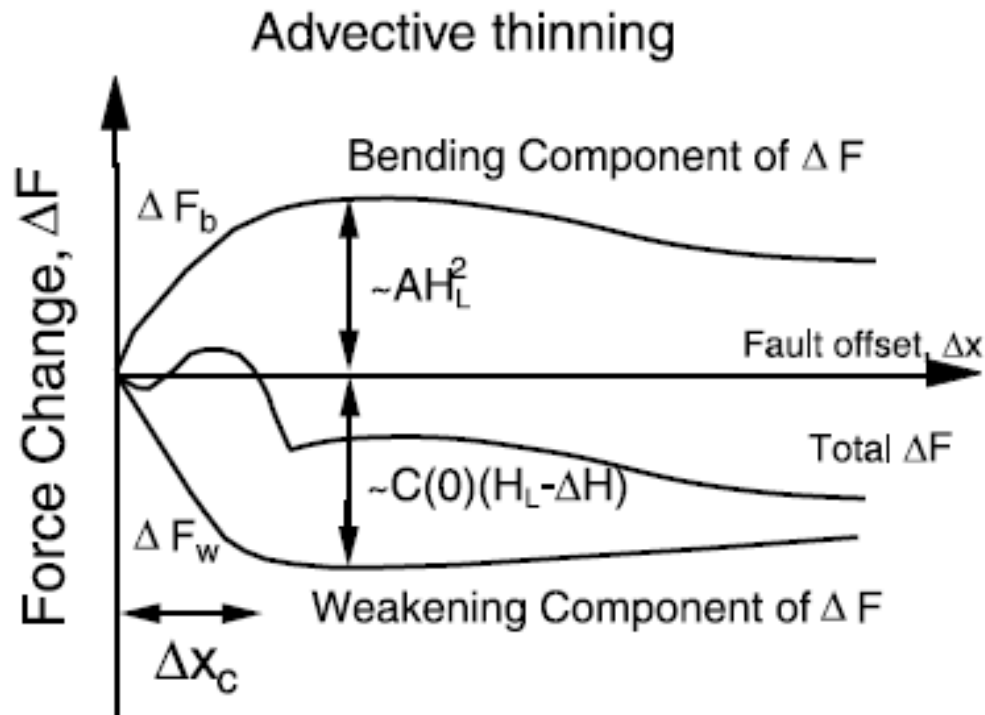


Fig. A.8: Representation of the weakening of the fault and bending component in the case of advective thinning (from Lavier and Buck, 2002). The advective thinning modify the thickness of the crust around the fault and modify the fault weakening.

1.4. The role of stress orientation

One of the ideas to explain the initiation of a low angle fault is a modification of the stress field. For a dip angle of 35° , it means that σ_1 is not vertical anymore but plunge with an angle of 65° (rotation of 25°). However, the question is how it is possible to explain this modification of the stress. Modelization with unusual loading condition were realised to understand how the stress field is modified and how it changes the fault geometry. In their article, Wills and Buck (1997) made a review of the different models concerning this topic. Yin (1989) proposed a model with ductile flow in the lower crust creating a shear stress at the base of the upper crust. The shear stress decreases from the base of the upper crust until the surface. This model creates low angle faults at depth, but the failure reaches the surface with a high angle. Spencer and Chase (1989) proposed model using an uncompensated Moho with a bulge at the base of the crust modifying the stress orientation. However even if the faults have low angle at depth none of them reach the surface with a low dip angle whatever parameter are used. The importance of dykes in the crust was analysed by Parsons and Thompson (1993). The shape of the dyke and the contrast of rheology between the dyke and the surrounding basement can modify locally the stress field (Fig. A.9). If the opening of the dyke is

Why large offset detachment faults are mechanically possible?

parallel to σ_{xx} a compression component from the dyke will decrease σ_{xx} . Therefore, there would be a rotation of the principal stress axis close to the dyke.

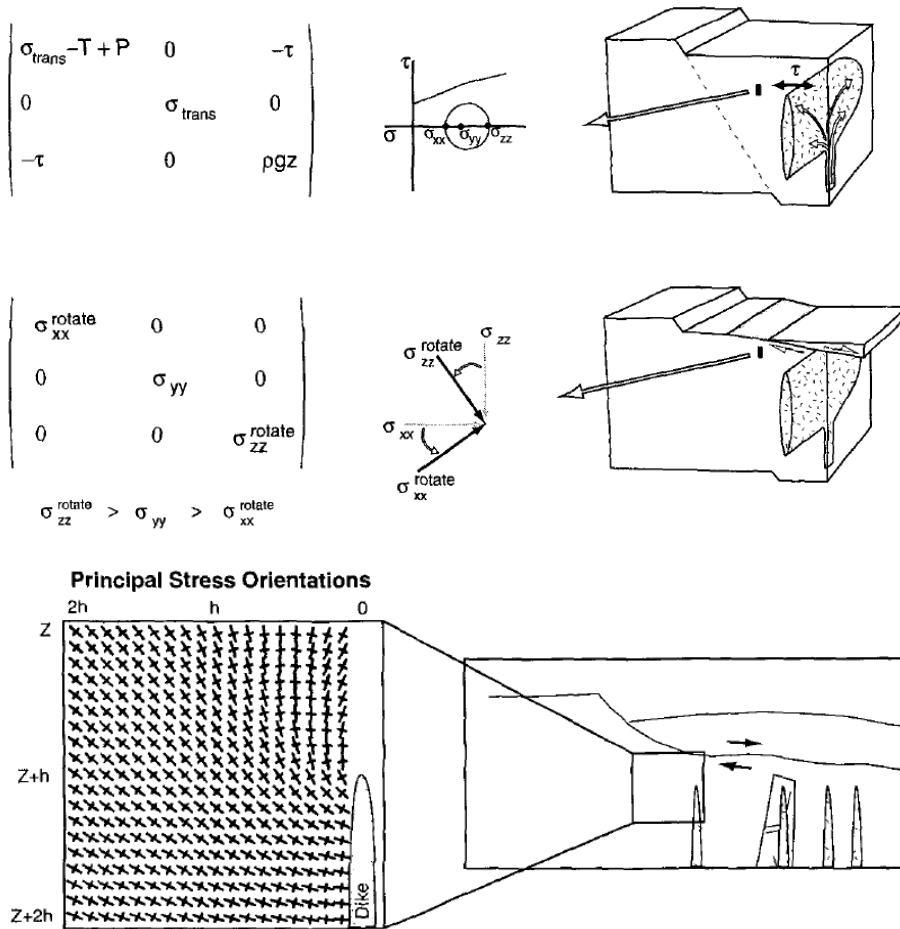


Fig. A.9: The opening of a dyke will modify locally the stress field (from Parsons and Thompson, 1993). There is apparition of shearing component (see matrix). The stress axis is no longer the principal stress axis. A rotation of a given angle is necessary to find the new principal axis.

Wills and Buck (1997) showed that with a localised near lithostatic pore pressure, it is possible to have a low angle fault (Fig. A.10). However, the pore pressure locally needs to be up to 0.96 of the lithostatic pressure. Such extremely high pore pressures at regional scale are relatively uncommon.

Why large offset detachment faults are mechanically possible?

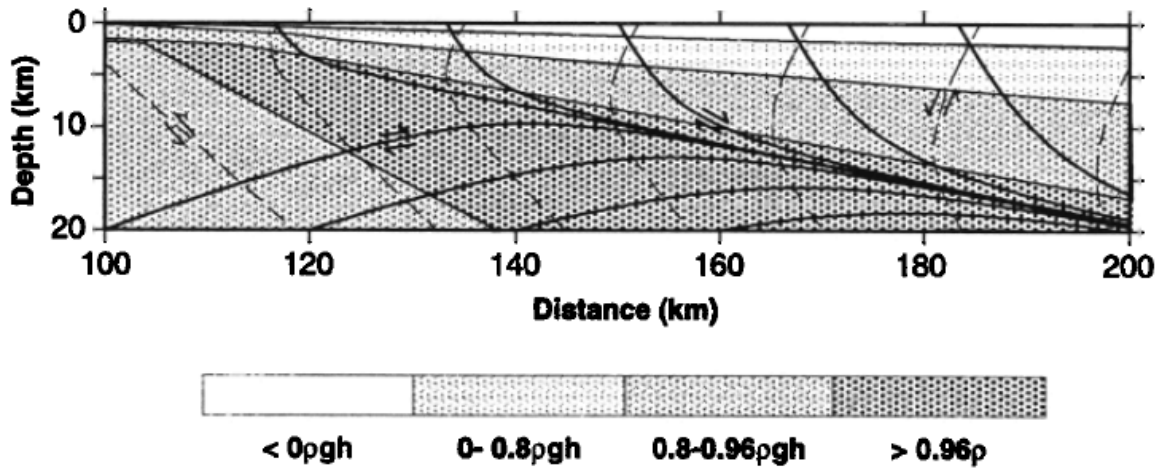


Fig. A.10: Pore pressure pattern necessary for having a low -angle fault reaching the surface (from Wills and Buck, 1997). An important pore pressure (0.96 of the lithostatic pressure) is needed locally.

The role of hydrothermal circulation in the rotation of the stress axis was proposed by (Bartley and Glazner, 1985). The opening and sealing (by mineral precipitation) of veins along a pre-existing plane will modify locally the stress along this plane. The stress field is given by the stress tensor:

$$S_{xy} = \begin{bmatrix} \sigma_h & 0 \\ 0 & \sigma_y \end{bmatrix} \quad (11)$$

With $\sigma_y = (1 - \lambda)\rho gh$

λ is the ratio of pore pressure to overburden pressure

The shear stress on the plane with a dip angle ϕ is

$$T_{xy} = \begin{bmatrix} 0 & \tau_s \\ \tau_s & 0 \end{bmatrix} \text{ with } \tau_s = \rho gh \sin(\phi) \quad (12)$$

Close to the plane with fluid circulation, the total stress is the sum of S_{xy} and T_{xy} . Therefore, an increase of λ will decrease S_{xy} and modify the orientation of the principal axis. (Bartley and Glazner, 1985) made a calculation that for $\phi=8^\circ$ and $\lambda=0.8$, σ_1 will rotate to an angle of 60° and the fault dip angle resulting from this stress-field would be 35° (Fig. A.11). However, in these models, high pore pressures predate the formation of the detachment and are not a consequence of faulting.

These models show that it is physically possible to create low angle fault. However, the stress conditions required for having low angle fault are not usual. It needs unusual loading of the crust, a complex repartition of pore pressure close to lithostatic pressure, dikes emplacement or hydrothermal circulation. Some of these conditions are met in nature but associated to a complex geological history and a strong inheritance such as former orogenic zones.

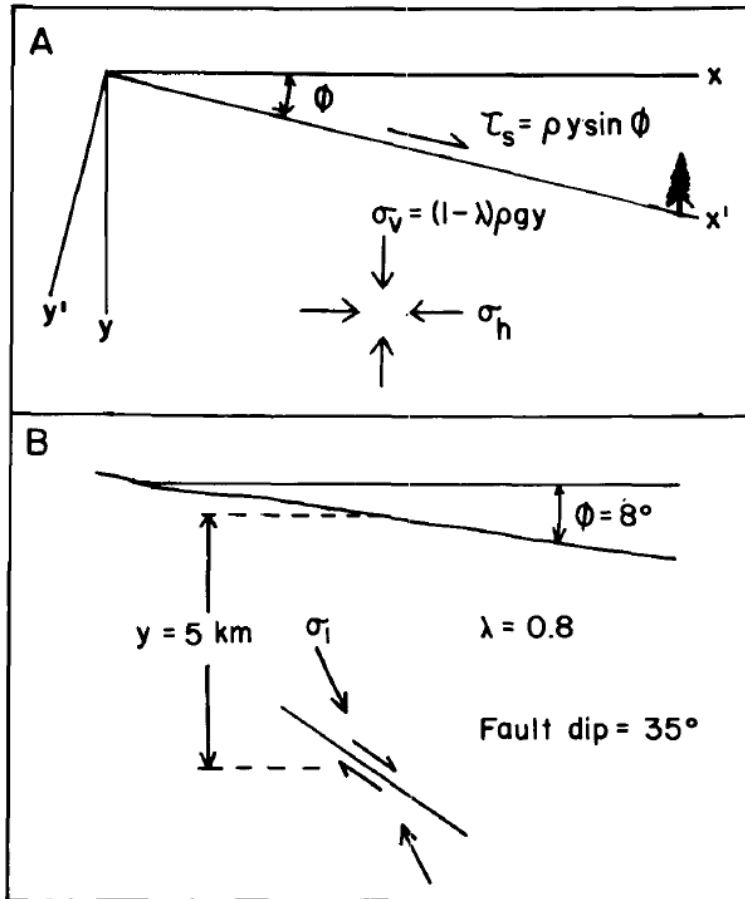


Fig. A.11: A- Illustration of the impact of a layer with hydrothermal circulation (dipping with an angle ϕ on the local stress field. B- Example for $\phi = 8^\circ$ and $\lambda=0.8$. The reorientation of the stress promote the formation of a fault dipping with an angle of 35° (from Bartley and Glazner, 1985).

2. Fault weakening

2.1. Acoustic fluidisation

As explained before, it is necessary to have a weakening of the fault, but the question is what are the processes responsible for the fault weakening (Boulton et al., 2009) : fluid overpressure, material properties, heating, self-healing slip pulse and acoustic fluidization. Acoustic fluidisation, self-healing slip pulse and fluid overpressure are mechanical processes. Vibrations passing through a granular material changes the stress between the grains; At certain time, it can decrease the friction between the grains and allow displacement on the fault. This mechanism was proposed by Melosh (1979) and can be applied for granular fault rocks (Fig. A.12). However, it needs a source for the vibration (decreasing the dynamic friction). It cannot trigger the displacement on the fault, but it can facilitate the displacement.

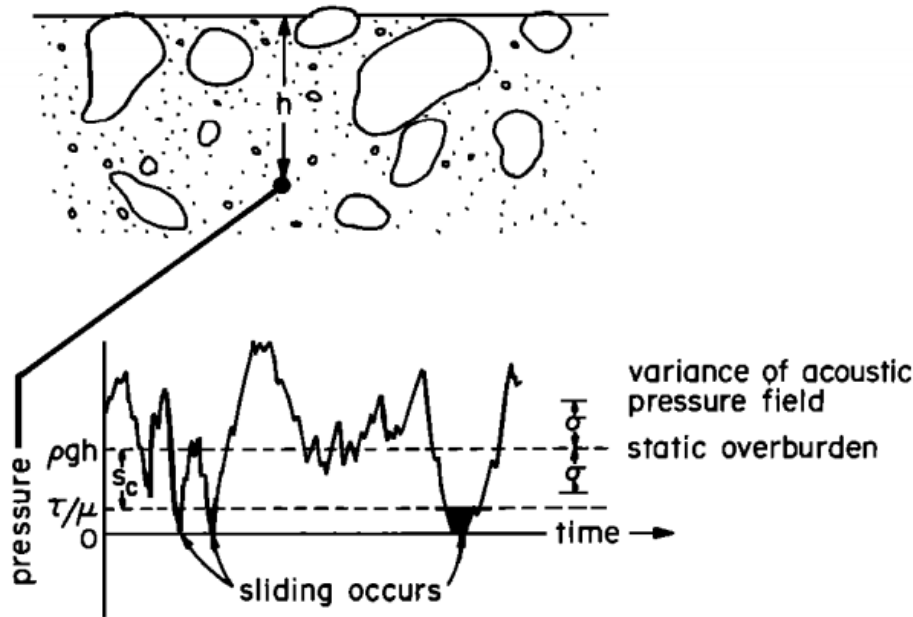


Fig. A.12: Variation of pressure during wave propagation in a granular material (from Melosh, 1979).

2.2. Fluid pressure

Fluids can circulate along the fault. The evolution of the permeability and porosity in the fault through time is complex. Permeability can increase during the seismic slip and the post seismic phase but remains low the remaining time leading to overpressure (fault-valve model). The pore pressure can also increase during the seismic slip due to the heating of the fault plane.

$$\tau = C_o + \mu(\sigma_n - P) \quad (14) \text{ with } P \text{ the pore pressure}$$

As written in the equation 14, the fluid pressure decreases the normal stress on the plane which make displacement on the fault easier.

2.3. Low friction minerals

Minerals have different friction coefficient. A weak material is considered to have a friction between 0.2 and 0.4 (Boulton et al., 2009). Common minerals with low friction are sheet silicate (clay, serpentine) and graphite even if the friction depends on the orientation of the minerals. According to (Boulton et al., 2009), the sericitization of the feldspath under greenschist facies. Sericitization is one of the reason of the low strength of the San Andrea fault (Evans and Chester, 1995). Under slow strain rate, amorphization of silica rich material can happened (see pseudotachylite section). These silica gel have a low friction and can decrease the friction on the fault plane. Frictional melt formed during the seismic slip behaved like the silica gel. However, they only impact the dynamic friction that can enhance the deformation during the earthquake instead of triggering it.

3. Mechanisms of deformation and fault rocks

3.1. Mechanism of deformation along fault zones

3.1.1. Plastic flow

Three main processes are acting during the plastic flow at the crystal scale: dislocation, diffusion and sliding (Fossen, 2016). The presence of defects in the crystal (vacancy of elements or substitution of element not adapted to the crystal lattice) induce stress in the crystal. These defects can be punctual or planar. At low temperature, it is not possible to resorb these defects but at higher temperature it is possible. The crystal lattice became less rigid and migration of these defects are possible. The energy required to start this process is called activation energy (Griggs and Handin, 1960). The increase of energy give can give to the system the amount of energy needed. The migration of punctual defects can be achieved by diffusion. For planar defects it is called dislocation creep. An increase of temperature will lead to the elimination of the defects. The deformation of the rock under high temperature lead diffusion and dislocation creep deformation of the mineral in response to the stress applied. The deformation will create new dislocation. There is a balance between the rate of creation of dislocation and the rate of disappearance at the border of the grain. This is called dynamic recrystallisation. The continental crust can be considered as a quartz-feldspath assemblage. The plastic deformation of quartz starts at around 300°C (Stipp et al., 2002). The first mechanism of dynamic recrystallisation is called bulging. New grains appear on the surface of the primary grain. The new grains with the lowest dislocation density will grow at the expense of the other. The accumulation of the dislocation on the edge of the sub grains lead to a permanent torsion of the crystal. This is called sub-grain rotation and occurs at around 400°C. At higher temperature (around 500°C), the dislocations are able to move easily. The grains with the lowest dislocation density will grow at the expense of the other. This is called Grain boundary migration (GBM).

The same mechanism can be applied for feldspar but for different temperature (Tullis and Yund, 1985). The bulging starts at 400°C, the sub-grain rotation at 600°C and the grain boundary migration at 850°C. The result of strong shearing under plastic flow is the formation of mylonite and ultramylonite. These mylonites usually show monomineralic bands. The grain size varies and is function of the mineral but also of the strain rate. The mylonitic bands form usually large shear zones (100's meters).

3.1.2. Frictional flow

Below the limit of plasticity, the deformation is brittle, controlled by the cohesion and the friction of the materials. The deformation is accommodated by fracturing or sliding of the grains. The fractures can be intra or inter-granular.

Important comminution grain comminution is related to frictional deformation with important grain comminution. From that moment, all the deformation is accommodated by the gouge. There are different hypotheses for explaining this loss of strength in the gouge. A diminution of the friction can be explained by phyllosilicates with low friction coefficients (depending however of the orientation of the phyllosilicates) or by fluid overpressures. (Boulton et al., 2009) in their review about fault gouge in low angle normal faults implied another mechanism coming from the theory of granular flow. They explain the mechanism responsible of the gouge with the concept of force chain in granular materials (Fig. A.13A). In these materials the friction between grains during shearing block the deformation and increase locally the pressure until one of the grains breaks allowing further deformation until it is blocked again by friction. The elastic energy stored by the grains is during fracturing released and transformed into kinetic energy. This kinetic energy can be responsible for the fluid behaviour of the gouge, but this is only temporary until kinetic energy is dissipated. As the deformation continues, fractures in the force chain continue creating smaller and smaller grains, which is responsible of the important grain comminution observed in the gouges in general. This leads to a diminution of the size of the force chains and a fractal appearance of the gouge with a gouge zone divided into smaller shear bands within these bands smaller shear bands. There is a fractal behaviour of the gouge (invariance of geometry of the gouge with the change of scale).

The grain size repartition in granular fault rocks was studied both with field sample (see An and Sammis, 1994) and experimental fault rock samples (Marone and Scholz, 1989). The measurements were done on 2D-sections. They give a fractal dimension of 1.6 (see Monzawa and Otsuki, 2003). Monzawa and Otsuki (2003) studied the processes of comminution (Fig. A.13B) using samples from major faults in Japan (the Tanakura shear zone, the Itoigawa–Shizuoka tectonic line, the Nojima fault, and the Koi fault). To find the fractal dimension they used the equation from (Otsuki, 1998):

$$P \equiv \frac{N}{N_t} = \left(1 + \left(\frac{D}{D_c}\right)^\alpha\right)^{-\frac{B}{\alpha}} \quad (13)$$

- N is the number of grains larger than the diameter D
- N_t is the total number of grains
- D_c is the characteristic diameter at the cut off
- B is the fractal dimension
- A is a measure of the cut-off sharpness

Why large offset detachment faults are mechanically possible?

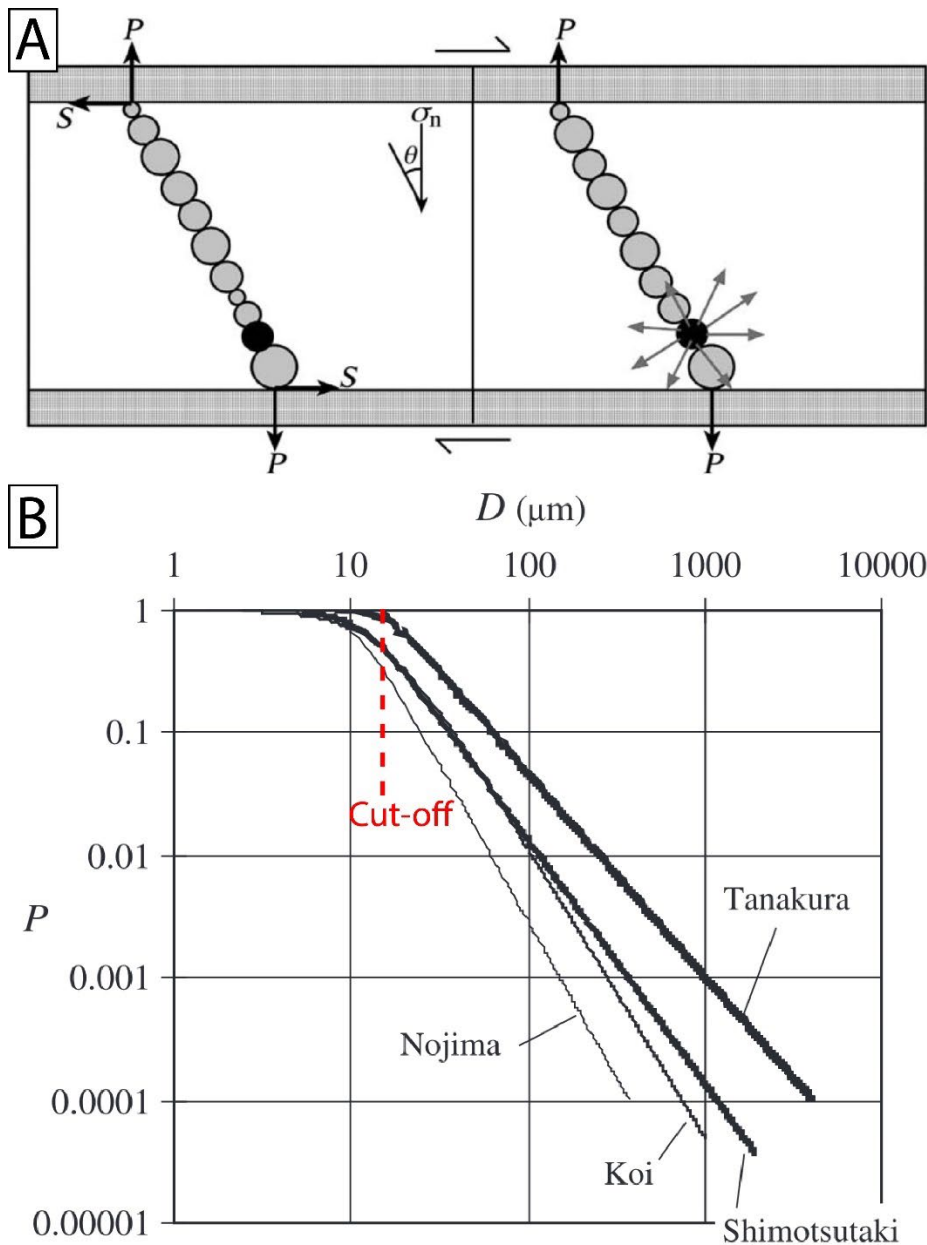


Fig. A.13:A- Force chain before and during fragmentation in response to shear stress (from Boulton et al., 2009). B- Size frequencies for granular fault rocks (from Monzawa and Otsuki, 2003). P represents the probability to find a grain larger than the diameter D .

The fractal dimension used for detachment fault is also around 1.6 ($5/3$ in (Boulton et al., 2009)).

Microstructures associated to frictional flow leads to the formation of YPR structures composed of a main shear plane (Y-plane) and secondary planes R (riedel), R' (antithetic riedel) and P-plane at specific angle to the Y-plane. These structures are similar to structures observed at macroscale on fault zones.

3.1.3. Frictional-viscous flow

However, another mechanism is common in the gouge, the frictional-viscous flow. This mechanism correspond to a "solution precipitation aided cataclasis in presence of chemically active

Why large offset detachment faults are mechanically possible?

fluid" (Imber et al., 2008). The fault weakening associated to frictional-viscous flow is associated to the formation of foliated cataclasite and gouges with fabric similar to mylonites (Bos and Spiers, 2002). These foliated cataclasite and gouges will form SCC' structures (Bos et al., 2000).

This type of mechanism is active at depth between ca. 3 to 15 km depending on the thermal gradient (Imber et al., 2008). At shallower depth, frictional flow will dominate while at depth, plastic flow will be the main mechanism of the deformation. The rheological profiles associated to Frictional-viscous flow are decreased up to 70% compared to calculation assuming only frictional flow (Imber et al., 2008).

3.2. Fault rocks in detachment

The fault rocks are the rocks formed along the shear zone in response to the strain. The response of the rock to the strain depends on the temperature and the pressure at which occurs the deformation. Two main mechanisms are found in nature. For high temperature, the rocks are deformed under plastic flow. The deformation is continuous (at least at the scale of the grain not the crystal). For quartz, the transition to plastic flow occurs at around 350°C which for a quartz feldspathic crust with a normal geothermal gradient of 30°/km means 10 km depth. However, the plastic transition for the feldspars is higher. For low temperature, the deformation is brittle which means that the deformation on the rocks is accommodated by fractures sliding and abrasion of the grains.

		← Deformation style →							
		Frictional flow			Plastic flow				
		← Dominant deformation mechanism →							
		Non-cohesive		Secondary cohesion		Primary cohesion		% matrix and grain-size	
			Cemented HB	Indurated HB		> 50% phyllosilicate	< 50% phyllosilicate		
Hydraulic breccia (HB)	Breccia series	Proto-breccia	Cemented proto-breccia	Indurated proto-breccia	Cataclasite series	Proto-cataclasite	Proto-phylionite	Proto-mylonite	0-50% matrix
		Breccia	Cemented breccia	Indurated breccia		Cataclasite	Phyllonite	Mylonite	50-90% matrix
		Ultra-breccia	Cemented ultra-breccia	Indurated ultra-breccia		Ultra-cataclasite	Ultra-phylionite	Ultra-mylonite	90-100% matrix
	Gouge	Cemented gouge	Indurated gouge					Sub-microscopic matrix	
Pseudotachylite									

Fig. A.14: Classification of fault rocks according to the mechanism of cohesion, the cohesion, the grain size and content of matrix (from Braathen et al., 2004).

The fault rock classifications are based on the mechanism of deformation, the cementation of the rock and the percentage and size of the matrix (Table A.1). When the deformation is

Why large offset detachment faults are mechanically possible?

dominated by plastic flow the fault rocks are mylonite or phyllonites depending on the content of phyllosilicates (Fig. A.14). When the brittle deformation, the rocks are breccias to gouge. The term breccia is used for coarse-grained rocks with low matrix content whereas the term gouge is used for ultra-fine-grained rocks (micro to nanometre). These breccias and gouges can be cemented or indurated. The term cataclasites correspond to coarse to fine-grained rocks with a mechanism of deformation at the transition between plastic and frictional flow (Table A.1). Pseudotachylite corresponds to ultra-fine-grained rocks formed during seismic slip. All these rocks will be described more in details below.

The minerals can be derived from the host rock with more or less deformation (called recrystallized if they show dynamic recrystallisation). However, their chemistry can be modified especially for the feldspars (albitisation of orthoses and anorthite rich feldspath). Neoformed minerals are also observed. They can come from the destabilisation of the initial minerals with often fluid circulation. The replacement of feldspath by sericite is an example.

For a normal fault, it is expected in the footwall a retrograde path which means a transition for higher temperature to lower temperature. The deeper part of the fault will start under plastic flow and as the exhumation goes on, the deformation will become brittle. This is the opposite to what is expected for thrust faults in the footwall.

Term	Description
Fault rocks or fault-related rocks	Commonly formed through strain concentration within a tabular or planar zone that experiences shear stress
Frictional flow	Pressure, subordinate temperature, and fluid-controlled deformation mechanisms which have a brittle style: granulation of grains by intergranular, intragranular, and transgranular microfracturing, and intragranular or intergranular frictional sliding with abrasion of fracture walls and grain margins
Plastic flow	Mainly thermally activated, continuous deformation without rupture, with a ductile style of deformation: dislocation creep and glide, solid state diffusion creep, diffusional mass transfer, and viscous grain boundary sliding
Noncohesive	Not consolidated
Secondary cohesion	Consolidated after formation, either through cementation of the matrix, or through compaction, recrystallization, or neomineralization (see indurated)
Primary cohesion	Cohesion preserved during formation
Hydraulic fracturing	Fracturing caused by fluid pressure: commonly random orientation of fractures and rough fracture surfaces. The resulting hydraulic breccia may not be tabular or planar, however, it is tectonically induced and frequently fault-related.
Cemented	Consolidated through mineral precipitation in pores of the matrix
Indurated	Consolidated by compaction due to directed pressure, annealing by recrystallization of grains, or neomineralization (e.g., muscovitization, silicification, albitization, epidotization, saussuritization). The term disregards cementation unless related to general neomineralization.
Phyllosilicate content	Content of sheet minerals (characterized by weak “001” bonds) of the phyllosilicate group
Matrix	Fine-grained material in a fault rock formed by granulation or dynamic recrystallization of grains, filling the interstices between larger clasts of original rock
Breccia	Mainly chaotic, noncohesive fault rock, generated by fractional flow
Cataclasite	Mainly chaotic fault rock that developed with cohesion, which is generated by mainly frictional flow
Phyllonite	Phyllosilicate-rich fault rock with distinct mineral fabric, and dominated plastic flow
Mylonite	Fault rock with distinct mineral fabric, and dominated by plastic flow
Blasto-mylonite	Fault rock in which dynamic recrystallization and/or neomineralization causing grain-size increase of clasts outpace grain-size reduction

Tab. A.1: Terminology of the fault rocks (from Braathen et al., 2004).

3.2.1. Cataclasite

Even if formed under frictional flow, cataclasites are different than the other friction dominated fault rocks because they keep their cohesion during the deformation (Fig. A.15B; Table A.1). The processes are different than in the other rocks. They are usually formed at higher temperature and metamorphic reactions play a bigger role. It is often observed an important deformation of the feldspars. The deformation occurs usually at sub-greenschist facies to pumpellyite facies. At these temperatures, the quartz is supposed to deform by bulging and by fracturing at lower temperature. The feldspars are supposed to be deformed only in a brittle way. However, what is commonly observed in the cataclasite is a localisation of the deformation on the feldspars. The style of deformation of the feldspars is complex. Even if fractures are formed at these temperatures, there is important recrystallisation of the feldspars with also neof ormation of feldspars, quartz, white micas and chlorite. The deformation, the fluid circulation and the changes of P-T lead to a destabilisation of the feldspath. A series of transformations was identified by Kerrich et al., (1980). The orthoclase can recrystallize or form albite if there is an input of Na. Oligoclase can also recrystallize or form orthoclase if there is an input of K. There is also formation of sericite as an alteration product of the feldspar during the deformation. Quartz can form if there is an excess of Si. The biotite with important deformation will disappear. They can form Fe-rich muscovite or chlorite with ilmenite, rutile or sphene. The Ca released by the oligoclase can be used to form epidotes and calcite.

Why large offset detachment faults are mechanically possible?

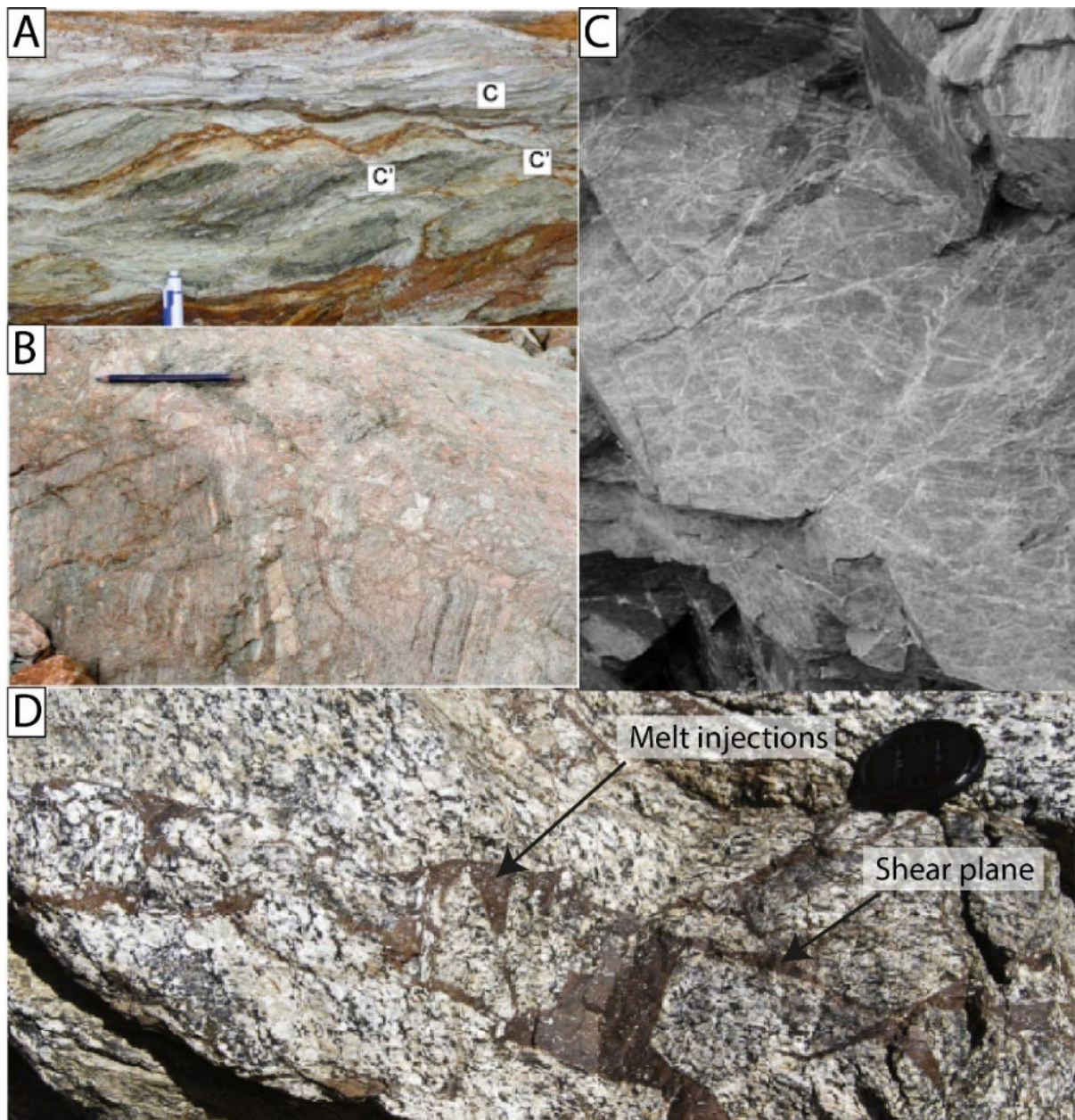


Fig. A.15: A- Illustration of a gouge showing SCC' structures (from Collettini et al., 2019). B- Cataclasite from the damaged of a detachment fault (from Mohn et al., 2012). C- Indurated hydraulic breccias from the Nordfjord-Sogn Detachment (from Braathen et al., 2004). D- Pristine pseudotachylite visible as veins injected in a granitic basement (from Kirkpatrick and Rowe 2013).

These deformations under lower greenschist facies are called 'green cataclasite' ((Fitz Gerald and Stünitz, 1993). Manatschal (1999) described green cataclasite from a Jurassic detachment in the Alps. The host rock is a granite. The K-feldspath were sericitized. Microcracks are present in the quartz grains with also undulose extinction. Secondary minerals show no sign of deformation. They are composed of illite, chlorite, albite, quartz, calcite, and epidote. The presence of hydrated phases indicate the presence of fluid during the deformation. These fluids include water and CO₂ associated to calcite precipitation.

3.2.2. Breccias

Contrary to the cataclasite, the breccias do not have cohesion during the deformation. If there is induration of the rock, it happens after the deformation. The breccias can be formed by two processes, fracturing during frictional flow and hydraulic fracturing. Breccias in detachment fault are formed by frictional flow. However fluid circulations along the fault plane can lead to hydraulic fracturing on the surrounding basement. More specifically, the hydraulic breccias show jigsaw fractures (Fig. A.15C) and are formed under high fluid pressure. The matrix can be made of the fault gouge and the cataclasite injected in the basement (Clark and James, 2003) or secondary minerals crystallized from the fluids.

3.2.3. Pseudotachylite

Pseudotachylite are glassy to fine grained rocks observed often in large scale faults. Two mechanisms of formation are often implied. The first one is local melting by frictional heating during seismic slip. They usually records paleo earthquake. Kirkpatrick and Rowe (2013), gives a list of features to recognize pseudotachylite. At macroscopic scale, large injection of molten material in the adjacent basement are visible (Fig. A.15D). They appear usually brown to dark. Sometimes, reaction front associated to contact metamorphic can be visible surrounding the veins. At the microscale, the shape of the grains can be modified during the melting event leading to embayed edge. The rapid cooling of the melt create features similar to the one observed in volcanic rocks like microcrystallites with dendritic habit, spherulites and vesicles or amygdules (Kirkpatrick and Rowe, 2013). Droplet of sulphur can be observed (indicating immiscibility of the sulphurs in the silicate melt). High temperature minerals in the fault rocks or changes of chemistry between the basement and the fault rock (more mafic and hydrous fault rock). However, pseudotachylite are scarcer than expected because frictional melt is rare or because the preservation of the pseudotachylite is bad (alteration of the glassy component).

Pseudotachylite-looking rocks can be formed during slow displacement of the fault (Pec et al., 2012). They form by amorphization of the crystal lattice during deformation at mid crustal conditions. They are therefore related to aseismic slip at depth.

3.2.4. Gouge

Gouges are ultra-fine-grained rocks (Fig. A.15A). The composition of the gouge is variable. It is composed of fine, crushed grains from the host rock with other neoformed minerals (quartz, albite, phyllosilicates, sulphurs). It can be in some cases dominated by neoformed phyllosilicates. These shear zones are really thin (from the centimetre to the meter maximum). The gouge can be white to greyish but some of the gouges are black. The coloration of the matrix can be due to the presence of

sulphurs or to the presence of graphite. The induration of some gouge can be due to neoformation of phyllosilicates along the shear zone.

4. Evolution of fault geometry

4.1. Evolution of the fault geometry during rifting

In this section, the crust is assumed to be equilibrated and no inheritance. The thickness of the brittle layer is around 15 km. Important thickness of the crust will favour half graben geometry with small offset to minimise the flexure. In an unstretched crust, the first fault to form generate half - graben structures.

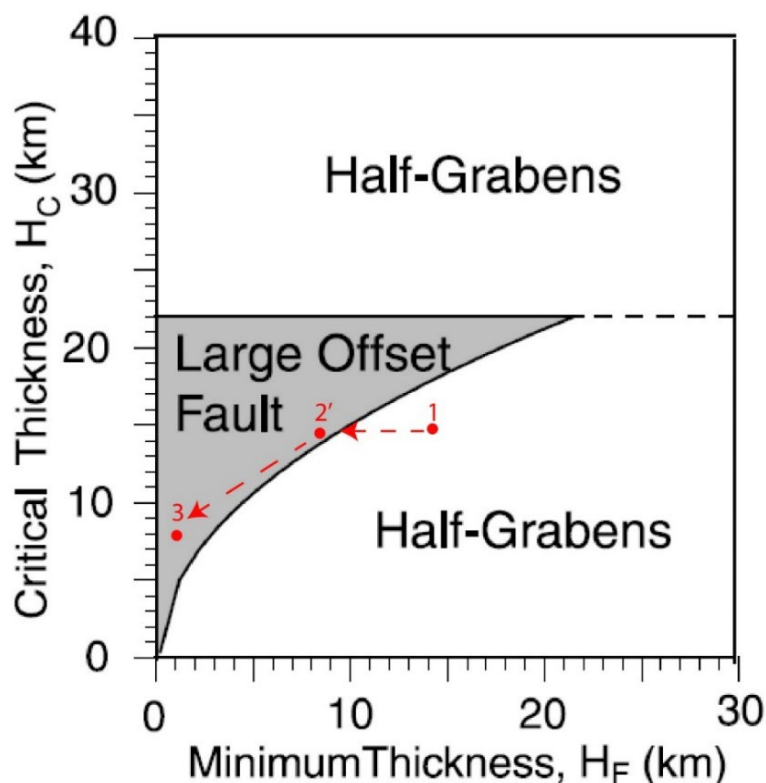


Fig. A.16: Plot of the critical thickness and the minimum thickness on the fault with the field corresponding to the half-graben and large offset fault (modified from Lavier and Buck, 2002). The points 1, 2 and 3 correspond to the possible evolution during rifting from stretching to hyperextension.

In the Fig. A.16, the point 1 correspond to the theoretical initial situation before the creation of the fault. It is found in the field of the half-graben. This situation corresponds actually to the stretching phase. The thermal advection created by the fault favours the creation of a new fault.

As the rifting continues, the crust gets thinner and thinner. The importance of the flexure decreases, enabling the formation of large offset faults. There is a relation between the thickness of the brittle layer (H_L) and the thickness in the area of the fault (H_F). If H_L decreases, then H_F decreases too. This is illustrated by the point 2 in the field of the large offset faults. However, it is also

Why large offset detachment faults are mechanically possible?

necessary to take the thermal advection into account. In absence of hydrothermal cooling, a secondary fault might form instead of continuing the deformation on the same one. To have the formation of a large offset-fault, it is necessary to have a decrease of the brittle layer and hydrothermal circulation to cool the crust.

Another interesting feature to understand the evolution of the fault geometry during rifting is the link between the geometry of the fault and the velocity of extension. Fig. A.17 plots the initial brittle thickness with the velocity of extension. For initial brittle layers above 30 km, only half-grabens are possible. However, under 30 km, there is a field of large offset faults as a function of the velocity of extension. The 2 curves represent different value of β . Actual data points from regions recording rifting were compared to the theoretical model (and show good agreement).

It is interesting to use this model to understand the evolution of the fault during rifting. During the stretching phase, the deformation is widespread across the region. It is accommodated by a multitude of normal faults. The regional extension velocity V_R is the sum of the velocity on the different faults: $V_R = V_1 + V_2 + \dots + V_n$ (15) with n the number of faults

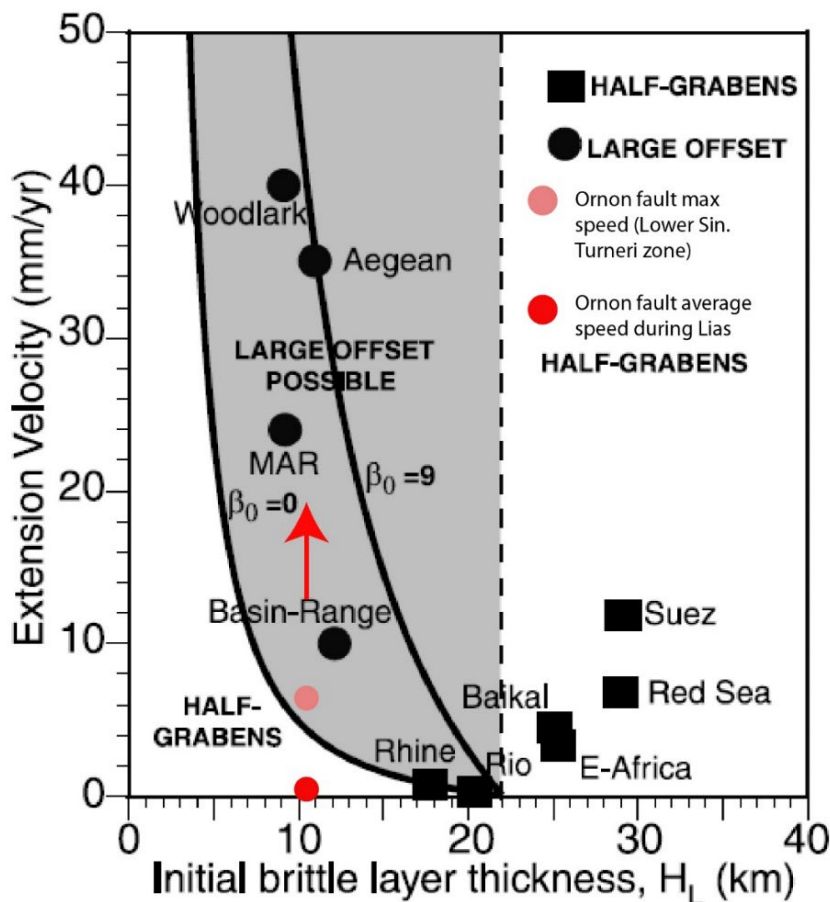


Fig. A.17: Plot of the extension velocity and the initial brittle layer thickness with the field corresponding to the half-graben and large offset fault (modified from Lavier and Buck, 2002). The points correspond to the Ornon fault in the Alps (Chevalier, 2002).

During the necking of the lithosphere, the deformation became localised on a small area with a smaller amount of fault accommodating the deformation on the surface. If V_R remains constant

Why large offset detachment faults are mechanically possible?

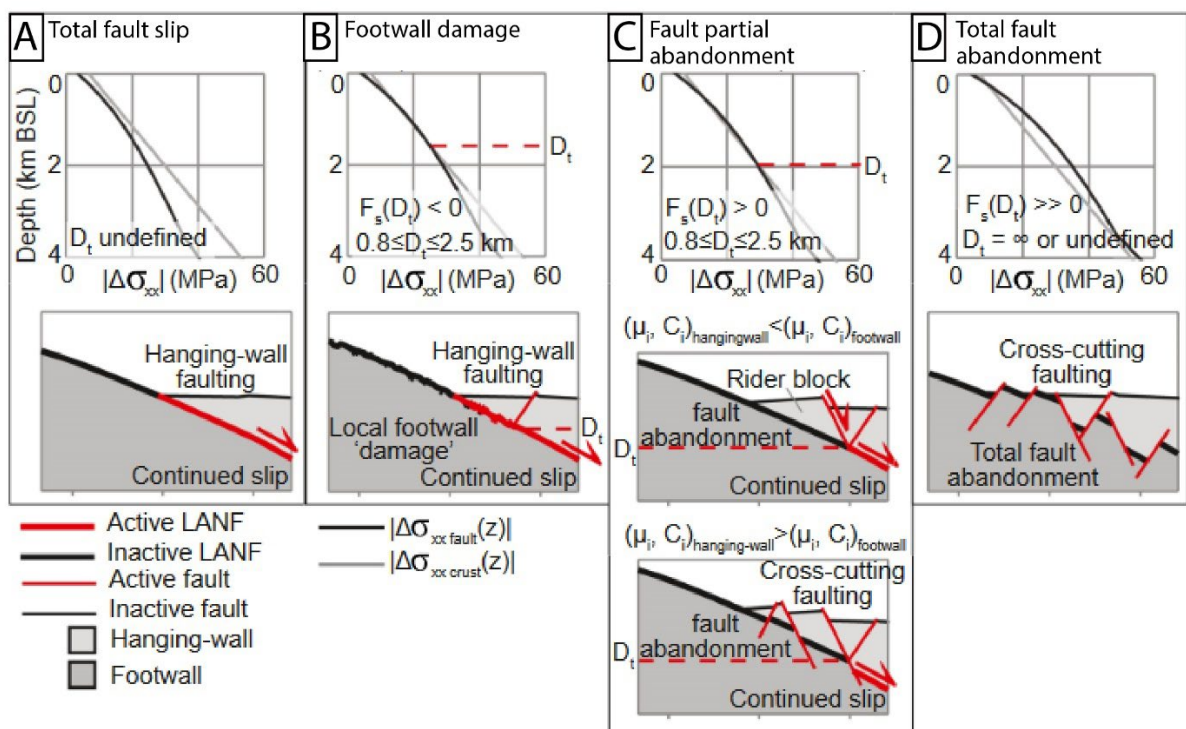
during the rifting, then each fault will have an extension velocity higher than during the stretching phase.

The example of the Ornon fault in the western alps is interesting (Chevalier, 2002). This fault was active during the Lias (0.318mm/yr in average) with a maximum of activity at the end of the Lower Sinemurian (7.5mm/yr for 400 kyr). The Ornon fault therefore lies in the field of the half-grabens (or at the limit of both field for the maximum value, Fig. A.17). During the necking of the crust each fault will accommodate more displacement as the deformation became localized shifting possibly into the field of large-offset faults.

The last step of the evolution of the rift is the hyperextension leading to the mantle exhumation. After the necking phase, the brittle layer is thin (few kilometres). The flexure of the crust is negligible. Large-offset faults are present even without necessity of hydrothermal circulation. This correspond to the point 3 on the Fig. A.15.

4.2. Evolution of a detachment fault through time

The shallowing of the fault toward the surface commonly observed on detachment fault led to a misorientation of the fault and fault abandonment. One of the factors controlling the fault abandonment is the difference between differential stress required for fault reactivation at depth z ($|\Delta\sigma_{xx \text{ fault}}|$) and the differential stress required to cut intact crust at depth z ($|\Delta\sigma_{xx \text{ crust}}|$). In general terms, if $|\Delta\sigma_{xx \text{ fault}}| < |\Delta\sigma_{xx \text{ crust}}|$ then the fault remains active while if $|\Delta\sigma_{xx \text{ fault}}| > |\Delta\sigma_{xx \text{ crust}}|$ then fault abandonment or partial abandonment is observed (Webber et al., 2022).



Why large offset detachment faults are mechanically possible?

Fig. A.18: Four main styles of fault abandonment (from Webber et al., (2022)). The model was made using $\mu_{crust}=0.65$, $\lambda=0.4$, $C_i=5$ MPa, and $C_f=0.5$ MPa while μ_{fault} increases from model A to D. A- Condition for continuous slip on the main fault B- Condition close to lock up leading to footwall damage. C- Conditions leading to partial fault abandonment. D- Condition leading to total fault abandonment.

Different scenarios however can be observed depending on the lock up depth Dt . If $|\Delta\sigma_{xx\ fault}| < |\Delta\sigma_{xx\ crust}|$ then the fault remains active entirely (Fig. A.18A). When the fault is close to locking up at a certain depth Dt , footwall damage is observed (Webber et al., 2022). This damage is characterized by roughness on the fault plane (Fig. A.18B). Partial abandonment means that above a certain depth, the fault is locked (Fig. A.18C). Below this depth, the main fault remains active while above this depth, new fault will form. Depending on the properties of the footwall and hanging wall these new faults will affect only the hangingwall merging at depth with the main fault forming a rieder block (extensional allochthons) or will crosscut the hangingwall and footwall (cross-cutting faulting). Finally, if $|\Delta\sigma_{xx\ fault}| > |\Delta\sigma_{xx\ crust}|$ at any depth, then the main fault will be totally abandonment and new fault will form (Fig. A.18D).

The parameter controlling the lock of the fault is the friction of the fault and the cohesion of the fault and the intact host rock (Reston, 2020). While fluid circulations usually lead to strain softening associated to formation of phyllosilicates, precipitation of quartz and calcite can lead to progressive strain hardening of the fault leading to abandonment of the fault. The behaviour of the fault is therefore a delicate interplay between the fault orientation and fluid circulations.

Conclusion

Large offset normal fault are associated to important shallowing and fault weakening with decrease of the friction. Other mechanisms responsible for change of stress orientation such as dike emplacement or high fluid pressure can lead to the formation of detachment fault but the conditions necessary for such processes are rather uncommon.

Fault weakening occurs mostly through strong fluid-rock interaction along the fault plane leading to formation of phyllosilicates. Significant amounts of phyllosilicate lower the friction of the fault. Besides, frictional-viscous flow associated to phyllosilicate-rich fault and chemically active fluid decrease dramatically the strength of the fault.

The evolution of fault during rifting is related to changes in the strain rate accommodated by each fault as well as decrease in the elastic thickness. Strong fluid circulation appears necessary to avoid advective thinning and creation of secondary faults.

Appendix B Supplementary Material Chapter III

<i>Sample: CB20-40</i>					
<i>Spectrum</i>	G position (cm-1)	G-FWHM	R1	R2	T (°C)
1	1594	30.00	1.80	0.73	316
2	1590	36.00	1.72	0.68	337
3	1593	29.00	1.75	0.72	320
4	1596	32.00	1.83	0.71	324
5	1595	28.00	1.64	0.72	322
6	1596	31.00	1.70	0.72	321
7	1592	34.00	1.55	0.71	326
8	1592	40.00	1.47	0.71	326
9	1595	31.00	1.53	0.73	316
10	1590	35.00	1.41	0.72	319
11	1592	36.00	1.59	0.71	324
12	1592	36.00	1.56	0.73	316
13	1590	38.00	1.66	0.72	319
14	1581	49.00	1.91	0.72	320
15	1595	32.00	1.47	0.69	335
16	1598	29.00	1.26	0.69	332
17	1596	28.00	1.79	0.73	314
18	1590	41.00	1.53	0.71	325
19	1593	29.00	19.27	0.68	341
20	1593	27.00	1.83	0.74	313
21	1595	28.00	1.75	0.73	315
<i>Average</i>	1592	33.29	2.48	0.71	323
<i>1σ</i>	3.5	5.36	3.76	0.02	7.57

Tab. B.1: RSCM data for each spectrum of sample CB20-40.

<i>Sample: CB20-41</i>					
<i>Spectrum</i>	G position (cm-1)	G-FWHM	R1	R2	T (°C)
1	1595	37	1.72	0.67	342
2	1594	34	1.89	0.70	331
3	1595	33	1.77	0.69	336
4	1596	31	1.65	0.69	334
5	1595	47	1.80	0.69	336

6	1595	31	1.85	0.70	330
7	1593	37	1.52	0.68	337
8	1591	35	1.85	0.69	334
9	1592	37	1.65	0.69	332
10	1589	42	1.58	0.68	339
11	1589	42	1.58	0.70	331
12	1595	31	1.61	0.68	338
13	1595	32	1.84	0.69	332
14	1595	35	1.91	0.68	339
15	1592	33	1.82	0.63	362
16	1593	32	1.78	0.70	330
17	1593	32	1.78	0.68	341
18	1590	39	1.59	0.68	336
<i>Average</i>	1593	35.56	1.73	0.68	337
1σ	2	4.40	0.12	0.02	6.99

Tab. B.2: RSCM data for each spectrum of sample CB20-41.

<i>Sample: MB1c</i>					
<i>Spectrum</i>	G position (cm-1)	G-FWHM	R1	R2	T (°C)
1	1592	36	2.42	0.71	327
2	1589	30	2.15	0.72	321
3	1595	30	2.69	0.72	322
4	1593	30	2.26	0.74	314
5	1593	41	4.80	0.70	330
6	1593	40	2.14	0.70	330
7	1590	45	2.20	0.70	331
8	1595	32	2.74	0.73	318
9	1593	36	2.49	0.68	337
10	1596	28	2.55	0.70	328
11	1594	28	2.44	0.73	318
12	1595	34	2.19	0.71	323
13	1592	42	1.89	0.68	337
14	1593	29	2.40	0.74	314
15	1592	54	2.42	0.69	333
16	1591	39	2.23	0.70	328
<i>Average</i>	1593	34.36	2.53	0.71	325
1σ	1.9	5.51	0.67	0.02	7.44

Tab. B.3: RSCM data for each spectrum of sample MB1c.

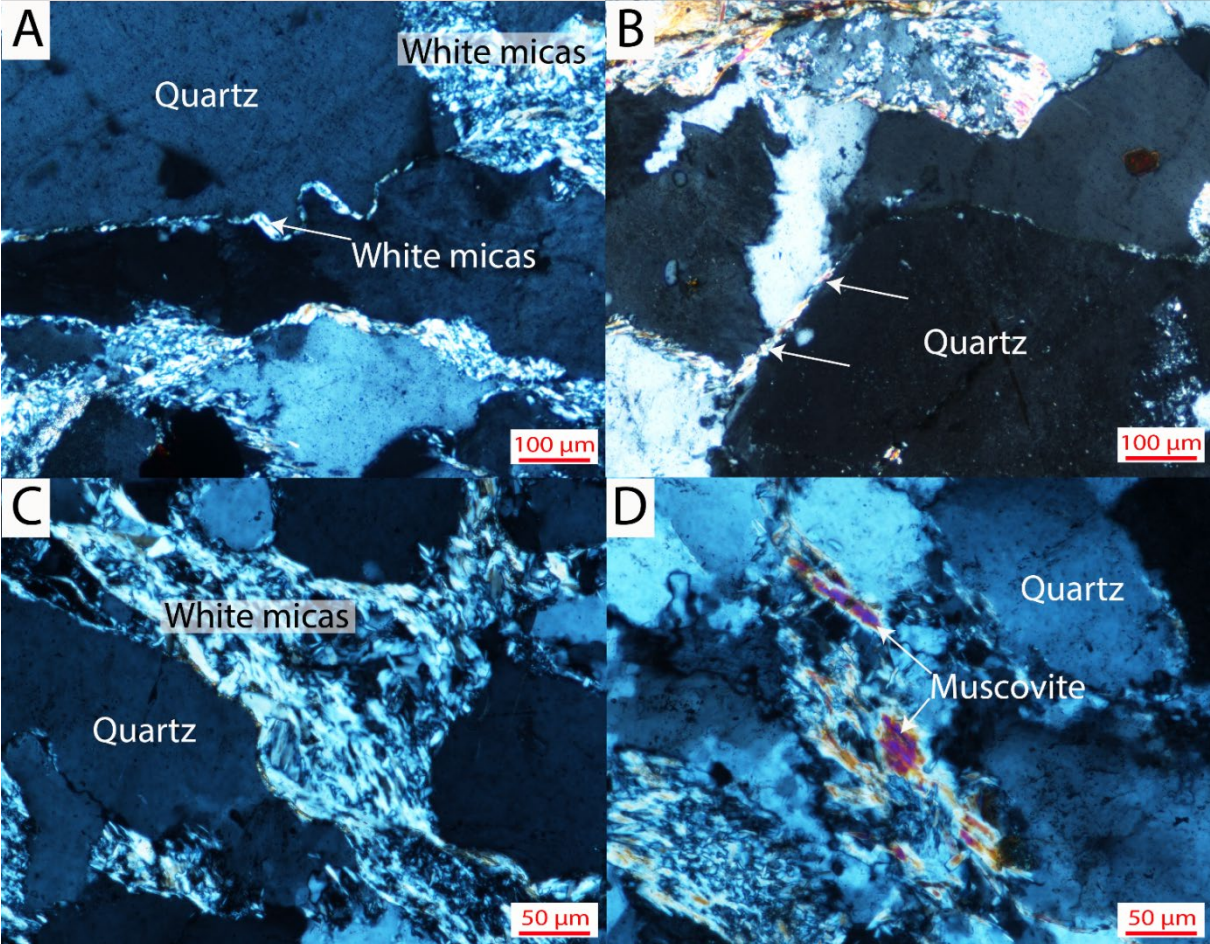


Fig. B.1: A- Grès Singuliers sample showing important compaction with convoluted sutured grains with with micas matrix caught between the two grains(XPL). B-Detrital grains with clay coating (white arrows, XPL). C- White micas (illite) matrix surrounding the quartz grains. D- Muscovite overgrowth over white micas (Illite, XPL).

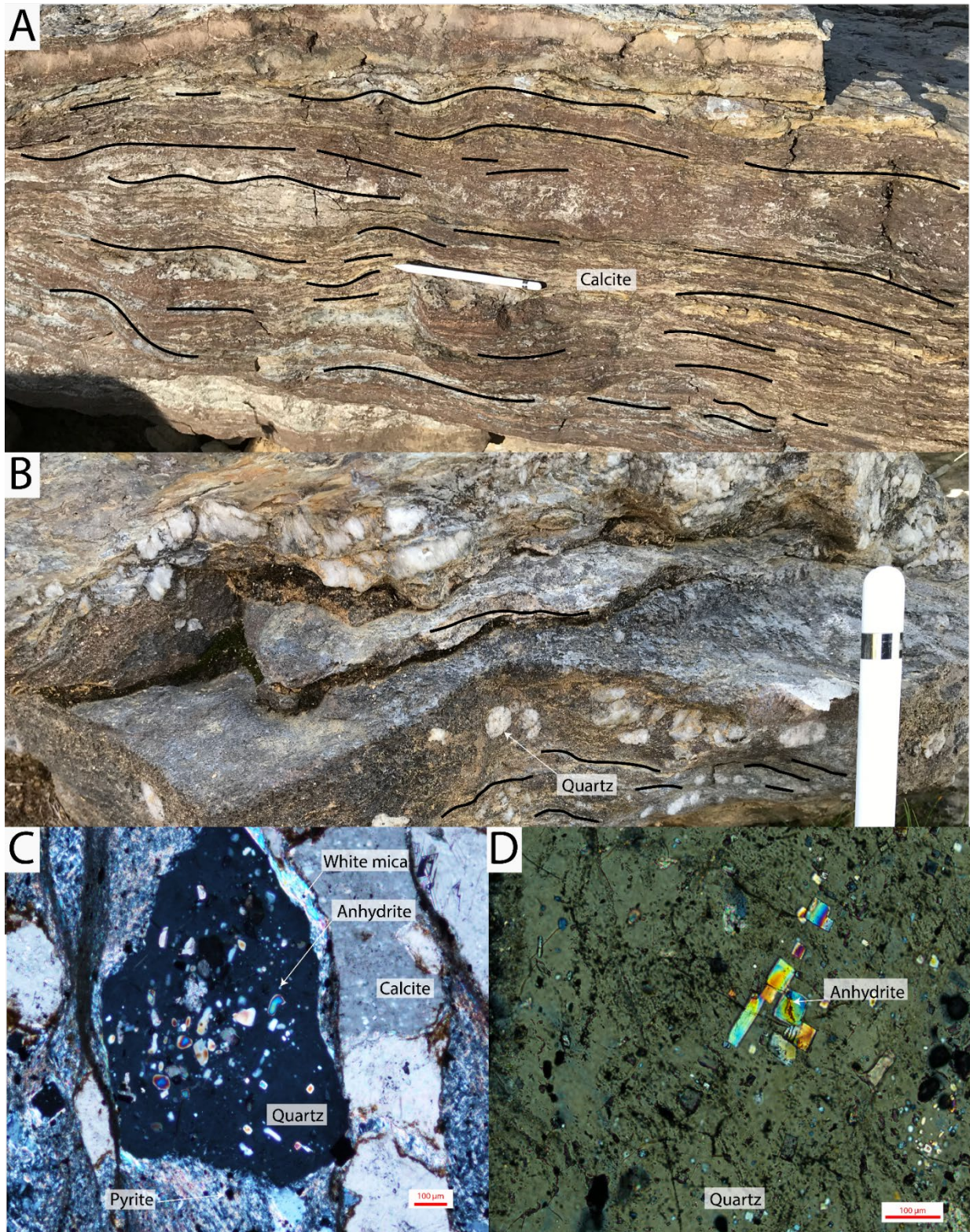


Fig. B.2: A and B- Highly-strained limestones with diagenetic quartz nodules (45°43'44.26"N/6°42'47.78"E). C- Microphotograph of diagenetic quartz with inclusions of anhydrites. The quartz is surrounded by microcrystalline calcite, white-micas and Fe-sulphides (XPL). D- Microphotograph of anhydrite inclusions in quartz (XPL).

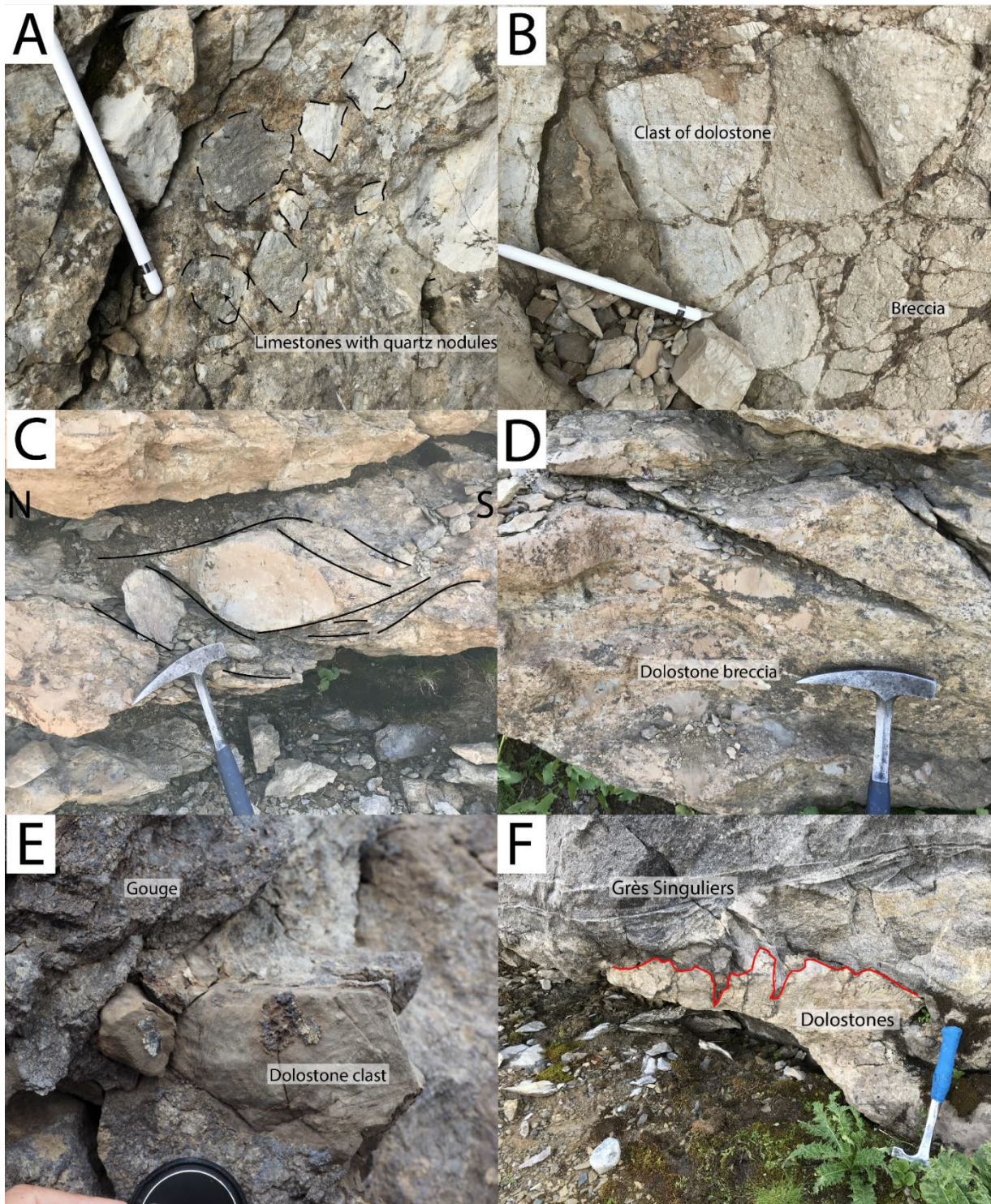


Fig. B.3: A- Breccia at the base of the pre-rift sediments showing clasts of highly strained limestone ($44^{\circ}43'46.52''N/6^{\circ}43'55.07''E$). B- Syn-sedimentary dolostone breccia affected by secondary brecciation at the base of the pre-rift cover. C- Dolostone breccia with boudins giving a N-S sense of shear ($45^{\circ}43'44.26''N/6^{\circ}42'47.78''E$). D- Dolostone breccia. E- Dolostone clasts in the gouge ($45^{\circ}43'58.53''N/6^{\circ}43'25.71''E$). F- Stratigraphic contact between the Grès Singuliers and the dolostone ($45^{\circ}43'36.84''N/6^{\circ}42'47.316''E$)

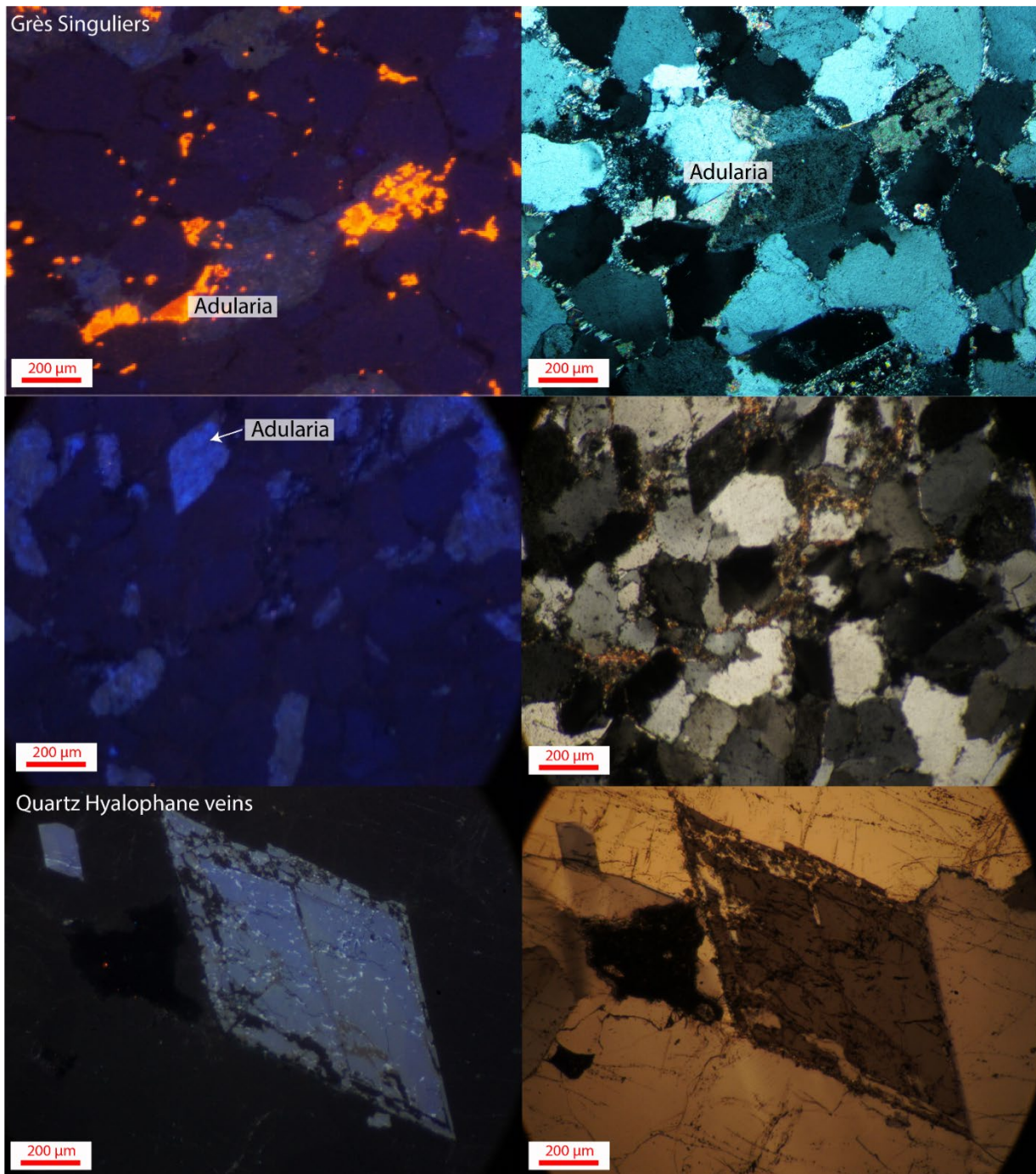


Fig. B.4: Comparison with detrital adularia crystals in the Grès Singuliers and hyalophane crystals in quartz hyalophane veins. The pictures in the left are taken under cathodoluminescence, the adularia appearing blue. The images on the right are optical microphotographs.

Appendix C Supplementary Material Chapter IV

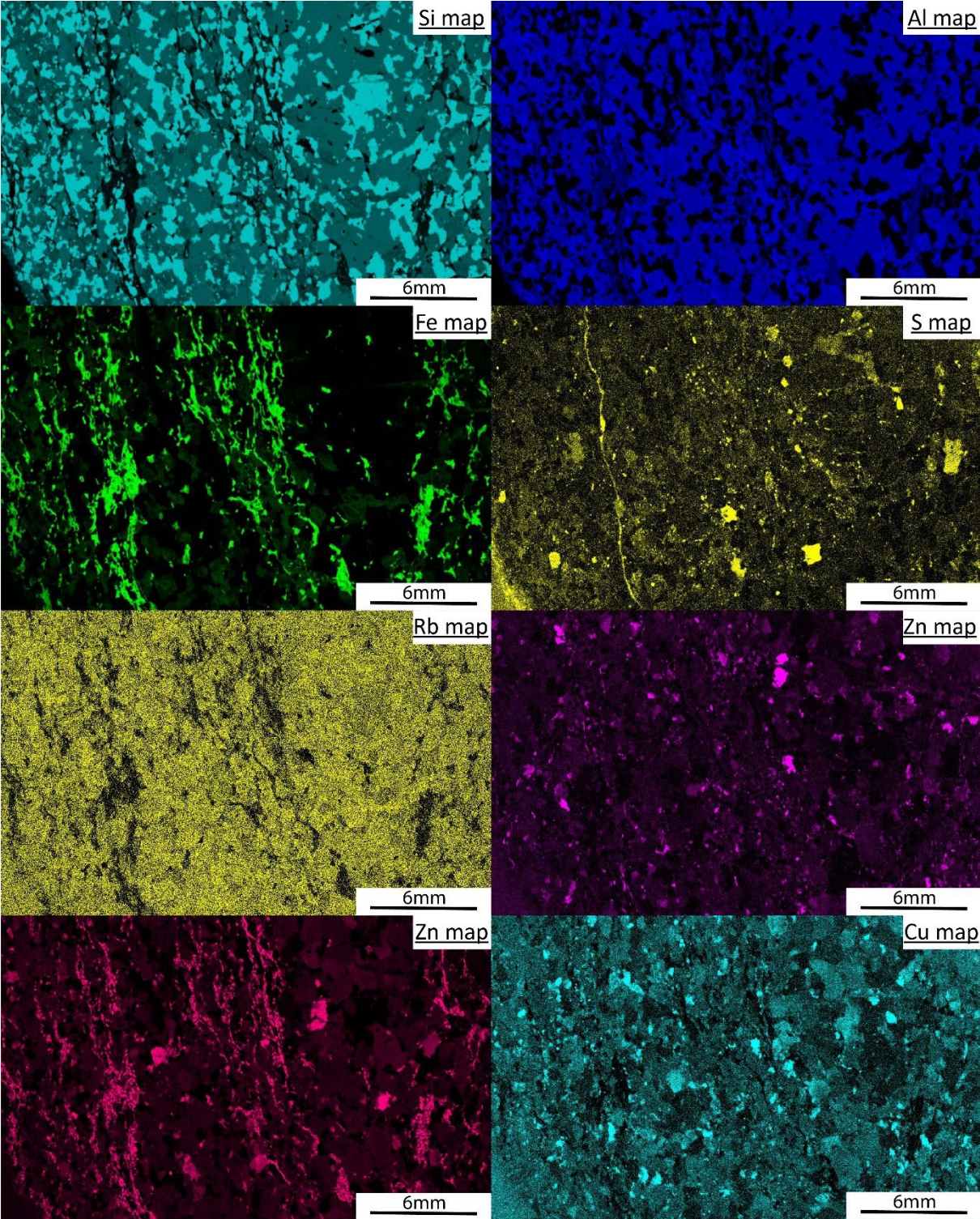


Fig. C.1: μ -XRF element map for the host rock.

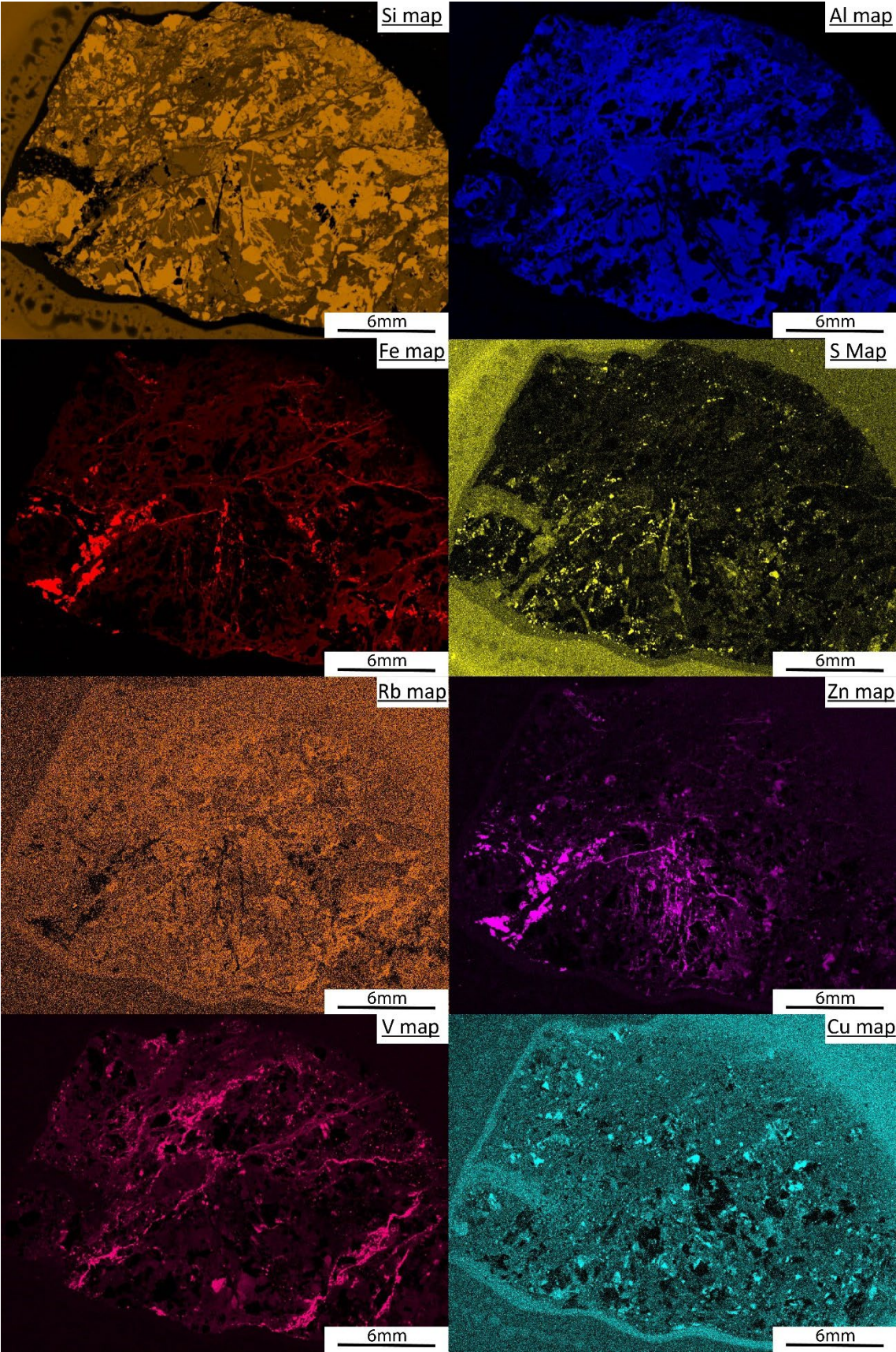


Fig. C.2: μ -XRF element map for the outer damage zone

<i>Sample: CB20-6a</i>					
<i>Spectrum</i>	G position (cm-1)	G-FWHM	R1	R2	T (°C)
1	1581	20	0.22	0.35	485
2	1581	20	0.26	0.37	475
3	1581	19	0.24	0.34	489
4	1581	21	0.49	0.51	414
5	1581	21	0.34	0.44	447
6	1581	22	0.51	0.50	420
7	1581	21	0.46	0.48	428
8	1581	18	0.33	0.45	442
9	1581	19	0.25	0.36	479
10	1581	18	0.43	0.46	437
11	1582	22	0.51	0.43	450
12	1581	20	0.37	0.49	423
13	1582	24	0.63	0.50	420
14	1583	31	0.58	0.44	445
15	1581	21	0.37	0.49	424
16	1581	32	0.38	0.50	420
<i>Average</i>	1581.25	21.81	0.40	0.44	444
<i>1σ</i>	0.56	3.96	0.12	0.06	24.83

Tab. C.1: RSCM data for each spectrum of sample CB20-6a.

<i>Sample: CB20-6b</i>					
<i>Spectrum</i>	G position (cm-1)	G-FWHM	R1	R2	T (°C)
1	1581	11	0.54	0.45	442
2	1580	23	0.59	0.42	455
3	1582	45	0.28	0.37	476
4	1582	27	0.67	0.48	429
5	1581	26	0.19	0.32	498
6	1581	26	0.42	0.47	433
7	1582	19	0.38	0.46	436
8	1581	19	0.28	0.38	470
9	1582	20	0.43	0.48	426
10	1582	19	0.52	0.51	413
11	1581	18	0.31	0.39	468
12	1582	19	0.33	0.42	452
13	1581	18	0.25	0.37	478
<i>Average</i>	1581.36	22.31	0.40	0.43	452
<i>1σ</i>	0.66	7.74	0.14	0.05	23.86

Tab. C.2: RSCM data for each spectrum of sample CB20-6b

<i>Sample: CB20-6a</i>					
<i>Spectrum</i>	G position (cm-1)	G-FWHM	R1	R2	T (°C)
1	1570	31	0.49	0.38	470
2	1583	27	0.96	0.53	404
3	1582	24	0.65	0.51	414
4	1579	56	0.78	0.50	418
5	1579	29	0.91	0.50	419
6	1578	29	0.80	0.51	413
7	1580	29	0.86	0.53	406
8	1580	27	0.72	0.44	444
9	1577	31	0.74	0.52	408
10	1579	27	0.83	0.47	433
11	1580	31	0.89	0.51	414
12	1577	36	0.75	0.42	453
13	1579	27	0.73	0.49	424
14	1579	27	0.78	0.52	409
15	1582	24	0.70	0.49	425
<i>Average</i>	1578.93	30.33	0.77	0.49	424
<i>1σ</i>	2.91	7.45	0.11	0.04	18.32

Tab. C.3: RSCM data for each spectrum of sample MB5c

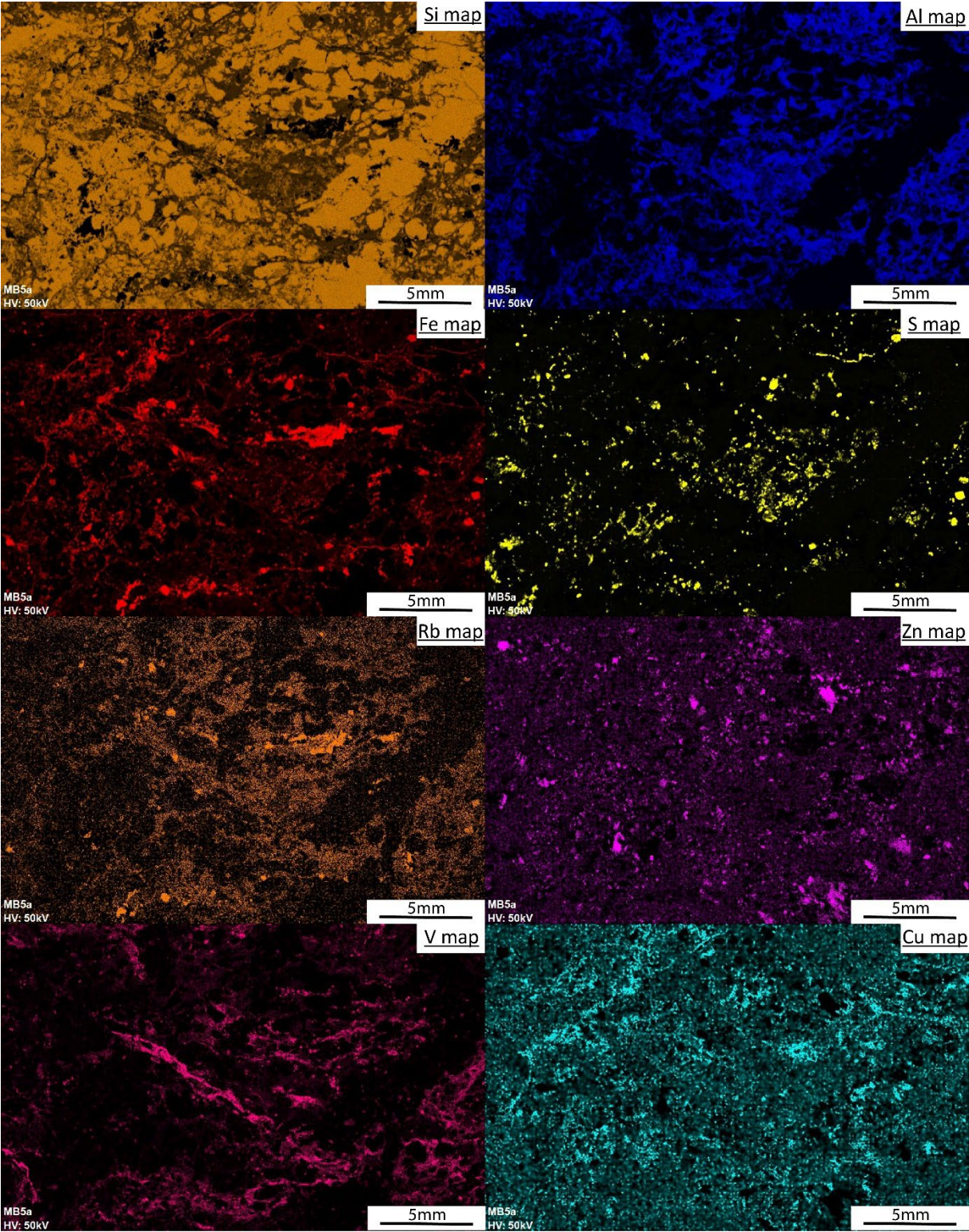


Fig. C.3: μ -XRF element map of the inner damage zone

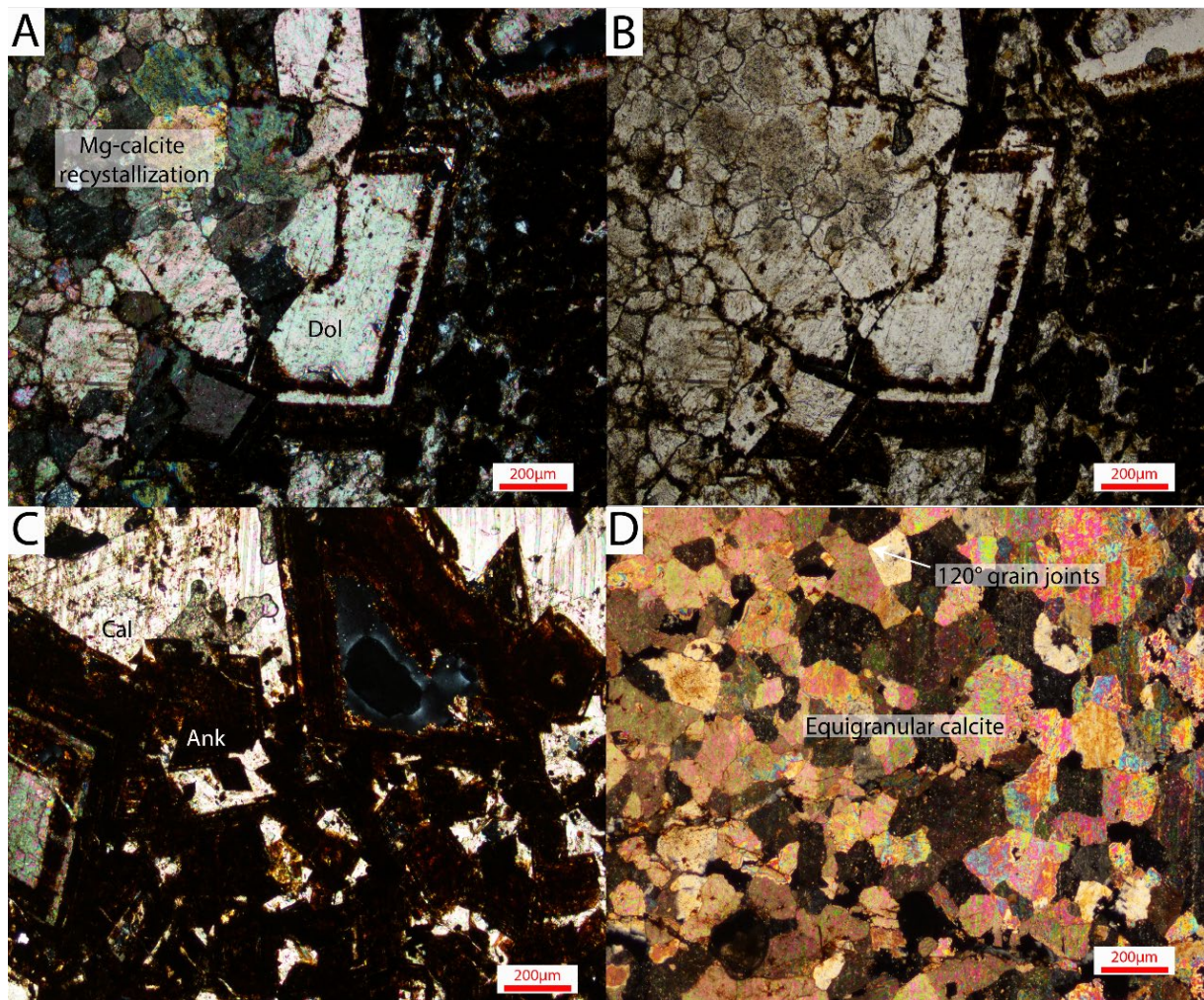


Fig. C.4: A and B- Optical microphotograph (XPL and PPL) from the hydraulic breccia cement showing the progressive replacement of dolomite by Mg-calcite. C- Optical microphotograph (PPL) of the hydraulic breccia cement showing small ankerite rhombs with calcite filling the voids. D- Equigranular recrystallized Mg-calcite (XPL)

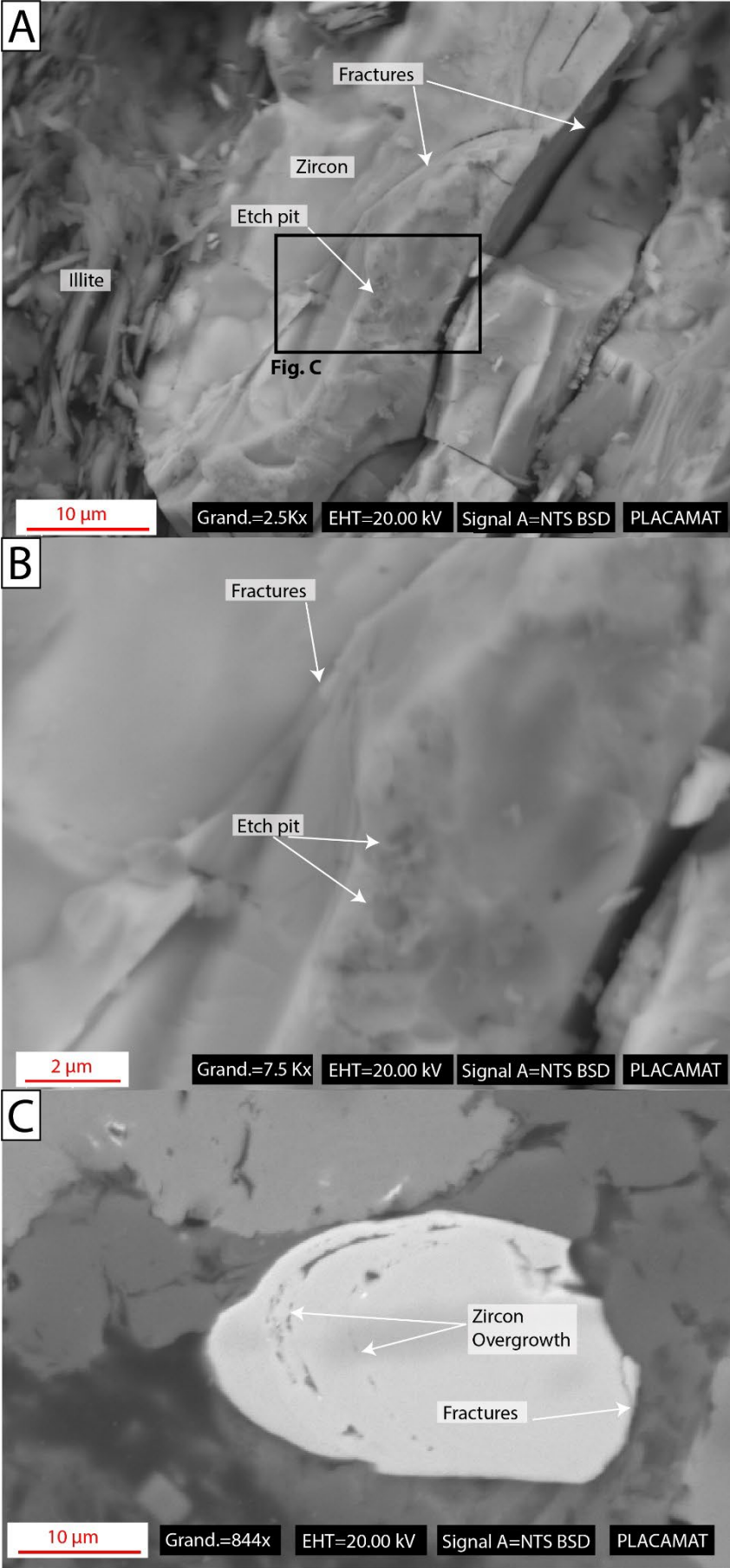


Fig. C.5: A- SEM image (BSE) of a zircon in the gouge affected by fractures. Possible traces of dissolution such as etch pits are visible on the surface of the zircon. B- Focus on the possible trace of dissolution on the zircons. C- Zircon in the cataclasite showing overgrowth truncated on the surface by fractures (polished thin section).

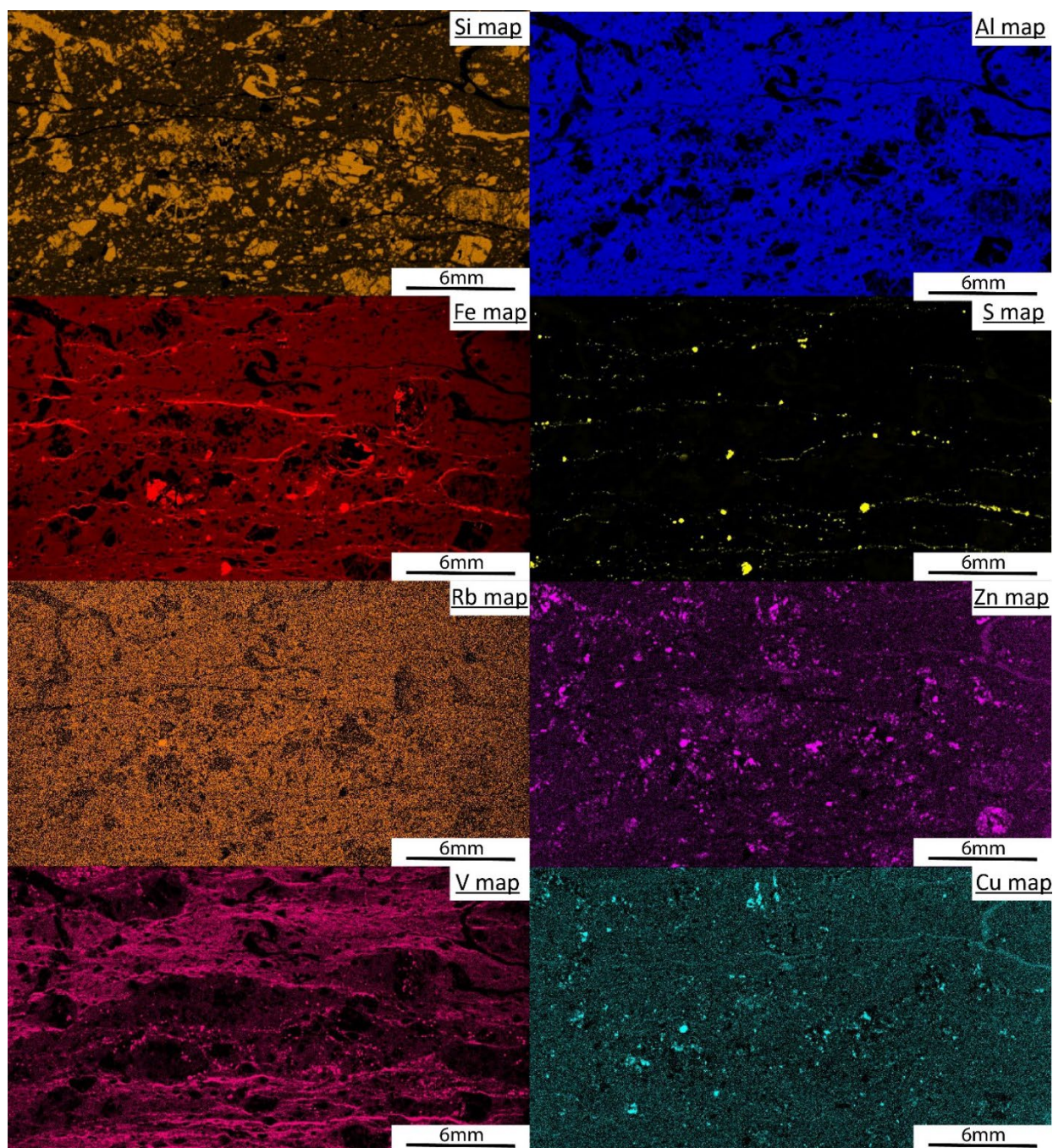


Fig. C.6: μ -XRF element map of the core zone

Supplementary Material Chapter IV

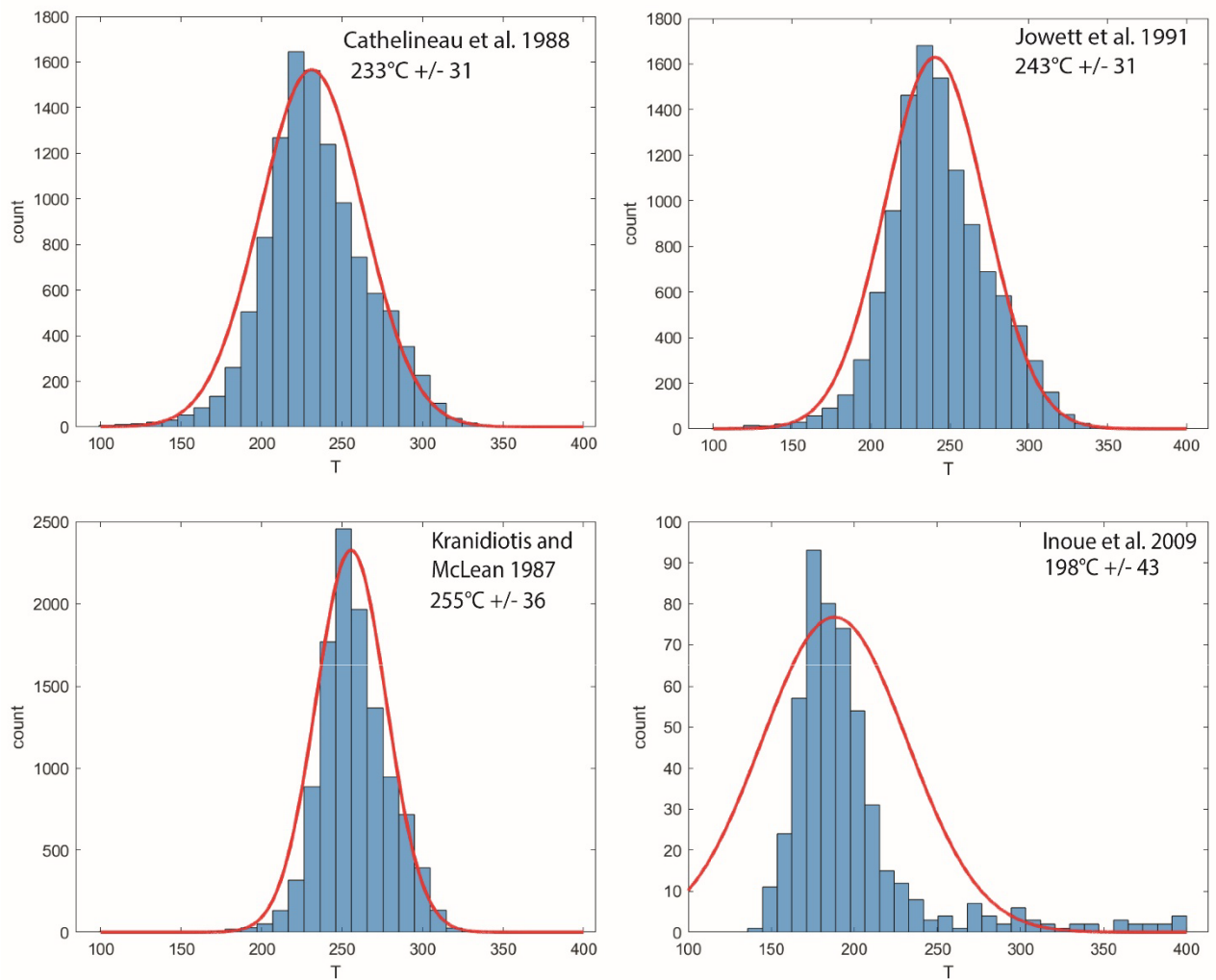
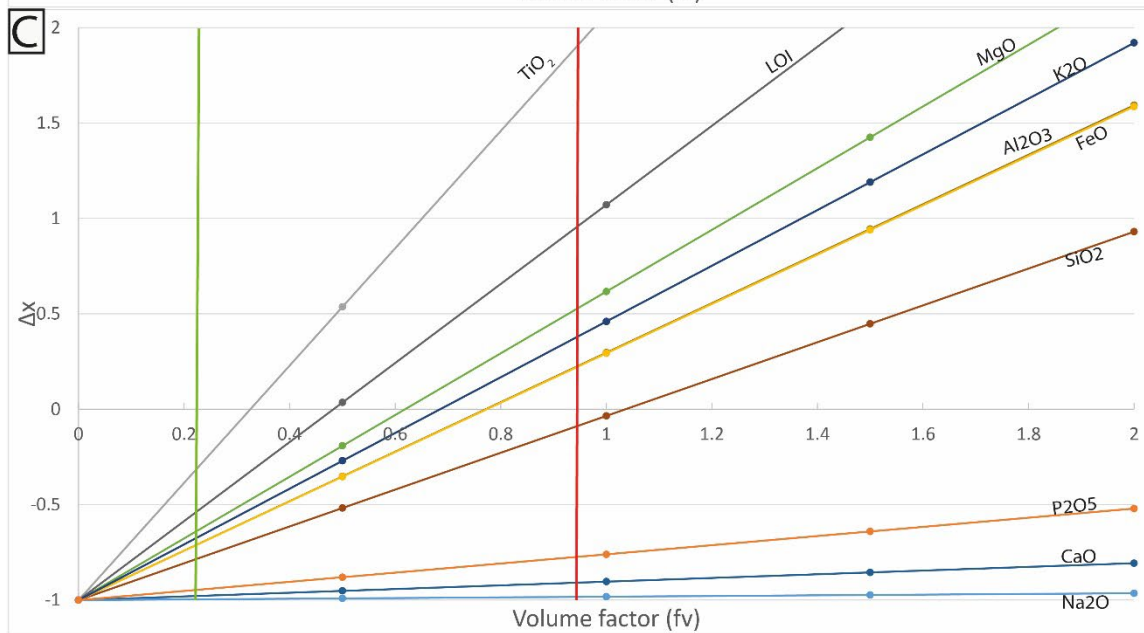
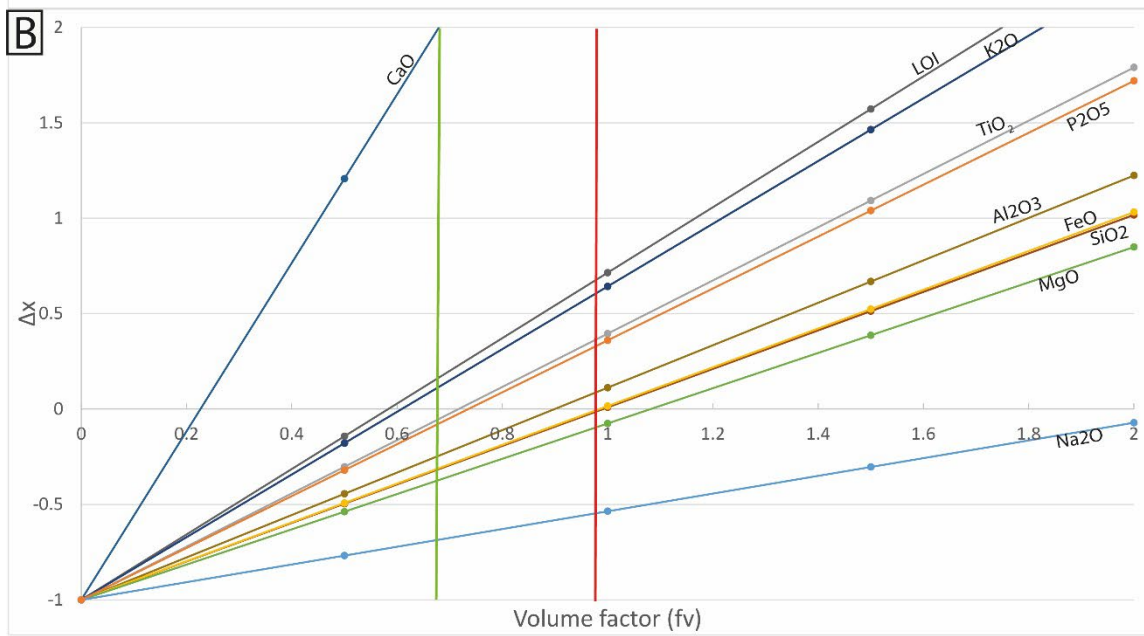
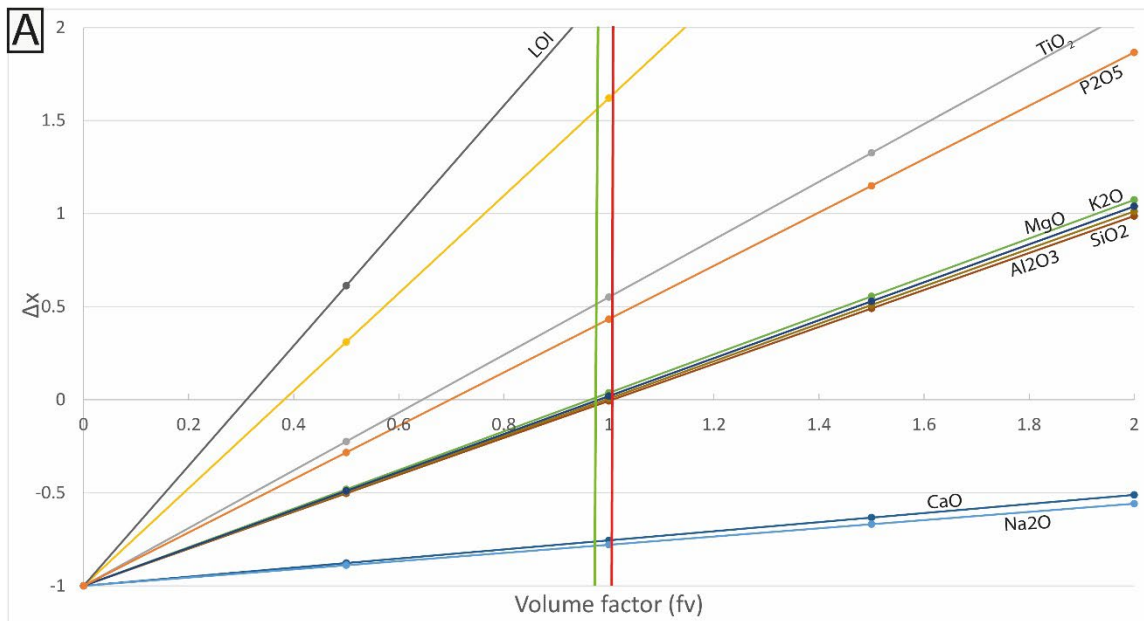


Fig. C.7: Temperature extracted from EPMA maps based on the calibration of Cathelineau (1988), Jowett (1991), Kranidiotis and MacLean (1987) and Inoue et al., (2009).



Supplementary Material Chapter IV

Fig. C.8: Normalized Gresen's plots ((Gresens, 1967b); (Potdevin and Marquer, 1987)) showing volume-composition variations. A- Outer damage zone-host rock plot B- Inner damage zone –host rock plot. C- Core zone-host rock plot.

Quartz Vein in cataclasite									
	Vein type1				Vein type2				
	Th (°C)	Tm (°C)	Salinity (wt%)	Salinity (Raman wt%)	Th (°C)	Tm (°C)	Te (°C)	Salinity (wt%)	Salinity (Raman wt%)
<i>Average</i>	200.4	-5.5	8.4	7.8	173.7	-5.9	-10.7	8.0	5.2
<i>SD (1σ)</i>	30.2	0.0	0.0	1.6	17.7	0.6	22.5	2.7	0.6
<i>Number of analysis</i>	21.0	2.0	2.0	34.0	49.0	19.0	4.0	21.0	10.0
	196.0			7.1	188.5				5.2
	145.0			7.4	152.0				6.6
	187.0			8.7	167.9				4.2
	200.3	-5.5	8.4	6.7	183.5				5.2
	184.0			8.9	150.1				5.1
	198.0			10.9	164.1				5.3
	199.8	-5.5	8.4	7.2	175.4				5.3
	202.0			7.5	161.0				4.8
	207.8			10.1	174.0				4.7
	204.0			8.3	172.0				5.4
	218.0			7.6	185.0				
	235.0			3.9	139.0				
	249.0			9.2					
	209.0			11.4					
	218.0			8.4	156.0				
	270.0			7.1	167.0				
	189.0			6.1	214.0				
	199.0			6.2	177.0				
	135.0			9.5	193.0				
	196.0			7.1	209.0				
	167.0			7.4	216.0				
				8.7	198.0				
				8.4	203.0	-6.0		9.0	
				8.4	177.0				
				8.1	170.0				
				9.6	189.0				
				7.1	169.0				
				5.6	182.0				
				6.1	175.5	-5.5	-21.0	8.4	
				6.4	175.0			0.0	
				6.9	146.0	-5.8		8.7	
				5.1	153.0	-6.0		9.0	
				8.5	172.0				

Supplementary Material Chapter IV

				8.8	150.5	-5.9		8.8	
					153.0	-6.0		9.0	
					147.0	-5.6		8.5	
					170.0	-5.3		8.1	
					152.5	-5.9		8.8	
					173.8	-5.2		8.0	
					180.3				
					167.0	-6.2		9.2	
					182.8	-4.5		7.1	
					183.0			0.0	
					153.0	-6.6		9.7	
					153.2	-5.7		8.6	
					180.0				
					186.0	-5.8		8.7	
					181.6	-6.3		9.3	
					177.0	-6.6	23.0	9.7	
					187.0	-7.4	-22.4	10.5	
					181.0	-6.1	-22.5	9.1	

Tab. C.4: Results of fluid inclusion thermometry and Raman spectrometry on the Qtz veins from the damage zone

Quartz-Hyalophane veins in core zone								
	Primary				Secondary			
	Th (°C)	Tm (°C)	Salinity (wt%)	Salinity (Raman wt%)	Th (°C)	Tm (°C)	Salinity (wt%)	Salinity (Raman wt%)
<i>Average</i>	199.7	-7.1	10.1	9.4	222.7	-7.0	10.1	10.1
<i>SD (1σ)</i>	14.2	1.8	1.8	4.5	6.3	0.4	0.4	1.9
<i>Number of analysis</i>	40.0	11.0	11.0	24.0	17.0	9.0	9.0	21.0
	170.0			22.9	222.0	-7.2	10.3	13.0
	198.0			13.9	224.0			13.8
	208.0			14.3	239.0			9.5
	173.0			8.4	212.0			10.4
	192.0			9.5	233.0			8.9
	212.0			19.1	222.0	-7.2	10.3	9.7
	193.0			10.1	217.0			7.9
	213.0			9.2	218.0	-6.6	9.7	13.8
	198.0			10.6	225.0	-6.7	9.8	9.0
	198.0			5.4	218.0			11.2
	214.0			8.7	224.0	-7.5	10.6	8.3
	209.0			9.1	223.0	-7.6	10.7	10.0
	200.0			7.8	225.0			7.2
	218.0			6.6	224.0	-6.8	9.9	8.4
	205.0	-9.2	12.2	7.9	217.0			8.6

Supplementary Material Chapter IV

	204.0	-10.0	12.8	6.8	218.0	-6.6	9.7	13.0
	187.0			4.4	225.0	-6.7	9.8	9.7
	203.0	-6.2	9.2	5.8				8.9
	204.0			4.6				9.3
	196.0	-7.0	10.1	5.2				10.8
	193.0			6.7				9.8
	212.0	-5.8	8.7	12.3				
	192.0			9.1				
	197.0			8.1				
	183.0							
	191.0							
	199.0							
	206.0	-6.4	9.4					
	204.0	-5.0	7.7					
	202.0	-10.0	12.8					
	168.0	-5.9	8.8					
	206.0							
	244.0							
	181.0							
	182.0							
	200.0							
	197.5	-7.6	10.7					
	210.0							
	221.0							
	204.0	-5.3	8.1					
	170.5							
	212.0							
	207.0							
	193.0	-6.6	9.7					
	198.0	-4.5	7.1					
	201.1	-5.4	8.2					
	213.0	-5.5	8.4					
	204.0	-9.3	12.3					
	206.0	-6.4	9.4					
	199.3							
	209.0							
	195.1	-5.8	8.7					
	171.0	-6.1	9.1					
	203.0	-7.3	10.4					
	207.0							
	208.0	-6.5	9.5					
	202.0							

Tab. C.5: Results of fluid inclusion thermometry and Raman spectrometry on the Qtz-Hy veins from the core zone.

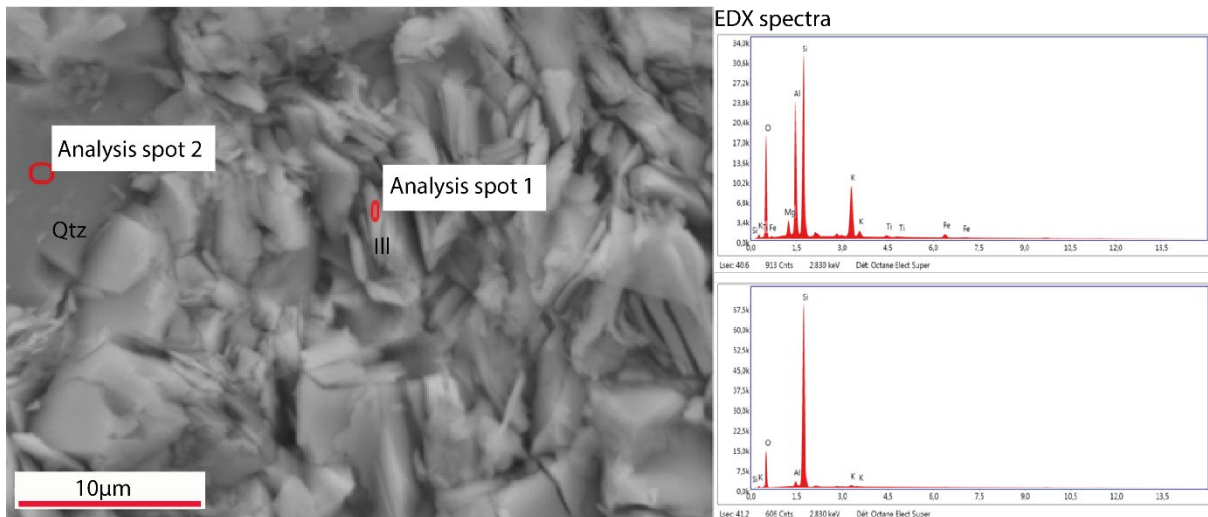


Fig. C.9: Electron scanning microscope image (Secondary electrons) of the gouge matrix. EDS spectra showing the presence of Ti in the illite.

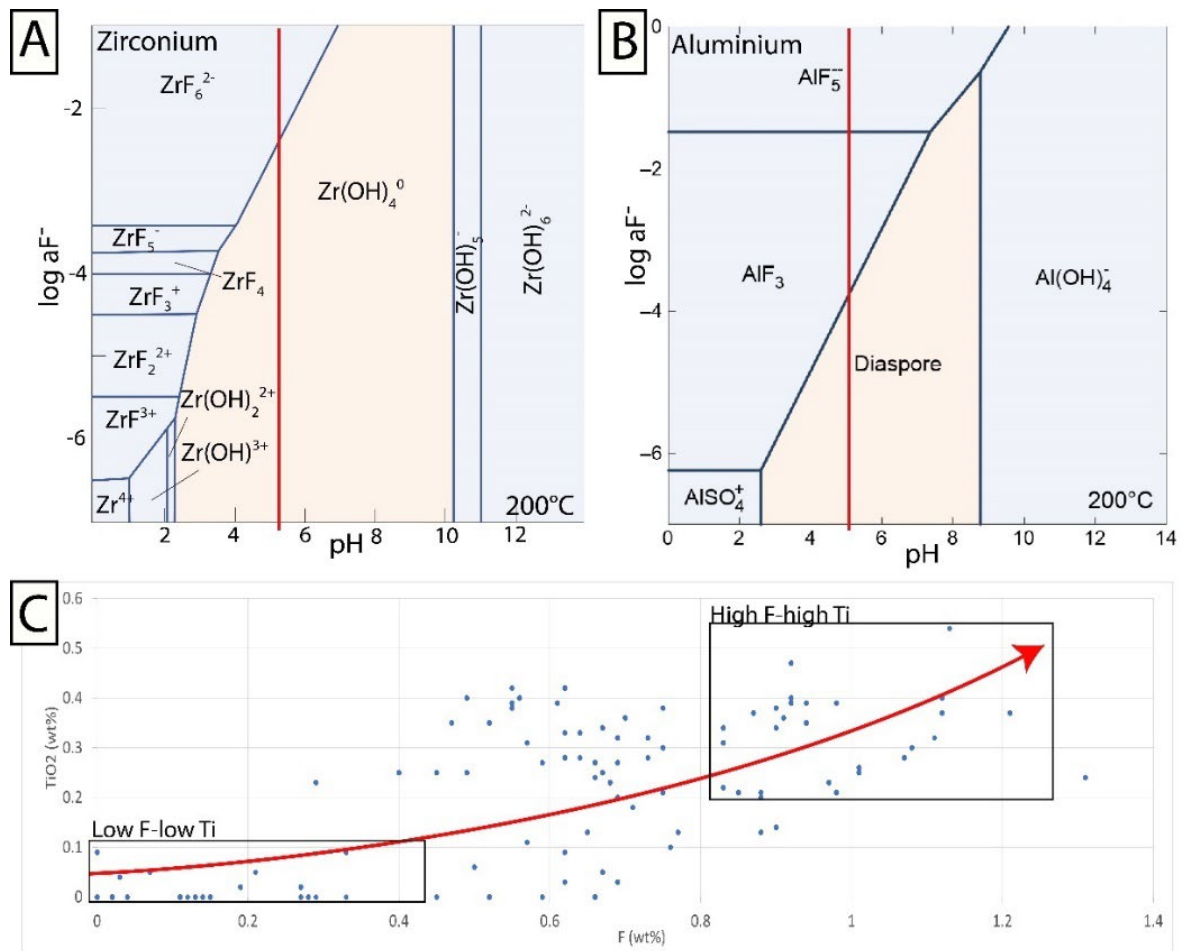


Fig. C.10: A- Speciation of Zr with F at 200°C from (Aja et al., 1995) in pure water. B- Modelling of the speciation of Al with F at 200°C. C- TiO₂-F content in the illite from the core zone.

Appendix D Dating of pre alpine event in the Mont-Blanc massif

Introduction

Different dating methods have been used in the Mont-Blanc massif and more specifically in the Col du Bonhomme area to date deformation events observed in this area. Dating was performed using U-Pb on calcite from the pre-rift cover and the fault breccia and Rb-Sr as well as Ar-Ar on hyalophane from the gouge. The results obtained corresponds to Alpine event or give age corresponding to no clear tectonic event highlighting the difficulty of dating pre-Alpine event in the Mont-Blanc. The results are discussed on the light of petrographical observations which can guide the interpretation of these ages.

1. Method

A total of 6 samples have been used for datations in the Mont-Blanc and 1 in the Pelvoux massif. Only the results of the Ar-Ar datations on hyalophane and U-Pb on calcite from tectonic breccias are presented in the chapter IV. The other results are presented in this appendix.

The method associated to the Ar-Ar and U-Pb datation are presented in the chapter IV. Only the method associated to the Rb-Sr datation of hyalophane is briefly described below.

1.1. List of samples

U-Pb dating (Table D.1) was realized on 4 samples from the Mont-Blanc and one from the Pelvoux massif while Rb-Sr dating and Ar-Ar were performed on 1 sample from the Mont-Blanc gouge (Table D.1).

Sample	Type	Coordinates	Method	Age
CB20-18	Evaporite pseudomorph	45°43'44.3"N 6°42'47.78"E	U-Pb on calcite	106 ± 35 Ma
CB20-17	Evaporite pseudomorph	45°43'44.3"N 6°42'47.78"E	U-Pb on calcite	U < 100 ppb
CB20-35	Calcite cement in tectonic breccia	45°44'11.3"N 6°43'46.6"E	U-Pb on calcite	50 ± 21 Ma
CB20-42	Calcite veins in rolling hinge	45°43'1.75"N 6°43'41.4"E	U-Pb on calcite	U < 100 ppb
Pv1	Calcite veins in cataclasite		U-Pb on calcite	U < 100 ppb
MB5b	Hyalophane veins in gouge	45°43'39.5"N 6°43'40.3"S	Rb-Sr	
MB5b	Hyalophane veins in gouge	45°43'39.5"N 6°43'40.3"S	Ar-Ar on hyalophanes	27.7 ± 1.79 Ma 28 ± 1.99 Ma

Tab. D.1: Location, type, method and ages obtained for samples in the Mont-Blanc massif (Col du Bonhomme) and in the Pelvoux massif

1.2. Rb-Sr on hyalophane

Rb-Sr dating was performed at the university of Gothenburg (Sweden) using an ESI 213 nm NWR laser ablation system connected to an Agilent 8800QQQ ICP-MS. They were realised on a thick section of the hyalophane veins. The separation of ^{87}Rb and ^{87}Sr was done by the reaction of ionized ^{87}Sr from ICP-MS plasma with N_2O forming ^{87}Sr oxides. The calibration of $^{87}\text{Rb}/^{86}\text{Sr}$ and $^{87}\text{Sr}/^{86}\text{Sr}$ was achieved by repeated measures of glass standards and NIST SRM 610 with known ratio. Analyses followed the analytical protocol described in detail by Tillberg et al., (2020).

2. Results

2.1. Calcite dating by U-Pb

2.1.1. Dating of tectonic event in the cover

The pre-rift cover in the Col du Bonhomme area appears strongly deformed at the base where evaporite pseudomorphs were recognized. It corresponds to a foliated limestone with large anhydrite-bearing quartz. At the thin-section scale, the limestones correspond to quartz nodules surrounded by phyllosilicates and bands of recrystallized calcite which appears to be the last event occurring in the limestones (Fig. D.1A). Therefore, dating the calcite might put a lower bound for the age of the shearing highlighted by the phyllosilicate-rich layers.

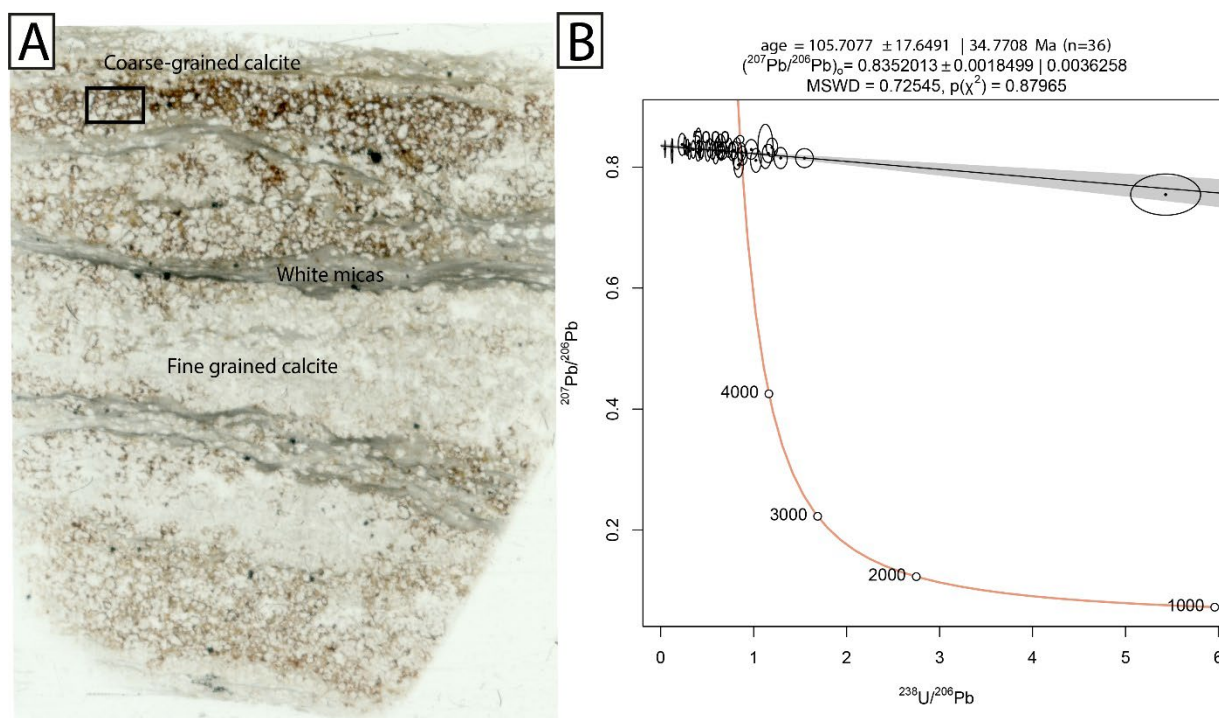


Fig. D.1: A-Microphotograph (PPL) of the recrystallized evaporite composed of white micas levels, fine grained calcite, coarse grained calcite and anhydrite bearing quartz. The dating was performed on the coarse-grained calcite. B- Tera-Wasserburg concordia diagram showing the result of U-Pb dating on the calcite.

Dating of pre alpine event in the Mont-Blanc massif

Two samples were analysed on this purpose. Isotopic mapping allows to define suitable area for dating without impurities in the calcite. However, one of the samples (CB21-17) showed values of U too low for dating. However, the second one gave an age of 106 ± 35 Ma with a MSWD of 0.72 (Fig. D.1B).

Another deformation observed in the pre-rift cover is associated to the folding of the pre-rift cover in response to high-angle normal faults observed in the Col du Bonhomme forming a rolling hinge fold. In the hinge of the folds, calcite-filled fractures were sampled to date this folding event. However, the amount of U was too low to obtain an age.

2.1.2. Dating of tectonic event in the basement

Tectonic breccia along the fault plane in the Col du Bonhomme have been dated using U-Pb on the calcite cement. The results are presented in the chapter IV.

In the Pelvoux massif, large calcite veins are observed in the basement associated to tectonic breccias and cataclasite. These veins are formed by a greyish cement reworking cataclasite clasts and in the centre a whitish cement (Fig. D.3). Locally, the veins are formed by an alternation of calcite and reddish to greenish clays.

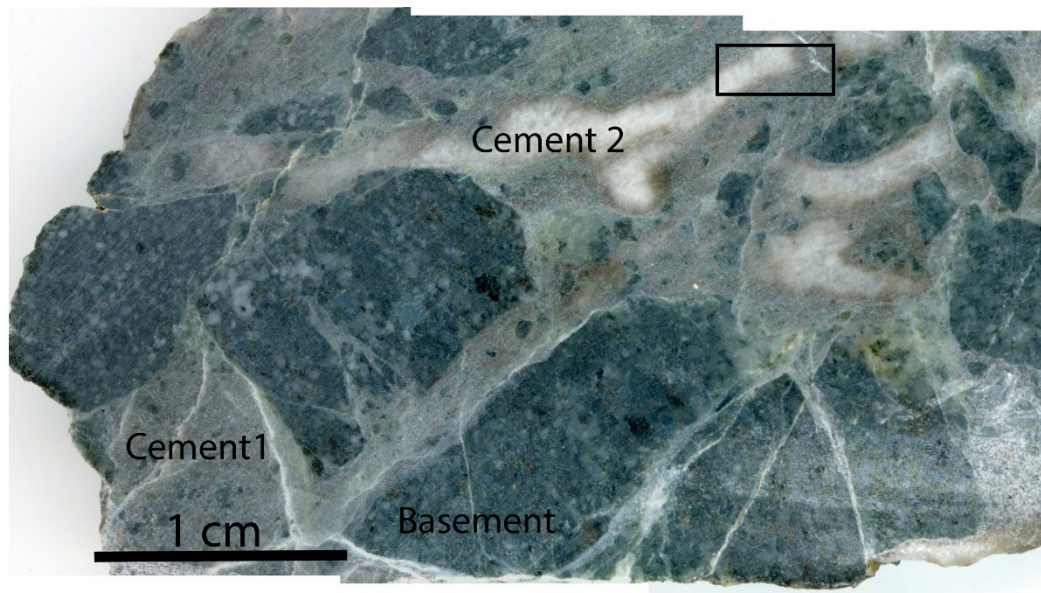


Fig. D.2: Microphotograph (PPL) of the fault breccia in the Pelvoux associated to calcite veins. Two type of cement are visible, a first fine-grained greyish cement and a second type corresponding to white coarse-grained calcite.

The white calcite was analysed but unfortunately, no age was obtained due to the low concentration in U.

2.2. Hyalophane dating

2.2.1. Rb-Sr dating

Hyalophane-Quartz veins are found in the black gouge from the Col du Bonhomme. Rb-Sr dating was realized (Fig. D.4A).

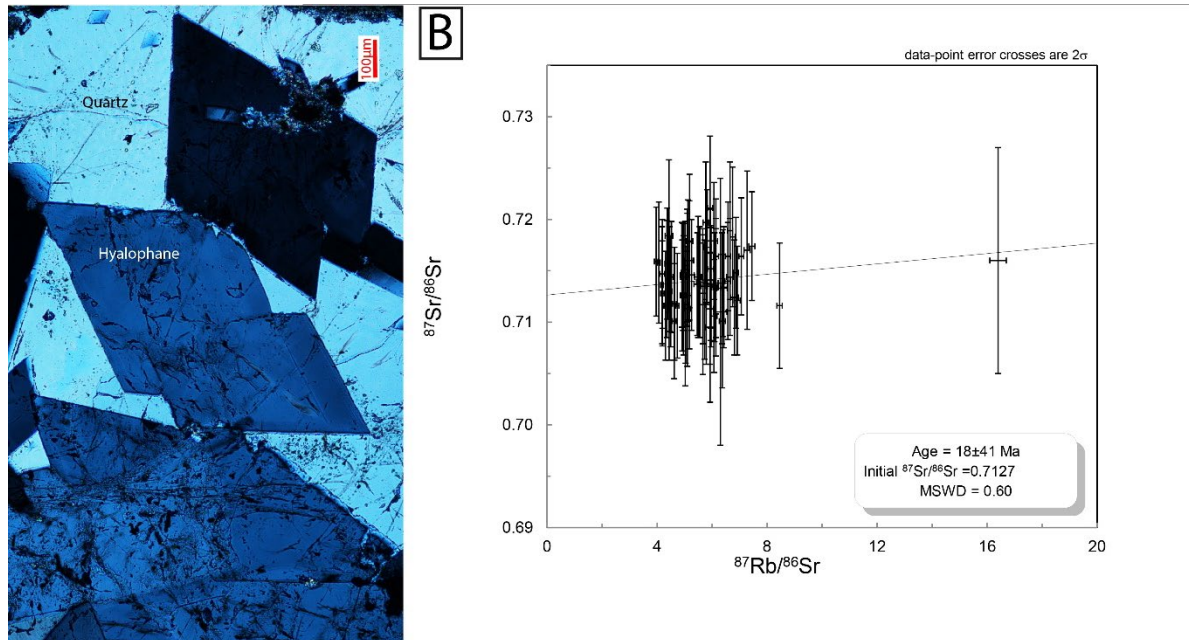


Fig. D.3: A- Hyalophane in hyalophane quartz veins B- Results of Rb-Sr dating on hyalophane. The isochron diagram corresponds to all the spots done on several hyalophane grains.

The analyses were realized by laser ablation on thick sections. A total of 5 crystals were analysed with between 5 to 20 ablation spots on each mineral (Table D.2). The age obtained using all the spots is 18 ± 41 Ma (Fig. D.4B). This extremely high and inconsistent uncertainty is the result of two main problems, (i) the important uncertainty for the Sr ratio, and (ii) the high isotopic homogeneity between the different crystals. This led to the impossibility to have a proper regression.

Dating of pre alpine event in the Mont-Blanc massif

Identifier	Concentration		Data for the Nicolaysen Diagram			
	Sr	Rb	$^{87}\text{Rb}/^{86}\text{Sr}$	2s	$^{87}\text{Sr}/^{86}\text{Sr}$	2s
	ppm	ppm		abs		abs
5C1-Adularia2-1	132	288	6.138	0.095	0.7134	0
5C1-Adularia2-2	103	311	8.456	0.1	0.7116	0
5C1-Adularia2-3	108	281	7.274	0.11	0.717	0
5C1-Adularia2-4	124	255	5.82	0.14	0.7173	0
5C1-Adularia2-5	55	116	5.927	0.093	0.7211	0
5C1-Adularia2-6	118	287	6.81	0.15	0.7124	0
5C1-Adularia2-7	81	192	6.651	0.092	0.7189	0
5C1-Adularia2-8	154	280	5.1	0.12	0.7113	0
5C1-Adularia2-10	88	156	5.026	0.11	0.7117	0
5C1-Adularia2-11	109	172	4.371	0.084	0.7157	0
5C1-Adularia2-12	157	235	4.183	0.052	0.7136	0
5C1-Adularia2-13	137	202	4.063	0.048	0.7158	0
5C1-Adularia2-14	137	291	5.96	0.13	0.7135	0
5C1-Adularia2-15	132	289	6.138	0.096	0.7164	0
5C1-Adularia2-16	127	232	5.12	0.14	0.716	0
5C1-Adularia2-17	92	223	6.742	0.094	0.7183	0
5C1-Adularia2-18	56	87	4.43	0.14	0.7184	0
5C1-Adularia2-19	115	286	6.866	0.085	0.7148	0
5C1-Adularia2-20	139	287	5.731	0.074	0.7122	0
			0.0001	1.5E-06	0.7	0
5C1-Adularia1-1	59	127	5.93	0.16	0.7095	0
5C1-Adularia1-2	69	133	5.18	0.12	0.7179	0
5C1-Adularia1-3	25	146	16.4	0.3	0.716	0
5C1-Adularia1-4	47	94	5.666	0.11	0.7117	0
5C1-Adularia1-5	25	55	6.3	0.24	0.711	0
			0.0001	1.5E-06	0.7127	0
5C1-Adularia5-1	143	258	5.036	0.066	0.7117	0
5C1-Adularia5-3	106	207	5.49	0.12	0.7144	0
5C1-Adularia5-4	146	266	5.093	0.09	0.7155	0
5C1-Adularia5-5	146	257	4.911	0.07	0.7126	0
5C1-Adularia5-6	144	262	5.17	0.16	0.716	0
5C1-Adularia5-7	162	267	4.63	0.072	0.7118	0
5C1-Adularia5-8	148	262	4.969	0.087	0.7144	0
5C1-Adularia5-9	156	258	4.624	0.071	0.7101	0
5C1-Adularia5-10	121	277	6.372	0.11	0.7101	0
			0.0001	1.5E-06	0.7127	0
5C1-Adularia6-1	135	277	5.769	0.1	0.7197	0
5C1-Adularia6-2	142	264	5.175	0.069	0.7126	0
5C1-Adularia6-3	149	243	4.514	0.092	0.7144	0

Dating of pre alpine event in the Mont-Blanc massif

5C1-Adularia6-4	168	253	4.191	0.06	0.7128	0
5C1-Adularia6-5	167	259	4.354	0.057	0.7142	0
5C1-Adularia6-6	164	253	4.305	0.058	0.7116	0
5C1-Adularia6-7	165	263	4.438	0.06	0.7112	0
5C1-Adularia6-8	162	258	4.449	0.058	0.7142	0
5C1-Adularia6-9	156	253	4.526	0.056	0.7144	0
5C1-Adularia6-10	165	246	4.19	0.092	0.7147	0
5C1-Adularia6-11	155	273	4.957	0.1	0.7126	0
5C1-Adularia6-12	156	264	4.736	0.057	0.7116	0
5C1-Adularia6-13	150	280	5.251	0.094	0.7146	0
5C1-Adularia6-14	156	276	5.02	0.14	0.7148	0
5C1-Adularia6-15	146	289	5.55	0.12	0.7139	0
5C1-Adularia6-16	145	292	5.67	0.13	0.7128	0
5C1-Adularia6-17	134	292	6.087	0.099	0.7134	0
5C1-Adularia6-18	122	288	6.581	0.093	0.7164	0
5C1-Adularia6-19	153	270	4.9	0.06	0.7146	0
5C1-Adularia6-20	161	259	4.494	0.051	0.713	0
			0.0001	1.5E-06	0.7127	0
5C1-Adularia3-1	151	276	5.1	0.087	0.7151	0
5C1-Adularia3-2	156	277	4.945	0.091	0.7144	0
5C1-Adularia3-3	143	278	5.46	0.12	0.7137	0
5C1-Adularia3-4	133	283	5.941	0.11	0.7137	0
5C1-Adularia3-5	138	293	5.945	0.11	0.7152	0
5C1-Adularia3-6	130	283	6.067	0.11	0.7106	0
5C1-Adularia3-7	133	280	5.92	0.13	0.7113	0
5C1-Adularia3-8	124	291	6.571	0.11	0.714	0
5C1-Adularia3-9	136	297	6.07	0.13	0.7179	0
5C1-Adularia3-10	125	297	6.65	0.13	0.7144	0
5C1-Adularia3-11	126	290	6.43	0.13	0.7134	0
5C1-Adularia3-12	117	297	7.063	0.09	0.7164	0
5C1-Adularia3-13	117	292	6.911	0.11	0.7121	0
5C1-Adularia3-14	129	293	6.39	0.17	0.7138	0
5C1-Adularia3-15	113	302	7.449	0.11	0.7174	0
5C1-Adularia3-16	134	272	5.661	0.076	0.7135	0
5C1-Adularia3-17	175	250	3.968	0.069	0.7159	0
5C1-Adularia3-18	127	287	6.36	0.19	0.7133	0
5C1-Adularia3-19	129	285	6.136	0.1	0.7138	0
5C1-Adularia3-20	139	288	5.79	0.13	0.7119	0
				0.0001	1.5E-06	1

Tab. D.2: Data from 5 hyalophane analysed giving the composition Rb and Sr and the isotopic ration for dating.

2.2.2. Ar-Ar dating

The result of the Ar-Ar dating on hyalophane are presented in the chapter IV. The table below corresponds to the data associated to the Ar-Ar dating.

Dating of pre alpine event in the Mont-Blanc massif

	36Ar	Error (%)	37Ar	Error (%)	38Ar	Error (%)	39Ar	Error (%)	40Ar	Error (%)	Age (Ma)	Error (Ma)	%40Ar rad	%39Ar
<i>Hyalophane 1</i>														
1	0.6415	0.15	0.193	27.39	0.3518	5.28	7.218	0.21	2846.544	0.01	1064.225	3.308	93.69	1.17
2	0.0606	0.65	0.000	0.07	0.0408	54.12	18.478	0.08	143.422	0.13	28.296	0.088	88.71	2.99
3	0.0113	3.36	0.075	82.63	0.0000	0.00	13.832	0.08	87.479	0.21	23.089	0.104	96.16	2.24
4	0.0269	1.62	0.086	63.69	0.0078	272.57	25.426	0.07	195.249	0.07	27.997	0.055	95.94	4.11
5	0.2071	0.37	0.152	73.21	0.0067	660.90	64.914	0.05	594.558	0.08	33.343	0.064	90.50	10.50
6	0.0206	3.41	0.091	113.82	0.0209	166.90	23.867	0.11	125.612	0.38	19.235	0.150	95.16	3.86
7	0.0230	2.73	0.000	0.09	0.0061	564.22	24.285	0.10	164.902	0.28	24.778	0.148	95.88	3.93
8	0.0369	2.06	0.000	0.10	0.0199	185.82	36.133	0.08	229.641	0.21	23.202	0.103	95.29	5.84
9	0.0207	2.94	0.000	0.10	0.0092	383.70	27.665	0.09	174.665	0.26	23.050	0.129	96.44	4.48
10	0.0386	1.01	0.023	316.29	0.0305	99.78	40.087	0.09	320.285	0.05	29.120	0.059	96.42	6.48
11	0.0335	1.29	0.189	39.60	0.0369	80.53	39.174	0.09	307.317	0.06	28.596	0.061	96.74	6.34
12	0.0156	2.12	0.066	71.77	0.0515	51.61	20.264	0.15	134.148	0.11	24.161	0.091	96.51	3.28
13	0.0344	0.94	0.000	0.06	0.0317	102.00	39.517	0.09	285.627	0.05	26.364	0.053	96.40	6.39
14	0.0262	1.40	0.000	0.07	0.0277	101.99	28.392	0.11	220.816	0.07	28.352	0.075	96.46	4.59
15	0.0506	1.05	0.124	50.05	0.0689	46.98	40.383	0.09	428.125	0.05	38.538	0.075	96.51	6.53
16	0.0384	1.15	0.202	30.62	0.0335	95.27	36.733	0.09	321.108	0.05	31.837	0.066	96.45	5.94
17	0.0259	1.29	0.000	0.06	0.0402	74.45	40.087	0.08	273.183	0.06	24.867	0.050	97.11	6.48
18	0.0175	2.30	0.070	94.15	0.0000	0.00	15.209	0.21	126.703	0.13	30.352	0.146	95.93	2.46
19	0.0172	1.90	0.000	0.07	0.0000	0.00	30.648	0.11	198.396	0.08	23.629	0.061	97.34	4.96
20	0.0123	2.71	0.033	198.66	0.0121	220.17	20.008	0.16	126.307	0.12	23.047	0.092	97.03	3.24
21	0.0234	1.68	0.079	75.51	0.0000	0.00	22.754	0.14	179.195	0.09	28.706	0.093	96.14	3.68
22	0.0104	4.20	0.016	317.89	0.0082	313.82	2.831	1.08	49.320	0.35	62.892	1.401	94.05	0.46
23	0.0047	5.50	0.089	58.45	0.0000	0.00	0.281	10.76	16.017	0.82	197.927	40.473	92.00	0.05
<i>Hyalophane 2</i>														
1	0.5011	0.35	0.189	33.63	0.1299	21.02	2.308	0.90	1214.279	0.05	1315.477	16.909	89.03	0.72
2	0.0294	4.05	0.000	0.06	0.0000	0.00	8.308	0.23	97.194	0.39	42.510	0.378	91.65	2.61
3	0.0221	5.40	0.159	46.51	0.0000	0.00	17.797	0.11	146.369	0.26	29.990	0.167	95.58	5.58
4	0.0184	6.32	0.128	107.55	0.0000	0.00	15.494	0.10	103.173	0.59	24.319	0.290	94.81	4.86
5	0.0179	6.37	0.000	0.13	0.0100	174.60	18.412	0.10	151.927	0.40	30.088	0.245	96.49	5.78
6	0.0343	3.43	0.016	874.31	0.0000	0.00	27.180	0.08	259.589	0.24	34.780	0.171	96.11	8.53
7	0.0233	4.90	0.000	0.13	0.0122	195.20	29.529	0.06	205.443	0.29	25.402	0.152	96.59	9.27
8	0.0193	6.01	0.065	220.82	0.0228	90.41	25.293	0.07	192.850	0.32	27.819	0.179	96.98	7.94
9	0.0194	5.97	0.088	150.21	0.0028	709.25	27.868	0.07	235.706	0.26	30.835	0.164	97.50	8.75

Dating of pre alpine event in the Mont-Blanc massif

10	0.0266	4.32	0.025	509.85	0.0000	0.00	33.853	0.06	290.489	0.21	31.279	0.135	97.24	10.62
11	0.0199	5.70	0.129	108.82	0.0000	0.00	32.300	0.06	220.188	0.27	24.893	0.139	97.24	10.14
12	0.0144	8.09	0.000	0.14	0.0000	0.00	26.538	0.06	163.493	0.37	22.512	0.169	97.30	8.33
13	0.0091	12.60	0.000	0.13	0.0238	80.81	14.193	0.10	97.072	0.62	24.974	0.313	97.15	4.45
14	0.0106	10.65	0.001	13564.60	0.0128	173.98	17.427	0.10	120.134	0.50	25.170	0.256	97.30	5.47
15	0.0092	12.22	0.000	0.13	0.0000	0.00	14.473	0.11	98.401	0.61	24.827	0.307	97.14	4.54
16	0.0035	32.08	0.000	0.14	0.0000	0.00	6.249	0.24	53.146	1.13	31.005	0.711	97.97	1.96
17	0.0002	448.79	0.000	0.13	0.0000	0.00	1.434	1.23	19.334	3.11	48.905	3.226	99.55	0.45

Tab. D.3: Ar Isotopic composition (V) measured for different release steps during heating for the two size fractions

Appendix E List and composition of the samples

1. List of the samples

Sample	Location	Mission	Coordinates	Type	Age	Analysis
Col du Bonhomme (South Mont-Blanc, France)						
1a	South of Col des Fours	2018	45°43'55.12N 6°44'16.39''S	Foliated top basement		
1b	South of Col des Fours	2018	45°43'55.12N 6°44'16.39''S	Top basement + black limestones	Sinemurian?	
1c	South of Col des Fours	2018	45°43'55.12N 6°44'16.39''S	Black limestones	Sinemurian?	RSCM
1d	South of Col des Fours	2018	45°43'55.12N 6°44'16.39''S	Base Grès Singuliers	Pliensbachian	
1e	South of Col des Fours	2018	45°43'55.12N 6°44'16.39''S	Top Grès Singuliers	Pliensbachian	
2a	South of Col des Fours	2018	45°43'53''N 6°44'13''S	Limestones with qtz grains and bioclasts	Lower Sinemurian?	
3a	South of Col des Fours	2018	45°43'53.3''N 6°43'34.3''S	Sandy injection in limestones		
4a	South of Col des Fours	2018	45°43'53.5''N 6°43'25.6''S	Top Grès Singuliers	Pliensbachian	
4b	South of Col des Fours	2018	45°43'53.7''N 6°43'26.3''S	Grès Singuliers	Pliensbachian	μXRF mapping
4c	South of Col des Fours	2018	45°43'54.4''N 6°43'26.1''S	Grès Singuliers - storm deposits	Pliensbachian	
4d	South of Col des Fours	2018	45°43'54.3''N 6°43'26.3''S	Grès Singuliers clinoforms	Pliensbachian	
4e	South of Col des Fours	2018	45°43'54.7''N 6°43'27.3''S	Grès Singuliers -seismite deposits	Pliensbachian	
4f	South of Col des Fours	2018	45°43'54.7''N 6°43'27.3''S	Grès Singuliers -seismite deposits	Pliensbachian	
4g	South of Col des Fours	2018	45°43'54.8''N 6°43'27.8''S	Grès Singuliers cross beds	Pliensbachian	
4h	South of Col des Fours	2018	45°43'55.6''N 6°43'27.3''S	Grès Singuliers	Pliensbachian	
4i	South of Col des Fours	2018	45°43'55.6''N 6°43'27.3''S	Basal conglomerate	Pliensbachian	
5a	South of Tete sud des Fours	2018	45°43'39.5''N 6°43'40.3''S	Cataclasite		Composition EPMA
5b	South of Tete sud des Fours	2018	45°43'39.5''N 6°43'40.3''S	Gouge with qtz-hy veins		Rb-Sr Ar-Ar
5c	South of Tete sud des Fours	2018	45°43'39.5''N 6°42'40.3''S	Gouge		Composition μXRF mapping EPMA mapping RSCM
5c-2	South of Tete sud des Fours	2018	45°43'39.5''N 6°42'40.3''S	Gouge		Composition
5d	South of Tete sud des Fours	2018	45°43'39.5''N 6°42'40.3''S	Triassic quartzite?		
5e	South of Tete sud des Fours	2018	45°43'39.5''N 6°42'40.3''S	Sandy injection in dolostone		
6a	Rocher du bonhomme	2018	45°44'1.45''N 6°42'42''S	Foliated Liassic limestones		
6b	Rocher du bonhomme	2018	45°44'0.8''N 6°42'40.1''S	Black veins in limestones		
8a	Tete Nord des Fours	2018	45°44'12.7''N 6°43'40.6''S	Coarse-grained Grès Singuliers	Pliensbachian	
8b	Tete Nord des Fours	2018	45°44'12.7''N 6°43'40.6''S	Grès Singuliers	Pliensbachian	
8c	Tete Nord des Fours	2018	45°44'12.7''N 6°43'40.6''S	Top Grès Singuliers	Pliensbachian	
9a	Tete Nord des Fours/couloir de Zub	2018	45°44'11.3''N 6°43'46.6''S	Foliated gouge		
9b	Tete Nord des Fours/couloir de Zub	2018	45°44'11.3''N 6°43'46.6''S	Top gouge		

List and composition of the samples

10a	Tete Nord des Fours	2018	45°44'7.1"N 6°43'39.4"S	Grès Singuliers		
10a	Col Tete des Fours	2018	45°43'58.7"N 6°43'25.7"S	Gneiss		
10b	Col Tete des Fours	2018	45°43'58.7"N 6°43'25.7"S	Cataclased gneiss		
10c	Col Tete des Fours	2018	45°43'58.7"N 6°43'25.7"S	Triassic quartzite?		
10d	Col Tete des Fours	2018	45°43'58.7"N 6°43'25.7"S	Triassic quartzite?		
CB20-1	South of Col des Fours	2020	45°43'56.5"N 6°43'15.2"S	Alpine quartz vein		
CB20-2	South of Col des Fours	2020	45°43'56.5"N 6°43'15.2"S			
CB20-3	South of Col des Fours	2020	45°43'56.5"N 6°43'15.2"S	Cataclased gneiss		
CB20-4 a,b,c,d,e	Col des Fours	2020	45°43'55.6"N 6°43'27.3"S	Conglomerate pebbles		
CB20-6 a	Tete Nord des Fours/couloir de Zub	2020	45°44'11.3"N 6°43'46.6"S	Pseudotachylite?		Composition RSCM μXRF mapping
CB20-6 b	Tete Nord des Fours/couloir de Zub	2020	45°44'11.3"N 6°43'46.6"S	Pseudotachylite?		RSCM
CB20-6 c	Tete Nord des Fours/couloir de Zub	2020	45°44'11.3"N 6°43'46.6"S	Pseudotachylite?		
CB20-7	Tete Nord des Fours/couloir de Zub	2020	45°44'11.3"N 6°43'46.6"S	Cataclase		Composition μXRF mapping
CB20-8	Tete Nord des Fours/couloir de Zub	2020	45°44'11.3"N 6°43'46.6"S	Phyllosilicate-rich cataclase		Composition
CB20-9	Tete Nord des Fours/couloir de Zub	2020	45°44'11.3"N 6°43'46.6"S	Magmatic intrusion		Composition
CB20-10	Tete Nord des Fours/couloir de Zub	2020	45°44'11.3"N 6°43'46.6"S	Variscan gneiss		Composition EPMA mapping μXRF mapping
CB20-10B	Tete Nord des Fours/couloir de Zub	2020	45°44'11.3"N 6°43'46.6"S	Variscan gneiss		Composition
CB20-11	Tete Nord des Fours/couloir de Zub	2020	45°44'11.3"N 6°43'46.6"S	Phyllosilicate-rich cataclase		
CB20-12	Tete Nord des Fours/couloir de Zub	2020	45°44'11.3"N 6°43'46.6"S	Cataclased gneiss		
CB20-13	Tete Nord des Fours/couloir de Zub	2020	45°44'11.3"N 6°43'46.6"S	Cataclased gneiss		Composition
CB20-14	Tete Nord des Fours/couloir de Zub	2020	45°44'11.3"N 6°43'46.6"S	Gouge		Composition
CB20-15	Col des Fours	2020	45°44'7.1"N 6°43'39.4"S	Contact basement- sediment		
CB20-16	Col des Fours	2020	45°44'7.1"N 6°43'39.4"S	Tectonic breccia with hydrothermal impregnation		Composition
CB20-17	Rocher du Bonhomme	2020	45°43'44.3"N 6°42'47.78"E	Evaporite pseudomorph		Composition U-Pb Calcite μXRF mapping
CB20-18	Rocher du Bonhomme	2020	45°43'44.3"N 6°42'47.78"E	Evaporite pseudomorph		U-Pb Calcite
CB20-19	Rocher du Bonhomme	2020		Grès Singuliers with calcite cement		
CB20-21	Rocher du Bonhomme	2020		Veins perpendicular to stertching direction in the sediments		
CB20-22	Rocher du Bonhomme	2020	45°43'55.9"N 6°42'41.6"E	Cataclased basement		Composition
CB20-23	Rocher du Bonhomme	2020	45°43'55.9"N 6°42'41.6"E	Cataclased basement		
CB20-24	Rocher du Bonhomme	2020	45°43'55.9"N 6°42'41.6"E	Cataclased basement		Composition
CB20-25	Rocher du Bonhomme	2020	45°43'55.9"N 6°42'41.6"E	Cataclased basement		
CB20-26	Rocher du Bonhomme	2020	45°43'55.9"N 6°42'41.6"E	Cataclased basement		

List and composition of the samples

CB20-27	Rocher du Bonhomme	2020	45°43'55.9"N 6°42'41.6"E	Cataclased basement		Composition
CB20-28	Rocher du Bonhomme	2020	45°43'55.9"N 6°42'41.6"E	Cataclased basement		
CB20-29	Rocher du Bonhomme	2020	45°43'55.9"N 6°42'41.6"E	Cataclased basement		Composition
CB20-30	Rocher du Bonhomme	2020	45°43'55.9"N 6°42'41.6"E	Cataclased basement		Composition
CB20-32	Rocher du Bonhomme	2020	45°43'55.9"N 6°42'41.6"E	Top basement sediment		Composition
CB20-34	Rocher du Bonhomme	2020	45°43'55.9"N 6°42'41.6"E			
CB20-35 a, b	Tete Nord des Fours/couloir de Zub	2020	45°44'11.3"N 6°43'46.6"E	Tectonic breccias		Composition U-Pb Calcite μXRF mapping
CB20-36	Col des Fours	2020	45°43'46.5"N6°43' 55.07"E	Dolostone breccias	Triassic	
CB20-37	Col des Fours	2020	45°43'46.5"N6°43' 55.07"E	Dolostone	Triassic	Composition
CB20-38	Col des Fours	2020		Black limestones	Sinemurian?	
CB20-39	Col des Fours	2020		Black shales	Aalenian	
CB20-40	Col des Fours	2020		Black shales	Aalenian	RSCM
CB20-41	Col des Fours	2020		Black shales	Aalenian	RSCM
CB20-42	Col des Fours	2020	45°43'1.75"N 6°43'41.4"E	Calcite veins in dolostone		U-Pb Calcite
CB20-43	Tete Nord des Fours/couloir de Zub	2020	45°44'11.3"N 6°43'46.6"S	Cataclasite		Composition
CB21-1	Rocher du Bonhomme	2020	45°43'39.5"N 6°42'40.3"S	Gouge		
CB21-2	Rocher du Bonhomme	2020	45°43'39.5"N 6°42'40.3"S	Gouge		Composition
CB21-2B	Rocher du Bonhomme	2020	45°43'39.5"N 6°42'40.3"S	Gouge		Composition
CB21-3	Rocher du Bonhomme	2020	45°43'39.5"N 6°42'40.3"S	Gouge		Composition
CB21-4	Rocher du Bonhomme	2020	45°43'39.5"N 6°42'40.3"S	Cataclasite		Composition
CB21-5	Rocher du Bonhomme	2020	45°43'39.5"N 6°42'40.3"S	Cataclasite		Composition
CB21-6	Rocher du Bonhomme	2020	45°43'39.5"N 6°42'40.3"S	Cataclasite		Composition
CB21-7	Rocher du Bonhomme	2020	45°43'39.5"N 6°42'40.3"S	Basement		
CB21-8	Rocher du Bonhomme	2020		Dolostone + Basement		
CB21-9	Rocher du Bonhomme	2020	45°43'39.6"N6°42' 46"E	Bioclast-rich fractures in basement	Upper Sinemurian	
CB21-10	Rocher du Bonhomme	2020	45°43'39.5"N 6°42'40.3"S	Basement		Composition
CB21-11	Rocher du Bonhomme	2020	45°43'39.5"N 6°42'40.3"S	Cataclasite		
CB21-12	Rocher du Bonhomme	2020	45°43'39.5"N 6°42'40.3"S	Phyllosilicate-rich cataclase		
CB21-13	Rocher du Bonhomme	2020	45°43'39.5"N 6°42'40.3"S	Cataclasite		Composition
CB21-14	Rocher du Bonhomme	2020	45°43'39.5"N 6°42'40.3"S	Cataclasite		
CB21-16	Rocher du Bonhomme	2020	45°43'39.6"N6°42' 46"E	Reddish shales		
CB21-17	Rocher du Bonhomme	2020	45°43'39.5"N 6°42'40.3"S	Cataclasite		Composition
Val Ferret (North Mont-Blanc, Switzerland)						
MB21-1a	Saleinaz	2021	45°49'8"N 7°06'37"E	Top basement siltstones		
MB21-1b	Saleinaz	2021	45°49'8"N 7°06'37"E	Top basement		

List and composition of the samples

MB21-2	Saleinaz	2021	45°49'8"N 7°06'37"E	Rhyolite top basement		Composition
MB20-3	Saleinaz	2021	45°49'8"N 7°06'37"E	Rhyolitic cataclasite		Composition
MB21-5	L'Amône	2021	45°56'31"N 7°05'32"E	Rhyolitic cataclasite		Composition
MB21-6	L'Amône	2021	45°56'31"N 7°05'32"E	Cataclasite		
MB21-7	L'Amône	2021	45°56'31"N 7°05'32"E	Micro granite		
MB21-8	L'Amône	2021	45°56'31"N 7°05'32"E	Contact microgranite		
MB21-9	L'Amône	2021	45°56'31"N 7°05'32"E	Phyllite		
MB21-10	L'Amône	2021	45°56'31"N 7°05'32"E	Phyllite		
MB21-11	L'Amône	2021	45°56'31"N 7°05'32"E	Rhyolitic sandstones		
MB21-12	L'Amône	2021	45°56'31"N 7°05'32"E	Rhyolite		
MB21-13	L'Amône	2021	45°56'31"N 7°05'32"E	Sandy limestone	Lower Aalenian	
19b	L'Amône	2021	45°56'31"N 7°05'32"E	Sandy fossiliferous limestones	Lower Aalenian	
19c	L'Amône	2021	45°56'31"N 7°05'32"E	Sandy limestones	Lower Aalenian	RSCM
19d	L'Amône	2021	45°56'31"N 7°05'32"E	Pelite with basement clasts	Upper Aalenian	
19e	L'Amône	2021	45°56'31"N 7°05'32"E	Encrinite	Upper Aalenian	
19f	L'Amône	2021	45°56'31"N 7°05'32"E	Sandstones above conglomerate	Lower Aalenian	
20a	Combe des Fonds	2021		Cataclasite		
20b	Combe des Fonds	2021		Conglomerate		
20c	Combe des Fonds	2021		Pelite with basement clasts	Aalenian	RSCM
20d	Combe des Fonds	2021		Echinoderm-rich limestone	Bajocian	
20as	Combe des Fonds	2021		Silicified cataclasite		
20ad	Combe des Fonds	2021		Cataclasite		
MB21-14	Col des Planches	2021	46°05'07"N 7°07'25"E	Microgranite		Composition
MB21-15	Col des Planches	2021	46°05'07"N 7°07'25"E	Altered basement		
MB21-16	Col des Planches	2021	46°05'07"N 7°07'25"E	Deformed basement		
MB21-17	Col des Planches	2021	46°05'07"N 7°07'25"E	Gouge		Composition
MB21-18	Col des Planches	2021	46°05'07"N 7°07'25"E	Basement		
MB21-19	Col des Planches	2021	46°05'07"N 7°07'25"E	Gouge		
MB21-20	Col des Planches	2021	46°05'07"N 7°07'25"E	Deformed basement		
MB21-21	Col des Planches	2021	46°05'07"N 7°07'25"E	Deformed basement		Composition
MB21-22	Col des Planches	2021	46°05'07"N 7°07'25"E	Deformed basement		Composition
MB21-23	Col des Planches	2021	46°05'07"N 7°07'25"E	Gouge		
MB21-24	Col des Planches	2021	46°05'07"N 7°07'25"E	Deformed basement		
MB21-25	Col des Planches	2021	46°05'07"N 7°07'25"E	Deformed basement		

List and composition of the samples

MB21-26	Col des Planches	2021	46°05'07"N 7°07'25"E	Deformed basement		
MB21-27	Col des Planches	2021	46°05'07"N 7°07'25"E	Cataclasite		
MB21-28	Col des Planches	2021	46°05'07"N 7°07'25"E	Gouge		
MB21-29	Col des Planches	2021	46°05'07"N 7°07'25"E	Arkose	Triassic	
MB21-30	Col des Planches	2021	46°05'07"N 7°07'25"E	Arkose	Triassic	
MB21-31	Col des Planches	2021	46°05'07"N 7°07'25"E	Dolostone	Triassic	
MB21-32	Col des Planches	2021	46°05'07"N 7°07'25"E	Dolostone	Triassic	
MB21-32	Trappistes mines	2021	46°04'49"N 7°07'34"E	Variscan mylonite		
MB21-34	Trappistes mines	2021	46°04'49"N 7°07'34"E	Variscan mylonite		
MB21-35	Trappistes mines	2021	46°04'49"N 7°07'34"E	Fluorite		
MB21-36	Breya	2021	46°01'24"N 7°05'46"E	Microgranite		Composition
MB21-37	Breya	2021	46°01'24"N 7°05'46"E	Granite		Composition
MB21-38	Breya	2021	46°01'25"N 7°06'08"E	Schlieren		Composition
MB21-39	Breya	2021	46°01'25"N 7°06'08"E	Shear zone		Composition
MB21-40	Breya	2021	46°01'25"N 7°06'08"E	Rhyolite supra contact		Composition
MB21-41	Breya	2021	46°01'0.0"N 7°05'48"E	Granite		
MB21-42	Breya	2021	46°01'0.0"N 7°05'48"E	Cataclase		
MB21-43	Breya	2021	46°01'0.0"N 7°05'48"E	Gouge		
MB21-44	Breya	2021	46°01'0.0"N 7°05'48"E	Tectonic breccias		
MB21-45	Breya	2021	46°01'13"N 7°05'59"E	Rhyolite		Composition
MB21-46	Breya	2021	46°01'13"N 7°05'59"E	Gouge		Composition
<i>Helvetic and Ultrahelvetic domain (Switzerland)</i>						
LM19-1	Lias des Mines	2019	46°17'08"N 7°03'38"E	Gypsum/anhydrite	Trias (Keuper)	
LM19-2	Lias des Mines	2019	46°17'08"N 7°03'38"E	Gypsum	Trias (Keuper)	
LM19-3	Lias des Mines	2019	46°17'08"N 7°03'38"E	Greenish clay	Trias (Keuper)	
LM19-4	Lias des Mines	2019	46°17'10"N 7°02'51"E	Dark shales	Rhetian	RSCM
LM19-5	Lias des Mines	2019	46°17'10"N 7°02'48"E	Indurated marls	Toarcien	
LM19-6	Lias des Mines	2019	46°17'11"N 7°02'43"E	Indurated marls	Pliensbachian	
LM19-7	Lias des Mines	2019	46°17'11"N 7°02'43"E	Indurated marls	Pliensbachian	
LM19-8	Lias des Mines	2019	46°17'11"N 7°02'43"E	Indurated marls	Pliensbachian	
LM19-9	Lias des Mines	2019	46°17'11"N 7°02'43"E	Indurated marls	Pliensbachian	
UH19-1	Ardèves	2019		Black shales	Toarcien sup/Aalenien	
UH19-2	Ardèves	2019		Indurated marls+limestones	Toarcien	
UH19-3	Ardèves	2019		Indurated marls+limestones	Toarcien	
21f	Ardeve	2018		Marls to shales	Toarcien- Aalenian	

List and composition of the samples

21g	Ardeve	2018		Black shales	Aalenian	
UH19-4	Saillon	2019		Laminated limestones	Pliensbachien	
UH19-5	Saillon	2019		Siliceous limestones	Pliensbachien	
UH19-6	Saillon	2019		Marls to shales	Pliensbachien	
21a	Saillon	2018		Sandy limestones	Upper Sinemurian	
21b	Saillon	2018		Limestones	Upper Sinemurian	
21c	Saillon	2018		Limestones	Upper Sinemurian	
21d	Saillon	2018		quartzite		
21e	Saillon	2018		Limestones	Hettangian-Sinemurian	

Tab. E.1: List of the samples with their coordinates

2. Composition of the samples from the Col du Bonhomme

2.1. Composition in major elements

	SiO ₂	Al ₂ O ₃	Fe ₂ O ₃	MnO	MgO	CaO	Na ₂ O	K ₂ O	TiO ₂	P ₂ O ₅	PF	Total
CB20-6	67.83	9.95	8.78	0.015	1.29	0.07	0.30	3.03	0.48	0.21	8.22	100.17
CB20-7	73.70	12.76	2.79	< L.D.	0.82	0.04	0.78	4.97	0.46	< L.D.	2.66	98.97
CB20-8	56.88	17.43	9.83	0.016	1.53	< L.D.	0.60	6.30	0.91	0.30	5.19	98.98
CB20-9	74.66	12.96	0.36	0.069	0.03	0.19	2.17	7.66	0.024	0.23	1.31	99.65
CB20-10	69.97	14.16	3.18	0.043	1.25	0.26	2.11	5.62	0.43	0.19	1.72	98.93
CB20-10B	72.59	13.91	2.83	0.068	1.04	0.31	3.05	4.72	0.36	0.19	1.55	100.61
CB20-13	71.46	13.54	1.98	< L.D.	1.11	0.09	0.15	8.46	0.40	0	1.95	99.14
CB20-14	68.94	14.16	3.59	< L.D.	1.60	0.06	0.12	6.97	0.50	0	3.40	99.33
CB20-16	85.39	5.71	2.54	< L.D.	0.17	< L.D.	0.05	3.32	0.039	0	1.80	99.02
CB20-17	17.75	6.56	3.90	0.79	10.74	22.42	0.05	3.20	0.30	0	31.19	96.89
CB20-22	70.66	14.54	2.71	0.044	1.14	0.14	2.98	4.64	0.48	0	2.05	99.37
CB20-24	61.35	18.95	2.46	0.031	1.17	0.22	1.97	10.14	0.57	0.20	1.82	98.85
CB20-27	57.91	18.81	2.32	0.10	1.17	2.09	2.29	9.96	0.62	0.36	3.37	99.00
CB20-29	59.08	19.55	1.93	0.11	0.71	0.88	2.08	11.37	0.58	0.36	2.22	98.88
CB20-30	64.55	14.93	1.26	0.097	1.46	2.86	2.70	5.83	0.41	0.53	4.51	99.13
CB20-32	12.71	4.15	2.14	0.26	1.15	42.24	0.14	1.75	0.15	0	34.59	99.29
CB20-35	50.75	9.75	1.52	0.23	5.73	9.93	0.51	5.20	0.36	0.15	14.72	98.85
CB20-37	18.19	1.29	1.16	0.20	16.40	24.14	0.04	0.55	0.031	0	37.52	99.52
CB20-43	66.76	14.57	2.42	0.053	1.61	1.71	1.35	5.73	0.83	0.19	3.82	99.04
CB21-2	62.03	17.23	2.06	0	1.05	< L.D.	0.16	7.68	0.43	0	3.42	94.06
CB21-2B	65.54	18.40	1.72	0	1.98	0.06	0.27	6.58	0.90	0	4.43	99.88
CB21-3	64.78	16.71	2.49	0	1.90	< L.D.	0.06	6.49	1.02	0	6.41	99.85
CB21-5	60.41	18.68	6.49	0.055	2.59	0.29	1.62	4.93	0.66	0.21	3.96	99.89
CB21-6	64.43	16.45	5.46	0.033	2.06	< L.D.	1.36	5.04	0.59	0	4.19	99.61
CB21-10	67.01	14.96	0.79	0.12	1.44	2.10	2.80	5.90	0.078	0.11	4.56	99.87
CB21-13	74.08	13.39	1.57	0.030	0.39	0.23	2.08	5.04	0.34	0.17	2.00	99.33
CB21-17	60.81	17.49	6.38	0.049	2.94	0.28	0.96	5.19	0.93	0.21	4.03	99.28
MB5C	62.55	19.52	1.88	0	2.16	< L.D.	0.06	7.37	1.17	0	4.33	99.03
MB5C-2	56.22	18.84	5.54	0	2.37	0.07	0.05	7.74	1.80	0.22	6.76	99.61
MB5A	80.56	7.51	5.17	0.029	0.81	0.11	0.03	2.89	0.34	0.15	2.88	100.47

Tab. E.2: Composition in major elements of the samples from the col du Bonhomme area

2.2. Composition in trace elements

List and composition of the samples

	F	Be	Sc	V	Cr	Co	Ni	Cu	Zn	Ga	Ge	As	Rb	Sr	Y	Zr	Nb	Mo	Cd	In	Sn	Sb	Cs	Ba	Hf	Ta	W	Pb	Bi	Th	U
CB20-6		3.23	11.00	536	99.6	5.33	29.8	28.6	135	16.7	1.23	449	157	11.1	12.1	107	6.86	55.5	0.09	0.09	13.4	21.4	10.2	540	2.67	0.60	6.37	234	4.12	7.31	5.76
CB20-7		3.44	10.51	47.8	42.7	1.95	16.1	34.2	361	34.2	1.90	108	223	24.0	7.16	192	12.8	0.72	0.42	1.46	8.57	10.3	10.9	790	4.97	1.11	8.37	75.6	0.62	3.43	3.08
CB20-8		5.43	20.24	145	131	1.02	9.1	12.6	103	31.9	1.70	151	362	22.1	33.5	130	15.1	1.49	0.07	0.07	4.42	17.4	29.7	771	3.61	1.32	8.10	42.7	1.88	15.8	5.18
CB20-9		0.48	1.05	<L.D.	40.9	6.14	28.5	4.8	252	10.3	1.48	13.8	169	95.2	4.33	2.94	1.25	0.55	0.90	<L.D.	8.05	1.18	5.08	545	0.12	0.34	<L.D.	34.7	0.17	0.14	3.95
CB20-10		2.77	8.50	39.1	53.1	6.12	23.6	10.7	85.9	18.8	1.27	11.1	203	94.1	25.1	159	11.2	<L.D.	0.21	0.06	6.69	2.23	10.3	1169	4.68	1.80	3.56	26.8	0.32	11.1	4.09
CB20-13		4.27	4.32	38.7	53.6	8.09	23.2	32.3	<L.D.	18.2	1.64	50.6	247	19.9	8.81	332	7.14	2.23	0.04	<L.D.	2.99	9.83	10.7	871	8.32	0.69	6.54	17.8	0.80	10.8	3.03
CB20-14		6.26	8.24	79.2	68.6	6.66	24.9	41.5	12.2	22.4	1.93	50.0	295	23.0	12.0	219	9.45	1.65	0.04	0.03	14.7	12.2	29.3	777	6.06	1.84	8.04	12.7	0.53	10.4	3.90
CB20-16		0.57	<L.D.	6.0	15.3	0.26	5.3	2.2	7.0	4.13	1.23	42.6	108	18.5	3.38	45.5	0.72	<L.D.	<L.D.	<L.D.	1.11	21.1	1.95	5421	1.30	0.08	1.01	13.1	<L.D.	1.80	0.40
CB20-22		1.92	8.83	32.6	38.3	4.35	15.6	7.3	49.2	19.8	1.47	15.8	205	68.3	12.5	117	18.2	0.59	0.05	0.04	6.83	2.14	12.0	790	3.41	1.33	1.80	13.0	0.11	7.84	2.98
CB20-24		1.97	7.36	39.7	52.0	5.02	18.3	6.4	31.5	23.6	1.87	7.34	342	103	25.9	216	17.8	0.69	0.04	0.04	3.75	2.73	15.8	1641	6.26	1.19	1.38	29.5	0.23	27.6	4.00
CB20-27		1.92	6.65	42.2	44.3	4.34	13.7	11.6	20.1	24.0	1.75	3.91	356	94.5	22.3	226	20.1	<L.D.	0.09	0.06	3.87	3.04	17.6	1696	6.60	1.63	1.44	23.4	0.15	29.4	4.01
CB20-29		2.24	7.23	44.3	99.6	5.17	37.4	17.9	15.5	24.6	1.66	9.03	387	101	18.1	223	16.6	0.64	0.07	0.06	3.78	9.04	14.4	1635	6.38	1.53	1.98	27.1	0.18	22.5	2.33
CB20-30		3.10	5.96	70.9	164	4.46	58.4	4.8	10.3	22.7	1.60	8.25	258	66.7	22.1	170	15.1	1.04	0.11	0.04	7.98	6.69	18.0	664	4.92	1.93	3.15	21.4	0.38	19.7	2.53
CB20-32		2.89	4.41	28.1	27.6	3.81	14.4	9.5	16.9	5.73	0.61	14.9	101	47.0	9.82	23.6	2.92	0.55	0.04	<L.D.	0.81	2.82	11.9	202	0.64	0.27	0.98	8.03	0.09	2.59	1.45
CB20-35		2.03	7.98	50.9	67.3	3.44	14.5	6.6	12.7	14.5	1.44	7.92	171	82.1	20.8	80.2	6.03	<L.D.	0.04	0.04	2.88	4.84	12.3	639	2.23	0.57	3.38	10.6	0.29	4.28	1.58
CB20-43		3.48	15.23	105	95.3	5.19	19.4	9.1	19.7	29.1	1.86	20.2	295	25.2	19.1	233	14.0	<L.D.	0.05	0.04	6.59	11.2	30.9	779	5.97	1.33	16.1	5.38	0.37	11.0	2.22
CB21-2	2 350	5.48	6.25	76.8	49.8	5.53	25.0	44.2	82.5	23.9	1.54	33.1	273	66.3	6.03	116	6.41	1.97	0.08	<L.D.	6.31	7.83	15.2	43915	3.22	0.64	8.89	6.13	0.22	6.94	5.71
CB21-2B	4 080	9.16	17.19	123	89.8	1.21	10.5	12.0	31.1	12.0	1.82	28.9	346	14.7	11.7	257	12.2	<L.D.	0.07	<L.D.	19.1	10.9	24.4	4522	7.18	1.35	6.98	11.7	0.50	13.2	2.28
CB21-3	3 530	8.19	18.51	153	101	1.57	25.4	16.3	37.6	16.3	2.07	29.5	323	24.5	16.9	270	14.1	1.01	0.06	<L.D.	11.0	10.7	19.8	4600	7.43	1.33	12.2	13.2	0.44	14.7	3.22
CB21-5	1 370	3.05	15.64	105	83.5	11.3	35.4	81.8	81.9	81.8	1.73	36.6	259	64.8	23.6	130	8.59	1.18	0.09	0.06	4.97	4.47	18.4	1938	3.79	0.99	1.96	17.9	0.27	11.4	2.53
CB21-6	1 370	3.76	14.38	115	84.7	2.21	15.4	37.6	46.3	37.6	1.35	23.5	259	60.1	10.4	118	8.25	4.62	<L.D.	<L.D.	4.64	5.34	23.8	1163	3.41	0.99	2.49	21.3	0.40	7.76	2.39
CB21-10	1 520	3.89	3.07	14.5	28.3	1.58	4.6	6.5	8.1	6.5	1.34	3.74	219	45.1	12.3	24.2	2.99	<L.D.	<L.D.	5.85	2.31	12.0	2240	0.89	0.61	0.80	16.4	0.73	1.88	1.46	
CB21-13	725	2.32	2.32	15.8	18.8	4.34	9.9	9.0	26.6	9.0	1.78	89.0	226	66.0	8.16	114	9.19	<L.D.	0.10	0.04	6.15	9.32	8.58	914	3.33	1.21	3.18	9.96	0.15	14.7	3.84
CB21-17	1 480	3.75	20.05	138	98.5	12.5	37.6	20.9	107	20.9	1.77	29.8	293	38.3	19.6	199	13.4	1.63	0.09	0.05	6.88	3.72	18.2	2916	5.33	1.41	3.65	12.9	0.37	12.1	3.10
MB5C	4 090	10.5	21.31	205	123	1.65	24.6	9.8	36.5	9.8	2.18	19.0	384	17.7	10.4	305	16.3	1.03	0.06	<L.D.	13.6	8.13	24.5	5488	8.50	1.63	14.2	7.39	0.41	13.0	3.96
MB5c	4182.00	10.81	18.05	245	189.6	4.77	20.2	8.8	132.5	35.9	2.35	81.7	386	257.1	11.1	534	32.5	3.497	0.31	0.05	14.26	18.5	30.9	7408	13.71	2.87	23.6	17.9	0.83	26.3	5.10
MB5a	1516.00	3.44	8.71	58	39.6	3.94	18.8	54.2	55.9	14.0	2.27	28.3	155	15.8	35.2	121	4.9	8.329	0.10	0.05	4.74	17.8	8.4	2206	3.14	0.64	5.1	5.11	0.13	8.0	2.95
CB20-10	390.00	2.28	7.43	31	28.6	5.21	16.5	21.4	111.0	17.6	1.21	15.8	163	119.8	27.0	137	10.0	<L.D.	0.35	0.06	6.56	2.2	8.7	1034	3.98	1.61	3.1	38.5	0.32	10.4	3.19
CB20-17		5.13	7.68	46	47.4	4.57	16.2	12.6	13.4	9.5	1.49	9.35	165	239.5	15.2	48	5.9	3.281	0.04	0.03	1.58	6.4	9.8	4946	1.35	0.52	2.4	48.1	0.07	5.3	1.95
CB20-37		1.03	1.96	15	6.7	1.10	4.2	2.7	22.5	1.7	0.43	0.56	35.0	125.1	4.7	6	0.5	<L.D.	0.10	<L.D.	<L.D.	0.7	1.9	94	0.17	0.05	<L.D.	2.69	<L.D.	0.6	3.95

Tab. E.3: Composition in trace elements of the samples from the col du Bonhomme area

2.3. Composition in Rare Earth Elements (REE)

	La	Ce	Pr	Nd	Sm	Eu	Gd	Tb	Dy	Ho	Er	Tm	Yb	Lu
CB20-6	20.3	43.6	5.29	17.9	2.88	0.798	1.91	0.280	1.87	0.426	1.30	0.221	1.55	0.253
CB20-7	13.7	28.6	3.34	11.5	2.03	0.552	1.37	0.196	1.20	0.255	0.758	0.127	0.942	0.153
CB20-8	37.5	79.4	9.16	32.8	6.23	0.863	5.02	0.812	5.30	1.15	3.21	0.467	2.81	0.419
CB20-9	1.46	3.31	0.360	1.52	0.556	0.558	0.655	0.119	0.747	0.150	0.412	0.0680	0.498	0.077
CB20-10	27.2	54.8	6.67	24.9	5.24	0.968	4.53	0.724	4.44	0.914	2.51	0.375	2.41	0.359
CB20-10B	26.6	52.3	6.24	23.6	5.08	1.09	4.61	0.765	4.80	1.01	2.80	0.418	2.69	0.409
CB20-13	23.2	46.1	5.41	19.2	3.26	0.414	2.25	0.302	1.66	0.326	0.906	0.145	1.03	0.171
CB20-14	16.9	33.2	4.08	15.0	2.92	0.462	2.27	0.342	2.11	0.443	1.26	0.207	1.41	0.226
CB20-16	7.18	12.3	1.43	4.87	0.825	0.267	0.610	0.088	0.551	0.118	0.328	0.0509	0.321	0.048
CB20-17	13.4	29.1	3.51	13.7	2.88	0.755	2.54	0.415	2.56	0.530	1.39	0.188	1.30	0.191
CB20-22	18.8	39.6	4.90	18.5	3.63	0.652	2.89	0.426	2.41	0.451	1.13	0.156	0.970	0.142
CB20-24	41.5	97.8	12.0	46.1	10.2	1.04	7.50	0.992	5.14	0.907	2.26	0.302	1.85	0.264
CB20-27	42.1	102	12.5	48.5	10.8	1.02	7.82	1.00	4.99	0.837	2.04	0.286	1.76	0.247
CB20-29	31.5	75.9	9.26	36.5	8.41	0.928	6.39	0.821	4.00	0.670	1.60	0.222	1.37	0.202
CB20-30	27.1	64.3	8.24	33.1	7.93	0.727	6.11	0.847	4.47	0.792	2.03	0.307	1.90	0.268
CB20-32	11.5	24.3	3.07	11.9	2.49	0.595	2.04	0.310	1.84	0.354	0.925	0.135	0.863	0.123
CB20-35	16.8	35.8	4.26	16.3	3.52	0.871	3.30	0.561	3.63	0.753	2.03	0.307	1.97	0.288
CB20-37	5.27	10.3	1.27	5.04	1.10	0.275	0.932	0.147	0.879	0.170	0.434	0.0626	0.377	0.055
CB20-43	25.3	51.6	5.99	21.4	3.97	0.845	3.23	0.526	3.44	0.749	2.12	0.342	2.32	0.349
CB21-2	16.6	32.5	3.04	11.2	2.17	1.07	1.70	0.242	1.44	0.288	0.833	0.143	1.11	0.169
CB21-2B	36.3	71.9	7.56	27.2	4.54	0.884	3.16	0.425	2.36	0.481	1.37	0.219	1.54	0.238
CB21-3	50.2	104	10.7	39.9	6.75	1.04	4.66	0.614	3.43	0.687	1.87	0.293	1.91	0.292
CB21-5	39.0	81.3	8.42	31.9	6.18	0.943	5.00	0.759	4.55	0.937	2.59	0.385	2.46	0.367
CB21-6	18.2	36.2	3.60	13.3	2.44	0.534	1.96	0.299	1.81	0.389	1.13	0.187	1.27	0.203
CB21-10	8.96	18.4	0.975	3.81	1.01	0.355	1.22	0.249	1.79	0.400	1.18	0.198	1.37	0.203
CB21-13	27.3	60.0	6.01	22.8	4.86	0.577	3.40	0.416	1.94	0.323	0.780	0.106	0.673	0.098
CB21-17	22.0	44.2	5.19	20.2	3.95	1.11	3.46	0.549	3.41	0.739	2.02	0.307	1.97	0.292
MB5C	46.7	94.1	10.6	38.2	6.44	1.07	4.10	0.509	2.59	0.487	1.32	0.217	1.58	0.246
MB5C-2	45.0	89.2	10.1	35.7	5.77	1.23	3.55	0.440	2.36	0.478	1.39	0.235	1.75	0.289
MB5A	21.5	42.1	4.98	18.7	3.71	1.20	3.76	0.713	5.14	1.17	3.26	0.469	2.75	0.389

Tab. E.4: Composition in REE of the samples from the col du Bonhomme area

3. Composition of the samples from the Val Ferret

3.1. Composition in major elements

List and composition of the samples

	SiO2	Al2O3	Fe2O3	MnO	MgO	CaO	Na2O	K2O	TiO2	P2O5	LOI	Total
MB21-2	64.58	18.71	2.96	0.083	0.92	0.44	7.79	2.38	0.44	0.16	1.25	99.71
MB21-3	73.48	13.43	2.26	0.055	0.52	0.44	3.73	4.34	0.22	< L.D.	1.68	100.14
MB21-5	77.08	11.51	1.22	< L.D.	0.28	0.16	3.60	3.99	0.047	< L.D.	1.11	98.99
MB21-14	66.47	15.02	2.91	0.038	1.23	1.65	1.17	7.93	0.37	< L.D.	2.53	99.31
MB21-17	73.56	8.91	3.93	0.065	1.55	2.77	0.47	3.47	0.55	< L.D.	4.07	99.35
MB21-21	63.98	16.49	4.37	0.11	2.09	1.74	3.60	3.85	0.53	0.11	3.55	100.41
MB21-22	60.40	16.91	7.29	0.12	3.31	1.18	2.78	3.91	0.89	< L.D.	3.39	100.20
MB21-36	66.78	15.36	5.33	0.16	2.12	1.57	4.20	2.00	0.66	0.13	2.12	100.42
MB21-37	76.72	11.79	1.07	0.019	0.18	0.44	3.24	4.73	0.10	< L.D.	0.91	99.21
MB21-38	60.49	16.49	7.42	0.15	2.98	1.83	2.77	4.37	0.90	0.15	2.80	100.34
MB21-39	58.42	16.65	8.12	0.18	3.52	2.02	3.45	4.35	1.02	0.27	1.82	99.82
MB21-40	73.05	13.77	2.05	0.043	0.51	1.17	3.65	4.35	0.18	< L.D.	0.91	99.68
MB21-45	55.17	15.22	6.96	0.19	3.27	3.29	2.49	5.04	0.85	0.63	6.07	99.18
MB21-46	47.83	20.02	10.14	0.086	3.20	2.32	0.38	8.87	0.63	< L.D.	5.76	99.23

Tab. E.5: Composition in major elements of the samples from the Val Ferret

3.2. Composition in trace elements

List and composition of the samples

	F	Be	Sc	V	Cr	Co	Ni	Cu	Zn	Ga	Ge	As	Rb	Sr	Y	Zr	Nb	Mo	Cd	In	Sn	Sb	Cs	Ba	Hf	Ta	W	Pb	Bi	Th	U
MB21-2	680	3.50	7.77	28.1	7.5	2.13	3.3	6.8	600	22.5	1.00	2.21	142	151	20.4	182	12.2	0.66	0.92	0.23	17.4	0.25	17.7	500	5.08	1.36	4.22	183	5.95	19.6	2.61
MB21-5	160	1.69	2.82	6.6	3.6	0.42	3.7	15.1	80.2	13.3	0.97	<L.D.	129	86.6	15.5	83.7	10.8	<L.D.	0.13	0.08	4.95	0.14	6.97	1079	3.19	1.41	1.14	20.1	0.55	15.4	2.64
MB21-14	477	2.05	7.69	49.4	37.5	8.56	17.3	10.6	89.0	15.1	1.48	17.3	318	45.4	10.3	66.0	6.96	<L.D.	1.02	0.17	6.26	0.51	5.92	1499	2.01	0.88	3.35	8.14	0.30	6.90	3.50
MB21-17	8230	2.17	14.31	106	67.0	8.07	29.9	18.4	61.7	20.0	3.15	6.72	181	26.4	61.5	93.0	6.05	3.20	0.13	0.10	1.99	0.77	16.8	873	2.65	0.40	6.86	17.1	0.12	5.14	2.10
MB21-21	925	3.22	10.26	81.1	51.4	6.37	20.8	8.1	78.3	22.4	1.17	2.83	159	139	25.2	126	11.5	0.68	0.25	0.17	17.1	0.51	9.17	810	3.73	1.02	3.18	33.5	0.10	13.4	3.55
MB21-22	975	3.24	19.33	139	93.4	16.8	39.1	31.6	280	25.6	1.21	6.20	187	240	11.3	289	10.1	0.76	0.87	0.07	4.16	1.02	15.3	793	8.03	0.72	2.94	40.7	0.10	4.58	1.51
MB21-36	425	1.45	15.04	88.1	58.2	11.3	23.6	18.3	201	19.1	1.14	0.73	71.1	283	23.4	159	7.13	<L.D.	0.42	0.10	6.79	0.24	6.76	659	4.52	0.56	<L.D.	39.5	0.10	4.72	1.45
MB21-37	208	5.14	6.11	3.7	4.5	0.70	2.2	5.3	12.1	17.6	1.86	0.79	303	31.6	66.7	92.0	33.6	<L.D.	<L.D.	<L.D.	3.45	0.18	4.12	102	4.04	4.22	3.21	39.5	<L.D.	35.6	9.97
MB21-38	2150	3.30	21.76	125	100	16.8	40.0	6.7	119	24.7	1.90	<L.D.	312	241	27.6	229	12.9	0.56	0.07	0.05	7.52	0.17	15.7	742	6.07	1.20	2.22	19.0	0.09	10.0	2.26
MB21-39	2790	2.76	20.79	139	110	21.2	58.2	10.4	142	23.8	1.70	<L.D.	330	204	37.5	227	14.2	0.58	0.08	0.06	6.53	0.15	17.6	803	6.17	1.20	3.08	62.6	0.06	13.2	3.28
MB21-40	485	2.57	4.15	8.6	6.3	1.68	3.2	4.4	31.7	16.5	1.47	<L.D.	147	145	21.0	146	11.3	<L.D.	0.05	<L.D.	2.10	0.17	3.01	773	4.50	1.38	0.95	16.2	<L.D.	14.9	4.13
MB21-45	2360	5.31	16.36	108	106	15.3	46.7	4.7	94.4	25.2	1.54	2.01	378	115	51.1	152	14.7	<L.D.	0.04	0.06	4.66	0.23	17.1	523	4.38	1.81	5.07	46.2	<L.D.	5.07	2.60
MB21-46	1140	10.3	36.75	64.8	318	11.9	41.0	4.4	165	28.0	4.50	4.36	327	22.7	27.4	32.7	1.58	<L.D.	0.06	0.35	14.0	0.93	35.0	812	1.10	0.38	23.2	5.87	0.34	0.75	3.15

List and composition of the samples

Tab. E.6: Composition in trace elements of the samples from the Val Ferret

3.3. Composition in Rare Earth Elements

	La	Ce	Pr	Nd	Sm	Eu	Gd	Tb	Dy	Ho	Er	Tm	Yb	Lu
MB21-2	27.2	53.1	5.23	18.2	3.46	0.663	3.00	0.509	3.38	0.745	2.20	0.355	2.36	0.367
MB21-3	22.4	48.6	4.24	15.0	2.89	0.601	2.46	0.422	2.65	0.561	1.65	0.275	1.91	0.310
MB21-5	29.4	57.0	5.66	19.2	3.66	0.480	2.97	0.462	2.79	0.580	1.62	0.264	1.83	0.279
MB21-14	32.4	64.7	7.13	25.5	4.97	1.43	3.28	0.429	2.21	0.421	1.20	0.197	1.39	0.222
MB21-17	272	538	62.8	237	44.7	8.94	33.9	3.80	15.7	2.19	4.10	0.438	2.54	0.380
MB21-21	36.6	71.3	7.71	27.6	5.45	1.52	4.64	0.736	4.60	0.957	2.60	0.393	2.42	0.337
MB21-22	22.2	46.0	5.20	19.4	3.62	1.17	2.63	0.360	2.08	0.455	1.43	0.257	1.99	0.350
MB21-36	21.2	43.7	5.19	20.4	4.21	0.868	3.79	0.625	4.05	0.871	2.49	0.397	2.64	0.410
MB21-37	18.0	41.6	5.06	19.1	5.73	0.181	6.48	1.40	10.2	2.34	6.99	1.18	8.03	1.21
MB21-38	33.5	67.9	7.23	27.8	5.58	1.32	4.94	0.778	4.85	1.02	2.84	0.438	2.89	0.439
MB21-39	44.3	89.3	10.1	38.7	7.79	1.51	6.91	1.10	6.82	1.39	3.75	0.553	3.52	0.517
MB21-40	31.3	62.7	5.98	21.4	4.23	0.703	3.57	0.593	3.64	0.757	2.14	0.347	2.31	0.354
MB21-45	30.3	67.1	6.40	26.6	6.93	0.943	7.53	1.41	9.03	1.88	4.89	0.716	4.28	0.630
MB21-46	16.4	33.2	3.24	13.1	3.84	1.33	4.69	0.855	5.33	1.02	2.57	0.374	2.20	0.297

Tab. E.7: Composition in REE of the samples from the Val Ferret

4. Uncertainty on the composition

	Uncertainty (%) according to the concentration							Limit of detection
	>100µg/ g	>50 µg/g	>10 µg/g	>1 µg/g	>0.5 µg/g	>0.1 µg/g	>0.01 µg/g	L.D. µg/g
ICP-MS iCapQ et ICP- OES iCap650 0 (Sc only)								
As		<5%	<15%	<20%		**		0.50
Ba		<5%	<15%	**				5.5
Be		<5%	<15%			<20%	**	0.05
Bi			<5%	<10%		<20%	**	0.045
Cd		<10%	<15%			<20%	**	0.02
Co		<5%	<10%	<20%		**		0.08
Cr			<5%	<10%		**		0.50
Cs			<5%	<15%		<20%	**	0.02
Cu		<8%	<20%	**				2.0

List and composition of the samples

Ga			<5%	<10%		<20%	**	0.02
Ge		<5%		<10%		<20%	**	0.04
Hf			<5%	<10%		<15%	**	0.03
In		<5%		<15%		<20%	**	0.03
Mo		<5%	<15%	<20%		**		0.50
Nb		<5%		<10%		<20%	**	0.015
Ni			<5%	**				2.0
Pb		<10%		<20%		**		0.45
Rb		<5%	<15%	<20%		**		0.15
Sb			<5%	<10%		<20%	**	0.06
Sc	<5%	<10%		<15%	**			0.6
Sn		<5%	<15%	<20%		**		0.30
Sr		<5%	<10%	<20%		**		0.70
Ta		<5%		<10%		<20%	**	0.004
Th		<5%		<10%		<20%	**	0.015
U		<5%	<10%	<15%		<20%	**	0.01
V		<5%	<10%	<15%		**		0.85
W		<5%	<10%	<20%		**		0.80
Y		<5%		<15%		<20%	**	0.02
Zn		<10%	<20%	**				7.0
Zr		<5%	<15%	**				1.50
La			<5%	<15%		<20%	**	0.02
Ce		<5%	<10%	<15%		<20%	**	0.03
Pr		<5%	<10%			<20%	**	0.004
Nd		<5%	<15%			<20%	**	0.016
Sm			<5%	<15%		<20%	**	0.005
Eu				<5%		<10%	**	0.002
Gd			<5%	<10%		<20%	**	0.005
Tb		<5%	<10%	<15%		<20%	**	0.001
Dy			<5%	<10%		<15%	**	0.004
Ho		<5%		<10%		<20%	**	0.001
Er				<5%		<10%	**	0.002
Tm		<5%		<10%		<20%	**	0.001
Yb		<5%	<10%	<15%		<20%	**	0.002
Lu			<5%	<10%		<20%	**	0.001

Tab. E.8: Uncertainty on the measure for trace elements and REE as provided by the SARM

ICP-OES iCap6500	>10 %	>5 %	>1 %	>0.5 %	>0.1 %	>0.05 %	>0.01 %	L.D. %
SiO2	<2%			<10%	<20%	**		0.05
Al2O3	<2%	<10%	<15%		<20%	**		0.04

List and composition of the samples

Fe₂O₃	<2%		<10%	<15%		<20%	**	0.015
MnO			<5%	<15%		<20%	**	0.015
MgO		<2%	<10%	<15%		<20%	**	0.03
CaO	<2%	<5%		<15%		<25%	**	0.03
Na₂O		<5%	<10%	<15%		<25%	**	0.02
K₂O		<5%	<10%	<20%		<25%	**	0.03
TiO₂		<5%	<10%	<20%		<25%	**	0.02
P₂O₅			<5%	<15%	**			0.10

Tab. E.9: Uncertainty on the measure for major elements as provided by the SARM

Appendix F Biostratigraphic data of the Helvetic domain

1. Ultrahelvetic domain (Lias des Mines)

Age	Ammonites	Brachiopod Lamellibranch	Belemnite	References
Hettangian	Schloteimia sp. (200-199Ma)	Ostrea sublamellosa Cardinia sp (252.3 to 2.588)		<i>Trumpy (1951)</i>
Upper Sinemurian	Arnioceras sp. (198-196Ma) Asterocheras (brooki) Avicula Sinemurensis (196.5 to 189.6 Ma) Asterocheras stellare (195Ma) Arnioceras sp. Echioceras sp. (Echioceras raricostatum 192Ma)	Brachiopodes: Spiriferina alpine (201.6 to 182.0 Ma) Terebratula punctata		<i>Trumpy (1951)</i> <i>Haas (1885)</i> <i>Renevier (1852)</i>
Pliensbachian	Androgynoceras Hybrida (189.6 to 183.0 Ma) Androgynoceras sp. Phylloceras sp. Lytoceras sp. Derolytoceras tortum (189.6 to 183.0 Ma)			<i>Trumpy (1951)</i> <i>Renevier (1852)</i>

Biostratigraphic data of the Helvetic domain

	<p>Amaltheus margaritatus (188-185Ma)</p> <p>Arieticerias algovianum (186-184Ma)</p> <p>Arieticerias bertrandi (189.6 to 183.0 Ma)</p> <p>Arieticerias ruthenense (185.7 to 184.1 Ma)</p> <p>Protogrammoceras fieldingii</p> <p>Protogrammoceras cf. exiguum</p> <p>Protogrammoceras isseli (183Ma)</p> <p>Hildoceratoides laviniaitus</p> <p>Paltopleuceras</p>			
Lower Toarcian	<p>Posidonomya (Steinmannia) bronni</p> <p>Harpoceratidés (183-180Ma)</p> <p>Dactylioceras sp. (184-183Ma)</p>	Lamellibranch		<i>Trumphy (1951)</i> <i>Renevier (1890)</i>
Middle Toarcian	<p>Coeloceras raquinianum (189.6 to 168.4 Ma)</p> <p>Crassiusculosum Aptychus</p> <p>Hildoceras bifron (180-178Ma)</p> <p>Hildoceras sublevisoni</p>			
Upper Toarcian	<p>Dumortieria striatulocostata</p>			

	(182.0 to 175.6 Ma)			
	Dumortieria cf. levesquei (174Ma)			
	Dumortieria costula (180.1 to 175.6 Ma)			

2. Helvetic domain

2.1. Morcles basin

2.1.1. SW Morcles nappe

Age	Ammonite	Brachiopod lamellibranch	Belemnite	References
Lower Hettangian	Caloceras Langei (201Ma)			<i>Barfety and Mouterde (1978)</i> <i>Parejas (1922)</i> <i>Epard (1989)</i>
Upper Hettangian	Schlotheimia angulata (200-199Ma) Wahneroceras sp Alsatites laqueus (201-200Ma)			<i>Eltchaninoff (1980)</i> <i>Dumas (1964)</i> <i>Landry (1976)</i> <i>Triboulet (1980)</i> <i>Epard (1989)</i> <i>Barfety and Mouterde (1978)</i>

Lower Sinemurian	<p>Coroniceras sp. (198-196Ma)</p> <p>Coroniceras cf. rotiforme</p> <p>Arietites cf. bucklandi (199-198Ma)</p> <p>Arnioceras semicostatum (198-196Ma)</p>			<p><i>Triboulet (1980)</i></p> <p><i>Paréjas (1922)</i></p> <p><i>Paréjas (1920)</i></p> <p><i>Epard (1989)</i></p>
Upper Sinemurian	Asteroceras sp. (Asteroceras obtusum 196-194Ma)			<i>Eltchaninoff (1980)</i>
Upper Toarcian Lower Aalenian	Pleydellia sp. (174Ma)			<p><i>Massaad (1973)</i></p> <p><i>Epard (1989)</i></p> <p><i>Badoux (1971)</i></p>
Aalenian	<p>Leioceras sp. (Leioceras opalinum 174-172 Ma)</p> <p>Ludwigia sp. (172-171Ma)</p> <p>Tmetoceras sp. (175.6 to 171.6 Ma)</p>			<p><i>Antal (1971)</i></p> <p><i>Favre (1867)</i></p> <p><i>Massaad (1973)</i></p> <p><i>Ritter (1897)</i></p> <p><i>Epard (1989)</i></p> <p><i>Paréjas (1925)</i></p>
Aalenian Bajocian	Graphoceras concavum (Graphoceras Concavum 170Ma)			<i>Ritter (1897)</i>

2.1.2. Arbignon

Age	Ammonite	Brachiopod	Other	References
-----	----------	------------	-------	------------

Biostratigraphic data of the Helvetic domain

		Lamellibranch		
Hettangian	Schlotheimia sp. (200-199Ma)			<i>Loup (1992)</i>
Sinemurian		Pecten sp.	Belemnites Siliceous sponges	<i>Loup (1992)</i>
Upper Sinemurian		Gryphaea sp (232.0 to 33.9 Ma)	Foramnières Benthiques: Lenticulina sp (235.0 to 0.012 Ma) Nodosaria sp (298.9 to 0.0 Ma) Involutina liasica	<i>Loup (1992)</i>

2.1.3. Catogne Mt.

Pliensbachian	Aegoceras maculatum Aegoceras sp. (186.7 to 185.7 Ma)	Terebratula sp. aff. Punctata Rhynchonella sp. Zeilleria numismalis Zeilleria cf. scalprata Zeilleria quadrifida (183.0 to 182.0 Ma)	Belemnites: Belemnites sp Microfaune: Textularia sp. (326.4 to 0.0 Ma) Nodosaria s. 1. sp	<i>Trümpy (1945) Loup (1992)</i>
----------------------	---	--	--	--

2.1.1. Ardève

Age	Ammonites	Brachiopod Lamellibranch	Belemnites	References
Upper Hettangian 201-199 Ma	Schlotheimia angulata (200-199Ma)			<i>Badoux (1971) Epard (1989)</i>
Upper Toarcian Aalenian	Pleydellia aalense (174Ma)			<i>Badoux (1971) Epard (1989)</i>
Aalenian	Ludwigia sp.,			<i>Antal (1971)</i>

	(172-171Ma)			<i>Epard (1989)</i>
	Harpoceratina sp.			

2.2. Mont-Blanc autochthonous cover

2.2.1. Col du Bonhomme

Age	Ammonite	Brachiopod Lammellibranch	Fish tooth	References
Rhetian			Acrodus Agassiz (298.9 to 55.8 Ma) Hybodus Agassiz (295.0 to 66.043 Ma) Polyacrodus jacket (279.5 to 70.6 Ma)	<i>Eltchaninoff (1980)</i>
Hettangian sinemurian	Scholteima sp. (200-199Ma) Arietites sp. (199-198Ma) Waechneroceras sp. (201-200Ma)	Gryphée remaniés dans GS Lima sp. (298.9 to 0.012 Ma) Plagiostoma aff. Valoniensis (221.5 to 201.6 Ma) Pinna sp. (345.0 to 0.012 Ma)		<i>Eltchaninoff (1980)</i>
Pliensbachian	Dated by surrounding formations			
Aalenian				
Age	Ammonites	Brachiopod Lamellibranch	Belemnites	References
Upper Hettangian 201-199 Ma	Schlotheimia angulate (200-199Ma)			<i>Grasmück (1961)</i>
Sinemurian	Entolium cf. hehli			<i>Grasmück (1961)</i>
Pliensbachian (possibly Sinemurian)		Pseudopecten aequalvis (189-182Ma)		<i>Grasmück (1961)</i>

2.2.2. Amône

Age	Ammonites	Brachiopod Lamellibranch	Other	References
Lower Aalenian	Ludwigia sp. Ludwigia murchisonae (172-171Ma)	Pseudomelania cf. Simplex Pecten Ostraea	Isastraea (coral)	<i>Grasmück (1961)</i>
Upper Aalenian	Ludwigia sp. Ludwigia murchisonae Ludwigella nodata	Terebratula sp		<i>Grasmück (1961)</i>
Bajocian- Bathonian		Chlamys cf lotharingica Chlamys cf meriani Lima (Plagiostoma) annoni (Bajocien-Bathonien) Lima (Plagiostoma) aff. Alticosta (Toarcien-Bajocien) Pholadomya cf. bellula (Aalenien- Bathonien) Alectryonia cf. costata (Bathonien)	Serpula sp. indet. (bryozoaire) Thamnasteria sp. indet. (coral) Montlivaltia sp. Indet (coral)	<i>Grasmück (1961)</i>

2.3. Aiguilles-Rouges cover

2.3.1. Vieux Emosson

Age	Ammonite	Brachiopods Lammellibranch	Other	References
-----	----------	-------------------------------	-------	------------

Ladinien-Carnien			Archosaurian footprint	<i>Demathieu and Weidmann (1982)</i>
-------------------------	--	--	------------------------	--------------------------------------

2.4. Aar cover

2.4.1. Federthorn

Age	Ammonites	Brachiopod Lamellibranch	Belemnites	References
Upper Hettangian 201-199 Ma	Schlotheimia extranodosa (Schlotheimia angulata 200-199Ma)			<i>Meister and Loup (1989)</i>
Lower Sinemurian	Charmesseiceras charmasseis Charmesseiceras sp. Metophioceras rotarium (196.5 to 189.6 Ma) Coroniceras lyra (196.5 to 183.0 Ma)			<i>Meister and Loup (1989)</i> <i>Lugeon (1905)</i> <i>Collet (1947)</i>
Upper Sinemurian	Leptochioceras sp. Echioceras raricostatum (193-191 Ma)			<i>Meister and Loup (1989)</i>
Pliensbachian	Tragophylloceras sp. (189.6 to 183.0 Ma) Platyleuroceras caprarium (189.6 to 183.0 Ma) Brevispina-brevispinoides (191 190 Ma) P. gr. Tenullobus-amplinatrix Eoderocerotidae gen. sp. Productyloceras davoei (189 188 Ma)	Zeilleria sp (242.0 to 109.0 Ma) Spiriferina sp (422.9 to 171.6 Ma) Spiriferina walcotti (196.5 to 189.6 Ma) Lamellibranche: Chlamys sp. (265.0 to 0.0 Ma) Pseudopecten sp (201.6 to 150.8 Ma) Gryphaea cymbium		<i>Meister and Loup (1989)</i> <i>Von Fellenberg (1893)</i> <i>Lugeon (1905)</i>

Biostratigraphic data of the Helvetic domain

	Derolytoceras tortum (189.6 to 183.0 Ma)	(189.6 to 183.0 Ma)		
	Oistoceras figulinum (190-189 Ma)	Liostrea sp. (235.0 to 37.2 Ma)		
		Plagiostoma sp. (295.0 to 61.7 Ma)		
		Pholadomya sp. (251.3 to 258.8 Ma)		
Upper Pliensbachian 190- 186Ma	Amalteus sp. (188-185Ma)			<i>Meister and Loup (1989)</i>
Toarcian - Aalenian	Harpoceras Pleydellia sp. (174Ma) Leioceras sp. (174-172 Ma)			<i>Lugeon (1905) Schlappi (1980)</i>

2.4.2. Lotschepass

Age	Ammonites	Brachiopod Lamellibranch	Belemnites	References
Upper Toarcian Aalenian	Ludwigia arcitenens (172-171Ma)			<i>Collet (1947/1989)</i>

Résumé:

Ce travail propose un aperçu de l'évolution tectono-stratigraphique et des circulations fluides associés à l'amincissement de la croûte (crustal necking) durant le rifting à parti de l'exemple d'une marge fossile préservée dans le massif du Mont-Blanc. L'élément clé pour comprendre l'évolution préalpine du Mont-Blanc est l'identification d'une faille de détachement jurassique préservée dans la partie sud du massif du Mont-Blanc. Une caractérisation détaillée de ce contact montre qu'il s'agit d'un socle déformé composé de cataclasites et gouges scellées par des sédiments syn-rift d'âge Sinémurien à Pliensbachien remaniant partiellement la faille. Ce détachement est associé à une réponse stratigraphique spécifique liée à la formation d'un haut topographique (Ile du Mont-Blanc) durant le Sinémurien supérieur. Ce haut topographique est responsable de la formation de dépôts gréseux d'âge Sinémurien et Pliensbachien autour du Mont-Blanc.

L'analyse géochimique et pétrologique des roches de failles dans le détachement montre une hydratation importante le long de la faille associée à l'altération des feldspaths et biotites à environ 250°C. L'utilisation d'une nouvelle méthode de calcul de bilan de masse basée sur la minimisation du transfert de masse montre que ces réactions minéralogiques sont responsables de gains en K, Fe, Ti, Mg, Ba, F, As, V et pertes en Si, Na, Ca, Pb, Zn dans les roches de failles. L'analyse des inclusions fluides dans les veines syn-cinématiques de la faille donne un fluide composé de H₂O-NaCl (-K₂O) avec une salinité de 7 to 9 wt% et une température d'homogénéisation de 200°C. Il s'agit de la première étude sur les circulations de fluides liées à l'amincissement crustal dans les massifs cristallins externes.

Un lien génétique entre les minéralisations préalpine à Pb-Zn-Ba-F dans le massif du Mont-Blanc et les circulations de fluides le long du détachement est proposé, ainsi que le premier modèle de circulation fluides durant la phase d'amincissement crustal (crustal necking).

Mots-clés : Massif du Mont-Blanc, Téthys alpine, amincissement crustal, Faille de détachement, Circulations de fluides

Abstract:

This work provides a new insight on the tectono-stratigraphic evolution and fluid circulation during crustal necking based on the study of a fossil necking domain preserved in the Mont-Blanc Massif (Western Alps). The key element to understand the pre-Alpine evolution of the Mont-Blanc is the recognition of a Jurassic detachment fault sealed by syn-rift sandstones was identified in the southern part of the massif. Detailed examination of this contact shows that it corresponds to a top tectonized basement formed by cataclasite and black gouge sealed by Upper Sinemurian to Pliensbachian sediments reworking the fault rock. This detachment faulting is associated to a specific stratigraphic response. Crustal necking is responsible for the formation of a topographic high (e.g., Mont-Blanc Island) during Upper Sinemurian leading to the formation of Sinemurian to Pliensbachian massive sandstones around the massif.

The petrological and geochemical analysis of the fault rocks indicates significant fluid circulations and basement hydration responsible for biotite and feldspars breakdown under temperature of ca. 250°C. Mass balance calculation using a new method of mass transfer minimization indicates a gain of K, Fe, Ti, Mg, Ba, F, As, V and loss in Si, Na, Ca, Pb, Zn in the fault rocks. The fluids inclusion studies show that the paleo fluids correspond to H₂O-NaCl (-K₂O) brines with a salinity of 7 to 9 wt% and a homogenization temperature up to 200°C. This provides the first observations of fluid circulations associated to crustal necking in the external crystalline massifs.

A genetic link between the pre-Alpine Pb-Zn-Ba-F ore deposits in the Mont-Blanc massif and the fluid circulations along the fault is proposed providing a first model for fluid circulations associated to crustal necking.

Keywords: Mont-Blanc massif, Alpine Tethys, Crustal necking, Detachment fault, Fluid circulation